Lecture Notes in Civil Engineering

Krishna R. Reddy
Susheel Kalia
Srinivas Tangellapalli
Divya Prakash *Editors*

Recent Advances in Sustainable Environment

Select Proceedings of RAiSE 2022

Springer

Lecture Notes in Civil Engineering

Volume 285

Series Editors

Marco di Prisco, Politecnico di Milano, Milano, Italy

Sheng-Hong Chen, School of Water Resources and Hydropower Engineering, Wuhan University, Wuhan, China

Ioannis Vayas, Institute of Steel Structures, National Technical University of Athens, Athens, Greece

Sanjay Kumar Shukla, School of Engineering, Edith Cowan University, Joondalup, WA, Australia

Anuj Sharma, Iowa State University, Ames, IA, USA

Nagesh Kumar, Department of Civil Engineering, Indian Institute of Science Bangalore, Bengaluru, Karnataka, India

Chien Ming Wang, School of Civil Engineering, The University of Queensland, Brisbane, QLD, Australia

Lecture Notes in Civil Engineering (LNCE) publishes the latest developments in Civil Engineering—quickly, informally and in top quality. Though original research reported in proceedings and post-proceedings represents the core of LNCE, edited volumes of exceptionally high quality and interest may also be considered for publication. Volumes published in LNCE embrace all aspects and subfields of, as well as new challenges in, Civil Engineering. Topics in the series include:

- Construction and Structural Mechanics
- Building Materials
- Concrete, Steel and Timber Structures
- Geotechnical Engineering
- Earthquake Engineering
- Coastal Engineering
- Ocean and Offshore Engineering; Ships and Floating Structures
- Hydraulics, Hydrology and Water Resources Engineering
- Environmental Engineering and Sustainability
- Structural Health and Monitoring
- Surveying and Geographical Information Systems
- Indoor Environments
- Transportation and Traffic
- Risk Analysis
- Safety and Security

To submit a proposal or request further information, please contact the appropriate Springer Editor:

– Pierpaolo Riva at pierpaolo.riva@springer.com (Europe and Americas);
– Swati Meherishi at swati.meherishi@springer.com (Asia—except China, Australia, and New Zealand);
– Wayne Hu at wayne.hu@springer.com (China).

All books in the series now indexed by Scopus and EI Compendex database!

Krishna R. Reddy · Susheel Kalia ·
Srinivas Tangellapalli · Divya Prakash
Editors

Recent Advances in Sustainable Environment

Select Proceedings of RAiSE 2022

Springer

Editors
Krishna R. Reddy
Department of Civil and Materials Engineering
University of Illinois
Chicago, IL, USA

Srinivas Tangellapalli
Department of Mechanical Engineering
Dr. B. R. Ambedkar National Institute of Technology
Jalandhar, India

Susheel Kalia
Army Cadet College Wing
Indian Military Academy
Dehradun, Uttarakhand, India

Divya Prakash
School of Environmental Sciences
Shobhit University Gangoh
Gangoh, India

ISSN 2366-2557 ISSN 2366-2565 (electronic)
Lecture Notes in Civil Engineering
ISBN 978-981-19-5076-6 ISBN 978-981-19-5077-3 (eBook)
https://doi.org/10.1007/978-981-19-5077-3

© The Editor(s) (if applicable) and The Author(s), under exclusive license to Springer Nature Singapore Pte Ltd. 2023
This work is subject to copyright. All rights are solely and exclusively licensed by the Publisher, whether the whole or part of the material is concerned, specifically the rights of translation, reprinting, reuse of illustrations, recitation, broadcasting, reproduction on microfilms or in any other physical way, and transmission or information storage and retrieval, electronic adaptation, computer software, or by similar or dissimilar methodology now known or hereafter developed.
The use of general descriptive names, registered names, trademarks, service marks, etc. in this publication does not imply, even in the absence of a specific statement, that such names are exempt from the relevant protective laws and regulations and therefore free for general use.
The publisher, the authors, and the editors are safe to assume that the advice and information in this book are believed to be true and accurate at the date of publication. Neither the publisher nor the authors or the editors give a warranty, expressed or implied, with respect to the material contained herein or for any errors or omissions that may have been made. The publisher remains neutral with regard to jurisdictional claims in published maps and institutional affiliations.

This Springer imprint is published by the registered company Springer Nature Singapore Pte Ltd.
The registered company address is: 152 Beach Road, #21-01/04 Gateway East, Singapore 189721, Singapore

Preface

RAiSE is one of the leading international conferences for presenting novel and fundamental advances in the fields of sustainable environment. It also serves to foster communication among researchers and practitioners working in a wide variety of scientific areas with a common interest in improving sustainable environment and related techniques.

The international conference is one of the leading international conferences dedicated to bringing together a significant number of diverse scholarly events for presentation within the conference program. Events will run over a span of time during the conference depending on the number and length of the presentations. With its high quality, it provides an exceptional value for students, academics, and industry researchers.

International Conference on Recent Advances in Sustainable Environment aims to bring together leading academic scientists, researchers, and research scholars to exchange and share their experiences and research results on all aspects of advances in sustainable ecological engineering and design. It also provides a premier interdisciplinary platform for researchers, practitioners, and educators to present and discuss the most recent innovations, trends, and concerns as well as practical challenges encountered and solutions adopted in the fields of advances in sustainable ecological engineering and design.

Theme of the Conference—RAiSE 2022.

Environmental Sustainability: Health Care, Soil Conservation and Water; Food and Environmental Legislation; Renewable Energies; Waste and Recycled Materials, Civil Infrastructure, and Environmental Geotechnologies.

Chicago, USA — Krishna R. Reddy
Dehradun, India — Susheel Kalia
Jalandhar, India — Srinivas Tangellapalli
Gangoh, India — Divya Prakash

Acknowledgement

It is our privilege and honor to welcome you all to the First International Conference on Recent Advances in Sustainable Environment (RAiSE 2022) jointly organized by Shobhit University Gangoh and Shobhit Institute of Engineering & Technology (Deemed to be University) Meerut, and in technical collaboration with Dr B.R. Ambedkar National Institute of Technology, Jalandhar, India, and supported by STEM Research Society during February 26–27, 2022.

It is our great pleasure to present the souvenir/book of abstracts with ISBN of the First International Conference on Recent Advances in Sustainable Environment (RAiSE 2022). We were honored to have Shri. Kunwar Shekhar Vijendra, Chancellor, Shobhit University, Prof. Krishna R. Reddy, Director, Sustainable Engineering Research Laboratory and Geotechnical & Geoenvironmental Engineering Laboratory, University of Illinois at Chicago, Guest of Honor, and Prof. Gaurav Manik, IIT Roorkee, as a special invitee on this special occasion.

We have received 121 research papers, and after review, 47 papers were accepted. These 47 papers were presented in different categories of 11 oral sessions, 1 poster session, and 6 invited talks. The theme of the RAiSE 2022 is "Environmental Sustainability," that covered health care, soil conservation and water; food and environmental legislation; renewable energies; waste and recycled materials, civil infrastructure, and environmental geotechnologies. Scientists, technologists, engineers, academicians, and researchers from national laboratories, research centers, academic institutions, and industries from different parts of India and abroad gathered on a common platform to interact with one another and shared their research activities in RAiSE-2015.

As the organizing team of the conference, we extend our gratitude to Prof. Ranjit Singh, Vice-Chancellor; Prof. Mahipal Singh, Registrar; Mr. Jasveer Singh, Accounts Manager, Shobhit University Gangoh, Saharanpur; Prof. G. K. Aseri, Provost, Dean—Academics, Director—AIMT; IQAC, Amity University Rajasthan, Jaipur, and Director—STEM Research Society; Dr. Srinivas Tangellapalli and Dr. Dwesh K. Singh from Dr. B. R. Ambedkar National Institute of Technology Jalandhar for their support. I would like to thank advisory committee, technical program committee, local organizing committee, potential reviewers, volunteers, and the staff members

of the Shobhit University, Gangoh, for their dedicated support. Special gratitude is paid here to Springer Nature Group for publishing the select proceedings of RAiSE 2022 in their Lecture Notes in Civil Engineering (LNCE) book series, indexed in EI Compendex, INSPEC, Norwegian Register for Scientific Journals and Series, SCImago, SCOPUS, and zbMATH. We would like to thank all the authors, volunteers, and persons who directly or indirectly contributed to the conference. Without their cooperation and full support, this conference would not have been possible.

We expect this conference will prove a memorable and productive discourse for all those who are a part of this event. I hope this event will motivate and profit everybody.

Divya Prakash
Om Prakash Verma
Tarun K. Sharma

Contents

About the Editors

Prof. Krishna R. Reddy is University Scholar, Distinguished Researcher, and Professor of Civil and Environmental Engineering, the Director of Sustainable Engineering Research Laboratory (SERL), and also the Director of the Geotechnical and Geoenvironmental Engineering Laboratory (GAGEL) in the Department of Civil, Materials, and Environmental Engineering at the University of Illinois at Chicago (UIC). Dr. Reddy received Ph.D. in Civil Engineering from the Illinois Institute of Technology, Chicago, USA. He received gold medals for being first in his class of B.S. (Civil Engineering) at Osmania University, India, and M.S. (Civil Engineering) at the Indian Institute of Technology (IIT) Roorkee. Prof. Reddy has over 28 years of research, teaching, and consulting experience within the broad fields of civil, geotechnical, materials, environmental, and sustainable/resilient engineering, addressing the nexus among sustainability, resiliency, infrastructure, water, energy, and the environment. His research expertise includes environmental remediation of soils, sediments, groundwater, and stormwater; solid and hazardous waste management, waste containment, and landfill engineering; characterization and engineering applications of waste/recycled materials; life cycle assessment and sustainable & resilient engineering; and geotechnical engineering. His research includes laboratory studies, field experiments, and computer modeling, ultimately leading to fundamental advances and practical solutions to the real-world problems.

Dr. Susheel Kalia is an Associate Professor & Head in the Department of Chemistry at Army Cadet College Wing of Indian Military Academy, Dehradun, India. He was a postdoctoral researcher in 2013 and a Visiting Professor at the University of Bologna, Italy, in 2020. Dr. Kalia has around 88 research articles in international journals along with 20 books, 11 book chapters and more than 7900 citations with 39 h-index in his academic career. He has guided several M.Phil. and Ph.D. students and delivered many invited talks at national and international conferences. His research interests include polymeric bio- and nanocomposites, surface modification, conducting polymers, nanofibers, nanoparticles, nanoferrites, hybrid materials and hydrogels. In addition, he is a member of a number of professional organizations, including the Asian Polymer Association, Indian Cryogenics Council, the Society

for Polymer Science, Indian Society of Analytical Scientists, and the International Association of Advanced Materials.

Dr. Srinivas Tangellapalli is an Associate Professor in the Department of Mechanical Engineering at Dr B. R. Ambedkar National Institute of Technology, Jalandhar, Punjab, India. He previously worked as a Professor at the CO_2 Research and Green Technologies Centre of the School of Mechanical Engineering at Vellore Institute of Technology, India. He received his Ph.D. from JNT University College of Engineering, Telangana in 2008 and was a Postdoctoral fellow at University of Ontario Institute of Technology (UOIT), Canada in 2010 and 2013. He has completed various research projects funded by CSIR, SERB, SERB (IMPRINT) and DST. He has one copyright to his credit and registered 5 patents. He has authored 4 full books, 12 book chapters, 125 journal publications, and 85 conference proceedings. His current areas of research are solar thermal energy and poly-generation. He has given 60 invited lectures and has supervised 5 Ph.D. students, 35 M.Tech. thesis and 40 undergraduate projects.

Dr. Divya Prakash obtained her Ph.D. in Industrial Environmental Engineering in 2007 from the Indian Institute of Technology (IIT) Roorkee, India. Since August 2019, she has been associated with Shobhit University, Saharanpur as a Professor & Dean—School of Biological Engineering and Sciences. Earlier she worked with Amity University Rajasthan as an Associate Professor & Head—Department of Chemistry. She has supervised 1 Ph.D., 4 in the submission process, 19 M.Sc. dissertations, and several undergraduate projects. She has over 41 research publications in international journals, chapters in edited books, and conferences of repute (SCI & SCOPUS). She has filed 5 patents. She has developed one application for the awareness of farmers. Her areas of interest are waste management, soil chemistry, water chemistry and environmental chemistry.

Landscape Degradation: The August 2019 Puthumala Landslide in Kerala, India

Nirmala Vasudevan, Kaushik Ramanathan, R. S. Parvathy, Aravind Ramesh, and Varun Joshy K

Abstract In recent times, landslides have been occurring with greater frequency and impact in the Western Ghats mountain ranges of India. The Western Ghats of Kerala State in particular have been witnessing several fatal and devastating landslides, especially during the annual monsoons. While heavy rainfall has triggered many of these slides, human intervention is also responsible for creating and reactivating landslides in the region, whether through deforestation, improper land use practices, slope modification, mining, or improper drainage. Thus, both natural causes and anthropogenic activity, individually or in combination, are responsible for creating conducive conditions for the occurrence of landslides. In this paper, we present the results of preliminary field investigations at the Puthumala landslide site in Wayanad District, Kerala. The slide occurred on August 8, 2019, killing 17 people and leading to an entire village being abandoned, making it one of the most catastrophic landslides in Kerala.

Keywords Landslide · Puthumala · Wayanad · Western Ghats · Kerala · India

1 Introduction

The Western Ghats are an approximately 1,600-km long mountain range stretching along the western coast of India and traversing the states of Gujarat, Maharashtra, Goa, Karnataka, Kerala, and Tamil Nadu. In recent times, the Western Ghats of Kerala

N. Vasudevan (✉)
Amrita Center for Wireless Networks & Applications, Amrita School of Engineering, Amrita Vishwa Vidyapeetham, Amritapuri, India
e-mail: nirmalav@am.amrita.edu

N. Vasudevan · R. S. Parvathy · A. Ramesh · V. Joshy K
Department of Physics, Amrita School of Arts & Sciences, Amrita Vishwa Vidyapeetham, Amritapuri, India

K. Ramanathan
Department of Civil Engineering, Amrita School of Engineering, Amrita Vishwa Vidyapeetham, Coimbatore, India
e-mail: rkaushik@am.amrita.edu

© The Author(s), under exclusive license to Springer Nature Singapore Pte Ltd. 2023

K. R. Reddy et al. (eds.), *Recent Advances in Sustainable Environment*, Lecture Notes in Civil Engineering 285, https://doi.org/10.1007/978-981-19-5077-3_1

have been witnessing frequent and devastating landslides. Since 2018, there have been at least one or two fatal landslides each year [1, 2], with some of them resulting in entire villages becoming uninhabitable [3, 4]. While each of these landslides is unique, they are not always isolated events, and a study of an individual landslide may give insights into the overall problem of mass wasting in the region. With this perspective, we initiated studies on one of the largest and most destructive landslides of the Kerala Western Ghats: the 2019 Puthumala landslide.

Puthumala locality and the adjoining Pachakkad Hill are situated in Meppadi, Wayanad District (Fig. 1).[1] Until recently, the hill slopes were covered primarily by forests and tea plantations. There were a few human settlements at both Pachakkad and Puthumala (possibly around 200 people [5]).

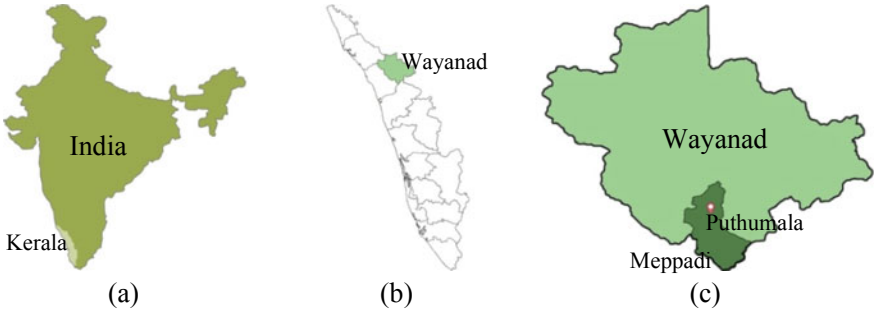

Fig. 1 **a** Kerala State, India, **b** Wayanad District, Kerala, **c** Puthumala landslide, Meppadi Grama Panchayat, Wayanad.[2]

Torrential rains triggered quite a few landslides at Puthumala and Pachakkad on August 7–8, 2019. There was over 500 mm of rain on August 8 as per a rain gauge installed near Puthumala by the Irrigation Department [5]. At around 4:20 pm, a landslide started in the Pachakkad forest. The slide became massive, covering an area of more than 2×10^5 m^2 and extending over a distance of around 2 km. Seventeen lives were lost, but only twelve bodies were recovered [6, 7]. The entire area became uninhabitable and survivors were relocated to a nearby village.

We visited Puthumala and Pachakkad on September 4, 2019. In this paper, we present the results of our site investigations, propose a plausible failure mechanism, and discuss possible causes of the slide. Though the village is not inhabited anymore,

[1] Puthumala lies in Vellarimala Village in Meppadi Grama Panchayat. Meppadi, in turn, lies in Kalpetta Block, which is situated in Vythiri Taluk, Wayanad District. A grama panchayat (also called panchayat) is an administrative unit comprising either a large village or a cluster of smaller villages; block and taluk are successively higher administrative (and geographical) units. The locations Pachakkad, Puthumala, Vellarimala, Meppadi, Kalpetta, and Vythiri are all used to refer to the Puthumala landslide.

[2] The maps are for illustrative purposes only and do not express any opinion of the Publisher or Authors regarding the legal status of any country, area, or territory, or of its authorities, or concerning the delimitation of any border. The depiction and use of boundaries, geographic names, and related data shown in this paper are not warranted to be error-free.

there is a lot of loose, unconsolidated material that may be mobilized to cause more landslides during future extreme weather events. In light of this, we also suggest a few simple remedial measures which would help improve slope stability.

2 Geology, Geomorphology, and Climate at the Landslide Site

Meppadi Panchayat consists of denudational structural hills and piedmont zones[3] [10] (Fig. 2). The rocks in Meppadi belong to the Charnockite Group and the Peninsular Gneissic Complex, both of the Archean Eon. The Charnockite Group comprises charnockite, with narrow bands of pyroxene granulite and magnetite quartzite; the Peninsular Gneissic Complex comprises hornblende biotite gneiss and pink granite gneiss [10]. Variably weathered hornblende biotite gneisses were observed in rock outcrops on Pachakkad Hill. The soil thickness was estimated to be 1.5–2 m at a few locations.

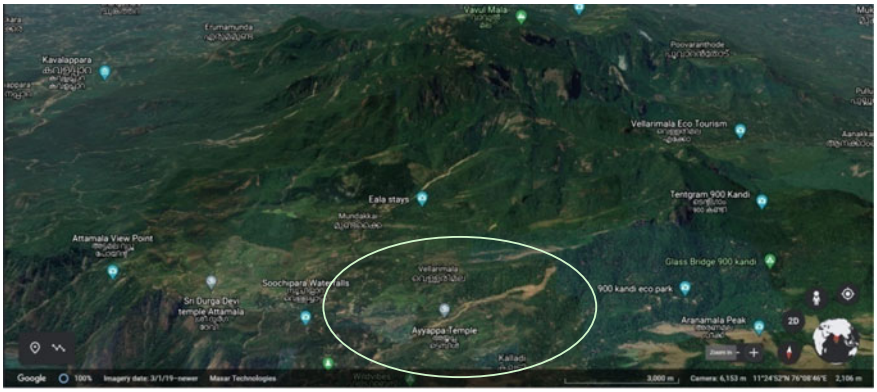

Fig. 2 Google Earth [11] image of Vellarimala Village in Meppadi Panchayat, and its surroundings (imagery date: after March 1, 2019); the main Puthumala landslide is circled

The main landslide initiated at an elevation of 1,230 m above mean sea level, approximately 110 m below the peak of the slope (Fig. 3). The slide occurred along the course of a higher-order stream (called *thodu* in the native language, Malayalam) that drained into the Kalladi River at the base of the hill (Fig. 3); the Kalladi River,

[3] A structural hill is one whose form is governed by the underlying geological structure and distribution of rocks. For instance, outcrops of rocks with lesser resistance to erosion or fractures (faults, joints, etc.) may be preferentially weathered and eroded, leaving behind a feature whose form is directly controlled by the geological structure of the region [8, 9]. Denudation refers to weathering, erosion, and other mass wasting related slope processes. A denudational structural hill is a structural hill subsequently subjected to denudation. A piedmont zone is the region at the foot (pied) of a mountain range (mont).

in turn, is a tributary of the Chaliyar, one of the major rivers in Kerala. The stream (Pachakkad-Puthumala thodu) was flooded due to extreme rains and destroyed houses close to its banks (Figs. 3 and 4). Smaller landslides occurred on the hill along the courses of lower-order tributaries of the stream [12].

Puthumala receives about 3,000 mm of annual rainfall, of which over 2,000 mm falls during the main monsoon season from June to September. During this period, moisture-laden winds from the southwest are intercepted by the Western Ghats, causing orographic rainfall over the windward slopes in the region. This season is closely followed by the northeast monsoon season from October to December, accounting for over 300 mm of rainfall. There is very little rainfall during January and February, while some pre-monsoon showers occur during the summer months from March to May [13, 14].

Fig. 3 Google Earth image of the Puthumala landslide site (imagery date: after February 23, 2021): the slide occurred along the course of a stream (Pachakkad-Puthumala thodu) that eventually drained into the Kalladi River flowing north of Puthumala Hill; the flood plain of the stream is circled

Fig. 4 Stream originating in the hill was flooded due to extreme rainfall and damaged property along its path. The hill and crown of the slide (circled) can be seen in the photo on the left

3 Rainfall Before and During the Landslide

In 2019, there was lesser rainfall than normal in Wayanad during the months of June and July (Table 1).

There was torrential downpour at Puthumala from August 4–8 (conversations with locals). There was over 500 mm of rain on August 8 as per a rain gauge installed near Puthumala by the Irrigation Department [5]. Figure 5 presents the India Meteorological Department (IMD) rainfall data (in mm) for the period April 1–August 31, 2019, from Vythiri, the nearest rain gauge station, located about 12.3 km away from the main Puthumala landslide (11°29′51″ N, 76°7′45″ E). Rainfall data available from other IMD rain gauge stations in Wayanad (Ambalavayal, Kuppady, and Mananthavady, located approximately 15.6 km, 25.4 km, and 35.5 km, respectively, from Puthumala) show a similar rainfall trend.

Table 1 2019 Wayanad District rainfall

	Jan	Feb	Mar	Apr	May	Jun	Jul	Aug 1–7
Actual rainfall (mm)	0	14.5	12.7	156.1	100.5	249.3	527.6	252.3
Normal rainfall (mm)	4.9	6.7	20.2	84.4	170.3	673.8	1055.2	184.5
Departure from normal (%)	−100	116	−37	85	−41	−63	−50	37

Source India Meteorological Department, IMD [15]

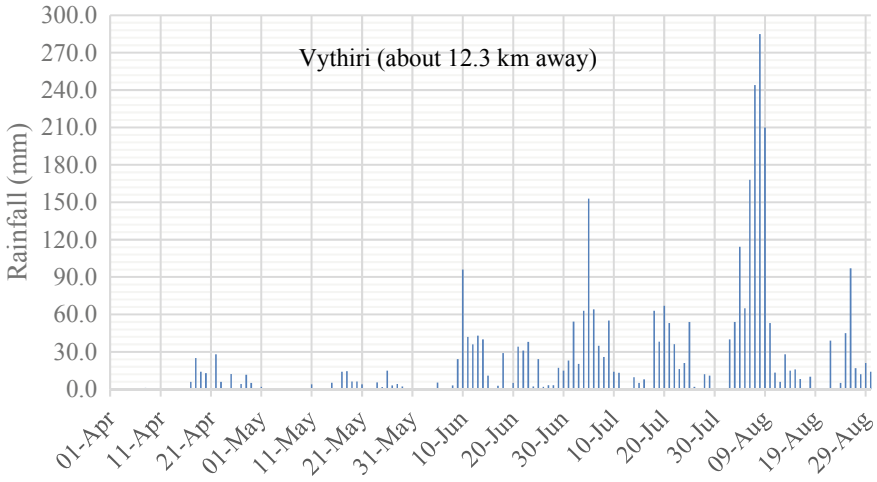

Fig. 5 Rainfall data from Vythiri (11°33′0″ N, 76°1′48″ E): The rainfall was 244 mm and 285 mm on August 7 and 8, respectively

4 August 2019 Landslides at Puthumala

The downpours triggered a number of minor landslides and one main landslide.

4.1 Minor Puthumala Landslides on August 7–8, 2019

A slide occurred at around 11 pm on August 7, 2019, in the vicinity of a house on the higher slopes of Pachakkad Hill. Rock was first dislodged and came crashing down. The residents rushed out and less than five minutes later, a mass of saturated overburden failed, destroying the house (Fig. 6). The debris traveled a few hundred meters downslope. A 5-m wide, slightly curved slope of weathered hornblende biotite gneiss lay exposed after the slide. Fearing more landslides, most Pachakkad and Puthumala residents shifted to relief camps.

Fig. 6 House completely destroyed by a minor landslide on August 7, 2019

At around 3:30 pm on August 8, another minor slide (most likely a shallow planar debris slide) occurred along Pachakkad Road (Fig. 7), a few hundred meters downslope of the slide mentioned above. The slide brought down some boulders, and three houses were damaged by the debris (Fig. 7); since the residents had moved to relief camps, no one was hurt.[4]

Apart from these two slides, there were other minor slides on the hill (Fig. 8), with at least some of them occurring along the overburden-rock interface. Also, the water level in the Pachakkad-Puthumala thodu started rising on account of both the rain and debris feeding it; eventually, the stream was flooded.

[4] Two residents returned to inspect the damage to the houses and unfortunately lost their lives in the main Puthumala landslide.

Fig. 7 House damaged by a minor landslide on August 8, 2019

Fig. 8 Two more minor slides that occurred on August 7–8; one of the authors (circled) climbing a slide. Some of the slides occurred along the tributaries of the Pachakkad-Puthumala thodu [12]

4.2 The Main Puthumala Landslide on August 8, 2019

At around 4:20 pm on August 8, a slide initiated on Pachakkad Hill at approximately 11°29′51″ N, 76°7′45″ E, 1,230 m above mean sea level. The slide was accompanied by an exceptionally loud sound, and very soon, it developed into a massive debris flow with soil and trees sent rocketing into the air [7]. The flow was extremely rapid and within seconds, a huge portion of the ground, trees, and gravel came down followed by an enormous gush of water which swept away the village. Over 50 houses, a post office, a canteen, a playground, a mosque, and a temple got buried under the debris [6, 7].

5 Landslide Mechanism

Google Earth slope profiles of the landslide site before and after the incident revealed that the main slide was shallow and began on a not-so-steep slope. Moreover, the material traveled quite a distance downslope (Fig. 3).

From our interactions with the locals, we learnt that there was heavy to extremely heavy rainfall in Puthumala in the days preceding the main landslide on August 8 and also on that day. This is further validated by the rainfall data presented in Sect. 3. A rain gauge, maintained by the Irrigation Department and situated near the slide location, recorded a rainfall of over 500 mm on the day of the slide [5]. The rains triggered floods which destroyed a few bridges. The rains would have caused an increase in pore pressure since they continued to batter the slope, giving little time for the excess pore pressures to dissipate.

There had been a few smaller slides before the main slide, and the waters had a dark brown tinge due to the floods carrying a significant quantity of debris from the slope. The slope would have been saturated on account of the antecedent rainfall conditions and was further disturbed by the landslide debris from upslope. The accounts of locals indicated that the floods and slide moved very quickly.

The gentle slope, long runout, and rapid floods and landslide indicated a shallow debris flow plausibly caused by progressive undrained loading of the slope materials, given that the slope gradient was minimal a short distance after the point of initiation.

6 Discussion

In recent years, Kerala has borne the brunt of climate change. Since 2018, episodes of extreme rainfall each year have led to fatal landslides in the hilly regions of the state. The southwest monsoon, the main season during which most of India receives heavy rainfall, has become unpredictable. Earlier, rains would begin in Kerala around June 1, but they are getting increasingly delayed. The months of June and July used

to witness the heaviest showers, but nowadays there is lesser rain in these months, while there are heavy showers in the months of August, September, and sometimes even in October, as witnessed in 2021. Another worrisome trend is the number of extreme rainfall events, especially since 2018. This has often given rise to both flash floods and floods, further increasing the likelihood of landslides.

Anthropogenic activity has been a very significant driving factor in worsening slope instability in Kerala. Improper land use practices including deforestation for plantations, settlements, and agriculture; over exploitation of groundwater resources; improper drainage practices; ill-planned construction and urbanization; and illegal quarrying and mining have made the state vulnerable to multiple hazards like floods and landslides, especially in the hilly regions. In the face of these continuing activities, we must consider the effects of the various causative and triggering factors of landslides, and not rely solely on rainfall thresholds (which are computed without cognizance of these activities).

At Puthumala, intense rainfall in a short span of time was both the trigger as well as one of the main causes of the landslides. The rainfall led to supersaturation of the soil overburden and increased pore water pressure; the rains also caused the flooding of the small streams (the Pachakkad-Puthumala thodu and its lower-order tributaries) that cut into the slopes. Further, there were several rainfall-triggered minor slides before the main Puthumala slide; these smaller slides may have caused a sudden redistribution of load, which could have subsequently contributed to the main slide.

Google Earth images indicated that there has been loss of green cover in recent years. Deforestation destabilizes the topsoil, making it more prone to erosion and mass wasting. Also, such activity eases the infiltration of water and promotes the washing away of soil particles, further exposing underlying slope material to weathering and erosion. Additionally, the locals had built their homes on natural drainage paths, obstructing the free flow of water. Such activities exacerbate the problem of slope instability.

Other human activity which was detrimental to slope stability included unplanned quarrying. We were informed that a Pachakkad resident lived near an abandoned granite quarry, and when it was operational, his home would often be hit by small rock pieces from the site. This indicates that the quarrying was neither regulated nor in conformity with standard practices, having severe adverse impact on slope stability and the environment as a whole.

The government has declared the entire village unfit for habitation [16] and all the survivors have been relocated. To ensure that Puthumala is safe from future landslides, it would be beneficial to demolish all structures obstructing natural drainage. It would also help to afforest with endemic vegetation. These simple measures would go a long way in preventing further deterioration of slope stability. Based on detailed site investigations, other remedial measures, if required, may be suggested.

7 Conclusion

Since 2018, successive years of heavy rains in Kerala have triggered landslides in the hilly tracts of the state. The causes of many of these landslides are fairly similar: a combination of human activity and natural processes weakens the slope over time, making it ready to fail. The final trigger—rainfall—then washes away the loose unconsolidated slope material, causing debris slides and flows. Many regions previously considered stable are now facing the threat of landslides.

Thorough site investigation is critical to identifying weak zones and possible landslide locations. As such, certain landslides recur during heavy rains. Identifying such landslides and understanding their causes and mechanisms would go a long way in remediating them and reducing landslide risk. With landslide occurrences increasing all over the country, such activity is the need of the hour.

Acknowledgments We are extremely grateful to the Chancellor of our university, Dr. Sri Mata Amritanandamayi Devi, Amma, for enabling this study. We thank Dr. Maneesha V. Ramesh, Dr. Sudesh K. Wadhawan, Mr. Balmukund Singh, Mr. Ansu, and Mr. Sudarshan Navada for their help and support during our visit and Dr. Sudesh K. Wadhawan for technical discussions. We sincerely thank the residents of Puthumala and surrounding areas for sharing their experiences and pertinent details with us. We are especially grateful to Mr. Prasad and his family, who helped with our accommodation. The former accompanied us on the visit and shared important details of the event. Mr. Ranjith N. Sasidharan prepared Fig. 1—we thank him for his help. Finally, we thank the two anonymous reviewers who helped improve the paper.

References

1. Jain N, Martha TR, Khanna K, Roy P, Kumar KV (2021) Major landslides in Kerala, India, during 2018–2020 period: an analysis using rainfall data and debris flow model. Landslides 18(11):3629–3645
2. Vasudevan N, Ramanathan K, Syali TS (2022) Land degradation in the Western Ghats: the case of the Kavalappara landslide in Kerala, India. In: Ashish DK, de Brito J (eds) F-EIR conference 2021, Lecture notes in civil engineering, vol 232. Springer, Cham, pp 199–207
3. Manoj AK, Sreekumar S (2017) Assessment of debris flow disaster in a reserve forest area, Kerala. Int J Appl Adv Sci Res 2(2):315–322
4. Sarun S, Vineetha P, Rajesh R, Sheela AM, Anil Kumar R (2021) Post landslide investigation of shallow landslide: a case study from the Southern Western Ghats, India. Disast Adv 14(7):52–59
5. Kerala rains: 4 bodies recovered from landslip debris in Wayanad district. The Hindu, August 9, 2019, https://www.thehindu.com/news/national/kerala/kerala-rains-4-bodies-recovered-from-landslip-debris-in-wayanad-district/article28923695.ece. Last accessed 11 Feb 2022
6. Anandan S (2019) As Malabar faces deadly landslides, debate shifts to ecologically sensitive areas and human intervention. The Hindu, August 24, 2019. https://www.thehindu.com/news/national/kerala/the-deadly-landslides-of-malabar/article29235741.ece. Last accessed 11 Feb 2022
7. Puthumala Tragedy (2020) A year after Kerala village was wiped out, residents still in distress. The New Indian Express, August 8, 2020. https://www.newindianexpress.com/states/kerala/2020/aug/08/puthumala-tragedy-a-year-after-kerala-village-was-wiped-out-residents-still-in-distress-2180841.html. Last accessed 11 Feb 2022

8. Gutiérrez F, Gutiérrez M (2016) Landforms of the earth: an illustrated guide. Springer, Switzerland
9. Twidale CR (1971) Structural landforms: landforms associated with granitic rocks, faults and folded strata. Australian National University Press, Canberra
10. Kerala State Land Use Board (2022) Natural resources data bank for Wayanad District, pp 33–35. https://kslub.kerala.gov.in/images/pdf/natural_resources/11Wayanad.compressed.pdf. Last accessed 11 Feb 2022
11. Google Earth, earth.google.com/web/
12. Wadhawan SK, Singh B, Ramesh MV (2020) Causative factors of landslides 2019: case study in Malappuram and Wayanad districts of Kerala, India. Landslides 17(11):2689–2697
13. Ramesh MV, Vasudevan N (2012) The deployment of deep-earth sensor probes for landslide detection. Landslides 9(4):457–474
14. Madhu V, Namboodiri GA, Vijay G (2021) An analytical study of rainfall characteristics over Wayanad District of Kerala. Turk J Comput Math Educ 12(13):1971–1979
15. India Meteorological Department (IMD)
16. Rajeev KR (2020) Scars of landslide tragedy still afresh at Kerala's Puthumala. The Times of India, 8 Aug 2020. https://timesofindia.indiatimes.com/city/kozhikode/scars-of-landslide-tragedy-still-afresh-at-keralasputhumala/articleshow/77427438.cms. Last accessed 11 Feb 2022

Understanding the Role of Biological Oxygen Demand in Aquaculture Waters in the Western Delta Region of Andhra Pradesh

T. V. Nagaraju, B. M. Sunil, and Babloo Chaudhary

Abstract The aquaculture industry with intensive farming activities has been gaining potential benefits to the nation's economic growth and food security. However, due to intensive farming, harmful pollutants are emerging with a higher concentration of biological oxygen demand (BOD), chemical oxygen demand (COD), and ammonia nitrates are more concerns. This study presents the role and assessment of BOD for the aquaculture ponds in the western delta region of Andhra Pradesh. The collected water samples at various locations in the study area have been tested for physicochemical characteristics and the test data used for BOD prediction. For evaluating the sensitivity of the prediction model, particle swarm optimization (PSO) with variations of inertia weight and damping factors is used to obtain the best global solution. As a result, prediction models developed for assessing BOD using PSO show convergent predictions. So, based on the prediction results, the implementation of prediction models of BOD using PSO could be helpful for sustainable aquaculture management in the western delta region of Andhra Pradesh.

Keywords Aquaculture · Biological oxygen demand · Soft computing · Sustainable environment

1 Introduction

Monitoring the water quality and quantity is very important to understand and assess the water resources and management. Further, water quality assessment could be helpful to human health and a sustainable environment. In general, the aquaculture industry allows large-scale production of fish and shrimp. However, due to intensive farming and high production of fish, it may generate a high amount of aquaculture waste such as fish or shrimp shells, unconsumed feed, disinfectants, chemicals, and minerals, which contributes negative impact on the environment [1]. The treatment of aquaculture waste is one of the challenging tasks in the aquaculture industry.

T. V. Nagaraju (✉) · B. M. Sunil · B. Chaudhary
Department of Civil Engineering, National Institute of Technology Karnataka, Mangaluru, Karnataka, India
e-mail: varshith.varma@gmail.com

© The Author(s), under exclusive license to Springer Nature Singapore Pte Ltd. 2023

K. R. Reddy et al. (eds.), *Recent Advances in Sustainable Environment*, Lecture Notes in Civil Engineering 285, https://doi.org/10.1007/978-981-19-5077-3_2

Conventionally, the aquaculture contaminated water pumped out from the ponds and merges into the nearby canals and lakes. The aquaculture contaminants with a high COD, BOD, and ammonia nitrates may pollute surface water and groundwater [2]. This practice with long-term farming results in hazardous to the groundwater environment. In general, physicochemical parameters of aquaculture water, BOD play a vital role in aquaculture practices because of organic waste (excess feed, shrimp effluents, and manure from poultry) generated from aquaculture ponds [3]. Water quality parameters such as pH, EC, salinity, TDS, and temperature can be measured adequately in the field with the help of digital tools [4]. In the case of BOD determination, it takes a time of 5 days in the laboratory. In this context, many researchers have focused on the regression models for the prediction of BOD. Classical regression analysis using statistical data is the traditional way to develop correlations between two or more parameters [5]. Estimating or predicting the dependent parameters such as BOD and COD, multi-linear regression models could be helpful to understand and identify the water quality parameters variation. Multi-variable prediction models for estimating water quality parameters at Tigris River, Iraq found successful results [6]. Apart from multi-variable regression models, using the regression tree, induction method is also helpful to predict BOD, COD, and ammonia concentrations. Moreover, the biological state of water bodies could be affected by seasonal variations and temperatures, so it would be more complicated to predict the problems associated with water quality [7].

In recent years, the research trend shifts toward the potential application of soft computing tools for predicting water quality parameters due to the rational and systematic approaches. Abyaneh (2014) reported that water quality parameters can be predicted using multi-linear regression (MLR) and artificial neural networks (ANNs). By comparison, MLR and ANN models, for predicting the BOD and the COD, ANN prediction models were better convergent than the MLR prediction models [8]. Tomic et al. (2016) reported that assessment of BOD in the Danube River, Serbia, using general regression neural networks (GRNNs) is found convergent results with fewer datasets for training and validation. Moreover, even it could be helpful for real-time prediction of BOD values in the Danube River, Serbia [9]. Other hand, at the sewage treatment plant, effluents rate can be predicted using an advanced PSO-RRBF neural network model, which gives more efficient findings due to the compact structure of the model. PSO-RRBF model for predicting BOD is simple, reliable, and rational to develop correlations between BOD and dependent variables [10]. PSO-ANN-based models are best suitable to predict the heavy metals concentration in the Toyserkan Plain, Hamedan Province [11]. In PSO-ANN-based models, the ANN-based model can enhance by the training data with PSO algorithm to achieve better performance and convergence [11]. Nowadays, soft computing approaches are emerging in the field of environmental engineering to assess groundwater quality, heavy contaminants rate, groundwater management, and effluents discharge.

Therefore, the purpose of this paper is to assess the biological oxygen demand (BOD) values in the aquaculture ponds in the western delta region of Andhra Pradesh. BOD is a significant parameter in aquaculture waterbodies due to the high-biological activity (effluents, feed load, and organic matter).

2 Experimental Investigation

In this study, primarily, experimental investigation is carried out to determine the physicochemical characteristics of the aquaculture water samples in the western delta region of Andhra Pradesh. Physicochemical characteristics such as pH, TDS, EC, salinity, total ammonia, PO_4, SO_4, DO, and temperature are helpful for the productive nature of the aquaculture pond. Aquaculture is major activity in the study area, and many aquaculture water quality laboratories were emerged in the recent years to monitor the water quality in the aquaculture ponds. Moreover, biological activity is major concern due to the intensive farming in terms of excessive usage of chemicals, minerals, and feed. So, it was much needed to have continuous assessment of aquaculture pond water for better management.

Table 1 shows the experimental values obtained during the investigation. Further, to assess future predictions, aforementioned parameters were used as input variables to predict 5 day BOD using PSO.

PSO is a simple learning metaheuristic algorithm based on the data learning approach, which has rational and systematic structure inspired by the nature or behavior of the fish group. For testing and training any data, sensitive variables play a vital role in a random search. In PSO, for a random search of particles position or iterations for finding a global solution, there is no need for any evolutionary operators. PSO is gaining potential in all disciplines including civil engineering, medical, and electrical engineering [12–14].

In general, predicting any variable, PSO algorithm involves the following steps: (i) choosing input variables, (ii) generating initial swarm, (iii) individual particle analysis for best fitness, (iv) listing out best fitness of all swarms, (v) finding the best global swarm, (vi) velocity, (vii) position of the swarms to be updated, and (viii) generate the best value. For developing prediction models on 5 day biological oxygen demand (BOD), the data information of pH (X1), TDS (X2), EC (X3), salinity (X4), total ammonia (X5), PO4 (X6), SO4 (X7), DO (X8), and temperature (X9) was considered as input variables. For this BOD prediction model, a linear equation was

Table 1 Physicochemical characteristics of western delta region

Property	Range
pH	8.4
Temperature (°C)	27
Dissolved oxygen, DO (ppm)	5.5
Electrical conductivity, EC (µs/cm)	3200
Total dissolved solids, TDS (ppm)	1850
Salinity (ppt)	6
NH3 (ppm)	3.15
PO4 (ppm)	0.25
SO4 (ppm)	0.3

developed, which consists of each parameter was multiplied by random coefficients (c1, c2, c3, c4, c5, c6, c7, c8, and c9) to find a global solution.

$$BOD_{(est)} = c_1.X1 + c_2.X2 + c_3.X3 + c_4.X4 + c_5.X5 + c_6.X6 + c_7.X7 + c_8X8 + c_9X9 \quad (1)$$

For evaluation of the overall test data, BOD is predicted, and error of the data was calculated using the below formula.

$$\mathrm{E(k)} = \sum_{\mathrm{i=1}}^{\mathrm{N}} \left(\mathrm{BOD_{(act)}(i,k)} - \mathrm{BOD(i,k)}\right)^2 \quad (2)$$

where k and i represent the number of iterations and total number of test data, respectively. The objective function of the given problem is represented by Eq. (3)

$$J = \min(E) \quad (3)$$

3 Results and Discussion

3.1 Effect of Inertia Weight on BOD Prediction

For predicting BOD, input variables such as pH (X1), TDS (X2), EC (X3), salinity (X4), total ammonia (X5), PO_4 (X6), SO_4 (X7), DO (X8), and temperature (X9) were considered. Moreover, inertia weight 0.5 is chosen for BOD estimation. The following equation was generated after the update of velocity and position of particles.

$$BOD_{(est)} = 0.889.X1 - 0.048.\mathrm{X2} + 0.028.\mathrm{X3} - 0.02.\mathrm{X4} + 0.003.\mathrm{X5} - 1.657.X6 - 12.241.X7 + 1.640.X8 + 0.009.X9 \quad (4)$$

Table 2 shows the effect of inertia weights on the global solution, and the BOD estimation models are determined by using PSO. The best global solution was found with the inertia weight of 0.5. This can be due to the best fitness of the swarm to generate efficient location of particle.

By comparison, Figs. 1 and 2 show the actual data and predicted data. The predicted results of the BOD values with the inertia weight 0.8 exhibit a larger deviation of estimated data (400% error) compared with the actual data. This could be due to the poor velocity and location of the particle during the random search.

Table 2 Effect of inertia weight on BOD estimation

Inertia weight (ω)	c_1	c_2	c_3	c_4	c_5	c_6	c_7	c_8	c_9	Error
0.1	0.818	−0.049	0.029	−0.019	0.003	−1.625	−12.248	2.1631	0.009	19.97
0.2	0.915	−0.051	0.031	−0.021	0.003	−1.581	−12.275	1.479	0.009	19.94
0.3	0.920	−0.051	0.031	−0.021	0.003	−1.578	−12.278	1.444	0.009	19.94
0.4	0.919	−0.051	0.031	−0.021	0.003	−1.579	−12.277	1.451	0.009	19.94
0.5	0.889	−0.048	0.028	−0.02	0.003	−1.657	−12.241	1.640	0.009	19.94
0.6	0.990	−0.055	0.033	−0.021	0.003	−1.563	−12.471	0.951	0.009	19.99
0.7	2.471	−0.082	0.052	−0.031	0.003	−0.705	−12.177	10.791	0.009	26.00
0.8	209.3	7.394	−4.83	−1.115	1.230	−71.25	1105.8	−1558.7	0.055	466.6

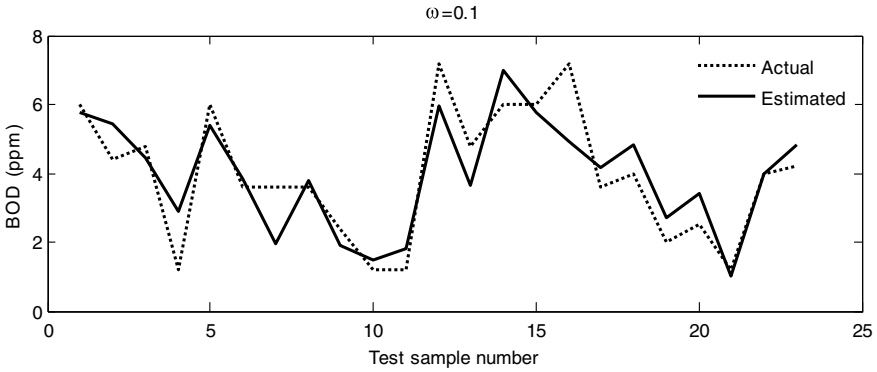

Fig. 1 Models BOD estimated values vs actual values with inertia weight 0.1

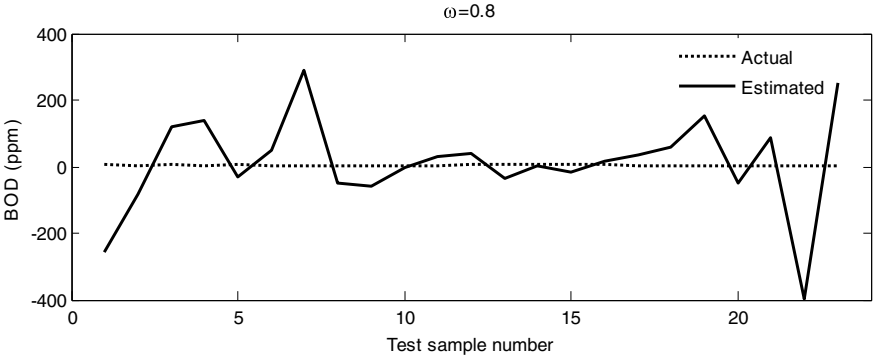

Fig. 2 Models BOD estimated values vs actual values with inertia weight 0.8

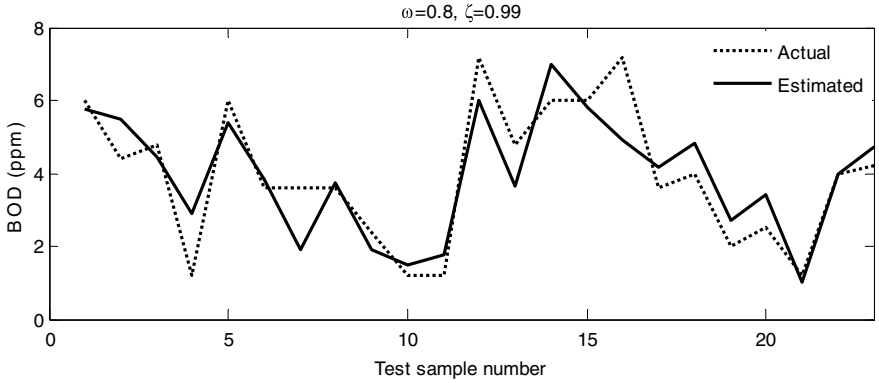

Fig. 3 Models BOD estimated values versus actual values with inertia weight 0.1 and damping factor 0.99

3.2 Effect of Damping Factor on BOD Prediction

In PSO prediction process, it involves the following steps to evaluate BOD estimated values such as choosing of input variables, inertia weights, and damping factor. The goal of the BOD estimation is to achieve efficient global solution. However, biological activity in aquatic bodies involves highly dynamic, nonlinearity, and nonstationary particles, which exhibit noises and poor performance. So, damping factor is an additional factor to reduce the dynamic position and increase the accuracy. In this study, an additional damping factor of 0.99 is used, and BOD estimations are examined with varying inertia weights to make it more realistic (Fig. 3).

Table 3 shows the satisfactory results for a dataset with varying inertia weights, and PSO is applied for the worst case (inertia weight 0.8). To verify all possible values of getting convergent results, a damping factor of 0.99 was included. So, after the number of trails, even BOD at inertia weight of 0.8 improved as well as got the best solution. While deploying optimization approaches to make variable prediction, it was not the sensitivity of the input variables. If the input variables particles displacement was enhanced by the damping factors, then the accuracy of the prediction model could be improved [15, 16]. Moreover, with an addition of damping coefficient running time of the execution is larger than the model with only inertia weights, but accuracy is more with an addition of damping coefficient.

Table 3 Effect of damping factor on BOD estimation

Inertia weight (ω)	c_1	c_2	c_3	c_4	c_5	c_6	c_7	c_8	c_9	Error
0.1	0.833	−0.050	0.030	−0.020	0.003	−1.617	−12.264	2.127	0.021	19.99
0.2	0.736	−0.049	0.029	−0.019	0.003	−1.693	−12.193	2.863	0.021	20.00
0.3	1.111	−0.055	0.033	−0.022	0.003	−1.466	−12.272	−0.50	0.021	19.96
0.4	0.877	−0.051	0.030	−0.020	0.003	−1.597	−12.272	1.778	0.021	19.44
0.5	0.941	−0.051	0.031	−0.021	0.003	−1.570	−12.266	1.271	0.021	19.96
0.6	0.837	−0.049	0.029	−0.020	0.003	−1.631	−12.231	2.076	0.021	20.00
0.7	0.746	−0.049	0.029	−0.020	0.003	−1.693	−12.284	2.793	0.021	20.00
0.8	0.993	−0.049	0.029	−0.021	0.003	−1.600	−12.189	0.834	0.021	19.99

4 Conclusions

In this study, a metaheuristic algorithm, PSO, has been applied to estimate the BOD values of aquaculture ponds in the western delta region of Andhra Pradesh. Besides, for estimating BOD value, the paper explores the aquaculture activities are more concern due to the intensive farming with high-biological activity. The following conclusions drawn from this study.

(1) The biological oxygen demand (BOD) is one of the vital water quality properties. Biological oxygen demand determination of water samples involves control temperature, time-consuming (5 days), and cumbersome tasks. PSO is an integrated tool for predicting BOD values with input variables. PSO is used for the estimation of weighted coefficients of multiple linear regression models of the BOD estimation function.
(2) Simulations of BOD estimation with varying inertia weights deliver a group of constants. In this study, inertia weights of 0.4 and 0.8 show the best and worst global solutions, respectively.
(3) BOD models with PSO produced with dapping factor 0.99 show significant improvement in the finding of the best global solution. Hence, PSO models generated with damping factor show dynamic particles would seem to get quite compatible with the velocity and position of particles. The comparison of the BOD predicted model showed that the PSO algorithm with a damping ratio can enhance the global solution.
(4) PSO approach provided better convergent results with fewer data. The proposed PSO model with a damping coefficient could be helpful to estimate BOD value rather than relying on time-consuming laboratory testing.

References

1. Cao L, Wang W, Yang Y, Yang C, Yuan Z, Xiong S, Diana J (2007) Environmental impact of aquaculture and countermeasures to aquaculture pollution in China. Environ Sci Pollut Res-Int 14(7):452–462
2. Coldebella A, Gentelini AL, Piana PA, Coldebella PF, Boscolo WR, Feiden A (2018) Effluents from fish farming ponds: A view from the perspective of its main components. Sustainability 10(1):3
3. Deka, P. (2008). A comparative study of the seasonal trend of Biological Oxygen Demand, Chemical Oxygen Demand and Dissolved Organic Matter in two freshwater aquaculture ponds of Assam. *Parameters*, *2009*
4. Noori R, Karbassi A, Ashrafi K, Ardestani M, Mehrdadi N, Bidhendi GRN (2012) Active and online prediction of BOD 5 in river systems using reduced-order support vector machine. Environ Earth Sci 67(1):141–149
5. Basant N, Gupta S, Malik A, Singh KP (2010) Linear and nonlinear modeling for simultaneous prediction of dissolved oxygen and biochemical oxygen demand of the surface water—a case study. Chemom Intell Lab Syst 104(2):172–180
6. Ewaid SH, Abed SA, Kadhum SA (2018) Predicting the Tigris River water quality within Baghdad, Iraq by using water quality index and regression analysis. Environ Technol Innov 11:390–398
7. Džeroski S, Demšar D, Grbović J (2000) Predicting chemical parameters of river water quality from bioindicator data. Appl Intell 13(1):7–17
8. Abyaneh HZ (2014) Evaluation of multivariate linear regression and artificial neural networks in prediction of water quality parameters. J Environ Health Sci Eng 12(1):1–8
9. Tomić ANŠ, Antanasijević DZ, Ristić MĐ, Perić-Grujić AA, Pocajt VV (2016) Modeling the BOD of Danube River in Serbia using spatial, temporal, and input variables optimized artificial neural network models. Environ Monit Assess 188(5):300
10. Chu M, Li W, Qiao J (2019, July) A PSO-RRBF neural network for BOD prediction in sewage treatment. In *2019 Chinese Control Conference (CCC)* . IEEE. pp. 1593–1597
11. Alizamir M, Sobhanardakani S (2018). An artificial neural Network-Particle swarm Optimization (ANN-PSO) approach to predict heavy metals contamination in groundwater resources. *Jundishapur J Health Sci*, *10*(2)
12. Nagaraju TV, Prasad CD (2020) Swarm-assisted multiple linear regression models for compression index (C c) estimation of blended expansive clays. Arab J Geosci 13(9):1–11
13. Chen YW, Lin CL, Mimori A (2008, November). Multimodal medical image registration using particle swarm optimization. In *2008 Eighth International Conference on Intelligent Systems Design and Applications* . IEEE. 3, pp. 127–131
14. Lei XJ, Fu AL, Sun JJ (2010) Performance analyzing and researching of improved PSO algorithm. Appl Res Comput 27(2):453–458
15. Armaghani DJ, Raja RSNSB, Faizi K, Rashid ASA (2017) Developing a hybrid PSO–ANN model for estimating the ultimate bearing capacity of rock-socketed piles. Neural Comput Appl 28(2):391–405
16. Guleryuz D (2021) Determination of industrial energy demand in Turkey using MLR, ANFIS and PSO-ANFIS. J Artif Intell Syst 3(1):16–34

Interpreting Different Timeslot Precipitation Characteristics in the Seonath River Basin, Chhattisgarh During 1901–2017

Ramgopal T. Sahu, Mani Kant Verma, and Ishtiyaq Ahmad

Abstract The study focuses on interpreting precipitation characteristics for assessing variability (time behavioral change) in the Seonath River basin. The Maximum loading value (MLV) approach, an eigen-based spatial pattern analysis, is presented to process grid-based monthly precipitation data of 0.25° × 0.25° resolution. The meteorological records of 117 years (1901–2017) have spatial provision for temporal and spatial modes that help recognize the region for precipitation characterization. The different timeslot precipitation characteristics identified were then assessed for their deviation from the annual precipitation observed at different stations by employing dissimilar/similar properties of the inter-cluster and between-cluster, respectively. Validation of the identified characteristics for distinctness and pairwise comparisons of CDFs using the Kolmogorov–Smirnov 'D' statistic test. Implementation results of temporal (T)-mode of spatial pattern analysis indicate that the 3rd (1979–2017) timeslot interval does not have a region with spatial pattern variability of precipitation during summer. Implementation results of spatial (S)-mode of spatial pattern analysis indicate that the northeast Mahanadi has significantly decreased from 42.49 to 28.13% (i.e., dropped by 14.36%), while the southeast Mahanadi has significantly increased by 10.36% (i.e., from 18.16 to 28.52%) of total variance. Spatial pattern variability in mid-autumn (October) was influenced during the 3rd (1979–2017) timeslot interval.

Keywords Eigenvalue decomposition · Spatial pattern analysis · Loadings · Core origin · Spatio-temporal

1 Introduction

The warming climate and precipitation variability is a long process and this undisputed fact, along with IPCC's 5th assessment, has raised a serious concern about global warming, suggesting a 0.85 °C rise in temperature during 1880–2012 [IPCC,

R. T. Sahu (✉) · M. K. Verma · I. Ahmad
National Institute of Technology, Raipur, Chhattisgarh, India
e-mail: ramgopal_sahu@yahoo.com

© The Author(s), under exclusive license to Springer Nature Singapore Pte Ltd. 2023

K. R. Reddy et al. (eds.), *Recent Advances in Sustainable Environment*, Lecture Notes in Civil Engineering 285, https://doi.org/10.1007/978-981-19-5077-3_3

2013]. To ascertain the precipitation characteristics during the said span of period, the meteorological records of 117 years (1901–2017) were analyzed in three different time intervals to study the aging effect. Based on these two concerns: the general hydrological cycle process, in which water evaporates and is stored as vapor in the atmosphere as well as the temperature required for effective condensation and evaporation, the spatial and temporal form of precipitation characteristics change. The limits for spatial and temporal terms where global or regional characteristics are likely to change is atmospheric water retention capacity. Precipitation characteristics such as wet days and precipitation intensities have been exacerbated by the warming climate. Changes in precipitation intensity, quantity, and pattern can lead to more frequent extreme events such as droughts and floods. The people who are ultimately influenced are those for whom extreme events are unforeseeable occurrences. Thus, historical data analysis is critical for extracting information about changing precipitation characteristics.

The research was prompted by phenological changes (e.g., uncertain, heavy, sudden, or low) in precipitation. The uncertainty and inconsistencies associated with precipitation have a negative impact on stakeholders from various sectors, including dependent farmers, health and safety (not limited to living creatures but also the environment). The research aspect is critical for water resource management and planning, as well as for assessing flood and drought risk [8, 18]. As a result, precipitation is critical, and its variability must be investigated. Consequently, the objective of the study is to investigate the precipitation characteristics in three different timeslots using grid monthly relative precipitation data in the Seonath River basin, Chhattisgarh. Comparatively, enormous studies have been published on precipitation variability [1, 15, 16, 28, 34, 35, 38, 39], saptio-temporal analysis [1, 2, 27, 29, 30, 42, 43], hydrological frequency analysis [4, 5, 9, 25, 32], and precipitation regionalization [3, 21–24, 26, 31, 36, 41] concerning precipitation characteristics for assessing a wide range of problems.

In this investigation, the monthly precipitation data record was partitioned into three equal timeslots and then applied to eigen-based spatial pattern analysis. The gridded precipitation data with a resolution of $0.25° \times 0.25°$ and a record of 117 years (1901–2017) is analyzed into three intervals of 39 years each: (1) 1901–1939, (2) 1940–1978, and (3) 1979–2017. A pattern interpretation for extracting different patterns of time variability information in meteorological records using spatial (S)—mode. The magnitude of monthly relative precipitation as an observation and station as a variable for spatial (S)—mode of spatial pattern analysis. The strong spatial pattern that emerges indicates high component loadings on interconnected stations, whereas dispersed stations have loadings that are congruent to zero. The Seonath River basin has vast climatological characteristics, so the timeslot approach will depict different precipitation characteristics and reveal different aspects of the Seonath's precipitation regimes.

2 Study Area and Data

The Seonath River is a tributary of the Mahanadi River that flows east (see Fig. 1). The Basin is located between latitudes 20°16′N and 22°41′N, and longitudes 80°25′E and 82°35′E. The river thalweg runs for 380 km and has a catchment area of 30,860 square kilometers. The river flows from Panabaras village in Chhattisgarh's Rajnandgaon district, merging with the Mahanadi River at Kharghani on the left (nearby city Shivrinarayan G&D site). The Tandula, Kharun, Arpa, Hamp, Agar, and Maniyari rivers are the main tributaries of the Seonath River. Annual rainfall in the basin ranges from 1005 to 1255 mm. Monthly relative precipitation data is derived from gridded precipitation data with a resolution of 0.25° × 0.25° [19, 20]. Meteorological data is disseminated by the Indian Meteorological Department (IMD), Pune.

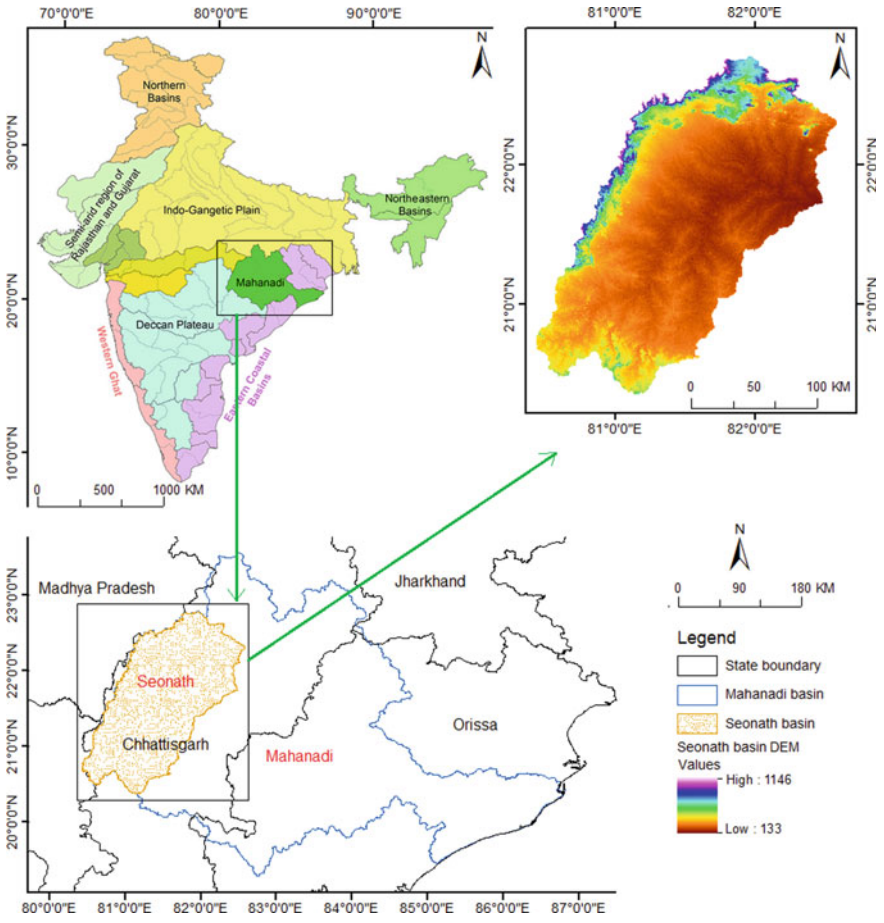

Fig. 1 The Mahanadi River basin

The high-resolution gridded precipitation data was processed from 2140 selected stations out of 6329 available stations in India using the interpolation scheme described by Shepard [33]. The data is assessed for spatial dependency to ascertain data accuracy and quality. "The closer spatial entities are more strongly related to each other than distant ones" [37]. "So spatial events therefore need to be spatially clustered for which spatial analysis is an important technique" [40]. The Moran's I test [13] results a p-value = 2.2e–16 (statistically significant), Z-score = 23.609, the Moran's Index = 0.876. The statistics implies that the data points tend to group spatially, in general, high value data points attract closer other high valued data points and vice-versa and reliable to infer that the dataset is spatially dependent.

3 Methodology

The Eigen-based technique, also known as spatial pattern analysis resembling PCA [17]. The spatial (S)-mode and temporal (T)-modes of spatial pattern analysis were used to assess precipitation time variability and precipitation regimes, respectively. The investigation was divided into two parts: (1) Timeslot analysis, i.e., the eigenvalue decomposition of different timeslots of time series data. (2) Pattern interpretation using the maximum loading value approach. The identified patterns from the three timeslots were then evaluated for their dispersion of annual precipitation observed at different stations using dissimilar/similar inter-cluster and between-cluster characteristics. The regionalized patterns were validated for their distinctness and a pairwise comparison of CDFs using the (Kolmogorov–Smirnov) KS-'D' statistic test [7].

3.1 Precipitation Time Variability and Regionalization

Prior to using spatial pattern analysis, data must be prepared, which includes data segmentation and normalization. (1) The task of Segmentation is to divide and visualize the data into three equal timeslot intervals. The timeslot perspective view of interpreting precipitation characteristics can help portray a realistic justification of the warming climate's influence on precipitation patterns. (2) The objective of data normalization is to obtain a stable distributed (congruent to normal distribution) and dimensionalized dataset. Point (2) is achieved by transforming the dataset to a low-skewed property by subjecting the dataset to the square root, cube root, or log transformation. The lowest skewed transformation results for cubic root and is a prerequisite for PCA application. The cubic root transformed dataset is checked for sampling adequacy, and the Kaiser-Mayer-Olkin (KMO) measure [11] of 0.99 for all timeslot interval results indicates 'marvelous' for PCA implementation. The entire Mahanadi River basin was evaluated for time variability precipitation pattern using cubic root transformed time series data of [M × N] matrix, where M = 53 denotes stations and N = 468 (39 × 12 years) observations applied to spatial (S)-mode of

spatial pattern analysis. In PCA implementation, an eigenvector is assigned to each component (variable), and eigenvalue decomposition yields as many components as variables in the dataset. Another engineering task is judging PCA implementation results for retaining components for further analysis, for which adjacent tools such as scree plot in conjunction with parallel analysis and the North test for accomplishing sampling error in the estimated eigenvalues are used.

For spatial pattern analysis, a scree plot [6] is defined as a line plot between eigenvalue and eigenvector, whose optimism lies in a sharp reduction of eigenvalue. The judgment of its sharp reduction is arbitrary and intuitive, suggesting two or three components. As a result, using the scree plot as the sole criterion for determining optimal components is impractical because eigenvalues are subject to errors and bias. As a consequence, a supplemental tool (Parallel analysis) for interpreting and considering the feasibility of eigenvalue by eigenvalue decomposition, where the error and bias are adjusted. "The rationale of parallel analysis [10] is to figure out that factor accounting for maximum variance, whose probability existence is not expected by chance". North's thumb rule [14] states "if the sampling error of an eigenvalue is comparable to or larger than the linear spacing of its closest eigenvalue, then these two eigenvectors are mixed", alternatively, it is a degree of separation between the eigenvalues. Lawley's [12] defined a formula for estimating the standard error (Eq. 1).

$$\Delta\lambda_i = \left(\frac{2}{n^*}\right)^{1/2} \lambda_i \tag{1}$$

where

n^* = effective sample size,

λ_i = eigenvalue for *i*th order.

Equation 1 suggests that "The error associated with each eigenvalue depends on the eigenvalue itself and the effective sample size, which means the error is directly proportional to the eigenvalue and inversely proportional to effective sample size" [12]. The error limit associated with equation-1 at a 95% confidence interval is defined as Error $= \lambda_i \pm 1.96\Delta\lambda_i$

3.2 Pattern Delineation (Maximum Loading Value Approach)

The retained components obtained by the subjecting transformed dataset to spatial (S)-mode of spatial pattern analysis are orthogonally rotated with the use of the varimax rotation criterion. Extracting sufficient localized information is the objective and beneficial for interpreting patterns. For studying the spatial and temporal form of characteristics and the warming climate's influence, components accounting for max variance within each timeslot interval are considered. The precipitation characteristics, shifting of patterns, and variability can be mapped by plotting the rotated loadings of eigenvectors of the delineated patterns using the loading value (y) as a

threshold. Regionalization of the Mahanadi River basin is characterized by patterns of time variability for each timeslot interval into few distinctive regions. Satisfactory regionalization by employing a maximum loading value approach such that the stations are well classified and within the boundary limit. Refer Sahu et al. [24] for DBSCAN-based regionalization and spatio-temporal analysis in the Mahanadi River basin. The identified regions can also be studied for regional frequency analysis, which is a supplementary content excluded in this work. Readers can refer to Sahu et al. [25] for l-moment based regional frequency analysis.

The Temporal (T)-mode of spatial pattern analysis is used to investigate the temporal form of precipitation characteristics in order to identify various timeslot precipitation regimes. The approach identifies stations with similar annual precipitation characteristics, regardless of magnitude, at each station. To ascertain the objective, the relative form of the monthly precipitation dataset in the [N × M] matrix, where M = 53 denotes stations and N = 12 represents observations (precipitation), is implemented to the temporal (T)-mode of spatial pattern analysis. Transforming the dataset to its relative form is simply a kind of standardization to ascertain dominating high precipitation values of the station. The principal component scores of the monthly relative precipitation implemented to the temporal (T)-mode of spatial pattern analysis were orthogonally rotated (Varimax criteria) to extract localized information for interpreting spatial patterns of monthly precipitation.

4 Results and Discussion

4.1 Implementation Results of Spatial (S)—Mode Spatial Pattern Analysis

Cubic root transformed monthly precipitation data implemented in spatial (S)-mode of spatial pattern analysis. The summary statistics of the implementation suggest that the first unrotated component accounts for more than 87% of the total variance for all timeslot data (see Fig. 3). The resulting eigenvalue from the implementation is assessed for bias and errors using parallel analysis and suggests an optimal number of components for later analysis (see Fig. 2a). Now, how are the loadings associated with the components? The retained components are rotated orthogonally using varimax criteria and the summary statistics suggest that for a timeslot (1901–1939), the northeast (including major portions of the middle and some portions of the Seonath and lower sub-division of the Mahanadi basin) pattern explains 42.49% of the total variance. The southwest (which includes major portions of the Seonath basin and some parts of the middle and lower sub-divisions of the Mahanadi basin) pattern explains 34.24% of the total variance. Whereas the southeast (which includes major portions of the lower sub-division of the Mahanadi basin) pattern explains 18.16% of total variance.

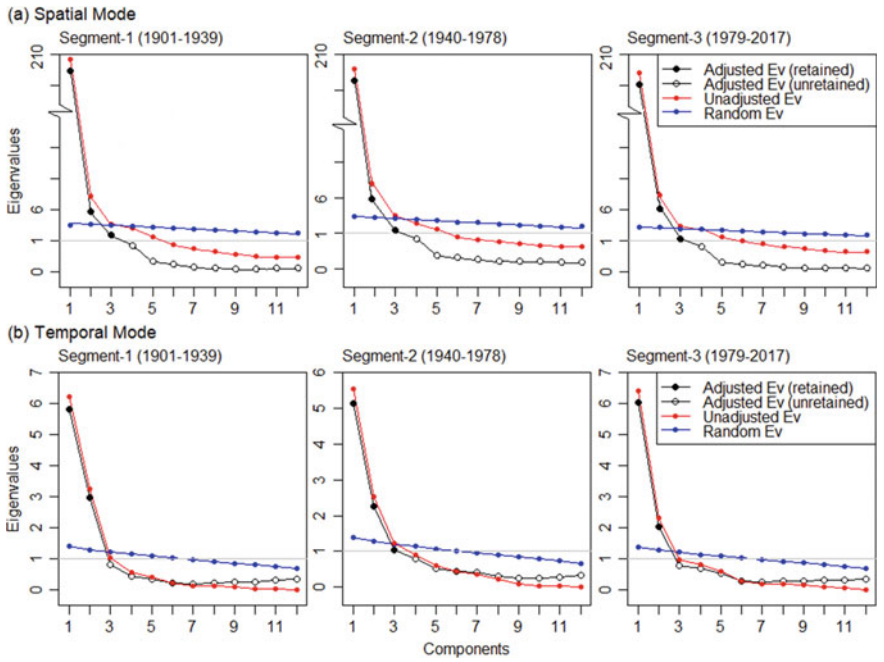

Fig. 2 Eigenvalue decomposition of the correlation matrix for the three timeslots obtained using the spatial (S)-and Temporal (T) mode of the spatial pattern analysis with the application of Horn's parallel analysis for component retention

The second timeslot (1940–1978), where the southwest (including the Seonath basin and some portions of the middle and lower sub-divisions of the Mahanadi basin) pattern increased by 5% approx. and explains 39.07% of the total variance. The northeast (includes major portions of the middle and some parts of the lower sub-division of the Mahanadi basin) pattern decreased by 9% approx. and explains 33.78% of the total variance. Similarly, the southeast (which includes major portions of the lower sub-division of the Mahanadi basin) pattern explains 20.75% of the total variance. The third timeslot (1979–2017), for which the northeast pattern has significantly decreased, contains merely half of the portion of the middle and some parts of the lower sub-division of the Mahanadi basin, explaining only 28.13% of the total variance. The southeast pattern (which includes major portions of the lower sub-division of the Mahanadi basin) has significantly increased to 28.52% of the total variance. The southwest pattern (now in-between southwest and northwest) decreased by 3% compared to the preceding timeslot and explains the Seonath basin and half of the middle sub-division of the Mahanadi basin, covering 35.75% of the total variance.

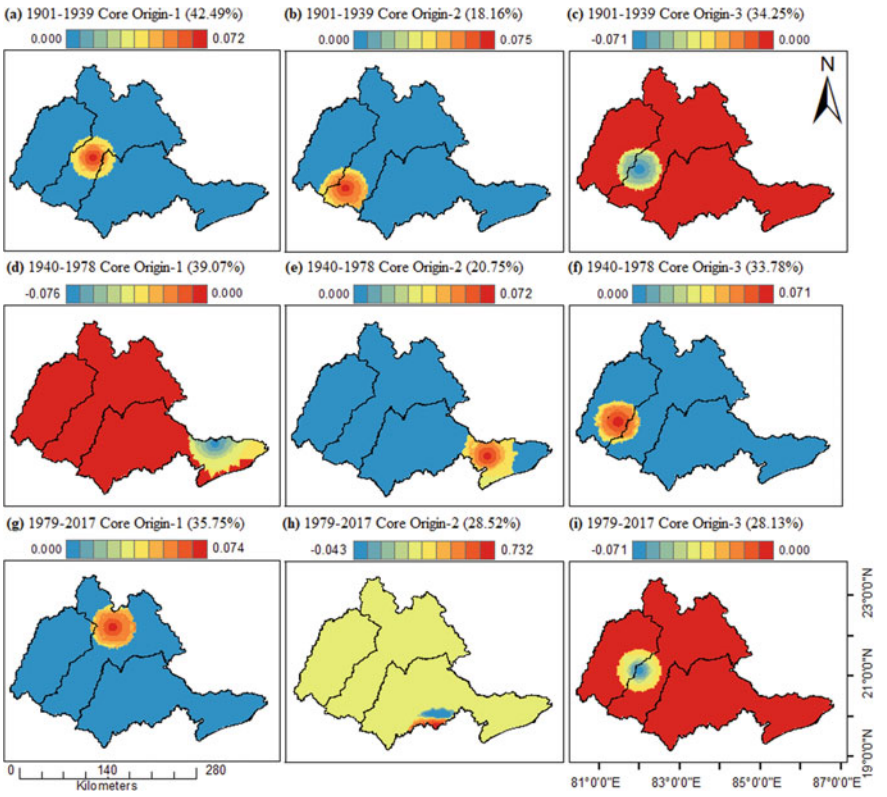

Fig. 3 Spatial distribution of the core origin for high loadings (positive or negative), a graphical representation of EOF coefficient upon the component it loads highly

4.2 Characterization of Core Origin

Empirical orthogonal function analysis for assessing rotated loading (negative and positive) and core origin to understand the characteristics of negative and positive rotated loadings and the emergence of core origin. Figure 3 shows the statistical representation of EOF coefficient. Statistics are the loadings (spatial patterns) and are distributed among the stations to which they load highly. Statistics of EOF coefficient revels the influential point (core point) of patterns resulting from spatial pattern analysis. The statistics in Table 1 describe the points of core origin for different timeslot intervals and suggest that the Seonath basin is highly influenced by all three patterns of timeslot (1901–1939) with a cumulative variance of 94.90%. The 3rd Pattern (33.78% variance) of the timeslot (1940–1978) and for recent past timeslot (1979–2017), the 1st and 3rd patterns with cumulative variance of 63.88% are other that influence the Seonath basin. Sahu et al. [26] investigated the Mahanadi basin for regionalizing precipitation on the same data set using Maximum loading value (MLV) approach and

Table 1 Core point description

Segment	Components	Geographical location	Sharing basin	Location description	Core nature
1901–1939	1	82°30′E × 21°15′N	U-M-L	Mahasamund	Positive
	2	81°45′E × 20°30′N	U-M	Dhamtari	Positive
	3	82°00′E × 21°15′N	U-M	Raipur	Negative
1940–1978	1	85°30′E × 20°30′N	L	Cuttack	Negative
	2	85°15′E × 20°30′N	L	Nayagarh/Khordha	Positive
	3	81°30′E × 21°00′N	U-M	Durg	Positive
1979–2017	1	83°00′E × 22°15′N	U-M	Raigarh/Korba	Positive
	2	84°00′E × 20°00′N	L	Khandhamal	Dual(±)
	3	82°00′E × 21°00′N	U-M	Raipur	Negative

Note: Geographical locations are approximate locations; Upper sub-division is specifically Seonath basin; U—Upper sub-division, M—Middle sub-division, L—Lower sub-division

found four homogenized regions, among which the third region is similar to what was expected in this study. It can be concluded that any change prevailing in the Mahanadi River basin is the influence that emerges from the uppermost sub-division (probably the Seonath basin), see Fig. 3 and Table 1.

4.3 Implementation Results of Temporal (T)—Mode Spatial Pattern Analysis

Eigenvalue decomposition of monthly relative precipitation for characterizing precipitation regimes. The statistics of temporal (T)-mode of spatial pattern analysis is illustrated in Fig. 4. According to implementation results, the first three unrotated components cover more than 75% of total variance, whereas parallel analysis suggests two optimum components for timeslots 1 and 3 and three for timeslot-2 (see Fig. 2b). Figure 4 depicts the spatial distribution of the varimax rotated principal component scores for the Seonath basin, which are the dominant components for their respective timeslot intervals. The following section discusses statistics in Table 2 and pictorial interpolation of Fig. 4 for various timeslot intervals.

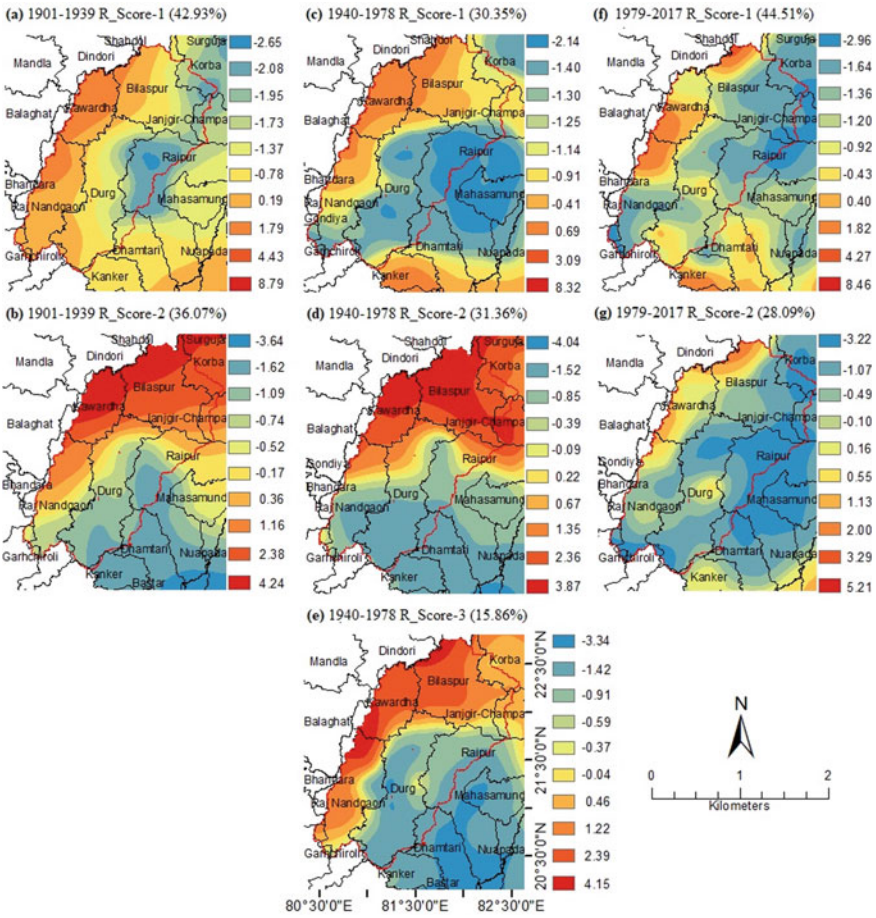

Fig. 4 Spatial distribution of rotated PC Scores for the Seonath basin obtained from implementing Temporal (T)-mode of Spatial pattern analysis

Timeslot—1 (1901–1939). For component−1, Durg, Raipur (portion of Seonath), and major portions of Bilaspur consist of spatial pattern variability during early winter (December), spring (April and May), and autumn (September, October, and November) featuring negative loading. Summer (July and August) spatial pattern variability is observed in Rajnandgaon, Kawardha, and some parts of Durg and Bilaspur feature positive loadings, accounting for 42.93% of the total variance (see Fig. 4a). Whereas 36.07% of the total variance is shared in meridional form with north (south) Seonath features positive (negative) loadings for component-2, see Fig. 4b. The north Seonath basin features spatial pattern variability during winter (January and February) and early spring (March). Whereas the south Seonath basin features spatial pattern variability during early summer (June), see Table 2.

Table 2 Results of varimax rotated loadings obtained from Temporal (T)-mode of the spatial pattern analysis

	Segment—1 (1901–1939)		Segment—2 (1940–1978)			Segment –3 (1979–2017)	
Month	Comp. 1	Comp. 2	Comp. 1	Comp. 2	Comp. 3	Comp. 1	Comp. 2
January	0.110	***0.488***		***0.543***	−0.118	0.154	***0.561***
February		***0.506***	−0.139	***0.567***	0.123	−0.173	***0.495***
March	−0.102	***0.423***	−0.245	***0.282***	0.218	***−0.296***	0.182
April	***−0.283***	−0.156	***−0.411***		0.334	***−0.339***	
May	***−0.358***		***−0.429***			***−0.378***	
June		***−0.421***			***0.645***	***0.235***	−0.18
July	***0.379***	0.106	***0.393***		0.111	***0.383***	0.104
August	***0.389***		***0.406***			***0.311***	−0.114
September	***−0.307***	−0.203	−0.149	***−0.487***	0.117	−0.161	***−0.201***
October	***−0.386***		***−0.338***		−0.301	***−0.381***	
November	***−0.381***		−0.307		***−0.378***	***−0.361***	
December	***−0.280***	0.253		0.199	***−0.357***		***0.541***

Timeslot—2 (1940–1978). For component-1, Durg, Raipur, and some parts of Bilaspur and Rajnandgaon experienced spatial pattern variability during spring (April and May), summer (July and August), and mid-autumn (October) featured negative loading, accounting for 30.35% of the total variance (see Fig. 4c). Similar to component-2 of timeslot-1, component-2 (Fig. 4d) accounts for 31.36% of the total variance and is shared in meridional form with north (south) Seonath features positive (negative) loadings. The north Seonath basin experiences spatial pattern variability in winter (January and February) and early spring (March), whereas the south Seonath basin experiences spatial pattern variability during early autumn (September). While, component-3 (Fig. 4e) accounts for 15.86% of the total variance, such that Bilaspur, Kawardha, and major portions of Rajnandgaon feature positive loadings and spatial pattern variability during early summer (June). During the late autumn (November) and early winter (December), Durg and Raipur feature negative loading and spatial pattern variability (see Table 2).

Timeslot—3 (1979–2017). Almost the entire Seonath basin had negative component-1 loadings (Fig. 4f), indicating spatial pattern variability during spring (March, April, and May) and winter (October and November), accounting for 44.51% of total variance. Similarly, component-2 (Fig. 4g) accounts for 28.09% of the total variance in which the entire Seonath basin had negative loadings, indicating spatial pattern variability in early autumn (September). See Table 2.

4.4 *Characterization of Patterns for Different Timeslot Interval*

The characterized patterns of different timeslot intervals were assessed for the annual dispersion of precipitation using similar and dissimilar properties of inter-cluster and between-cluster, respectively. Figure 5b depicts a boxplot with a centered median, suggesting a symmetric distribution for all timeslot intervals. The identified patterns of different timeslot intervals exhibit good agreement, implying compact and homogeneous inter-cluster variability of precipitation. Figure 5a illustrates the application of empirical cumulative distribution to validate the distinctness of different timeslot intervals. Kolmogorov–Smirnov 'D' statistic test [7] for pairwise comparison of eCDFs as depicted in Fig. 5b. The CDF plot (Fig. 5a) appears similar and close on visual interpretation, and to ascertain their distinctness, the D-statistics of the KS test were used for pairwise comparison of all CDFs. The statistics indicate that the timeslot pairs 1–3 and 2–3 are well below 0.01 (p-value), whereas timeslot pair 1–2 evidently has a 27.2% similarity. Thus, it is reliable to infer that the results of D-statistics are distinct from one another.

Figure 6 exhibits boxplot analysis for the monthly relative precipitation to assess any form of non-uniformity present in different timeslot intervals. The interpretation of the boxplot suggests the nature of inter-cluster variations and the analysis result statistics as depicted in the patterns of precipitation regime range from medium to low, i.e., possible to acceptable homogeneous among the different timeslot intervals. Figure 6 depicts three timeslot intervals that are well-defined, distinct, and compact, covering the central table plains and high mountains of 53 station

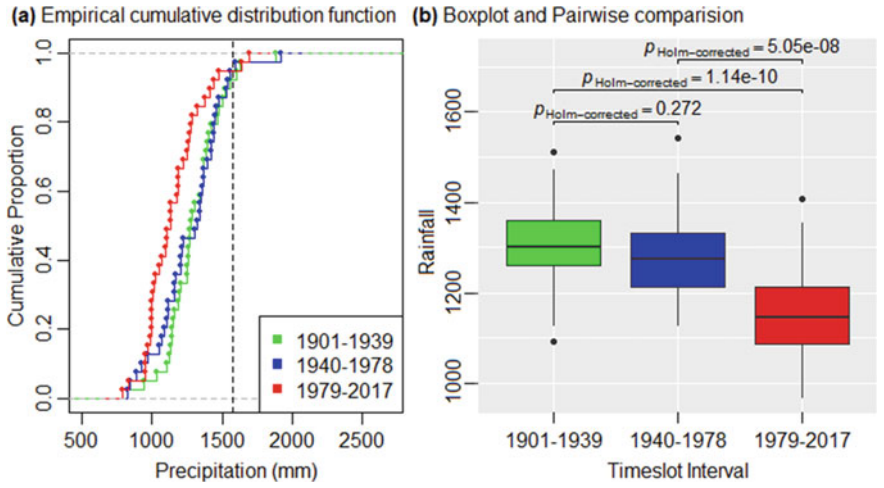

Fig. 5 **a** Comparison of empirical cumulative distribution function for different timeslot interval, the black dash vertical line represents the mean annual precipitation of the Mahanadi basin (1572 mm). **b** Boxplot and KS 'D – test' (pairwise comparison) for each timeslot pairs

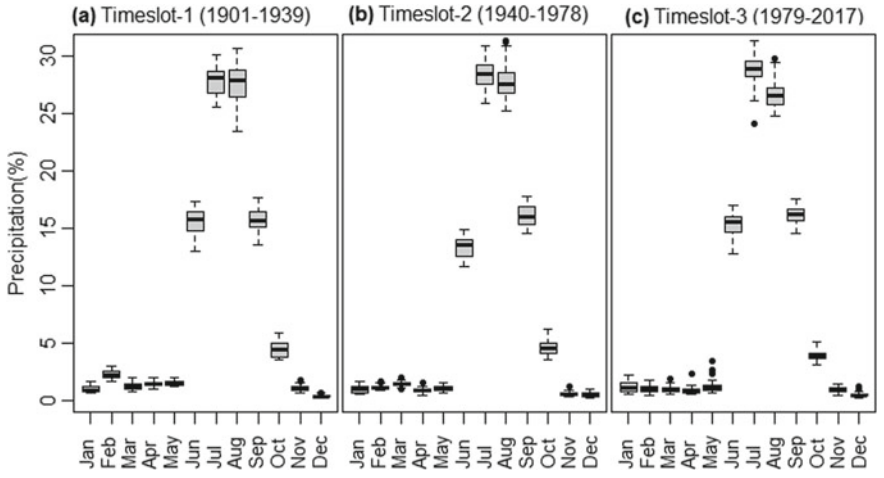

Fig. 6 Boxplots of the monthly march of relative monthly precipitation for the different timeslot patterns

points. The median's relative distance of some station points has distracted, e.g., July (Fig. 6a) and June (Fig. 6b, c). Overall, the statistics of boxplot analysis suggest well-defined and homogeneous patterns of precipitation. Except October month of the 3rd timeslot interval exhibits a similar march of months for precipitation, i.e., reasonable precipitation during (June to September) and some noticeable precipitation during October month. Figure 6 illustrates a boxplot implying a symmetric distribution of precipitation in all timeslot intervals in connection with the march of months. Thereafter follows the natural cycle of the dry season that ends in May. The spatial distribution of station points that are spatially scattered over the basin features moderate precipitation during summer (JJA) and noticeable precipitation during autumn (SO) (see Figs. 3 and 4). The Summary of this section states that summer is the main rainy season with standard marching months such as June, July, August, and September.

5 Conclusion

The maximum loading value approach (eigen-based spatial pattern analysis) resembles PCA for extracting more localized information for interpreting the spatial and temporal form of variability in different time slot intervals. The objective behind the eigenvalue decomposition of the cubic root transformed monthly precipitation and monthly relative precipitation data in different timeslot intervals is to study the aging effect. High resolution ($0.25° \times 0.25°$) grid precipitation data partitioned into three equal intervals was used to investigate the spatial characteristics of precipitation. The following are the findings of the aforementioned investigation.

1. Implementation results of spatial (S)-mode of spatial pattern analysis indicate a minimum deviation for the first three unrotated components of different timeslot intervals (i.e., 94.9%–93.6–92.4%). For varimax rotated components, the northeast Mahanadi has significantly decreased from 42.49 to 28.13% (i.e., dropped by 14.36%), while the southeast Mahanadi has significantly increased by 10.36% (i.e., from 18.16 to 28.52%).
2. Characterization of core origin, i.e., EOF coefficient statistics (loadings) for quantifying the negative and positive loadings and emergence of core points. Figure 3a–c, f–i confirm and conclude that any change (spatial or temporal form) in the entire Mahanadi is due to the northwest portion (probably the Seonath basin).
3. Implementation results of temporal (T)-mode of spatial pattern analysis indicate that the 3rd timeslot interval does not have a region with spatial pattern variability of precipitation during summer in two of the components.
4. The characterization of patterns for different timeslot intervals for the Seonath suggests that the timeslot pairs were distinct except pair 1–2, which had a 27.2% (p-value—0.272) similarity. The median line in the boxplot of the 3rd timeslot was at 1154 mm, comparatively less than the 1st (1303 mm) and 2nd (1275 mm) timeslots, which means that the annual precipitation magnitude is in a decreasing trend.
5. Spatial pattern variability in mid-autumn (October) was influenced during the 3rd timeslot interval, and thus the standard marching months of rain are June, July, August, and September.

Concluding remark of investigation: The three different timeslot patterns of precipitation variability for the Seonath basin are the local-dependent phenological changes that emerge because of the substantial effect of hydrology, climatology, and local topography. The spatial pattern variability of precipitation is based on the summer monsoon moist current moving northeast from the Indian Ocean toward the Himalayas and retreating toward the southeast. October and sometimes November are the retreating monsoon and is evident from the boxplot results (Figs. 5b and 6), an intimation of precipitation variability (magnitude) at different locations. The characterized patterns of the different timeslot precipitation using the MLV approach have different uses and applications. Regions with known precipitation characteristics are helpful for better water resource management practices by simplifying the prediction of future precipitation. This can be accomplished by defining a regionalized time series and associating a climatological index (predictors) using a statistical and stochastic approach. Activities such as agricultural planning, irrigation scheduling, rain-fed and dry farming practice, planting time of different crops are helpful with known precipitation regime.

The limitations are based on the results of the spatial characteristics of precipitation patterns, which may be substantially different for different methods and size of patterns characterized by the different time periods and spatial resolution.

References

1. Aher S, Shinde S, Gawali P, Deshmukh P, Venkata LB (2019) Spatio-temporal analysis and estimation of rainfall variability in and around upper Godavari River basin, India. Arab J Geosci 12(22):1–16. https://doi.org/10.1007/s12517-019-4869-z
2. Azharuddin M, Verma S, Verma MK, Prasad AD (2022) A synoptic-scale assessment of flood events and ENSO—streamflow variability in Sheonath River Basin, India. In: Rao CM, Patra KC, Jhajharia D, Kumari S (eds) Advanced modelling and innovations in water resources engineering. Lecture notes in civil engineering, vol 176. Springer, Singapore, pp 93–104. https://doi.org/10.1007/978-981-16-4629-4_8
3. Bharath R, Srinivas VV (2015) Regionalization of extreme rainfall in India. Int J Climatol 35(6):1142–1156. https://doi.org/10.1002/joc.4044
4. Burn DH (1990) Evaluation of regional flood frequency analysis with a region of influence approach. Water Resour Res 26(10):2257–2265. https://doi.org/10.1029/WR026i010p02257
5. Burn DH (1990) An appraisal of the region of influence approach to flood frequency analysis. Hydrol Sci J 35(2):149–165. https://doi.org/10.1080/02626669009492415
6. Cattell RB (1966) The scree test for the number of factors. Multivar Behav Res 1(2):245–276. https://doi.org/10.1207/s15327906mbr0102_10
7. Conover WJ (1998) Practical nonparametric statistics, 3rd edn, vol 350. Wiley, New York
8. Dhiwar BK, Verma S, Prasad AD (2022) Identification of flood vulnerable area for Kharun River basin by GIS techniques. In: Rao CM, Patra KC, Jhajharia D, Kumari S (eds) Advanced modelling and innovations in water resources engineering. Lecture notes in civil engineering, vol 176. Springer, Singapore, pp 385–408. https://doi.org/10.1007/978-981-16-4629-4_27
9. Gabriele S, Arnell N (1991) A hierarchical approach to regional flood frequency analysis. Water Resour Res 27(6):1281–1289. https://doi.org/10.1029/91WR00238
10. Horn JL (1965) A rationale and test for the number of factors in factor analysis. Psychometrika 30:179–185. https://doi.org/10.1007/BF02289447
11. Kaiser HF (1960) The application of electronic computers to factor analysis. Educ Psychol Measur 20:141–151. https://doi.org/10.1177/001316446002000116
12. Lawley DN (1956) Tests for significance for the latent roots of covariance and correlation matrices. Biometrica 43(1–2):128–136. https://doi.org/10.1093/biomet/43.1-2.128
13. Moran PA (1950) Notes on continuous stochastic phenomena. Biometrika 37(1/2):17–23. https://doi.org/10.2307/2332142
14. North GR, Bell TL, Cahalan RF, Moeng FJ (1982) Sampling errors in the estimation of empirical orthogonal functions. Mon Weather Rev 110(7):699–706. https://doi.org/10.1175/1520049 3(1982)110%3C0699:SEITEO%3E2.0.CO;2
15. Parthasarathy B (1984) Interannual and long-term variability of Indian summer monsoon rainfall. Proc Indian Acad Sci Earth Planet Sci 93(4):371–385. https://doi.org/10.1007/BF0284 3255
16. Parthasarathy B, Kumar RK, Munot AA (1993) Homogeneous Indian monsoon rainfall: variability and prediction. Proc Indian Acad Sci Earth Planet Sci 102(1):121–155. https://doi.org/10.1007/BF02839187
17. Pearson K (1901) On lines and planes of closest fit to systems of points in space. Phil Mag 2(11):559–572. https://doi.org/10.1080/14786440109462720
18. Pradhan D, Sahu RT, Verma MK (2022) Flood inundation mapping using GIS and hydraulic model (HEC-RAS): a case study of the Burhi Gandak river, Bihar, India. In: Kumar R, Ahn CW, Sharma TK, Verma OP, Agarwal A (eds) Soft computing: theories and applications. Lecture notes in networks and systems, vol 425. Springer, Singapore, pp 135–145. https://doi.org/10.1007/978-981-19-0707-4_14
19. Rajeevan M, Bhate J, Kale JD, Lal B (2005) Development of a high resolution daily gridded rainfall data for the Indian Region (version 2). Meteorological Monograph Climatology 22/2005, India Meteorological Department, New Delhi (2005)

20. Rajeevan M, Bhate J, Kale JD, Lal B (2006) High resolution daily gridded rainfall data for the Indian region: analysis of break and active monsoon spells. Curr Sci 91(3):296:306. https://www.jstor.org/stable/24094135
21. Rao AR, Srinivas VV (2006) Regionalization of watersheds by hybrid-cluster analysis. J Hydrol 318(1–4):37–56. https://doi.org/10.1016/j.jhydrol.2005.06.003
22. Rao AR, Srinivas VV (2006) Regionalization of watersheds by fuzzy cluster analysis. J Hydrol 318(1–4):57–79 (2006). https://doi.org/10.1016%2Fj.jhydrol.2005.06.004
23. Raziei T (2018) A precipitation regionalization and regime for Iran based on multivariate analysis. Theoret Appl Climatol 131(3):1429–1448. https://doi.org/10.1007/s00704-017-2065-1
24. Sahu RT, Verma MK, Ahmad I (in press) Density-based spatial clustering of application with noise approach for regionalization and its effect on hierarchical clustering. [Manuscript accepted for publication]. Int J Hydrol Sci Technol. http://dx.doi.org/10.1504/IJHST.2022.10048476
25. Sahu RT, Verma MK, Ahmad I (2021) Regional frequency analysis using L-moment methodology—a review. In: Pathak KK, Bandara JMSJ, Agrawal R (eds) Recent trends in civil engineering. Lecture notes in civil engineering, vol 77. Springer, Singapore, pp 822–832. https://doi.org/10.1007/978-981-15-5195-6_60
26. Sahu RT, Verma MK, Ahmad I (2022) Segmental variability of precipitation in the Mahanadi River basin from 1901 to 2017. Geocarto Int. https://doi.org/10.1080/10106049.2022.2091163
27. Sahu RT, Verma MK, Ahmad I (2021) Some non-uniformity patterns spread over the lower Mahanadi River basin, India. Geocarto Int. https://doi.org/10.1080/10106049.2021.2005699
28. Sahu RT, Verma MK, Ahmad I (2021) Segmental variability of precipitation in the Mahanadi River basin during 1901–2017, 24 August 2021, PREPRINT (Version 1) available at Research Square (2021). https://doi.org/10.21203/rs.3.rs-542786/v1
29. Sahu RT, Verma MK, Ahmad I (2021) Characterization of precipitation in the sub-divisions of the Mahanadi River basin, India. Acta Sci Agric 5(12):50–61 (2021). https://doi.org/10.31080/ASAG.2021.05.1085
30. Sahu N, Panda A, Nayak S, Saini A, Mishra M, Sayama T, Sahu L, Duan W, Avtar R, Behera S (2020) Impact of Indo-Pacific climate variability on high streamflow events in Mahanadi River Basin, India. Water 12(7):1952. https://doi.org/10.3390/w12071952
31. Satyanarayana P, Srinivas VV (2011) Regionalization of precipitation in data sparse areas using large scale atmospheric variables—a fuzzy clustering approach. J Hydrol 405(3–4):462–473. https://doi.org/10.1016/j.jhydrol.2011.05.044
32. Satyanarayana P, Srinivas VV (2008) Regional frequency analysis of precipitation using large-scale atmospheric variables. J Geophys Res—Atmos 113:D24110. https://doi.org/10.1029/2008JD010412
33. Shepard D (1968) A two-dimensional interpolation function for irregularly spaced data. In: Richard BB, Arthur MR (eds) 23rd ACM national conference. Association for Computing Machinery, New York, pp 517–524 (1968). https://doi.org/10.1145/800186.810616
34. Shukla J (1987) Interannual variability of monsoons. In: Fein JS, Stephens PL (eds) Monsoons, Chapter 14, pp 399–464. Wiley, New York (1987)
35. Singh G, Panda RK, Nair A (2020) Regional-scale trend and variability of rainfall pattern over agro-climatic zones in the mid-Mahanadi River basin of eastern India. J Hydro-Environ Res 29:5–19. https://doi.org/10.1016/j.jher.2019.11.001
36. Srinivas VV (2013) Regionalization of precipitation in India—a review. J Indian Inst Sci 93(2):153–162 (2013). http://eprints.iisc.ac.in/id/eprint/47265
37. Tobler W (1970) A computer movie simulating urban growth in the Detroit region. Econ Geogr 46(2):234–240. https://doi.org/10.2307/143141
38. Verma S, Prasad AD, Verma MK (2021) Trend analysis and rainfall variability of monthly rainfall in Sheonath River Basin, Chhattisgarh. In: Pathak KK, Bandara JMSJ, Agrawal R (eds) Recent trends in civil engineering. Lecture notes in civil engineering, vol 77. Springer, Singapore, pp 777–790. https://doi.org/10.1007/978-981-15-5195-6_58

39. Verma S, Prasad AD, Verma MK (2022) Trends of rainfall and temperature over Chhattisgarh during 1901–2010. In: Rao CM, Patra KC, Jhajharia D, Kumari S (eds) Advanced modelling and innovations in water resources engineering. Lecture Notes in Civil Engineering, vol 176. Springer, Singapore, pp 3–19. https://doi.org/10.1007/978-981-16-4629-4_1
40. Waller LA (2009) Detection of clustering in spatial data. In: Fotheringham AS, Rogerson PA (eds) The SAGE handbook of spatial analysis. Thousand Oaks, London, SAGE Publications, pp 299–320. https://doi.org/10.4135/9780857020130.n16
41. Wotling G, Bouvier C, Danloux J, Fritsch JM (2000) Regionalization of extreme precipitation distribution using the principal components of the topographical environment. J Hydrol 233(1–4):86–101. https://doi.org/10.1016/S0022-1694(00)00232-8
42. Yin Y, Pan X, Yang X, Wang X, Wang G, Sun S (2019) Spatiotemporal changes and frequency analysis of multiday extreme precipitation in the Huai River Basin during 1960 to 2014. Adv Meteorol 2019. https://doi.org/10.1155/2019/6324878
43. Yuan L, Yang G, Li H, Zhang Z (2016) Spatio-temporal variation analysis of precipitation during 1960–2008 in the Poyang Lake basin, China. Open J Mod Hydrol 6(2):115–127. https://doi.org/10.4236/ojmh.2016.62010

To Study the Effect of Confining Walls on Flexible Circular Particle Using Immersed Boundary Method

Rekha Panghal, Sudeshna Ghosh, and Reeta Bhardwaj

Abstract We researched the impact of the medium bounded with walls on sedimenting flexible circular particle immersed in a Newtonian, incompressible and viscous fluid. The fluid-structure interaction was studied using Immersed boundary method (IBM). We concluded that the settling velocity (terminal velocity) of the particle is directly proportional to the gap between the confining walls, i.e. wall gap. We further observed that by increasing the flexibilities of the particle, the corresponding settling velocity of the particle also increases. It was also found that by increasing the wall gap, the distortion of the flexible circular particle also increases.

Keywords Immersed boundary method · Flexible · Viscosity · Velocity · Pressure · Fluid

1 Introduction

The major focus of this research is to examine in two dimensions the impact of the medium bounded with walls on the immersed flexible circular particle in a bounded medium infused with Newtonian, incompressible and viscous fluid. The interaction between the fluid and immersed structure has been captured by using the immersed boundary method (IBM).

Sedimentation of flexible particles is encountered in different areas, such as the clinical application of flexible needles [1], settling of floating particles with shapes of different flexibilities in manufacturing industries [2], procedure of diffusion of carbon nanotubes which are used as reinforcing filament [3] and in the analysis of the mash and paper industries squander water [4], corrosion of pipelines and food chain in the rivers [5], etc.

R. Panghal · S. Ghosh (✉) · R. Bhardwaj
Amity School of Applied Sciences, Amity University Haryana, Gurgaon, India
e-mail: sudeshnagh108@gmail.com

R. Bhardwaj
e-mail: rbhardwaj@ggn.amity.edu

© The Author(s), under exclusive license to Springer Nature Singapore Pte Ltd. 2023

K. R. Reddy etal. (eds.), *Recent Advances in Sustainable Environment*, Lecture Notes in Civil Engineering 285, https://doi.org/10.1007/978-981-19-5077-3_4

To study the current research, Immersed boundary method has been implemented. The method was first used for simulating the motion of heart valves by Charles Peskin in 1972. Various fluid-structure interaction problems including biological and engineering problems have been studied through IBM [6–11]. For solving sedimentation-related problem, many of the authors [12–17] have used IBM.

It has been a topic of interest for researchers on how the confining wall affects the sedimenting rigid particles [12, 18–20] but to the best of the knowledge of the authors till date the effect of the confining wall on flexible particle has not been studied. The novelty of the work can be divided into two different categories. First of all, researchers have not studied the wall effect on settling flexible particle and also IBM has not been implemented for studying flexible particles.

2 Immersed Boundary Method (IBM)

The numerical approach considered for studying the current research is immersed boundary method. This method is both a fluid-structure interaction calculating mathematical formulation and numerical scheme with the assumption of fluid being viscous, Newtonian and incompressible. Fluid and the immersed structure interact with each other with the help of the Dirac delta function. In this paper, we will only be reporting the governing equations. The equations are already well documented in [12].

2.1 Governing Equations

In this subsection, the delta function formulation of the studied problem is discussed. The following parameters and variables used in the equations are listed as follows:

Ω = Domain of fluid
Γ = Structure
$\Delta\rho$ = Difference between the fluid and structure density
ρ_f = fluid density
μ = viscosity of the fluid
v = velocity of fluid
F_{IB} = Force density
$\mathbf{x} = (x, y)$ Eulerian coordinates
$\mathbf{s}$ = parametrization of the immersed structure Γ.

To calculate the fluid motion, the incompressible Navier-Stokes equation is implemented.

$$\rho_f \frac{\partial \mathbf{v}}{\partial t} + \rho_f \mathbf{v} \cdot \nabla \mathbf{v} = \mu \nabla^2 \mathbf{v} - \nabla p + \mathbf{f}_{IB} + \mathbf{f}_{Gr}. \tag{1}$$

$$\nabla \cdot \mathbf{v} = 0. \tag{2}$$

Effect of the particle on the fluid is designated by $\mathbf{f}_{IB}(\mathbf{x}, t)$ and is indicated in Eq. 3:

$$\mathbf{f}_{IB} = \int_{\Gamma} \mathbf{F}_{IB}\, \delta(\mathbf{x} - \mathbf{X})\, d\mathbf{s}. \tag{3}$$

In this study, we take the added lagrangian mass, $M(s)$, which has been considered constant, and also in the model, we assume that the density difference $\Delta\rho$ is much more smaller than ρ_f. Therefore, the density of the fluid-structure composite material is $\rho(x, t) = \rho_f + \Delta\rho(x, t)$, whereas $\Delta\rho$ is expressed in the way shown in [12].

$$\Delta\rho(x, t) = \int_{\Gamma} M(s)\delta(\mathbf{x} - \mathbf{X}(s, t))ds. \tag{4}$$

The settling term due to gravity $\mathbf{f}_{Gr}(\mathbf{x}, t)$ is represented by Eq. 5:

$$\mathbf{f}_{Gr} = -g\hat{k}\,\Delta\rho = -g\hat{k}\int_{\Gamma} M(\mathbf{s})\,\delta(\mathbf{x} - \mathbf{X})\,d\mathbf{s}, \tag{5}$$

where $g = 980$ (cm/s^2) is the gravitational acceleration and $\hat{k} = (0, 1)$ is the vertical unit vector. Finally, the immersed boundary is assumed to move according to

$$\frac{\partial \mathbf{X}}{\partial t} = \int_{\Omega} \mathbf{v}(x, t)\delta(\mathbf{x} - \mathbf{X}(s, t))d\mathbf{x} \tag{6}$$

which is simply the "no-slip" boundary condition.

For the numerical implementation of the above-mentioned governing equation, there are numerous versions of the delta function accessible in IBM literature. In this work, we have used cosine delta function [6, 21, 22].

Before winding up this section, we will briefly explain the algorithm of immersed boundary method.

1. We calculate the force generated by the structure immersed in the fluid (F_{IB}).
2. Spreading of the force generated by the structure to the fluid grid points by using a discrete version of the delta function.
3. To compute the fluid motion by using the incompressible Navier-Stokes equation by implementing Chorin's split step scheme.
4. Evolving the structure by using the First-order Forward Euler scheme.

2.2 Problem Setup for Flexible Circular Particle

Figure 1 illustrates the geometry of the current problem. The size of the fluid domain considered here is $L_x \times L_y$ along with two vertical walls placed at a gap ΔW from each other. The circular flexible particle is positioned along the centreline of the channel.

2.3 Modeling of Flexible Circular-Shaped Particle

The particle is constituted with Lagrangian points which are lying on its periphery and all through its interior. The unstructured mesh is made with the help of a triangular mesh code generator called Distmesh [23] (refer Fig. 2). The immersed structure points are the nodes of the triangulation and the nodes are connected by edges that represent the network of springs. We have varied the flexibility of the particle by varying the stiffness parameter σ_c of the spring connecting the edges and it has been assumed to be constant for all edges. The forces acting on a particular IB point are discussed and well documented in [12].

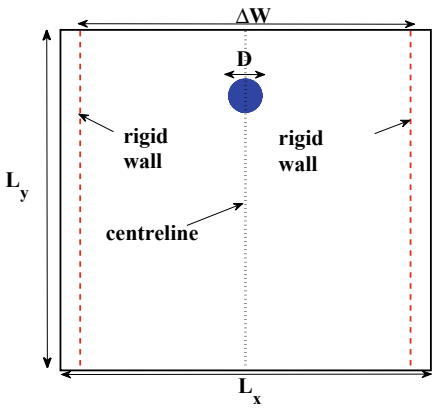

Fig. 1 Problem setup for gravitational settling of flexible circular particle

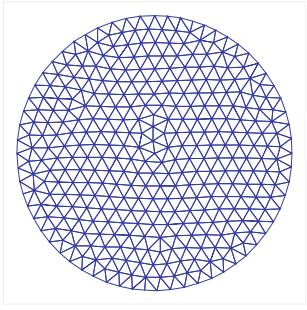

Fig. 2 Uniform triangular mesh generated by `distmesh2d` for a circular particle

3 Numerical Results

In the section on numerical results, we will be reporting the simulations done by using IBM for the above-mentioned problem setup discussed in Sect. 2.2. For our study, we have considered two viscosities $\mu = 1$ (g/cm s) and $\mu = 0.01$ (g/cm s). We have kept the density difference between the structure and the fluid at $\Delta\rho = 0.16$ (g/cm^3). The particle flexibilities considered in this study belong to the range $\sigma_c = [0.16, 160000]$ (g/cm s^2). The fluid domain considered here are $L_x = 1$, $L_y = 16$ (cm) and ΔW has been varied from [0.20, 0.98] (cm). We have also done an analysis on the deformation of the particle.

In the coming subsection, we will perform a sensitivity study by considering two different viscosities of the fluid.

3.1 Sensitivity Study of Flexible Circular Particle for Varying Viscosities

In this section, we will be investigating how the change in fluid viscosity affects the wall and flexible particle interaction. The results obtained are summarized in Table 1 and Fig. 3 for $\mu = 1$ and Table 2 and Fig. 4 for $\mu = 0.01$.

The following conclusion can be made from the tables and figures:

Table 1 Settling velocities (V_c) of the particles of variable flexibilities for different values of wall gaps for $\mu = 1$ and $\Delta\rho = 0.16$

σ_c (g/cm s^2)	ΔW			
	0.20	0.24	0.48	0.98
160000	0.0065	0.0116	0.0550	0.1081
1.6	0.0076	0.0157	0.0608	0.1165
0.16	0.0142	0.0420	0.1027	0.1391

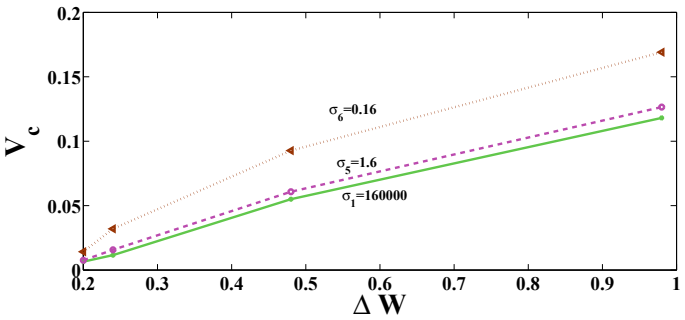

Fig. 3 Dependence of settling velocity (V_c) of the circular particle on ΔW for different particle flexibilities with $\mu = 1$

Table 2 Settling velocities (V_c) of the particles of variable flexibilities for different values of wall gap for $\mu = 1$ and $\Delta\rho = 0.16$

σ_c (g/cm s^2)	ΔW			
	0.20	0.24	0.48	0.98
160000	0.6214	1.0797	2.2969	4.3088
1.6	0.6625	1.8858	2.6301	4.7368
0.16	0.7740	1.5037	3.1527	5.1317

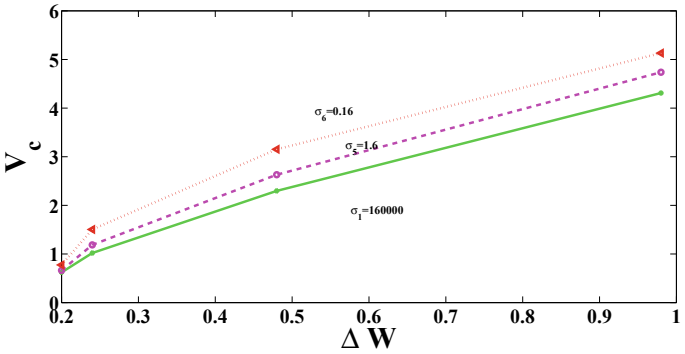

Fig. 4 Dependence of settling velocity (V_c) of the circular particle on ΔW for different particle flexibilities with $\mu = 0.01$

– For a fixed flexibility, as the wall gap increases, the settling velocity increases. This result which we have obtained is in tune with the results obtained for the wall effect experienced by rigid circular particle [12, 19, 20]. The physical justification behind this result is that the confining walls exert an extra retarding effect on the particle settling under gravity which in turn lowers the magnitude of the settling velocity when compared with the unbounded domain under the same conditions.
– For a fixed wall gap, as the flexibility increases, the settling velocity also increases.
– Also we have observed that when viscosity increases, the settling velocity decreases for a fixed wall gap and flexibility. The obtained results are justified since it is a verifiable truth as the viscosity of the particle escalates, the settling velocity decreases as shown in [12] for rigid particles.

3.2 Distortion Analysis

In this section, we have analyzed the deformation experienced by the particle for different scenarios discussed above in Sect. 3.1. The distortion of flexible circular particle has been calculated in the following way.

– The initial and final coordinate of the boundary represented by $(X_{(init,bd)}, Y_{(init,bd)})$, $(X_{(f,bd)}, Y_{(f,bd)})$, respectively, are calculated.
– Calculate the difference between the initial and final coordinates for all boundary nodes. $D_1(i) = \left(X_{(init,bd)}(i) - X_{(f,bd)}(i)\right)^2 + \left(Y_{(init,bd)}(i) - Y_{(f,bd)}(i)\right)^2$.
– Then distortion is calculated by root mean square: $Distortion_1 = \sqrt{\frac{1}{n_b}\sum_{i=1}^{n_b} D_1(i)} \times 100$ where n_b is the number of boundary points.

Distortions experienced for different values of wall gap with different flexibilities range [0.16, 160000] are listed in Tables 3 and 4 for $\mu = 1$ and $\mu = 0.01$, respectively. Distortion is expressed in percentage.

For better visualization, we have shown the deformation experienced by the particle for the case $\mu = 0.01$ in Figs. 5, 6, 7 and 8.

The following inferences can be made about the distortion experienced by the particle:

– As the flexibilities of the particle increases, the distortion also increases for a fixed wall gap and a given viscosity.
– For a fixed wall gap and flexibility of the particle, the distortion experienced by the particle increases as the viscosity of the fluid decreases.

Table 3 Distortion analysis for different values of wall gaps and $\mu = 1$ with flexibilities range [0.16, 160000]

σ_c (g/cm s^2)	ΔW			
	0.20	0.24	0.48	0.98
160000	0.0009	0.0013	0.0056	0.0082
1.6	0.5325	0.6686	4.8172	5.1225
0.16	7.1878	8.2963	9.1641	10.1935

Table 4 Distortion analysis for different values of wall gap and $\mu = 0.01$ with flexibilities range [0.16, 160000]

σ_c (g/cm s^2)	ΔW			
	0.20	0.24	0.48	0.98
160000	0.0013	0.0018	0.3176	0.6512
1.6	2.3774	2.8371	4.9249	5.7487
0.16	5.6326	5.8552	6.2725	40.9735

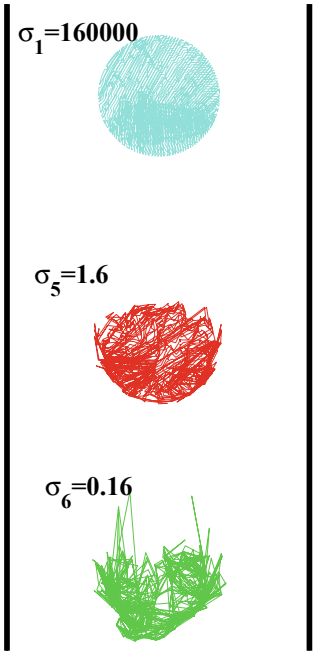

Fig. 5 Distortion in the particle shape for different flexibilities with wall gap $\Delta W = 0.20$ and $\mu = 0.01$

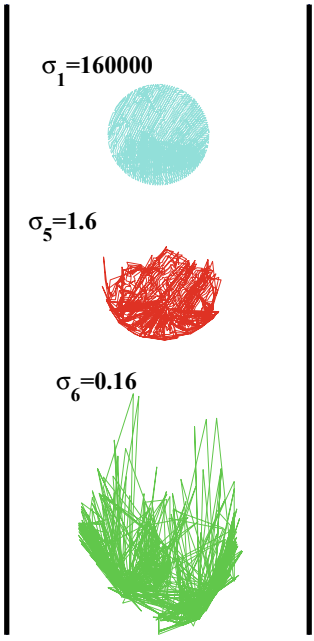

Fig. 6 Distortion in the particle shape for different flexibilities with wall gap $\Delta W = 0.24$ and $\mu = 0.01$

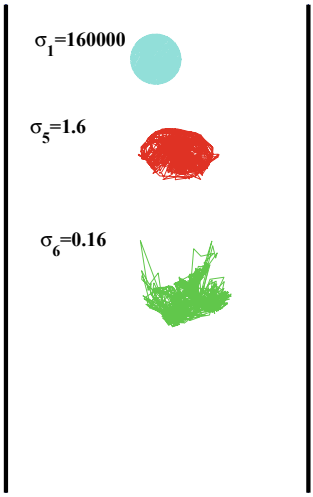

Fig. 7 Distortion in the particle shape for different flexibilities with wall gap $\Delta W = 0.48$ and $\mu = 0.01$

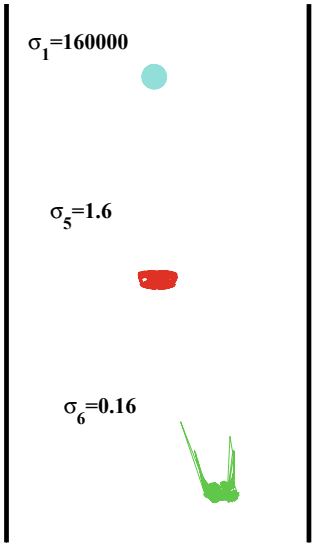

Fig. 8 Distortion in the particle shape for different flexibilities with wall gap $\Delta W = 0.98$ and $\mu = 0.01$

4 Conclusions

The main focus of this research was to study the effect of confining walls on a flexible circular particle using immersed boundary method. The key observations done are that for a fixed flexibility as the wall gap increases, the settling velocity increases. This result is in tune with already obtained results for the wall effect on the particles which are rigid in nature. For a constant wall gap and density difference,

as the flexibility of the particle increases, correspondingly the settling velocity also increases. The results obtained in the study are physically justified.

The study done ascertains the validity of immersed boundary method for studying flexible sedimenting particles. In the future, the authors will like to extend the study for different shapes of sedimenting particles like semi-torous, planktonic-shaped particles. Also in the future, the authors will like to investigate the dynamics of two interacting flexible particles under the effect of confining walls.

References

1. Cai C, Sun C, Han Y, Zhang Q (2020) Clinical flexible needle puncture path planning based on particle swarm optimization. Comput Methods Programs Biomed 193:105511. https://doi.org/10.1016/j.cmpb.2020.105511
2. Li L, Manikantan H, Saintillan D (2013) The sedimentation of flexible filaments 735:705–736. https://doi.org/10.1017/jfm.2013.512
3. Jiang L, Gao L, Sun J (2003) Production of aqueous colloidal dispersions of carbon. J Colloid Interface Sci Nanotubes 260:89–94. https://doi.org/10.1016/S0021-9797(02)00176-5
4. Kamali M, Khodaparast Z (2015) Review on recent developments on pulp and paper mill wastewater treatment. Ecotoxicol Environ Saf 114:326–342. https://doi.org/10.1016/S0021-9797(02)00176-5
5. Gooday AJ, Turley CM (1990) Responses by benthic organisms to inputs of organic material to the ocean floor: a review. Philos Trans R Soc Lond Ser A Math Phys Sci 331:119–138. https://doi.org/10.1098/rsta.1990.0060
6. Peskin CS (2002) The immersed boundary method. Acta Numer 11:1–39. https://doi.org/10.1017/S0962492902000077
7. Fogelson AL (1984) A mathematical model and numerical method for studying platelet adhesion and aggregation during blood clotting. J Comput Phys 56:111–134. https://doi.org/10.1016/0021-9991(84)90086-X
8. Bottino DC, Fauci LJ (1998) A computational model of ameboid deformation and locomotion. Eur Biophys J 27:532–539. https://doi.org/10.1007/s002490050163
9. Arthurs KM, Moore LC, Peskin CS, Pitman EB, Layton HE (1998) Modeling arteriolar flow and mass transport using the immersed boundary method. J Comput Phys 147:402–440. https://doi.org/10.1006/jcph.1998.6097
10. Fauci LJ, Peskin CS (1988) A computational model of aquatic animal locomotion. J Comput Phys 77:85–108. https://doi.org/10.1016/0021-9991(88)90158-1
11. Dillon RH, Fauci LJ (2000) An integrative model of internal axoneme mechanics and external fluid dynamics in ciliary beating. J Theoret Biol 207:415–430. https://doi.org/10.1006/jtbi.2000.2182
12. Ghosh S, Stockie JM (2015) Numerical simulations of particle sedimentation using the immersed boundary method. Commun Comput Phys 18(2):380–416. https://doi.org/10.4208/cicp.061113.050115a
13. Ghosh S, Kumar M (2020) Study of drafting, kissing and tumbling process of two particles with different sizes using immersed boundary method in a confined medium. Math Comput Simulat 177:341–357. https://doi.org/10.1016/j.matcom.2020.04.029
14. Wang L, Guo ZL, Mi JC (2014) Drafting, kissing and tumbling process of two particles with different sizes. Comput Fluid 96:20–34. https://doi.org/10.1016/j.compfluid.2014.03.005
15. Ghosh S, Kumar M (2018) Study of drafting, kissing and tumbling process of two particles with different densities using immersed boundary method in a confined medium. J Adv Res Appl Mech Comput Fluid Dyn 5:15–22

16. Hopkins MM, Fauci LJ (2002) A computational model of the collective fluid dynamics of motile micro-organisms. J Fluid Mech 455:149–174. https://doi.org/10.1017/S0022112001007339
17. Uhlmann M (2005) An immersed boundary method with direct forcing for the simulation of particulate flows. J Comput Phys 209:448–476. https://doi.org/10.1016/j.jcp.2005.03.017
18. Chhabra RP, Agarwal S, Chaudhary K (2003) A note on wall effect on the terminal falling velocity of a sphere in quiescent Newtonian media in cylindrical tubes. Powder Technol 129:53–58. https://doi.org/10.1016/S0032-5910(02)00164-X
19. Takaisi Y (1995) The drag on a circular cylinder moving with low speeds in a viscous liquid between two parallel walls. J Phys Soc Jpn 10:685–693. https://doi.org/10.1143/JPSJ.10.685
20. Pianet G, Arquis E (2008) Simulation of particles in fluid: a two-dimensional benchmark for a cylinder settling in a wall-bounded box. Eur J Mech-B/Fluids 27:309–321. https://doi.org/10.1016/j.euromechflu.2007.07.001
21. Leveque R, Li Z (1994) The immersed interface method for elliptic equations with discontinuous coefficients and singular sources. SIAM J Numer Anal 31(4):1019–1044. https://doi.org/10.1137/0731054
22. Roma AM, Peskin CS, Berger MJ (1999) An adaptive version of the immersed boundary method. J Comput Phys 152(2):509–534. https://doi.org/10.1006/jcph.1999.6293
23. Persson PO, Strang G (2004) A simple mesh generator in MATLAB. SIAM Rev 46(2):329–345. https://doi.org/10.1137/S0036144503429121

Time Series Modelling and Forecasting of Mean Annual Rainfall Over MRP Complex Region Chhattisgarh Associated with Climate Variability

Shashikant Verma, A. D. Prasad, and Mani Kant Verma

Abstract The purpose of time series analysis is to model random processes and forecast future series using historical data. Nine rain gauge stations over the MRP complex were studied using a single-variable autoregressive integrated moving average model, compared to CORDEX South Asia experiments conducted under scenarios RCP 4.5 and RCP 8.5, respectively. This study focusses on determining the extreme rainfall indices by using historical rainfall data set from 9 rain gauge stations from 1994 to 2018 for 24 years and a short-term future forecast of the behaviour of rainfall with the help of the ARIMA model. Interestingly, the mean annual rainfall for all nine stations over MRP complex region chhattisgarh is the best-fitted ARIMA model (1,0,1). Climate model CCCma-Can_ESM2 has good relation concerning forecasted mean annual rainfall. This model is considered appropriate for short-term forecasting the mean annual rainfall in the study area for the next 20 years to assist decision-makers and policymakers in setting water demand, storage, distribution, water resource managers, producers, and urban engineers may use this knowledge to determine water supply and disaster management priorities.

Keywords ARIMA model · CORDEX · Climate variability · Time series modelling · Forecasting · MRP complex

S. Verma (✉) · A. D. Prasad · M. K. Verma
Civil Engineering Department, National Institute of Technology Raipur, Raipur, Chhattisgarh, India
e-mail: shashiv50@gmail.com

A. D. Prasad
e-mail: adprasadiit@gmail.com

M. K. Verma
e-mail: manikverma.ce@nitrr.ac.in

© The Author(s), under exclusive license to Springer Nature Singapore Pte Ltd. 2023

K. R. Reddy et al. (eds.), *Recent Advances in Sustainable Environment*, Lecture Notes in Civil Engineering 285, https://doi.org/10.1007/978-981-19-5077-3_5

1 Introduction

Climate change is widely recognized as a significant problem in today's world. Global changes are the integrated form of regional-scale changes. Moreover, the regional-scale changes are much important than the global changes, whether intensities are negative or positive. Rainfall is a most critical hydrologic component that has a significant impact on human life and the socio-economic development of any country. Most of the fresh water come from rainfall, making suitable conditions for our ecosystem, irrigation, and hydropower plants. Water is one of the prime important and valuable natural resources which requires special attention because excess or extended absence of rainfall can lead to a condition of flooding and drought, respectively [1]. As the climate changes at an alarming rate, freshwater availability in many streams will decline shortly [2]. Due to the significant economic and social impacts of extreme weather events, there has been a significant increase in scientific interest in climate change. It is critical to examine changes in variability and magnitude of extreme behaviour as well as long-term trends and fluctuations in climatic signals as part of climate change research [3]. In context of current climate models, this framework has become increasingly popular, because extreme events are expected to increase in the twenty-first century. Understanding of climate variability and patterns is critical in many areas, accurate forecasts and predictions of climate variables are also essential for policymakers, planners, and others involved in water resource management and climate change adaptation. In addition to predicting future water supply and demand, Forecasting Monthly Maximum Temperaturesfuture flood and drought risks, maintaining reservoir water levels, and preparing for calamities, and predictions can help improve water resource allocation and management [4–7]. The Mann–Kendall test, the Kruskal–Walli test, and Sen's slope estimator are amongst the many parametric and nonparametric methods documented in the literature [8–11].

Another important tool used in climate prediction is time series modelling, which is used to predict changes in a climate time series over the short and long term (Nury et al. 2019) [12]. It is common practice to use time series analysis for monitoring and forecasting, as well as for providing feedback. In a variety of fields, the time series analyzes are typical scientific methodologies in fields like regional development and planning, business management, meteorology, market forecasting, hydrology, pollution control, astronomy, and oceanography. In order to examine patterns in time series data and make forecasts, many different techniques have been developed, including moving averages, autoregressive models, autoregressive and moving averages, combined models, exponential smoothing, seasonal decomposition, neural networks, and spectral analysis [13–15]. Precipitation time series, in particular, are notoriously difficult to forecast because they are made up of a variety of different components, including periodic patterns, cyclic behaviour, and white noise (randomness).

Time series analysis is to relate features of the stochastic process and the properties of the historical data set. In this view, time series analysis has been done to detect the change in the rainfall pattern of the state. In Chhattisgarh, rainfall decreases

during the pre-monsoon, annual, and monsoon seasons [16, 17]. Also reported that over many states in India like Chhattisgarh, there is a decline in rainfall annually. However, at the regional level and basin wise, no research has been done yet. So, in this context, it was necessary to detect trends at the micro-level in the state. A paramount tool for modelling and foreseeing rainfall data is time series analysis [12, 18]. Prediction of rainfall is equally important and demanding with relevant to the agriculture sector. ARIMA model is used to the greatest extent in hydrologic and climatic time series modelling [19, 20]. As the data hold a methodical pattern and some random noise called error, it is usually not easy to identify the pattern under time series analysis patterns can be of two classes: (1) trend and (2) seasonality. A linear or nonlinear component that does not repeat and changes with time is trend but seasonality repeats itself at systematic time intervals. Also, this technique includes some methods for filtering out the noise to make the pattern more salient. Thus, the objectives of the study are (1) to assess the extreme events of mean annual rainfall over the study area, (2) to predict the near term, mean annual rainfall, i.e. 2019–2038 relative of baseline period 1994–2018, and (3) comparative study between predicted rainfall and mean annual rainfall of CORDEX climate models over the study region.

2 Study Area and Data Used

The Mahanadi is a major river that originates in Chhattisgarh's Dhamtari district and flows into the Bay of Bengal. From its origin to its outflow into the Bay of Bengal, the river's total length is 851 km. The basin of the Mahanadi is split into three sub-basins, namely the upper, middle, and lower Mahanadi. The MRP complex, located in the upper Mahanadi basin drained by the Sheonath River, is a plain region with an elevation range of 200–300 m, surrounded by higher hills between 300 and 400 m high on its west. Having an area of upper Mahanadi basin (UMB) is around 29796.65 sq. km. The MRP complex in UMB consists of 9 rain gauge stations that are shown in the figure. With summer temperatures of about 29 °C and winter temperatures of 21 °C, the climate in the Mahanadi River region is predominantly sub-tropical. Most of the precipitation are in the period from July to September (800 to over 1200 mm) and less than 50 mm from January to February [19–22] (Fig. 1)

The daily rainfall data have been collected from the State Data Centre, Water Resources Department of Chhattisgarh, Raipur, for 24 years from 1994–2018. The consistency test is used to assess whether the behaviour of the process that produces a section of time series data is taken into account. The standard normal homogeneity test (SNHT) is used for this reason, and the station is considered compatible if the p-value is >0.05. The stations such as Sikaser, Gurur, Sarangpal, and Kanker having p-value consist of less than 0.5, thus the above stations have been discarded for the further analysis (refer Table 1). A coordinated regional downscaling experiment (CORDEX) South Asia regional climate model has been downloaded from (https://esgf-data.dkrz.de/search/cordex-dkrz/) as shown in Table 2 and extreme rainfall indicator along with indicator name, description, and their unit of measurements as depicted in Table 3 (Fig. 2).

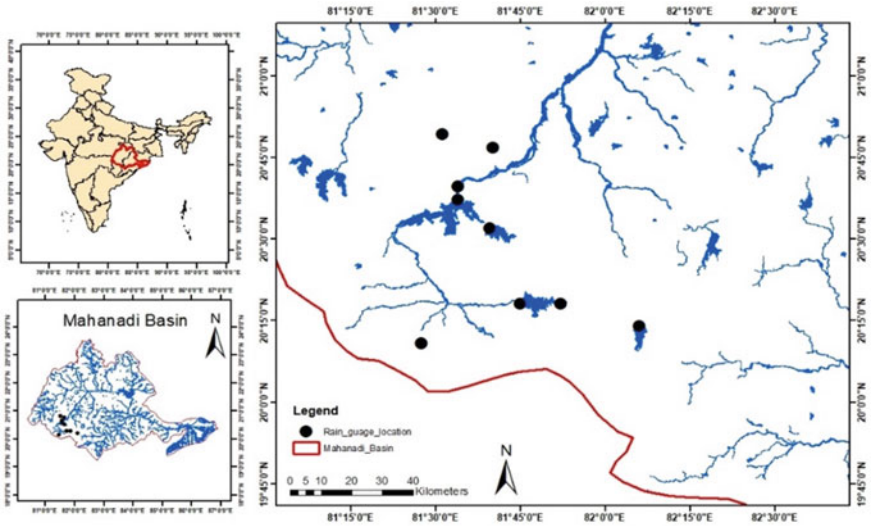

Fig. 1 Study area map

Table 1 List of rainfall stations and their locations over the study area

S. No	Station name	Location	P-value
1	Birgudi	(20.30 N-81.87E)	0.210
2	Chatti	(20.78 N-81.67E)	0.204
3	Dudhawa	(20.18 N-81.46E)	0.271
4	Dhamtari	(20.82 N-81.52E)	0.846
5	Gangrel	(20.62 N-81.56E)	0.445
6	Khajrawan Kanker	(20.30 N-81.75E)	0.344
7	Moorumsilli	(20.53 N-81.66E)	0.132
8	Rudri	(20.63 N-81.56E)	0.942
9	Sondur	(20.23 N-82.10E)	0.448
10	*Sikasar*	*(20.52 N-82.32E)*	*0.028*
11	*Gurur*	*(20.68 N-81.40E)*	*0.034*
12	*Sarangpal*	*(20.26 N-81.49E)*	*0.021*
13	*Kanker*	*(20.30 N-81.52E)*	*0.042*

3 Methodology

3.1 Time Series Modelling and Forecasting

In the time series models, data may be in different forms and can represent unalike stochastic processes [23]. A time series without trends or seasonal effects means

Table 2 List of CORDEX South Asia RCM experiments

CORDEX South Asia RCM	CORDEX modelling centre	Driving CMIP-5 AOGCM
IITM_RegCM4	Centre for Climate Change Research (CCCR), Indian Institute of Tropical Meteorology (IITM), India	Can_ESM-2
		GFDL_ESM2M
		CNRM_CM-5
		MPI_ESM_MR
		IPSL_CM5A_LR
		CSIRO_Mk-3.6
MPI_CSC_REMO2009	Climate Service Centre (CSC), Germany	MPI_ESM_LR

Table 3 List of extreme rainfall indicators

Extreme rainfall indicator	Indicator name	Description	Units
PRCP_TOT	Annual total rainfall	Annual total rainfall from days > 2.5 mm	mm
R_D	Days with rainy condition	Number of days with rainfall > 2.5 mm	days
SD-II	Intensity index	"Basic day-by-day intensity list. Normal precipitation on wet days (DR $\geq$ 1 mm)"	mm per day
R_1day maximum	1_day maximum rainfall	"Most extreme 1-day storm precipitation"	mm
R_5day maximum	5_day maximum rainfall	"Most extreme 5-day storm precipitation"	mm
R_mod	Days with moderate rainfall	"Number of days with annual precipitation $\geq$ 7.5 mm and < 64.5 mm, respectively"	days
R_heavy	Days with heavy rainfall	"Number of days with annual precipitation $\geq$ 64.5 mm and < 124.5 mm, respectively"	days
CDD	Consecutive dry days	"Successive dry days. The greatest number of continuous dry days (DR < 1 mm)"	days
CWD	Consecutive wet days	"Most number of successive days when rainfall $\geq$ 2.5 mm"	days

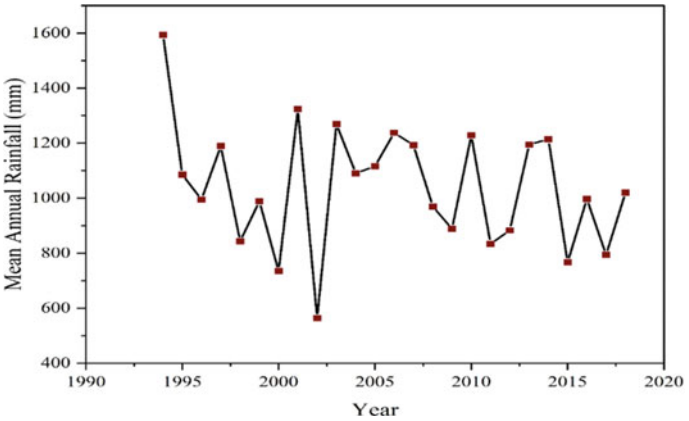

Fig. 2 Pictorial representation of observed mean annual rainfall for MRP complex region Chhattisgarh

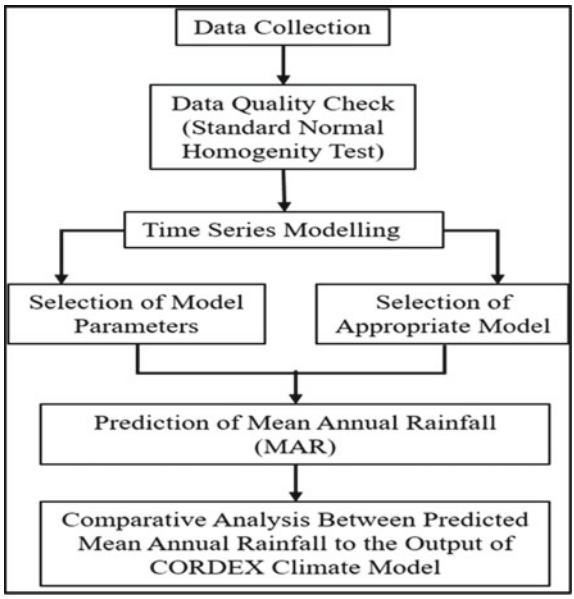

Fig. 3 Methodology flow chart

trends or seasonal effects, if any, have been removed from the series previously [24] (Fig. 3).

3.1.1 Autoregressive Moving Average (ARMA) Models

An ARMA model of order p and q combines the AR and MA models of order p and q. Mathematically; the AR(p) model can be represented as

Here, y_t is the actual value and ε_t is a random error (or random shock) at period t. $\varphi_i (i = 1, 2\ldots, p)$, y_t, and ε_t are model parameters, and c is a constant. For estimating AR parameters for any time series, generally, the Yule–Walker equations are used.

$$y_t = \mu + \sum_{j=1}^{q} \theta_j \varepsilon_{t-j} + \varepsilon_t = \pi + \theta_1 \varepsilon_{t-1} + \theta_2 \varepsilon_{t-2} + \cdots\cdots\cdots + \theta_q \varepsilon_{t-q} + \varepsilon_t \quad (2)$$

Here, μ (mean value of the series) and θ_j $(j = 1, 2\ldots, q)$ are the model parameters. Fitting an AR model is quite easy than fitting an MA model to a time series, because the random errors in MA are unforeseeable.

The combination of autoregressive (AR) and moving average (MA) models is known as the ARMA models. An ARMA (p, q) model is represented as

$$y_t = c + \varepsilon_t + \sum_{i=1}^{p} \varphi_i y_{t-i} + \sum_{j=1}^{q} \theta_j \varepsilon_{t-j} \quad (3)$$

Here, the orders p, q represent to terms of AR and MA, respectively. The lag or backshift operator is defined as $L\ y_t = y_{t-1}$.

AR(p) model:

$$\varepsilon_t = \varphi(L) y_t \quad (4)$$

MA(q) model:

$$y_t = \theta(L) \varepsilon_t \quad (5)$$

ARMA (p, q) model:

$$\varphi(L) y_t = \theta(L) \varepsilon_t \quad (6)$$

$$\varphi(L) = 1 - \sum_{i=1}^{p} \varphi_i L^i \quad (7)$$

$$\theta(L) = 1 + \sum_{j=1}^{q} \theta_j L^j \quad (8)$$

3.1.2 Autocorrelation and Partial Autocorrelation Functions

ACF and PACF analysis are necessary to determine a proper model. Both reflect the relationship between observations of a time series. In time series modelling, plotting the ACF and PACF against successive time lags is useful for calculating p and q.

The autocorrelation coefficient (ACF) at lag k is defined as

$$\rho_k = \frac{\gamma_k}{\gamma_0} \tag{9}$$

Here, for the time series, *x(t)* for $t = 0,1, 2, \ldots$, γ_k is defined as autocovariance at lag k and γ_0 is autocovariance at lag 0. As shown, it is clear that the coefficient of the autocorrelation function (ACF) is dimensionless. In another term, the association between an observation at lag k and the current observation is measured by the partial autocorrelation function (PACF). The optimum order of an AR process can be identified from the PACF plot, and the ACF plot can identify the optimum order of an MA term.

3.1.3 Autoregressive Integrated Moving Average Model

Stationary time series data can be used with ARMA models. However, data with a pattern or seasonality may be non-stationary. To deal with non-stationarity, the ARIMA model is proposed, which is a simplified version of an ARMA model. Differencing of the data is essential in ARIMA models to remove non-stationarity.

$$\varphi(L)(1 - L)^d y_t = \theta(L)\varepsilon_t \tag{10}$$

$$\left(1 - \sum_{i=1}^{p} \varphi_i L^i\right)(1 - L)^d y_t = \left(1 + \sum_{j=1}^{q} \theta_j L^j\right)\varepsilon_t \tag{11}$$

Here, order p of AR, d of I, and q of MA terms of the model are integers. The integer d accounts for the level of difference. Generally, $d = 1$ is enough in most cases. When $d = 0$, then it comes to an ARMA (p, q) model and ARIMA (0,1,0), i.e. $y_t = y_{t-1} + \varepsilon_t$ is known as the random walk model. The best model selection method starts with deciding the optimum model parameters. Various parameters are used to evaluate the best model order, which minimizes either the Akaike information criterion (AIC). The method of maximum likelihood is used for optimization. Yule–Walker equation was used for the primary estimation of model parameters.

3.1.4 Bias Correction of Climate Model

Biases are systemic errors caused by climate models and algorithms of estimation used in remote sensing [25], i.e. inaccuracy within the system [24]. Bias is defined as the correspondence averaged over a certain domain and time between a mean forecast and means observation. Bias is used to an error in average precipitation. Bias is the proportional difference between mean simulated output and mean observed value over a given period. Here, we focus on minimizing or removing the bias of precipitation [26]. Mathematically expressed as

$$\mathrm{B_R} = \frac{R_{RCM} - R_{obs}}{R_{obs}} \times 100\% \tag{12}$$

$\mathrm{B_R}$ is biased, $\mathrm{R_{RCM}}$ is the mean precipitation of simulated model output, and $\mathrm{R_{obs}}$ is the mean of observed precipitation values.

3.2 Performance Evaluation Indices

The World Meteorological Organization (WMO) and other investigations have presented the evaluation and comparison of various models that can be compared using graphical representations and numerical computations [2, 27, 28]. The graphical performance indices consists of.

(1) A linear plot of observed and predicted time series for both model and test data set, respectively.
(2) A scatter plot for both observed and predicted mean annual rainfall time series.

In comparison, numerical performance indices related to RMSE, MAE, and MAPE error are given below.

$$\mathrm{RMSE} = \sqrt{\frac{\sum_{i=1}^{N}\left(x_i - \widehat{x_i}\right)^2}{N}} \tag{13}$$

$$\mathrm{MAE} = \frac{1}{N} * \sum_{i=1}^{N}\left|\left(x_i - \widehat{x_i}\right)\right| \tag{14}$$

$$\mathrm{MAPE} = \frac{1}{n} * \sum_{i=1}^{n}\left|\frac{\left(x_i - \widehat{x_i}\right)}{x_i}\right| \tag{15}$$

Here, N = Total number in series, x_i = Actual observed time series, and $\widehat{x_i}$ = Predicted time series.

Table 4 Statistical parameter

Statistical parameter	Mean	Median	Std	Cov	Skewness	Kurtosis	Annual percentage change
	1156.052	1131.222	330.6416	18.07266	0.195117	0.59767	27.61375

4 Results and Discussion

4.1 Extreme Rainfall Indices

The statistical parameters such as mean, standard deviation, kurtosis, coefficient of variation, and annual percentage change were calculated to check the variability of mean annual rainfall in the entire study area as shown in Table 2. Extreme rainfall indices for MRP, complex region as shown in Table 5. Amongst all the rain gauge stations, Chhatti station is showing higher 1-day and 5-day maximum rainfall, i.e. 340 and 746.4 mm, respectively, except Sondur. Continuous dry days over the study period for Chhatti are higher which is 228 days except Dhamtari and Rudri. Number of heavy rainfall days for Chhatti is 67 which is higher as compared to other stations except Birgudi. Apart from that total annual rainfall, days with rainy condition, intensity index, and days with moderate rainfall for Chhatti are slightly differ from others rain gauge stations during study period (Table 4).

4.2 Time Series Modelling

Figure 4a, b represents the plot of the autocorrelation function (ACF) and partial autocorrelation function (PACF) with respect to time lag for observed mean annual rainfall. Figure 4a is used to evaluate the number of autoregressive model parameter which is denoted by p. Similarly, Fig. 4b is used to evaluate the number of moving average model parameter which is denoted by q. Combination of above two parameters time series model can be written as ARMA. Meanwhile introducing the order of differencing to remove the seasonality effect in a time series, which is denoted by d. Thus, the combination of model parameters p, q, and d, the time series model can be written as autoregressive integrated moving average (ARIMA). At the present study, performance evaluation of the ARIMA model in terms of error measure is shown in Table 6. The table indicates that the ARIMA (1,0,1) is the best-fitted model over the study region. The root means squared error for the model data set and test data set for the ARIMA model is 48.73 and 100.71, respectively. Whilst the other performance measures such as MAE, MAPE, and AIC as shown in Table 5. The coefficient of determination (R^2) for the model and test data sets is 0.74 and 0.60, respectively, (see Fig. 5). Based on R^2, test data set considerably satisfactory simulates the model data set, and ARIMA (1,0,1) is an appropriate tool to model and short-term future forecast

Table 5 Extreme rainfall indices of MRP complex region, Chhattisgarh

Indicator name	Birgudi	Chatti	Dhamtari	Dudhawa	Gangrel	Khajrawan Kanker	Moorumsilli	Rudri	Sondur
PRCP_TOT	28,636.4	29,371.6	28,525.34	26,091.55	27,159.05	27,380.21	31,098.8	27,984.15	29,658.61
R_D	1366	1377	1407	1351	1472	1323	1396	1328	1390
SD-II	20.96369	21.33014	20.27387	19.31277	18.45044	20.69555	22.27708	21.0724	21.33713
R_1day Maximum	232	340	247	212.4	262	240	228	252	385.6
R_5day Maximum	319.2	746.4	364.6	602.6	508	367	437	489	780
R_mod	807	838	850	767	828	771	869	913	855
R_heavy	68	67	60	48	60	60	60	56	57
CDD	134	228	277	145	158	119	217	234	155
CWD	11	14	8	11	20	8	8	15	22

of mean annual rainfall. Figure 6 shows the pictorial representation of observed and predicted mean annual rainfall for MRP complex, during 1994–2018. According to Fig. 6, the predicted mean annual rainfall is higher than the observed mean annual rainfall and maximum predicted mean annual rainfall (MAR) occurred in year 1994 is 1700 mm which is slightly higher than observed mean annual rainfall, similarly rest of the years predicted mean annual rainfall is slightly higher than the observed mean annual rainfall. In addition, predicted mean annual rainfall has been observed more variation in year 2000, 2001, 2002, and 2009, respectively, as compared to observed mean annual rainfall.

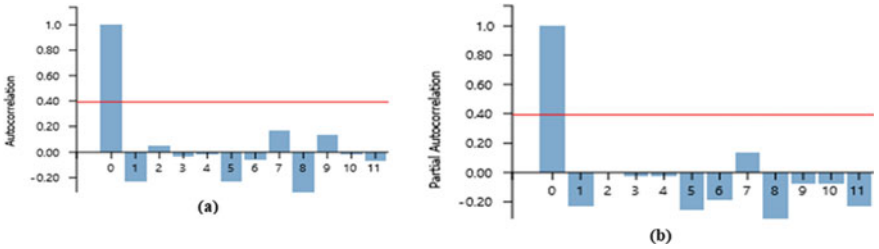

Fig. 4 (**a**, **b**) Plot of the autocorrelation function (ACF) and partial autocorrelation function with respect to time lag

Table 6 Performance evaluation indices

Techniques	Error measure for mean annual rainfall model data set					Error measure for mean annual rainfall test data set				
ARIMA (1, 0, 1)	RMSE	MAE	MAPE	R^2	AIC	RMSE	MAE	MAPE	R^2	AIC
	48.73	177.71	0.196	0.74	271.9	100.71	220.51	0.240	0.60	88.99

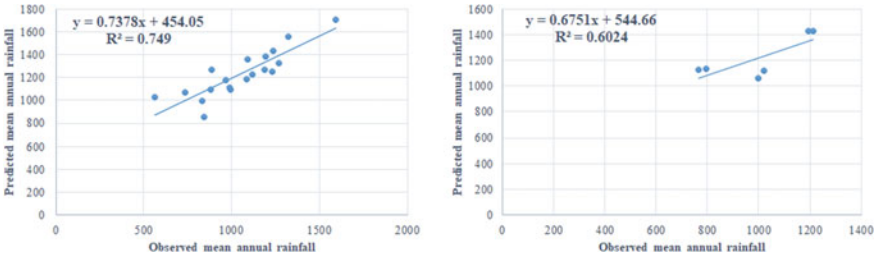

Fig. 5 Linear plot between observed and predicted mean annual rainfall for test data set and model data set, respectively

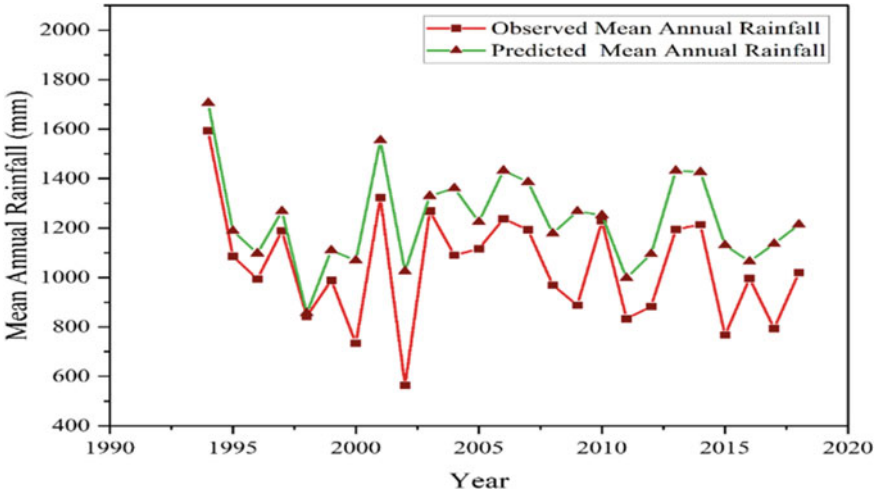

Fig. 6 Pictorial representation of observed and predicted mean annual rainfall for MRP complex region Chhattisgarh

4.3 Forecasting

When the appropriately selected model passes the diagnostic testing process, we estimate the model coefficients, which are then used in the final forecasting stage to calculate new time series data set observations and confidence intervals for expected values based on the previous observations. This section presented the short-term future forecast of the mean annual time series for the rainfall data set of all the stations under MRP complex region Chhattisgarh at a different scenario RCP 4.5 and RCP 8.5 (see Figs. 7 and 8). Table 7 showing the error terms for the CORDEX South Asia climate model concerning forecasted mean annual rainfall. According to Table 7, the CCCma-CanESM2 model having less RMSE, MAE, and MAPE which is 163.51, 612.10, and 0.43 as compared to other models.

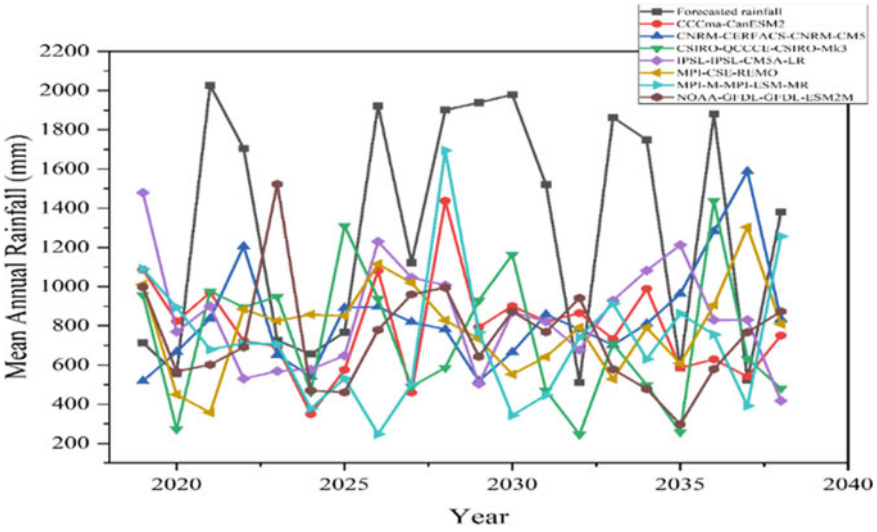

Fig. 7 Projected mean annual rainfall of 7 CORDEX South Asia climate models under scenario RCP 4.5 for the period of 20 years from (2019–2038)

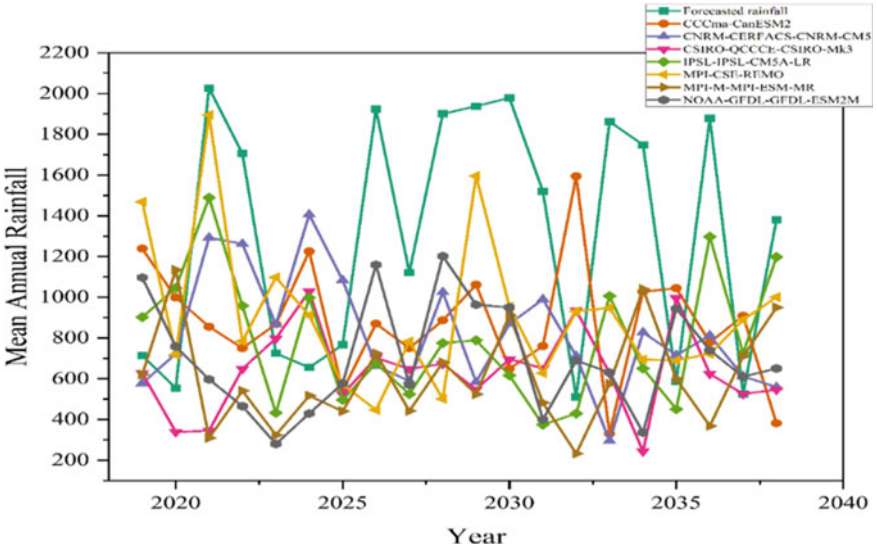

Fig. 8 Projected mean annual rainfall of 7 CORDEX South Asia climate models under scenario RCP 8.5 for the period of 20 years from (2019–2038)

Table 7 Error terms for the CORDEX South Asia climate models with respect to predicted mean annual rainfall

Error terms	CCCma Can ESM-2	CNRM CERFACS CNRM CM-5	CSIRO QCCCE CSIRO Mk-3	IPSL IPSL CM-5A LR	MPI CSE REMO	MPI M-MPI ESM MR	NOAA GFDL GFDL ESM-2 M
RMSE	163.51	177.23	175.02	175.01	189.43	195.01	194.12
MAE	612.10	655.77	679.98	662.76	684.52	696.44	735.90
MAPE	0.43	0.51	0.50	0.50	0.49	0.49	0.54

5 Conclusion

This study focuses on determining the extreme rainfall indices and short-term future forecasting by using historical rainfall data set from 9 rain gauge stations situated over MRP complex region Chhattisgarh for 24 years from 1994 to 2018. This study reveals that the ARIMA model is an effective method for modelling and forecasting rainfall. ARIMA model cannot be performed with non-stationary time series data without pre-processing the input data set. The rainfall time series were pre-processed using transformations and then to fit the ARIMA model. For mean annual rainfall for all the nine stations over MRP complex region Chhattisgarh, the best-fitted ARIMA model is (1,0,1). Climate model CCCma-Can_ESM2 has good relation concerning forecasted mean annual rainfall. Changes in rainfall have a significant impact on water resource management, irrigation, hydrology, and habitats. As a result, understanding the extent of changes in temporal and spatial rainfall patterns is crucial for developing effective strategies for the long-term management of water supplies, agriculture, the atmosphere, and ecosystems. This could be used to improve the model's long-term predicting capabilities. MRP complex region Chhattisgarh stream bowls will be severely affected by climatic fluctuation.

Acknowledgements The authors are grateful to NIT, Raipur Chhattisgarh.

Conflict of Interest There are no conflicts of interest disclosed by the authors.

References

1. Nyatuame M, Owusu-Gyimah V, Ampiaw F (2014) Statistical analysis of rainfall trend for Volta region in Ghana. Int J Atmos Sci. https://doi.org/10.1155/2014/203245
2. Mahajan DR, Dodamani BM (2015) Trend analysis of drought events over upper Krishna basin in Maharashtra. Aquat Procedia 4:1250–1257. https://doi.org/10.1016/j.aqpro.2015.02.163
3. Manobavan M (2003) The responses of terrestrial vegetation to El Niño Southern Oscillation perturbations. PhD dissertation, Kingston University. https://ethos.bl.uk/OrderDetails.do?uin=uk.bl.ethos.289669

4. Shathir AK, Saleh LAM, Majeed SAAD (2019) Forecasting monthly maximum temperatures in Kerbala using seasonal ARIMA models. J Univ Babylon Eng Sci 27(2):223–232. https://doi.org/10.29196/jubes.v27i2.2341
5. Feng G, Cobb S, Abdo Z, Fisher DK, Ouyang Y, Adeli A, Jenkins JN (2016) Trend analysis and forecast of precipitation, reference evapotranspiration, and rainfall deficit in the Blackland Prairie of Eastern Mississippi. J Appl Meteorol Climatol 7(55):1425–1439. https://doi.org/10.1175/JAMC-D-15-0265.1
6. Reyna TM, Guillén NF, Lábaque MdR, Alvarez JA, Eder M, Funes F (2015) Using time series analysis to support the water resources management in the upper basin of the Suquía River. http://hdl.handle.net/11336/65556
7. Verma S, Prasad AD, Verma MK (2021) Trend analysis and rainfall variability of monthly rainfall in Sheonath River Basin, Chhattisgarh. In: Pathak KK, Bandara JMSJ, Agrawal R (eds) Recent trends in civil engineering lecture notes in civil engineering, vol 77. Springer, Singapore, pp 777–790. https://doi.org/10.1007/978-981-15-5195-6_58
8. Esterby SR (1996) Review of methods for the detection and estimation of trends with emphasis on water quality applications. Hydrol Process 2(10):127–149. https://doi.org/10.1002/(SICI)10991085(199602)10:2%3c127::AID-HYP354%3e3.0.CO;2-8
9. Sonali P, Nagesh Kumar D (2013) Review of trend detection methods and their application to detect temperature changes in India. J Hydrol 476:212–227 (2013). https://doi.org/10.1016/j.jhydrol.2012.10.034
10. Zhang Q, Liu C, Xu C-Y, Xu Y, Jiang T (2006) Observed trends of annual maximum water level and streamflow during past 130 years in the Yangtze River basin, China. J Hydrol 1–4(324):255–265 (2006). https://doi.org/10.1016/j.jhydrol.2005.09.023
11. Verma S, Prasad AD, Verma MK (2022) Trends of rainfall and temperature over Chhattisgarh during 1901–2010. In: Rao CM, Patra KC, Jhajharia D, Kumari S (eds) Advanced modelling and innovations in water resources engineering. Lecture notes in civil engineering, vol 77. Springer, Singapore, pp 3–19. https://doi.org/10.1007/978-981-16-4629-4_1
12. Soltani S, Modarres R, Eslamian SS (2007) The use of time series modeling for the determination of rainfall climates of Iran. Int J Climatol: A J Royal Meteorol Soc 6(27):819–829. https://doi.org/10.1002/joc.1427
13. Hill T, Lewicki P, Lewicki P (2006) Statistics: methods and applications: a comprehensive reference for science, industry, and data mining. StatSoft, Inc.,
14. Sahu RT, Verma MK, Ahmad I (2021) Regional frequency analysis using L-moment methodology—a review. In: Pathak KK, Bandara JMSJ, Agrawal R (eds) Recent trends in civil engineering. lecture notes in civil engineering, vol 77. Springer, Singapore, pp 811–832. https://doi.org/10.1007/978-981-15-5195-6_60
15. Dhiwar BK, Verma S, Prasad AD (2022) Identification of flood vulnerable area for Kharun River Basin by GIS Techniques. In: Chintalacheruvu MR, Patra KC, Jhajharia D, Kumari S (eds) Advanced modelling and innovations in water resources engineering lecture notes in civil engineering, vol 77. Springer, Singapore, pp 385–408. https://doi.org/10.1007/978-981-16-4629-4_27
16. Meher J, Jha R (2013) Time-series analysis of monthly rainfall data for the Mahanadi River Basin, India. Sci Cold Arid Regions (SCAR)
17. Sahu RT, Verma MK, Ahmad I (2022) Segmental variability of precipitation in the Mahanadi River basin from 1901 to 2017. Geocarto Int. http://dx.doi.org/10.1080/10106049.2022.2091163
18. Sahu RT, Verma MK, Ahmad I (2021) Characterization of precipitation in the subdivisions of the Mahanadi River Basin, India. Acta Sci Agric 5(12). https://doi.org/10.31080/ASAG.2021.05.1085. ISSN: 2581-365X
19. Sahu RT, Verma MK, Ahmad I (2021) Some non-uniformity patterns spread over the lower Mahanadi River Basin, India. Geocarto Int 1–23. https://doi.org/10.1080/10106049.2021.2005699
20. Somvanshi VK, Pandey OP, Agrawal PK, Kalanker NV, Ravi Prakash M, Chand R (2006) Modeling and prediction of rainfall using artificial neural network and ARIMA techniques. J Ind Geophys Union 2(10):141–151

21. Alsudani RSA, Liu J (2017) The use of some of the information criterion in determining the best model for forecasting of thalassemia cases depending on Iraqi patient data using ARIMA model. J Appl Math Phys 3(5):667–679. https://doi.org/10.4236/jamp.2017.53056
22. Azharuddin M, Verma S, Verma MK, Prasad AD (2022) A synoptic-scale assessment of flood events and ENSO—streamflow variability in Sheonath River Basin, India. In: Chintalacheruvu MR, Patra KC, Jhajharia D, Kumari S (eds) Advanced modelling and innovations in water resources engineering, lecture notes in civil engineering, vol 7. Springer, Singapore, pp. 93–104. DOI https://doi.org/10.1007/978-981-16-4629-4_8
23. Kachroo RK (1992) River flow forecasting. Part 5. Applications of a conceptual model. J Hydrol 1–2(133):141–178. https://doi.org/10.1016/0022-1694(92)90150-T
24. Ehret U, Zehe E, Wulfmeyer V, Liebert J (2012) Should we apply bias correction to global and regional climate model data? HESS 16:3391–3404
25. Heo J-H, Ahn H, Shin J-Y, Kjeldsen TR, Jeong C (2019) Probability distributions for a quantile mapping technique for a bias correction of precipitation data: a case study to precipitation data under climate change. Water 7(11):1475. https://doi.org/10.3390/w11071475
26. Bennett JC, Grose MR, Corney SP, White CJ, Holz GK, Katzfey JJ, Post DA, Bindoff NL (2014) Performance of an empirical bias-correction of a high-resolution climate dataset. Int J Climatol 7(34). https://doi.org/10.1002/joc.3830
27. Krishnakumar KN, Prasada Rao GSLHV, Gopakumar CS (2009) Rainfall trends in twentieth century over Kerala, India. Atmos Environ 11(43):1940–1944. https://doi.org/10.1016/j.atmosenv.2008.12.053
28. Mahmood R, Jia S, Zhu W (2019) Analysis of climate variability, trends, and prediction in the most active parts of the Lake Chad basin, Africa. Sci Rep 1(9):1–18 (2019). https://doi.org/10.1038/s41598-019-42811-9
29. Aitken AP (1973) Assessing systematic errors in rainfall-runoff models. J Hydrol 2(20). https://doi.org/10.1016/0022-1694(73)90035-8
30. Kripalani RH, Kulkarni A (1997) Rainfall variability over South–east Asia—connections with Indian monsoon and ENSO extremes: new perspectives. Int J Climatol*:* A J Royal Meteorol Soc 11(17):1155–1168. https://doi.org/10.1002/(SICI)1097-0088(199709)17:11<1155::AIDJOC188>3.0.CO;2-B
31. Rajurkar MP, Kothyari UC, Chaube UC (2004) Modeling of the daily rainfall-runoff relationship with artificial neural network. J Hydrol 285(1–4):96–113. https://doi.org/10.1016/j.jhydrol.2003.08.011

Studies on Strength Characteristic of Recycled Aggregate Concrete Using Supplementary Cementitious Materials and Hybrid Fibres

Musa Aminu Alhaji and Pushpendra Kumar Sharma

Abstract It is critical to improve the strength parameters of recycled coarse aggregate concrete to be equal to virgin aggregate concrete. Thus, the research focusses on using different percentages of replacements of ordinary Portland cement with a supplementary cementitious materials (SCMs) to determine the best combination for structural purposes by adding a hybrid of glass and steel fibres. In the experimentation, the recycled coarse aggregate was used at a constant percentage of 75% as a partial substitute of natural coarse aggregate, and SCMs used as a partial substitute of ordinary Portland cement were rice husk ash at 10, 15, and 20% and also silica fume at 8, 12, and 16% by weight of cement. The hybrid of a glass of steel fibres was also added by volume fraction of concrete in ratios of 50:50, 25:75, and 75:25 in all of the percentage replacements of rice husk ash and silica fume. Mechanical parameters like compressive, flexural, and split tensile strength were assessed. Result revealed that the target strength of M25 was achieved with the combinations of RCA75-RHA15-GF0.5-XSF0.5 (i.e.75% recycled coarse aggregate, 15% cement replacement with rice husk ash, 0.5% glass fibre, and 0.5% steel fibre) and RCA75-SF8-GF0.25-XSF0.75 (i.e.75% recycled coarse aggregate, 8% cement replacement with silica fume, 0.5% glass fibre, and 0.5% steel fibre). Similar trends were observed in split tensile and flexural strength. The study concludes that these combinations can be used for structural purposes.

Keywords Hybrid fibres · Recycled aggregate concrete · Strength

1 Introduction

Concrete is a heterogeneous matrix comprised of cement, fine aggregate, coarse aggregate, water, and occasionally admixtures are added to modify certain properties of concrete. However, there is a problem associated with the production of cement which is the main binder in concrete, therefore, to minimize the impact of

M. A. Alhaji · P. K. Sharma (✉)
School of Civil Engineering, Lovely Professional University, Phagwara 144411, Punjab, India
e-mail: p.sharmaji10@gmail.com

© The Author(s), under exclusive license to Springer Nature Singapore Pte Ltd. 2023

K. R. Reddy et al. (eds.), *Recent Advances in Sustainable Environment*, Lecture Notes in Civil Engineering 285, https://doi.org/10.1007/978-981-19-5077-3_6

environmental pollution associated with the manufacture of cement and also cost of concrete production, thus supplementary cementing materials (SCMs) are utilized as a partial substitute of cement. These SCMs are mineral admixtures which are either fly ash, metakaolin, silica fume, wood ash, pumice, or rice husk ash. Whilst, virgin coarse aggregate is the major constituent in a concrete matrix which occupies 60–70% volume of the concrete matrix [1, 2].

In the light of sustainable development goals and measures for mitigating climate change, it is critical to prioritize management of construction and demolition (C&D). With housing for all and other infrastructural projects underway, construction is accelerating at an unprecedented rate, as is C&D waste. As a result, technology interventions that not only minimize and manage C&D waste but also convert it to useful resources are critical for the construction sector's sustainable development. Thus, there is an urgent need to use recycled coarse aggregate from demolished concrete structures to substitute the virgin coarse aggregate. The main advantage of using recycled coarse aggregate (RCA) is minimizing the ecological imbalance associated with the extraction of natural aggregate and also saving the landfills where the waste demolished concrete is dumped. However, the main issue with the recycled aggregate concrete (RAC) is the high-water absorption of the RCA because of the old mortar on the RCA which resulted in low strength and durability performance in comparison with those of concrete produced with virgin aggregates [3].

In the recent trends of researches, adding fibres to "recycled aggregate concrete" improves its mechanical strength parameters [4]. But, fibres in higher volume fractions reduce concrete mix workability [4]. Furthermore, Revathi et al. [5] concrete is brittle and breaks easily, but adding fibres to cement concrete improves ductility and reduces brittleness. Compared to traditional concrete, fibre-reinforced concrete showed a slower crack propagation, indicating a ductile failure mode, whilst plain concrete showed a brittle failure mode. However, besides fibres, supplementary cementing materials are used in concrete as a partial substitute of cement to enhance durability and fresh characteristics of the "recycled aggregate concrete" [4]. For example, Indumathi and Gnanadevi [6] experimentally studied the durability characteristic of polypropylene fibre and fly ash concrete. In their experiments, they found that replacing ordinary Portland cement with fly ash and fibre reduced concrete density. However, adding fly ash to concrete enhanced workability, which was reduced by polypropylene fibre. The freeze–thaw resistance of polypropylene fibre concrete was also found to be slightly higher than without fibres. After, adding fibre to the concrete, the mechanical properties improved after silica fume and fly ash were utilized to replace cement. In conclusion, the utilization of silica fume and fly ash not only improves the strength behaviours of the RAC but also reduces costs [7, 8]. Adding different proportions of hybrid fibres to concrete as a cement replacement has been found to improve its mechanical properties. Thus, the supplementary cementing materials improved compressive strength, whilst fibres improved split tensile and flexural strength [9–15].

Furthermore, past research works in the area of RAC revealed that the mechanical performance of RAC can be enhanced using fibres, whilst SCMs showed significant improvement in the durability and mechanical characteristics of RAC. However, no

study so far in the existing literature reported the combined impacts of SCMs and hybrid fibre on the strength characteristics of recycled coarse aggregate concrete. Therefore, this research work fills this gap and presents mechanical performances of recycled aggregate concrete with supplementary cementitious materials (i.e. rice husk ash and silica fume) as well as a hybrid of glass and steel fibres. The study is aimed at investigating the fresh and mechanical behaviours of "recycled aggregate concrete" with a view to improving its strength performance so that it can be comparable to that of normal concrete.

2 Experimental Programmes

2.1 Materials

2.1.1 Cement

In experimentation, the concrete specimens were cast using a grade 43 ordinary Portland cement. The cement has satisfied the requirement of IS 269:2015 ordinary Portland cement, and the details of the chemical compositions are presented in Table 1.

2.1.2 Aggregates

The recycled coarse and natural aggregate are of size 20 mm to 10 mm minimum whilst fine aggregate is river sand that satisfies Zone III of grading. The specific gravity of the fine and natural coarse and recycled coarse aggregate is 2.78, 2.84,

Table 1 Oxide compositions and physical properties of ordinary Portland cement rice husk ash and silica fume

Elements	Percentages of oxides compositions (%)		
	OPC	Rice husk ash	Silica fume
Calcium oxide	65.5	0.6	0.03
Silicon oxide	23.2	91.5	95.1
Aluminium oxide	5.3	0.2	0.02
Iron oxide	4.5	0.4	1.2
Sulphur oxide	2.8	0.2	0.02
Alkalis	0.9	3.5	0.43
Magnesium oxide	–	0.4	0.01
Loss of ignition	–	6.7	3.28
Specific surface area (m^2/kg)	350	36.47	16,000

and 2.34, respectively, whilst the water absorption values are 5.32, 0.60 and 3.10%, respectively.

2.1.3 Supplementary Cementitious Materials (SCMs)

The SCMs used in the experiment are rice husk ash and silica fume. These materials have satisfied the pozzolanic requirements of ASTM C618-2005. The details of the chemical compositions are presented in Table 1.

2.1.4 Fibres

The hybrid of the fibres consists of Alkali resistant glass fibre and super XR crimped steel fibres. Table 2 presents the physical and mechanical behaviours of the fibres.

2.2 Methods

2.2.1 Preparation of the Fresh Concrete Mix

A grade of M25 concrete was designed as per Indian standard 10262 (2009) to determine the proportions of the mixes as presented in Table 3. In this experimental work, there are four series of concrete mixes, in which series I contains 75%NCA-100%OPC and series II contains 75%RCA-100%OPC which served as a control mixes. Furthermore, series III contains 75%RCA with OPC being partially replaced with rice husk ash (RHA) at 10, 15, and 20% with a hybrid of glass (GF) and steel

Table 2 Physical and mechanical properties of the fibres

Property	Types of fibres	
	Glass fibre	Steel fibre
Specific gravity	2.7	7.8
Density (Kg/m^3)	2700	7800
Tensile strength (MPa)	1400	510–1100
Elastic modulus (GPa)	72	210
Length (mm)	30	50
Diameter (mm)	0.038	1.14
Fibre (type)	**Micro**	**Macro**
Aspect ratio	789	44
Strain to failure (%)	2	3.5
Fibre material	Alkali resistant	Xorex crimped

Table 3 Materials mix proportions for different mix combinations

Mix			Binders (kg/m^3)			Aggregates (kg/m^3)			Fibres (kg/m^3)		Water (kg/m^3)
Family	Mix combinations	Notations	OPC	RHA	SF	FA	NCA	RCA	GF	XSF	
Series I	NCA100-OPC100	**S1-0**	433	–	–	618	1195	–	–	–	186
Series II	RCA75-OPC100	**S2-0**	433	–	–	618	299	896	–	–	186
Series III	RCA75-RHA10-GF0.5-XSF0.5	**S3-1**	390	43	–	618	299	896	13.5	39	186
	RCA75-RHA10-GF0.25-XSF0.75	**S3-2**	390	43	–	618	299	896	6.8	58.5	186
	RCA75-RHA10-GF0.75-XSF0.25	**S3-3**	390	43	–	618	299	896	20.3	19.5	186
	RCA75-RHA15-GF0.5-XSF0.5	**S3-4**	368	65	–	618	299	896	13.5	39	186
	RCA75-RHA15-GF0.25-XSF0.75	**S3-5**	368	65	–	618	299	896	6.8	58.5	186
	RCA75-RHA15-GF0.75-XSF0.25	**S3-6**	368	65	–	618	299	896	20.3	19.5	186
	RCA75-RHA20-GF0.5-XSF0.5	**S3-7**	346	87	–	618	299	896	13.5	39	186
	RCA75-RHA20-GF0.25-XSF0.75	**S3-8**	346	87	–	618	299	896	6.8	58.5	186
	RCA75-RHA20-GF0.75-XSF0.25	**S3-9**	346	87	–	618	299	896	20.3	19.5	186
Series IV	RCA75-SF8-GF0.5-XSF0.5	**S4-1**	398	–	35	618	299	896	13.5	39	186
	RCA75-SF8-GF0.25-XSF0.75	**S4-2**	398	–	35	618	299	896	6.8	58.5	186
	RCA75-SF8-GF0.75-XSF0.25	**S4-3**	398	–	35	618	299	896	20.3	19.5	186
	RCA75-SF12-GF0.5-XSF0.5	**S4-4**	381	–	52	618	299	896	13.5	39	186
	RCA75-SF12-GF0.25-XSF0.75	**S4-5**	381	–	52	618	299	896	6.8	58.5	186
	RCA75-SF12-GF0.75-XSF0.25	**S4-6**	381	–	52	618	299	896	20.3	19.5	186
	RCA75-SF16-GF0.5-XSF0.5	**S4-7**	364	–	69	618	299	896	13.5	39	186
	RCA75-SF16-GF0.25-XSF0.75	**S4-8**	364	–	69	618	299	896	6.8	58.5	186

(continued)

Table 3 (continued)

Mix			Binders (kg/m^3)			Aggregates (kg/m^3)			Fibres (kg/m^3)		Water (kg/m^3)
Family	Mix combinations	Notations	OPC	RHA	SF	FA	NCA	RCA	GF	XSF	
	RCA75-SF16-GF0.75-XSF0.25	**S4-9**	364	–	69	618	299	896	20.3	19.5	186

NCA = Natural coarse aggregate, **OPC =** Ordinary Portland cement, **RCA =** Recycled coarse aggregate, **RHA =** Rice husk ash, **SF =** Silica fume, **GF =** Glass fibre, and **XSF =** Xorex steel fibre

(XSF) fibres being added by volume fraction in percentage dosage of 0.5–0.5, 0.25–0.75, and 0.75–0.25% in all the percentage replacements of RHA, whilst, series IV is the same as series III except silica fume (SF) replaces OPC instead of RHA at 8, 12, and 16% by weight of cement.

2.2.2 Assessment of the Properties of the Fresh Concrete Mixes

The measurement of workability was done using the slump cone test per IS: 1199 (1959). Three readings were taken, and average value was obtained to represent a slump value for each mix, and the test was conducted at a room temperature.

2.2.3 Assessment Mechanical Parameters of the Hardened Concrete Specimens

In this study, compressive, split tensile, and flexural behaviours of hardened concrete specimens were the three main mechanical strength characteristics measured in this study. At the end of each hydration interval of 7, 14, and 28 days, the compressive behaviour of each concrete samples was evaluated. The concrete metal cube of size $100 \times 100 \times 100$ mm was used for casting the specimens. To determine split tensile strength, metal cylinder of size 100 mm diameter and 200 mm height was used and tested at the end of 14 days and 28 days hydration periods. Furthermore, flexural strength was evaluated by testing $100 \times 100 \times 500$ mm specimens at the end of 14 and 28 days. Three concrete specimens were used to determine a strength parameter at a specific curing duration, and the average value was taken. All the three strength parameters were tested as per IS 516—(1959).

2.2.4 Assessment of the Microstructural Characteristics

The concrete specimens of the best combinations and control samples were characterized in terms of functional groups qualitative analysis to determine the positions of peaks and their bands using Fourier transform infrared (FTIR). The FTIR measurements of the concrete sample were carried out with a spectrometer and diamond attenuated total reflectance ATR (Perkin-Elmer Spectrum 2) equipped with the ATR and Pellet accessories method, which allowed for direct measurements of the solid concrete sample without making it into powder form. The bands and wavenumbers were measured in transmittance mode, with a resolution of 5 cm^{-1}, over a range of 4000–500 cm^{-1}.

3 Results and Discussion

3.1 Workability of the Fresh Concrete Mixes

The slump cone test was adopted to measure the workability in accordance with IS: 1199. (1959). The average of three readings was taken from each concrete mix to represent the slump values. The results are presented in Fig. 1 as it can be observed that the workability of the recycled aggregate concrete decreased in all the percentage combinations compared to the control mix (i.e. S1-0) which is in line with the similar findings by Mi et al. [16]. The reason for this decrease could due to porosity of recycled coarse aggregate as a result of adhered mortar on the aggregates.

Furthermore, the decrease in the slump is more pronounced in series IV; the reason for this decrease can be ascribed to the high-surface area of silica fume (16,000 m^2/kg) compared to cement. Because silica fume particles have a large specific surface area; thus, more water is required to achieve the required workability [17]. Although the workability of the mixtures is reduced when silica fume is added, but the mix remains extremely cohesive.

3.2 Mechanical Behaviours of Hardened Concrete Specimens

3.2.1 Compressive Behaviours of the Hardened Concrete Specimens

The most essential concrete parameter for determining the load-carrying capability of structural parts is compressive strength. Figure 2 presents the compressive behaviours

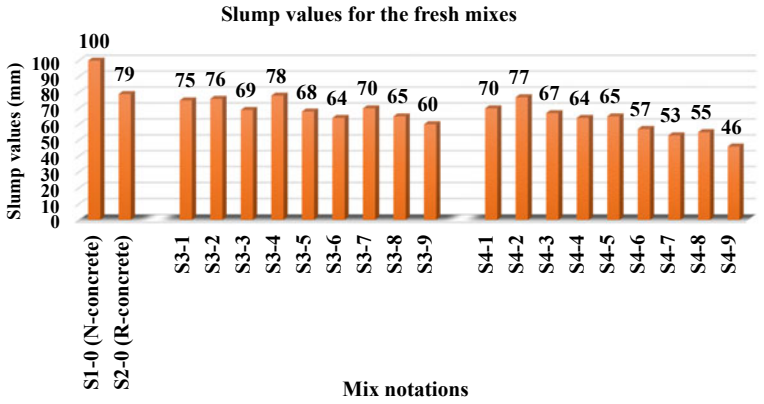

Fig. 1 Slump values of the mix combinations

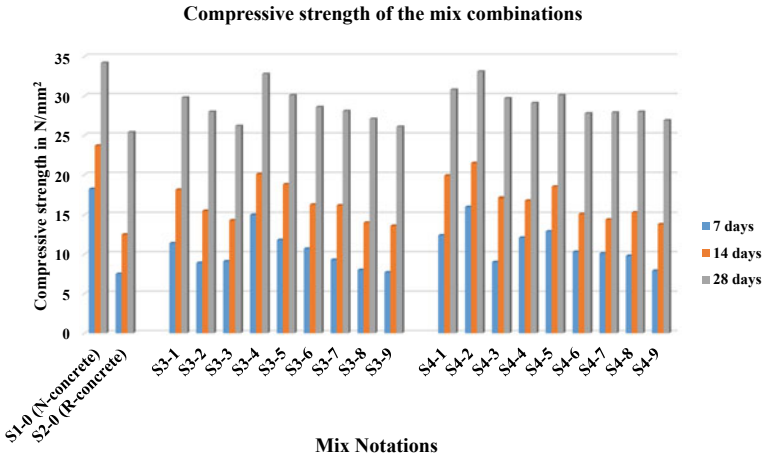

Fig. 2 Compressive strength of the mix combinations at the end 7, 14, and 28 days

values of the mix combinations. As it can be seen from the results that the compressive strength of **series II** (i.e. **S2-0 R-concrete**) decreased drastically by 25.6% in strength at 28 days in comparison with the reference mix made with natural aggregate concrete (i.e. **S1-0N-concrete**). However, with incorporation of rice husk ash and hybrid of glass and steel fibres in **series III**, the compressive strength of "recycled aggregate concrete" improved significantly at the end of 28 days hydration period. Amongst the mix combinations in **series III**, the combination with mix notation **S3-4** is the only one that attained the target strength of M25 (32 N/mm^2) with a least reduction in compressive strength of 2.6% in comparison with the reference mix (i.e. **S1-2N-concrete**). The reason for this phenomenal could be due to a pozzolanic interaction between RHA particles and free CH [18]. Furthermore, RHA improves particle size distribution by filling gaps between OPC particles and aggregates in the binder matrix, lowering the CH concentration and converting it to calcium silica hydrate gel. On the other hand, the crack propagation and crack width in the cement matrix are controlled by the randomly oriented fibres. Due to the crack arresting capability or bridging impact of fibres in concrete, the compressive behaviour increased [18]. It was observed also that under axial stresses, micro-cracks formed in the microstructure, and that when fibres were introduced, the formation and development of these micro-cracks were reduced, and thus, the compressive behaviour of concrete is improved [13].

Furthermore, in **series IV**, an increase in compressive behaviours of the specimens was noticed more than that of **series III**. The best combination in this series is RCA75%-SF8%-GF0.25%-XSF0.75% (i.e. **S4-2**). The reasons for this can be related with the calcium silicate hydrate which is formed as a result of the reaction of silica fume with calcium hydroxide generated at the hydration process. It was also because of the filling role of SF because of its fine particles [19]. As a result, the usage of silica

fume in the interfacial region strengthens the cement paste aggregate connection, resulting in a microstructure that is less porous and more homogeneous.

3.2.2 Split Tensile Behaviours of Hardened Specimens

Although split tensile behaviours of concrete does not represent genuine tensile strength, the failure pattern of specimens under splitting loads provides a good indication of the material's tensile behaviour. At the end of 14 and 28 days hydration periods, the split tensile behaviour of each mix combination was tested, and results are given in Fig. 3. As it can be noticed, the split tensile behaviour is influenced in a same way to compressive strength at 14 and 28 hydration periods for both the mix combinations. In **series III**, the mix combination with notation **S3-4** had a negligible reduction of only 1.0% in split tensile behaviour in comparison with the reference mix (i.e. **S1-0 N-concrete**), whilst in **series IV**, the mix combination of notation **S4-2** is the best combination in terms of split tensile strength. The reason for the increase in split tensile behaviour could be due to the pozzolanic interaction between mineral admixtures and calcium hydroxide, which resulted in improved microstructure at 28 days, which aids in the formation of a strong bond between the fibres and the binder matrix. Additionally, when RAC is made using "mineral admixtures as a partial replacement of ordinary Portland cement"; two mechanisms may work to improve the characteristics of the finished product: (1) A portion of the mineral admixtures would permeate into the pores of RA, improving the bonding zone between the paste and the aggregate; and (2) hydration products would fill cracks previously existing in the aggregates [20].

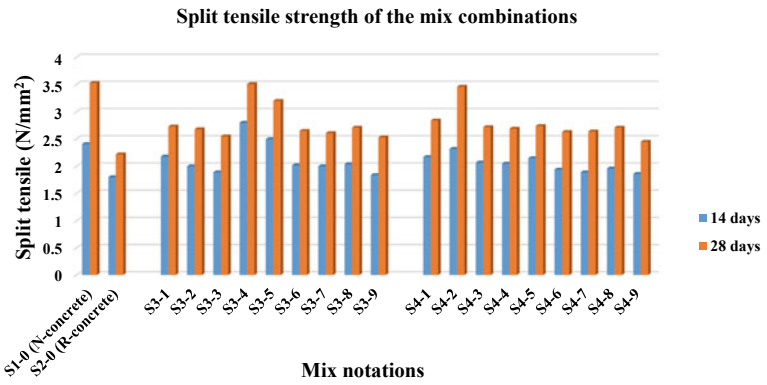

Fig. 3 Split tensile behaviour of mix combinations at 14 and 28 days hydration

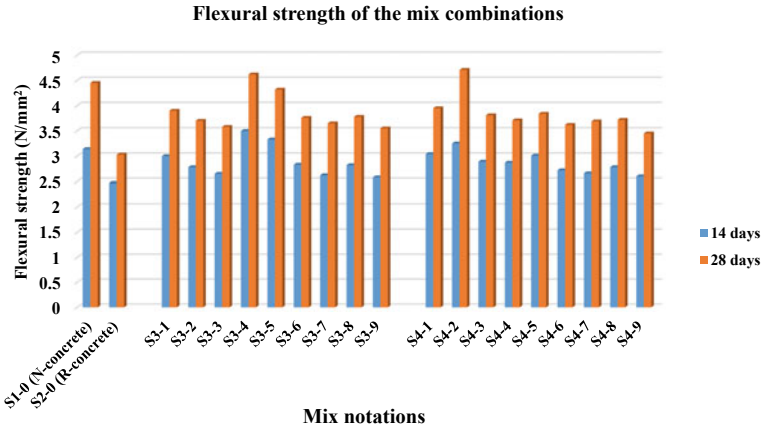

Fig. 4 Flexural strength behaviour of mix combinations at 14 and 28 days of hydration

3.2.3 Flexural Strength

Flexural behaviour of a concrete is another indirect measure of concrete tensile behaviour. Figure 4 depicts the flexural strength of the mix combinations after 14 and 28 days hydration periods. It can be noticed that the similar trend was observed as that of split tensile. The mix combination with notation **S3-4** had better flexural strength behaviour than control (i.e. **S1-0**) by 3.6% at 28 days. Also, **S4-2** exhibits a good performance in flexural strength than control (i.e. **S1-0**) by 5.5% at the end of 28 days of hydration period. The reason for the increased in flexural behaviour of RAC could be owing to the addition of SCMs in the mix which resulted to a strong binding matrix and improves the bond between the fibres and the cement paste [11]. The efficiency of glass and steel fibres in resisting cracks at the bonding zone caused a strong bond with the binder matrix. Furthermore, Koushkbaghi et al. [21] have found that employing pozzolanic materials like RHA in steel fibre-reinforced concrete can strengthen the connection between the fibres and the binder matrix and thus, improved the strength behaviour of a concrete.

3.3 Microstructural Study

Fourier transform infrared (FTIR) spectroscopy was conducted to study the microstructural characteristics of the best combinations of series III (i.e. **S3-4**) and series IV (i.e. **S4-2**) with the control mix that is series I and II (i.e. **S1-0** and **S2-0**). The result of FTIR of the **S1-0**, **S2-0** and **S3-4** is presented in Fig. 5. It can be inferred from the result that there is a shifting of peaks in **S3-4** compared to the control mixes of **S1-0** and **S2-0**. This can be ascribed to the pozzolanic reactions of RHA in **S3-4**. The reduction in intensity of the peaks in **S3-4** and **S1-0** was observed

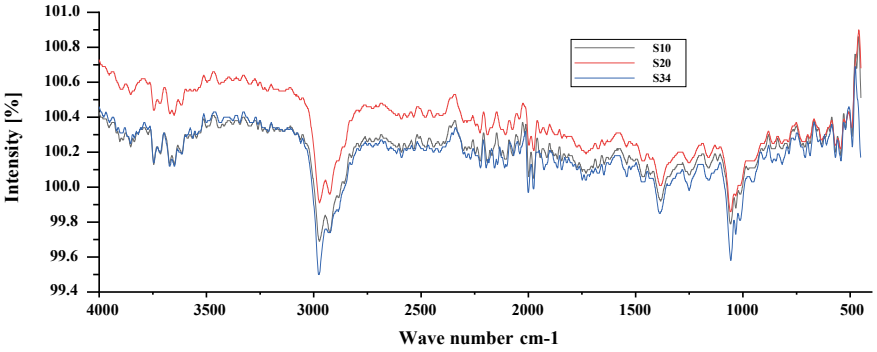

Fig. 5 FTIR of the best combination of S3-4 and control series of S1-0 and S2-0

compared with **S2-0** which can be associated with the reductions in the strength of **S2-0** at all the hydration periods. Furthermore, bands at 1680 cm^{-1} (O–H bend) and 3200–3600 cm^{-1} (O–H stretch) were observed due to the hydration of C_3S and C_2S. The band observed at 1400 cm^{-1} is associated with carbon–oxygen C–O stretch (CO_3^{2-}). Additionally, the band corresponding to alumina ettringite AlO_6 (octahedral) was observed at 850 cm^{-1} for **S3-4**. Also, FTIR spectroscopy can easily detect the portlandite (CH), which is well detected by a strong unique signal at 3640 cm^{-1}. At 1150–1100 cm^{-1}, the S–O stretch (SO_4^{2-}) is also found.

On the other hand, Fig. 6 showed the result of FTIR of the best percentage combinations in series IV (i.e. **S4-2**) with control mixes series I and series II (i.e. **S1-0** and **S2-0**). As it can be observed that because of the silica fume presence in **S4-2**, the bands tend to shift towards the lower wavenumber side of 1450–1460 cm^{-1}, whereas control mixes without silica fume show no or only a modest shift in these bands. This is because of the pozzolanic feature of silica fume, which speeds up the hydration reaction and consumes more calcium hydroxide to generate the C–S–H phase. The existence of C_3S and C_3A in concrete matrices is confirmed by the occurrence of bands at 626 and 528 cm^{-1} in FTIR spectra. Aside from that, the emergence of FTIR bands at 1180, 1120, and 980 cm^{-1} during the hydration process can be ascribed to the formation of monosulphate, ettringite, and C-S–H molecules.

4 Conclusions

To effectively enhance the mechanical parameters of “recycled aggregate concrete”, the combined impacts of supplementary cementing materials and hybrid glass and steel fibres on the physical and mechanical properties of the RAC were assessed in this study. Therefore, the following served as a conclusion from the findings of the experimental study;

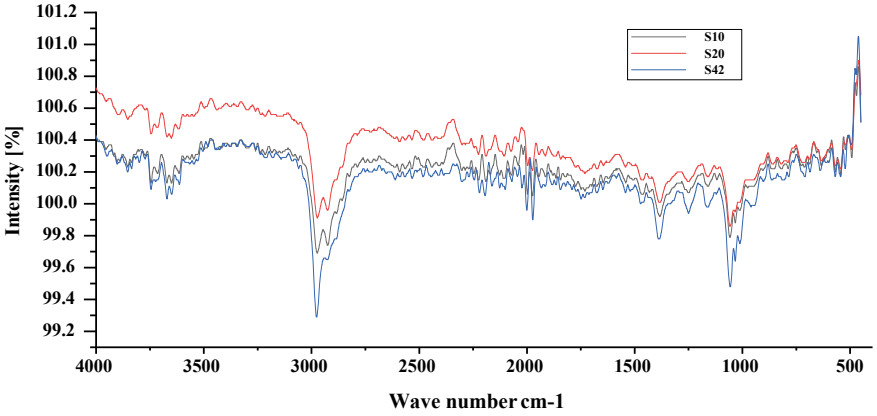

Fig. 6 FTIR of the best combination of S4-2 and control series of S1-0 and S2-0

1. The incorporation of the fibres and SCMs decreased the workability of the fresh concrete, but a water-reducing admixture was used to offset the loss in the workability.
2. The combined effects of hybrid fibres and SCMs improved the compressive strength by more than 11.4% for mix combination of **S3-4** and 13.2% for mix combination of **S4-2** at the age of 28 days.
3. The inclusion of a hybrid of fibres and SCMs improved the splitting tensile strength of RAC at both 14 and 28 days. The mix combination of **S3-4** and **S4-2** had better and flexural behaviour than the control series (i.e. **S1-0**).
4. The higher SiO_2 concentration of RHA and SF facilitated the hydration process of concrete, resulting in an additional continuous layer of C–S–H and C–AS–H, which improved the concrete's binding properties and increased its strength.
5. The bands corresponding to ettringite, monosulphate, and C–S–H molecules at 1180, 1120, and 980 cm^{-1} shift to the lower number side in **S3-4** and **S4-2** due to the pozzolanic reaction as a result of the concentration of rice husk ash and silica fume.
6. The inclusion of SCMs in the concrete binder matrix is believed to improve fibre pullout and bond strength. As a result of the combined effects of SCMs and a hybrid of glass and steel fibres, the mechanical properties of "recycled aggregate concrete" were improved.

References

1. Salim K, Janet R, Azadeh P (2019) Experimental investigation on the properties of recycled concrete using hybrid fibers. Open J Compos Mater 9:183–196
2. Rampit R, Smith J, Ray I (2020) A review of recycled concrete aggregates as a sustainable construction material. In: The international conference on emerging trends in engineering and technology IConETech, vol 1 (1)
3. Sheetal JSC, Mathew MD, Jose AM (2015) Experimental study on fiber reinforced concrete using lathe scrap fiber. Int J Adv Technol Eng Sci 3:622–630
4. Ulape Y, Narule G (2015) Experimental investigation on steel fiber reinforced concrete using metakolin. Int J Emerg Technol Adv Eng Sci 5:105–111
5. Revathi S, Gandhimathi RS, Saranya S (2016) Experimental investigation on mechanical properties of hybrid fibres in M25 grade concrete. Int J Innov Eng Technol 6:213–220
6. Indumathi B, Gnanadevi V (2015) An experimental investigation on properties of hybrid fiber reinforced concrete with GGBS and fly ash. Int J Emerg Technol Comput Sci Electron 13:120–123
7. Kanagavel R, Arunachalam K (2018) Experimental investigation on mechanical properties of hybrid fiber reinforced quaternary cement concrete. J Eng Fibers Fabr 10:139–147
8. Seshadri R, Ramesh B, Niramala S (2016) A study of high performance fiber reinforced polymers (FRP). Int J Innov Res Sci Eng Technol 5
9. Vignesh P, Krishnaraja AR, Nandhaini N (2014) Study on mechanical properties of geopolymer concrete using M-sand and glass fibers. Int J Innov Res Sci Eng Technol 3:110–116
10. Yashwanth MK, Nareshkumar BG, Sandeep Kumar DS (2019) Potential of bagasse ash as alternative cementitious material in recycled aggregate concrete. Int J Innov Technol Explor Eng 6(2):271–276
11. Qureshi LA, Ali B, Ali A (2020) Combined effects of supplementary cementitious materials (silica fume, GGBS, fly ash and rice husk ash) and steel fiber on the hardened properties of recycled aggregate concrete Constr Build Mater 263. https://doi.org/10.1016/j.conbuildmat.2020.120636
12. Garg A, Sharma PK (2021) Mechanical properties of glass fibre reinforced concrete with recycled aggregates. J Appl Sci Eng 24(6):1033–1039
13. Gao D, Gu Z, Pang Y, Yang L (2021) Mechanical properties of recycled fine aggregate concrete incorporating different types of fibers. Constr Build Mater 298. https://doi.org/10.1016/j.conbuildmat.2021.123732
14. Sharma P, Verma M, Sharma N (2021) Examine the mechanical properties of recycled coarse aggregate with MK GGBS. IOP Conf Ser Mater Sci Eng 1116:012152
15. Savva P, Ioannou S, Oikonomopoulou K, Nicolaides D, Petrou MF (2021) A mechanical treatment method for recycled aggregates and its effect on recycled aggregate-based concrete. Materials 14. 103390/ma14092186
16. Mi R, Pan G, Liew KM, Kuang T (2020) Utilizing recycled aggregate concrete in sustainable construction for a required compressive strength ratio. J Clean Prod 276. https://doi.org/10.1016/j.jclepro.2020.124249
17. Masood B, Elahi A, Barbhuiya S, Ali B (2019) Mechanical and durability performance of recycled aggregate concrete incorporating low calcium bentonite. Constr Build Mater 237. https://doi.org/10.1016/j.conbuildmat.2019.117760
18. Meesala CR (2019) Influence of different types of fiber on the properties of recycled aggregate concrete. Struct Concr 20:1656–1669. https://doi.org/10.1002/suco.201900052
19. Nazarimofrad E, Shaikh FUA, Nili M (2016) Effects of steel fibre and silica fume on impact behaviour of recycled aggregate concrete. J Sustain Cement-Based Mater 6(1):54–68
20. Ali B, Raza SS, Hussain I, Iqbal M (2020) Influence of different fibers on mechanical and durability performance of concrete with silica fume. Fib Wiley. https://doi.org/10.1002/suco.201900422

21. Koushkbaghi M, Kazemi MJ, Mosavi H, Mohseni E (2019) Acid resistance and durability properties of steel fiber-reinforced concrete incorporating rice husk ash and recycled aggregate. Constr Build Mater 202:266–275. https://doi.org/10.1016/j.conbuildmat.2018.12.224
22. Indian Standard IS 269 (2015) Specification of requirements of ordinary Portland cement. Bureau of Indian Standards, New Delhi, India
23. American Society for Testing and Material, ASTM C618-05 (2005) Specification for fly ash and raw or calcined natural Pozzolana or use in as a mineral admixture in Portland cements concrete. American Society for Testing and Material, West Conshohocken, No C618, USA
24. Indian Standard IS: 10262 (2009) Proportioning-guidelines. Bureau of Indian Standards. Bureau of Indian Standards, New Delhi, India
25. Indian Standard IS 383 (1970) Specification for coarse and fine aggregates from natural sources for concrete. Bureau of Indian Standards, New Delhi, India
26. Indian Standard IS: 2720-3 (1980) Sect/2. Determination of specific gravity of fine, medium & coarse-grained soil. Bureau of Indian Standards, New Delhi, India
27. Indian Standard IS: 2720-3 (1980) Sect/1. Determination of water content (moisture content). Bureau of Indian Standards, New Delhi, India
28. Indian Standard IS: 1199 (1959) Determination of slump of fresh concrete. Bureau of Indian Standards, New Delhi, India
29. Indian Standard IS 516—(1959) Specification for compressive strength, flexural strength. Bureau of Indian Standards, New Delhi, India

Conceptualisation of Sustainable Low-Cost Earthquake Resistant Bamboo-Reinforced Mud Brick House in North-East India

Yashdeep Sarmah, Manash Protim Goswami, Nayan Deka, Debanga Bikash Bora, Rajanya Kashyap Gogoi, Nikita Mandal, and Olympa Baro

Abstract Advancement in science and technology has led to the development of stronger and durable materials such as steel and concrete. However, these materials are contributors of greenhouse gases. With the ever increasing temperatures of the planet and its associated hazards, it has become essential to look for greener alternatives. The new era demands reviving the forgotten materials and technologies of the past with a more sustainable and environmental friendly outlook. This study attempts to provide such an alternative low-cost housing method for seismically active regions with bamboo and mud at its core.

The house is proposed to be made of mud bricks as an alternative to conventional bricks and bamboo reinforcement as an alternative for steel. The proposed bricks will be made of mud, straw, and rice husk and provided with two holes to insert the bamboo poles. Due to its excellent tensile strength, the addition of bamboo poles to the mud brick walls will help resist the lateral loads coming from earthquake forces. The foundation is proposed to be built using boulders and bamboo reinforcement. GI sheet roof is proposed to be placed over a bamboo truss. The cost of the various materials required for the construction of this house is also provided to ascertain the low-cost factor.

Keywords Mud brick · Bamboo reinforcement · Low-cost house · Earthquakes

1 Introduction

People have been building houses made of bamboo and mud from ancient times. The potential and benefits of such houses have been known from a long time due to which such houses are still built in rural areas in many parts of India. Mud and bamboo are abundantly available and have numerous applications and benefits as building materials. Mud is an eco-friendly sticky substance which has very good adhesive properties, and hence, it serves as a good mortar. Bamboo is a tall tree like grass

Y. Sarmah (✉) · M. P. Goswami · N. Deka · D. B. Bora · R. K. Gogoi · N. Mandal · O. Baro
Department of Civil Engineering, National Institute of Technology, Silchar, Assam, India
e-mail: yashdsarma41@gmail.com

© The Author(s), under exclusive license to Springer Nature Singapore Pte Ltd. 2023

K. R. Reddy et al. (eds.), *Recent Advances in Sustainable Environment*, Lecture Notes in Civil Engineering 285, https://doi.org/10.1007/978-981-19-5077-3_7

which can be bent easily and is known to provide tensile strength which makes it suitable for building houses. Bamboo generally takes 3–5 years to fully harvest and with age its growth rate increases rapidly. The property of bamboo plants to re-grow from the nodes gives it an edge over timber.

Mud and bamboo houses can also withstand earthquake forces. The conventional houses in north-east India have always relied on mud and bamboo to withstand the forces coming from earthquakes which are quite common to this region. With the advent of reinforced concrete houses, the safety and social status that come along with these houses, people have left the conventional housing methods. However, a section of the society in the north-east India still relies on bamboo to build their houses. The conventional mud and bamboo houses, however, are not spared from their share of disadvantages. One of the most common disadvantages is the chipping off of the old and dried mud plaster and exposing the Ikora wall (mat woven with thin pieces of bamboo), thus reducing the aesthetics as well as the strength of the walls. This requires periodic plastering of the walls with mud and cow dung. Further, safety and security from antisocial elements also raise a concern in the conventional mud and bamboo houses. Thus, this study proposes a new low-cost earthquake resistant house made of mud bricks and bamboo reinforcement. The conventional houses are generally either entirely made of bamboo or mud bricks. Moreover, the columns of such houses consist of only single bamboo. But our proposed house will have walls constructed of unconventional mud bricks consisting of two holes for the insertion of bamboo poles, and the columns will be constructed in the similar manner consisting of four bamboo poles. The bamboo poles will act as reinforcement to withstand the lateral earthquake forces. The easy availability and the abundance of mud and bamboo in the north-eastern region of India will ensure the affordability of the proposed houses. A detailed report of the design, costing, treatment of bamboo and other particulars is discussed in the following paragraphs.

2 Properties of Bamboo

The most common types of bamboo available in north-east India are *Bambusa tulda* (Jati Baah) and *Bambusa balcooa* (Bhaluka Baah). These bamboo varieties have found their uses in the Assam type houses built in the north-east Indian state of Assam. Thus, in this study, the primarily focus is on the mechanical properties of *Bambusa tulda* (Jati Baah) and *Bambusa balcooa* (Bhaluka Baah) [1].

3 Cost of Materials

The cost of different types of materials used in the construction of the house is shown in the Table 2 below—

Table 1 Properties of bamboo

Sl No.	Property	*Bambusa Tulda*	*Bambusa Balcooa*
Compressive strength (N/mm^2)			
1	Bottom	40.7	39.4–50.6
	Middle	68	51–57.3
	Top	79	69
2	Tensile strength (N/mm^2)	207	164
	Modulus of rupture (N/mm^2)		
3	Bottom	51.1	62.4–85
	Middle	66.7	69.6–92.6
	Top	194	151
4	Shear strength (N/mm^2)	9.9	11.9
5	Modulus of elasticity (N/mm^2)	20,000–25,000	20,000–25,000

Table 2 Cost of different materials used in construction

Sl No	Material	Price
1	Jati Baah (*Bambusa Tulda*)	Rs. 80–100 per piece
2	Bhaluka Baah (*Bambusa Balcooa*)	Rs. 150–180 per piece
3	Straw	Rs. 4000 per vehicle (size of the vehicle—3 m × 2 m × 4 m)
4	Boulder stone	Rs. 1100 per m^3
5	Steel wire	Rs. 120 per kg
6	Bolts	Rs. 100 per kg

4 Manufacture of Mud Brick

Earth containing fairly high-clay content and straw will be used for construction of the mud bricks. Practically, the soil of paddy field after harvesting would be used as the source. Clay soil will be taken to a mud pit where it will be churned up adding water to it. In this process, materials like straw, hay, or rice husks will also be added to the mud pit. The mixture will be collected from the mud pit and placed into the moulds of inner dimensions 474 mm × 200 mm × 150 mm. To provide reinforcement, the brick will consist of two holes having 90 mm diameter (see Figs. 1 and 2). Whilst placing in the moulds, the mud will be compressed and flattened. The surface of the mud should be smoothened properly. Each surface of the mud brick will be dried under the sun, flipping the brick until it is hardened and ready for use. After complete drying, he perfect mud brick for the proposed house will be prepared [2].

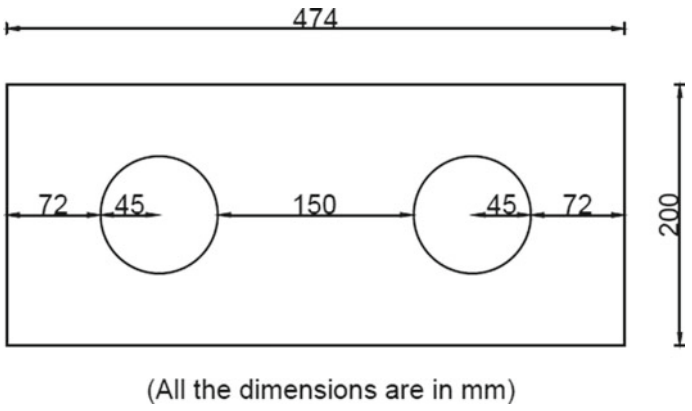

Fig.1 Top view of the brick

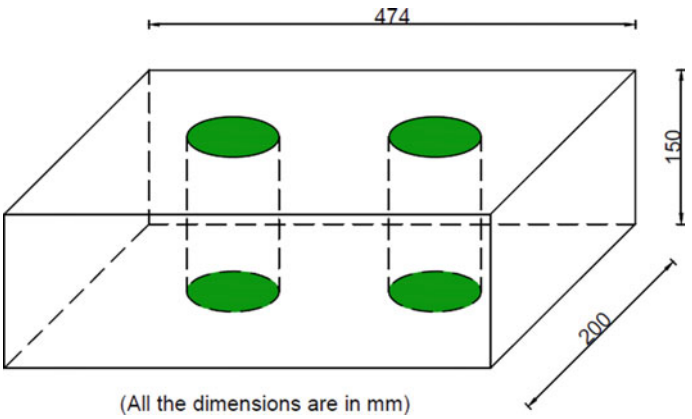

Fig.2 3D view of the mud brick

5 Design of the House

The proposed idea of constructing a house plan with mud bricks and bamboo as reinforcement is prepared. The house will consist of ten columns, sufficient number of beams, a truss for the roof, walls, and a foundation. It will have a bedroom of size 3600 mm × 2500 mm, a drawing room of size 3600 mm × 2635 mm, a kitchen of size 2430 mm × 2255 mm, and a bathroom of size 2430 × 1145 mm. (see Fig. 3).

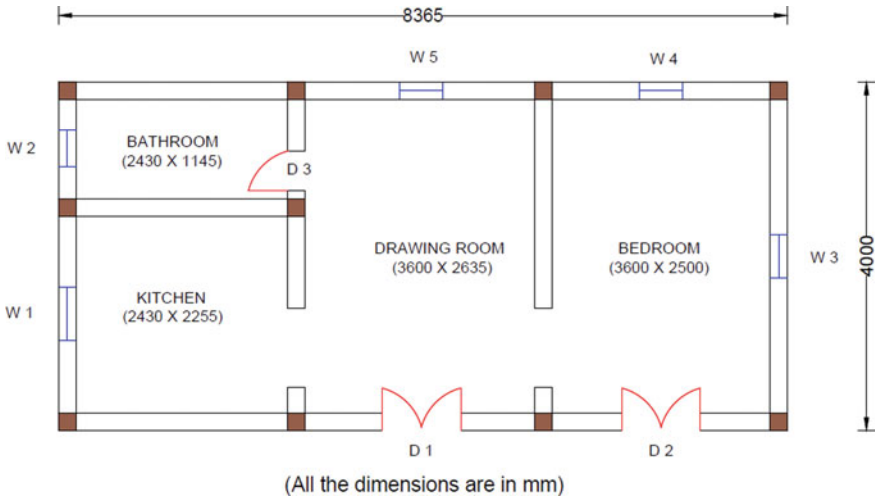

Fig. 3 Floor plan of the house

6 Different Structures of the House

6.1 Foundation

Foundation is the most essential part of any house construction which supports the entire structure. The designing of the foundation will consist of excavating a trench of depth 500 mm and a width of 540 mm along the outline of the walls of the house. At first, a layer of bamboos will be placed horizontally along the outline of sides of this trench. The bamboos that will meet at the corners of the sides will be tied with steel wires to resist displacement. This is followed by the placing of bamboos in a vertical manner along the mid-way of the trench at a distance of 150 mm from each other. These vertical bamboos will be extended up to a height of 2500 mm from the ground surface which will serve as the reinforcements for the wall. Now, there will be some free spaces in between the horizontally and vertically placed bamboos. This space will be filled up with boulder stones up to mid-height of the trench; holding the vertical bamboos in place. Another layer of horizontal bamboos will be placed above this stone layer in a similar manner. Finally, the excavated soil will be dampened and placed back to fill the trench completely [3]. Consolidation of this soil will be done with the help of a rammer (see Fig. 4).

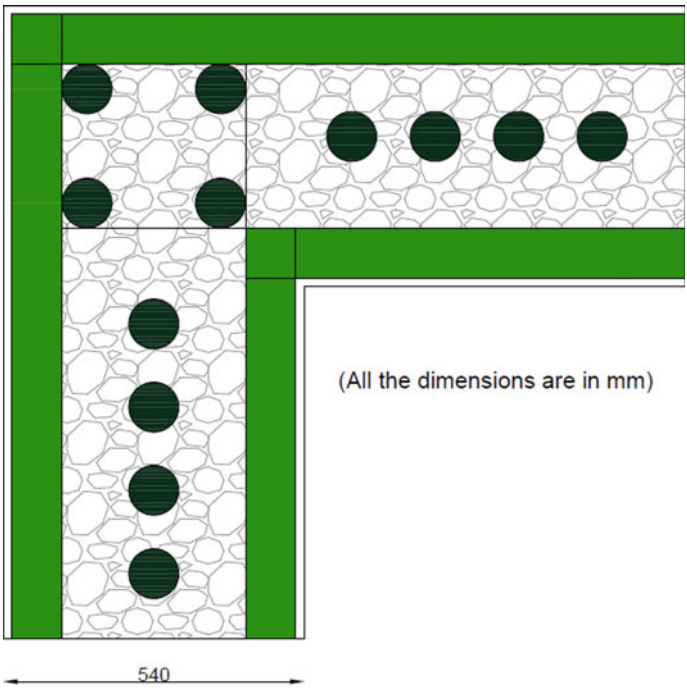

Fig.4 Top view of the corner of the foundation

6.2 Column

The columns will be of mud and straw bricks along with bamboo erected vertically through the bricks. The design procedure for the columns will be similar to that of the walls; except that in walls in each layer, the adjacent bricks will be placed along the width of the bricks, whilst in columns, the adjacent bricks in each layer will be placed along the length thus increasing its overall width. Bamboos of specific uniform height and cross-sectional dimension are erected vertically from the foundation level in 2 $\times$ 2 layouts. The bricks having holes will be inserted through these bamboos, two bricks in each layer. The subsequent layers of the bricks will be stacked up, through the bamboos, with mud mortar as the binding material. The increased area of the base along with the cross-sectional area will provide enough loads bearing capacity to these columns. The length x breadth x height of the bricks is 474 mm $\times$ 200 mm $\times$ 150 mm. (see Fig. 5).

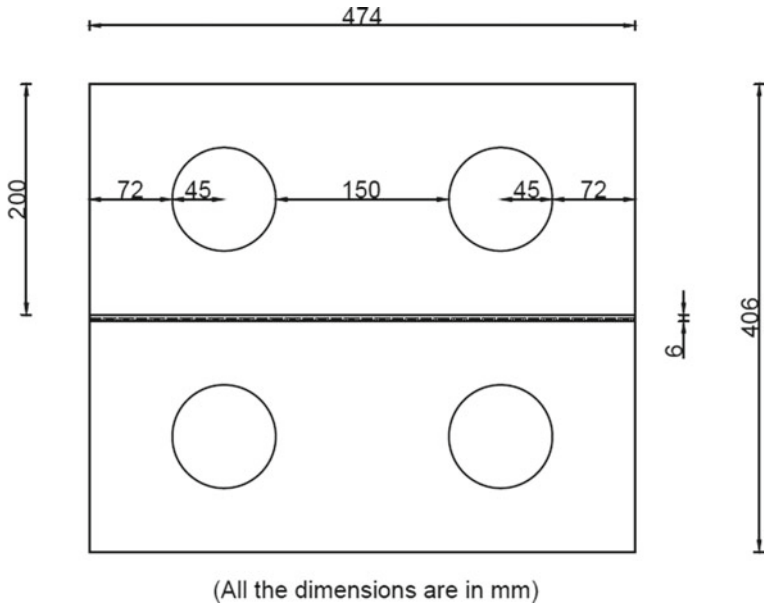

Fig.5 Top view of the column

6.3 Walls

The walls of the house are the main highlight of this study. The mud brick and the bamboos are the main components of the wall. The mud brick has two holes in it at a distance of 150 mm apart. Each brick will be slid through two bamboos from the top. Mud mortar will be used for binding since it has very good adhesive property. In this way, the first layer of brick will be laid. Similarly, the second layer of brick will be laid alternately with respect to the first layer (see Fig. 6). In this way, the entire wall will be built up to a height of 2500 mm from the ground level. Then, the wall will be plastered with a mixture of mud and slaked lime. The main advantage of using this is that it provides a good finishing surface and keeps the insects away from the wall. The wall is about 220 mm thick reinforced with bamboo, and it will be structurally very strong owing to its thickness compared to conventional wall.

6.4 Truss and Roof

The roof and truss are also an essential part of any building as the roof provides safety against incoming natural extremities, and the truss helps in transferring the roof loads to the underlying structures. The proposed house will have a double pitch roof truss of bamboo and GI sheets as roof. The bamboo in the truss will be bolted

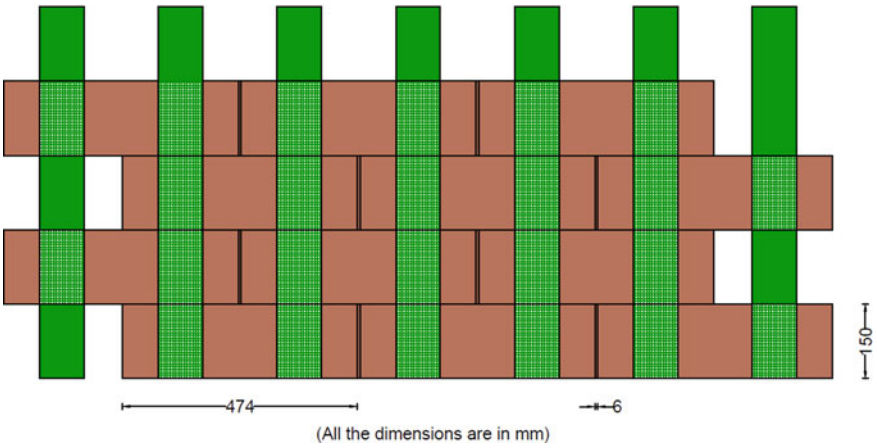

Fig. 6 Section of the wall

with each other. The iron sheets will also be bolted with the bamboo of the truss frame (see Fig. 7). For the ceiling, interwoven bamboo strips will be used to prevent the heat coming from the roof, primarily supported on the columns and the beams [4] (see Fig. 8).

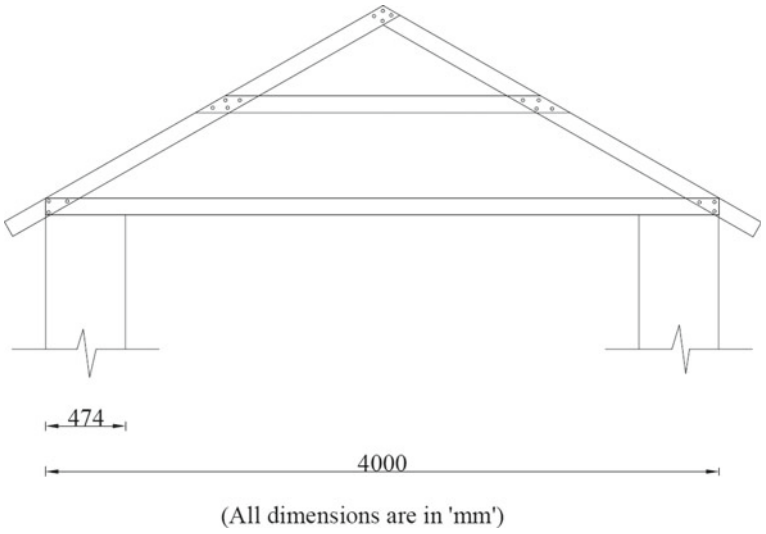

Fig. 7 Truss of the house

Fig. 8 Ceiling of the house

7 Methods to Increase the Durability of the House

Since the entire house will be made of natural materials like mud and bamboo, the house remains vulnerable to small insects and fungal infections. Hence, pre- and post-treatments of the structural elements are essential to increase the durability. The following methods are proposed as pre- and post-treatments.

7.1 Water Soaking

Before commencing upon the construction, the bamboo poles will be soaked in either running water or in stagnant water of ponds for a desirable period of time. This process will cut down the natural starch content from the bamboo which will protect it from insects and fungi attacks. Split bamboo takes as little as a week, but round culms take 10–14 days. In case of stagnant water, the water needs to be changed frequently to avoid fouling [5].

7.2 Smoking Treatment

Another pre-treatment is where the bamboo poles will be exposed to heat and smoke for a considerable period of time inside a closed room. The bamboo poles will be

smoked at an air temperature of 50–60 °C. This causes reduction of the water-soluble constituents which protects the bamboo from fungi and insect attacks [6]. Moreover, the toxic agents present in the smoke, and heat will destroy the starch in bamboo making it immune to attacks of insects and fungi and blacken the culms, thereby giving it a protective layer.

7.3 White Washing Treatment

Post the construction of the house, the walls will be painted with slaked lime. Although this approach is mostly used for aesthetic purposes, it will also preserve the wall by keeping the moisture from entering it. This coating is highly effective when it is applied repeatedly to cut or cracked surfaces. So, it will be less susceptible to fungal attack and extend the life of the wall [5].

8 Advantages of Bamboo-Mud House

Since the construction of bamboo-mud houses is mostly environment friendly and requires only natural ingredients, so the proposed house is expected to possess minimum adverse effect to the nature. Some of the points highlighting the advantages are discussed below:

1. Bamboo-mud houses and its components are recyclable and biodegradable, which makes it nature friendly in an utmost way. If a bamboo-mud house requires to be rebuilt, one can re-use the whole material [7].
2. Walls made of mud are thermally insulated. So there is always a thermal comfort inside the house irrespective of the season [8].
3. There will be barely any concrete or cement used in the making of mud houses, so the carbon footprints of such houses will be negligible. Moreover the raw materials can be collected locally, so transportation cost will also very less.

9 Future Work

It has to be mentioned here that this study aims to propose the idea of an unconventional mud and bamboo house which is sustainable as well as earthquake resistant in nature. The claim of this house being earthquake resistant is based on the findings of past studies where bamboo has been found to be able to counter the earthquake forces. Further, the good performance of bamboo houses in the north-eastern region during past earthquakes has also been taken into account. However, the proposed house is yet to be tested for resistance to different levels of earthquake shaking. This part of the work will be carried out in the near future.

10 Conclusion

The proposed house is aimed at providing a low-cost earthquake resistant living quarter for the economically weaker sections of the society. As bamboo and mud are abundantly available in the north-eastern region of India, this study proposes to make use of these materials. Mud bricks of dimensions 474 × 200 × 150 mm with holes for insertion of bamboo poles are proposed to be used for the walls of the house. Such types of brick walls will be different from the conventional Ikora walls of Assam type houses generally found in the region. The proposed bricks walls will provide additional strength, thermal insulation, and security to the house without compromising its earthquake resistant properties. The addition of bamboo poles to the walls, columns, and foundation shall provide for the ductility necessary to counter the lateral earthquake forces. Further as mud and bamboo are natural elements, construction of this house will have minimum impact on the environment. Thus, for a sustainable environment, this house can be very useful in the coming future.

References

1. Bamboo Import Europe, Mechanical Properties for Bamboo. https://www.bambooimport.com/en/what-are-the-mechanical-properties-of-bamboo. Last accessed 10 November 2021
2. Abundant Edge (2021) Adobe: The tradition and techniques of bricks. https://abundantedge.com/articles-1-2016-5-29-adobe-the-tradition-and-techniques-of-mud-bricks/.
3. Archinomy, Mud Architecture—Construction Details and Techniques. https://www.archinomy.com/case-studies/mud-architecture-construction-details-and-techniques/. Last accessed 10 November 2021
4. She LY, Shan B, Xiao Y (2008) Development of prefabricated bamboo mobile house. Mod Bamboo Struct 209–2013. ISBN 978-0-415-47597-6
5. All About Bamboo, Bamboo Treatment and Preservation. https://www.allaboutbamboo.org/p/bamboo-treatment.html
6. Kaur PJ, Satya S, Pant KK, Naik S (2016) N, **Eco-friendly preservation of bamboo species: traditional to modern techniques**. BioResources 11:10604–10624
7. The better India, Cooler, Cheaper & Recyclable: 7 Reasons Why Our Grandparents' Mud Walls Are The Best, Gopi Karelia. https://www.thebetterindia.com/227726/mud-house-benefit-tradition-cool-summer-hack-cheap-eco-friendly-india-gop94/. Last accessed 10 November 2021
8. Manandhar R, Kim JH, Kim JT (2019) Environmental, social and economic sustainability of bamboo and bamboo-based construction materials in buildings. J Asian Archit Build Eng 18(2):49–59

Seismic Response of Setback RC Buildings with Shear Wall

Yash Verma and Rama Debbarma

Abstract Construction of tall buildings is now becoming popular because of the increment in the population and due to limited space in urban areas. Irregular buildings are mostly in fashion because of their aesthetic view and their functional efficiency. A G+10 storeyed setback building with a fixed base and shear wall is considered for the present study. In this study, two types of shear walls, i.e. L-shape and T-shape have been considered. For comparative study, a regular RC building with and without shear walls is also considered. Analysis has been made for both types of building as per IS1893:2016. The responses of some parameters like storey drift, storey displacement, storey shear, bending moment, and base shear are obtained for comparative study. The time period and modal participation factor have been checked for all the models.

Keywords Earthquake loading · Regular building · Setback building · And Shear wall

1 Introduction

In recent years, due to limited space, economical requirements and advanced construction techniques have caused a significant increase in the height of structures. The buildings have become considerably more flexible, lighter, and inherent low damping due to the use of high-strength materials that leads to the possibility of more sway as compared to the high-rise buildings built earlier which can be dangerous during seismic activities, i.e. earthquake loading and wind load. An earthquake exerts lateral as well as vertical forces so to dissipate those forces and vibration in structure, an earth-quake-resistant system has to be designed. Shear walls are one of the best means to provide earthquake resistance in a multistorey building. Shear walls incorporated in the building reduce the effect of an earthquake by improving the effectiveness of the building and ensuring adequate lateral stiffness to resist lateral

Y. Verma (✉) · R. Debbarma
Department of Civil Engineering, National Institute of Technology Agartala, Tripura 799046, India
e-mail: yashverma1807@gmail.com

© The Author(s), under exclusive license to Springer Nature Singapore Pte Ltd. 2023

K. R. Reddy et al. (eds.), *Recent Advances in Sustainable Environment*, Lecture Notes in Civil Engineering 285, https://doi.org/10.1007/978-981-19-5077-3_8

loads [1]. Tidke et al. (2016) analyzed the effect of seismic loading on a building with different locations of a shear wall to check the effectiveness of the shear wall and stated that the presence of a shear wall can affect the seismic behaviour of the frame structure to large extent and it increases the strength of stiffness of structure [2]. Anshuman et al. (2011) analyzed the multistorey building to find out the most suitable location for the shear wall based on its elastic and elastoplastic behaviours [3]. Aktar et al. (2017) acknowledge the effect of P-delta in designing a structure rather than the first-order effect and also help to minimize the pounding action between two tall buildings [4]. Chittiprolu and Kumar (2014) discussed the significance of shear walls in high-rise irregular buildings and show that it can be used to reduce the effect of torsion and provide more resistance to lateral loads [5]. El-Sokkary and Galal (2012) investigate the behaviour of RC shear wall rehabilitated using carbon fibre-reinforced polymer (CFRP) composite sheets to enhance the shear behaviour of the rehabilitated panels [6]. Anya and Ghosh (2021) shown that the position of the shear wall in the core, as well as the corners, shows minimum storey drift and displacement [7].The objective of this paper is to study the seismic response of a G+10 storeyed setback building with two different types of shear walls. In this paper, response spectrum analysis and time history analysis are used to estimate the expected seismic response of the building. For the comparative study, results from a regular building have also been drawn.

2 Methodology

In this present work, all the models are analyzed by both linear and static method which is also known as equivalent static force method and linear dynamic methods that are response spectrum analysis and time history analysis. The details related to all the analysis method are provided below.

2.1 Equivalent Static Force Method (ESFM)

To analyze the models in ESFM, all the load combinations mentioned in IS 1893 (Part 1): 2016 [8] for the limit state design of reinforced and pre-stressed concrete structures are taken.

2.2 Response Spectrum Analysis Method (RSM)

Response spectrum analysis is the linear dynamic method, in which modes of vibrations are considered. The total sum of the modal masses should be more than 90% of the total seismic mass. All the modes are combined by using complete quadratic

combination method (CQC), and the directional combination is done using square root of the sum of the squares (SRSS) method. The scaling for the response spectrum load case is done according to the IS1893 (Part 1): 2016 guidelines, i.e. equating the base shear obtained from ESFM to that obtained from RSM.

2.3 Time History Analysis (THA)

For the time history analysis, the ground motion data of Northwest Calif-02 earthquake are considered of 6.6 magnitude.

3 Structure Modelling

In order to evaluate the seismic response of the buildings with and without shear wall, two buildings (G+10 storeys with basement) have been modelled [9] in ETABs software version 17.0.1. The details of the building are (Fig. 1):

• Plan (Regular building) (Setback building)	27 m × 16 m 432 m^2 (up to 4th storey) 272 m^2 (5th to 8th storey) 160 m^2 (9th to terrace)
• Height of each storey	3.2 m
• Height of basement	3.5 m
• Grade of concrete	M35 (For column) M30 (For beam) M25 (For slab)
• Grade of steel for rebar	HYSD 415 (tie bars) HYSD 550 (longitudinal bars)
• Size of beam	300 mm × 450 mm
• Size of column	450 mm × 450 mm
• Thickness of slab	140 mm
• Live load on floors:	3 kN/m^2
• Live load on roof:	1.5 kN/m^2
• Wall load:	12.88 kN/m^2
• Floor finish:	1.2 kN/m^2 2 kN/m^2 (for terrace)
• Seismic zone:	V
• Zone factor (Z):	0.36
• Soil type:	Type II (medium soil)
• Damping ratio:	5%

(continued)

(continued)

• Frame type:	Special moment resisting frame
• Response reduction factor:	5
• Importance factor (I):	1.2
• Attributes of real earthquake records:	The real earthquake ground motion, Northwest Calif-02 of 6.6 magnitude is used for the present study

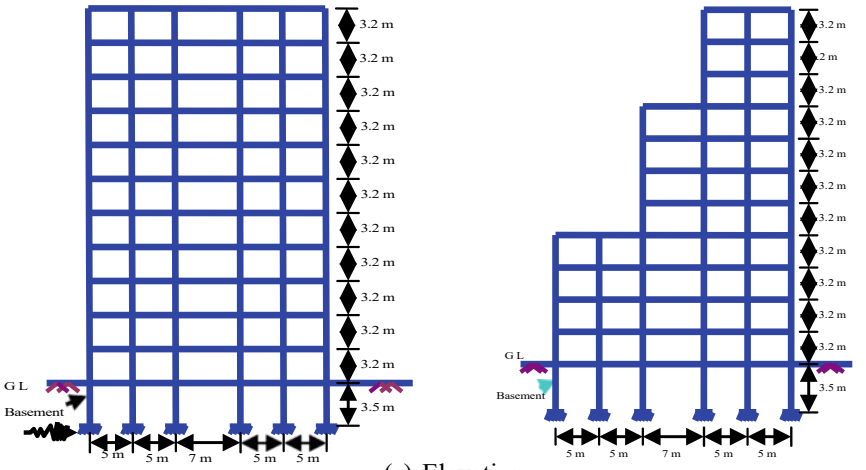

(a) Elevation

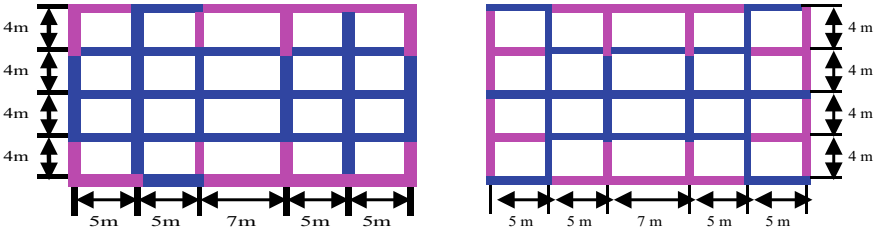

(b) Plan with L-shape and T-shape Shear wall

Fig. 1 G+10 storeyed regular and setback RC buildings with shear wall

4 Results and Discussion

4.1 Regular Building Model

- **Storey Displacement**: The variation of displacement of regular RC buildings with or without shear wall is shown in Fig. 2. The displacement is controlled with the shear wall. From the graph, it can be seen that the displacement reduction is more in L-shape shear wall compared to T-shape shear wall.
- **Storey drift**: The storey drift ratio is the relative displacement between the adjacent floors. The results obtained by both methods are shown in Figs. 3 and 4. It is observed that the L-shape shear wall is more effective to reduce the storey drift as compared to T-shape shear wall.
- **Storey stiffness**: It is observed from the Fig. 5 that the building with L-shape shear wall has the maximum storey stiffness, whereas the building model without shear wall shows the minimum.

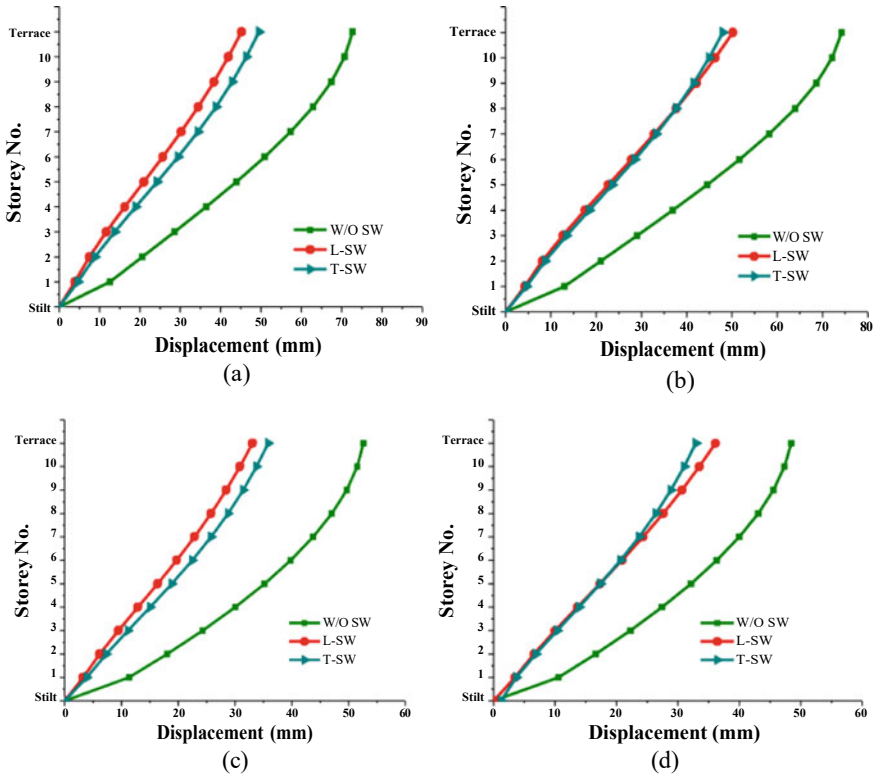

Fig. 2 Variation of displacements of regular buildings in **a** x-direction by ESFM, **b** y-direction by ESFM, **c** x-direction by RSM, and **d** y-direction by RSM

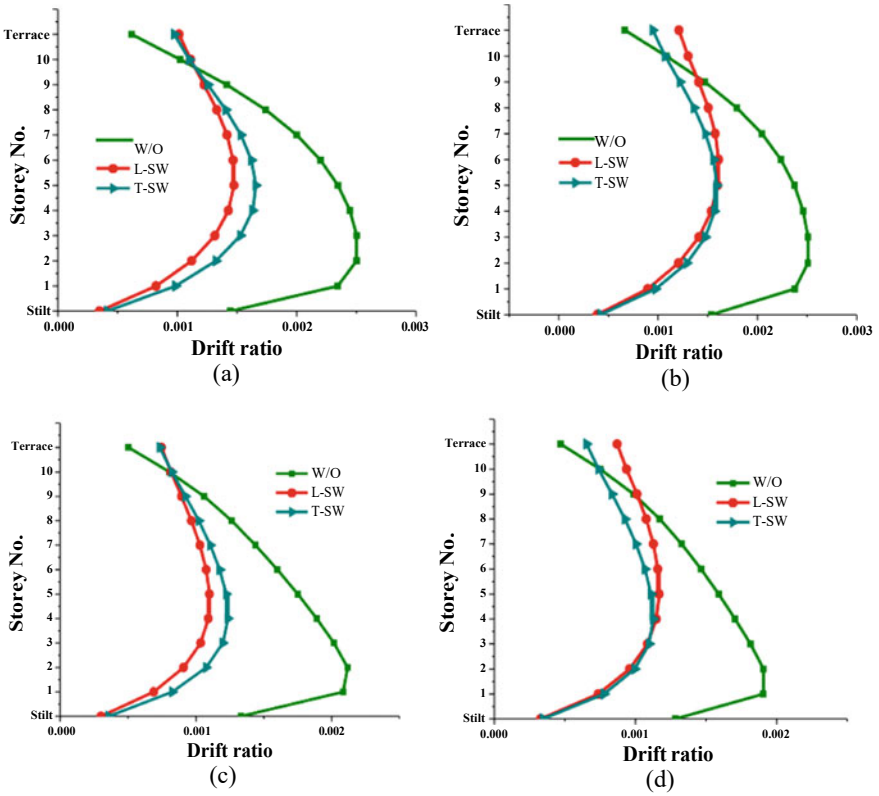

Fig. 3. Variation of inter-storey drift of regular buildings **a** x-direction by ESFM, **b** y-direction by ESFM, **c** x-direction by RSM, and **d** y-direction by RSM

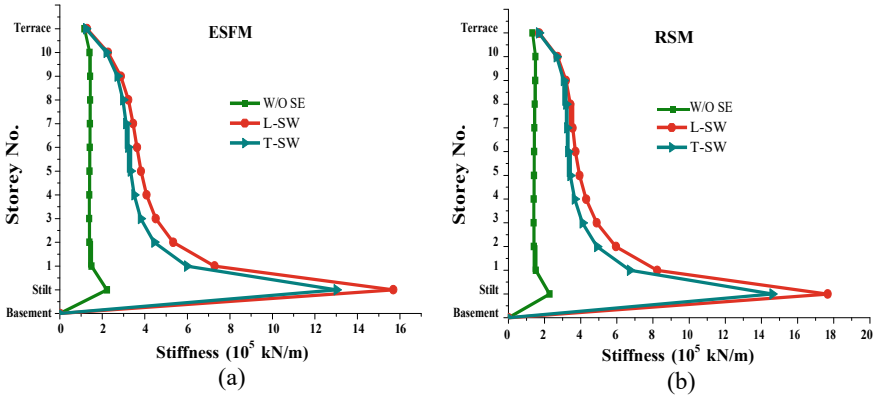

Fig. 4. Variation of stiffness for regular buildings **a** in ESFM and **b** in RSM

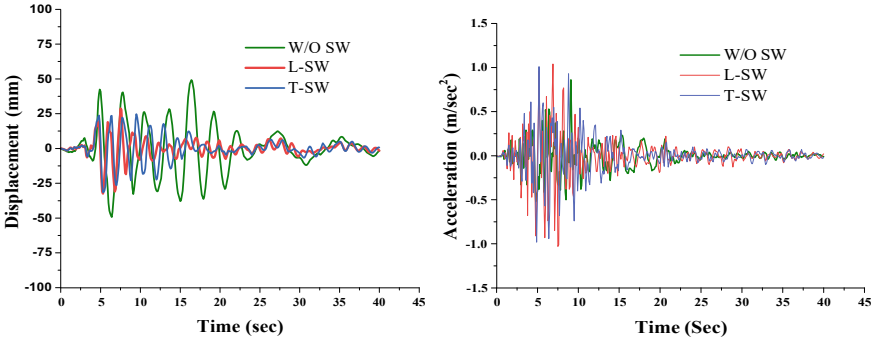

Fig. 5 Variation of displacement and acceleration of regular buildings considering real earth- quake ground motions

- **Time history results**: From the figure, it can be observed that L-SW is more effective to reduce the top storey displacement of the building considering the 5% damping ratio of the structure. The variation in the acceleration of the structure with time is shown in Fig. 6. From the figure, it can be observed that the acceleration is maximum for L-SW, and the significant duration of the earthquake is 5–10 s.

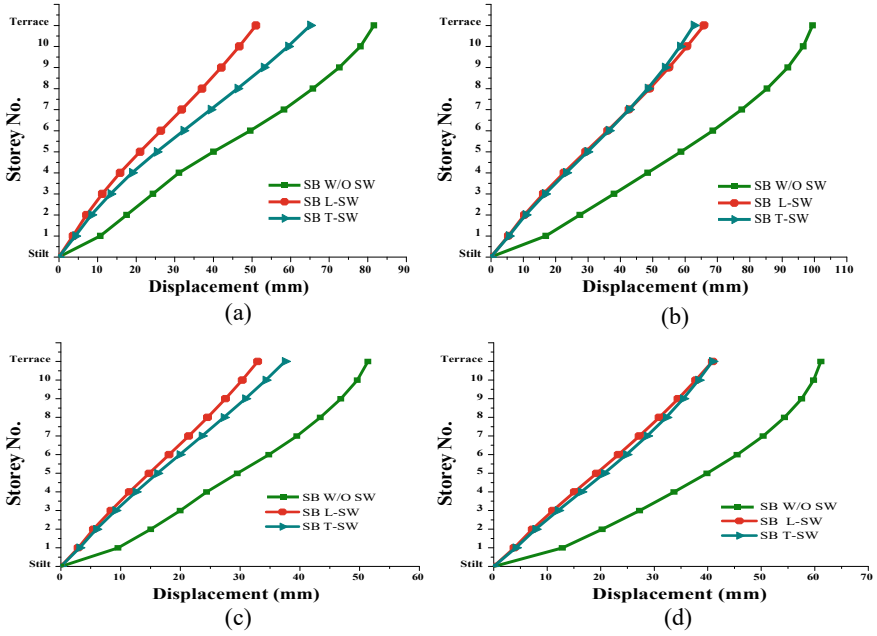

Fig. 6 Variation of displacements of setback buildings in **a** x-direction by ESFM, **b** y- direction by ESFM, **c** x-direction by RSM, and **d** y-direction by RSM

Table 1 Fundamental time period of regular buildings

Regular building	Mode	Time period	Model mass participating ratio	
			Sum Ux	Sum Uy
Without shear wall	1	2.774	0.8164	0
	2	2.548	0.8164	0.8175
	3	2.455	0.8164	0.8175
L-shape shear wall	1	1.482	0.7274	0
	2	1.39	0.7274	0.7109
	3	1.07	0.7274	0.7198
T-shape shear wall	1	1.668	0.7397	0
	2	1.497	0.7397	0.7429
	3	1.232	0.7397	0.7429

- **Time period**: The time period of all the models for the first three modes is shown in the Table 1.

4.2 Setback Building Model

- **Storey displacement**: In the direction of the force and transverse direction, the maximum displacement is recorded for without shear wall model, because of lesser vertical geometric irregularity and lesser stiffness caused by the absence of shear wall. Out of both the shear walls, the L-shape shear wall has shown minimum dis- placement in y-direction, whereas in x-direction, both shear walls have shown almost equal displacement control, with L-SW being minimum as shown in Fig. 7.
- **Storey drift**: The results are shown in Fig. 8. It is observed that the L-shape shear wall is more effective to reduce the storey drift as compared to T-shape.
- **Storey Stiffness**: It is observed from the Fig. 9 that the building with L-shape shear wall has the maximum storey stiffness, whereas the building model without shear wall shows the minimum.
- **Time history results**: The time history results also reveal the vulnerability of without shear wall setback structure as the top storey displacement and acceleration are maximum in Fig. 10. The other two models have been excellent in displacement control.
- **Time period**: The time period of all the models for the first three modes is shown in the Table 2.

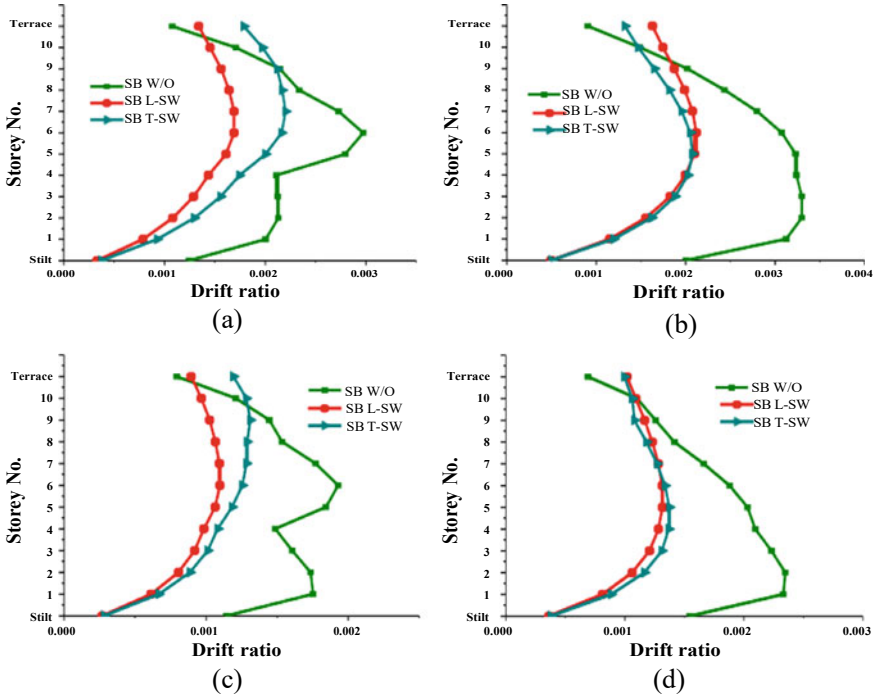

Fig. 7 Variation of inter-storey drift of setback buildings in **a** x-direction by ESFM, **b** y-direction by ESFM, **c** x-direction by RSM, and **d** y-direction by RSM

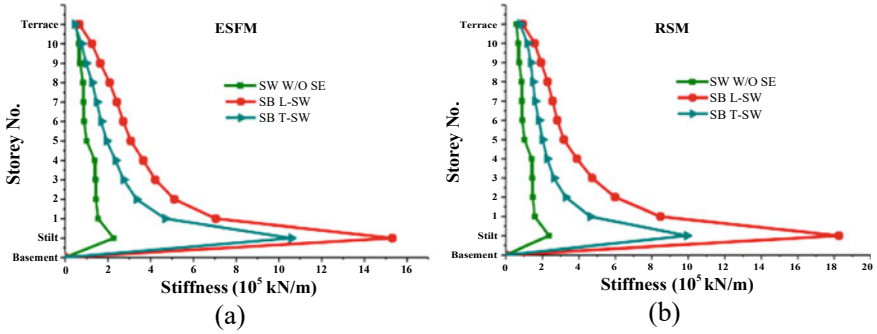

Fig. 8 Variation of stiffness for setback buildings **a** in ESFM and **b** in RSM

4.3 Comparative Study Between Both Buildings

- **Base shear**: Base shear due to earthquake force has been obtained in both of the methods ESFM and RSM are balanced by the scale factor as per IS 1893 (Part 1): 2002. For both the buildings, it has been observed that the base shear is a

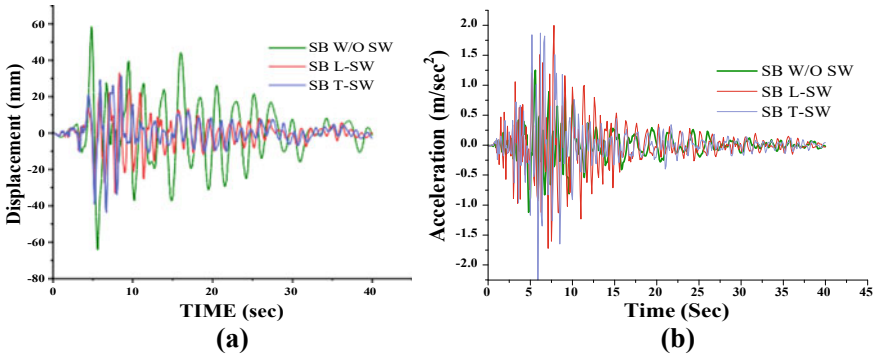

Fig. 9 Variation of displacement and acceleration of setback buildings considering real earth- quake ground motions

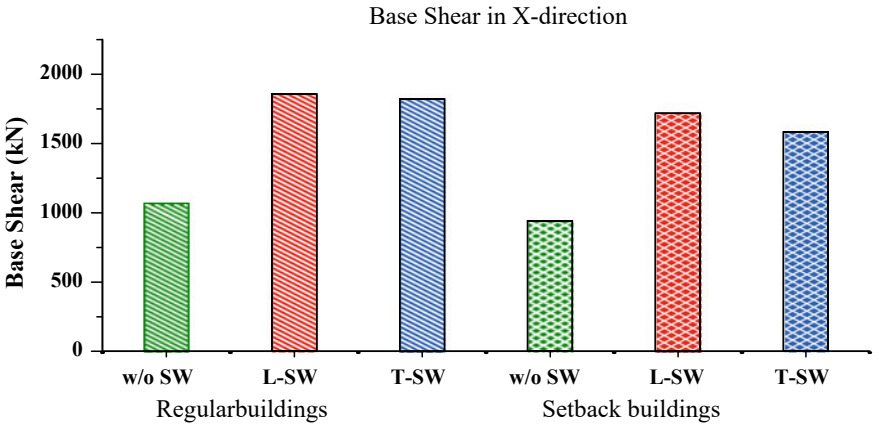

Fig. 10 Variations of base shear for all the models

Table 2 Fundamental time period of setback buildings

Setback building	Mode	Time period	Model mass ratio sum Ux	Participating sum Uy
Without shear wall	1	2.402	0	0.544
	2	2.303	0.7384	0.544
	3	1.548	0.7384	0.7617
L-shape shear wall	1	1.288	0	0.5401
	2	1.25	0.6571	0.5401
	3	0.656	0.6571	0.661
T-shape shear wall	1	1.385	0.6602	0
	2	1.319	0.6602	0.5694
	3	0.788	0.6603	0.6522

function of mass and stiffness of the structure, so except bare frame models, in all other models, the base shear has increased due to the stiffness and mass by the inducement of the shear walls.

4.4 Conclusions

A G+10 storeyed RC building with or without shear wall has been considered for the present study. The following conclusion has been drawn based on the present study which is as follows:

- The displacement of regular RC buildings is controlled with the shear wall. From the graph, it can be seen that the displacement reduction is more in L- shape shear wall compared to T-shape shear wall. The storey displacement is reduced to 38% by installing L-shape shear walls in the corners, whereas the storey displacement is reduced to 32% by installing T-shape shear wall at the intermediate sides of the building whereas in the y-direction, storey dis- placement is reduced to 32% for L-SW and around 35% for T-SW.
- In the case of the setback building, the storey displacement in x-direction is reduced to 37% by L-shape shear wall whereas T-shape shear wall was able to restrict it by 20%, whereas in the y-direction, storey displacement was restricted by 33% and 36% by L-shape and T-shape shear wall, respectively.
- The inter-storey drift ratio shows that the L-shape shear wall is more effective than T-shape shear wall for both buildings as it has the minimum drift ratio, all the models are under the maximum drift ratio limit stated by the IS 1893:2002, i.e. 0.004.
- The top storey displacement with time considering time history data of Northwest Calif-02 and 5% damping ratio is observed, and it is found out that L-SW minimizes the displacement very efficiently and considering variation in acceleration, buildings without shear wall has the minimum acceleration.

References

1. Dwivedi A, Tyagi BS (2020) Seismic analysis of building with and without shear wall for building with RCC and composite column. Int J Eng Res Technol (IJERT) 09(06):172–179
2. Tidke K, Patil R, Gandhe GR (2016) Seismic analysis of building with and without shear wall. Int J Innov Res Sci Eng Technol 05(10):17852–17858
3. Anshuman S, Bhunia D, Ramjiyani B (2011) Solution of shear wall location in multistorey building. Int J Civ Struct Eng 2(2):493–506
4. Akhter R, Prakash S, Baig MA (2017) P-delta effect on high rise building subjected to earth quake and wind load. Int J Eng Sci Comput 7(2):14441–14446
5. Chittiprolu R, Kumar RP (2014) Significance of shear wall in high-rise irregular buildings. Int J Educ Appl Res IJEAR 4(2):35–37

6. El-Sokkary H, Galal K (2012) Shake table tests on FRP-rehabilitated RC shear walls. In: 6th international conference on advanced composite materials in bridges and structures, Kingston, Ontario, Canada, pp 1–8
7. Boria A, Ghosh T (2021) A study on effect of shear wall in seismic analysis of building. In: IOP conference series: earth and environmental science
8. IS 1893 (part 1) (2016) Indian standard code of practice for criteria for design of earth-quake resistant structures. Bureau of Indian Standards, New Delhi
9. IS 456 (2000) Indian standard code of practice for criteria for plain and reinforcement concrete. Bureau of Indian Standards, New Delhi

Development of ANN-Based Risk Prediction Model in Construction Projects

N. Anirudh, S. P. Sreenivas Padala, and H. N. Eshwar Reddy

Abstract Construction projects are one among various major businesses which need high investments like time, money, resources to meet project requirements. As a result, risk is involved in executing construction projects. Timely completion of project within allocated budget is the main goal of any project. However, due to various risks involved, most of the projects are delayed and result in cost overruns. Thus, prediction of risk impacts on time and cost before their occurrence is essential for successful management of projects. Therefore, the objective of the study is to develop a model to predict risks using artificial neural network (ANN) approach. To achieve this objective initially, through literature review, 60 risk factors are identified. A questionnaire survey was conducted with 100 respondents to determine the probability and impact values of all risk factors. Based on survey data, an ANN model was developed using MATLAB software to predict risks. The findings revealed that ANN-based prediction can be utilized effectively to predict risks at early stages of construction project.

Keywords Risks · Risk prediction · Artificial neural network · Delays

1 Introduction

Construction projects are risky, complex, and difficult to manage. Different risks such as technical, financial, contractual, operational, and environmental risk affect the time and cost of the project. Risk is defined as product of probability of occurrence and impact of an event [1]. Early identification of these risks is essential to minimize impacts. The vital risk factors are schedule and cost risk [1]. Construction projects involve various number of resources and activities, and proper risk management may decrease the percentage of risk in projects [2, 3]. The construction industries are undergoing a technological shift for advanced productivity with artificial neural network to predict the level of risk occurring in construction projects [4–7]. Cost

N. Anirudh · S. P. S. Padala (✉) · H. N. E. Reddy
Department of Civil Engineering, M.S. Ramaiah University of Applied Sciences, Bangalore 560058, India
e-mail: sreenivasiit@gmail.com

© The Author(s), under exclusive license to Springer Nature Singapore Pte Ltd. 2023

K. R. Reddy et al. (eds.), *Recent Advances in Sustainable Environment*, Lecture Notes in Civil Engineering 285, https://doi.org/10.1007/978-981-19-5077-3_9

risk is the risk involved with the budget, cost quotation, execution cost, equipment expenses, manpower expenses, material expenses, equipment maintenance expenses documentation expenditures, etc. When there is cost variation between the planned and actual cost, the cost risk arises. There are many techniques that determine the variation of cost in the project like cost performance index, cost index, etc. Schedule risk is the risk involved with the duration, duration quoted for completion of project, time to start execution and end time of completion, equipment time, manpower mobilization, material delivery time, equipment maintenance time, documentation time, etc. [8, 9]. When there is schedule variation between the planned duration and actual duration, the schedule risk arises [10–14]. Therefore, the objectives of this study are to propose a model to predict risk affecting time and cost in construction project using artificial neural network (ANN) approach.

2 Background Study

Yaseen et al. [4] proposed a integrated artificial intelligence model known as integrative random forest to predict delay in construction. Two algorithms were used—random forest model and RF-GA model to develop a prediction model. The questionnaire was received from 40 projects with different time overrun levels. A questionnaire was distributed among 300 respondents. Delay level was classified as less than 50% of delay, 50–100% of delay, and more than 100% delay. The RF-GA model evaluation was done by measuring its indices and comparing the classical model. RF-GA showed a better results than classical model. The RF-GA values showed more accuracy, classification of error and Kappa are 91.67%, 8.3%, and 87%, respectively. Gondia et al. [15] developed prediction model to determine project delay based on risk factors. The methodology used is literature survey, and algorithms used are decision tree classifier and Naive Bayesian classifier. The results showed that the Naive Bayesian model offers better performance. The DT classifier errors for misclassification and accuracy are 25.5% (52.8%) and 74.5% (47.2%). Similarly, the errors for the NB classifier are 21.6% (48.8%) and 78.4% (51.2%). Chattapadhyay et al. [16] proposed a model to predict risk in megaproject construction. The study focused on using cross analytical-machine learning model. The questionnaire contains 150 total questions, among which 70 valid responses were received. A total of 63 risk variables were framed depending on responses received. The responses were received based on a five-point scale ranging from extremely low impact to high and extremely high impact. The research uses the genetic algorithm k-mean-assisted risk to classify high-risk factor. The findings revealed that that delay is caused due to the temporary traffic regulation orders, followed by inappropriate equipment and quality of the material. Sanni-Anibire et al. [7] proposed an ML model for assessing delay risk in tall building projects. The methodology used is a questionnaire survey, and algorithms used are K-nearest neighbors (KNNs), ANN, and support vector machines (SVMs). The study has identified 36 risk factors. The questionnaire survey contains two domains that are consequence and likelihood, Likert scale 1 to 5 is

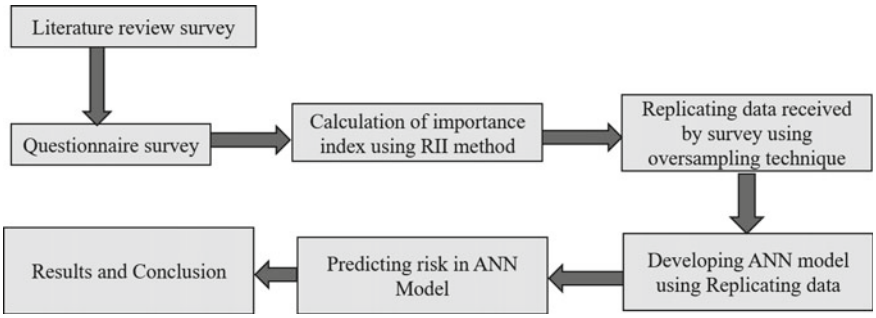

Fig. 1 Methodology for development of risk prediction model

used to measure the degree of risk. A total of 62 responses were received among water which 48 responses were considered valid. The critical factors are decision-making delay, sub-contractors works delay, late instructions by architects and structural engineers, and shop drawings approval delay and delay in material samples. The results indicated that ANN has good level of performance with 93.75% classification accuracy.

3 Research Methodology

The methodology to develop ANN-based prediction model is shown in the Fig. 1 Initially, literature survey is done to identify 60 factors which are grouped under seven factors. A questionnaire survey was conducted to determine mean values and critical risk factors. Last, the survey data were considered as input for ANN model to predict risks. The errors are determined by comparing predict risk values with actual risk values generated from survey.

4 Dataset Establishment

Data collection has been carried out to collect information from all relevant sources pertaining to the present study. The preliminary survey is carried out for various construction projects, and standard literature reviews have been referred to choose the appropriate methodology and for framing questions. Questionnaire survey has been carried out by distribution of questionnaires among industrialists working in various reputed civil industries. Questionnaire consists of two domains, i.e., cost and time causing risk in construction projects. A total of 100 questionnaires have been circulated to the industry experts. Respondents majorly consist of site engineers, QC and QA engineers, and junior engineers shown in Fig. 2. The respondent reposed was majorly industrialists, i.e., 95% industrialists and 5% research scholars. The

responses have been received based on various types of projects such as residential, commercial, and infrastructure projects, i.e., 27.6%, 34.5%, and 37.9%, respectively, shown in Fig. 3. From the literature survey, factors have been adopted based on the probability and impact of risk on time and cost. The following factors have been adopted to study the risk involved in risk of construction projects. Risk factors in construction projects are shown in Tables 1 and 2.

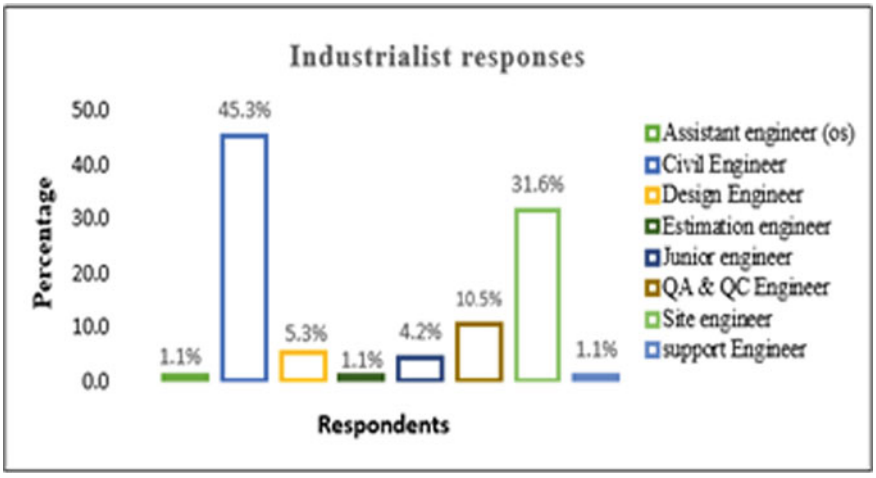

Fig. 2 Industrialist responses

Fig. 3 Type of projects

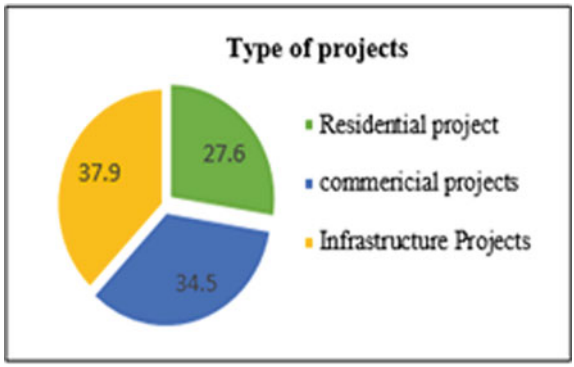

Table 1 Risk factors

S. no	Risk factors
1	Construction risk factor
2	Technical risk factor
3	Economical risk factor
4	Environmental risk factor
5	Social risk factor
6	Political risk factor
7	Health and safety risk factor

5 ANN-Based Prediction Model

To develop ANN prediction model, MATLAB software is utilized. MATLAB provides tools such as nntool and nftool for developing prediction models. An artificial neural network uses neuron principles in brain as a basis for developing algorithms that can be used to model complex patterns and prediction problems. These models are usually based on computational models that are intended to replicate the behavior of biological neurons in neural networks. These algorithms represent an adaptive system of reconnected neurons arranged in a network of multi-layered. ANN is based on three main layers—input, hidden, and output. ANN is a type of ML algorithm that is used to model complex patterns in the datasets by using multiple hidden layers and non-linear activation functions. The overfitting is avoided using random oversampling technique. This technique involves supplementing the existing data with multiple copies such as 2x,3x,4x,5x,6x…, etc. In this study, total of 60 risk factors are considered to predict risk on time and cost. Through survey, initially, data on probability and impact of 60 risk factors are collected individually for time and cost. The revised dataset size was 240 Nos which was further replicated to 3 times. Thus, total dataset considered for training ANN model is 720 Nos. Using ANN, prediction models can be trained iteratively, and error minimization can be done using optimization technique—gradient descent. In this study, regression algorithm is used for developing a prediction model.

6 Results and Discussion

The training technique used in the work is supervised training method where in input and target both are fed to train the neural network. This robust technique used to train models, the dataset can be randomly replaced to achieve the perfect prediction model. Inputs and targets are used to train the model. Simulation is done whose outputs are required in present work inputs, and targets are generated using oversampling techniques, and the response and number of respondents for each element are used as a simulation and assigned to model for predicting the RII mean as output which

Table 2 Sub-risk factors

S. no	Sub-risk factors
1	Poor site supervision by the contractor
2	Adoption of improper construction methods/techniques
3	Improper planning, scheduling, and controlling
4	Rework in construction due to various errors
5	Poor workmanship
6	Changes in construction methodology
7	Low skilled/incompetent workforce
8	Lack of availability of skilled labor
9	Non-conforming materials
10	Change of sub-contractors frequently
11	Consultants delay in inspection and testing
12	Damage material
13	Shortage in manpower supply and availability
14	Lack of material availability
15	Lack of equipments
16	Improper material delivery schedule
17	Incompetency of designers
18	Design changes
19	Inadequate or poor design briefing
20	Poor project quality management
21	Complexity of proposed design solutions
22	Un-use of advanced engineering design software
23	Insufficient feasibility study
24	Late issue of drawings and documents
25	Lack of site access
26	Incorrect take off calculation
27	Lack of constructability analysis
28	Changes in foreign exchange rate and interest rate
29	Changes in tax rates
30	Incorrect cost estimate
31	Market demand changes
32	Delays and interruptions
33	Unrealistic project duration
34	Delay in progress payments by owner
35	Owners sudden bankruptcy
36	Natural disaster

(continued)

Table 2 (continued)

S. no	Sub-risk factors
37	Inadequate site investigations
38	Force majeure
39	Effects of subsurface conditions
40	Unavailability of utilities in site
41	Unexpected inclement weather
42	Environment issues
43	Unforeseen site conditions
44	Requirements of neighboring society
45	Changes in local body regulations
46	Cultural and heritage sights
47	Conflicts due to differences in culture
48	Changing government regulations/funding policy
49	Legal disputes
50	Fragmented decision-making by clients
51	Political issues
52	Corruption
53	Expropriation and nationalization of assets/facilities
54	Unfairness in tendering
55	Difficulty in claiming insurance compensation
56	Lack of safety measures
57	Non-compliance with health, safety, and environmental standards
58	Ineffective protection of surrounding environment
59	Epidemic illness
60	Inexperienced equipment operators

then is compared with theoretically calculated RII mean to check the accuracy of output by ANN model. To obtain a proper model with the least mean square error and maximum regression value, 12 trails have been carried out with two hidden layers and a different number of nodes to find best model. For 100 dataset, 70% data are used for training, 15% data are used for validation and 15% for testing.

Two inputs—probability and impact values are used as inputs and risk as target values, Levenbergs Marquart algorithm is used to train the model with training function of tan sigmodal. The model has taken 65 epochs to reach the precise targeted values. The ANN shows 0.99 R^2 value indicating that model is satisfactorily trained and predicts the risk values. Network architecture, training of neural network is shown in Fig. 4, and regression results, training state, and performance graphs are shown in Figs. 5, 6, and 7, respectively. The ANN trails are shown in Table 3 and Fig. 8. It is evident that hidden layer with 14 neurons has low training, testing, and

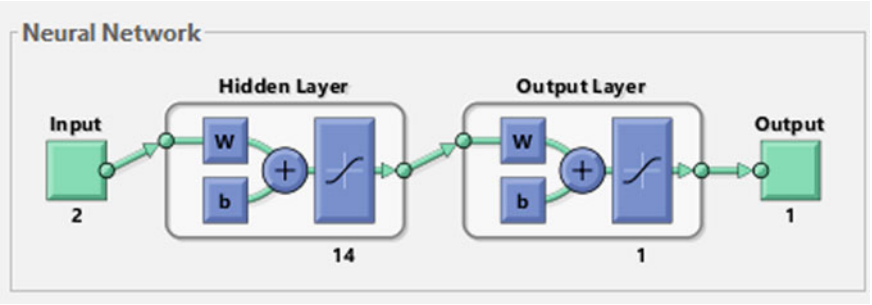

Fig. 4 ANN risk prediction model architecture

validation error. Finally, the predicted risk values on time and cost are determined from ANN model, and results are presented in Table 4.

7 Conclusions

Risk prediction is one of the critical tasks of project management. Early prediction of risks can minimize the unnecessary schedule and cost overruns of the projects. In the present study, ANN approach is used to predict the risk involved in the construction sector. The proposed methodology that is adopted was found to be effective for the prediction of the impact of risk on time and on cost, probability of risk on time and on cost. The MSE found to be 2.86 (training), 3.22 (testing), and 3.64 (validation) for selected ANN model. The developed ANN model can be used in future to predict risk in different type of construction projects with the help of same or different respondents inputs. The risk identification can be carried out with existing questionnaires in different locations to predict the impact and probability of factors on risk. Other machine learning algorithms can be used to develop the prediction model, and comparison between the models can be carried out to select a suitable model.

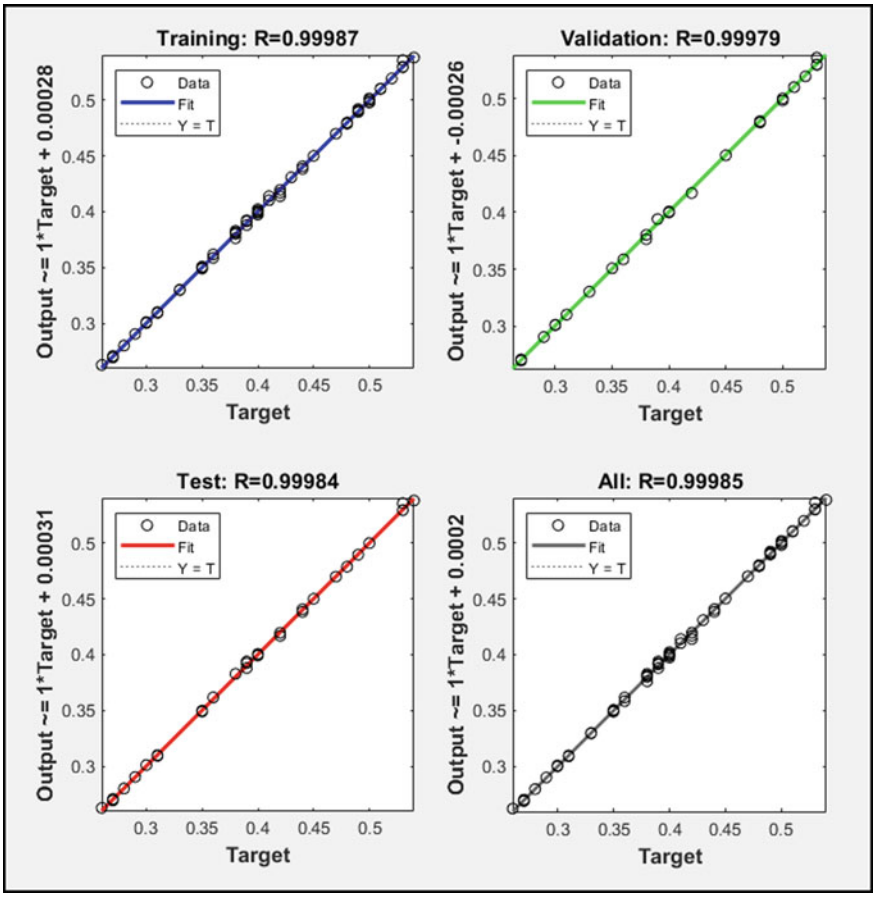

Fig. 5 Regression results of ANN model

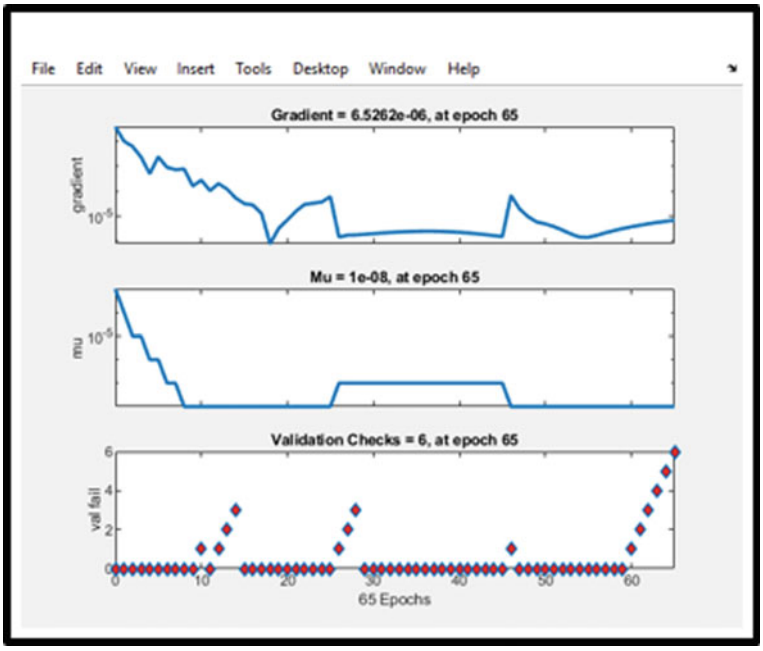

Fig. 6 Training state

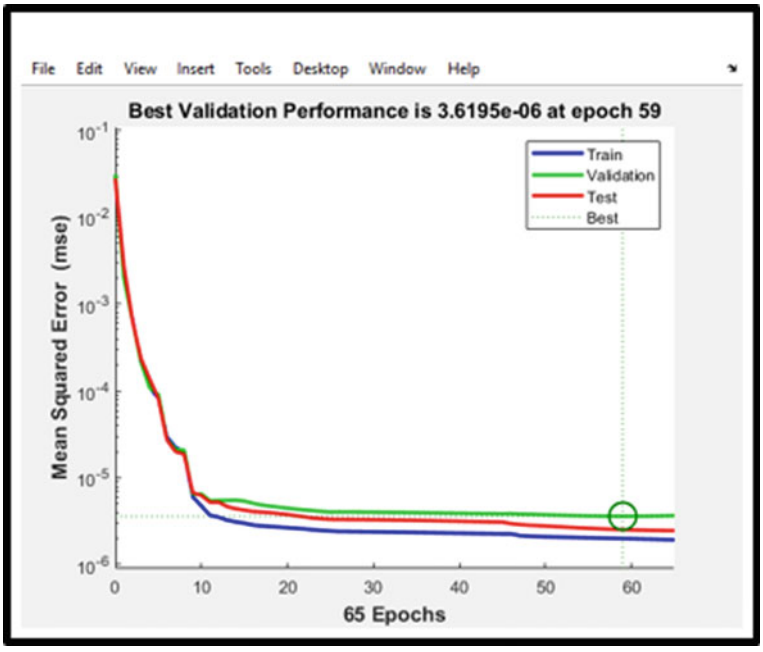

Fig. 7 Performance graph

Table 3 Trials to train ANN model

Trails	No. of nodes	Training		Testing		Validation		Overall *R*-value
		MSE	R^2	MSE	R^2	MSE	R^2	
1	1	68.67	0.6	97	0.53	91.99	0.54	0.58
2	2	46.23	0.76	51.69	0.75	74.86	0.67	0.751
3	3	20.31	0.9	13.1	0.94	29.08	0.88	0.906
4	5	6.18	0.97	11.27	0.94	8.69	0.96	0.967
5	6	3.54	0.98	5.73	0.97	6.09	0.97	0.981
6	8	3.45	0.98	3.34	0.98	2.15	0.99	0.985
7	10	3.1	0.98	3.39	0.98	3.32	0.98	0.985
8	11	3.1	0.98	3.93	0.98	3.32	0.98	0.986
9	12	3.09	0.98	3.33	0.98	3.43	0.98	0.999
10	14	2.86	0.99	3.22	0.99	3.64	0.99	0.986
11	15	2.9	0.98	3.25	0.98	4.32	0.98	0.986
12	18	3.58	0.98	5.11	0.98	5.21	0.98	0.986

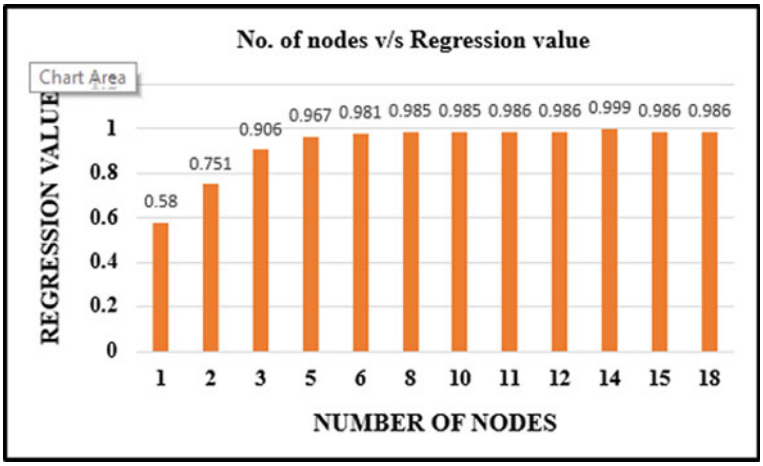

Fig. 8 Different trails graph

Table 4 Predicted risk from ANN model

S. no	Risk factors	Time		Cost	
		Risk	Rank	Risk	Rank
1	Construction risk factor	0.40	2	0.44	1
2	Technical risk factor	0.35	3	0.36	3
3	Economical risk factor	0.26	4	0.38	2
4	Environmental risk factor	0.17	6	0.18	6
5	Social risk factor	0.11	7	0.11	7
6	Political risk factor	0.21	5	0.28	4
7	Health and safety risk factor	0.42	1	0.24	5

References

1. Siraj NB, Fayek AR (2019) Risk identification and common risks in construction: literature review and content analysis. J Constr Eng Manage
2. Gupta VK, Thakkar JJ (2018) A quantitative risk assessment methodology for construction project. Sadhana 43:116
3. Ling CX, Li C (1998) Data mining for direct marketing: problems and solutions. Am Assoc Artif Intell
4. Yaseen ZM, Ali ZH, Salih SQ, Al-Ansari N (2020) Prediction of risk delay in construction projects using a hybrid artificial intelligence mode. Sustainability 12:1514
5. Asadi A, Alsubaey M, Makatsoris C (2015) A machine learning approach for predicting delays in construction logistics. Int J Adv Logistics 115–130
6. Keshk AM, Maarouf I, Annany Y (2018) Special studies in management of construction project risks, risk concept, plan building, risk quantitative and qualitative analysis, risk response strategies. Production and hosting by Elsevier B.V. on behalf of Faculty of Engineering, Alexandria University
7. Sanni-Anibire MO, Zin RM, Olatunji O (2020) Machine learning model for delay risk assessment in tall building projects. International journal of construction management. Informa UK Limited, trading as Taylor & Francis Group
8. El-Sayegh SM (2008) Risk assessment and allocation in the UAE construction industry. Int J Project Manage 431–438
9. Choi H-H, Cho H-N, Seo JW (2004) Risk assessment methodology for underground construction projects. J Constr Eng Manage 130:258–272
10. Tah JHM (2000) A proposal for construction project risk assessment using fuzzy logic. Constr Manag Econ 18:491–500
11. Padala SPS, Maheswari JU (2019) Axiomatic design framework for changeability in design of construction projects. Asian J Civil Eng 21(2):201–215
12. Subramanyan H, Sawant H, Batt V (2012) Construction project risk assessment: development of model based on investigation of opinion of construction project experts from India. J Constr Eng Manage 138:409–421

13. Padala SPS, Maheswari JU, Hirani H (2020) Identification and classification of change causes and effects in construction projects. Int J Constr Manage. https://doi.org/10.1080/15623599.2020.1827186
14. Ebrat M, Ghodsi R (2014) Construction project risk assessment by using adaptive-network-based fuzzy inference system: an empirical study. KSCE J Civil Eng
15. Gondia A, Siam A, El-Dakhakhni W, Nassar AH (2020) Machine learning algorithms for construction projects delay risk prediction. J Constr Eng Manage 146(1):04019085
16. Chattopadhyay DB, Putta J, Rao RM (2021) Risk identification, assessments, and prediction for mega construction projects: a risk prediction paradigm based on cross analytical-machine learning model. Buildings 11:172

Evaluation of the Phytoremediation Potential of Pegaga (*Centella asiatica*) under Shrimp Farm Effluent

D.-N. Yen, H.-V. Hieu, Tran Thanh, and L.-Q. Tuong

Abstract The commercial aquaculture sector in culturing shrimp (*Macrobrachium rosenbergii*) may be increased contaminants in the waterbody without proper treatment. Our research is directed to examine the morphology and the survival rate of wetland plants as *Centella asiatica* had a fresh weight 20.73 ± 0.019 g, length of tree 23.5 ± 0.17 cm, and length of roots 4.5 ± 0.03 cm (e.g., a plant group/reactor) for raising in an aquarium containing 7 L of shrimp farm effluent in a period from the start time to the 15 days. In the experimental design, the Control aquarium is a non-planted aquarium ($n = 2$), and the Experiment aquarium is an aquarium planted with *Centella asiatica* ($n = 3$). Physical and chemical indicators are temperature, pH, EC, TDS, and DO for daily monitoring in a period from the start time to fifteen dates. Water samples are collected on the start time, 5 days, 10 days, and 15 days for analysis of indicators ammonium-nitrogen (NH_4^+-N), phosphate (PO_4^{3-}), iron (Fe), and copper (Cu). The findings show that *C. asiatica* grow well in the shrimp farm effluent with 100% high survival rate, especially a new plant that grows from a vegetative part of *C. asiatica* (i.e., it is usually a stem of the parent plant of *C. asiatica*) on the 10 days and 15 days. In conclusion, *C. asiatica* has the capacity to adapt and remove NH_4^+-N and PO_4^{3-} pollutants under static conditions. The growth and development of *C. asiatica* have a positive effect on reducing pollutants from shrimp farm effluent for 15 days experiments as phytoremediation potential of biological treatment.

Keywords Phytoremediation · Shrimp farm effluent · *Centella asiatica*

D.-N. Yen · L.-Q. Tuong (✉)
Faculty of Food and Environmental Engineering, Nguyen Tat Thanh University, Ho Chi Minh City 70000, Vietnam
e-mail: lqtuong@ntt.edu.vn

H.-V. Hieu
Faculty of Biotechnology, Nguyen Tat Thanh University, Ho Chi Minh City 70000, Vietnam

T. Thanh
NTT Hi-Tech Institute, Nguyen Tat Thanh University, Ho Chi Minh City 70000, Vietnam

© The Author(s), under exclusive license to Springer Nature Singapore Pte Ltd. 2023

K. R. Reddy et al. (eds.), *Recent Advances in Sustainable Environment*, Lecture Notes in Civil Engineering 285, https://doi.org/10.1007/978-981-19-5077-3_10

1 Introduction

The development of aquaculture production in Vietnam already caused wastewater generation, and the water resource protection is challenged in high pressure. The clearest example of the devastation people cause is the decline of water quality in intensive shrimp culture (*Macrobrachium rosenbergii*) which means shrimp farm effluent. High stocking density prompts the high amount of feed given to shrimp. The untreated effluent contains many sorts of toxins that comprise of organic and inorganic materials with various concentrations in wastewater. The untreated shrimp effluent is discharged without any form of treatment that can influence environment quality and ecosystem. Phytoremediation by aquatic plants handles this issue, as a general rule, a plant-based innovation called phytoremediation is utilized to clean contaminated water bodies [1]. These methods are thought of as effective, economy, and eco-accommodating for the ecosystem. Phytoremediation innovation has been known over the most recent twenty years that the capacity of plants reduces nutrient concentration from polluted area by the plant roots [2]. The process is harmless to the ecosystem conditions and also likewise builds the worth of biodiversity and diminishes undesirable substances to remove the contaminant from water [3]. Plant species *Centella* are chosen in terms of the phytoremediation agents because the plant shows their rapid growth rate and tolerance to contaminated areas. Overall, *Centella* species comprises approximately 50 species belonging to the plant family *Apiaceae* which includes the medicinally important *Centella asiatica* (L.) Urban (herein *C. asiatica*) [4]. The plant comes from the tropical and subtropical regions [5], being a weakly aromatic, slender, and creeping perennial plant that flourishes in wet areas [6]. The growth of *C. asiatica* is influenced by different nutrients including nitrogen, carbon, potassium, phosphorous, magnesium, and manganese concentration [7]. According to the International Union for Conservation of Nature's Red List (https://www.iucnredlist.org/species/168725/88308182), *C. asiatica* is one of the local herbs, which is recently mentioned for The IUCN Red List of threatened species. The plant may exhibit phytoremediation potential in nickel-ore contaminated soils [8] and plants used as phytoremediation for controlling erosion and soil contamination [9]. The previous study shows that *C. asiatica* is utilized for the phytoremediation of BOD5, COD, and NH_4^+-N in municipal wastewater [10]. Yet, studies have rarely investigated how *C. asiatica* shows phytoremediation of the shrimp farm effluent. Therefore, the objective of this study was to evaluate the effectiveness of *C. asiatica* in the phytoremediation of the shrimp farm effluent in culturing shrimp (*M. rosenbergii*).

2 Materials and Methods

2.1 Plant Materials

The in situ study investigated the impacts of *C. asiatica* L. Urban on shrimp farming effluent because of the negative effect of shrimp farm effluent on waterbodies. Plants of *C. asiatica* were bought from a business nursery, and these plants were painstakingly washed utilizing regular water and then to eliminate all the debris. Two treatments separated the control without plants and the experimental plot in Fig. 1. Plants per experimental plot were totally randomized in this study. Both treatments had 4 special periods of time as the start time, 5 days, 10 days, and 15 days. *C. asiatica* was harvested and the water sample was stored at various times. An aquarium contained 7 L of shrimp farm effluent (i.e., *Macrobrachium rosenbergii*). The selective *C. asiatica* in the experimental design had a plant height 23.5 ± 0.17 cm, length of roots 4.5 ± 0.03 cm, and 20.73 ± 0.019 g of the plant's total fresh weight/aquarium (e.g., a plant group/reactor), groups of *C. asiatica* were well carefully selected with similar morphology to conduct this study.

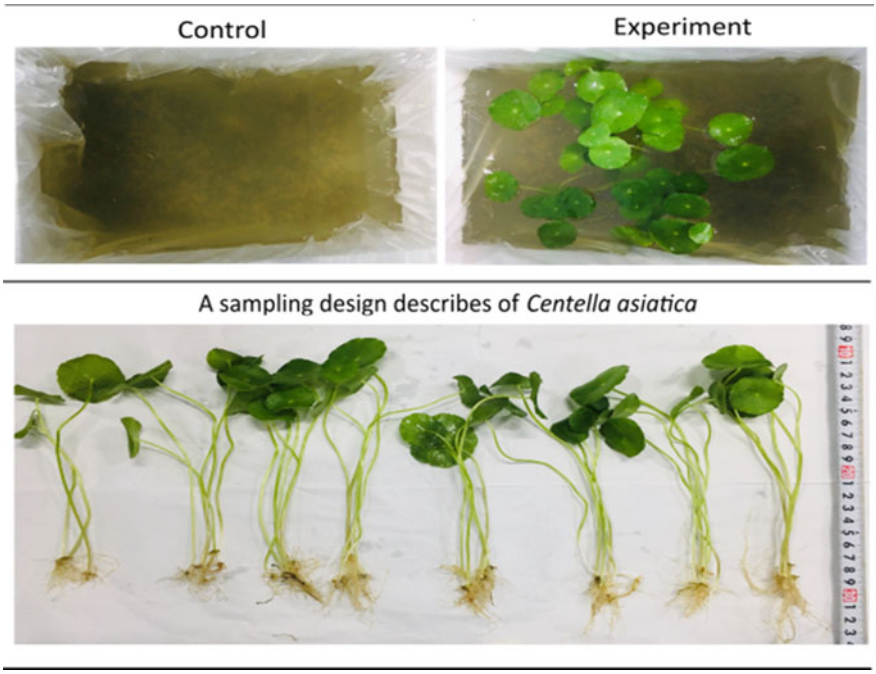

Fig. 1 Morphology of *C. asiatica* cultured in shrimp farm effluent in this study

2.2 Samples Collection and Analysis

The main reason for an examination of a plant's dry weight is clarified by the specified time. Plants in every aquarium were collected and washed with tap water, followed by distilled water. And afterward, plants were washed any leftover soil and contaminants residue from the plant shoots and roots, followed by drying on a filter paper. The plants are gauged, estimated the root size, and dried at 65 °C (dried to steady weight after two gaugings) to affirm the last dry weight. Second, a comparison of physical and chemical indicators between the control and the experiment was analyzed to find out the changes during experimental periods. The finding indicated that the water quality before and after treatment was examined the different concentrations in ammonium-nitrogen (NH_4^+-N), phosphate (PO_4^{3-}), iron (Fe), and copper (Cu) in shrimp rearing wastewater through the phytoremediation method by *C. asiatica.* There are analyzing methods as (1) water temperature (°C), pH, EC, and TDS by using measurement Mi805 Milwaukee, CO, USA. (2) Dissolved Oxygen by Milwaukee 600, CO, USA. (3) The HI83399-02 was a multi-parameter photometer for measuring important water quality parameters such as NH_4^+-N (a sample solution: HI93715A-O), phosphate PO_4^{3-} (a sample solution: HI93717-01), Cu (a sample solution: HI93702-01), and Fe (a sample solution: HI 93,721-01). Mean values and standard errors of water quality parameters were conducted from replicates (mean $\pm$ S.E, $n = 3$), to be done within each treatment at four special periods of time as the start time, 5, 10, and 15 days. These distinctions in findings were compared to the water quality standards of Vietnam [11, 12], and water quality standards of the World Health Organization (WHO) [13].

3 Results

3.1 Growth of C. asiatica

The responses of *C. asiatica* were investigated based on their morphological and physiological parameters in aquarium experiments. The in situ and laboratory tests in Fig. 2 presented that an increase of total dry weight of the *C. asiatica* was 3.6 g in 5 days, 2.84 g in 10 days, 5.03 g in 15 days, being higher than 1.81 $\pm$ 0.16 g of dry weight/aquarium at the start time. According to the observations of *C. asiatica* in 15 days, the plant looked healthy with green leaves and shoot proliferation of *C. asiatica* well grown at various times. The increase of plant biomass with a 100% survival rate of *C. asiatica* showed that *C. asiatica* is one of the important requirements in the phytoremediation process with the ability to treat shrimp farm effluent.

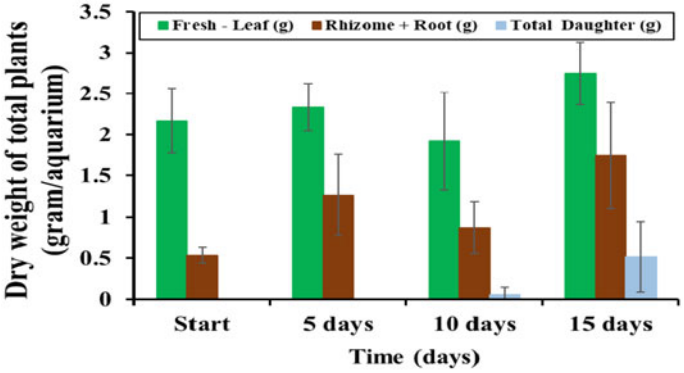

Fig. 2 Expression of dry weight growth of *C. asiatica* in this study

3.2 Water Quality

The study mentioned only a role for plants in the phytoremediation process with the ability to treat shrimp farm effluent. A range of air temperature was 26–28 ºC in the laboratory condition and water temperature in 15 day's period ranges from 25.7 ± 0.0 to 29.2 ± 0.06 ºC for the control and ranges from 25.3 ± 0.1 to 29.0 ± 0.2 ºC for the experiment. Optimal growth performance of aquatic plants and animals in water temperatures was in a range of 20–30 ºC [14]. The pH in the control ranged from 7.03 ± 0.02 to 8.25 ± 0.16, and the pH in the experimental ranged from 7.05 ± 0.07 to 8.05 ± 0.24. The pH was within the allowable standards of class B2 in (QCVN 08, 2015) and World Health Organization (WHO) with the threshold of pH 6–9 for a purpose of conserving aquatic ecology. The conductivity in the control ranged from 1213 ± 11 to 1380 ± 12 µs/cm with the conductivity average of 1274 ± 42 µs/cm, and the conductivity in the experimental ranges 1225 ± 4 to 1399 ± 11 µs/cm with the conductivity average of 1302 ± 48 µs/cm, therefore, it is difference of conductivity of control and experiment in this study. The trend of total dissolved solids (TDS) in all control and experiment was a limit standard of allowable standards as a concentration of TDS < 1000 mg/l. The dissolved oxygen concentration (DO) examination of control had a range from 0.68 ± 0.08 mg/l to 9.1 ± 0.28 mg/l with 6.49 ± 2.74 mg/l of an average concentration. And the average dissolved oxygen concentration (DO) of the experiment had a range from 0.63 ± 0.06 mg/l to 7.97 ± 1.25 mg/l with 5.73 ± 2.32 mg/l of an average concentration. Therefore, examination of the water temperature (°C) pH, EC, TDS, and DO provides useful information to better understand the survival rate of *C. asiatica* with new plants (Fig. 2) in the shrimp farm effluent.

The control contains only shrimp farm effluent, and the result found a stable concentration of nitrogen and phosphate in the effluent in situ study. The decreased NH_4^+-N value presented from the start time to 5 days, and then kept the stable concentration from 5 days 10 days, and 15 days that the ammonium ions or nitrogen

explained by the growth of plants through the root system (i.e., a healthy root system looks white and provides a lot of lateral roots and rootlets) because *C. asiatica* usually needed nitrogen (e.g., NH_4^+-N) for growth and development and NH_4^+-N concentration of the experiment was lower than the control level during the experimental duration in Fig. 3a. The trend of NH_4^+-N concentration at the start time was 3.27 ± 0.46 mg/l, and then, a reduction trend of NH_4^+-N concentration at 15 days was of 0.473 ± 0.04 mg/l of experiment, it means that the phytoremediation of NH_4^+-N by *C. asiatica* was in the permitted limit of class B2 in the water quality standards of Vietnam [11], regulating NH_4^+-N < 0.9 mg/l. The effectiveness of the treatment by *C. asiatica* through phytoremediation may be enhanced by choosing aquatic macrophytes with high tolerance toward ammonia levels in wastewater [15, 16]. In general, ammonia was also considered one of the important nutrients for *C. asiatica* to grow, and the presence of NH_4^+-N in the shrimp farm effluent explains of the processes of organic waste matter decomposition as well as nitrogen fixation. The roots of *C. asiatica* seem an important role in this method, and the roots can fix the suspended particles in effluent samples. The previous study [17] showed that, *C. asiatica* plants can able to remove 98% of NH_3-N, 90% of TSS, and 64% of phosphate PO_4^{3-}. And *C. asiatica* can accumulate heavy metals through its roots, stems, and leaves in the previous study [18]. Figure 3b showed that the PO_4^{3-}concentration at the start time was 18.2 ± 0.4 mg/l both treatments, and a trend of the experiment significantly decreased 11.4 ± 1.6 mg/l of 15 days. *Centella asiatica* was considered phytoremediation agent as its capacity absorbs different concentrations of contaminants in the water body [1] and phosphorus adsorption by plants in this effluent was the main factor in this study. The trend of the PO_4^{3-}concentration in the experiment decreased because of the processes and mechanisms for aquatic plants to take up nitrogen (N) and phosphorus (P) in contaminated water [16]. These *C. asiatica* can take up phosphorus continuously which reveals the suitability of applying to *C. asiatica* for treating the shrimp farm effluent.

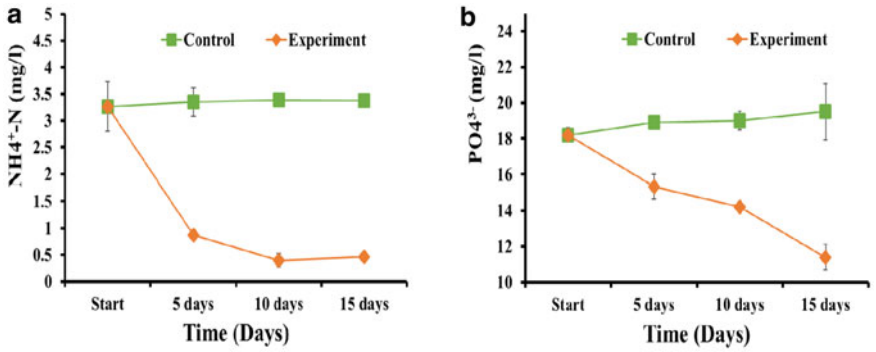

Fig. 3 Remaining concentration of ammonium-nitrogen (**a**) and phosphate (**b**) in shrimp farm effluent treated with *C. asiatica* at various times under static conditions

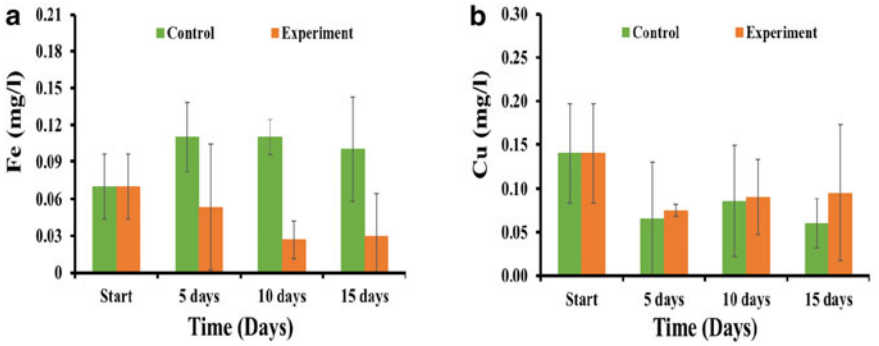

Fig. 4 Remaining concentration of iron (**a**) and copper (**b**) in shrimp farm effluent treated with *C. asiatica* at various times under static conditions

Figure 4a showed that the trend of Fe concentration of the experiment was strikingly lower than the trend of Fe concentration of the control. It means that the Fe concentration of the experiment may be absorbed by *C. asiatica* uptake at various times under static conditions, and the Fe concentration at the start time was 0.07 ± 0.03 mg/l and a trend of Fe concentration at the end of this study at 15 days was of 0.03 ± 0.03 mg/l. According to the previous study of Marlia Mohd Hanafia [19], *C. asiatica* can be used as phytoremediation plants for removing iron (Fe) from industrial wastewater. Figure 4b indicated that the Cu concentration at the start time was 0.14 ± 0.06 mg/l in a limit < 2 mg/l of Cu standard from World Health Organization (WHO) [13]. This Cu concentration in a solution of both treatments presented on the 5, 10, 15 days, being lower than the start time. Another study also confirmed the maximum removal of copper in the waste water by *C. asiatica* was 99.6% [20].

4 Conclusion

The effectiveness of *C. asiatica* in removing NH_4^+-N, PO_4^{3-}, Fe, and Cu from shrimp farm water effluent was investigated in this study. These findings indicated that the growth of plants in the phytoremediation system showed a positive response by the increasing biomass growth of *C. asiatica* on the 5 days, 10 days, and 15 days, compared to the start time which reveals the suitability of applying to *C. asiatica* for treating the shrimp farm effluent. The study concluded that the shrimp farm effluent can be treated by *C. asiatica* like phytoremediation potential of biological treatment of wastewater containing nitrogen and phosphate from the shrimp farm effluent.

References

1. Muthusaravanan S et al (2018) Phytoremediation of heavy metals: mechanisms, methods and enhancements. Environ Chem Lett 16(4):1339–1359
2. Lai WL, Wang SQ, Peng CL, Chen ZH (2011) Root features related to plant growth and nutrient removal of 35 wetland plants. Water Res 45(13):3941–3950
3. Quang-Tuong L, Thanh T (2021) Contaminant removal from shrimp rearing wastewater by wetland plant species (*Echinodorus amazonicus*). IOP Conf Ser Earth Environ Sci 785(1):0–4
4. James J, Dubery I (2011) Identification and quantification of triterpenoid centelloids in *Centella asiatica* (L.) Urban by densitometric TLC. J Planar Chromatogr Mod TLC 24(1):82–87
5. Müller V, Lankes C, Zimmermann BF, Noga G, Hunsche M (2013) Centelloside accumulation in leaves of *Centella asiatica* is determined by resource partitioning between primary and secondary metabolism while influenced by supply levels of either nitrogen, phosphorus or potassium. J Plant Physiol 170(13):1165–1175
6. Aziz ZA, Davey MR, Power JB, Anthony P, Smith RM, Lowe KC (2007) Production of asiaticoside and madecassoside in Centella asiatica in vitro and in vivo. Biol Plant 51(1):34–42
7. Roy A, Bharadvaja N, Krishnan ML (2018) Influence of different macro and micro nutrients on the shoot multiplication of *Centella asiatica.* J Plant Biochem Physiol 6(2):1–5
8. Madjos GG (2018) Phytoremediation potential of *Centella asiatica* (gotu kola) in nickel ore-contaminated soils. J Biodivers Environ Sci 13(6):99–108
9. Roslan R, Omar RC, Baharuddin INZ (2016) Erosion and soil contamination control using coconut flakes and plantation of *Centella Asiatica* and *Chrysopogon Zizanioides.* IOP Conf Ser Mater Sci Eng 160(012082):1–7
10. Azarpira H, Behdarvand P, Dhumal K, Pondhe G (2013) Phytoremediation of municipal wastewater by using aquatic plants. Adv Environ Biol 7(14):4649–4654
11. QCVN 08-MT (2015) National technical regulation on surface water quality (Quy Chuẩn Kỹ Thuật Quốc Gia Về Chất Lượng Nước Mặt)
12. QCVN 01-BYT (2009) Vietnamese National technical regulation on drinking water quality (Quy Chuẩn Kỹ Thuật Quốc Gia Về Chất Lượng Nước Ăn Uống)
13. World Health Organization (WHO) (2006) A compendium of standards for wastewater reuse in the Eastern Mediterranean Region. Regional Centre for Environmental Health Activities CEHA
14. Tuong LQ, Nam NP (2017) Different growth performance - tilapia (Oreochromis Niloticus) in using two different types of feed at Hoa my Reservoir, Thua Thien Hue Province, Vietnam. Khoa Học Kỹ Thuật Thủy Lợi Và Môi Trường. J Water Resour Environ Eng 56:9–15. ISSN 1859–3941
15. Ting WHT, Tan IAW, Salleh SF, Wahab NA (2018) Application of water hyacinth (*Eichhornia crassipes*) for phytoremediation of ammoniacal nitrogen: a review. J Water Process Eng 22:239–249
16. Tuong LQ, Nhan (NTT) Potential of *Echinodorus cordifolius* and *Vallisneria natans* in constructed wetlands for the removal of water pollution from shrimp farm effluent. In: IOP conference series: materials science and engineering, pp 1–11 (2020)
17. Nizam NUM, Hanafiah MM, Noor IM, Karim HIA (2020) Efficiency of five selected aquatic plants in phytoremediation of aquaculture wastewater. Appl Sci 10(8)
18. Yap CK, Fitri MRM, Mazyhar Y, Tan SG (2010) Effects of metal-contaminated soils on the accumulation of heavy metals in different parts of *Centella asiatica*: a laboratory study. Sains Malaysiana 39(3):347–352
19. Hanafiah MM, Zainuddin MF, Nizam NUM, Halim AA, Rasool A (2020) Phytoremediation of aluminum and iron from industrial wastewater using *Ipomoea aquatica* and *Centella asiatica.* Appl Sci 10(9):1–13
20. Fizri FFA, Mokhtar H, Morad N (2011) Phytoaccumulation of copper from aqueous solutions using *Eichhornia Crassipes* and *Centella Asiatica.* Int J Environ Sci Dev 2(3):205–210

Performance Evaluation of Sustainable Concrete at Elevated Temperature Using Recycled Concrete Aggregate and Copper Slag

Anasuya Sahu, Adarsh Srivastav, and Sanjay Kumar

Abstract The requirement of sustainable development is a prime focus of today's world. In this regard, utilization of construction and industrial waste possessing characteristics to be used as building materials will be a great push to achieve an equitable balance of environmental, social, and economic sufficiency for completing the trilogy of sustainable development. Incorporation of recycled concrete aggregate as replacement of natural coarse aggregate and replacement of fine aggregate with copper slag will guide us to the goal of sustainable development at a specific percentage of replacement levels. Recycled concrete aggregate is different from natural aggregate in terms of interfacial zone characterization as a new bond has to establish when we use RCA. A significant study has been done on RCA but a great deal of work is needed to understand the effect of elevated temperature on RCA through this experimental approach proper relationship between different replacement levels, and their impact on mechanical properties is discussed. To test the mechanical property at elevated temperatures of 150, 300, 450, 600 °C with replacement levels of 0, 33, 67, and 100% of natural aggregate with recycled concrete aggregate is performed and then keeping RCA replacement as 33% as control mix, replacement of fine aggregate up to 60% is done. From the experimental results, it is found that replacement of NA with 33% RCA shows better result in compressive and split tensile test. Fine aggregate is replaced by copper slag, and it is found that replacement of copper slag between 40 and 60% with 33% RCA as control mix shown better compressive strength.

Keywords Sustainable development · Recycled concrete aggregate (RCA) · Copper slag (CS) · Elevated temperature

A. Sahu · A. Srivastav (✉) · S. Kumar
National Institute of Technology Jamshedpur, Jamshedpur 831014, Jharkhand, India
e-mail: Adarsh991926@gmail.com

© The Author(s), under exclusive license to Springer Nature Singapore Pte Ltd. 2023

K. R. Reddy et al. (eds.), *Recent Advances in Sustainable Environment*, Lecture Notes in Civil Engineering 285, https://doi.org/10.1007/978-981-19-5077-3_11

1 Introduction

Concept of circular economy is requirement of time especially, construction industry which utilizes huge volume of raw materials putting enormous pressure on natural material, impacting the environment to great extent. In terms of volume, worldwide construction aggregates consumption is predicted to reach 62.9 billion metric tonnes by the end of 2024, up from 43.3 billion metric tonnes in 2016. Sand will have the highest demand, with an absolute incremental opportunity of about US$ 89 billion between 2016 and 2024 [1]. Increasing demand of construction material paved a path to look for more sustainable way of developing construction sector. One of the innovative solutions to be adopted in the future is use of material passport which track the life cycle of construction material and ensure their proper utilization [2]. In context of achieving sustainable development goals, we have to incorporate huge volume of construction and demolition waste, and one way is to use recycled concrete aggregate as the replacement of natural aggregate (NA), and utilization of industrial waste such as copper slag as replacement of fine aggregate. To maintain environmental balance today, lot of research is going on eco-friendly and economical building materials, and recycled concrete aggregate is most prominent amongst all, extensive research is carried in last decade to understand the effect of replacement of NA with RCA so as to produce concrete which maintain structural integrity under various condition. The basic difference one can define between RCA and NA is that RCA composed of natural aggregate and adhered mortar. Recycled concrete aggregate is different from natural aggregate in terms of interfacial zone characterization as new bond has to establish when we use RCA. RCA is more porous and higher water absorption which may lead to lower strength and design mix complexity [3], however, optimizing above-mentioned drawbacks are not a big issue. When we use RCA in concrete mix proportioning, three type of ITZ is observed mainly between old natural aggregate and old mortar, new cement paste and RCA, and between new cement paste and NA [4]. Extraordinary development is made in last decade to understand RCA characteristics still wide adoption and awareness towards the use of RCA is need of hour, and lot of work still required to understand its behaviour at elevated temperature.

Various researchers stated in their work that replacement of natural aggregate with recycled concrete produce concrete of strength same as conventional concrete [5–10] and recycled aggregate concrete at elevated temperature shows trend similar to conventional concrete. Secondly, utilization of copper slag as replacement of fine aggregate helps to achieve more sustainable way to reduce industrial waste with proper replacement level, Maharishi et al. [11] in his paper stated that replacement of fine aggregate with copper slag up to 40% improve compressive strength of concrete compared to control. And if fraction is increase beyond 40%, there is reduction in compressive strength because of excess free water. Same behaviour is observed with split tensile strength test. On acid and sulphate exposure, change in mass accompanied by a reduction in compressive strength was shown by all concrete mixes. The results showed a decrement in water absorption with an increment in copper slag fraction up to 40% of natural fine aggregates.

Table 1 Behaviour of conventional concrete with natural aggregate

Temperature	Behaviour of conventional concrete
20–80 °C	Reduction of capillary water at slow rate [12, 13]
80–100 °C	Dehydration of ettringite and decomposes [13]
100–200 °C	Dehydration of calcium silicate hydrate of cement paste starts and decompose forming αC_2s [12]
120–300 °C	Closeness of cement gel layer, van der Waals force increases leads to increase in strength up to 300 °C [14]
350 °C	Porosity increases, significant loss of strength and stiffness [12]
400–600 °C	Decomposition of CH (portlandite), leads to micro-cracks in cement paste [12, 13]
600–800 °C	Significant amount of loss in compressive strength [13]
800–1200 °C	Melting of aggregate starts at temperature higher than 1000 °C [12]

This paper aims to first fix the replacement of natural aggregate with replacement level of 0, 33, 67, 100% recycled concrete aggregate and testing it at elevated temperature of 150, 300, 450, 600 °C. And selecting best replacement level based on results and then using that replacement level as constant and varying replacement of copper slag of 0, 20, 40, 60% finally a sustainable concrete is developed and tested at elevated temperature and comparing with conventional concrete.

1.1 Behaviour of Conventional Concrete at Elevated Temperature

Understanding the behaviour of recycled concrete aggregate becomes more crystal clear once the behaviour of conventional concrete with natural aggregate at elevated temperature properly understood. Table 1 shows behaviour of conventional concrete with natural aggregate.

2 Experimental Program

2.1 Material

Ordinary Portland cement grade 53 with specific gravity 3.10 is used as cementitious material in all design mix. Natural River sand is used as fine aggregate having specific gravity 2.65 and water absorption of 0.8% and fineness modulus after proper grading is 2.7, and by sieve analysis, it is found that it belongs to grading zone 2. Coarse aggregate is replaced by recycled concrete aggregate shown in Fig. 1 where we fixed

replacement level showing best result under compressive strength and split tensile strength test. RCA is obtained from demolition of old petrol pump nearly 10-year-old near chouka area of Jamshedpur. Recycled concrete aggregate hiving specific gravity 2.38, water absorption 5.5%, proper sieving of recycled aggregate is ensured such that maximum size does not exceed 20 mm, to understand the physical and mechanical property of recycled concrete impact test, Los Angeles test is performed shown in Table 2.

In second part of experiments, replacement of recycled aggregate is kept constant, and replacement of fine aggregate is performed with copper slag. Copper slag is obtained from Hindustan Copper Limited, Jamshedpur shown in Fig. 2 possessing blackish grey, glassy appearance having specific gravity of 3.6 and moisture content less than 0.1%, its composition is given in Table 3. Different physical properties of fine aggregate and copper slag are mentioned in Table 4. da Silva [3] in his paper stated that RCA possesses porosity nearly three times the natural aggregate, so absorption of water is more so utilization of superplasticizer used to reduce water content which help to acquire required compressive strength, water reducing admixture is polycarboxylic ether based having specific gravity 1.09, and provider is Asian paints.

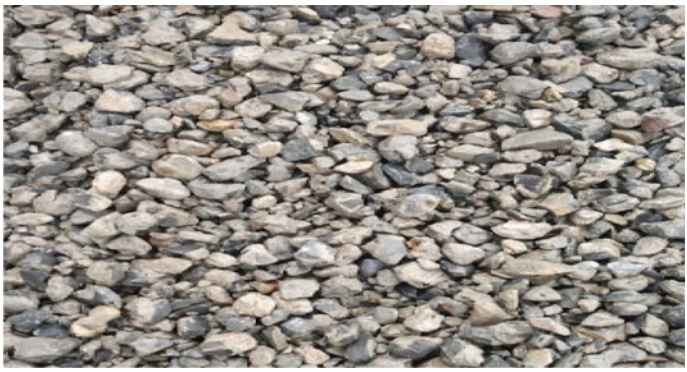

Fig. 1 Recycled concrete aggregate

Table 2 Properties of recycled concrete aggregate and natural aggregate

Test item	Natural aggregate	Recycled concrete aggregate
Impact value	23	22.74
Los Angeles abrasion (%)	22.8	31.7
Density (kg/m^3)	2662	2374
Water absorption	0.82	5.5%
SG	2.67	2.38

Fig. 2 Copper slag

Table 3 Chemical composition of copper slag

Material-copper slag	
Cu	0.6–0.9%
*Fe (total)	40–44%
S	0.8–1.2%
Sio_2 (combined as silicate)	33–35%
Free silica	<0.5%
Al_2o_3	4–6%
Cao	0.8–1.5%
MgO	1–2%
Ni	0.01–0.03%
Pb	0.01–0.04%
Zn	0.20–0.30%
Bi	0.01–0.02%
Co	0.04–0.13%

Table 4 Properties of fine aggregate and copper slag

Properties	Bulk density (Kg/m^3)		SG	FM	Zone	Colour	Texture	WA (%)
	Loose	Compacted						
Sand	1500	1625	2.65	2.7	2	Brown	Granular	0.6–1
Copper slag	1850	1950	3.6	3.1	2	Blackish grey	Glassy	0.1–0.15

Note SG—specific gravity, FM = fineness modulus WA = water absorption

Table 5 Mix proportioning—replacement of coarse aggregate with recycled coarse aggregate

Replacement of NA (%)	W/C	WC	CC	AD	WRA	FA	Coarse aggregate	
							Natural	RCA
0	0.45	177	393	–	3.6	865	1210	–
33	0.45	177	393	20	3.6	865	811	399
67	0.45	177	393	20	3.6	865	400	810
100	0.45	177	393	20	3.6	865	–	1210

Note Unit weight-Kg/m^3, WC = Water content, CC = Cement content, AD = Additional water, WRA = Water reducing admixture

2.2 Mix Proportions

Mix design consists of two parts firstly replacement of natural aggregate is made with recycled concrete aggregate, then various tests are performed to fix the best replacement level, then second set of mix design is made with replacement of fine aggregate keeping replacement of recycled concrete aggregate constant, then specimens are tested at elevated temperature, and finally, most sustainable concrete with replacement of coarse and fine aggregate is obtained. In mix design, superplasticizer is used which reduced water quantity as attached mortar in recycled concrete aggregate absorb more water, and it is found that water absorption of recycled concrete aggregate is about three times the natural aggregate. Recycled aggregate is soaked for 24 h before the mix design and left for drying for 1 h before used in concrete mix so as to achieve saturated surface dry condition.

For first batch, natural aggregate is replaced by recycled concrete aggregate as 33, 67, and 100% and mixed for about 2 min and then 1/3 of water is added after that natural coarse aggregate is added and mixed for another 1 min. Remaining half of fine aggregate and cement is added and mixed for other 2 min, and finally, remaining water, cement, and fine aggregate are mixed for another 2 min. For each concrete mix with selected percentage of recycled concrete aggregate 26 cubes of size 150 mm * 150 mm, 26 cylinder of 150 mm * 300 mm and 26 prism of 100 mm * 100 mm * 500* were casted. These were demolded about 24 h after casting and put for curing. The details of mix proportioning are given in Tables 5 and 6.

2.3 Experimental Setup

This experiment is based on two step, firstly replacement of natural coarse aggregate with recycled course aggregate whose properties is mentioned in Table 2, and then, mix design is performed with replacement level of 0% that is conventional concrete and consecutive replacement of 33, 67, 100% is made, and concrete is tested for 3 days, 7 days, 28 days for compressive strength, split tensile strength, and ultrasonic

Table 6 Mix proportioning—replacement of fine aggregate with copper slag

Replacement of FA (%)	W/C	WC	CC	AD	WRA	FA		CA	
						Natural	CS	Natural	RCA
20	0.45	177	393	18	3.6	692	173	811	399
40	0.45	177	393	18	3.6	519	346	811	399
60	0.45	177	393	18	3.6	519	346	811	399

Note WC = Water content, CC = Cement content, AD = Additional water, WRA = Water reducing agent, FA = Fine aggregate, CA = Coarse aggregate, RCA = Recycled concrete aggregate, CS = Copper slag

pulse velocity at elevated temperature of 150, 300, 450, 600 °C. Comparing the results with conventional concrete is made, and best replacement level is commented. Once the replacement of recycled aggregate is fixed, we replaced fine aggregate with copper slag, replacement level of 10, 20, 30, and 40% is made, and concrete specimen is then tested at elevated temperature of 150, 300, 450, 600 °C.

2.4 Heating Process

For heating, muffle furnace is used where temperature is increased at rate of 1 °C/min, and after reaching, the targeted temperature constant heating of 2 h is given, and then, specimens are allowed to cool this completes the one complete cycle of heating.

Figure 3 shows heating curve, and Fig. 4 shows the muffle furnace used for heating purpose. We have attained the required temperature and then maintained the temperature for 2 h, and then, proper cooling is provided so that spalling of concrete can be avoided, generally two methods are utilized in various research papers first residual method and second one is hot heat state; in residual method, we give time to cool concrete specimen, and then, test is performed, but in hot state, concrete specimens are taken out from muffle furnace and tested for various mechanical properties.

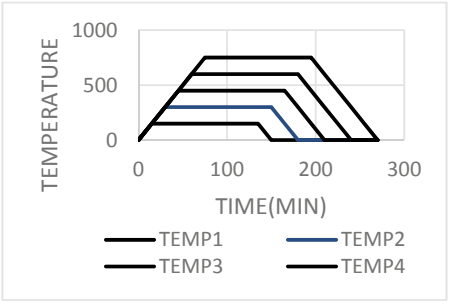

Fig. 3 Variation of temperature with time

Fig. 4 Muffle furnace

2.5 Surface Treatment of Attached Mortar

When we use recycled aggregate with different replacement level in concrete mixture, three type of ITZ is obtained mainly between old natural aggregate and old mortar, between new cement paste and RCA, and between new cement paste and NA. Attached mortar is most important factor which effects the strength of concrete in mechanical and durability test. Surface treatment is given to recycled aggregate, i.e. ball milling method; in this technique, Los Angeles abrasion machine is used; in this mechanical treatment, method 12 steel spheres are used, and total revolution of 200 is given after which the aggregate is passed through 4.75 mm sieve. Then, the aggregate is washed to remove the dust particle present on the surface. In Los Angeles, abrasion test 5 kg of recycled aggregate is taken, and percentage mortar removed is 20%. This treatment improves surface parameters and greatly impact the strength and durability.

3 Result and Analysis

Experimental result obtained from compressive strength and split tensile strength of recycled concrete with different replacement levels is discussed, and secondly, replacement of fine aggregate with copper slag is made, and its compressive strength is discussed. Reports presented are average of three samples.

3.1 Compressive Strength

Figure 6 shows the compressive strength of concrete made with different replacement level compared with conventional concrete at 3 days. Similarly, Figs. 7 and 8 show the compressive strength at 7 days and 28 days. It is observed that compressive strength of concrete specimen decreases with increase in temperature, and it may be due to physical and chemical changes primarily due to loss of free and absorbed water and attached mortar which affect the ITZ properties. Similar finding was also observed by Salahuddin et al. [15] and Bui et al. [16]. Figure 5 shows failed cube under compressive test of conventional and 33% replaced RC concrete.

It is observed from the Fig. that replacement level of 33% of recycled concrete aggregate shows compressive strength higher than corresponding replacements made, and corresponding strength is higher than other replacement at elevated temperature. So fixing this replacement level as control mix Fig. 9 shows compressive strength of replacement of fine aggregate by copper slag at 28 days, and compressive strength of replaced fine aggregate by 40% with copper slag and 33% replacement of coarse aggregate shows higher strength compared to control mix and other replacement made. With increase in % of copper slag, compressive strength increases

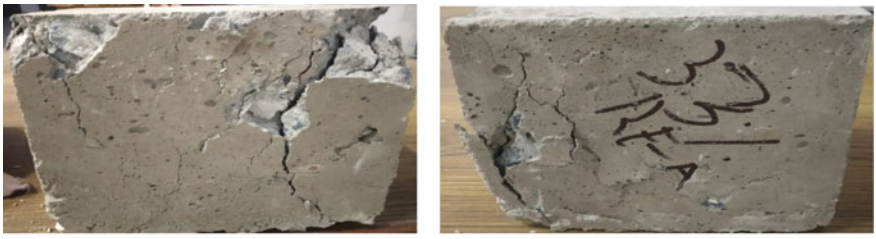

(a) (b)

Fig. 5 **a** Conventional concrete, **b** concrete with 33% RCA compression strength test

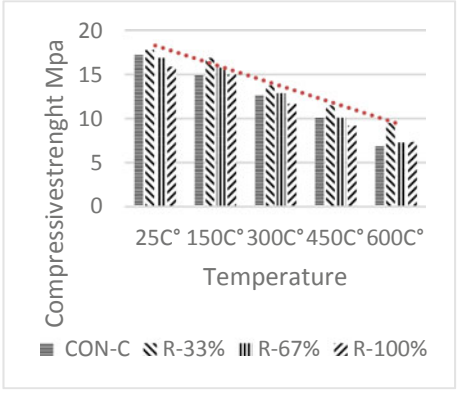

Fig. 6 Compressive strength of concrete mix with replacement level of natural aggregate with recycled concrete aggregate at 3 days

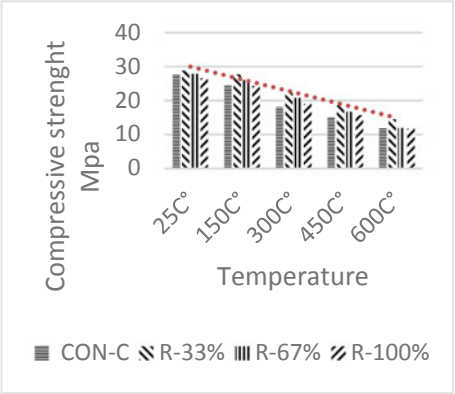

Fig. 7 Compressive strength of concrete mix with varies replacement level of natural aggregate with recycled concrete aggregate at 7 days

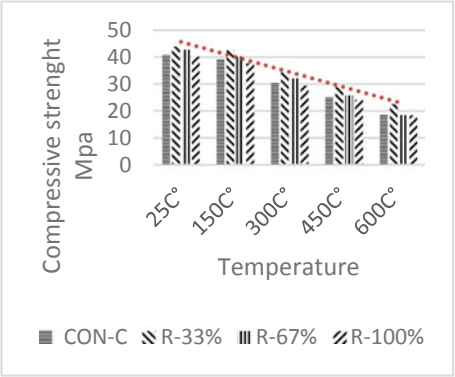

Fig. 8 Compressive strength of concrete mix with varies replacement level of natural aggregate with recycled concrete aggregate at 28 days

between 40 and 60% and starts to reduce with further increase in replacement level of copper slag. Similar observation is stated by Babu and Ravitheja [17]. Increase in compressive strength can be attributed to better compressibility of copper slag which increase cohesiveness of concrete mix, and copper slag fills the pores of attached mortar of recycled concrete aggregate which improves the overall strength.

3.2 Split Tensile Strength

Figure 10 shows the split tensile strength of concrete with various replacement levels, and Fig. 11 shows the cylinder with 33% RCA after split tensile strength test. It is found that split tensile strength of concrete specimen decreases with increase in temperature, and best result is found out at replacement level of 33% of recycled coarse aggregate. It may be due to thermal and micro-cracks effect on tensile strength of concrete. Similar behaviour was observed by Laneyrie et al. [18].

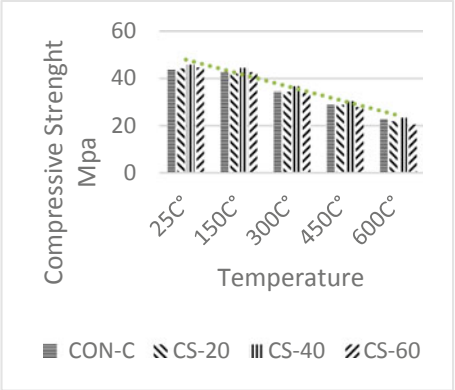

Fig. 9 Compressive strength of concrete mix with 33% replacement of RCA as control mix with different percentage of copper slag as replacement

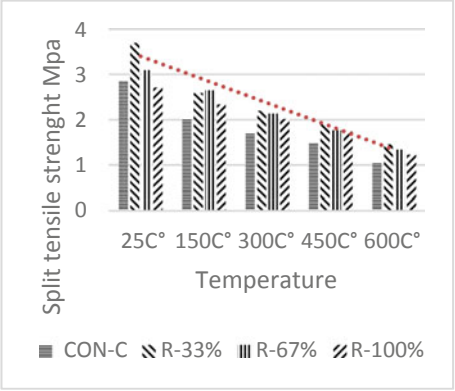

Fig. 10 Split tensile strength of concrete mix with various replacement level of natural aggregate with recycled concrete aggregate at 28 days

Fig. 11 Split tensile strength with 33% RCA

4 Conclusion

- It is observed that replacement level of 33% of recycled concrete aggregate shows compressive strength higher than other replacement levels with increase of 6.56% higher at 28 days when compared to conventional concrete.
- It is observed that at 33% replacement of NA with RCA, there is increase in split tensile strength of about 23% higher than conventional concrete at 28 days which goes on decreasing with increase in temperature.
- With RCA, 33% as constant further replacement of fine aggregate by copper slag up to 60% is made, and it is observed that replacement up to 40% shows higher compressive strength than other replacement made with increase of strength of 4.4% when compared to conventional concrete at 28 days.
- Replacement of NA with RCA by 33% and fine aggregate with copper slag by 40–60% is recommended to use in sustainable development of concrete as they possess sustainability even at elevated temperature.

References

1. Construction aggregates market: global trends, growth and forecast
2. Heinrich M, Lang W, Materials passports—best practice—innovative solutions for a transition to a circular economy in the built environment. Technische Universität München. ISBN: 978-3-941370-96-8
3. da Silva JB, Pepe M, Toledo Filho RD (2020) High temperatures effect on mechanical and physical performance of normal and high strength recycled aggregate concrete. Fire Safety J
4. Fernandes B, Carre H, Mindeguia J-C, Perlot C (2021) Effect of elevated temperature on concrete made with recycled concrete aggregates-an overview. J Build Eng
5. Xiao J (2018) Recycled aggregate concrete. In: Recycled aggregate concrete structures. Springer, pp 65–98
6. Xiao J, Li J, Zhang C (2005) Mechanical properties of recycled aggregate concrete under uniaxial loading. Cem Concr Res 6:1187–1194
7. Choi W-C, Yun H-D (2012) Compressive behavior of reinforced concrete columns with recycled aggregate under uniaxial loading. Eng Struct 285–293
8. Xiao J, Huang Y, Yang J, Zhang C (2012) Mechanical properties of confined recycled aggregate concrete under axial compression. Constr Build Mater 1:591–603
9. Behera M, Bhattacharyya SK, Minocha AK, Deoliya R, Maiti S (2014) Recycled Aggregate from C&D waste & its use in concrete—a breakthrough towards sustainability in construction sector: a review. Constr Build Mater 501–516
10. Zhou C, Chen Z (2017) Mechanical properties of recycled concrete made with Different types of coarse aggregate. Constr Build Mater 497–506
11. Maharishi A, Singh SP, Gupta LK, Shehnazdeep (2020) Strength and durability studies on slag cement concrete made with copper slag as fine aggregate. Mater Today Proc
12. Pimienta P, Alonso MC, McNamee RJ, Mindeguia J-C (2017) Behaviour of high performance concrete at high temperatures: some highlights. RILEM Tech Lett 2:45. https://doi.org/10.21809/rilemtechlett.2017.53.
13. Alonso MC, Schneider U (2019) Degradation reactions in concretes exposed to high temperatures. In: Physical properties and behaviour of high-performance concrete at high temperature. Springer, pp 5–40

14. Naus DJ (2005) The effect of elevated temperature on concrete materials and structures—a literature review. Tech Rep 41
15. Salahuddin H, Nawaz A, Maqsoom A, Mehmood T, ul Ali Zeeshan B (2019) Effects of elevated temperature on performance of recycled coarse aggregate concrete, construction and building. Materials
16. Bui NK, Satomi T, Takahashi H (2018) Effect of mineral admixture on properties of recycled concrete aggregate at high temperature, construction and building. Materials
17. Babu KM, Ravitheja A (2019) Effect of copper slag as fine aggregate replacement in high strength concrete. Mater Today Proc
18. Laneyrie C, Beaucour A-L, Green MF, Hebert RL, Ledesert B, Noumowe A (2016) Influence of recycled coarse aggregates on normal and high-performance concrete subjected to elevated temperatures. Construct Build Mater 111:368–378

Comparative Study on Natural and Recycled Concrete Aggregate in Sustainable Concrete: A Review

Anasuya Sahu, Sanjay Kumar, and A. K. L. Srivastava

Abstract Utilization of recycled concrete aggregates (RCA) as a replacement for natural aggregates in innovative concrete has gained fame around the world as a way to decrease natural aggregate use. The building sector produces a huge amount of concrete waste as a result of the quick rise of population and urbanization over the last 20 years, which not only depletes natural resources but also poses a severe environmental issue. In this framework, recycled concrete aggregates (RCA) made from construction and demolition (C&D) wastes could be a good option because they not only give an alternative to natural aggregates (both fine and coarse), but they also help to reduce landfill space and dispose of C&D wastes. Several investigations have been done to explore how the proportions of the mixture design affect the hardened qualities of concrete made with RCA, but still, some systematic review is required to enhance the performance of RCA. This manuscript presents a comparative study of fresh mechanical and durability properties between normal and recycled concrete by replacing both fine and coarse natural aggregate with recycled concrete aggregates. The analysis has been done by incorporating coarse RCA, fine RCA and both in various proportions to the concrete mix and compared its properties (like workability, compressive strength, tensile strength, flexural strength, and modulus of elasticity) with conventional concrete and the viability of its application in construction industry toward sustainable development. The study shows that the workability of RCA mix was increased from 1.4 to 40% as compared to the normal concrete with 50% replacement. Similarly, replacement level up to 50% fine RCA, the compressive strength was 2.1% more than that of normal mix as compared to the coarse RCA or incorporation of both coarse and fine RCA. But with the increasing of replacement level of RCA, strength gradually decreases. This is credited to higher water absorption of RCA due to attached mortar. However, by addition of suitable chemical and mineral admixtures, the strength of RCA can be enhanced to 20% than the normal concrete.

Keywords Construction and demolition waste · Recycled concrete aggregate · Mechanical properties

A. Sahu (✉) · S. Kumar · A. K. L. Srivastava
National Institute of Technology, Jamshedpur, Jamshedpur 831014, Jharkhand, India
e-mail: anasuyasahu1980@gmail.com

© The Author(s), under exclusive license to Springer Nature Singapore Pte Ltd. 2023

K. R. Reddy et al. (eds.), *Recent Advances in Sustainable Environment*, Lecture Notes in Civil Engineering 285, https://doi.org/10.1007/978-981-19-5077-3_12

1 Introduction

The need for concrete has risen dramatically in the last fifty years as a result of population growth, which raised the requirement for residential and infrastructural projects. This raises the demand of raw materials for construction, particularly aggregate, which accounts for 70–80% of total concrete volume [1, 2]. In 2015, aggregate consumption in the construction industry was estimated to be 48.3 billion metric tons globally. This consumption rises by roughly 5% per year, with Asia and the Pacific having the biggest consumption [3]. As an outcome, the concrete industry consumes an important quantity of natural resources, leading to significant environmental losses, energy losses, and economic crises, as it consumes 50% of basic materials, 40% of total energy, and creates 50% of total waste [4]. Thus, restraining ecological consequences, energy consumption, and CO_2 emission for concrete has become extra apparent for the construction sector, which leads to sustainable development.

On the other hand, due to rapid growth of industrialization and urbanization, huge amounts of wastes produced from construction and demolition (C&D) waste which create disposal problem due to scarcity of land, environmental pollution, heavy transportation cost, and environmental imbalance. According to the World Bank's annual report (2012), the global buildup of C&D waste is almost 1.3 billion tons per year. Furthermore, by 2025, the annual buildup of C&D waste is predicted to reach 2.2 billion tones. According to data, the United States, France, China, and Germany are the top garbage creators, accounting for 48%, 62%, 40%, and 86% of waste generated, respectively. Thus, dealing with such debris has become one of the most challenging issues in advanced economies, as well as a global matter that need a long-term solution. So, the review paper has focused on the usage of recycled concrete aggregate (RCA) derived from C&D wastes as an alternative to natural aggregates (NA) which can minimized the disposal of C&D waste and reduced the consumption of natural resources. This study could help to alleviate consumer concerns and promote the use of recycled aggregate in civil engineering projects on a larger scale.

1.1 Recycled Concrete Aggregates

Recycled concrete aggregate (RCA) is obtained from recycled aggregate (RA) which is extracted from recycling process of C&D waste. Recycling is the technique of reusing wasted materials to create new products with added value. The procedure comprises crushing of demolished concrete to generate minor size fragments by exposing it to a series of operations like elimination of pollutants, multiple phases of screening, and sorting. The schematic representation of recycling process has been shown in Fig. 1. Depending on the effectiveness of crushing procedures, different crushers have varying effects on the physical and mechanical properties of RAs [5], which impacts the concrete performance as well. The main purpose of using RCA

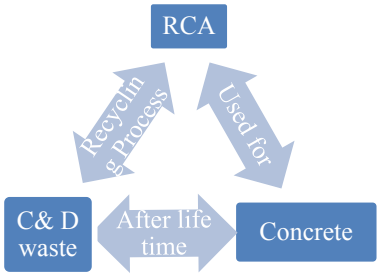

Fig. 1 Recycling technique of C&D waste

in construction sector is to make a greener and sustainable concrete. The application of RCA in concrete has developed a keen attention in various construction projects for sustainable development as it provides a technique of generating environmentally friendly concrete. It saves lot of energy and minimizes the quantity of CO_2 released by the aggregate's manufacturer as well as minimizes the waste disposal and conserve the natural resources. The proper utilization of RCA in construction industry minimizes the quarry of natural aggregate, and also the costs for amenity and bio-diversity can be reduced [6]. The benefits of RCA have been shown schematically in Fig. 2. The concept of utilization of RCA in construction sector was first occurred during the Second World War in England [7], but due to a lack of knowledge policies and specifications, the application of RCA in building activities in many developing nations remains limited.

The RCA is composed of coarse recycled concrete aggregate (CRCA) and fine recycled concrete aggregate (FRCA). The CRCA is a small concrete component made up of old coarse aggregate, mortar, and interfacial transition zone (ITZ), whereas the FRCA (>5 mm) is made up of crushed and sieved waste concrete mortar fragments. Fine RCA, like coarse RCA, can be utilized in concrete production to alleviate the severe scarcity of river sand while simultaneously addressing key environmental concerns. According to the studies [8, 9], utilizing FRCA reduces the strength of concrete since it contains old mortar, which makes the concrete porous and less

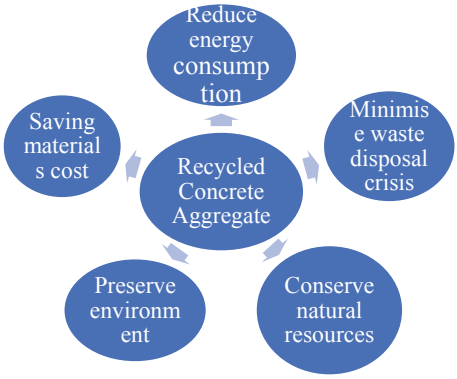

Fig. 2 Benefits of RCA

dense. Though there has been limited research on FRCA, recent research [10, 11] has found that if the RCA mix is adjusted to reward for the water absorbed by FRA during mixing, the basic mechanical properties of FRCA can be equal to those of normal aggregate concrete. It has also been discovered that [12] using CRCA and FRCA together can produce more sustainable concrete than using CRCA and FRCA separately because combined use does not require sieving to separate fractions, and all of the recycled material produced is utilized, resulting in no new by-waste. In this context, this review paper highlights the different properties of concrete made with both coarse and fine recycled concrete aggregate from various literatures and make a comparative analysis with the conventional concrete so as to make it easier to provide specific guidelines for its use and to encourage more study in this area.

1.2 Characteristics of Recycled Concrete Aggregate

RCA is made by crushing of discarded concrete into aggregate size particles using mechanically powered equipment. The main distinguish feature of RCA and NA is the attached old mortar which is adhered to the NA present at the core. With increasing nominal aggregate size, the fraction of adhering mortar decreases [13]. The quality of RCA is decided by the approaches of recycling technique to be used, but the quality of RCA is primarily determined by the W/C ratio of the parent concrete [13, 14]. The water absorption (WA) capacity of RCA is greater than the NA due to the attached mortar and porous. Physical properties of RCA are greatly influenced by an interfacial transition zone (ITZ) present among the aggregate and adhered mortar. The amount of mortar indicates the original concrete's strength properties, the efficiency of the crushing technique, crushing method, and the particle size of RCA. As compared to NA, RCA has high-water absorption capacity, lower density, lesser specific gravity, high-moisture content, high porosity, and poor particle size distribution. These properties of RCA can affect the workability, strength, durability, setting and hardening, shrinkage, and creep of concrete. According to many studies, RCA is porous in nature due to the high-mortar content, which results in higher WA capacity and modifies the recycled concrete properties to a greater extent. Hansen et al. [13] observed water absorption capacity of coarse RCA is 2.3–4.6 times greater than that of NA. However, it has been found that the WA of fine RCA is more than that of coarse RCA [15] as the amount of attached mortar increases with the reduction of particle size. This can be attributed to the recycling techniques used, where the use of multiple processing steps increases the amount of paste accumulated in the fine fraction. Pedro et al. [12] obtained the WA value of 6.9% for FRCA (5.8% more than natural fine aggregate), whereas the value was 3.6% for CRCA (2.7% more than that of natural coarse aggregate). The attached mortar has a low density and specific gravity, which accounts for the low-specific gravity, bulk density, and surface saturated density (SSD) of RCA [9]. Although SSD is unaffected by the grade of parent concrete, it does affect the original concrete's W/C ratio. The experimental examination reveals that the SSD of RCA is decreases to 7–9% as compared to

natural aggregate [16]. According to Pedro et al. [12], the density of fine RCA is expected to lower than that of CRCA as the more amount of mortar attached to the fine particle which can be attributed by the recycling process.

Concrete's characteristics are generally determined by the aggregates used. As a result, the mechanical properties and chemical properties of RCA are considered essential considerations in aggregate research. The review shows the crushing strength of RCA is higher than the parent aggregates because of the adhered mortar. According to Suryavanshi et al. [17], for 20–10 mm and 10–4.75 mm sized aggregates, crushing strength of RCA was found to be much higher (33 and 45%) as compared to natural aggregates. Durability of RCA is generally determined by its chemical properties (amount of sulfate and chloride exist). According to Nagataki et al. [18], the sulfate losses for RCA vary between 29.1 and 49% depending on the source, whereas the value for coarse NA was 9.1 and 2.6% for Fine NA. The research work revealed that when higher degree of crushing was applied to RCAs, their performance enhanced dramatically. Another critical chemical property is chloride content, as high levels of chloride can cause reinforcement steel to corrode quickly. Debieb et al. [19] suggested that if the aggregate contains an excessive amount of chloride, it can be removed by pouring the aggregate in water. However, based on the literature, the properties of RCAs were solely dependent on the aggregate source used, the age, and the nature of the concrete from which it is derived.

2 Fresh Properties

Fresh properties of concrete include workability of concrete mix. It is greatly influenced by a number of parameters, aggregate size, moisture content, water absorption, and aggregate shape and texture [19, 20]. Due to the porous nature of RCA, it attains low workability than the natural aggregate. It has also been found that with the increase in RCA replacement ratio, the workability reduces and also has a greater loss in slump as compared to the natural concrete aggregate [20]. When coarse RCA is utilized in a dry environment, the workability of the concrete is severely impeded, depending on the amount of RCA used. At greater percentage replacements, especially when it exceeds 50%, the loss in workability in RCA is extremely noticeable [21]. Some literature proposed that by using coarse RCA in surface saturated dry condition instead of oven dried condition, the initial slump has been increased with the increase amount of RCA [22]. Similarly, adding up to 20% fine RCA into the concrete mix has been shown to have no significant influence on its workability. However, increasing the fine RCA content causes a significant reduction in workability [19]. Some study conveys that, by replacing both fine and coarse RCA (50%) into the concrete mix, the workability increases to 18% than the control mix. However, by using high-performance superplasticizers for concrete mixes with a 25% and 100% replacement of coarse, RCA increases slump by around 7.31% and 25.80%, respectively [23]. However, workability of mix with 30% coarse recycled and 50% fine

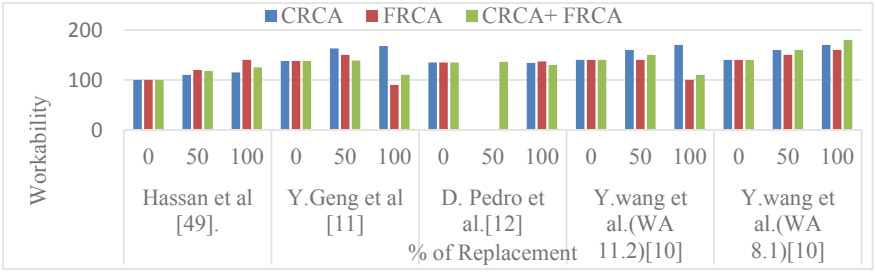

Fig. 3 Workability of concrete with RCA from different literature studies

RCA is comparable to control concrete with natural aggregates when superplasticizer is added. Figure 3 shows the values of workability of concrete made up of RCA at various replacement % from different literature study. The graph shows that with the incorporation of 50% RCA, the workability increases to 20% approximately as compared to conventional concrete.

3 Mechanical Properties

3.1 Compressive Strength

Compressive strength of concrete is an important quality of concrete that affects its strength, durability, and performance. Many factors influenced the qualities of RCA, including the water-binder ratio, the replacement level of RCA, the properties of adhering mortar, and use of admixture. It is also determined by the mechanical and physical qualities of RCA, such as the impact and crushing strength of aggregate, which controls the resistance to compression. Experimental studies have found that with increasing the RCA replacement percentage having same w/c ratio has a significant impact on the strength of RAC which is 10% lower than the control concrete [24–26]. It has also been studied that, the strength of concrete decreases by using fine RCA [9], which could be attributed to the old attached mortar in fine RCA making concrete additionally porous and less dense. However, researchers practically shown that, the replacement of coarse RCA up to 30% or 20% fine RCA has minor effect on the strength development of concrete but as the replacement level of RCA increases, strength gradually decreases [27]. Some literatures also suggest that, in an average 20–30% strength loss occurs in concrete by incorporating 100% CRCA or 50% FRCA to natural aggregate. Pedro et al. [12] incorporated both coarse and fine RCAs by replacing NA and found that concrete having both coarse and fine RCAs at the same time may reach equal performance to regular concrete. Sim and Park [28] investigated the properties of concrete by taking 100% coarse RCA and fine RCA in the range of 30–100% and observed that there was a maximum loss of 14%

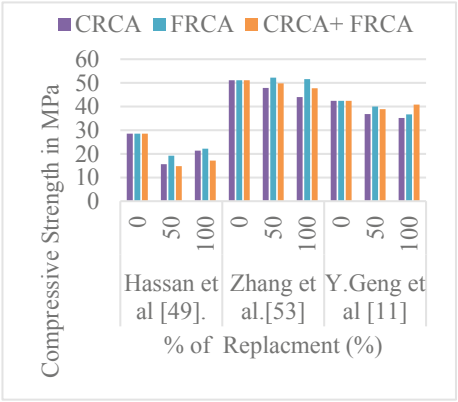

Fig. 4 Compressive strength of RCA from various literature studies

compared to standard concretes with compressive strengths of above 40 MPa. Wang et al. [10] found a greater loss in compressive strength of 10% in the mix including a 100% recycled granular skeleton when both coarse and fine (50 and 100%) concrete aggregate were used together.

However, compressive strength of RCA may be improved by increasing the cement content or employing admixtures [29, 30]. According to Dilbas et al. [31], the compressive strength increased by 11.4%, 5%, 3.2%, and 14%, respectively, with the addition of silica fume (5%) to 100% natural aggregate, to 100% FRCA, CRCA, and both. Manzi et al. [32] replaced the natural aggregate with RCA (both fine and coarse) fluctuating from 27 to 63.5% of total amount of aggregates by adding acrylic based superplasticizer (SP) to achieve compressive strength of 30 Mpa and observed that, the strength was increased about 27% higher than the reference concrete. Figure 4 depicts the influence of the various replacement % of coarse and fine RCA or both on the compressive strength of recycled aggregate concrete. The plot shows that the concrete made with FRCA with 50% replacement achieve almost similar strength to the natural concrete, whereas the concrete made with only CRCA and combination of both shows marginal loss in strength relative to conventional mix with the same replacement percentage. But with 100% replacement of RCA (CRCA, FRCA, and FRCA + FRCA) shows comparatively less strength than the control mix. Whereas, the loss in strength is marginal, and recycled aggregate could be used in regular structures with minimum strength.

3.2 Split Tensile Strength

Split strength is the common indirect method to determine the tensile strength of concrete. The tensile strength of RCA exhibits similar behavior to compressive strength as it is affected by a number of variables, including RCA replacement, w/c ratio, mixing procedures, cement type, and RCA properties. The reviews convey that

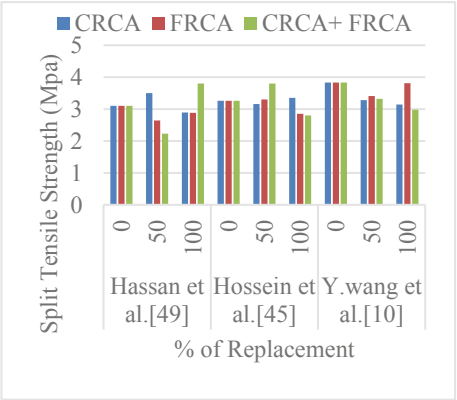

Fig. 5 Split tensile strength of RCA from various literature studies

tensile strength diminishes as the replacement percentage of RCA increases [33–35]. Many investigations reveal that the RACs tensile strength up to 30% replacement is comparable to or exceeds that of fresh concrete [31, 36, 37]. However, the strength of RCA was decreased with the increase in FRCA replacement with natural sand [38, 39]. According to Nedeljkovic et al. [39], tensile strength of RCA was reduced to 10.2%, 10.8%, 17.8%, and 33%, respectively, when the fine aggregate is replaced by 10%, 30%, 50%, and 100% replacement of FRCA. Similarly, when RCA made with both fine and coarse RCA, the tensile strength was reduced to 20% than control concrete [40]. As a result, it is concluded that the usage of fine aggregate limits the tensile strength of RAC. Plaza et al. [41] observed that, simultaneous use of both fine (50%) and coarse (100%) fraction of RCA decreased the strength up to 14.13% than the control mix. However, the negative effects of RCA substitution can be overcome by addition of superplasticizers and using mineral admixtures. Hossein et al. [42] reported that, polycarboxylate-based superplasticizers increased the strength from 10 to 29% relative to control mix with the replacement of 50% coarse RCA. Whereas with 50% replacement of fine RCA and both of fine and coarse, RCAs increased the tensile strength to 4% and 22%, respectively. Figure 5 shows the variation of split tensile strength versus RCA (CRCA, FRCA, and FRCA + FRCA) replacement % as observed by several researchers. It shows that, as the replacement ratio increases, the split tensile strength of concrete made with RCA decreases than the control concrete. This literature review not only identifies the different aspects that may influence the tensile strength of concrete produced from RCA, but it also imparts a clear image of the criterions that may affect it, allowing them to be modified as needed.

3.3 Flexural Strength

Another aspect affecting concrete's structural performance is its flexural strength. It is determined by the RCA replacement ratio, aggregate moisture content, concrete

curing time, and water-binder ratio, among other factors. Literature shows that flexural strength of concrete produced with RCA has been decreased when the replacement ratio of RCA increases [20, 37]. Review shows that the flexural strength up to 40% replacement of CRCA [43] and FRCA [44] is comparable to normal concrete. According to James et al. [45], the flexural strength dropped to 2.5% at 28 days by replacing NA with 25% RCA with W/C ratio 0.55 as compared to reference concrete. Whereas Hassan et al. [34] replaced fine and coarse RCA (50 and 100%) combinedly by natural aggregate and found that, the flexural strength was reduced (43, 33%) with the upsurge of replacement ratio as compared to the control mix. Increases in the W/C ratio have been revealed to recover the flexural strength of recycled concrete. Mas et al. [36] made RCA-based concrete with varying W/C ratio (0.65, 0.72, and 0.45) and observed that by replacing up to 75% of NA with RCA of inferior quality, flexural strength was reduced in the range of 13–30%. But the real flexural strength decreases when the W/C ratio rises. The flexural strength of concrete was ameliorated by using RCA with a reduced water absorption capacity [46].

However, by replacing 10 and 15% of OPC with fly ash having W/C ratio 0.55 improves flexural strength of RAC as compared to normal mix. Manzi et al. [32] used an acrylic-based superplasticizer and observed that by replacing 20%, 30%, and 60% RCA (both fine and coarse) with NA leads to reduction of flexural strength by 9.3%, 23%, and 25%, respectively.

3.4 Modulus of Elasticity

Incorporation of RCA has been shown to reduce modulus of elasticity [47, 48]. Moreover, the aggregate modulus of elasticity has been identified as a key factor which influences the modulus of elasticity of concrete with RCA. As recycled concrete aggregate is more vulnerable to deformation than raw aggregate, the aggregates' weakness reduces the Young's modulus for concrete when RCA is used. According to Kou et al. [48], by replacing 50% coarse RCA, the elasticity modulus decreased by 12.6%, whereas with the100% replacement ratio, it is decreased by 25.2%. Zhang et al. [53] determined the effect of elastic modulus by incorporating CRCA, FRCA and combination of both into the concrete mix with the replacement ratio 0%, 50%, and 100%, respectively. He observed that the elastic modulus is decreased by 10.8 and 22% at 50 and 100% replacement of CRCA as compared to conventional concrete, whereas, it is decreased by 2.07% and 14% at same % of replacement of FRCA. Similarly, the elastic modulus is also decreased up to 24% by replacing both CRCA and FRCA (50 and 100%) than the control mix. So, it is concluded that, as compared to CRCA, FRCA exhibited minor effect on the elastic modulus of the resulting concrete.

However, the modulus of elasticity of concrete with RCA can be improved by using mineral admixtures. The literature reviews that the modulus of elasticity of RCA mix exhibit more or less similar to conventional concrete with the addition of 5% silica fume and by replacing CRCA (30%), FRCA (40%), or both (70%) [31]. Figure 6 depicts the effects of elasticity modulus of RCA with the various percentages

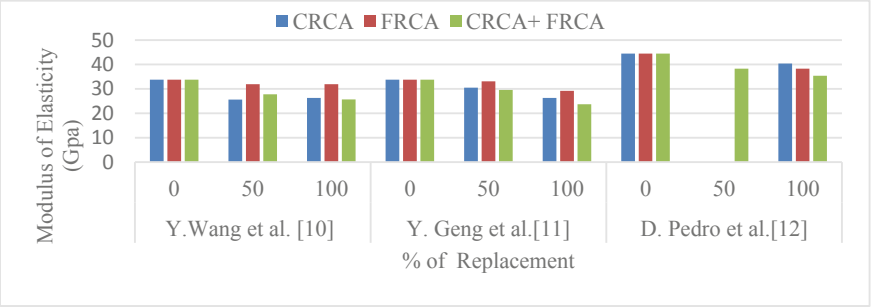

Fig. 6 Elastic modulus of RCA for different literature studies

of RCA replacement. The graph clearly shows that the elasticity modulus decreases as the percentage of replacement increases. However, it should be noted that the influence of FRCA was less significant in comparison with the influence of CRCA and (FRCA + CRCA), at 50% replacement ratio.

4 Durability Properties

Durability is the most important properties of concrete which determine the ability of concrete to withstand weathering action, chemical attack, and abrasion. Durability of concrete mainly depends upon the cement content, quality of aggregate, permeability, proportion of mixing, type of admixtures used and temperature. Various researchers from their investigations observed that the durability of concrete made with RCA exhibit inferior result as compared to the natural concrete due to high porosity. A comparative analysis has been made between the concrete made with RCA and NA on various properties influencing durability from different experimental studies which is summarized in Table 1.

5 Conclusion

According to the study, the properties of concrete with recycled concrete aggregates appear to be slightly lesser to their conventional counterparts.

- The review shows that the physical and durability properties of both fine and coarse RCA exhibit lower result than the virgin aggregates due to the old attached mortar and porous nature.
- The study shows that the workability of concrete increased from 0 to 40% at various replacement of RCA relative to the conventional concrete.

Table 1 Comparative analysis of durability properties

Sl. No.	Properties	Effects on concrete
1	Resistant to sulfate attack	1. With the incorporation of 50% coarse RCA to NA (immersed in $MgSo_4$ solution), loss of strength was found to be 27.36% more than that of control mix, and corresponding mass loss was found to be 21.62% [49] 2. By replacing both coarse and fine RCA (20%) to NA (immersed in Na_2So_4 solution), the strength reduced to 11.77% and mass reduced to 0.13% relative to control concrete [50]
2	Resistant to acid attack	1. With the incorporation of 50% coarse RCA to NA (immersed in H_2So_4 solution), loss of strength was found to be 29.82% more than that of control mix, and corresponding mass loss was found to be 14.81% [49] 2. Vinay Kumar [50] replaced both coarse and fine RCA (20%) to NA (immersed in H_2So_4 solution) and observed that, the strength reduced to 39.50% and weight reduced to 5.37% relative to control concrete
3	Chloride penetration	1. With 50 and 100% replacement of coarse RCA, the depth of chloride ingress was found to be 67 and 33% more than that of normal concrete [49] 2. According to Sim and Park [28], the replacement of FRCA was not affected the chloride penetration depth, but with the incorporation of 100% FRCA, the compressive strength decreased up to 33%
4	Resistance to carbonation	1. Pedro et al. [12] simultaneously incorporated fine and coarse RCA (25, 50, and 100%) to NA, and the concrete was kept in carbonation chamber for 28 and 91 days. He observed that the depth of different RCA mix at 28 days was found to be more (73–160%) than that of normal mix 2. According to Evangelista and De Brito [9], the carbonation depth was increased to 40% than that of normal concrete at 21 days with the replacement of 30% FRCA

- The literatures recommended that the compressive strength of concrete produced with RCA (CRCA, FRCA, FRCA + CRCA) for replacement ratios of up to 50% is comparable to that of fresh aggregate concrete.
- The study shows that, though in some cases, the performance of concrete made with both FRCA and CRCA is poor, but they can produce sustainable concrete as compared to the use of CRCA and FRCA alone because in combined use, most of the recycled materials are utilized without generating new by-products.
- RCA derived from C&D waste can be regarded as a satisfactory construction material in future, and this RCA may be referred to as a basic material for low-cost construction. As a result, there is the likelihood of substantial use of C&D waste in the construction industries by gathering existing knowledge, allowing for future research and the development of practical guidelines that are acceptable to industries.

References

1. Neville AM (1995) Properties of concrete, vol 4. Longman, London
2. Alexander M, Mindess S (2005) Aggregates in concrete. Taylor & Francis, London
3. Yehia S et al (2015) Strength and durability evaluation of recycled aggregate concrete. Int J Concr Struct Mater 9(2):219–239
4. Anik D, Boonstra C, Mak J (1996) Handbook of sustainable building. James & James
5. Matias D, de Brito J, Rosa A, Pedro D (2013) Mechanical properties of concrete produced with recycled coarse aggregates—influence of the use of superplasticizers. Constr Build Mater 44:101–109
6. Tam VW, Soomro M, Evangelista ACJ (2018) A review of recycled aggregate in concrete applications (2000–2017). Constr Build Mater 172:272–292
7. Best practice guide for the use of "RAs in new concrete". Technical report TR 14, Cement & Concrete Association of New Zealand (CCANZ), October 2011
8. Khatib JM (2005) Properties of concrete incorporating fine recycled aggregate. Cem Concr Res 35:763–769
9. Evangelista L, de Brito J (2007) Mechanical behaviour of concrete made with fine recycled concrete aggregates. Cem Concr Compos 29:397–401
10. Wang Y, Zhang H, Geng Y, Wang Q, Zhang S (2019) Prediction of the elastic modulus and the splitting tensile strength of concrete incorporating both fine and coarse recycled aggregate. Constr Build Mater 215:332–346
11. Geng Y, Zhao M, Yang H, Wang Y (2019) Creep model of concrete with recycled coarse and fine aggregates that accounts for creep development trend difference between recycled and natural aggregate concrete. Cement Concr Compos 103:303–317
12. Pedro D, de Brito J, Evangelista L (2017) Structural concrete with simultaneous incorporation of fine and coarse recycled concrete aggregates: mechanical, durability and long-term properties. Constr Build Mater 154:294–309
13. Hansen TC, Henrik N (1983) Strength of recycled concrete made from crushed concrete coarse aggregate. Concr Int 5(1):79–83
14. Hansen TC, Boegh E (1985) Elasticity and drying shrinkage of recycled aggregate concrete. J ACI 82(5):648–652
15. Juan M, Gutiérrez P (2009) Study on the influence of attached mortar content on properties of recycled concrete aggregate. Constr Build Mater 23(2):872–877
16. Limbachiya MC, Leelawat T, Dhir RK (2000) Use of recycled concrete aggregate in high-strength concrete. Mater Struct 33:574–580
17. Suryawanshi SR, Singh B, Bhargava P (2015) Characterization of RAC. Advances in structural engineering. Springer, India, pp 1813–1822
18. Nagatakia S, Gokceb A, Saekic T, Hisada M (2004) Assessment of recycling process induced damage sensitivity of recycled concrete aggregates. Cem Concr Res 34(6):965–971
19. Debieb F, Courard L, Kenai S, Degeimbre R (2009) Roller compacted concrete with contaminated RAs. Constr Build Mater 23(11):3382–3387
20. Malešev M, Radonjanin V, Marinkovic´ S (2010) Recycled concrete as aggregate for structural concrete production. Sustainability 2(5):1204–1225
21. Tavakoli M, Soroushian P (1996) Drying shrinkage behavior of recycled aggregate concrete. Concre Int 18:58–61 (Compendex)
22. McNeil K, Kang TH-K (2013) Recycled concrete aggregates: a review. Int J Concr Struct Mater 7(1):619
23. Zhu YG, Kou SC, Poon CS, Dai JG, Li QY (2013) Influence of silane-based water repellent on the durability properties of RAC. Cem Concr Compos 35(1):32–38
24. Frondistou-Yannas S (1977) Waste concrete as aggregate for new concrete. J Proc 74(8):373–376
25. Malhotra VM (1978) Recycled concrete—a new aggregate. Can J Civ Eng 5(1):42–52
26. Rahal K (2007) Mechanical properties of concrete with recycled coarse aggregate. Build Environ 42(1):407–415

27. Silvaa RV, de Britob J, Dhircd RK. The influence of the use of recycled aggregates on the compressive strength of concrete: a review. Eur J Environ Civ Eng
28. Sim J, Park C (2011) Compressive strength and resistance to chloride ion penetration and carbonation of recycled aggregate concrete with varying amount of fly ash and fine recycled aggregate. Waste Manag 31:2352–2360
29. González-Fonteboa B, Martínez-Abella F (2008) Concretes with aggregates from demolition waste and silica fume. Mater Mech Prop Build Environ 43(4):429–437
30. Kou SC, Poon CS (2012) Enhancing the durability properties of concrete prepared with coarse RA. Constr Build Mater 35:69–76
31. Dilbas H, Simsek M, Çakır Ö (2014) An investigation on mechanical and physical properties of RAC (RAC) with and without silica fume. Constr Build Mater 61:50–59
32. Manzi S, Mazzotti C, Bignozzi MC (2013) Short and long-term behavior of structural concrete with recycled concrete aggregate. Cem Concr Compos 37:312–318
33. Kou SC, Poon CS, Agrela F (2011) Comparisons of natural and RACs prepared with the addition of different mineral admixtures. Cem Concr Compos 33:788–795
34. Yang KH, Chung HS, Ashour AF (2008) Influence of type and replacement level of RAs on concrete properties. ACI Mater J 105:289
35. Mas B, Cladera A, del Olmo T, Pitarch F (2012) Influence of the amount of mixed RAs on the properties of concrete for non-structural use. Constr Build Mater 27(1):612–622
36. Padmini AK, Ramamurthy K, Mathews MS (2009) Influence of parent concrete on the properties of RAC. Constr Build Mater 23(2):829–836
37. Santos S, Da Silva PR, De Brito J (2019) Self-compacting concrete with recycled aggregates—a literature review. J Build Eng 22:349–371
38. Nedeljkovic M, Visser J, Savija B, Valcke S, Schlangen E (2021) Use of fine recycled concrete aggregates in concrete: a critical review. J Build Eng 38:102196
39. Sri R, Tam CT (1985) Properties of concrete made with crushed concrete as coarse aggregate. Mag Concr Res 37(130)
40. Plaza P, Sáez del Bosqua IF, Frías M, Sánchez de Rojas MI (2021) Medina. Constr Build Mater 285:122926
41. Sasanipour H, Aslani F (2020) Durability properties evaluation of self-compacting concrete prepared with waste fine and coarse recycled concrete aggregate. Constr Build Mater 236:117–540
42. Chen ZP, Huang K, Zhang XG, Xue JY (2010) Experimental research on the flexural strength of recycled coarse aggregate concrete. In: International conference on mechanic automation and control engineering (MACE). IEEE, pp 1041–1043
43. Ahmed SFU (2014) Properties of concrete containing recycled fine aggregate and fly ash. J Solid Waste Technol Manag 40(1):70–78
44. James MN, Choi W, Abu-Lebdeh T (2011) Use of RA and fly ash in concrete pavement. Am J Eng Appl Sci 4:201–208
45. Hassan RY, Faroun GA, Mohammed SK. Mechanical properties of concrete made with coarse and fine recycled aggregates. Mater Today: Proc
46. Zega CJ, Di Maio AA (2011) Use of recycled fine aggregate in concretes with durable requirements. Waste Manag 31:2336–2340
47. Kou SC, Poon CS (2013) Long-term mechanical and durability properties of RAC prepared with the incorporation of fly ash. Cem Concr Compos 37:12–19
48. Zhang H, Wang Y, Lehman DE, Geng Y, Kuder K (2020) Time-dependent drying shrinkage model for concrete with coarse and fine recycled aggregate. Cem Concr Compos 105:103426

49. Majhi RK, Nayak AN (2019) Bond, durability and microstructural characteristics of ground granulated blast furnace slag based recycled aggregate concrete. Constr Build Mater 212:578–595
50. Vinay Kumar BM, Ananthan H, Balaji KVA (2018) Experimental studies on utilization of coarse and finer fractions of recycled concrete aggregates in high performance concrete mixes. Alex Eng J 57:1749–1759

Neo-Tectonic Activities in Darjeeling Himalaya

Vartika Singh, Amit Kumar, Rakesh Singh, Richa Singh, CharanJeet Singh, Santosh Kumar Sharma, and Nisha Tripathi

Abstract The present research has been particularly mentioned in response to plate shift toward north, northwest direction in the area of the Darjeeling Himalaya in West Bengal. The Himalaya range is well-known as the highest and youngest mountain range of the world. In the Great Himalayan terrain, the outer Himalaya shows the sign of dynamic tectonics. Outer Himalaya and lesser Himalaya parted by Main Boundary Thrust (MBT) show the history of active tectonics in the region. The shape of the Darjeeling Himalaya has been changing as a result of continuous movement of tectonic plates of the Himalayas. As the plates shift across the outside as far as the planet, it strikes each and every one, causing enormous influence slipup lines. Occasionally, plates slide attached each other, whereas afterward they rumple frequently form the Himalayas.

Keywords Himalaya · Environmental hazard · Neo-tectonic · Plate movement · Hazard management

V. Singh (✉)
Amity Institute of Global Warming and Ecological Studies (AIGWES), Amity University, Noida, Uttar Pradesh, India
e-mail: vsingh3@amity.edu

A. Kumar
Indra Gandhi Institute of Physical Education and Sports Sciences, New Delhi, India

R. Singh
Department of Chemistry, D. B. S. P. G. College, Dehradun, Uttarakhand, India

R. Singh · C. Singh
Amity School of Natural Resource and Sustainable Development, Amity University, Noida, Uttar Pradesh, India

S. K. Sharma · N. Tripathi
Sanjeevani Foundation for Health Education & Environment Research Action (SFHEERA), New Delhi, India

© The Author(s), under exclusive license to Springer Nature Singapore Pte Ltd. 2023

K. R. Reddy et al. (eds.), *Recent Advances in Sustainable Environment*, Lecture Notes in Civil Engineering 285, https://doi.org/10.1007/978-981-19-5077-3_13

1 Introduction

In the northern portion of the area of research, geo-tectonics activities are supervised by local compression, and southern part is categorized by the local extension activities. In the northern part of the study area, thrust faults are dominated, and in southern part, normal faults are broadly developed face of the study area. In the field, we can easily observable some faults; these faults are common in natural environment, and they are slanted toward at great angles to the Darjeeling Himalayan front thrust. Such a 'neo-tectonic activity' in Darjeeling Himalayan belt created the frequent hazards day after day. The main motive of this research is study the neo-tectonic activity happing to the Darjeeling Himalaya and identify the types and nature of geo-environmental hazard due neo-tectonic activity in this region. We find medium-grade metamorphism around the Darjeeling Himalaya, and it is a great example of inverted Himalayan metamorphism. Due to this tectonic activity, this area comes under higher vulnerable area and very prone to the disaster. At the end of the study, we suggest some effect full remedial measures for the study area.

2 Methodology

The following work is based on availability of primary and secondary sources which is gathered from different resources. The date, information, and records were collected from Geological Survey of India, Hazard management Bureau, etc. We can also use thematic and cartographic maps lucid illustration of the panoramic view of the study area.

2.1 Location of Darjeeling Himalaya

Darjeeling Himalayan belt is the parts of Eastern Himalaya. It lies in the top most northern part of West Bengal. It is located between 22°40′15″ N to 22°44′45″ N latitude and 88°26′45″ E to 89°31′15″ E longitude. It covers an area of 3010 ha.

Origen of Himalaya is wedge shaped and categorized by basal impartiality [1–8]. In Darjeeling District, we find plane and hilly areas, and hilly area is belonging to sub-Himalayan belts and lesser Himalayan belt of the Eastern Himalayas. The study area is covered by Sikkim Himalaya in northern part and Nepal Himalaya in western side Bhutan Himalaya in eastern part of the area. The southern part of the study area is established by extremely dissolute platform of famous terrace deposits which is spreading alongside the east–west axis of the study area. The inner belt of the hills is defined by ridgeline which is stretch from the Kalimpong Hill to the east and Darjeeling Hills to west, overseeing the southerly flowing Tista valley in among

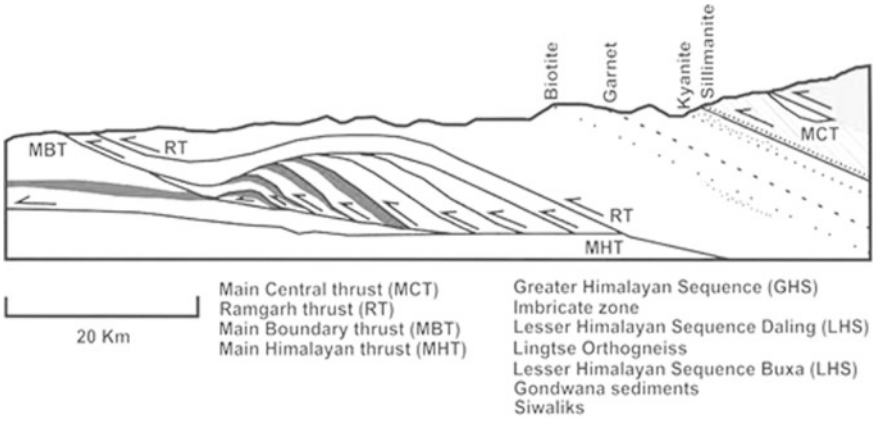

Fig. 1 Cross-section of Himalaya. *Source* Amit Kumar

area. Small streams are contributing the basin of Rammam-Rangitand disintegrate the northern slope of Darjeeling Hills.

2.2 Geology

The Darjeeling Hills characterize by exceptional geo-environmental insight. It is largely collected through erosional landform which is formed by southerly flowing water bodies, which exposed different tectonic units with the help of cross-section. In this area, we find nearly same type of structures, lithology, soil, climatic condition, and green cover. Auden [9], Mallet [10] brief about the different tectonic units in this area are found in the opposite order of stratigraphic superimposition, and it is characterized by the Siwalik and Gondwana. Thrusted sheets of Daling and Darjeeling group of crystalline rocks succeed toward the inner Himalayas. We find very clear interaction among diverse groups of rocks which is denoted by thrusts, dipping at high angles near north direction (Fig. 1, Table 1).

2.3 Physical Structure of Darjeeling Himalaya

In West Bengal, Northwestern side of the hilly region goes to Darjeeling Himalayas. This area is also known as the Eastern Himalaya range. It cover the total Darjeeling district apart from the Siliguri subdivision region. It arises continually from the Terai region and slopes fall from south to north direction. Teesta River separates the region into two parts East of Teesta and West of Teesta region. In the west of the Teesta River, we find high hill ranges which belongs to the Darjeeling Himalaya. Here, we find two

Table 1 Detail of several formations of the Darjeeling Himalaya

S. No	Formations of Darjeeling Himalaya	Description	Places
1	High Terraces	A recent establishment forms a fringe end to end the hills, particularly at the meetings of the rivers. These terraces are formed of pebbles, gravels, and boulders which is mixed with clay and sand. The formation is semi-consolidated, stratified end to end with the evidences of disruption at places	A 40 m high terrace is originate in the Tista valley at Kalijhora
2	Siwalik	The Siwalik system which we find near the Darjeeling hill contained the shale, sandstone, mudstones, and conglomerates. These formations are associated with the different bands of lignite and shale	Along with Tista River and Hill Cart Road
3	Damuda Series	After the formation of Siwalik range, we find carbonaceous shale, coarse-grained sandstone which is hard in nature, quartzite, and slates which is belong to Damuda series. This series is comparable to the Gondwanas of Indian peninsular region. The extreme thickness of the Damuda is about 2.5 km along the Tista valley	Adjacent Tindharia region, Gish and Lish Rivers
4	Daling Series	The Daling series included the phyllites chlorite shales and schist which is related with quartzite and rest over Damuda series. Well-developed form of Damuda series. The significant feature of present series is we find increasing rate of metamorphism toward upward and slates form the lowest bed	Along the Tista River and the stretches along the Tindharia –Paglajhora on the Hill Cart Road

(continued)

Table 1 (continued)

S. No	Formations of Darjeeling Himalaya	Description	Places
5	Darjeeling Gneiss	In the upper part of the Darjeeling Hill, the Dalings progressively grade into the more metamorphosed rocks which is famous as Darjeeling Gneiss. We find irregularity in dip of the rocks and vary in among 40°–70°. Darjeeling gneisses are extremely foliated due to high rate of metamorphism in this area	Darjeeling Hill areas

different ranges; one is Singalila range, and another one is the Darjeeling-Karsiang range. Singalila range covers the western part of the region and separates Nepal from West Bengal. Four famous peaks of the Singalila are—Sandakfu (3,630 m) and Fault (3,595 m) of West Bengal and Sabargram (3,543 m) and Tonglu (3,036 m) of Darjeeling-Karsiang range. Singalila National Park is located here. Two famous peaks of this range are Senchal and Tiger Hill are found east to Teesta, and Chola range is found near Bhutan and Sikkim border. The well-known town in this region is Kalimpong, and highest peak is Rishila. Near the low-height Buxa-Jayanti range, Neora Valley National Park is situated, and it is a part of Shivalik.

2.4 Soils

Development of soil is depending upon the underlying geological strata, lithological disintegration, and fluvial action around the area. Soils developed around the Darjeeling hills are predominantly dark reddish in color due to widespread existence of schists and phyllitic. Soil we find near the highland or interfluvial areas we find sandy loam to loamy mainly near the water body, some time we also find clayey loam soil. Most of the soils are acidic in nature which is continuous increasing with the depth; this is due to the lacking of base from exterior and collect in to the lesser horizons. The thickness of soil and regolith is varying from place to place. Thickness of soil is depending on the gradient of the longitudinal slope outlines, weathering rate, and gravity of mass movement. In this area, generally, we find red, yellow, and brown soil (Table 2).

In the different size of soil grains, we find reflection of bedrock. In the study area, we find vary coarse-grained particles range from 80 to 50%. We find coarse sand particles in the Damuda and Daling series. In the Siwalik range, we find high clay-silty fraction. In Darjeeling gneiss soil, we find high amount of potassium which is

Table 2 Soil color disruption

S. No	Color of soil	Disruption
1	Yellow and red soils	Settled from gneiss
2	Brownish soil	Developed from schists and shales
3	Red brown to pale yellow coarse soils	Siwaliks
4	Clayey dark soils	Daling series

find from the source of muscovite mica and feldspar, and it is poor in iron oxide, magnesium, nitrogen, lime, and nitrogen.

3 On Geo-Environmental Hazard and Neo-Tectonic Activities in Darjeeling Himalaya

Neo-tectonism in the Darjeeling Himalayan belt is regular activities for the area. 'Darjeeling Himalaya' is very active in 'neo-tectonic activity'. In the current research work, researcher finds some scientific structural and geomorphic evidence of neo-tectonic activity which is belong to Darjeeling Himalayan belt in the Nahan area. In field work, we find some faults, and they are sloping at high angles to the Darjeeling Himalayan Frontal Thrust (DHFT). A lot of peoples who belong to eastern Himalaya (Sikkim) have direct experience of disturbing power of earthquakes. It is a common disaster who belong to this area and disturb the life of humans. Earthquakes happen after the pressure builds up end to end a fault line. It is measured on the Richter scale in the form of magnitude [11, 12]. It helps to measure released energy during the earthquake activity. During the earthquake, energy is released underground, and shock waves are felt on the earth surface (Fig. 2).

The most specious geomorphic indication comes from the more or less straightforward line of the Darjeeling Himalayan Front in this region. A visual study of the DHFT is straight in comparison of DHFT of the adjacent reentrants. At few places, DHFT marked as discontinuous and small scraps at some places. But, we don't have a direct proof of thrusting along with the front. DHFT has a tectonic importance which shows the fact that it is generated among the two different geomorphic entities like plain and hills. In the detailed study, we find DHFT is parallel to topographic profile, and tectonic line is parallel to geographic profile [13–16]. It is a most dynamic tool for the identifying of geomorphic evidence which is related to the deformation of the study area. In the present study, we find to type of topographic patterns which is more or less parallel to the Darjeeling Himalaya; it conforms the strike of DHFT and has been form the topographic data.

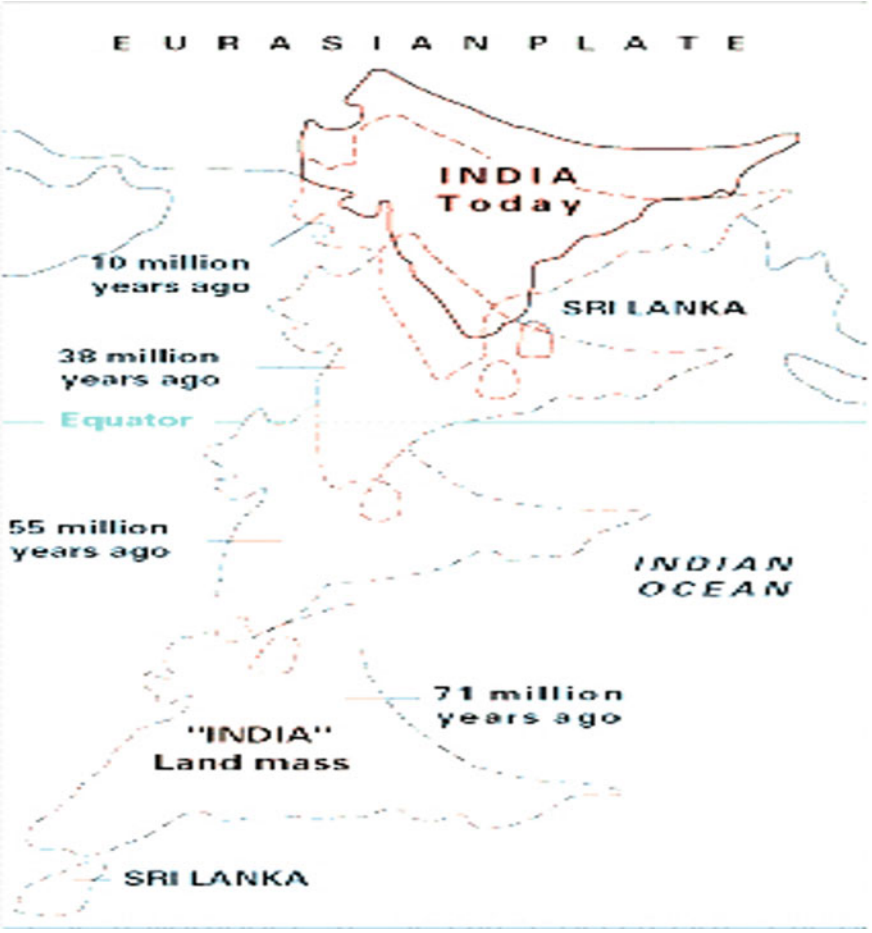

Fig. 2 Neo-tectonic activities in Darjeeling Himalaya*. *Source* www.pmfias.com

3.1 The Nature of Hazard Due to Neo-Tectonic Activity

In monsoon season of September 2007 rainfall in Kalimpong region of Darjeeling area, we face large number of landslide in the zone and cause of lots of death and economic loss of the state [17]. This event highlights the issue of environmental degradation and regular landslide in the Himalayan region. Darjeeling is a small-scale version of complications arising throughout the Himalaya region. Regular increasing event of landslide creates problems at district level and state level. It is a famous tourist place and hub of tea plantation because the moderate temperatures, topography and high rainfall [18]. These conditions are good for plantation but very critical for landslides and slope stability. Researcher is searching the solution to landscape preservation to reduce landslide and promotes tea plantation in the area. In Himalayan

Fig. 3 Landslide along with the road. PC: Vartika Singh

region, due to strong strome condition, disaster is common and has a great impact on population growth and plantation. The outcome is all too likely—more records of landslides with a growing level of influences. The following photograph shows the Kalimpong town which is situated at a high ridge area [19, 20]. We find active landslide below scarred slopes. Mostly, old landscape is made up of landslide scars and old landslide. Kalimpong area is affected by several active land sliding problems in last few years (Fig. 3).

4 Major Reasons of Landslide Risks in the Darjeeling Hills

1. In the rising process of young mountains are one of the reason of landslide in the Himalaya. Due to this activity, we find tectonic disturbances, insecure geological structure, and parallel subsidence of Himalayan fore deep of slopes.
2. Conservation and erosion of soil play major role in the landslide activities in hill areas. The toe erosion of the rivers also one of the region of landslides in the valley area [21–23]. If we find very thin soil cover in the hilly area, it effects the socioeconomic development of the hilly people and their agriculture practices.
3. The soil near by the Darjeeling hill area is formed by phyllite, Darjeeling gneiss, and schists. Due to wrong practice of crop selection and excess of deforestation, intensity of soil erosion is increased. In Darjeeling Hill areas, we don't find deposition of soil; only in valley region along with the river, we find layer of soil. Due to the present situation, it is very important to go for soil conservation

practices in the study area. Without soil cover, we can't think about the plantation and agriculture activities in the area.

4. From last few years, if we observe the land use land cover pattern, we find forest cover is sinking due to urbanization and cultivation in the area. We notice the degradation of forest near the tea plantation area. In most of the tea gardens in the hills, any type of shade tree or trees sideways, the fringe line of the garden for the protection of the soil is irrelevant.
5. New development in the hilly region especially along with the road side is main region of disaster and deforestation. We go for high rise building without any permission of government and in unplanned way, and at the end, this activity of steeper slope upturns the load on the already deteriorated slopes.
6. In the higher altitude area, rural people are depend on forest wood for fuel; it is a mail cause of deforestation and slop failure in hilly region. Another region is unscientific mining of the minerals in the area and unlawful felling of trees for the industries.
7. From last fifty to thirty year, we observe the uncontrolled growth of population in the area particularly in the town area. With the population, the traffic and vehicular movement also increases. The nonstop horizontal vibration due to heavy vehicle along the roads slowly weakens the geological formations and unstable slopes.
8. Demand of water for the society is also increased with the urbanization in hilly region. Water resources of the hilly region are dried up with the cutting of forest and road slop in the hilly region because with the cutting we cut several drainage and water resources. So, year after year, our spring shed is drying up.
9. At the end of the all these research, we find the future of the Darjeeling hill is not so good, and we are ready for the water problem in this area [24]. For these type of area, we want strong government policy and awareness among the hilly people.
10. We suggest the watershed and spring shed programs in the study area, with the help of that we are also try to control the soil erosion and landslide problem in the area.

5 Conclusion

In Darjeeling, though there is one shine of expectation, which is extraordinary campaigning will be a campaign to lift the consciousness of issues linked with slope instability in Darjeeling. We should target local people through awareness program and pre-digester preparation activities. The local community of the hilly region needs to be sensitized toward the environmental issues, and we have make a clear picture of the hilly region that if we ignore the cutting of forest in the region, so at the end, there is no forest, no water, no soil, no life. We have to follow the rules and laws as relating to many growing actions going on the hilly region. We want a good coordination among local administration, state, and central government. We also

promote the local NGO's and self-help groups. Still, the same needs to be done in right direction by all the stakeholders. Historical record of the area reflects that the intense rainfall and seismicity are major key factors for the landslide in the area. As the developmental activity is increased in the mountainous region, thereby, the land use management is significant to reduce the vulnerability of the landslides. The analysis and curative measures recommended above for Darjeeling Himalayas are applied to every part of the country.

References

1. DeCelles PG, Robinson DM, Zandt G (2002) Implications of shortening in the Himalayan fold-thrust belt for uplift of the Tibetan Plateau. Tectonics 21:1062
2. Goscombe B, Gray D, Hand M (2006) Crustal architecture of the Himalayan metamorphic front in eastern Nepal. Gondwana Res 10:232–255
3. Mukul M (2000) The geometry and kinematics of the main boundary thrust and related neotectonics in the Darjiling Himalayan fold-and-thrust belt, West Bengal, India. J Struct Geol 22:1261–1283
4. Nelson KD et al (1996) Partially molten middle crust beneath Southern Tibet: synthesis of project INDEPTH results. Science 274:1684–1696
5. Powers PM, Lillie RJ, Yeats RS (1998) Structure and shortening of the Kangra and Debra Dun reentrants, sub-Himalaya, India. Geol Soc Am Bull 110:1010–1027
6. Schelling D (1992) The tectonostratigraphy and structure of the eastern Nepal Himalaya. Tectonics 11:925–943
7. Schelling D, Arita K (1991) Thrust tectonics, crustal shortening, and the structure of the far-eastern Nepal, Himalayas. Tectonics 10:851–862
8. Srivastava P, Mitra G (1994) Thrust geometries and deep structure of the outer and Lesser Himalaya, Jumoan and Garhwal (India): implications for evolution of the Himalayan fold and thrust belt. Tectonics 13:89–109
9. Auden JB (1935) Traverses in Himalaya. Rec Geol Surv India 69(2):161–167
10. Mallet FR (1875) On the geology and mineral resources of the Darjeeling district and the western Duars. Geol Surv India Memoir 11(I):1–50
11. Hengl T, Gruber S, Shreshta DP (2003) Digital terrain analysis in ILWIS. Lecture notes, and user guide. International Institute for Geo-Information Science and Earth Observation (ITC), Enschede, Netherlands
12. Landslide Hazard Zonation Atlas of India (2004) Building material and technology promotion council. New Delhi, India
13. BIS (1998) Indian Standard Preparation of landslide hazard zonation maps in mountainous terrains—guidelines. Part 2 macro-zonation, Bureau of Indian Standards, New Delhi, India, IS:44496 (Part2)
14. Consortium for Spatial Information (CGIAR-CSI) of the Consultative Group for International Agricultural Research (CGIAR) (2005) SRTM data processing methodology
15. Foumelis M, Lekkas E, Parcharidis I (2004) Space data from earth sciences. Elsevier, Amsterdam, pp 321–332
16. Geological Map of India (1998) Geological survey of India. Kolkata, India
17. Martin G (2004) Free and low-cost datasets for international mountain cartography. http://www.icc.es/workshop/abstracts/ica_paper_web3.pdf. Accessed 24 May 2006
18. Ramakrishnan S, Santee Kumar V, Afar Sadie MGSM, Venugopal K (2002) Landslide zonation for hill area development
19. Saha A, Gupta RP, Arora MK (2002) GIS-based landslide hazard zonation in the Bhagirathi (Ganga) valley, Himalayas. Int J Remote Sens 23(2):357–369

20. Saha AK, Gupta RP, Sarkar I, Arora MK, Csaplovics E (2005) An approach for GIS-based statistical landslide susceptibility zonation—with a case study in the Himalayas. Landslides 2(1):61–69
21. Agarwal A, Chak A (1991) Floods, flood plains and environmental myths. Centre for Science and Environment
22. Jarvis A, Rubiano J, Nelson A, Farrow A, Mulligan M (2004) Practical use of SRTM data in the tropics: comparisons with digital elevation models generated from cartographic data. International Centre for Tropical Agriculture (CIAT) and the International Plant Genetic Resources Institute (IPGRI), Cali, Colombia, Working Document no. 198
23. De SK, Jamatia M, Bandyopadhyay S (2009) A geo-technical investigation of Mirik landslide in Darjiling Himalayas, India. In: Sharma HS, Kale VS (eds) Geomorphology of India. PrayagPustakBhavan, Allahabad, pp 207–216
24. Seismotectonic Atlas of India and its environs (2000) Geological survey of India. Kolkata, India, pp 12–13

Application of Fuzzy TOPSIS for Selection of MSW Disposal/Treatment Alternatives

Atul Sharma and Nekram Rawal

Abstract In present time, rapidly increasing urbanization has increased the generation of solid waste sharply, and it has become a serious concern for every city and town. The effective and efficient solid waste management system for a city is a very complex problem. It has to be thoughtfully investigated based on considering various economic, environmental, and social parameters. The selection of appropriate options is the key to an efficient waste management system for a city. In the present study, Jabalpur, which is one of the oldest city in central India, is considered for the selection of appropriate solid waste disposal/treatment option, and their combinations from available options, i.e., are sanitary landfilling, mechanical biological treatment (aerobic), and incineration with energy recovery for economic evaluations. The different scenarios were analyzed with sets of criteria based on economical, technological, and social and environmental using multi-criteria decision-making tools fuzzy TOPSIS technique. Results show scenario: 2 SLF_MBT receives highest priority due to its economic and environmental merits over other alternatives, whereas scenario: 3 SLF_INC, the incineration with the energy recovery scenario receives second-highest priority due to the high energy generation.

Keywords Municipal solid waste · Sanitary landfill · Mechanical biological treatment · Incineration with energy recovery · Fuzzy TOPSIS

1 Introduction

India is the second-largest country in the world with a population of 1.21 billion, about 18% of the world's human population, but still not have enough systems for the treatment of its solid waste [2]. Rapid urbanization and improved living standards are causing higher municipal solid waste generation in Indian cities. Since the waste collection and safe disposal of collected waste is equally important, local bodies must choose appropriate treatment/disposal methods. The selection of solid waste

A. Sharma (✉) · N. Rawal
Department of Civil Engineering, Motilal Nehru National Institute of Technology Allahabad, Prayagraj, India
e-mail: atul@mnnit.ac.in

© The Author(s), under exclusive license to Springer Nature Singapore Pte Ltd. 2023

K. R. Reddy et al. (eds.), *Recent Advances in Sustainable Environment*, Lecture Notes in Civil Engineering 285, https://doi.org/10.1007/978-981-19-5077-3_14

treatment options is still a complex major problem, but it can be tackled through multi-criteria analysis. In our country, local authorities are responsible for this waste collection, installation, and selection of recycling activities suitable for waste treatment options [4]. The solid waste management system should include appropriate environmental and social indicators, potentially used in MCDM analysis. Morrissey and Browne [10] said that every effective waste management strategy should be considered environmental, social, and economic aspects. The MCDA technique is an evaluation process that allows comparison and evaluation of quantitative and qualitative data systematically and consistently. In the MCDA process, a panel of people (which may include experts, field engineers or a combination of two) selects the criteria that are important decisions to be taken (for example, cost, environmental impact, impact on employment), measures the criteria of importance, scores each option (landfill, incineration, advanced thermal processing) against each criterion and determines the weighted score for each option [6]. Previous studies in the field of solid waste decision and LCA to select and offer aid in waste management decision-making process. Many researchers have implemented the MCDM and LCA methods for this waste treatment options ranking to determine the best waste management strategies for site selection or specific waste streams [9, 14]. In some studies, the author assessed waste treatment strategies within the methodological framework taking into account the economic, social, and environmental impacts of LCA.

This article applies Fuzzy TOPSIS methodology to analyze and compare sanitary landfill performance, mechanical biologicals treatment (composting), and waste-to-energy (WtE), in terms of economic, technological and social, and environmental three-pillar criteria. Four treatment/disposal scenarios are made, and each treatment/disposal option scenario is analyzed to find out the most appropriate solution.

2 Methodology

2.1 Study Area

Jabalpur is one of the major cities in Madhya Pradesh, India, and famous for marble rocks and cultural heritage. As per provisional reports of Census India, the population of Jabalpur in 2011 is 1,081,678 with a population density of 7092 people per sq. km. Jabalpur city is governed by Municipal Corporation, which comes under the Jabalpur Metropolitan Region. The total area under JMC is 153 sq. km (Census Commissioner). The city is currently divided into 79 wards. It is under Smart City Mission, started by GOI.

The primary sources of municipal solid waste of the city are as follows: residential, commercial, instructional, street sweeping, and open spaces. Using forecasted population by geometric increase method and per capita generation rate of 460 g/day/person, MSW generation by 2021 is 620 TPD is estimated. According to

the Madhya Pradesh pollution control board report year 2018, about 462 tons per day MSW is processed by kathonda waste-to-energy plant by incineration. The plant is designed to treat 580 TPD waste and generate 11.5 MW electricity.

2.2 *Structuring the Multi-criteria Decision Making Problem for MSW Disposal Alternative*

For structuring the MCDM problem, alternatives, i.e., treatment/disposal methodology, are defined. The next step is to determine the evaluation criteria [8, 13]. Thirteen criteria are selected based on surveys and interviews with experts. Data related to solid waste management are obtained from many sources such as experts, literature, and local corporation bodies [3]. Besides experts interview, data are also acquired from site observation to obtain more information on solid waste disposal methodology at Jabalpur city. Finally, fuzzy TOPSIS, well-known MCDM technique, is used to determine the most appropriate solid waste disposal methodology.

2.3 *Fuzzy TOPSIS Methodology*

TOPSIS (The Technique for Order of Preference by Similarity to Ideal Solution) was developed by Hwang and Yoon [7] on MCDM problems, based on the concept that the chosen alternatives should be the shortest distance from the positive-ideal solution (PIS) and the farthest from the negative ideal solution. After calculating the criteria's significant weighting and ranking, the fuzzy TOPSIS approach is applied to conduct the option's ranking process [12]. To build the fuzzy decision matrix, each decision maker uses the linguistic variables depicted in the Table 1.

The following steps involved in the F-TOPSIS:

Step 1: Assignment of ratings to the criteria and the alternatives.

Step 2: Compute aggregate fuzzy ratings for the criteria and the alternatives.

Step 3: Compute the fuzzy decision matrix.

Step 4: Normalize the fuzzy decision matrix.

Step 5: Compute the weighted normalized matrix.

Table 1 Linguistic scale and the corresponding triangular fuzzy numbers

Linguistic scale	Triangular fuzzy number
Equally important	(1, 1, 3)
Weakly more important	(1, 3, 5)
Strong more important	(3, 5, 7)
Very strong more important	(5, 7, 9)
Absolutely more important	(7, 9, 9)

Step 6: Compute the fuzzy positive-ideal solution (FPIS) and fuzzy negative ideal.
Step 7: Compute the distance of each alternative from FPIS and FNIS.
Step 8: Compute the closeness coefficient (CCi) of each alternative.
Step 9: Rank the alternatives.

In step 9, the different alternatives are ranked according to the closeness coefficient (CCi) in decreasing order. The best alternative is closest to the FPIS and farthest from the FNIS.

2.4 Identification of Municipal Solid Waste Disposal/Treatment Alternatives

In this study, the appropriate MSW treatment/disposal option is selected from the many available waste treatment options considering local waste characteristics and suitability by location. Selected options are sanitary landfilling, mechanical biological treatment (MBT), and incineration; open dumping is the base line scenario, and according to the solid waste management rule, open dumping is not allowed in 2016, so land dumping is not considered in the evaluation of alternatives. Because the capacity of each wastewater treatment plant plays an important role in establishing an integrated waste management system in medium-sized cities, the following treatment/disposal option scenarios are designed.

Scenario 1: Sanitary landfill (SLF).
Scenario 2: Sanitary landfill along with composting (SLF_MBT).
Scenario 3: Sanitary landfill and incineration (SLF_INC).
Scenario 4: Sanitary landfill along with composting and incineration (SLF_COM_INC).

2.5 Delineation of Selected Treatment/Disposal Options

The sanitary landfill is an engineered facility designed adequately for safe, solid waste disposal in a planned manner, properly laid out and compacted with a top cover material. This includes leachate collection and treatment facilities and appropriate landfill gas mitigation measures [17].

A mechanical biological treatment system (MBT) is a waste processing facility that combines a waste sorting facility and biological treatment. The MBT facilities are designed for the treatment of mixed municipal solid waste. In composting, organic matter is decomposed into organic manure by the biological activities of microorganisms that require oxygen to complete the entire process. Windrow composting is commonly used for MSW [11].

Waste-to-energy (WtE) is treating waste and generating energy in the form of electricity from it [15]. To increase process efficiency, the preprocessing of MSW

involves removal of inorganic material. The heat from the burning converts the water into steam, which is then sent to the turbine generator to produce electricity. Volume reduction of up to 90% is achieved through combustion.

2.6 Description of Selected Criteria

Three main criteria, namely, the economic aspect, the technical aspect, and the social and environmental aspect, have been chosen by considering the elaborated literature review and expert opinion [1]. To maintain any chosen technology for a long time, economics Xin-Gang et al. [16] plays an important role, so in criterion selection, economic aspects are given more weightage although technical and social and there is enough space for environmental concerns. The details of the criteria and sub-criteria are summarized in Table 2, and the outline of treatment/disposal alternative selection is shown in Fig. 1.

3 Result and Discussion

According to the methodology of the fuzzy TOPSIS [5, 12], the criteria were compared and evaluated against the overall goal (i.e., choosing the most preferred waste management scenario). The options are then compared with each criterion. There are four scenarios of options formed and used for comparison: SLF, SLF_MBT, SLF_INC, and SLF_COM_INC, respectively. Figure 1 illustrates the hierarchical decision model structure, with targets at the top level and options at the bottom-most level, while the intermediate level includes criteria and sub-criteria elements. F-TOPSIS evaluates four treatment/disposal scenarios Alt.1, Alt.2, Alt.3, and Alt.4 based on thirteen evaluation criteria. There are differences in quantitative and subjective judgments between each assessment criterion; the overall evaluation of the decision is employed to synthesize the opinions of various experts to obtain a fair and objective assessment. Each decision maker establishes a decision matrix in which each choice is evaluated in relation to each criterion. In TOPSIS, the evaluation of options with respect to each criterion decision matrix is made with the help of linguistic assessments from Table 1 to rate criteria and options. After that, the collected fuzzy weights of each criterion are calculated and are presented in Table 3. Then, the total fuzzy weights of the alternatives are calculated and are given in Table 4. In the next step, normalization of the fuzzy decision matrix of alternatives is done. The normalized fuzzy decision matrix for the four alternatives is given in Table 5. A fuzzy weighted decision matrix for the four alternatives is then formed using the values obtained from Tables 3 and 5, the fuzzy weighted decision matrix for the alternatives given in Table 6. Then, the fuzzy positive-ideal solution (FPIS) and the fuzzy negative ideal solutions (FNIS) are computed for alternatives and presented in Table 7. After that, from fuzzy positive-ideal solutions and fuzzy negative ideal solutions,

Table 2 Description of selected criteria

Criteria	Sub criteria	Description
1. Economic aspects	Capital cost	It includes the expenses for the plant and machinery, construction of the treatment/disposal facility
	Operation cost	It includes expenses in the operation of the treatment/disposal facility
	Maintenance cost	These are expenses in periodic maintenance and change/repair of damaged parts of the treatment/disposal facility
	Cost recovery/revenue	These are total earnings from the sale of end products like compost, electricity, etc.
2. Technological aspects	Operational ease	The requirement of a technically skilled workforce and their quantum
	Maintenance ease	Availability of spares and technicians
	Reliability	To handle variation in incoming waste characteristics up to a certain extent without affecting output
	Robustness of technology	It should work under adverse conditions
3. Social and environmental aspects	Health and safety	The potential impact on workers' health in the plant and people living surrounding the treatment/disposal facility
	Social acceptability	Cooperation and involvement of local people affected by the treatment/disposal facility
	Employment potential	The number of wages generated by the treatment/disposal facility
	Global warming potential	It is in terms of greenhouse gas generation potential from the treatment/disposal facility
	Surface and subsurface water quality	Potential usage and impact on surface and subsurface water bodies in the vicinity of treatment/disposal facility

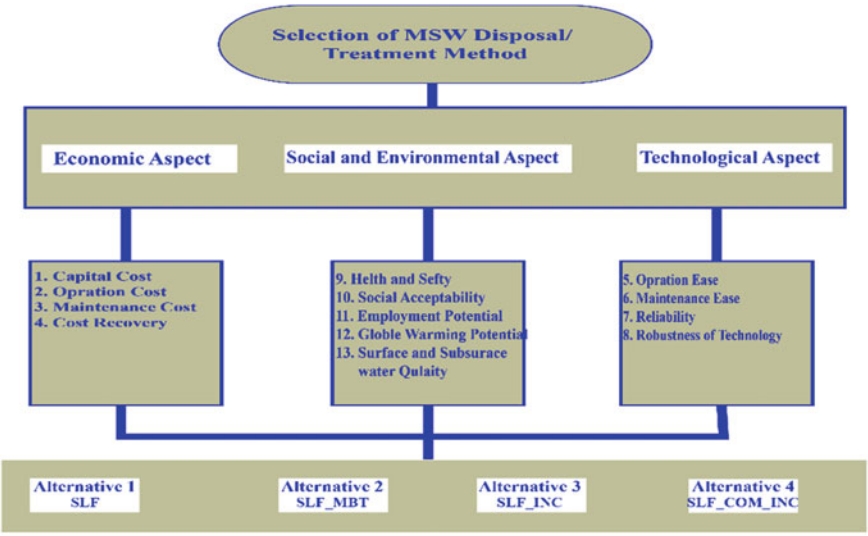

Fig. 1 Framework for alternative selection

the distance of each alternative is calculated in Table 8. The results are presented in Table 9 and Fig. 2, which shows that alternative 2 SLF_MBT has the maximum closeness coefficient (CCi) value, then SLF_INC scores the second closeness coefficient. Therefore, alternative A2 is recommended as the best treatment/disposal option for Jabalpur city.

Table 3 Aggregated fuzzy weights of each criterion

Criteria	Aggregate fuzzy criteria weight		
C:1	7.00	9.00	9.00
C:2	7.00	9.00	9.00
C:3	7.00	9.00	9.00
C:4	7.00	9.00	9.00
C:5	1.00	4.33	7.00
C:6	3.00	6.33	9.00
C:7	1.00	4.33	7.00
C:8	3.00	5.67	9.00
C:9	5.00	8.33	9.00
C:10	3.00	6.33	9.00
C:11	7.00	9.00	9.00
C:12	5.00	7.67	9.00
C:13	3.00	6.33	9.00

Table 4 Aggregate fuzzy matrix of alternatives

Criteria	A:1			A:2			A:3			A:4		
C:1	3.00	6.33	9.00	3.00	5.00	7.00	5.00	8.33	9.00	5.00	8.33	9.00
C:2	1.00	4.33	7.00	5.00	7.00	9.00	3.00	6.33	9.00	3.00	6.33	9.00
C:3	1.00	4.33	7.00	5.00	7.00	9.00	3.00	6.33	9.00	3.00	6.33	9.00
C:4	5.00	8.33	9.00	1.00	1.00	3.00	1.00	2.33	5.00	3.00	6.33	9.00
C:5	1.00	3.67	7.00	5.00	7.00	9.00	3.00	5.67	9.00	3.00	5.67	9.00
C:6	1.00	4.33	7.00	5.00	7.00	9.00	1.00	4.33	7.00	3.00	6.33	9.00
C:7	3.00	5.00	7.00	7.00	9.00	9.00	5.00	8.33	9.00	5.00	7.00	9.00
C:8	3.00	5.00	7.00	7.00	9.00	9.00	5.00	7.67	9.00	3.00	6.33	9.00
C:9	1.00	3.00	5.00	5.00	7.00	9.00	3.00	6.33	9.00	3.00	6.33	9.00
C:10	5.00	8.33	9.00	5.00	7.00	9.00	5.00	7.00	9.00	5.00	7.00	9.00
C:11	5.00	8.33	9.00	1.00	1.00	3.00	1.00	1.67	5.00	1.00	4.33	7.00
C:12	1.00	2.33	5.00	7.00	9.00	9.00	3.00	6.33	9.00	1.00	2.33	5.00
C:13	1.00	3.67	7.00	5.00	7.00	9.00	3.00	6.33	9.00	3.00	5.00	7.00

Table 5 Normalized aggregate fuzzy matrix

Criteria	A:1			A:2			A:3			A:4		
C:1	0.33	0.47	1.00	0.43	0.60	1.00	0.33	0.36	0.60	0.33	0.36	0.60
C:2	0.14	0.23	1.00	0.11	0.14	0.20	0.11	0.16	0.33	0.11	0.16	0.33
C:3	0.14	0.23	1.00	0.11	0.14	0.20	0.11	0.16	0.33	0.11	0.16	0.33
C:4	0.56	0.93	1.00	0.11	0.11	0.33	0.11	0.26	0.56	0.33	0.70	1.00
C:5	0.14	0.27	1.00	0.11	0.14	0.20	0.11	0.18	0.33	0.11	0.18	0.33
C:6	0.14	0.23	1.00	0.11	0.14	0.20	0.14	0.23	1.00	0.11	0.16	0.33
C:7	0.43	0.60	1.00	0.33	0.33	0.43	0.33	0.36	0.60	0.33	0.43	0.60
C:8	0.43	0.60	1.00	0.33	0.33	0.43	0.33	0.39	0.60	0.33	0.47	1.00
C:9	0.20	0.33	1.00	0.11	0.14	0.20	0.11	0.16	0.33	0.11	0.16	0.33
C:10	0.56	0.93	1.00	0.56	0.78	1.00	0.56	0.78	1.00	0.56	0.78	1.00
C:11	0.56	0.93	1.00	0.11	0.11	0.33	0.11	0.19	0.56	0.11	0.48	0.78
C:12	0.20	0.43	1.00	0.11	0.11	0.14	0.11	0.16	0.33	0.20	0.43	1.00
C:13	0.14	0.27	1.00	0.11	0.14	0.20	0.11	0.16	0.33	0.14	0.20	0.33

4 Conclusions

In this study, a multi-criteria decision-making approach is used to select the best solid waste treatment/disposal method under a fuzzy environment in Jabalpur. In this approach, criteria for evaluating the appropriate treatment/disposal method are identified. These criteria are related to capital cost, O&M cost, cost recovery, and technical and social and environmental aspects. From this study, fuzzy multi-criteria

Table 6 Weighted normalized fuzzy matrix of alternatives

Criteria	A:1			A:2			A:3			A:4		
C:1	2.33	4.26	9.00	3.00	5.40	9.00	2.33	3.24	5.40	2.33	3.24	5.40
C:2	1.00	2.08	9.00	0.78	1.29	1.80	0.78	1.42	3.00	0.78	1.42	3.00
C:3	1.00	2.08	9.00	0.78	1.29	1.80	0.78	1.42	3.00	0.78	1.42	3.00
C:4	3.89	8.33	9.00	0.78	1.00	3.00	0.78	2.33	5.00	2.33	6.33	9.00
C:5	0.14	1.18	7.00	0.11	0.62	1.40	0.11	0.76	2.33	0.11	0.76	2.33
C:6	0.43	1.46	9.00	0.33	0.90	1.80	0.43	1.46	9.00	0.33	1.00	3.00
C:7	0.43	2.60	7.00	0.33	1.44	3.00	0.33	1.56	4.20	0.33	1.86	4.20
C:8	1.29	3.40	9.00	1.00	1.89	3.86	1.00	2.22	5.40	1.00	2.68	9.00
C:9	1.00	2.78	9.00	0.56	1.19	1.80	0.56	1.32	3.00	0.56	1.32	3.00
C:10	1.67	5.86	9.00	1.67	4.93	9.00	1.67	4.93	9.00	1.67	4.93	9.00
C:11	3.89	8.33	9.00	0.78	1.00	3.00	0.78	1.67	5.00	0.78	4.33	7.00
C:12	1.00	3.29	9.00	0.56	0.85	1.29	0.56	1.21	3.00	1.00	3.29	9.00
C:13	0.43	1.73	9.00	0.33	0.90	1.80	0.33	1.00	3.00	0.43	1.27	3.00

Table 7 FPIS and FNIS of alternatives

Criteria	FNIS (A^-)			FPIS		
C:1	2.3	2.3	2.3	9.0	9.0	9.0
C:2	0.8	0.8	0.8	9.0	9.0	9.0
C:3	0.8	0.8	0.8	9.0	9.0	9.0
C:4	0.8	0.8	0.8	9.0	9.0	9.0
C:5	0.1	0.1	0.1	7.0	7.0	7.0
C:6	0.3	0.3	0.3	9.0	9.0	9.0
C:7	0.3	0.3	0.3	7.0	7.0	7.0
C:8	1.0	1.0	1.0	9.0	9.0	9.0
C:9	0.6	0.6	0.6	9.0	9.0	9.0
C:10	1.7	1.7	1.7	9.0	9.0	9.0
C:11	0.8	0.8	0.8	9.0	9.0	9.0
C:12	0.6	0.6	0.6	9.0	9.0	9.0
C:13	0.3	0.3	0.3	9.0	9.0	9.0

decision-making approach has been identified as an important tool for evaluation of proper treatment/disposal method considering the factors related to solid waste and their management in Jabalpur city. F-TOPSIS is used to select the best and appropriate solid waste treatment/disposal method for the city. In order to identify the MCDM assessment process and criteria, it is important to assign appropriate weights to the criteria and options. It is also important to have consistent goals and

Table 8 Distance of alternatives from FPIS and FNIS

Criteria	d^+				d^-			
	A:1	A:2	A:3	A:4	A:1	A:2	A:3	A:4
C:1	6.94	7.37	3.20	3.20	8.18	7.00	9.52	9.52
C:2	8.33	1.14	2.31	2.31	10.58	13.38	12.69	12.69
C:3	8.33	1.14	2.31	2.31	10.58	13.38	12.69	12.69
C:4	11.59	2.23	4.50	10.04	5.15	12.95	11.32	7.18
C:5	6.97	1.39	2.32	2.32	8.99	10.93	10.40	10.40
C:6	8.74	1.57	8.74	2.75	11.41	13.87	11.41	13.23
C:7	7.04	2.89	4.06	4.16	7.91	9.56	9.05	8.87
C:8	8.36	2.99	4.57	8.18	9.53	11.88	11.09	10.19
C:9	8.74	1.40	2.56	2.56	10.13	13.57	12.90	12.90
C:10	8.45	8.02	8.02	8.02	7.98	8.39	8.39	8.39
C:11	11.59	2.23	4.31	7.17	5.15	12.95	11.72	9.66
C:12	8.89	0.79	2.53	8.89	9.83	14.04	12.96	9.83
C:13	8.78	1.57	2.75	2.83	11.24	13.87	13.23	13.01

Table 9 Closeness coefficient (CC_i) of alternatives

	A1:SLF	A2:SLF_MBT	A3:SLF_INC	A4:SLF_COM_INC
d^+	112.75	34.74	52.18	64.73
d^-	116.68	155.76	147.37	138.57
CC_i	0.51	0.82	0.74	0.68

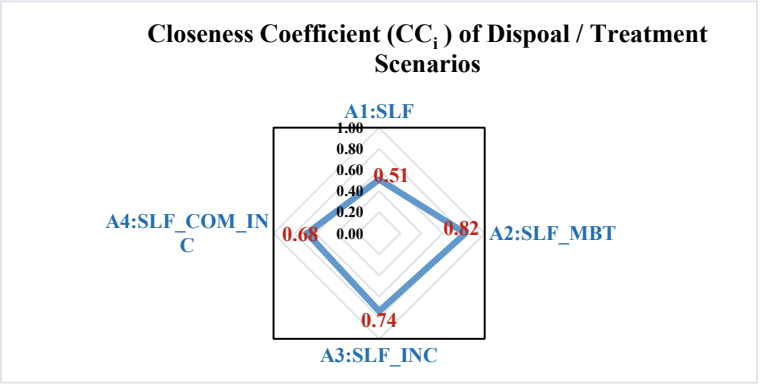

Fig. 2 Priority of treatment/disposal scenarios

objectives for evaluating treatment methodology for solid waste based on socio-cultural, technical, economic, and environmental criteria. Comparing the treatment options for the four treatment/disposal scenarios shows that SLF_MBT (A2) is the most appropriate treatment/disposal option as it offers separation and recycling from waste, which adds to the revenue and load on the environment and disposal facility reduces after Scenario: 3 (SLF_INC), Scenario: 4 (SLF_COM_INC), and Scenario: 1 (SLF) in fuzzy TOPSIS. Thus, it is expected that the results of this study will be used as a decision support system for the selection of a suitable solid waste disposal method for the city and minimize problems related to solid waste management.

Acknowledgements The authors would like to thank the Jabalpur Nagar Nigam (JNN), all experts and field engineers, and local people for their help in data collection and survey during fieldwork.

References

1. Allesch A, Brunner PH (2014) Assessment methods for solid waste management: a literature review. Waste Manage Res 32(6):461–473. https://doi.org/10.1177/0734242X14535653
2. Census of India (2011) Census of India. [Online]
3. Central Public Health and Environmental Engineering Organisation (CPHEEO) (2016) Municipal solid waste management plan: step-wise guidance Swachh Bharat mission municipal solid waste management manual. Municipal Solid Waste Management Manual, part II, pp 3–561. www.moud.gov.in or www.swachhbharaturban.gov.in
4. Cherubini F et al (2009) Life cycle assessment (LCA) of waste management strategies: landfilling, sorting plant and incineration. Energy 34(12):2116–2123. Elsevier Ltd. https://doi.org/10.1016/j.energy.2008.08.023
5. Ekmekçioğlu M et al (2010) Fuzzy multicriteria disposal method and site selection for municipal solid waste. Waste Manag 30(8–9):1729–1736. https://doi.org/10.1016/j.wasman.2010.02.031
6. Hanan D et al (2013) A multi-criteria decision analysis assessment of waste paper management options. Waste Manag 33(3):566–573. https://doi.org/10.1016/j.wasman.2012.06.007
7. Hwang C-L, Yoon K (1981) Methods for multiple attribute decision making. 58–191. https://doi.org/10.1007/978-3-642-48318-9_3
8. Jovanovic S et al (2016) Using multi-criteria decision making for selection of the optimal strategy for municipal solid waste management. https://doi.org/10.1177/0734242X16654753
9. Karagiannidis A et al (2010) A multi-criteria assessment of scenarios on thermal processing of infectious hospital wastes: a case study for central Macedonia. Waste Manag 30(2):251–262. Elsevier Ltd. https://doi.org/10.1016/j.wasman.2009.08.015
10. Morrissey AJ, Browne J (2004) Waste management models and their application to sustainable waste management. 24:297–308. https://doi.org/10.1016/j.wasman.2003.09.005
11. Municipal, integrated, and solid waste (2000). Users manual
12. Nădăban S et al (2016) Fuzzy TOPSIS: a general view. Proc Comput Sci 91(Itqm):823–831. https://doi.org/10.1016/j.procs.2016.07.088
13. Rathi S (2006) Alternative approaches for better municipal solid waste management in Mumbai, India. Waste Manage 26(10):1192–1200. https://doi.org/10.1016/j.wasman.2005.09.006
14. Roussat N et al (2009) Choosing a sustainable demolition waste management strategy using multicriteria decision analysis. Waste Manag 29(1):12–20. Elsevier Ltd. https://doi.org/10.1016/j.wasman.2008.04.010
15. Tozlu A, Özahi E (2016) Waste to energy technologies for municipal solid waste management in Gaziantep. 54:809–815. https://doi.org/10.1016/j.rser.2015.10.097

16. Xin-Gang Z et al (2016) Technology, cost, a performance of waste-to-energy incineration industry in China. Renew Sustain Energy Rev 55:115–130. Elsevier. https://doi.org/10.1016/j.rser.2015.10.137
17. Yadav P, Samadder SR (2018) A critical review of the life cycle assessment studies on solid waste management in Asian countries. J Clean Prod 185:492–515. Elsevier Ltd. https://doi.org/10.1016/j.jclepro.2018.02.298

Implementing Machine Learning Models for Drought Prediction Based on Metrological Drought Indices with Varying Time Scales: A Case of Latur Region

Tuba Firdaus, Preeti Gupta, and S. Sangita Mishra

Abstract Droughts have a huge socioeconomic impact, thus globally affecting the people, the environment, and the economy on a massive scale. Proper monitoring and accurate predictions can help mitigate the ill effects of such natural calamities to a considerable level. Providing warning signals and proper preplanning can provide further solutions. Drought occurrences highly depend on the environmental characteristics of the region. To identify drought and analyze its severity level, metrological drought indices like Standard Precipitation Index (SPI), Standardized Precipitation and Evapotranspiration Index (SPEI), and Reconnaissance Drought Index (RDI) are popularly used. The present work focuses on drought prediction using three drought indices SPI, SPEI, RDI. The case of Latur region of Maharashtra, India, has been taken for the research work. The prediction model is developed using support vector regression (SVR) and long short-term memory (LSTM) for varying timescales 1, 3, 6, 9 and 12 months, and the performance of the model is evaluated across measures like mean absolute error (MAE) and root mean squared error (RMSE).

Keywords Drought prediction · Support vector regression · Long short-term memory · Standard precipitation index · Standardized precipitation and evapotranspiration index · Reconnaissance drought index

1 Introduction

Defining the natural phenomena of drought is complex owing to its region-specific nature. However, precipitation deficit can be considered as the root cause of drought. In the absence of start and end times of this, natural phenomenon its impact can be detrimental for decades, influencing socioeconomic conditions of the region. Based on its impact, drought can be classified in following four categories, as depicted in Fig. 1:

- Metrological Drought—a persistent and abnormal precipitation deficiency.

T. Firdaus (✉) · P. Gupta · S. Sangita Mishra
Amity University Maharashtra, Mumbai, India
e-mail: tubafirdaus@gmail.com

© The Author(s), under exclusive license to Springer Nature Singapore Pte Ltd. 2023

K. R. Reddy et al. (eds.), *Recent Advances in Sustainable Environment*, Lecture Notes in Civil Engineering 285, https://doi.org/10.1007/978-981-19-5077-3_15

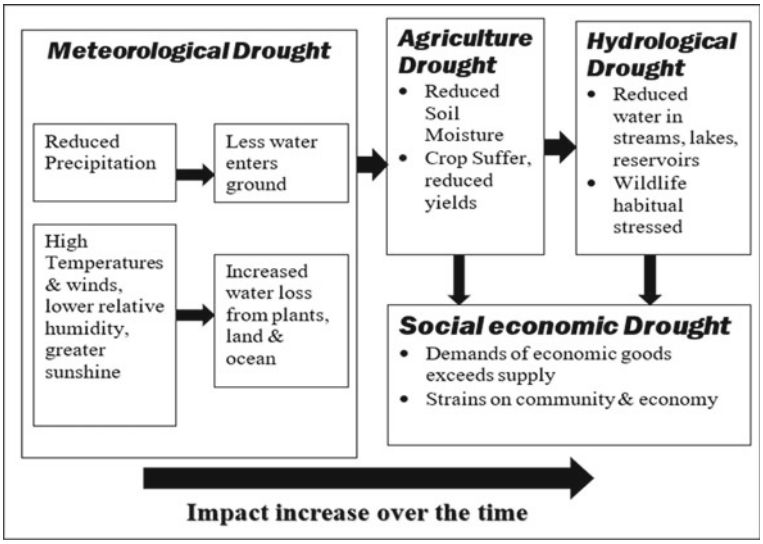

Fig. 1 Drought classification

- Agriculture Drought—deficiency in soil moisture which affects crop growth.
- Hydrological Drought—a fall in lake water level, stream flow, and groundwater level.
- Socioeconomic Drought—When these different forms of deficiencies become visible at social level, then it is considered as socioeconomic drought.

The India Meteorological Department (IMD) describes drought based on rainfall deficiency compared with long-term average as if it falls below 25% it is normal; 26–50% is moderate, and more than 50% deficiency is severe drought condition.

According to Area Authority of India, about 60% of the total fertile area in India depends on natural rainfall (rainfed agriculture), and hence, any change in rainfall will adversely affects Indian economy. Drought prediction is challenging as it involves complex interaction of multiple environmental variables. Early drought prediction is much required for implementing necessary actions such as better use of resources and change of crop for beating the adverse effect of drought.

Accuracy of drought prediction and monitoring systems highly depends on the indices selected for evaluation as these are variables which define regional climatic characteristics. Most important characteristics of a region for drought classification are precipitation. Along with precipitation, temperature, humidity, and wind speed are also some of important characteristics for drought. Numerous drought monitoring and prediction indices have been given by researchers suitable for different regions with various data requirements. These indices can be very simple as percentage of normal precipitation or complex as Palmer drought severity index (PDSI) which requires a lot of mathematical calculations [1]. One of the most widely acceptable indexes is Standard Precipitation Index (SPI), given by McKee et al. in 1993 at Colorado state

University [2]. In 2009, World Meteorological Organization (WMO) recommended SPI as a standard index [3] to monitor meteorological drought conditions in countries. SPI is widely acceptable due to its simplicity as it requires only precipitation as input which can be easily available for most of the regions. SPI can be evaluated at multiple timescales like 1, 3, 6, 9, 12, 24, and 48 which makes it suitable to be used for short-term and long-term applications. Shorter time scales of SPI can be used for meteorological and agricultural drought as soil moisture indicates lack of precipitation at short scales, while longer time scales can be used for hydrological drought as reservoir, streamflow, and ground water indicates lack of precipitation at longer scale. Calculation of SPI requires at least 30 years of monthly precipitation data. Usually, precipitation data are negatively skewed as less precipitation has more frequencies due to which Gamma probability distribution function mentioned in Eq. (1) provides better fit for the data.

$$G_x = \int_0^x g_x dx = \frac{1}{\beta^\alpha \tau(\alpha)} \int_0^x x^{\alpha-1} e^{-x/\beta} dx \tag{1}$$

Gamma function has two parameters α (shape factor) and β (scale factor) which can be evaluated by Thomas Eqs. (2), (3), and (4).

$$\alpha = \frac{1}{4A}\left(1 + \sqrt{1 + \frac{4A}{3}}\right) \tag{2}$$

$$\beta = \frac{\overline{x}}{\alpha} \tag{3}$$

$$A = \ln(\overline{x}) - \frac{\sum \ln(x)}{n} \tag{4}$$

After this, the data will be normalized by taking mean as 0 and standard deviation as 1 (factsheet SPI); the final SPI value is the measure of deviation from mean. Once the SPI values have been evaluated, Mackee scale can be used to classify the severity of the drought Table 1 [2].

SPI at different time scale will be evaluated following similar method, e.g., for 3-month SPI, the aggregated value of three months has to be taken like to calculate 3-month SPI at March end will take January–March precipitation data of that particular

Table 1 SPI range for drought classification

SPI values	Drought category
0 to −0.99	Mild drought
−1.00 to −1.49	Moderate drought
1.50 to −1.99	Severe drought
=< −2.00	Extreme drought

year and compare it with the same 3-month precipitation data of all the years included in data. Same procedure will be followed for all the scales.

Though SPI is widely acceptable, but as it includes only precipitation data for drought prediction, the effect of other environmental characteristics is considered as negligible which is addressed by researchers, and various indices have been proposed which include temperature, potential evapotranspiration, humidity, and wind speed along with precipitation. Reconnaissance drought index (RDI) [4] is proposed in 2005 which includes precipitation and potential evapotranspiration as input for drought prediction. RDI is evaluated in three forms initial, normalized, and standardized at different time scales. Standardized RDI can be compared with SPI. RDI uses Penman–Monteith method to evaluate evapotranspiration. RDI has been used by many researchers for meteorological drought prediction [5, 6] as it includes both precipitation and potential evapotranspiration and makes it possible to compare areas with different climatic scenarios. SPEI [7] is another widely acceptable index which is an enhancement over SPI. Similar to SPI, SPEI is also very easy to calculate as it utilizes same mathematical formulation used in SPI. It takes potential evapotranspiration (PET) along with precipitation and simply calculate the difference between precipitation and PET as depicted in Eq. (5).

$$D_i = P_i - \mathrm{PET}_i \tag{5}$$

D_i is simply the surplus water for analyzed month. This D_i values will be aggregated for various time scales, by using same method as SPI.

Considering climate variability is important for drought assessment as there is almost 2-degree improvement in last 150 years [8] which is going to continue even faster. Therefore, including evapotranspiration or temperature in drought indices is preferable, especially for regions with variable climatic scenario.

2 Literature Survey

Droughts have severe environmental, social, and economic impact which enters slowly and affects widespread geographies. Therefore, drought early warning systems are very much required to mitigate the effects of drought in particular area. Various approaches can be used for drought prediction such as statistical models, dynamical models, and hybrid models are assumed prominence.

The commonly used statistical models can be implemented using various algorithm like fuzzy logic, classification and regression algorithms of machine learning, Markov chain models, deep learning algorithms, or even different hybrid algorithms can also be used. The approach in dynamical method uses climate models or hydrologic models that simulate physical processes of ocean, land, and atmosphere. The hybrid methods for drought prediction involve merging forecasts from both methods—statistical and dynamical.

In this work, statistical models have been studied and implemented. Fuzzy model is one of this which is widely used by researcher, Malik [9] used different variations of fuzzy logic such as multiple linear regression (MLR), multi-layer perceptron neural network (MLPNN), and co-active neuro-fuzzy inference system (CANFIS) for meteorological drought prediction using Effective Drought Index (EDI) and concluded that CANFIS and MLPN outperforms MLR. Adnan [10] has used three adaptive neuro-fuzzy inference system (ANFIS)–embedded grid partition (GP), fuzzy c-means clustering (FCM), and subtractive clustering (SC) have been used to estimate PAN evaporation and find that ANFIS-FCM normally gives better EPAN estimates compared to other two methods.

A variety of models have been implemented by using either classification or regression algorithms of machine learning and comparative assessment between these algorithms has been done, Khan [11] compared the performance of ANN, KNN, and SVM and found that SVM models can better capture the spatial and temporal features of droughts in some region of Pakistan. Borji [12] implemented SVR for hydrological drought forecasting and compared it with ANN and found that SVR outperforms in long-term drought prediction. Agana [13] used Standardized Streamflow Index (SSI) as input and implemented a deep belief network with two Boltzmann machines to predict SSI and compare the efficiency of proposed model with multilayer perceptron (MLP) and support vector regression (SVR). The results showed that DBN gives significant improvement over SVR and MLP. Park [14] has used different machine learning algorithms for predicting SPI like boosted regression trees (BRT), random forest (RF), and Cubist to detect drought in various regions of USA and concluded that RF gives better results.

Same algorithms perform differently for different drought indicators like autoregressive integrated moving average (ARIMA) model gives better long-term prediction for SPEI [15] and better short-term prediction for SPI [16]. Dehghani [17] has implemented dynamic linear spatiotemporal model (DLSTM) and ANN to predict Standardized Hydrological Drought Index (SHDI) and found that DLSTM can accurately forecast SHDI at short time scales.

Among deep learning algorithms, LSTM is widely used for drought prediction as it is a type of recurrent neural network (RNN) that can remember important things of the input they receive because of their internal memory due to which it is very suitable for sequence data like time series data. It has high applicability in time series forecasting [18]. Zhang [19] proposed LSTM-based model to predict soil moisture data which outperforms ARIMA model which is widely acceptable by researcher for drought variables prediction. Very similar work has been done by Poornima [20]; they implemented both algorithms and found LSTM has given better prediction results for longer lead times, and also, LSTM gives improved results when additional variables are getting added which is having positive correlation with SPI and SPEI, but ARIMA gives better results for short-term prediction.

These algorithms can also be combined and give better prediction results when compared individually like, Rehmat [21] implemented a hybrid model using ANN and Markov chain model to predict standardized streamflow index (SSI) and confirmed that combining two models improve short-term prediction. Though various

hybrid algorithm has been implemented by researchers like Nabipour [22] implemented a hybrid model by hybridizing the ANN algorithm with various nature-inspired algorithms like SSA, BBO, PSO, and GOA and found that ANN optimized with PSO has given better results as compared to others. This nature-inspired algorithms can also been used differently like Subedi [23] used a deep belief network to predict drought in prior and then used swarm optimization (SO) for drought mitigation by finding re-routed path for rivers. Hosseini-Moghari [24] compared ARIMA model with two hybridized algorithm recursive support vector regression (RSVR) and recursive multi-layer perceptron (RMLP); both were optimized via an imperialist competitive algorithm (ICA) to evaluate SPI. Various comparisons have been made to find better solution and found that ICA-RSVR and ICA-RMLP outperform ARIMA in majority of the cases.

3 Implementation

3.1 Dataset

The data are collected for Latur (latitudes 18.4088° N and longitudes 76.5604° E) region of Marathwada, India from year 1930 to 2002. For the study, Latur which is about 400 km east of Mumbai is chosen as it is a drought ravaged land in the state of Maharashtra, India and since years its half a million population is immensely suffering due to below par monsoon rains leading to crop failure. The research data comprise of precipitation, average temperature, and potential evapotranspiration on monthly basis. The data are converted into monthly time series data by taking date element which includes same date of each month from year 1930 to 2002 to give it a comparative base. As all the indices taken into consideration take monthly time series data.

The first 54-year (1930–1983) of data has been taken for training, and last 18 years (1984–2002) have been taken for testing. Three indices have been evaluated: SPI, SPEI, and RDI at different time scales 1, 3, 6, 9, and 12. The objective is to find accurate prediction of these parameters. An exploratory analysis of the data has been done to understand the behavior of it as depicted in Fig. 2.

3.2 Support Vector Regression (SVR)

SVR is an advance machine learning algorithm developed in 1992 by Vladimir Vapnik. SVR and ANN are two most widely used data-driven models for machine learning [25]; various comparative assessments have been done on these for different drought indices in different regions, and SVR outperforms in most of the scenarios [12] as ANN models suffers the problem of overfitting, underfitting, and local minima

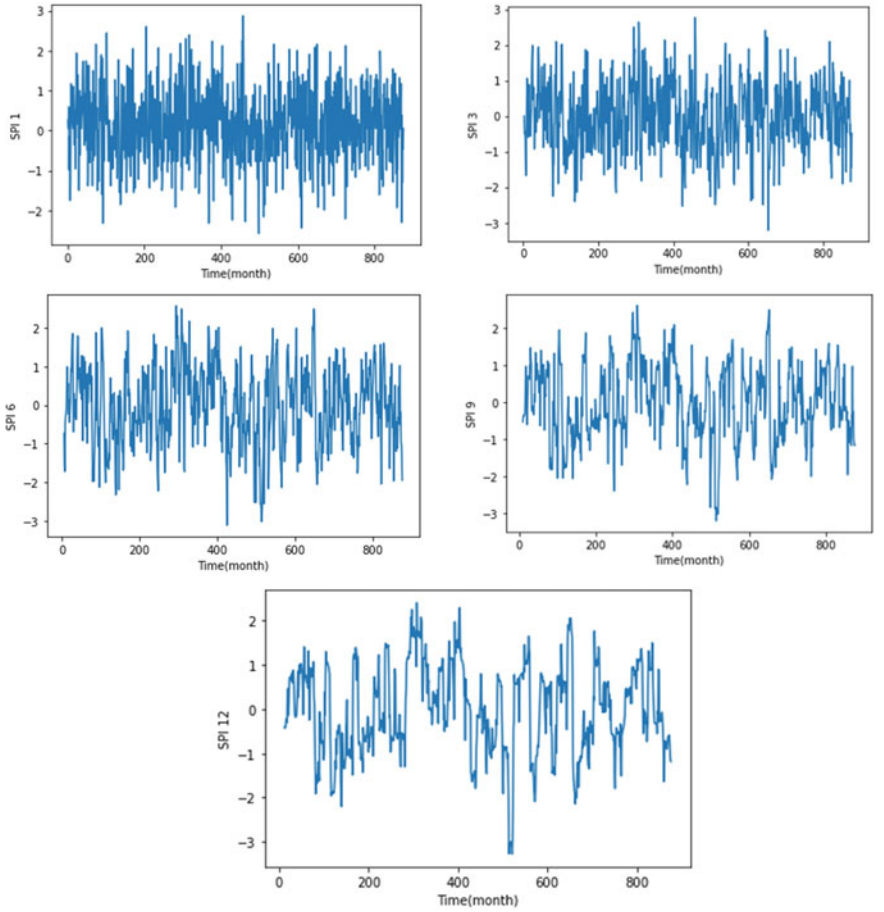

Fig. 2 SPI values in different time scales

though SVR also is vulnerable to overfitting and underfitting problems, but as it works on the principles of structural risk minimization, which minimizes the expected error and preserves it to get trapped in local minima and achieves global optimum. Other than this, there are many advantages of SVR over ANN which makes it better in most of the scenarios as it requires lesser parameters for model building, more suitable for generalizing training datasets, and lesser possibility of overfitting are few of them.

3.3 SVR Implementation

The proposed model of work implements SVR for SPI, SPEI, and RDI for timescales 1, 3, 6, 9, and 12 month. A radial basis function (RBF) kernel is used in SVR; kernel

functions are used to map training dataset into higher dimensional dataset to give a linear view of data; RBF is most popular kernel functions which overcomes space complexity problem which arises due to this conversion.

3.4 Long Short-Term Memory

Long short-term memory (LSTM) is an advancement over basic recurrent neural network (RNN). LSTM architecture was proposed in 1997 by Hochreiter and Schmidhuber. RNNs were first algorithm which remembers its input due to an internal memory which makes it suitable for sequential data or time series data. The range of data that traditional RNNs can remember is quite limited because of repeated weight adjustments in neural network influence of previous input either decreases or increases exponentially in every pass (epochs). This problem of RNN is known as vanishing gradient problem. Due to this problem, RNNs are not suitable to be used in time series data with long-term dependency; it is resolved by LSTM using a memory unit called cell state and sequence of 'gates' which remembers long-term dependencies.

LSTM network is designed in such a way it can learn from previous inputs and its suitable when the data sizes are huge. As mentioned, LSTM uses gates; these gates are arranged in sequential order like a chain. First, forget gate selects which values to be dropped from old cell state considering the current input. Second, input gate allows the normal flow of input; third candidate gate chooses what values to be updated in cell state, and finally, output gate chooses the final output from cell state. In basic LSTM architecture, forget gate and input gate use sigmoid activation; candidate gate uses tanh, and output gate uses both sigmoid and tanh as activation function. All these functions are going to be computed like a traditional neural network by applying weights and bias which triggers the neurons. This LSTM unit will be present in every neuron of hidden layer of RNN. The structure can be depicted as shown in Fig. 3.

As mentioned in LSTM, input gate uses sigmoid function, so it doesn't get activated until it receives value zero. Output gate is taking care when to allow any output go out; with this structure when both gates are closed, the value generated by activation function will be trapped in memory cell, and it will not be allowed to grow or shrink. In back propagation, same applies for errors the gates will learn when to read input and when to generate input. LSTM changes its weight as per change in its derivative with error which minimizes total error of LSTM.

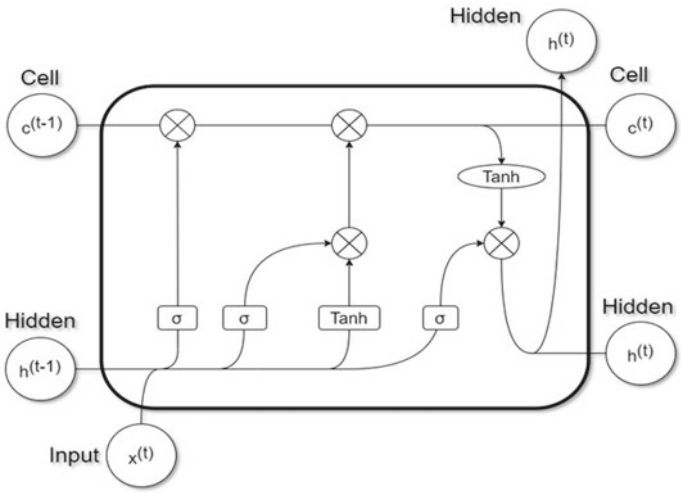

Fig. 3 LSTM architecture

3.5 LSTM Implementation

The LSTM model developed in this work is multivariate model which takes different input for different indices. As we have taken three drought indices SPI, SPEI, RDI for model evaluation and to find out which index can best predict by LSTM model.

All these indices are evaluated at different timescales of 1, 3, 6, 9, and 12 month, but input for all indices is different as for SPI we have taken date and precipitation as input; for RDI, we have given three inputs as date, precipitation, average temperature. And for SPEI, inputs are date, precipitation, and potential evapotranspiration.

4 Results and Discussion

As mentioned earlier, the input data of prediction model are precipitation, evapotranspiration, and average temperature for predicting SPI, SPEI, and RDI values, taken in different combination for each value. Figure 3 shows SPI values at different timescales with respect to time. It can be seen from the figure that the fluctuations of SPI in shorter time scales are greater than longer time scales. Thus, highest fluctuations can be seen in SPI1 and least fluctuations in spi12. Same applies for other indices as well. RMSE and MAE are taken as performance criteria, with this a clear performance evaluation can be done for each model implementation. Both the model is implemented for all 3 indices in consideration at 1, 3, 6, 9, and 12 timescales.

Table 2 SVR results

Prediction for SPI, SPEI, and RDI			
Index	Scale	Measures	
		RMSE	MAE
SPI	1	0.59	0.556
	3	0.985	0.782
	6	0.937	0.772
	9	0.985	0.789
	12	0.981	0.798
SPEI	1	0.875	0.691
	3	0.97	0.791
	6	0.994	0.842
	9	0.988	0.819
	12	0.987	0.803
RDI	1	0.954	0.76
	3	0.956	0.756
	6	0.781	0.599
	9	0.732	0.605
	12	0.656	0.53

4.1 SVR Results

The result of SVR for SPI, SPEI, and RDI predictions is shown in Table 2. As shown in the results, it can be identified that SVR is not able to give good results for these indices though it shows slight improved results for shorter time scales (1 and 3) as compared to longer time scales (6, 9, and 12) for SPI and SPEI, while for RDI, it shows improved results for longer timescales.

4.2 LSTM Results

The results of LSTM for SPI, SPEI, and RDI predictions are shown in Table 3. The same pattern can be identified here again that LSTM is able to better capture SPI and SPEI for shorter time scales, and for RDI, they are able to capture longer time scales. It is clear from the results that overall prediction performance is improved for LSTM for all three indices. Though RDI is better predictable by both algorithms, it can be further utilized for drought severity classification.

Table 3 LSTM results

Prediction for SPI, SPEI, and RDI			
Model	Scale	Measures	
		RMSE	MAE
SPI	1	0.439	0.411
	3	0.507	0.480
	6	0.596	0.566
	9	0.573	0.490
	12	0.607	0.513
SPEI	1	0.621	0.580
	3	0.573	0.493
	6	0.698	0.620
	9	0.647	0.606
	12	0.807	0.684
RDI	1	0.525	0.498
	3	0.525	0.496
	6	0.562	0.537
	9	0.602	0.570
	12	0.453	0.402

5 Conclusion

Extensive climate change, causing decline in precipitation, elevates severe drought conditions. This creates requirement for improved drought prediction and forecasting system for mitigation of severity. In this work, a region-specific study of Latur, a drought ravaged region of the state of Maharashtra, was conducted. For predicting drought indices at varying timescales, SVR and LSTM models were used. It can be seen from the results, that LSTM model outperforms for all three indices as compared to SVR. It can also be seen that LSTM gives better prediction for RDI index than SPI and SPEI. Further, it can be observed that both SVR and LSTM are able to better capture RDI at longer time scales as compared to SPI and SPEI which perform well at shorter time scales.

This work can further be extended to calculate drought class to find drought severity by taking the index whichever is giving better accuracy. Larger datasets can be used to achieve better results. Further, deep learning algorithms or hybrid metaheuristic algorithms can be used to optimize prediction accuracy.

References

1. Svoboda MD, Fuchs BA (2016) Handbook of drought indicators and indices. World Meteorological Organization, Geneva
2. McKee TB, Doesken NJ, Kleist J (1993) The relationship of drought frequency and duration to time scales. In: Proceedings of the 8th conference on applied climatology, vol 17, no 22
3. Svoboda M, Hayes M, Wood DA (2012) Standardized precipitation index user guide
4. Tsakiris G, Vangelis HJEW (2005) Establishing a drought index incorporating evapotranspiration. Eur Water 9(10):3–11
5. Farajalla N, Ziade R (2010) Drought frequency under a changing climate in the eastern Mediterranean: the Beka'a Valley, Lebanon. Geophys Res Abstracts 12
6. Khalili D, Farnoud T, Jamshidi H, Kamgar-Haghighi AA, Zand-Parsa S (2011) Comparability analyses of the SPI and RDI meteorological drought indices in different climatic zones. Water Resour Manag 25(6):1737–1757
7. Vicente-Serrano SM, Beguería S, López-Moreno JI (2010) A multiscalar drought index sensitive to global warming: the standardized precipitation evapotranspiration index. J Clim 23(7):1696–1718
8. Jones PD, Moberg A (2003) Hemispheric and large-scale surface air temperature variations: an extensive revision and an update to 2001. J Clim 16:206–223
9. Malik A, Kumar A, Salih SQ, Kim S, Kim NW, Yaseen ZM, Singh VP (2020) Drought index prediction using advanced fuzzy logic model: regional case study over Kumaon in India. PLoS ONE 15(5):e0233280
10. Adnan RM, Malik A, Kumar A, Parmar KS, Kisi O (2019) Pan evaporation modeling by three different neuro-fuzzy intelligent systems using climatic inputs. Arab J Geosci 12(19):1–14
11. Khan N, Sachindra DA, Shahid S, Ahmed K, Shiru MS, Nawaz N (2020) Prediction of droughts over Pakistan using machine learning algorithms. Adv Water Resour 139:103562
12. Borji M, Malekian A, Salajegheh A, Ghadimi M (2016) Multi-time-scale analysis of hydrological drought forecasting using support vector regression (SVR) and artificial neural networks (ANN). Arab J Geosci 9(19):1–10
13. Agana NA, Homaifar A (2017) A deep learning based approach for long-term drought prediction. In: SoutheastCon 2017. IEEE, pp 1–8
14. Park S, Im J, Jang E, Rhee J (2016) Drought assessment and monitoring through blending of multi-sensor indices using machine learning approaches for different climate regions. Agric For Meteorol 216:157–169
15. Mossad A, Alazba AA (2015) Drought forecasting using stochastic models in a hyper-arid climate. Atmosphere 6(4):410–430
16. Han P, Wang P, Tian M, Zhang S, Liu J, Zhu D (2012) Application of the ARIMA models in drought forecasting using the standardized precipitation index. In: International conference on computer and computing technologies in agriculture. Springer, Berlin, Heidelberg, pp 352–358
17. Dehghani M, Saghafian B, Rivaz F, Khodadadi A (2017) Evaluation of dynamic regression and artificial neural networks models for real-time hydrological drought forecasting. Arab J Geosci 10(12):1–13
18. Tan YF, Ong LY, Leow MC, Goh YX (2021) Exploring time-series forecasting models for dynamic pricing in digital signage advertising. Future Internet 13(10):241
19. Zhang N, Dai X, Ehsan MA, Deksissa T (2020) Development of a drought prediction system based on long short-term memory networks (LSTM). In: International symposium on neural networks. Springer, Cham, pp 142–153
20. Poornima S, Pushpalatha M (2019) Drought prediction based on SPI and SPEI with varying timescales using LSTM recurrent neural network. Soft Comput 23(18):8399–8412
21. Rahmat SN, Jayasuriya N, Bhuiyan MA (2017) Short-term droughts forecast using Markov chain model in Victoria, Australia. Theor Appl Climatol 129(1):445–457
22. Nabipour N, Dehghani M, Mosavi A, Shamshirband S (2020) Short-term hydrological drought forecasting based on different nature-inspired optimization algorithms hybridized with artificial neural networks. IEEE Access 8:15210–15222

23. Subedi S, Pasalkar K, Navani G, Kadam S, Lalitha PRN (2019) Drought prediction and river network optimization in Maharashtra region. In: International conference on advances in computing and data sciences. Springer, Singapore, pp 390–398
24. Hosseini-Moghari SM, Araghinejad S, Azarnivand A (2017) Drought forecasting using data-driven methods and an evolutionary algorithm. Model Earth Syst Environ 3(4):1675–1689
25. Deo RC, Salcedo-Sanz S, Carro-Calvo L, Saavedra-Moreno B (2018) Drought prediction with standardized precipitation and evapotranspiration index and support vector regression models. In: Integrating disaster science and management. Elsevier, pp 151–174

Impact of Climate Variability on Streamflow Using Swat Model on Kharun River Basin

Shubha Soni, Samir Bajpai, and Manikant Verma

Abstract The impacts of climate variability and human activities in the Kharun watershed of Chhattisgarh state have been investigated with Soil and Water Assessment Tool (SWAT), calibrated and validated for the period 1989–2001 during calibration and period 2002–2010 during validation. In this study, 30 years of weather data from 1980 to 2010 is used. Calibration and Validation are carried out in SWAT-CUP using the SUFI-2 algorithm and satisfactory performance of the model is achieved as NS value is 0.83 and RSR value is 0.42. Also, Sensitivity analysis showed that the most sensitive parameter in this watershed model is CN2 followed by ALPHABF, GWDELAY, GWQMN, SOLBD, and SLSUBBASIN on basis of t-stat and p-value. Discharges for future rainfall during the year 2012–2100 have been simulated using calibrated SWAT Model. The results indicate that there is a decrease in discharge by 29.85% with a decrease in rainfall by 4.5% during the period 2012–2100. Climate change can result in a decrease in runoff along with changing Landuse patterns. Water demand of Raipur city will increase by 52.38% in the year 2038 with reference to the year 2016 along with a decrease in flow by 35% during the period 2016–2038. Also, River runs dry during April and June months. Deficit starts from March and ends in the last of June month and peak flow occurs in august and September month as per 2017–2018 analysis of inflow and outflow in upper Kharun catchment. Water scarcity may indicate poor management of water in the Kharun watershed and the need for the temporary storage of water.

Keywords Climate · Hydrological modeling · Calibration · SWAT-CUP · SUFI-2 · Sensitivity analysis

S. Soni (✉) · S. Bajpai · M. Verma
Department of Civil Engineering, National Institute of Technology, Raipur, Chhattisgarh, India
e-mail: Shubhasoni1902@gmail.com

S. Bajpai
e-mail: sb@nitrr.ac.in

M. Verma
e-mail: manikverma.ce@nitrr.ac.in

© The Author(s), under exclusive license to Springer Nature Singapore Pte Ltd. 2023

K. R. Reddy et al. (eds.), *Recent Advances in Sustainable Environment*, Lecture Notes in Civil Engineering 285, https://doi.org/10.1007/978-981-19-5077-3_16

1 Introduction

Water scarcity is a big concern in recent years with the growing population, increased food production, and human activity causing a serious impact on the surface as well as groundwater resources. All these factors have exacerbated water stress situations in many parts of the world, especially in arid and semi-arid regions. This human-induced water stress along with unsustainable use of water has contributed to "Anthropogenic Drought" [1]. The Global water cycle is also seriously affected by water management-related human practices (dams, reservoirs, irrigation withdrawals, industrial withdrawals, etc.). Among different components of the water cycle, streamflow is considered as the most crucial reflecting variability in water use pattern. Change in streamflow is due to many factors but broadly speaking two main factors which contribute to this change are Climate change and anthropogenic factor.

In recent years, many researchers have used long-term streamflow data to quantify the separate impacts of human activities and climate change on streamflow [2–4]. Sea temperature rise due to global warming will affect runoff magnitude along with soil moisture disturbs the balance between rainfall and evaporation [5]. Whereas due to human actions like change in land cover, the rate of evapotranspiration would be changed consequently altering vital parameters of the hydrological cycle, such as rainfall and runoff [6–8]. The magnitudes as well as frequency of extreme events are also affected by the change in hydrological parameters [9, 10]. Climate change is a global phenomenon whereas the effect of human activities on streamflow is scale-dependent and highly location-specific [11, 12].

The increase in population along with decreasing water availability causes severe challenges to water resources creating water stress and anthropogenic droughts. Thus, decision-makers and policymakers are now driven toward sustainable water resource management, handling the consequences of the hydrological impact of human activities and climate variability on streamflow [13–15].

2 Methods and Materials

2.1 Study Area: Kharun Basin

The Kharun is the most important tributary of Shivnath River which is tributary of Mahanadi, the longest flowing river of Chhattisgarh. Kharun is a Non-Perennial River that originates from Petechua hills at Balod district and after flowing through 129 km joins Shivnath at Somnath in Raipur district. The Kharun basin's latitudinal extent is between 20° 38′ N to 21° 36′ N and longitudinal extent is 81° 20′ E to 81° 55′ E. This river mainly flows through three districts namely, the Raipur, Dhamtri, and Durg districts of Chhattisgarh state. Kharun river basin covers an area of 4034 km2 and is situated in the plains of Chhattisgarh state as in Fig. 1.

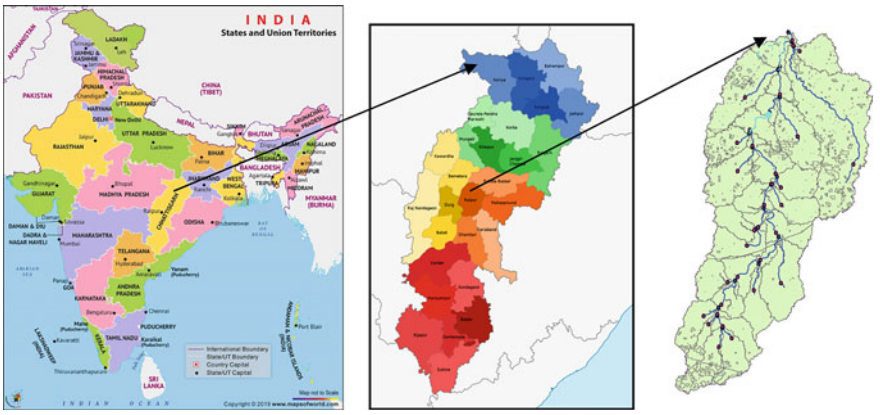

Fig. 1 Map of Chhattisgarh state showing Kharun river basin and its location

Kharun watershed is in the plains of Chhattisgarh which comprises cuddapah series of rocks rich in limestone. Soil profile mostly comprises of coarse gravel, coarse to medium sand, and silts with a thickness of 10–20 m along Kharun and Shivnath basin. This region mainly receives rainfall from the southwest monsoon which starts at the end of June to mid-august with the heaviest shower in July and August. The annual average rainfall in this area is around 1300 mm. This region has a tropical wet and dry climate. The temperature remains constant throughout except in the months of March to June when the temperature reaches about 40 °C The highest temperature goes up to 45 °C in the month of June. Winters last from November to February with the lowest temperature of 13 °C

There are two gauges and discharge sites on river Kharun at "Pathardih" and "Kharun Amdi". Gauging site "Pathardih" is located at 21° 20′28″ N latitude and 81° 35′ 48″ E longitude and comprises an area of 2511 km^2.

2.2 Research Motivation

Kharun being an important tributary of Shivnath River provides drinking water supply to Raipur city and water to the industrial area around it in addition to other uses. The recent issues distinguishing the Kharun basin are water scarcity with an increase in water demand with the growing population and under exploitation of the available water resources [16]. There has been increasing industrial and domestic water demand of Kharun River because of rapid industrialization and urbanization in Raipur district and its surroundings due to which water is being diverted from Ravishankar Sagar Reservoir during dry seasons. As there is no temporary storage structure present in this basin, due to increasing population and water demand, water scarcity issues will increase further in the future.

2.3 Data sources

The brief descriptions of data required and collected from different agencies are discussed below:

1. **DEM** [digital elevation model) of 30 m resolution and **Landuse map** was obtained from SWAT Database for India from https://swat.tamu.edu/data/india-dataset.
2. **Soil map** for India is collected from FAO [Food and Agricultural Organization).
3. **Weather data** (maximum and minimum temperature, wind speed, solar radiation, and relative humidity) were collected from Climate Forecast System Reanalysis (CFSR).
4. **Rainfall data** for 34 years were collected from Indian Meteorological Department (IMD).
5. **Daily discharge data** were collected from Central Water Commission (CWC) and Water Resource Information System (WRIS) (Table 1).
6. **Toposheets** (64G-10, 64G-11, 64G-12, 64H-5, and 64H-9) were collected from the Survey of India.
7. **Season-wise crop production statistics** were collected from https://data.gov.in/resources/district-wise-season-wise-crop-production-statistics.
8. **Landuse map for the year 2017–2018** and **Landuse statistics** were collected from water resource information system (WRIS).
9. Other inflows, drinking water demand, industrial demand were collected from the CG State data center.
10. **Crop statistics** were obtained from CG Agriculture Development and Farmer Welfare and Bio-Technology Department
11. **Water Demand of Raipur City** is taken from revised Raipur development Plan.

3 Methodology

The series of steps involved in this study are expressed in the form of a flowchart as shown in Fig. 2. Climate data, DEM and soil map is taken as inputs to SWAT model. After calibration and validation of parameters and trend analysis, analysis of simulated streamflow is done. At present daily rainfall data of 34 years (1980–2014) of Pathardih station is considered along with meteorological data.

Table 1 Stream gauging station in Kharun watershed

S.no	Stream gauging station	Drainage area (km^2)	Data availability	Mean flow (in cms)	Standard deviation
1	Pathardih	2511	198−2010	29.23769263	45.6313269

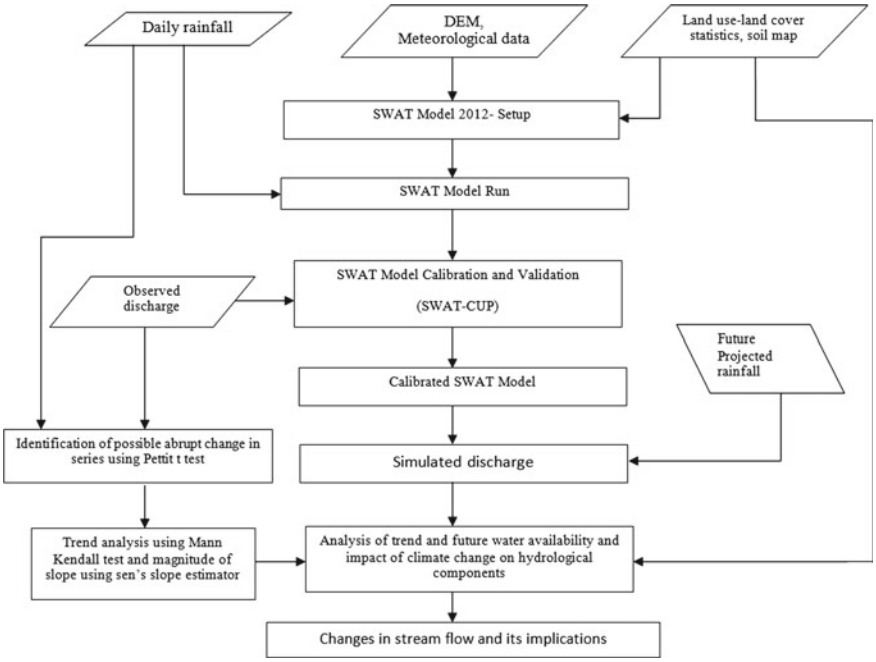

Fig. 2 Flowchart representing methodology and sequence of steps used in this study

3.1 Hydrological Modeling Using SWAT

A hydrological model is used to simulate flow or change in water storage with time in a natural hydrological cycle using watershed parameters with some input data [17]. Soil Water and Assessment Tool (SWAT) is a physical-based and semi-distributed continuous time step model of a river or basin or watershed that can operate on daily, monthly and annual time steps with varying land use, soil and management conditions with time [18, 19]. Also, it has been successfully used to predict the impact of climate variability and Landuse on hydrological cycles in various watersheds [20–22].

This model uses the concept of Hydrological Response Units (HRUs) to incorporate spatial heterogeneity of Landuse, soil type, and slope in the watershed and the main underlying equation is the water balance equation. SWAT divides watersheds into small sub-basins on basis of drainage patterns and sub-basins are further sub-divided into small modeling units called HRUs [23]. The volume of surface runoff/yield is estimated using the Soil Conservation Service Curve Number method (SCS-CN).

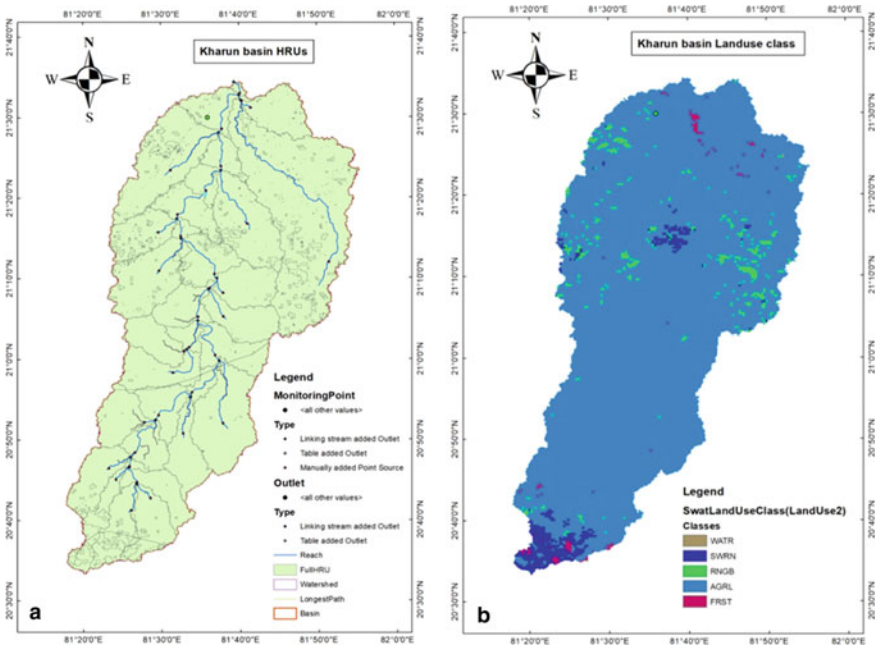

Fig. 3 **a** HRUs and Sub-Basins in Kharun Watershed. **b** Landuse map of Kharun Watershed

3.2 Watershed Delineation and Generation of Hydrological Response Units (HRUs)

Model is set up using DEM, soil map, and Landuse as input data. Delineation is carried out automatically on the area of 403,459.76 hectares. Consequently, the watershed is divided into 34 sub-basins and 42 HRUs on basis of soil type, Landuse, and slope as shown in Fig. 3.

3.3 Model Calibration and Validation

Model calibration and validation are essential steps before arriving at simulation results. By calibrating, we mean to set our input parameters in such a way so that it matches with observed data and Validation is basically testing of calibrated parameters with another set of independent data to obtain the performance of the calibrated model [24]. There are various techniques available for calibration and validation of parameters such as sequential uncertainty fitting (SUFI-2) algorithm, generalized likelihood uncertainty estimation (GLUE), parameter solution (PARASOL), particle swarm optimization (PSO), and Markov chain Monte Carlo (MCMC). In this study, a sequential uncertainty fitting algorithm (SUFI-2) is used [25–27].

Sequential uncertainty fitting (SUFI-2) algorithm [28–30] is a sequential process in which wide-ranging uncertainties at the initial stage in model parameters are reduced progressively till the particular requirement of calibration is satisfied within permissible uncertainties. SUFI-2 is a stochastic process and 95% probability distributions are evaluated on the cumulative distribution of an output variable at the 2.5 and 97.5% level, called 95% prediction uncertainty plot or 95PPU plot.

SWAT-CUP uses two statistical indicators for uncertainty estimation that is p-Factor and r-Factor. Theoretically, the p-factor that is the percentage of observed data enveloped by modeling results (95PPU) ranges from 0 to 100 %. R-factor that signifies thickness of 95PPU plot ranges from 0 to ∞. P-factor close to 1 represents a good model [31]. Regarding model performance indicators, the Nash–Sutcliffe coefficient (NS) was used as a major objective function along with the root mean squared error to standard deviation ratio of measured data (RSR), coefficient of determination (R^2), and percentage bias (PBIAS).

3.4 Detection of Trend and Change Point in Time Series

Identification of trends in series is essential to analyze the stationarity of the hydrological cycle in the region. Several methods are available for trend analysis and change point detection like the Mann Kendall test [32, 33], Pettit test [34], Double Mass Curve technique and moving t-test for detection of change point [35]. In this study, the Mann Kendall test and Pettit test are used for analyzing the time series.

4 Results and Discussion

4.1 Trend Analysis of Precipitation and Runoff

Precipitation data for the year 1980–2015 and flow data for the year 1980–2012 are used for trend analysis and the series is further categorized according to seasons as summer, spring, winter, and autumn [36]. Mann–Kendall test and Pettit test [37] are performed using Matlab software and results are shown in Table 2.

There is no significant trend present in precipitation and flow series except for the winter season where the decreasing trend in precipitation is visible. Further, no significant change point exists for flow and precipitation series. There is a 4.5% decrease in precipitation from the year 2012–2100 for future precipitation projected through MPI CSE REMO 2009 model.

Table 2 Trend analysis and change point detection using Mann Kendall test and Pettit test

Item	Period	Mann Kendall test			Pettit test	
		Z	β	H_O	P value	H_O
Precipitation	Spring	−1.31952	−0.763	Y	0.818	Y
	Summer	0.449338	1.882	Y	0.352	Y
	Winter	−1.6736	−0.683	N	0.94	Y
	Autumn	0.759226	1.467	Y	0.098	Y
Flow	Annual	0.700901	0.075	Y	0.812	Y

H_O= represents null hypothesis that there is no trend in series. β = Sen Slope estimator. Y = yes, N = no. P value is significance probability of statistics

Table 3 t-stat and p-value of parameters in sensitivity analysis

Parameter name	t-Stat	p-Value
R__CN2.mgt	0.80	0.42
R__SOL_AWC(..).sol	−8.09	0.00
R__HRU_SLP.hru	0.01	0.99
R__SOL_K(..).sol	−0.28	0.78
V__ALPHA_BNK.rte	−1.87	0.06
V__CH_K2.rte	−1.09	0.28
V__CH_N2.rte	0.56	0.58
V__GW_REVAP.gw	−65.92	0.00
V__ALPHA_BF.gw	0.62	0.53
V__GW_DELAY.gw	0.04	0.97
A__GWQMN.gw	−0.70	0.48
R__SOL_BD(..).sol	−2.90	0.00
R__SLSUBBSN.hru	−0.75	0.45
V__OV_N.hru	−0.62	0.53
V__ESCO.hru	3.86	0.00
V__REVAPMN.gw	−1.13	0.26

4.2 SWAT Model Calibration and Validation

In this study, the model is calibrated for streamflow on monthly basis from the year 1989–2001 and validated from the year 2002–2010 at Pathardih station using SWAT-CUP (Fig 4).

Parameterization also plays a significant role in regionalizing parameters in the model as it reflects which parameters need to be changed for accurate results. Parameters chosen can be relative, absolute, and replace. Types of parameters include spatial type (vary according to position) and non-spatial type (depends on region or basin

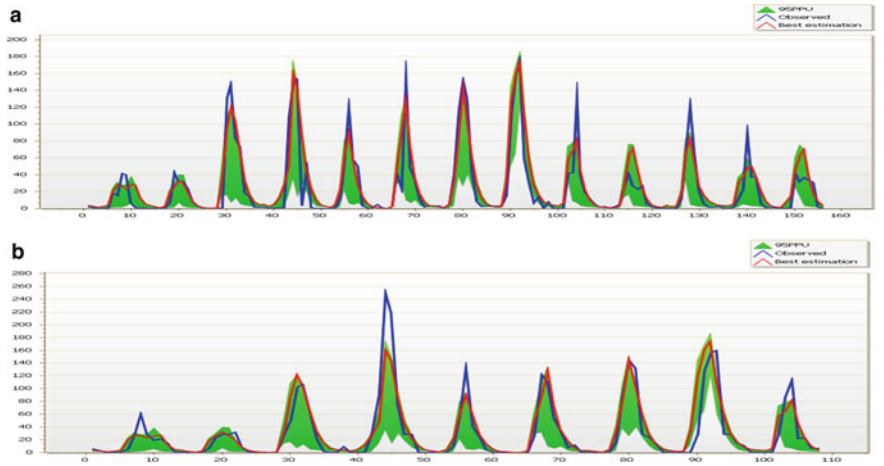

Fig. 4 **a** 95PPU Plot for calibration period (1989–2001) **b** 95PPU Plot for validation period (2002–2010)

only). Thus, to account for spatial heterogeneity, spatial type of parameters should be used as relative [38].

Sensitivity analysis showed that the most sensitive parameter in this watershed model is CN2 followed by ALPHABF, GWDELAY, GWQMN, SOLBD, and SLSUBBASIN based on t-stat and p-value as in Table 3.

In SWAT-CUP, parameter sensitivity is performed using multiple regressions. The t-stat value represents the significance of each parameter. The sensitivity given below represents the relative change in the objective function for change in each parameter while other parameters are changing. Also, a higher p-value indicates parameter is not much sensitive or vice-versa. Generally, the model simulations can be considered as satisfactory if NS value > 0.5, RSR value < 0.7, and PBIAS < 25% for streamflow [24, 26]. Also, the Model is said to be very good if the NS value is greater than 0.75. PBIAS of −12.5 and −5.6 for calibration and validation respectively suggest that the model under-estimated results by 12.5% during the calibration period and under-estimated by 5.6% during the validation period. In this study, satisfactory performance of the model is achieved as NS value is 0.83 and RSR value is 0.42 as shown in Table 4.

Table 4 Results of calibration and validation in SWAT-CUP

Criteria	Calibration	Validation
NS coefficient	0.83	0.82
R2	0.83	0.83
P–factor	0.58	0.54
R–factor	0.49	0.46
PBIAS	−12.5	−5.6
RSR	0.42	0.42

Table 5 Year wise 75% dependable flow

Year	75% dependable flow (in cms)
2012	0
2032	1.188
2052	2.029
2072	2.071
2092	1.295
2100	1.58

5 Analysis of Streamflow Change

Future projected rainfall from the year 2012–2100 is used for obtaining future runoff at basin outlet as shown in Fig 5. It can be seen that there is no significant trend of runoff in the future. Overall there is a decrease of flow from the year 2012–2100 by 29.85% in the period of 89 years as in Fig. 6. From past records, it can be seen that there is a 3.9% increase in discharges at Pathardih station from the year 1989–2010.

Flow duration curves for May month are plotted from the year 2012–2100 with an interval of 20 years. Dependable flow with 75% probability is as shown in Fig 5. It can be seen that there is no significant trend of increase or decrease of streamflow, however, the magnitude of 75% dependable flow decreases with time after increasing till 2072 as in Table 5.

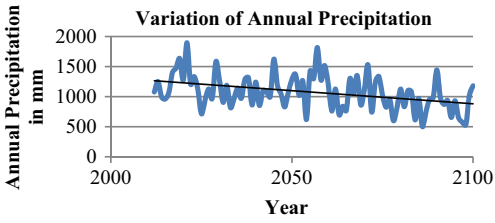

Fig. 5 Future projected rainfall from year 2012–2100

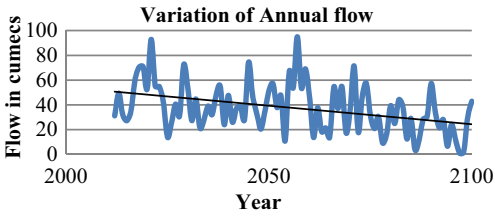

Fig. 6 Variation of flow with time during 2012–2100

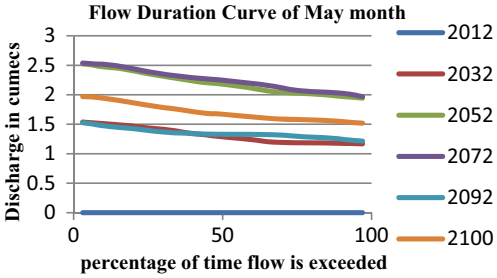

Fig. 7 Flow duration curve for May month

6 Supply-Demand Scenario of Raipur City

Raipur city is situated on the banks of the Kharun basin and is one of the most populated cities in Chhattisgarh state. The water supply in this area is entirely dependent on the Kharun River. However, being an intermittent river, demand for water supply cannot be met during dry seasons. Also, growing water demand with increasing population is a new concern in this region. The current population of Raipur city is 12.66 lakhs with a water demand of 209 MLD in total. Further, it is estimated that in 2023 population will grow to 15.34 lakhs and in 2038 it will be 21.36 lakhs [39] with estimated water demand of 231 MLD and 288 MLD respectively considering a per capita demand of 135 lpcd.

To meet the water demand of the city in dry season water is being diverted from Ravishankar reservoir (Gangrel dam) to Raipur using the Mahanadi feeder canal. Water from the Gangrel dam is diverted to the Bhatagaon intake well from which it is used for drinking water supply. Previously, water is required only for 2 months October and November, but from the last two years, water is being diverted for 9 months. Additionally, 2.15 TMC water is always reserved for the drinking water supply for Raipur city and 22 MLD of water at present is sourced through tube wells.

Apart from drinking water demand total industrial water demand is 36.5 MCM supplied from Kharun at present. For the rest of the industries like Bhilai Steel Plant, water is supplied from the Ravishankar reservoir.

Main crops grown include paddy, maize, wheat, and gram. The total yearly crop water requirement of this area is 21.80928 MCM for both Rabi and Kharif crops for the year 2017–2018. The contribution of groundwater for irrigation comes to nearly 10.25% of the net sown area. Irrigation water is mainly supplied through Mahanadi feeder canals and other networks.

Water supply and demand analysis is done. It can be seen that there is insufficiency of flow in months March, April, May, and June. Also, there is surplus flow most of the months in a year, especially in the monsoon season. However, due to the absence of any storage structure this region experiences scarcity of water in dry seasons. Also, as per census data and future projections of the population, there is high drinking water demand in the future which may not be satisfied with changing flow in a stream in the future. Consequently, from the year 2010 water is being diverted from the Ravi Shankar reservoir is increased by 62% in 2018 (Table 6).

Table 6 Year wise water diverted from Ravishankar reservoir for Raipur city

Year	Water diverted daily (in million liter)
2010	80
2012	90
2014	105
2016	140
2017	170
2018	210

7 Conclusion

The long-term trends in precipitation and runoff have been investigated in this study. The results showed a statistically insignificant trend in precipitation and runoff. The contributions of climate change and runoff have been found using the SWAT model for the Kharun watershed. The results showed that there is a decrease in the runoff by 3.9% and 29.85% during 1989–2010 and 2012–2100, respectively, along with a decrease in precipitation by 4.5% during 2012–2100.

Sensitivity analysis showed that the most sensitive parameter in this watershed model is CN2 followed by ALPHABF, GWDELAY, GWQMN, SOLBD, and SLSUBBASIN on basis of t-stat and p-value. In this study, the SWAT model is successfully applied to the Kharun watershed and calibration and validation of parameters are done. Also, satisfactory performance of the model is achieved as NS value is 0.83 and RSR value is 0.42.

Water supply and demand analysis is carried out in Raipur city. As per demographic data, the water demand of Raipur city will increase by 52.38% in the year 2038 with respect to the year 2016 along with a decrease in flow by 35% during the period 2016–2038. It is found that the river runs dry during April and June months. Deficit starts from March and ends in the last of June month and peak flow occurs in august and September month as per 2017–2018 analysis of inflow and outflow in upper Kharun catchment. For the rest of the months, there is sufficient flow to meet water demands. However, from the year 2010 water which is being diverted from the Ravi Shankar reservoir which is increased by 62% in 2018 which may indicate poor management of water in the Kharun watershed. Another source of abnormalities in the analysis may be due to the insufficiency of water use data of the Kharun watershed.

Presently, there is no water storage structure in the Kharun watershed. To overcome the shortage of water in the future, land management practices can be done to provide storage [40]. Also, provisions can be made for the temporary storage of water during high flow months so that it can be used during dry seasons. To deal with water scarcity issues that may exacerbate in the future due to decreasing trend of streamflow following approaches can be made:

1. Underground rainwater harvesting system can be designed. Water can flow through natural slopes to a drainage conduit during rainy seasons and through that

conduit it can be stored in any underground storage structure built in watershed. It can be used to meet water requirements during lean periods.
2. Artificial groundwater recharge techniques can be adopted.
3. Construction of more lakes in the watershed, or increasing the size of lakes to accommodate more water during rainy seasons can be done. Tanks can be made for each local area and can be maintained by locals. Water can be stored for domestic usage in rainy seasons which can be used in dry periods.
4. As no temporary storage structure is present in Kharun watershed, any temporary structure or dam can be constructed so as to store water during peak periods.
5. Dedicated canal directly from nearby reservoir can be constructed for water stress situations in dry periods.

References

1. AghaKouchak A, Feldman D, Hoerling M, Huxman T, Lund J (2015) Water and climate: Recognize anthropogenic drought. Nature 524(7566):409–411
2. Bai P, Liu W, Guo M (2014) Impacts of climate variability and human activities on decrease in streamflow in the Qinhe River, China. Theoret Appl Climatol 117(1):293–301
3. Bao Z, Zhang J, Wang G, Fu G, He R, Yan X, Jin J, Liu Y, Zhang A (2012) Attribution for decreasing streamflow of the Haihe River basin, northern China: climate variability or human activities? J Hydrol 460:117–129
4. Ila C, Mujumdar PP (2015) Isolating the impacts of land use and climate change on streamflow. Hydrol Earth Sys Sci 19(8):3633–3651
5. Gleick PH (1989) Climate change, hydrology, and water resources. Rev Geophys 27(3):329–344
6. Akpoti K, Antwi EO, Kabo-Bah AT (2016) Impacts of rainfall variability, land use and land cover change on stream flow of the black Volta Basin, West Africa. Hydrology 3:26
7. Jones RN, Chiew FHS, Boughton WC, Lu Z (2006) Estimating the sensitivity of mean annual runoff to climate change using selected hydrological models. Adv Wat Resour 29(10):1419–1429
8. Moraes JM, Pellegrino GQ, Ballester MV, Martinelli LA, Victoria RL, Krusche AV (1998) Trends in hydrological parameters of a southern Brazilian watershed and its relation to human induced changes. Water Resour Manage 12(4):295–311
9. Buendia C, Batalla RJ, Sabater S, Palau A, Marcé R (2016) Runoff trends driven by climate and afforestation in a Pyrenean Basin. Land Degrad Dev 27(3):823–838
10. Zhu Y, Wang W, Liu Y, Wang H (2015) Runoff changes and their potential links with climate variability and anthropogenic activities: a case study in the upper Huaihe River Basin, China. Hydrol Res 46(6):1019–1036
11. Chomitz KM, Kumari K (1998) The domestic benefits of tropical forests: a critical review. World Bank Res Obs 13(1):13–35
12. Wang J, Hong Y, Gourley J, Adhikari P, Li L, Su F (2010) Quantitative assessment of climate change and human impacts on long-term hydrologic response: a case study in a sub-basin of the Yellow River, China. Int J Climatol 30(14):2130–2137
13. Huan MA, Yang D, Tan SK, Gao B, Hu Q (2010) Impact of climate variability and human activity on streamflow decrease in the Miyun Reservoir catchment. J Hydrol 389(3–4):317–324
14. Sharma PJ, Patel PL, Jothiprakash V (2019) Impact of rainfall variability and anthropogenic activities on streamflow changes and water stress conditions across Tapi Basin in India. Sci Total Environ 687:885–897

15. Zhan C, Niu C, Song X, Xu C (2013) The impacts of climate variability and human activities on streamflow in Bai River basin, northern China. Hydrol Res 44(5):875–885
16. Kumar N, Tischbein B, Kusche J, Laux P, Beg MK, Bogardi JJ (2017) Impact of climate change on water resources of upper Kharun catchment in Chhattisgarh, India. J Hydrol: Reg Stu 13:189–207
17. Gayathri KD, Ganasri BP, Dwarakish GS (2015) A review on hydrological models. Aquat Proc 4:1001–1007
18. Arnold JG, Moriasi DN, Gassman PW, Abbaspour KC, White MJ, Chinnasamy Santhi RS et al (2012) SWAT: model use, calibration, and validation. Trans ASABE 55(4):1491–1508
19. Tang FF, Xu HS, Xu ZX (2012) Model calibration and uncertainty analysis for runoff in the Chao River Basin using sequential uncertainty fitting. Proc Environ Sci 13:1760–1770
20. Edmonds NJ, Rosenberg JA (2005) Climate change impacts for the conterminous USA: an integrated assessment: from mink to the Lower 48. Clim Change 69(1):1
21. Xing MA, Xu J, Luo Y, Aggarwal SP, Li J (2009) Response of hydrological processes to land-cover and climate changes in Kejie watershed, south-west China. Hydrol Process: Int J 23(8):1179–1191
22. Zhang A, Zhang C, Fu G, Wang B, Bao Z, Zheng H (2012) Assessments of impacts of climate change and human activities on runoff with SWAT for the Huifa River Basin, Northeast China. Water Resour Manag 26(8):2199–2217
23. Swain S, Verma MK, Verma MK (2018) Streamflow estimation using SWAT model over Seonath river basin, Chhattisgarh, India. In: Hydrologic modeling. Springer, Singapore, pp 659–665
24. Verma MK, Verma MK (2019) Calibration of a hydrological model and sensitivity analysis of its parameters: a case study of Seonath river basin. Int J Hydrol Sci Technol 9(6):640–656
25. Abbaspour KC (2011) SWAT-CUP2: SWAT calibration and uncertainty programs manual version 2. Swiss Federal Institute of Aquatic Science and Technology Department of Systems Analysis, Eawag, Swiss Federal Institute of Aquatic Science and Technology
26. Abbaspour KC, Johnson CA, Van Genuchten MT (2004) Estimating uncertain flow and transport parameters using a sequential uncertainty fitting procedure. Vadose Zone J 3(4):1340–1352
27. Abbaspour KC, Vejdani M, Haghighat S, Yang J (2007) SWAT-CUP calibration and uncertainty programs for SWAT. In: MODSIM 2007 international congress on modelling and simulation, modelling and simulation society of Australia and New Zealand. Swiss Federal Institute of Aquatic Science and Technology, Dübendorf, Switzerland, pp 1596–1602
28. Narsimlu B, Gosain AK, Chahar BR, Sudhir Kumar Singh, Srivastava PK (2015) SWAT model calibration and uncertainty analysis for streamflow prediction in the Kunwari River Basin, India, using sequential uncertainty fitting. Environ Process 2(1):79–95
29. Nasiri S, Ansari H, Ziaeia AN (2020) Simulation of water balance equation components using SWAT model in Samalqan Watershed (Iran). Arab J Geosci 13(11):1–15
30. Tolson BA, Shoemaker CA (2007) Cannonsville reservoir watershed SWAT2000 model development, calibration and validation. J Hydrol 337(1–2):68–86
31. Wang Y, Jiang R, Xie J, Zhao Y, Yan D, Yang S (2019) Soil and water assessment tool (SWAT) model: a systemic review. J Coast Res 93:22–30
32. Hamed KH, Ramachandra Rao A (1998) A modified Mann–Kendall trend test for autocorrelated data. J Hydrol 204(1–4):182–196
33. Yue S, Wang CY (2004) The Mann–Kendall test modified by effective sample size to detect trend in serially correlated hydrological series. Water Resour Manag 18(3):201–218
34. Pettitt AN (1979) A non-parametric approach to the change-point problem. J Roy Stat Soc: Ser C (Appl Stat) 28(2):126–135
35. Ruan H, Zou S, Yang D, Wang Y, Yin Z, Lu Z, Li F, Xu B (2017) Runoff simulation by SWAT model using high-resolution gridded precipitation in the upper Heihe River Basin, Northeastern Tibetan Plateau. Water 9(11):866
36. Jaiswal RK, Lohani AK, Tiwari HL (2015) Statistical analysis for change detection and trend assessment in climatological parameters. Environ Process 2(4):729–749
37. Pettitt AN (1979) A non-parametric approach t Stat. Soc Ser C 28:126–135

38. Abbaspour KC, Vaghefi SA, Srinivasan R (2018) A guideline for successful calibration and uncertainty analysis for soil and water assessment: a review of papers from the 2016 international SWAT conference. Wat 10(1):6
39. Galkate RV, Pandey RP, Jaiswal RK, Thomas T (2015) Assessment of water demand and supply prospects in Kharun river basin
40. Aayog NITI (2018) Composite water management index. National Institution for Transforming India, GOI
41. Mengistu AG, van Rensburg LD, Woyessa YE (2019) Techniques for calibration and validation of SWAT model in data scarce arid and semi-arid catchments in South Africa. J Hydrol: Reg Stud 25:100621
42. Moriasi DN, Arnold JG, Van Liew MW, Bingner RL, Harmel RD, Veith TL (2007) Model evaluation guidelines for systematic quantification of accuracy in watershed simulations. Trans ASABE 50(3):885–900

Structural Evaluation and Retrofitting of a Commercial Building

Ashika A. Sharma, Manish Haveri, and Akshayakumar V. Hanagodimath

Abstract This thesis describes of structural evaluation and retrofitting of a commercial building. It explains the need for strengthening of columns as the building is being added with an extra storey. This procedure starts by gathering the information of the existing building from the building owner. The AutoCAD plan with structural details is acquired and then the non-destructive tests are performed to know the current strength of the existing building. The building is analysed for the current loads and the additional loads using ETABs software. Suitable retrofitting methods are then selected for the under-strength elements to increase the strength and the designs are done manually for selected methods. The best one is chosen and again analysed in ETABs after retrofitting is done to the building. The existing footings are checked for additional loads from adding an extra storey. The cost comparison is done between the selected retrofitting methods and then the thesis winded up with conclusions.

Keywords Retrofitting · Structural evaluation · NDT · AutoCAD · ETABs

1 Introduction

The construction industry is an always ever-growing field. People are enhancing and planning new and more perplexing structures. Concrete with its ability to be projected into any shape or structure is in extreme popularity as a construction material. Because of this there is an extremely appeal for new development in construction and most old structures might look great outwardly yet may have a tonne of basic issues like weak structural elements, helpless ventilation or potential issues. Old structures have tendency to moisture. To conquer these issues, it becomes basic to

A. A. Sharma
Civil Department, Ramaiah University of Applied Sciences, Bangalore, Karnataka 560058, India

M. Haveri (✉) · A. V. Hanagodimath
Civil Department, Ramaiah University of Applied Sciences, Bangalore, Karnataka 560058, India
e-mail: manish.ce.et@msruas.ac.in

© The Author(s), under exclusive license to Springer Nature Singapore Pte Ltd. 2023

K. R. Reddy et al. (eds.), *Recent Advances in Sustainable Environment*, Lecture Notes in Civil Engineering 285, https://doi.org/10.1007/978-981-19-5077-3_17

track down an elective strategy to stay away from the reconstruction of the structure. However, retrofitting old structures and making them more efficient to bear the loads by strengthening them, making them energy-effective sounds like a superior thought. Retrofitting of old structure is extremely fundamental to reduce pollution, rehabilitation, damaging of structures, expansion in the expense of construction and demolition of structures. Retrofitting is the course of adding new-features to already established old structures, historical structures, bridge and so on. Retrofitting of RCC elements is done to recover the strength of weakened primary structural elements and to mitigate further distresses in concrete.

2 Objective

The main objective of this case is to evaluate and analyse the commercial structure for its current performance to find the critical factor and to propose suitable retrofit techniques that improves its performance.

3 Methodology

A 5 year old G + 3 building for which the owner wants to add a storey was selected and the critical factors were identified by performing NDT. Structural analysis of the building before and after retrofitting was done using ETABs software. This complete work took 6 months to be completed (Table 1).

Table 1 Listing of Methods utilized

Sl.no	Statement	Methodology	Resources used
1	Preliminary test	Non-Destructive tests	Visual observation, Rebound hammer and UPV tests
2	Proposing retrofit techniques to the selected building and analysing	Field survey, Test results, Literature survey, case study	Rebound hammer and UPV test results
3	Structural analysis of building	Software	ETABs, AutoCAD
	Design of RC and Steel plate Jacketing Design of footing	Manual design for proposed retrofit schemes	Axial loads from ETABs, code books, MS Excel
4	Comparison	Certain parameters	Design, Cost estimation

4 Analysis

4.1 Selection of the Commercial Building

In this study, the selected commercial building has a dimension of 50' × 80' feet with G + 3 storeys which is located in chintamani which was constructed 5 years back. Now this building is being utilized as offices to 2 small companies. The structural details are taken from the AutoCAD drawings that were provided by the owner. It was said that the building was built with M25 grade concrete. The storey height is taken as 3.2 m from given AutoCAD elevation.

4.2 Non-destructive Tests

Presently, since the owner wants to add an extra storey to the building, the structural evaluation is done to check the stability of building whether it is capable to bear the extra load due to the same. Therefore, the non-destructive tests are conducted to find the present strength of concrete. The selected NDT for this case are Rebound Hammer test and Ultrasonic Pulse Velocity test. The UPV test was done to basement columns in the building in direct impact method and indirect impact to beams and slabs. The Rebound hammer test was done to basement columns with dry surface condition in horizontal direction of rebound and vertically up direction of rebound to beams and slabs in basement. From the NDT test results the UPV test showed excellent and good results therefore, we can inference that the concrete does not have any type of honey comb failure so, the rebound Hammer test results can be believed as actual compressive strength of concrete. From the rebound hammer test results, the grade of concrete in columns is reduced to M23 from M25. It is reduced by 2 numbers for short duration of 5 yrs. Hence the retrofitting of columns should be done for them to bear the additional load that comes from adding an extra storey. The results are safe and did not show any signs of deterioration for beams and slabs hence, Retrofitting is not necessary of the beams and slabs.

4.3 Structural Analysis Using ETABs Software

ETABS is a software that takes into account multi-storey building designing and analysing. "Its full structure is broadened 3-D analysing of building framework". ETABS is a unique PC programme grown explicitly for building structures. It furnishes the Structural Engineers with necessary tools that are important for creating, modifying, analysing, designing and optimizing the building models. Analysis of building that was built (G + 3), analysis of the building after adding an extra storey (G + 4) and the retrofitted building is done using ETABS (Figs. 1, 2 and 3).

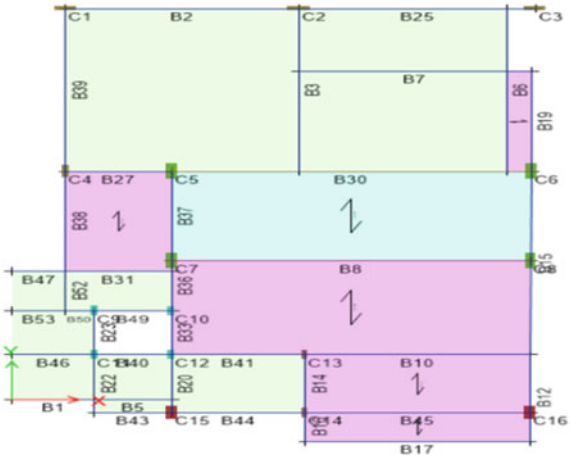

Fig. 1 The typical floor plan of the building

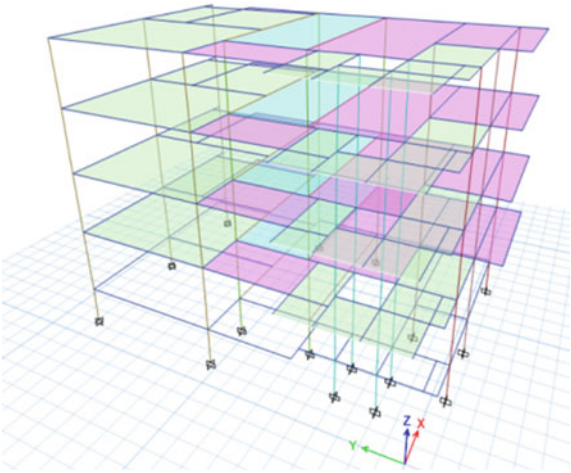

Fig. 2 The 3-D view of existing G + 3 building, after importing to ETABs through centre line method.

LOADING CRITERIA.

The load on slab—live load varies as per IS 875 Part-2, the super dead load for floor finish is taken as 1.25kN/m2, for ceiling or hanging loads is taken as 0.75kN/m2, for partition wall load, it is taken as 1kN/m2. So the total load on slab is 3kN/m2. Self-weigh of slab, beam and column will be taken automatically by ETABs as dead load. The load on beam- wall loads $= 0.2 \times 3.2 \times 22 = 14.02$ kN/m. The load combinations taken is 1.5D + 1.5L.

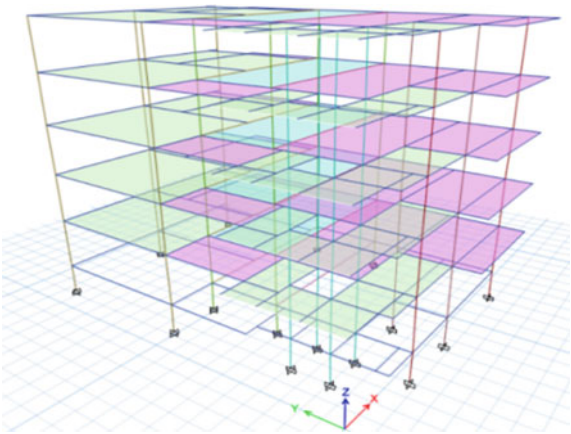

Fig. 3 The 3-D view after adding an extra storey(G + 4)building after the analysis

4.4 Calculation of Total Additional Load

The axial loads on basement columns of the existing building (G + 3) from the analysed results from ETABs are taken as **P** kN. The axial loads on basement columns after adding an additional storey (G + 4) which is analysed in ETABs are taken as **P'** kN. The difference between these two that is **(P'-P) kN** gives us the extra additional load on the basement columns due to the addition of extra storey to the building.

From the NDT results, it shows that the grade of concrete in basement columns have been deteriorated to grade M23 from grade M25. Therefore, the deficient 2 fck is converted into load using the formula $Pu = 0.4 \times f_{ck}$ x Ac and is being added to the additional load we have obtained from ETABs in table no. 3. The deficient fck* is converted into load and is named as **P*.** So the total additional load on the columns in basement is given by **(P'-P) + P*.** Hence, for this Total additional load **(P'-P) + P*** that has been calculated, the columns are retrofitted so they can bear this Total Additional load. This way the same procedure is followed for all the columns in the basement to find the total additional load that the columns have to bear (Table 2).

4.5 Proposing Suitable Retrofit Techniques

Columns are one of the main structural elements of any construction. Columns form the support structures that distribute the weight of the upper storeys, roof load and all the live loads in a structure to the foundations. Columns receive the loads from the slabs through the beams. The common and effective methods for retrofitting columns are RC jacketing and steel plate jacketing. These are the methods widely used in market because of the availability, cost and for its effective results. For the Total additional load **(P'-P)+P*** that has been calculated, the basements columns are given jacketing designs so they can bear this Total Additional load which is calculated

Table 2 The axial loads from ETABs results of basement columns and the total additional Load calculation

Col.no	Axial loads G + 3	Axial loads G + 3	Difference in axial force	Required additional force	Required additional grade of concrete	Total additional axial force kN
	P kN	P' kN	P'-P kN	P*	fck*	(P'-P) + P*
C1	1538.1	1902.7	364.5	96	2	460.5
C2	2403.7	2927.6	523.9	96	2	619.9
C3	1523.0	1889.6	366.6	96	2	462.6
C4	1654.9	2028.4	373.5	96	2	469.5
C5	3373.2	4125.3	752.2	180	2	932.2
C6	3839.5	4690	850.7	180	2	1030.7
C7	1956.4	2440.5	484.1	180	2	664.1
C8	2383.1	2960.2	577.2	180	2	757.2
C9	1238.3	1454.9	216.6	72	2	288.6
C10	390.8	569.7	178.9	72	2	250.9
C11	989.2	1164.1	174.9	72	2	246.9
C12	483.7	660.8	177.1	72	2	249.1
C13	1261.7	1496.7	235	54	2	289.0
C14	1184.1	1386.0	201.9	54	2	255.9
C15	1042.8	1328.9	286.1	144	2	430.1
C16	1971.0	2437.7	466.7	144	2	610.7

for load from addition of an extra storey and also the deficient concrete strength. The RC jacketing and steel plate jacketing designs are done manually for all the columns in basement to bear the total additional load. Here the sample design is shown for the column C4 of size 200 x 600 mm which is similarly done for all the columns in the basement.

RC Jacketing

RC jacketing of 75 mm was assumed and designed for which it seems to be safe to bear the total additional load, therefore the new column dimension would be 350 mm*750 mm (Fig. 4).

Steel Plate jacketing

Steel plate jacketing using four 100*6 mm plates and two 50*6 mm plates is assumed and designed for which it seems to be safe to bear the total additional load (Fig. 5).

The same procedure as shown for C4 column of basement is followed for all other columns to get results in the table no. 4 (Table 3).

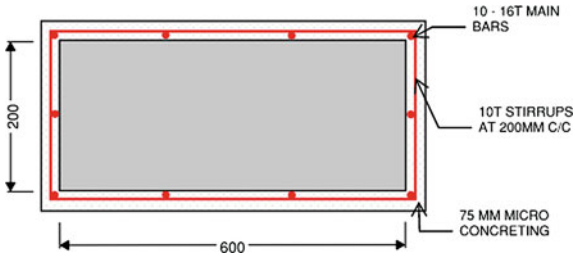

Fig. 4 Detailing diagram of the RC jacketing for the column C4

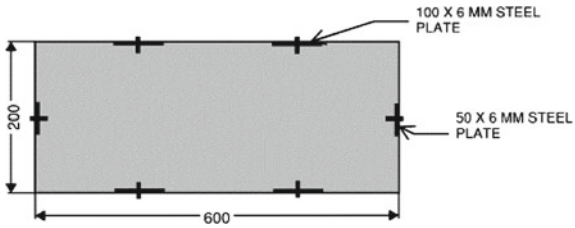

Fig. 5 Detailing diagram of Steel plate jacketing for the column C4

Table 3 Reinforcement and steel plate Jacketing for Retrofitting for all the basement columns

Sl.no	Column	RC jacketing Scheme	Steel Plate jacketing Scheme
1	C11	Provide 75 mm thick Micro-concrete jacketing on all 4 sides along with 10-T16 main bars & 10 T @ 200 mm stirrups. Also provide 12 mm shear pins at 300 mm C/C in staggered manner	Provide 4 no. of 100 X 6 mm and 2 no.s of 50 X 6 mm Steel Plate and M12 Bolts at 300 mm c/c in staggered manner on one plate
2	C12		
3	C10		
4	C14		
5	C9		
6	C13		
7	C15		
8	C1		
9	C3		
10	C4		
11	C16	Provide 100 mm thick Micro-concrete Jacketing on all 4 sides along with 10 - T16 main bars and 10 T @ 200 mm stirrups. Also provide 12 mm shear pins at 300 mm C/C in staggered manner	
12	C2		
13	C7		
14	C8		Provide 4 no. of 100 X 6 mm and 2 no.s of 75 X 6 mm Steel Plate and M12 Bolts at 300 mm c/c in staggered manner on one plate
15	C5		
16	C6		

Table 4 Elements forces on Basement column after Retrofitting

Element forces – columns in Basement		Element forces– columns in Basement	
Column no	P in kN	Column no	P in kN
C1	1922.22	C9	1516.95
C2	3029.83	C10	501.13
C3	1890.41	C11	1269.04
C4	2065.43	C12	620.87
C5	4108.97	C13	161.15
C6	4748.48	C14	1510.73
C7	2447.15	C15	1266.74
C8	2978.71	C16	2455.75

4.6 Structural Analysis Using ETABs Software After Retrofitting

RC Jacketing is considered here for retrofitting in ETABS and the axial forces on the revised columns in Basement are shown in table no. 5 (Table 4).

Since the manually designed columns have more capacity than the forces obtained here after retrofitting due to an additional storey on the building, it is said to be safe.

4.7 Check for Isolated Footing

As the columns takes the loads distributed from slabs and beams, it furthers distributes these loads on the footing. Hence, checking the footing is as vital and necessary inspite of the SBC. In this case the footing of column C4 is taken for sample design of the footing. The area and the depth has been assumed. The provided area of the footing is 5.72 m^2 which is safe for one way and two way shear before and after the retrofitting. The provided depth of 0.55 m for the footing is also safe for one way shear and two way shear when checked for both before and after retrofitting for the respective axial loads obtained from the analysis of the building from ETABS software.

5 Results and Discussion

1. From the NDT test results the UPV test showed good results therefore, we can inference that the concrete does not have any type of honey comb failure so, the rebound Hammer test results can be believed as actual compressive strength of

concrete. From the rebound hammer test results, the grade of concrete in columns is reduced to M23 from M25.

2. The results are safe and did not show any signs of deterioration for beams and slabs hence, Retrofitting is not necessary of the beams and slabs.
3. **For example,**

   For C4 column, **In table no.3** as shown above, the axial load on column **C4** of the existing building (G+3) from the analysed results from ETABs is **1654.9 kN**.

   The axial load on column **C4** after adding an additional storey (G+4) and analysed in ETABs is **2028.4 kN.**

   The difference between these two loads are **373.5 kN** gives us the extra additional load on the column C4 due to the addition of extra storey to the building.

   Now in **table no.3**

   From the NDT results, it shows that the grade of concrete in basement columns have been deteriorated to grade M23 from grade M25. Therefore, the deficient 2 fck is converted into load and is being added to the additional load we have obtained from ETABs.

   Pu = 0.4 x fck x Ac

   =0.4 x 2 x (200 x 600) (size of the C4 column as per AutoCAD plan is 200 x 600 mm)

   Pu = 96 kN

   So the **Total additional load is 373.5 + 96 = 469.5 kN** hence, for this Total additional load that has

   been calculated, the columns are given jacketing designs so they can bear this Total Additional load.

4. Columns receive the loads from the slabs through the beams. The common and effective methods for retrofitting columns are RC jacketing and steel plate jacketing. These are the methods widely used in market because of the availability, cost and for its effective results
5. In this case, the sample design is shown for the column C4 of size 200 × 600 mm which is similarly done for all the columns in the basement.
6. RC jacketing of 75 mm was assumed and designed for which it seems to be safe to bear the total additional load, therefore the new column dimension would be 350 mm x 750 mm. Where the additional load from the extra storey is 1654.9 + 469.5 kN = 2124.8 kN, the retrofitted column can bear 2919.4 kN (from manual design data), hence, safe.
7. Steel plate jacketing using four 100*6 mm plates and two 50*6 mm plates is assumed and designed for which it seems to be safe to bear the total additional load. The plates provided can bear 834 kN load (from manual design data). Therefore 1654.9 + 834 = 2488.5 kN.

   Hence, the retrofitted column can bear 2488.5 kN after providing 6 steel plates.

Where the additional load from the extra storey is 1654.9 + 469.5 kN = 2124.8 kN, the retrofitted column can bear 2488.5 kN, hence, safe

6. RC Jacketing is considered here for retrofitting in ETABS and the axial forces on the revised columns is found out after the analysis. Since the designed columns have more capacity than the forces obtained here after retrofitting due to an additional storey on the building, it is said to be safe. **For example**, **C4** column design sample is shown

   The axial force on the C4 column initially before adding a storey from ETABs was—1654.9 kN. The axial force on the C4 column after adding an additional storey from ETABs—2124.8 kN. The manually designed capacity of the C4 column for given retrofitting of 75 mm Jacketing n all four sides—2919.4 kN. The axial force on the column C4 after retrofitting from ETABs—2065.43 kN (from table no. 5)

   Since, **2919.4 kN > 2065.43 kN . It is safe.**

8. In this case, the footing of column C4 is taken for sample design of the footing. Before Retrofitting, the load of C4 column -1654.9 kN

   After Retrofitting, the load on C4 column—2065.8 kN

   The assumed and provided area of the footing is (2.2m*2.6m) = 5.72 m^2 which is designed and checked for one way and two way shear before and after the retrofitting is safe.

   The provided depth of 0.55m for the footing is also safe for one way shear and two way shear when checked both before and after retrofitting for the respective loads obtained from the analysis of the building from ETABS software.

   The nominal shear stress < the permissible shear stress for both loads before and after retrofitting, therefore it is safe.

9. Retrofit costs vary with a building's unique characteristics; e.g., building construction type, age and location. RC Jacketing cost from BOQ– 71,528/- Steel Plate Jacketing cost from BOQ– 91,210/-

6 Conclusions

1. Retrofitting of the building is necessary to mitigate the failures and to maintain the strength of the building. From the tests done on building, the grade of the concrete has depleted after some time due to various environmental changes. Due to this the structural stability is not sufficient to increase the number of storeys.
2. It is also observed that there was an increase in axial force on columns which has to be redesigned to increase the strength and capacity therefore, retrofitting is necessary for the future purpose. It was observed that the beams and slabs

were safe and had the required strength by non-destructive test results and that retrofitting is not needed for beams and slabs.
3. Here we have assumed the area and depth of the footing for a column and checked for one way and two way shear and it seems to be safe even after the retrofitting and addition of the extra storey.
4. RC jacketing is useful when reinforcement is safe from deterioration. This method is suitable when there is enough space for increase in area of column and when there is no allowance to change the rebar. Steel jacketing is suitable when the axial load difference is high. This method is applicable when there is no space for the dimension increase of the structural member.
5. The cost of construction is more for steel plate jacketing compare to RC jacketing. From the calculated BOQ steel plate jacketing is 30% more in cost requirement compare to RC jacketing. RC Jacketing looks more aesthetic than steel plate Jacketing.
6. From the above experimental investigations, it can be concluded that both the methods has advantages and disadvantages. The steel jacketing is strong compared to RC jacketing in strength but cost wise and availability of materials RC jacketing is good compare to steel jacketing.
7. Here we have chosen RC jacketing for this building since the cost for RC jacketing is less and steel plate jacketing requires skilled labours to work on but RC jacketing can be done by normal labours and also since the materials required for RC Jacketing is easily available compared to Steel plates. There is difficulty in availability of required size of steel plates.

Acknowledgements Expressing my gratitude to my Mr. Manish Haveri and Mr. Akshayakumar V Hannagodimath for their support and suggestions to improvise and Dr. Nayana N Patil, HOD Department of Civil Engineering, Ramaiah University of Applied Sciences for giving constant support to carry out this project.

References

1. Lorenz W (2007) In: 5th International Conference on Structural Analysis of Historical Constructions in New Delhi. Bautechnik, 84(2), pp.146–147
2. Ademović N, Oliveira D, Lourenço P (2019) Seismic evaluation and strengthening of an existing masonry building in sarajevo, B&H. Buildings 9(2):30
3. Saleem Muhammad Azhar, Siddique Zahid, Abbas Safeer, Aziz Mubasir (2016) Ultrasonic pulse velocity and rebound hammer testing for non destructive Evaluation of existing concrete Structure, Pak.J.Engg & Appl
4. Dingorkar Prathamesh, Srivastava Ayush (2016) Retrofitting—Comparative study of Rc Jacketing and Frp Wrapping, school of construction management, PGPACM, 7(5)

5. Ademović N, Oliveira D, Lourenço P (2019) Seismic evaluation and strengthening of an existing masonry building in sarajevo, B&H. Buildings 9(2):30
6. Nishanth C, Sai Swaroop Y, Jagarapu D, Kumar Jogi P (2020) "Analysis and design of commercial building with different slab arrangements using ETABS". In: Materials Today: Proceedings, 33, pp. 700–704
7. Gurudath C, Sah Arun Kumar, Kumar Manoj, Sharma Ram Babu, Sah Ramesh (2019) Analysis and Design of Commercial Building Using ETABS. J Innov Res Technol, 5(12)

Utilization of Waste Plastic in Dense Bituminous Macadam Mixes—An Experimental Study

Mukesh Saini, Sunil Chouhan, and Vikas Sofat

Abstract Bituminous pavements are now expected to perform better as traffic increases steadily and there is a significant change in daily and seasonal temperatures. Scientists attempt to find a way to change the better properties' of bituminous mixes under variable environmental conditions. This research work describes the effect of low density polyethylene (carry bags) on physical properties of coarse aggregates by dry process. The aim of present study is to understand the concept of utilization of waste plastic (LDPE) in flexible pavement in environmental friendly way along with withstand increased traffic load. Various physical properties of aggregates used in dense bituminous macadam mixes were studied with varying percentage of low density polyethylene (0, 6, 6.5, 7, 7.5, and 8%) of bitumen content. To evaluate the physical properties of aggregates tests such as Los Angles abrasion Test, Impact Value Test, Dorry Abrasion Value Test, Centrifugal Extractor Test, Crushing Strength Test, Stripping Test, Soundness Test, and Water Absorption Test are performed on conventional and waste plastic coated aggregates. Physical properties of aggregate coated with low density polyethylene are improved due to improvement in hardness and toughness, decrease in voids, resistance against weathering action, water resistance, better binding property with bitumen and improvement in abrasion resistance.

Keywords LDPE · Aggregates · Dense Bituminous Macadam

1 Introduction

Road networks are one of the elements of the transportation system that play important role in economy of any country. Roads must be able to carry heavy loads and meet the demand of road users by increasing pavement performance. Researchers are constantly striving to improve the quality of pavement for durability. This can be achieve using an inexpensive, durable, and versatile material for road construction, and have done most of their research in this area to protect the environment

M. Saini (✉) · S. Chouhan · V. Sofat
Department of Civil Engineering, Maharishi Markandeshwar (Deemed to be University) Mullana, Ambala 133207, India
e-mail: mukeshsaini512@mmumullana.org

© The Author(s), under exclusive license to Springer Nature Singapore Pte Ltd. 2023

K. R. Reddy et al. (eds.), *Recent Advances in Sustainable Environment*, Lecture Notes in Civil Engineering 285, https://doi.org/10.1007/978-981-19-5077-3_18

on the one hand and save energy on the other. Therefore, this material can be called plastic waste. Plastic is a non-biodegradable material which can stay on earth for 4,500 years without degradation. Bitumen polymer modifications were used first in the roofing industry and then in the road paving industry. Polypropylene production was first used to modify bitumen for roofing in Italy and was the first commercial product to be marketed. In the road construction waste plastic is used in two method, i.e. wet and dry process. In wet process waste plastic is added in bitumen. This significantly increases the adhesion of bitumen to aggregates. Due to the resistance to load deformation and temperature change, structural additives can be converted into cross joints and thus provide the required strength of the road surface, whereas in dry process aggregates are coated with waste plastic under controlled temperature condition for bituminous mixes. Dense Bituminous Macadam (DBM) is a connecting course used for all roads. For the large number of high tonnage commercial vehicles need to make a mix with 5–10% voids content. Due to its resistant surface, it performs well in almost all conditions and has become more popular amongst bituminous mixture for all pavement layers and compatible with all traffic situations. DBM improves smooth surface with good quality and non-slip resistance. To meet the design criteria, the DBM mix should consist of coarse aggregates, fine aggregates and fillers in proportion to the required adhesive content. Plastic coating decreases the porosity and improves the soundness of aggregates. Durability of bituminous mixes can be improved with polymer coated aggregates due to higher Marshall Stability value and suitable Marshall Coefficient as compared to conventional aggregates [1, 2]. Performance and durability of flexible pavement can be improved at 10% shredded plastic [3]. Acceptable range of polyethylene terephthalate is 6% for modified bituminous concrete mixes via dry process [4, 5]. Asphalt mix shows less permanent deformation and higher fatigue resistance due to better inherence between the bitumen and aggregates [6, 7]. Mechanical properties of dense bitumen mixtures are initially somewhat improved and the desired amount of PET is 10% by weight of the optimal bitumen content, which meets the need for modified mechanical properties. Bituminous mixes with addition of waste plastic in accordance with standard code developed by Indian Road Congress, suggest the use of plastic waste (PET) in flexible pavement in terms of disposal of this non-degradable plastic waste in environmentally friendly way [8]. The optimum amount of bitumen for conventional bituminous concrete mix is 5.66%, whereas 5.40% for 8% PET modified mix. The bitumen content was reduced to 4.59% by adding plastic waste bottles in bituminous concrete mixes due improvement in mechanical properties of bituminous mixtures [9]. High-density polyethylene and low density polyethylene are the main constituents of WPPM used milk bags and food bags, which make up the bulk of non-degradable plastic waste in different parts of each city. The result of his study is that WPPM can be easily used as a modifier in bituminous mixtures for the management and sustainability of plastic waste [10].

Table 1 Properties of Bitumen

Property	Observed value	Desired value	Method used
Penetration	50	Min. 45	IS:1203-1978
Softening point °C	52	Min. 47	IS:1205-1978
Ductility at 27° C, cm	55	Min. 40	IS:1208-1978
Specific gravity at 27 °C	1.01	–	IS:1202-1978

2 Objectives of the Study

The main objectives of study are:

- To study physical properties of conventional aggregates used in Dense Bituminous Macadam Mixes.
- To study utilization of waste plastic as per IRC: SP: 98-2013 code specifications.
- To identify effects of low density polyethylene on physical properties of aggregate used in Dense Bituminous Macadam Mixes.

3 Materials Used

3.1 Bitumen

Bitumen sample of VG-30 grade, collected from IOCL, Panipat Refinery (Haryana, India), was used in present study. Test results are summarized in Table 1.

3.2 Aggregates

Volume of bituminous mixes comprises coarse aggregates, so the quality of aggregate play important role in durability and performance of road. Coarse aggregates from Yamunanagar quarry (Haryana, India) were used in the present study. Test results on are compiled in Table 2.

Table 2 Physical properties of coarse aggregates

Property	Test	Observed values	Specification	Test method
Cleanliness	Grain size analysis	0.7	% passing 0.075 mm sieve (Max. 5)	IS:2386 (Part I)
Particle shape	Combined flakiness and elongation indices	21.35%	Max. 35%	IS:2386 (Part I)
Strength	Los Angeles abrasion value	20.54%	Max. 30%	IS:2386 (Part IV)
	Aggregate impact value	17.68%	Max. 24%	IS:2386 (Part IV)
Durability	Soundness: sodium sulphate	5.42%	Max. 12%	IS:2386 (Part V)
Water absorption	Water absorption	0.73%	Max. 2%	IS:2386 (Part III)
Stripping	Stripping test	Retained coating 96%	Retained coating 95% Min.	IS:6241
Density	Specific gravity	2.680	2.5–3.0	IS:2386 (Part III)

3.3 Waste Plastic

The waste plastic carry bags (Low Density Polyethylene (LDPE)) collected from MM (DU) Campus, Mullana, Ambala, Haryana wear used for present study. The carry bags were shredded in uniform size (2.36 mm–600 μm). Properties of carry bags (LDPE) are given in Table 3.

Table 3 Properties of low density polyethylene

Property	Value
Size	600 μm–2.36 mm
Density (gm/cc)	0.93
Melting Temperature (°C)	140–160

Table 4 Compositions of Dense Graded Bituminous Macadam layer

Grading	II
Nominal aggregate size	26.5 mm
Layer thickness	50–75 mm
IS Sieve (mm)	Cumulative % by weight of total aggregates passing
45	–
37.5	100
26.5	90–100
19	71–95
13.2	56–80
9.5	–
4.75	38–54
2.36	28–42
1.18	–
0.6	–
0.3	7–21
0.15	–
0.075	2–8
Bitumen content	Min. 4.5%

4 Experimental Programme

4.1 Bitumen Content

Optimum bitumen content is the amount of bitumen required for an ideal mix. To study the physical properties of aggregates coated with waste plastic optimum bitumen content was taken as 4.5%, i.e. minimum bitumen content required for dense graded bituminous macadam mixes of Grading—II as per Minister of Road Transport and Highway, 2013 specifications given in Table 4.

4.2 Process Used

Physical properties of aggregates were tested for conventional aggregates and aggregates coated with waste plastic (LDPE). As the percentage of waste plastic used in bituminous mixes suggested by IRC SP-98, 2013 Specifications is 6–8% of bitumen content, so percentage of waste plastic was taken as 6, 6.5, 7, 7.5, and 8% to study the physical properties of aggregate. Aggregates were heated at 165 °C temperature and waste plastic (shredded form) was sprayed on heated aggregates. Before testing aggregates were cooled at room temperature. Los Angles Abrasion Test, Impact Value

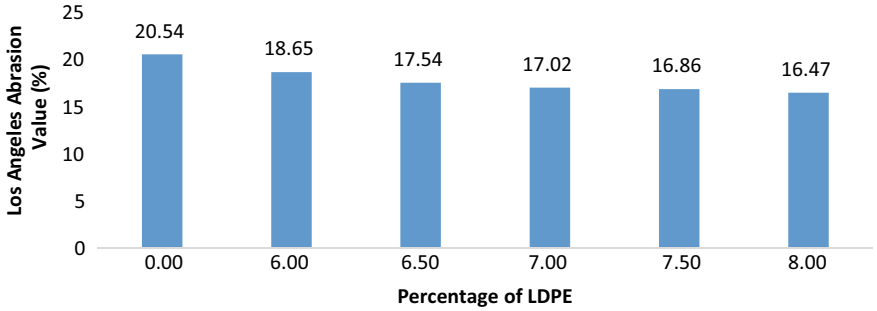

Fig. 1 Los Angles abrasion value

Test, Dorry Abrasion Value Test, Centrifugal Extractor Test, Crushing Strength Test, Stripping Test, Soundness, and Water Absorption Test are performed as per Indian Standards Codefor conventional and waste plastic (LDPE) coated aggregates.

5 Results and Discussion

5.1 Los Angles Abrasion Value

Abrasion resistance of aggregates used in pavement construction describes the hardness of aggregates. Abrasion resistance of aggregate (Fig. 1) decrease with increase in LDPE content, which shows improvement in hardness value of aggregate. Abrasion resistance of aggregates coated with 8% LDPE content is 19.85% higher as compared to conventional aggregates.

5.2 Aggregate Impact Value

Durability of road depends upon resistance of aggregates to withstand impact loading. Coating of LDPE improves aggregate impact value means improvement in quality of aggregates by coating of waste plastic. So, weak aggregates can be used by coating with polymers. Aggregate Impact value is 14.93% higher at 8% LDPE content as compared to conventional aggregates as shown in Fig. 2.

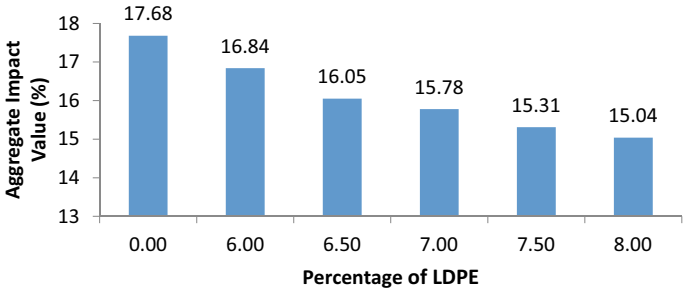

Fig. 2 Aggregate impact value

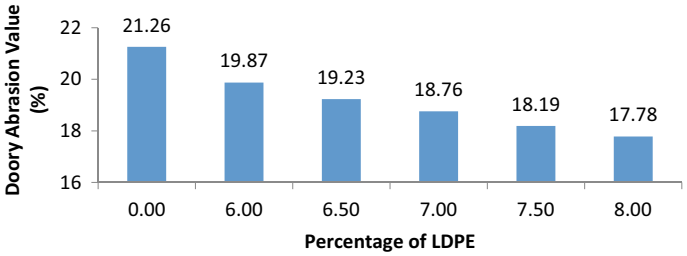

Fig. 3 Dorry abrasion value

5.3 Dorry Abrasion Value

Dorry abrasion test gives the abrasion resistance of aggregates. Figure 3 shows the Dorry Abrasion value of aggregates at different LDPE, which decrease with increase in LDPE content. This decrease in abrasion value shows that abrasion resistance of aggregates improves with addition of LDPE, which is 16.37% higher at 8% LDPE content as compared to conventional aggregates.

5.4 Bitumen Extraction Value

Extraction of bitumen from aggregate evaluates the bonding strength between aggregates and bitumen. The results as given in Fig. 4 shows that the removal of bitumen is slow in the case of waste coated aggregate as compared to conventional aggregate. Bonding strength of conventional aggregate is 5.37% less as compared to aggregates coated with 8% LDPE content.

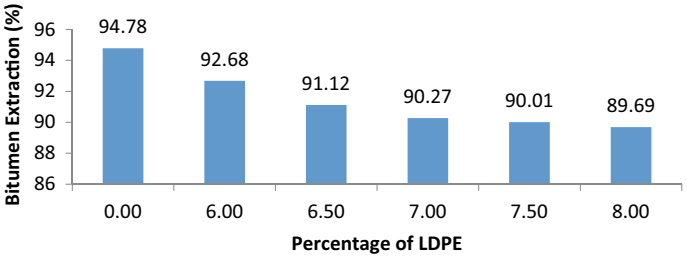

Fig. 4 Bitumen extraction value

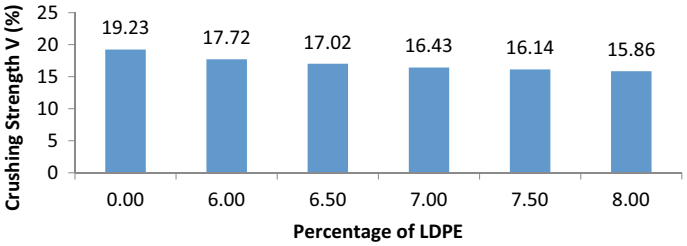

Fig. 5 Crushing strength value

5.5 Crushing Strength Value

The effect of gradually applied compressive load on aggregate is known as crushing strength. Figure 5 show that coating of LDPE improves crushing strength that means quality of weak aggregates can be improved by coating of waste plastic for durability of pavement. Crushing strength value is 21.24% more at 8% LDPE content as compared to conventional aggregates.

5.6 Stripping Value

The stripping is due to aggregates greater affinity towards water than bitumen and these phenomena depends on the physico-chemical forces acting on the system. Figure 6 shows that retained coating of bitumen increase with increase in LDPE content. This improvement in retained coating may be due to better binding property of the plastic over aggregates.

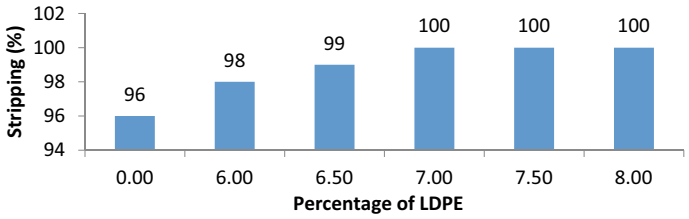

Fig. 6 Stripping value

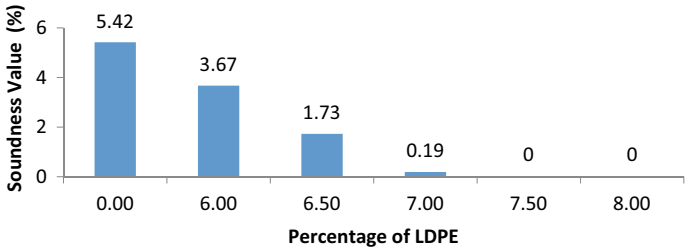

Fig. 7 Soundness value

5.7 Soundness Value

Resistance of aggregate to weathering action is an important property of aggregates, which increase the durability of pavement. Resistance of aggregates to weathering action improves with increase in LDPE content (Fig. 7). 7.5 and 8% LDPE content, confirming the 100% resistance of aggregates to weathering action.

5.8 Water Absorption Value

Water absorption value of waste plastic coated aggregates decreases with increase in low density polyethylene content as given in Fig. 8, which indicate improvement in water absorption resistance of aggregates. This improvement in water absorption resistance is due to decrease in voids. Hence, quality of aggregates can be improved by coating of waste plastic (LDPE).

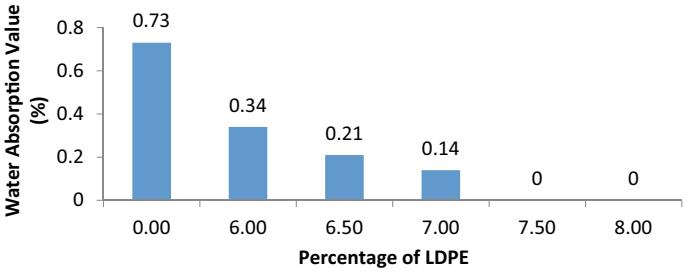

Fig. 8 Water absorption value

6 Conclusions

The main outcomes of study are:

- The hardness value of aggregates coated with waste plastic (LDPE) improves gradually.
- Resistance of the aggregate against fracture under repeated load improves, which further improves the durability of road.
- There is increase in abrasion resistance of aggregates by coating them with LDPE.
- Low density polyethylene coated aggregates have better binding property with bitumen due to less removal of bitumen from aggregates as compared to conventional aggregate.
- Quality of aggregate improved by coating with LDPE.
- Improvement in retained coating shows waste plastic coated aggregates less affinity towards water.
- Low density polyethylene coated aggregate has more resistance weathering action.
- Waste plastic (LDPE) coated aggregate are less porous as compared to conventional aggregates due to decrease in voids.
- Properties of bituminous mix can be improved by using waste plastic coated aggregates.
- Indian Road Congress Code SP: 98-2013 guidelines play important role to make modified bituminous mix.
- This methodology gives an alternate solution for disposal of waste plastic in environmental friendly way along with improvement in quality of bituminous mixes.

References

1. Vasudevan R, Nigam SK, Velkennedy R (2007) Utilization of waste polymers for flexible pavement and easy disposal of waste polymers. In: Proceedings of the international conference on sustainable solid waste manage, pp 105–111
2. Idris SE, Yassin KE (2012) The use of low density polyethylene carry-bags waste. In: Hot asphalt paving mixtures. Proceedings 01:22–27. www.uofk.edu
3. Beena KS, Bindu CS (2010) Waste plastic as a stabilizing additive in stone mastic asphalt. Int J Eng Technol 2(6):379–387
4. Ahmadinia E, Zargar M, Karim MR, Abdelaziz M, Shafigh P (2011) Using waste plastic bottles as additive for stone mastic asphalt. Mater Des 32(10):4844–4849
5. Ahmadinia E, Zargar M, Karim MR, Abdelaziz M, Ahmadinia E (2012) Performance evaluation of utilization of waste Polyethylene Terephthalate (PET) in stone mastic asphalt. Constr Build Mater 36:984–989
6. Osuolale OM, Agbalaya KS (2012) Influence of shredded waste water sachet on engineering properties of asphalt. J Nat Sci Res 2(10):134–140
7. Rokade S (2012) Use of waste plastic and waste rubber tyres in flexible highway pavements. In: International conference on future environment and energy, vol 28, pp 105–108. IACSIT Press, Singapore
8. Saini M, Aggarwal P (2019) Utilization of waste plastic in bituminous mixes—an experimental study. J Pollut Res 38(2):421–427. ISSN: 0257-8050
9. Saini M, Aggarwal P (2019) Bituminous concrete with waste plastic—an experimental study. Indian Highw 47(10):11–17
10. Jain R, Dwivedi S (2018) Influence of Zycosil in cold mix design of DBM (Dense Bituminous Macadam). Int Res J Eng Technol (IRJET) 5(3):1802–1807

Geopolymer Concrete: A Sustainable Development and Its Field Applications

Jotesh Gupta and Vanita Aggarwal

Abstract Ordinary Portland Cement usage has been increased day by day due to the massive growth of the infrastructure industry. In today's era, Geopolymer Concrete (GPC) is the utmost, economical source of replacement of Ordinary Portland Cement (OPC) that is creating depletion for the last many years, and also, many countries have already started imposing taxes carbon taxes. GPC can absorb waste materials from various industries like heavy metals, dyes, radioactive pollution that are also harmful to society. In comparison to OPC, GPC possesses better mechanical properties. Development of GPC is also dependent upon various factors like curing conditions and setting time, alkaline solution molarity, workability, binder ratio to an alkaline solution, Na_2SiO_3/NaOH and SiO_3/Al_2O_3 ratio. GPC can be considered an eco-friendly construction solution by having a proper mixed design with desirable mechanical properties under ambient curing conditions. Moreover, GPC is resistant to corrosion and fire too. This paper includes all the properties of GPC including long-term and short-term, the geopolymerization process of the creation of GPC, different sources of raw materials, various types of activators, mixed design of GPC, and various advancements to improve its mechanical properties.

Keywords GPC · OPC · Ambient curing · Geopolymerization · Alkaline solution · Molarity · Workability

1 Introduction

In recent years, OPC industries have grown immensely and the rate of growth of urban development is also continuous, leading to the huge requirement of Portland cement. OPC owns complications such as carbon emission, durability, corrosive nature but due to having good strength, it is the most commonly used material in the construction industry [1, 2]. It acts as a binding material and is resistant to chemical attacks like acid and sulfate. World widely, a total of 7% of greenhouse gas

J. Gupta (✉) · V. Aggarwal
M.M. Engineering College, M.M. (Deemed to be University) Mullana, Ambala 133207, Haryana, India
e-mail: guptajotesh@gmail.com

© The Author(s), under exclusive license to Springer Nature Singapore Pte Ltd. 2023

K. R. Reddy et al. (eds.), *Recent Advances in Sustainable Environment*, Lecture Notes in Civil Engineering 285, https://doi.org/10.1007/978-981-19-5077-3_19

emissions to the atmosphere is due to the production of OPC. 1 ton production of OPC by combustion of fossil fuels or calcination of limestone emits 1 ton of carbon dioxide to the environment and consumes 1 GJ of energy [3]. The construction and transportation industry mainly contributes to the emission of CO_2. A notification has been issued on November 3rd, 2009, and then revised on January 26th, 2016 by The Ministry of Environment, Forest and Climate Change of India (MoEF and CCS) regarding the achievement of 100% utilization of by-products of power industries, i.e., Fly Ash (FA) within 5 years by around 76 plants out of 194. Total in 2019-20, thermal plants produced 169.25 tons of FA, and 107.10 ton was used by various sectors.

Inorganic polymeric materials, i.e., "geopolymer" are developed by Davidovits. As geopolymers are made of inorganic polymer materials and also identified as Alkali-Activated Materials (AAMs) that yield leftover products of various industries like FA, Ground Granulated Blast Furnace Slag (GGBS), other silica-enrich by-products that are disposed of globally, and natural materials as raw materials for their composition that undergoes the activation process by using alkali or acid solution. Due to the properties like high durability, resistance to fire, chemicals, corrosion, high mechanical compressive strength, geopolymers are advantageous and are considered as a replacement for OPC [4–7]. Because in the production of OPC a huge amount of carbon dioxide gas is emitted that causes the greenhouse effect. 80% of CO_2 emissions can be reduced by using geopolymers. Geopolymers composed of low calcium Fly Ash (FA) activated by alkaline solution create a Si–O–Al bond, possess high mechanical and physical properties. Various materials are selected depending upon their availability and cost. Alkali-activated binders resulting from the alkali-mediated reaction of alumina, silica, and calcium are used as binder material. GPC possesses to have the good binding capability that is attained by the reaction between alkali solution and aluminosilicate compounds result into the alkali aluminosilicate compound just like calcium silicate hydrate (C–S–H) gel molded-in OPC. Geopolymers are used at commercial airports, railway sleepers, etc. in Australia because of their excellent properties. It can also be used in the construction of rigid pavements of military bases. Geopolymers are not only able to turn waste into a gem but also an ecological product [8].

2 Geopolymers Chemistry

An amorphous aluminosilicate inorganic polymer embraces silica and aluminum coupled through atoms of oxygen in a tetrahedral style called a geopolymer (GP). Si(iv) is substituted only by Al(iv) during the geopolymerization process. $Mn[(Si–O_2)\ z–Al–O_2]\ n\ wH_2O$. is the empirical formula of GP, where alkali metal cation such as potassium or sodium is denoted by M, degree of polycondensation is denoted by n, water molecules are denoted by w and z is the Si/Al ratio, which may be 1, 2, or 3 [9]. Due to the substitution of Si_4 with Al_3 the Si–O–Al–O structure transmits a negative charge which is balanced by present sodium and potassium. Based on

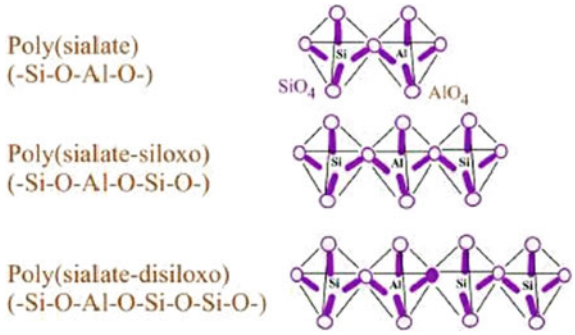

Fig. 1 Aluminosilicates types [11]

a ratio of aluminum and silicon atoms the aluminosilicate network gel molecular structure can have three types of monomeric units, i.e., 'sialate', 'sialate-siloxo', and 'sialate-disiloxo' which can be denoted as [–Si–O–Al–O–], [–Si–O–Al–O–Si–O–], and [–Si–O–Al–O–Si–O–Si–O–], respectively. Polymeric forms are classified as polysialate (PS), polysialate-siloxo (PSS), and polysialate-disiloxo (PSDS) by Davidovits [11] as depicted in Fig. 1. The Na–PSS demonstrates the range of Si surroundings using the frame structures of Al (Q4 (nAl)) having spectacles like surrounding characteristics. This structure looks like hydrated silicate glasses and minerals. Figure 2a, b depict the semi-schematic structure that represents the K-PSS structure that is deduced from Na-PSS. Si and Al are tetrahedrally coordinated by a participated oxygen snippet in both structures. In depression, the present Na or K balances the Al negative charge [10].

3 Geopolymerization Reaction Mechanism

During the geopolymerization process, initially monomers, i.e., Si $(OH)_4$ and Al $(OH)_4$ formed by the reaction of aluminosilicate sources with the alkaline solution. Then, by polymerization, these monomers are transformed into oligomeric species and poly-condensation of oligomers forms aluminosilicate gel. The geosynthetic geopolymerization process is dependent on the ability of aluminum ions (four-fold or six-fold coordination) for the introduction of Al in the silicate backbone.

The steps of the geopolymerization process are as follows:

I. Si and Al from aluminosilicate source materials atoms are dissolute by hydroxides.
II. Water molecules are eliminated by the condensation of SiO_4 and AlO_4 into monomers.
III. Aluminosilicate polymers are created by polycondensation/polymerization of silica aluminate monomers.

Various Ca+Si and Si+Al rich precursor materials are responsible for the type of binding system formed that affects the mechanical and durability properties (Fig. 3).

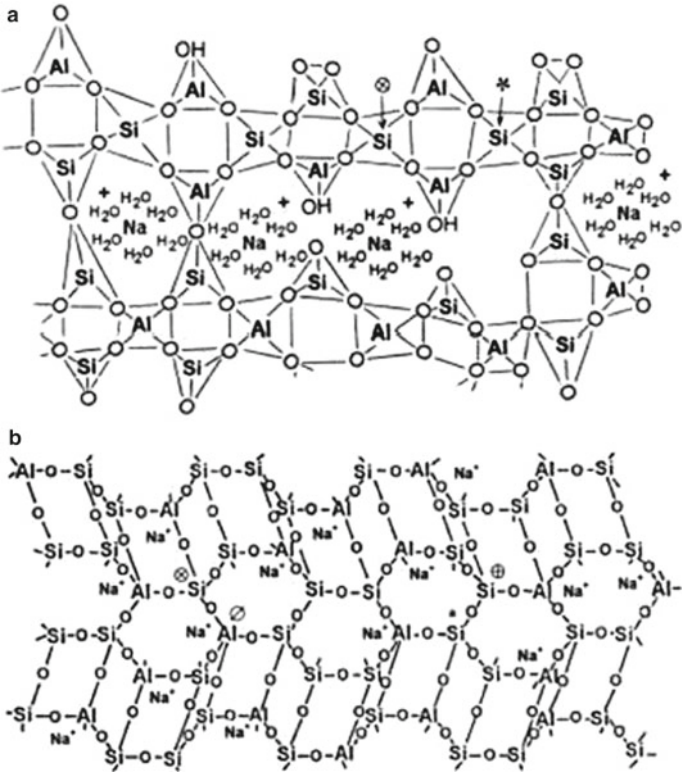

Fig. 2 **a** Semi schematic structure of Na-poly sialate polymer **b** 3-D framework structure based on suggested model for K-poly sialate polymer after Davidovits [12]

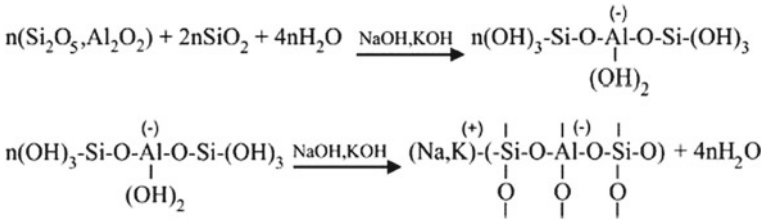

Fig. 3 Aluminosilicate network formation in GP [13]

4 Alkali Concentration Effect on Geopolymerization

GP and its properties are affected by the underlying state of reaction and the precursor material. Some most influencing parameters are the molarity of an alkaline solution, curing conditions, types of alkali activators, Si/Al ratio, network modifier content, additives, etc. In [2, 6, 14–18], it is shown that how the GP produced by RHA,

GGBS, FA, metakaolin, etc. is affected by the alkaline activator. As per [19], the mechanical properties of metakaolin-based GP are also affected by the Si/Al ratio as well as also dependent upon the type of activator used. Geopolymer material remains unchanged after 7 or 28 days by changing the K and Na activator and giving a positive response to compressive strength. Metakaolin reactivity has a direct relationship with compressive strength and polymerization degree in terms of activator type and alkaline concentration used [1]. Upon increasing the Si/Al ratio from 2 to 4, the compressive strength of the metakaolin-based GP increases. Mechanical properties also increased upon adding fused silica which behaves like a bridge element irrespective of low or high Si/Al. flexural and elastic modulus also increases upon increasing Si/Al ratio [17]. As per [20] pre- and post-curing conditions are also affected by the SiO_2/NaO_2 ratio and a high concentration of silicate shows a positive effect. In the case of GP constituted of FA and GGBS, the compressive strength increases upon the addition of superplasticizers like naphthalene and carboxylate, and its workability also increased and slump improved by 110–210 mm. Addition of GGBS increases the strength by not considering the curing temperature but the slump decreases [10].

5 Properties of GPC

Mechanical properties, fresh and hardened properties, and thermal properties of FA-GGBS-based GPC are discussed in this section. Also, the resistance to sulphuric acid, drying shrinkage, creep behavior under continuous load, sulfate tolerance like long-term properties is also investigated.

5.1 Mechanical Properties of GPC

According to the findings of Table 1, the compressive strength of FA-based increases by the increase in molarity of NaOH, and the addition of 20% GGBS also increases the compressive strength by 44%.

Table 1 Various mixed proportions and their respective Compressive Strength

References	FA: GGBS	NaOH molarity	Binder/Activators	Compressive strength
[19]	100:0	20M	0.5	46.69
[21]	60:40	12M	0.4	80.5
[22]	80:20	14M	0.4	51.1
[23]	0:100	10M	0.5	36.4
[24]	70:30	14M	0.4	58.0
[25]	100:0	12M	0.5	35.4

Hadi et al. [26] by changing the ratio of alkaline solution and binder mass, additional water to binder mass, and sodium silicate/sodium hydroxide, prepared a GP paste of FA-GGBS to predict the compressive strength, workability, and setting time of GPC. And it was found that at 7 and 28 days of curing the compressive strength is 48.69% and 45.37% of OPC respectively. As per [27] GPC paste was formed by considering and not considering wollastonite as binding material. GP: sand: gravel ratio 1:2.5:2.4 was considered. Wollastonite was 3% of weight added. And it was noticed that the addition of wollastonite microfibers fills the micro-cracks and improves the bond strength. It was also observed that the addition of 4M NaOH increases the compressive strength at indoor curing by 62.68% from 14 to 180 days and at outdoor curing 23.33% from 14 to 180 days [8] studied the effect of the alkaline solution to binder ratio by varying curing temperature and time, i.e., curing temperature 80, 90, and 100 °C and curing time 12 and 14 h, 0.45, the molarity of NaOH: 12M, Na_2SiO_3 to NaOH: 2.5 with a rest period of one day. It was noticed that compressive strength increases by 80% at 12 h, 90 °C and 3 days, 49.51% at 24 h 90 °C and 3 days, 50% at 12 h, 90 °C and 7 days, 5% at 24 h, 90 °C and 7 days, i.e., increase in curing time and temperature decreases the compressive strength. Mustafa R. et al. studied the mechanical properties of FA-GGBS based GPC by adding micro silica and lime dust by 5, 10, 15% of the weight of FA and 10M alkaline solution in 2.5:1 by weight and studied that compressive strength is affected by the types and quantity of additive added. Jena S. et al. investigated the FA-based GPC by adding 14M silica fume and observed that the compressive strength of GPC increased by 20–38 Mpa and a maximum of 48 Mpa.

5.2 Durability Properties of GPC

Amran et al. [28] studied the factors affecting the durability properties of FA-GPC and observed that the fineness of FA particles affects the durability and alkaline activators that are majorly used NaOH, KOH, and Na_2SiO_3. FA-GPC is resistant to the aggressive environment in case of durability. As per [29] investigations, durability properties of Fa and metakaolin-based GPC were affected by sulphuric acid attack, i.e., there was 1.71% and 3.23% loss in weight at 10M and 12M of alkaline solution, respectively. In the curing of 7 and 28 days, the weight loss is 4.67% and 5.16%, respectively. Paruthvi et al. [30] studied the durability and strength properties of FA-based GPC with silica fume, metakaolin, and GGBS when mixed with a 10M alkaline solution. It was concluded that this mixture can be used in highway applications as it shows efficient results of abrasion test i.e., its value is very small and showed satisfactory results for water permeability, Sorptivity, acid attack, and sulfate attack tests due to the presence of high binding particles. Luhar et al. [31] investigated the durability properties of rubberized GPC, i.e., sand is replaced by waste rubber fibers. After the conduction of the abrasion test, it was concluded that minimal wear was noticed in between reliable values. Kurtoglu et al. [32] compared the durability properties of FA-based GPC with slag-based GPC and concluded that slag-based

GPC is more resistant to chemicals than FA-based GPC and OPC-based. Moreover, it was noticed that due to deterioration, weight loss is less in slag-based GPC than the other two. Aleem and Priya [33] reported the FA from thermal plants and M-sand-based GPC durability properties mixed with an alkaline solution of sodium hydroxide and sodium silicate and the admixture showed efficient results for the sulphuric attack, chloride attack tests. Karthik and Mohan [34] analyzed the Taguchi approach to predict strength and durability properties of FA, silica fume, and GGBS-based GPC mix. And concluded that mixture shows optimal resistances to various attacks and optimal mixture after the tests comprised of 45% of FA, 45% of GGBFS and 10% of silica fume, 1.5% dosage of superplasticizer, Na_2SiO_3/NaOH ratio = 1.5, and 12 molar contents.

5.3 Effect of Elevated Temperature

GPC properties are also affected by elevated temperature and there are various studies performed on it. It was noticed by Kong and Sanjayan [35] that strength properties are proportional to specimen size. FA-based GPC showed small aggregates were seen at elevated temperature rest remained stable and temperature variation at surface and core of specimen could lead to surface cracking. GPC remained chemically stable at elevated temperature whereas OPC specimens dehydrated and decomposed due to the building of pore pressure [36]. Park et al. [37] synthesized a FA and slag-based GP with an alkaline solution of silica and concluded that the gel strength started increasing at 400 °C and decreasing at 800 °C and becoming microporous to microporous at 400 °C. Under elevated temperature, FA-based GP paste cylinders of different sizes were cast and their behavior was compared with mortar and concrete-based cylinders. It was observed due to core and surface temperature differences, GPC-based specimens remained stable with small aggregates and in others, thermal cracking was noticed [35]. Authors of [18] studied the mechanical properties of FA-based GPC under elevated temperature by adding crushed sand, river sand, and granite and basalt aggregates as aggregate material and observed that crushed sand showed more strength than river sand and granite aggregates showed more strength than basalt aggregates. As per the [38] considerations, an FA-GGBS-based GPC with an alkaline solution having 0.2 silica modulus and 4 and 8% dosage of sodium was synthesized by the authors. It was concluded by the authors that initially at high-temperature strength increases then decreases.

6 Field Applications of GPC

The first building using GPC Global Change Institute (GCI) of the University of Queensland was built in 2013 by the HASSELL in association with Bligh Tanner and Wagners [39]. GPC sewer pipes, railway sleepers, cemetery crypts, box culverts,

and wall panels were successfully executed by Rocla in Australia. GPC is an eco-friendly substitute in rigid pavement road construction of OPC. River sand, M-sand, coarse aggregates based on three mixtures were used. After a study of GPC, it can be concluded that its fresh properties seem equivalent to slump and spread fresh concrete. GPC flexural and compressive strength achieve its targeted value to be considered as a replacement [16]. Glass waste and metakaolin with an augmented ratio of SiO_2/Al_2O_3 under 7 days curing and ambient temperature, ecological ceramic tiles can be made and this admixture met the desired properties of civil construction activity [40].

Geopolymer Railway Sleepers [3]: It was noticed that load vs displacement of FA-based GPC sleepers behaved similarly to OPC-based sleepers under four-point bending (two-point loading) [41]. Railway sleepers were cast from a mixture of FA and 30% GGBS with 18M alkaline solution and liquid/binder ratio of 0.35 and it was found that their compressive strength is found to be the same under stem curing and ambient curing as recommended by the Indian Railway Code T39-85 for OPC, i.e., GPC can be used in the construction of railway sleepers and would be proved as an eco-friendly replacement of OPC.

Geopolymer Roads: Throughout India, road construction using GPC has been carried out. GPC-based paver blocks are also used in road construction. A GPC road 50 * 3 long and wide, respectively, was constructed at Council of Scientific and Industrial Research-Central Building Research Institute (CSIR-CBRI) Roorkee and [42] moreover, at Energy Technology Research Alliance-NTPC (NETRA-NTPC), UP.

7 Conclusion

After the study of literature review of mechanical, chemical properties of GP it can be concluded that GPC is a better replacement for OPC and can be used in the construction industry effectively. The summarized view of the above literature is as below:

- OPC can be effectively replaced by GPC because under ambient temperature it can acquire early setting time and strength gain and GGBS is the efficient binder that can be added.
- It is concluded that by replacing GGBS 40% from different precursors efficient durability properties can be seen under ambient curing, i.e., GGBS makes GP an alternate binder to OPC in the construction industry.
- The thermal stability and compatibility of GP binder gel and aggregate are directly dependent upon the types of aggregates and composition of the source material. At elevated temperatures, GP based on FA shows high thermal resistance properties by sustaining its mechanical strength. At ambient temperature replacement of FA by GGBs shows improved performance but negative in case of thermal stability.

- In comparison to OPC, GPC shows fine bond behavior and reinforcement by attaining high-stress values and their respective equations hold equally good results for GPC too.
- GP usage in field applications and construction is increasing around the world.
- In geopolymer-based tiles glass polishing industry waste has been used as an activator and precursor. Under high temperatures and exposed to environmental conditions, these tiles showed considerable stability.
- Geopolymer railway sleepers using GGBS as a by-product under ambient curing also met the recommendations of Indian Railway Code T39-85. Hence OPC-based railway sleepers can be replaced with GPC railway sleepers.
- In road applications, GPC has also proved itself as an efficient material and is used in industry nowadays. GPC-based paver blocks are also used in road construction.
- Geopolymer concrete is also used as a replacement material in the construction of water tanks, pavements, and precast beams.

References

1. De Vargas AS, Dal Molin DC, Vilela AC, Da Silva FJ, Pavao B, Veit H (2011) The effects of Na_2O/SiO_2 molar ratio, curing temperature and age on compressive strength, morphology, and microstructure of alkali-activated fly ash-based geopolymers. Cem Concr Compos 33(6):653–660. https://doi.org/10.1016/j.cemconcomp.2011.03.006
2. Li C, Sun H, Li L (2010) A review: the comparison between alkali-activated slag (Si+Ca) and metakaolin (Si+Al) cements. Cem Concr Res 40(9):1341–1349. https://doi.org/10.1016/j.cemconres.2010.03.020
3. Deivabalan B, Tamilamuthan B (2015) Development of geopolymer concrete on railway prestressed concrete sleeper under static loading. J Ind Eng Res 1(4):118–122. https://ssrn.com/abstract=2796683
4. Shaikh FU (2014) Effects of alkali solutions on corrosion durability of geopolymer concrete. Adv Concr Constr 2(2):109. https://doi.org/10.12989/acc.2014.2.2.109
5. Mathew G, Joseph B (2018) Flexural behavior of geopolymer concrete beams exposed to elevated temperatures. J Build Eng 15:311–317. https://doi.org/10.1016/j.jobe.2017.09.009
6. Huseien GF, Mirza J, Ismail M, Hussin MW (2016) Influence of different curing temperatures and alkali activators on properties of GBFS geopolymer mortars containing fly ash and palm-oil fuel ash. Constr Build Mater 125:1229–1240. https://doi.org/10.1016/j.conbuildmat.2016.08.153
7. Hardjito D, Rangan BV (2005) Development and properties of low-calcium fly ash-based geopolymer concrete. http://hdl.handle.net/20.500.11937/5594
8. Nagral MR, Ostwal T, Chitawadagi MV (2014) Effect of curing temperature and curing hours on the properties of geopolymer concrete. Int J Comput Eng Res 4(9):1–11. ISSN (e): 2250-3005
9. Davidovits J (1991) Geopolymers: inorganic polymeric new materials. J Therm Anal Calorim 37(8):1633–1656. https://doi.org/10.1007/bf01912193
10. Nguyen TT, Goodier CI, Austin SA (2020) Factors affecting the slump and strength development of geopolymer concrete. Constr Build Mater 261:119945. https://doi.org/10.1016/j.conbuildmat.2020.119945
11. Davidovits J (1999) Chemistry of geopolymeric systems, terminology. In: Geopolymer, vol 99, no 292, pp 9–39
12. Davidovits J (1994) Geopolymers: man-made rock synthesis and the resulting development of very early high strength cement. J Mater Educ 16:91–91

13. Davidovits J (2015) Geopolymer chemistry and applications, 4th edn. J. Davidovits.–Saint-Quentin, France
14. Singh B, Rahman MR, Paswan R, Bhattacharyya SK (2016) Effect of activator concentration on the strength, ITZ, and drying shrinkage of fly ash/slag geopolymer concrete. Constr Build Mater 118:171–179. https://doi.org/10.1016/j.conbuildmat.2016.05.008
15. Sivasakthi M, Jeyalakshmi R (2021) Effect of change in the silica modulus of sodium silicate solution on the microstructure of fly ash geopolymers. J Build Eng 44:102939. https://doi.org/10.1016/j.jobe.2021.102939
16. Girish MG, Shetty KK (2017) Geopolymer concrete an eco-friendly alternative to Portland cement paving grade concrete. Int J Civ Eng 8(7)
17. Mustafa R, Shivaprasad KN, Das BB (2019) Effect of various additives on the properties of fly ash based geopolymer mortar. In: Sustainable construction and building materials. Springer, Singapore, pp 707–715
18. Mane S, Jadhav HS (2012) Investigation of geopolymer mortar and concrete under high temperature. Magnesium 1(5). http://citeseerx.ist.psu.edu/viewdoc/download?doi=10.1.1.414.4307andrep=rep1andtype=pdf
19. Topark-Ngarm P, Chindaprasirt P, Sata V (2015) Setting time, strength, and bond of high-calcium fly ash geopolymer concrete. J Mater Civ Eng 27(7):04014198. https://doi.org/10.1061/(ASCE)MT.1943-5533.0001157
20. Gharzouni A, Joussein E, Samet B, Baklouti S, Rossignol S (2015) Effect of the reactivity of alkaline solution and metakaolin on geopolymer formation. J Non-Cryst Solids 410:127–134. https://doi.org/10.1016/j.jnoncrysol.2014.12.021
21. Krishnan L, Karthikeyan S, Nathiya S, Suganya K (2014) Geopolymer concrete an eco-friendly construction material. Magnesium 1(1)
22. Deb PS, Nath P, Sarker PK (2014) The effects of the ground granulated blast-furnace slag blending with fly ash and activator content on the workability and strength properties of geopolymer concrete cured at ambient temperature (1980–2015). Mater Des 62:22–39. https://doi.org/10.1016/j.matdes.2014.05.001
23. El-Gamal SMA, Selim FA (2017) Utilization of some industrial wastes for eco-friendly cement production. Sustain Mater Technol 12:9–17. https://doi.org/10.1016/j.susmat.2017.03.001
24. Nath P, Sarker PK (2014) Effect of GGBFS on setting, workability and early strength properties of fly ash geopolymer concrete cured in ambient condition. Constr Build Mater 66:163–171. https://doi.org/10.1016/j.conbuildmat.2014.05.080
25. Cui Y, Zhang P, Bao J (2020) Bond stress between steel-reinforced bars and fly ash-based geopolymer concrete. Adv Mater Sci Eng 2020. https://doi.org/10.1155/2020/9812526
26. Hadi MN, Zhang H, Parkinson S (2019) Optimum mix design of geopolymer pastes and concretes cured in ambient condition based on compressive strength, setting time and workability. J Build Eng 23:301–313. https://doi.org/10.1016/j.jobe.2019.02.006
27. Lee WH, Wang JH, Ding YC, Cheng TW (2019) A study on the characteristics and microstructures of GGBS/FA based geopolymer paste and concrete. Constr Build Mater 211:807–813. https://doi.org/10.1016/j.conbuildmat.2019.03.291
28. Amran M, Debbarma S, Ozbakkaloglu T (2021) Fly ash-based eco-friendly geopolymer concrete: a critical review of the long-term durability properties. Constr Build Mater 270:121857. https://doi.org/10.1016/j.conbuildmat.2020.121857. ISSN 0950-0618
29. Deepak A, Lakshmi TVS (2020) Durability properties of geopolymer concrete with flyash and metakaolin. Int J Sci Technol Res 9(1)
30. Paruthvi S, Dinesh HT, Bhavana B (2016) Characterization & durability properties of ultrafine fly ash based geopolymer concrete. J Res (J4R) 2(5)
31. Luhar S, Chaudhary S, Luhar I (2019) Development of rubberized geopolymer concrete: strength and durability studies. Constr Build Mater 204:740–753
32. Kurtoglu AE, Alzeebaree R, Aljumaili O, Nis A, Gulshan ME, Humor G, Cevik A (2018) Mechanical and durability properties of fly ash and slag based geopolymer concrete. Adv Concr Constr 6(4):345

33. Aleem A, Priya TS. Enhancement of durability characteristics of geopolymer concrete with manufactured sand
34. Karthik S, Mohan KSR (2021) A Taguchi approach for optimizing design mixture of geopolymer concrete incorporating fly ash, ground granulated blast furnace slag and silica fume. Curr Comput-Aided Drug Des 11:1279. https://doi.org/10.3390/cryst11111279
35. Kong DL, Sanjayan JG (2010) Effect of elevated temperatures on geopolymer paste, mortar, and concrete. Cem Concr Res 40(2):334–339. https://doi.org/10.1016/j.cemconres.2009.10.017
36. Pan Z, Sanjayan JG, Kong DL (2012) Effect of aggregate size on spalling of geopolymer and Portland cement concretes subjected to elevated temperatures. Constr Build Mater 36:365–372. https://doi.org/10.1016/j.conbuildmat.2012.04.120
37. Park SM, Jang JG, Lee NK, Lee HK (2016) Physicochemical properties of binder gel in alkali-activated fly ash/slag exposed to high temperatures. Cem Concr Res 89:72–79. https://doi.org/10.1016/j.cemconres.2016.08.004
38. Jena S, Panigrahi R, Sahu P (2019) Effect of silica fume on the properties of fly ash geopolymer concrete. In: Sustainable construction and building materials. Springer, Singapore, pp 145–153
39. World's first public building with structural Geopolymer Concrete | Durable building materials (wordpress.com)
40. Marvila MT, Azevedo AR, Delaqua GC, Mendes BC, Pedroti LG, Vieira CM (2021) Performance of geopolymer tiles in high temperature and saturation conditions. Constr Build Mater 286:122994. https://doi.org/10.1016/j.conbuildmat.2021.122994
41. Malipatil S, Patil SG (2015) Geopolymer concrete for railway sleepers. Int J Innov Res Sci Technol 2(3)
42. https://www.business-standard.com/article/pti-stories/irc-accredits-geopolymer-concrete-road-by-Netra-ntpc-and-118011201266_1.html/.2018. Accessed 05 Jan 2021

Study of Orange and Banana Peels as Natural Coagulants

Subhash Kumar Yadav and Atul Sharma

Abstract Turbidity is a characteristic related to the concentration of suspended solids particles in water and has been adopted as an easy and reasonably accurate measure of overall water quality. Turbidity imparts a great problem in raw and wastewater treatment and to remove this turbidity the most commonly applied treatment process is the combination of coagulation, flocculation, sedimentation, and filtration to reduce within the permissible limit or eliminate turbidity. The most commonly used chemical coagulant is alum but studies have shown that alum has certain drawbacks such as it producing a lot of sludge, being expensive, not environment friendly. Orange peels, Banana peels and blends of alum with orange peels and banana peels are used as coagulants in this study in place of regularly used chemical coagulants to reduce the turbidity of synthetically prepared turbid water of 100 ± 5 NTU. The tests were carried out using jar test apparatus to determine the optimum dose quantity of coagulants. Different concentration of the stock solution is prepared and mixed in synthetic turbid water in different quantity and the optimum doses of coagulants were found out. The efficiency of the orange peels, banana peels, blend of alum and banana peels, blend of alum and orange peels were 79.4%, 85.4%, 90.8% and 88.9%, respectively. The effect of the natural coagulant on other water quality parameters such as pH, hardness, alkalinity, was also found out. The use of natural coagulants is suitable, easier, and cheap, and environment friendly approach for water treatment as observed in this study.

Keywords Banana peels · Coagulation · Natural coagulant · Orange peels · Synthetic turbid water

1 Introduction

Water is undoubtedly one of the most important elements amongst natural resources. Most of the countries in the world do not have access to clear and safe drinking water

S. K. Yadav (✉) · A. Sharma
Jabalpur Engineering College, Jabalpur, India
e-mail: yadavsubhash199611@gmail.com

© The Author(s), under exclusive license to Springer Nature Singapore Pte Ltd. 2023

K. R. Reddy et al. (eds.), *Recent Advances in Sustainable Environment*, Lecture Notes in Civil Engineering 285, https://doi.org/10.1007/978-981-19-5077-3_20

as a result of which millions of people are suffering from diseases caused due to polluted water [12]. One of the best ways to remove turbidity from water in the water treatment process is by the use of a coagulant [8]. Coagulants play an important role in the treatment of water, waste water, the treatment and disposal of sludge [1]. Surface water sources traversing urban areas contain elevated levels of dissolved and suspended materials [13]. Coagulation and flocculation processes are widely used in water and wastewater treatment. Its main objective is to remove suspended colloidal particles and to reduce turbidity in water body [2]. The coagulant materials can be classified into inorganic and organic coagulants [9]. Conventionally, inorganic coagulants, such as alum and different salts of iron have been used to carry out coagulation [4]. However, the use of these chemical coagulants resulted in many downsides such as harmful voluminous sludge produced [11]. Recent studies have pointed out several serious drawbacks of using aluminium salts, such as Alzheimer's disease and similar health related problems associated with residual aluminium in treated waters [3]. Plant-based coagulants have long been recognized for their effectiveness in traditional water treatment [5]. Natural coagulants are safe and eco-friendly [6]. It can be extracted from plant, microorganisms and animals [7]. Some of the plants are able to be a coagulant because they are able to conduct some of the coagulation mechanisms which are neutralizing the charge in colloidal particles and perform polymer bridging [2, 10]. So natural coagulants came into the picture for cost-effective, environment friendly and easier turbidity removal than inorganic coagulants. In this study, Orange peels and Banana peels are used as a natural coagulant.

2 Materials and Methods

2.1 Preparation of Synthetic Turbid Water

Synthetic turbid water was prepared using clay. 10 gm of clay was weighed and mixed in 1 L of distilled water using Jar test apparatus. The solution of clay and distilled water were mixed at a high rpm (150 rpm) for 1 min in jar test apparatus followed by 30 min of slow mixing at 30–35 rpm to obtain a uniform solution of clay and distilled water. After this, the mixed clay sample was left to stand for 24 h for complete hydration of clay. The suspension is then stirred again so as to achieve uniform and homogenous sample, this sample is then used as stock solution to make desired synthetic turbid water of 100 NTU. The turbidity of the sample was measured by using nephelometer and expressed in nephelometric turbidity unit (NTU) and thus the synthetic turbid water of 100 ± 5 NTU was made.

2.2 Preparation of Alum Solution

Alum solution of 1% concentration was prepared by dissolving 1gm of alum in distilled water (pH = 7) and the solution volume was increased to 1L.

2.3 Preparation of Natural Coagulant Solution

Peels of orange and banana were collected from a local juice shop and were used to make natural coagulants solutions. The orange and banana peels were first weighed before drying; 200gm of orange and banana peels each was weighed again, the dried weights of the sample were 48.6gm and 19.9gm, respectively.

$$\%\text{moisture} = \frac{\text{Initialweight} - \text{Finalweight}}{\text{Initialweight}} \times 100$$

The dried sample is then grind using the home grinder to convert dried peels into powder. The powder thus obtained is then used to make stock solutions of different concentrations. The stock solution is then filtered using filter paper to finally obtain the desired stock solution to be used in the jar test.

2.4 Experimental Procedure

A standard jar test apparatus equipped with six paddles to be rotated in six beakers was used to imitate the process of coagulation, flocculation and sedimentation.

To determine the optimum conditions for coagulation and flocculation, the dosage of coagulant to be used is one of the important parameters. If the dosage is insufficient or overloaded then the desired results will not be obtained and would result in poor performance of turbidity removal. So, it is crucial to determine the optimum dosage to minimize the coagulant dose cost and to obtain the optimum performance in the treatment of water. To determine the optimum dosage a set of experiments were performed on synthetic turbid water of 100 ± 5 NTU using jar test apparatus at different dosages of natural coagulants ranging from 10−100 ml/L prepared from the stock solution of 2.5gm/L, 5gm/L and 10gm/L concentration.

Different dosages of coagulants were put in different beakers filled with 1000 ml of synthetic turbid water of 100 NTU after this the beakers are placed on jar test apparatus. The solution of turbid water and coagulant is mixed at a high rpm of 150 for 1 min and then at a lower rpm from 30–35 for 30 min. The solution is then allowed to settle for 30 min and then their turbidity is measured in a nephelometer. The samples to be tested for turbidity were taken out using a pipette from the beakers from approximately 2–2.5 cm below the water surface. The turbidity of the sample

is then test measured using Nephelometer. The efficiency of turbidity removal is measured as:

$$R = \frac{\text{Initialturbidity} - \text{Finalturbidity}}{\text{Initialturbidity}} \times 100$$

where R is percentage removal.

3 Results and Discussion

3.1 Orange Peel Turbidity Removal Efficiency

Figure 1 shows the turbidity removal efficiency of orange peel at different dosage of stock solution. The turbid removal efficiency was found to be maximum when concentration of stock solution was 2.5 gm/L and dosage was 50 gm/L. In the below case the turbidity removal efficiency increases up-to a certain dosage of coagulant and after that the efficiency starts to decrease.

3.2 Banana Peel Turbidity Removal Efficiency

Figure 2 shows the turbidity removal efficiency of banana peel at different dosage of stock solution. The maximum turbid removal efficiency of 85.4% was found to be when concentration of stock solution was 5 gm/L and dosage was 25 gm/L. In the below case the turbidity removal efficiency increases up-to a certain dosage and after that the efficiency starts to decrease. Banana peels efficiency was found to be more than orange peels.

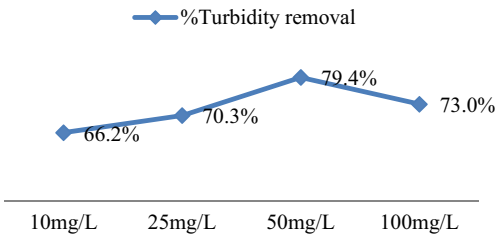

Fig. 1 Turbidity removal efficiency of Orange peels as cogaulant at different dosage

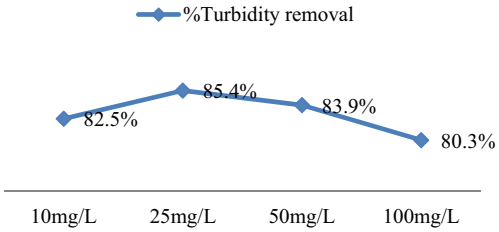

Fig. 2 Turbidity removal efficiency of Banana peels as cogaulant at different dosage

3.3 Alum-Orange Peel Turbidity Removal Efficiency

Figure 3 shows the turbidity removal efficiency of Alum + Orange peels at different dosages of stock solution. The maximum turbid removal efficiency of 88.9% was found to be when concentration of stock solution was 2.5 gm/L and dosage was 25 gm/L. The turbidity removal efficiency of Alum + Orange peels was found to better than the orange and banana peel when mixed in a ratio of 1:1.

3.4 Alum- Banana Peel Turbidity Removal Efficiency

Figure 4 shows the turbidity removal efficiency of Alum + Banana peels at different dosage of stock solution. The maximum turbid removal efficiency of 90.8% was found to be when concentration of stock solution was 5 gm/L and dosage was 25 gm/L. In the below case the turbidity removal efficiency increases up-to a certain dosage and after that the efficiency starts to decrease. The efficiency of Alum + Banana peels blend as coagulant gives the best result amongst the four coagulants when mixed in a ratio of 1:1 in this study.

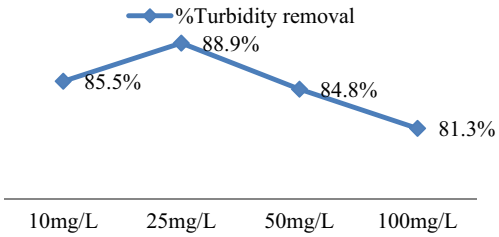

Fig. 3 Turbidity removal efficiency of Alum + Orange peels as coagulant at different dosage

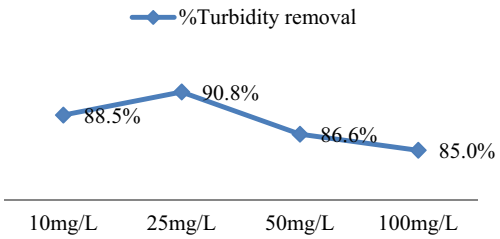

Fig. 4 Turbidity removal efficiency of Alum + Banana peels as coagulant at different dosage

3.5 Effect on Other Water Quality Parameters

Table 1 shows the water quality parameters of raw (untreated) water and after the treatment with coagulants of orange peels it is been observed that there are certain changes in the values of water quality. The values of pH and alkalinity decreased (shown in Table 2) but still are within the permissible limits whereas the values of hardness and TDS increased (shown in Table 2) although the value of TDS is within the permissible limits it is still one of the drawbacks with the use of orange peels as coagulants along with decrease in pH as it is making the water slightly acidic.

Similarly, when the raw water was treated with banana peels coagulant the values of pH and alkalinity decreased (shown in Table 3) but still are within the permissible limits whereas the values of hardness and TDS increased (shown in Table 3). The drawbacks of banana peels coagulant are similar to orange peels coagulant, the banana peels showed better turbid removal efficiency than orange peels. The blend of Alum + Orange peels as coagulant shows much better results than the other two

Table 1 Values of synthetic turbid water before coagulation

Water quality parameters	Measured value
Turbidity	100 NTU
pH	7.7
Hardness	320 mg/l
Alkalinity	160 mg/l
TDS	324 mg/l
Temperature	21.2 °C

Table 2 Values of synthetic turbid water after coagulation with Orange peels

Water quality parameters	Measured value
Turbidity	20.4 NTU
pH	6.84
Hardness	350gm/l
Alkalinity	110gm/l
TDS	534 mg/l
Temperature	21.0 °C

Table 3 Values of synthetic turbid water after coagulation with Banana peels

Water quality parameters	Measured value
Turbidity	14.6 NTU
pH	6.72
Hardness	360 mg/L
Alkalinity	60 mg/L
TDS	560 mg/L
Temperature	21.1 °C

coagulants (shown in Table 4); all the water quality parameters values are found to be within the permissible limits. The value of pH decreases but is closed to the neutral pH value, i.e. pH = 7, the value of alkalinity also decreases, whereas the value of hardness and TDS slightly increases and thus the blend of Alum + Orange peels shows better performance than the orange peels and banana peels coagulants.

The blend of Alum + Banana peels showed the best results of all the coagulants, the turbidity removal efficiency of the coagulant was more than 90% and the value of turbidity of treated water came out to below 10 NTU, not only does the turbidity result was satisfactory but the values of other water quality parameters such as hardness, alkalinity, TDS were found to be satisfactory and within the permissible limits as shown in Table 5.

Table 4 Values of synthetic turbid water after coagulation with Alum + Orange pee

Water quality parameters	Measured value
Turbidity	11.1 NTU
pH	6.89
Hardness	340 mg/L
Alkalinity	84 mg/L
TDS	350 mg/L
Temperature	21.4 °C

Table 5 Values of synthetic turbid water after coagulation with Alum + Banana peels

Water quality parameters	Measured value
Turbidity	9.2NTU
pH	6.94
Hardness	380 mg/L
Alkalinity	80 mg/L
TDS	346 mg/L
Temperature	21.2 C

4 Conclusion

The turbidity removal efficiency of coagulated and sedimented water was found out after a fixed interval of time in case of different coagulant such as orange peels, banana peels, Blend of Alum + Orange peels and Blend of Alum + Banana peels. Turbidity removal efficiency of orange peels was found to be highest at 2.5gm/L concentration of stock solution and at a dosage of 50 ml/L. Similarly, Turbidity removal efficiency of banana peels, Blend of Alum + Orange peels and Blend of Alum + Banana peels was found to be highest at 5gm/L, 2.5gm/L and 5gm/L concentration of stock solution and at a dosage of 25 ml/L, 25 ml/L and 25 ml/L, respectively. The turbidity removal efficiency was found to be maximum in case of blended coagulant of alum and banana peels in a definite proportion. In this study reduction of Alum dose upto 50% was observed thereby reducing alum drawbacks to someextent. Residual turbidity is slightly more in case of alum and orange peels blended coagulant and further more in case of banana and orange peels coagulants. Orange and banana peels present a viable alternative to alum not only in developing countries but also globally orange and banana peels have a great potential of water treatment.

Acknowledgements I would like to thank, my guide Prof. Atul Sharma, Faculty of Civil Engineering, Jabalpur Engineering College for guiding me through every point during this study. I would also like to thank Chemist Amreen Khan, Ranjhi Treatment plant for helping me perform the required water quality parameters test.

References

1. Al-Samawi A, Shokrala E (1996) An investigation into an indigenous natural coagulant. Environ Sci Health, 1881–1897
2. Amir Hariz Amran, Nur Syamimi Zaidi, Khalida Muda, Liew Wai Loan (2018) Effectiveness of natural coagulation process: A Review, Int J Eng Technol 7(3.9), 34–37
3. Anju S, Mophin-Kani K (2016) Int J Sci & Eng Res 7(4) 238–244
4. Kakoi B (2016) Banana pith as a natural coagulant for polluted river water. Ecol Eng 95:699–705
5. Dorea C (2006) Use of Moringa spp. seeds for coagulation: a review of a sustainable option, Water Sci Technol Water Supply, 6 219–217
6. Choy SY, Prasad KMN, Wu TY, Raghunandan ME, Ramanan RN (2014) Utilization of plant based natural coagulants as future alternatives towards sustainable water clarification. J Environ Sci 26(11):2178–2189
7. Fathinatul N, Nithyanandam R (2014) Wastewater Treatment by using Natural Coagulant, 2nd Eureca, 2–3
8. Ghulam Hussain (2019) Exploring the potential of pearl millet (Pennisetum glaucum) and black-eyed pea (Vigna unguiculata subsp. Unguiculata) as bio-coagulants for water treatment, Desalination and Water Treatment, 184–191
9. Montgomery JM (1985) Water Treatment-principles and design", Wiley Inter-Science

10. Kristianto H (2017) The potency of indonesia native plant as natural coagulant: A mini review. Water Conserv Sci Eng 2(2):51–60
11. Maya Shamira Shaharom, Dyg. Siti Quraisyah Abg. Adenan (2019) Potential of orange peel as a coagulant for water treatment, Infrastruct Univ Kuala Lumpur Res J, 7(1)
12. Asrafuzzaman Md., Fakhruddin ANM (2011) Reduction of turbidity of water using locally available natural coagulants, ISRN Microbiology, Volume 2011 1-6
13. Al-Sameraiy M (2012) A Novel water treatment approach for turbidity removal using date seeds and pollen sheath. J Water Resour Prot 4:79–92

Contribution of Site Remediation to Sustainable Development Goals

Mello Campos, Kamil Czaplinski, Jasper Gabriel, Thomas Pikowski, Gaurav Verma, and Krishna R. Reddy

Abstract Sustainability considers society, environment, culture, and economy in practices and projects to avoid hindering future generations' needs while meeting current needs. In 2015, the United Nations developed a set of 17 goals meant to help achieve sustainable practice worldwide by 2030. These 17 goals are the Sustainable Development Goals to create a more peaceful and prosperous world for the planet and its inhabitants. While site remediation does not intentionally or directly incorporate these 17 Sustainable Development Goals, four case studies of site remediation across North America are evaluated for the applicability of each goal. The four cases explored different sites that each used various remediation technologies, showing how some technologies can be considered more sustainable. By connecting the Sustainable Development Goals to site remediation, it was observed that these practices incorporate a majority of the goals but fail to address issues on poverty, gender equality, and clean energy. Through this classification of applicability for each case study, it can be determined that these goals are dependent on the geographical location, economics, governmental action, and the local communities. This paper will analyze the UN Sustainable Development Goals and highlight the contribution site remediation has toward them by examining four case studies.

Keywords Sustainability · Sustainable Development Goals · Site remediation

1 Introduction

Sustainability is defined as "meeting the needs of the present without compromising the ability of future generations to meet their own needs" by the United Nations Brundtland Commission [1]. To meet the needs, four aspects must be considered: society, the environment, culture, and the economy [2]. With these four considerations, the United Nations has created a list of 17 goals which they call the Sustainable Development Goals—SDGs as seen in Fig. 1. The Sustainable Development Goals

M. Campos · K. Czaplinski · J. Gabriel · T. Pikowski · G. Verma · K. R. Reddy (✉)
Department of Civil, Materials, and Environmental Engineering, University of Illinois at Chicago, 842 West Taylor Street, Chicago, IL 60607, USA
e-mail: kreddy@uic.edu

© The Author(s), under exclusive license to Springer Nature Singapore Pte Ltd. 2023

K. R. Reddy et al. (eds.), *Recent Advances in Sustainable Environment*, Lecture Notes in Civil Engineering 285, https://doi.org/10.1007/978-981-19-5077-3_21

Fig. 1 List of the Sustainable Development Goals developed by the United Nations

developed by the United Nations general assembly in 2015 are a plan that developing countries can use to create a more sustainable world by 2030. Each goal is further broken down into targets that describe all aspects of the respective objective. The UN recognizes events, publications, and actions that contribute toward a goal and is used during yearly evaluations on the worldwide progress made toward a goal.

Site remediation is "the remediation of already contaminated soils and groundwater using in situ or ex situ treatment methods" [3]. While the process of removing contamination from soils and groundwater is inherently sustainable, it only focuses on the environment and economy, while society and culture have not been the main focus during site remediation until recent years. Currently, site remediation focuses on involving all aspects of sustainability. The progress can be evaluated by evaluating a site remediation project to see which of the 17 Sustainable Development Goals it meets. This paper focuses on a total of four case studies to evaluate how they addressed and contributed to the goals. To highlight which SDGs are applicable to a case study (Table 1), a scale of 1–5 was developed where 1 represents that the SDG was not applicable to the case study, and 5 shows a direct applicability of the SDG to the site remediation in the case study.

The SDGs are typically interconnected in some ways, allowing for multiple to be applicable from one action that was performed during the remediation process. This

Table 1 Scale of Sustainable Development Goals

Scale 1–5	1: No applicability	2: Low applicability	3: Moderate applicability	4: Regular applicability	5: High applicability

shows the impact that small changes in site remediation can make, leading to more sustainable projects in future.

Furthermore, trends among the case studies will be discussed since evaluating the case studies may help expose areas of sustainability that need more focus in future site remediation projects. Various technologies used in site remediation may tend to allow for the inclusion of Sustainable Development Goals that other technologies do not offer. It is important to note such differences and trends as it progresses the ability for projects to be more sustainable, allowing for the goal set out by the United Nations of meeting all 17 SDGs by 2030. These goals are essential due to the pressing environmental, economic, and political issues that society has to face within the next coming decades to achieve a more sustainable, equal, and just society for future generations.

These case studies offer a different perspective on how the UN Sustainable Development Goals can be achieved in site remediation, where some countries need to develop infrastructure to include more social, ecological, or environmental aspects in their remediation projects. While site remediation is beneficial for the world, it can often have byproducts that are not favorable or may lack future use foresight. It is essential to evaluate various remediation projects on whether they are achieving as many sustainability goals as possible.

This paper will evaluate four case studies on the applicability and impact of the 17 Sustainable Development Goals in their site remediation projects. While some case studies may not have considered the Sustainable Development Goals or have not addressed all the goals in their project, it is essential to recognize the progress being made toward fulfilling as many goals as possible.

2 Case Study

2.1 Case Study 1: Phoenix, Arizona

Case study 1 is focused on the Motorola 52nd Street Superfund Site (M52 Site) located in Phoenix, Arizona. The site was added to the National Priorities List as a Superfund site in 1989 after the initial discovery in 1983 of a plume of 93,000 gallons of trichloroethylene (TCE) that had reached and contaminated the groundwater at the site. While trichloroethylene remained the most prominent contaminant at the site, further investigations showed that there were more contaminants such as volatile organic compounds (VOCs) and tetrachloroethene (PCE) were also present in the groundwater [4]. All these contaminants are carcinogens which were affecting the local community.

After the initial findings, pump and treat methods were established in 1986 to help contain the plume. Additional groundwater extraction and treatment have been added along the way in 2001, which now discharges into the Salt River Project Grand Canal and has functional uses in local agriculture. Since then, monitoring wells have

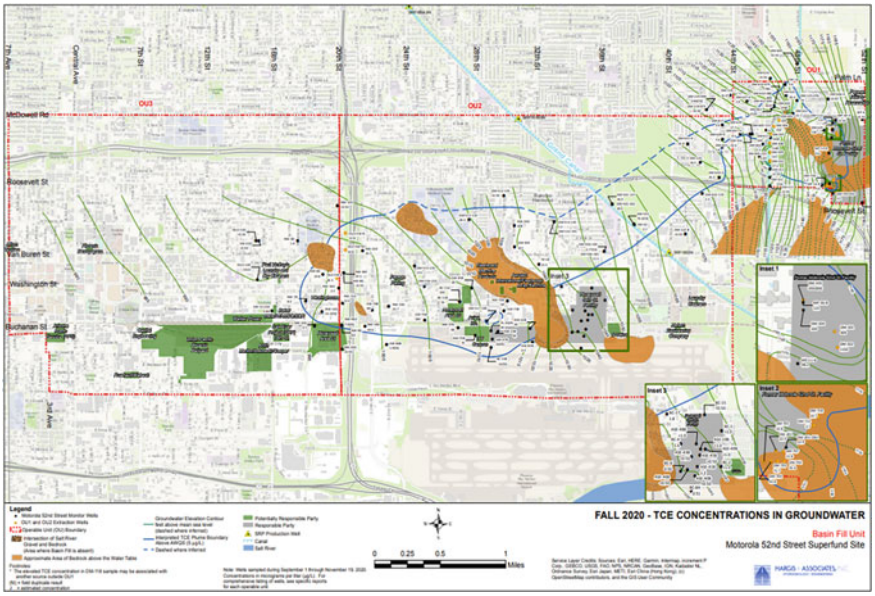

Fig. 2 Map of the Motorola Superfund Site with plumes showing the concentrations of TCE in groundwater from the basin fill unit (EPA)

been added throughout the area of impact to make sure the groundwater remains within acceptable limits. The community has not had much further concern with the groundwater, but rather with the soil vapors. For this reason, soil vapor monitoring wells and indoor mitigation systems have been implemented throughout the affected community [4]. An updated map of the Motorola Superfund Site from Fall of 2020 showing the plumes of the TCE in groundwater can be found below as Fig. 2.

This involves many of the United Nations' Sustainable Development Goals, even though the remediation had started in the 1980s, well before the goals were established. The M52 Superfund Site has done nothing to address the local economy that was largely low income during the time of this site joining the NPL. The Sustainable Development Goal 1 of "no poverty" is not applicable to this case study and receives a 1 (Table 2). The M52 Superfund Site discharges part of the water that is treated on site into the Grand Canal. The Grand Canal is part of the Salt River Project in which part of the water gets used for the irrigation of crops and for agricultural use. For this reason, the M52 Superfund Site receives a 2 for SDG 2 due to the low applicability of the goal in the remediation. Most remediation sites address SDG 3 of good health and well-being simply by making the contaminated area more usable than it previously was. The M52 Superfund Site is no different in that manner. A large amount of contamination was cleaned up, allowing for the use of local groundwater and the site again. On the site, there are residential, commercial, and industrial land zones to which people must go to or live in. The remediation of this site directly improves the health of all on site. This is a tangential benefit of site remediation, and therefore,

Table 2 List of the Sustainable Development Goals applicable to each of the case study

	Case study 1 Phoenix, Arizona	Case study 2 Montreal, Canada	Case study 3 Hartford, Illinois	Case study 4 Chicago, Illinois
SGD 1	1	1	1	1
SDG 2	2	5	1	3
SDG 3	3	3	5	4
SDG 4	1	2	1	3
SDG 5	1	1	1	1
SDG 6	5	4	5	4
SDG 7	2	2	2	1
SDG 8	3	2	2	2
SDG 9	2	5	4	2
SDG 10	3	1	2	3
SDG 11	2	5	1	3
SDG 12	5	5	1	5
SDG 13	2	5	5	5
SDG 14	2	4	5	5
SDG 15	4	4	5	5
SDG 16	3	2	5	4
SDG 17	5	4	5	4

the M52 Superfund Site receives a 3 for moderate applicability of SDG 3 to the site. The Motorola Superfund Site does not have any association with education which shows no applicability, a 1 of 5, of SDG 4 to the site remediation.

The Motorola Site had contained a lot of groundwater contamination which is what Sustainable Development Goal 6, “Clean Water and Sanitation”, speaks about in its targets. A large portion of the contamination removal process was to treat the water with air stripping by synthetic resin adsorption, advanced oxidation, reinjection of treated water into the aquifer, carbon absorption, and ultraviolet oxidation. This treated water is then either reinjected into the aquifer or put into the Grand Canal where it flows into the Salt River. There the water is being managed to avoid a shortage or overflow during drought and rain seasons. The site remediation meets multiple of the targets set out to achieve this goal by the UN and receives a 4 for applicability. Through the M52 Superfund Sites’ contribution to the Salt River Project, the water being treated and discharged goes to a dam that generates hydroelectric power. The M52 Superfund Site indirectly contributes to the generation of alternative energy which aligns with the UN goal for affordable and clean energy. Following the same rationale for the applicability of SDG 2, SDG 7 also receives a 2 for applicability.

The M52 Superfund Site currently provides 1,712 jobs across 26 businesses. The annual sales revenue that these businesses are estimated to bring in is $380,342,310. For this reason, SDG 8 receives a rating of 3 for the applicability. Industrial zoning is within the contaminated zone of the Motorola Superfund Site, however, the quality, sustainability, and innovation of these businesses in their respective industry is unknown. This goal is barely met with the site remediation that occurred at the M52 Superfund Site, only brushing on some of the targets to meet such a goal. Since the goal is barely applicable at this site, a 2 of 5 for applicability is given. SDG 10 is moderately applicable to the site remediation that occurred due to the inclusion of the low-income and Latino communities during the community involvement events. These community involvement events that happened during the decision-making were to allow for questions and suggestions to be made, giving these communities a voice. The local communities were also able to ask for monitoring of the indoor air mitigation systems in homes and apartments. From these involvements, the goal receives an applicability rating of 3. Sustainable cities and communities are not very applicable to the site remediation that occurred on the Motorola Superfund Site. There is a small connection between the sustainability of hydroelectric power that is generated from some of the on-site treated water by the dams in the Salt River Project. This hydroelectric energy is sustainable and is used by those connected to the Phoenix electricity grid. SDG 11 is applicable enough to get a rating of 2. In the United Nations' targets that define SDG 12, Target 12.4 speaks on being able to manage the chemicals and wastes in an environmental manner that reduces their quantity. This directly relates to clean up and remediation of the M52 Site, however, this is only one of many targets. Many other targets speak on sustainability, which once again is vaguely addressed in the remediation process. For these reasons, SDG 12 is highly applicable to this case study, deserving the rating of 5.

The applicability of SDG 13 once again goes to the Salt River Project where multiple dams are being used to be resilient toward the drought and rain seasons that occur in Phoenix, Arizona. This follows the same rationale as SDG 11 and therefore will also receive the same score of 2 for applicability. SDG 14 largely deals with marine ecosystems which Phoenix, Arizona has little to no part in. The only applicability of goal 14 to the site remediation is the reservoirs of the Salt River can be considered to be small-scale fisheries. Once again, the treated water being pumped into the Grand Canal helps aid in maintaining a water level that resists the drought and rain seasons of the region. This protects the small-scale fisheries, showing a low applicability of SDG 14 to the site remediation at the Motorola Superfund Site. While the site remediation being done at the M52 site does not promote any biodiversity, it does address many efforts on improving the local land and ecosystem that was affected by the contamination. Site remediation is restoring the land, and the treated groundwater from the contaminated site is being used to combat droughts and floods via the Salt River Project. This sort of relationship shows an applicability of SDG 15 in the site remediation of the Motorola Site worthy of a 4. The Motorola Superfund Site in Phoenix helped expose a lot of the unfortunate occurrences that can happen when working on a project with multiple stakeholders, as discussed in the article "ideal and reality of multi-stakeholder collaboration on sustainability problems: a

case study on a large-scale industrial contamination on Phoenix, Arizona". In particular, the period where the local community had issues with power struggle between the governmental agencies and themselves. While the community demanded more support and monitoring with and on the site, they were unable to get a fair representation in the cases until another party stepped in and settled the dispute by addressing the wants and needs of the local community. This is an example of Target 16.7 for the SDG 16 that shows a moderate applicability of the goal to the site remediation. The lack of international interaction on the site is what reduces the applicability of the goal to remediation to a 3. A shortcoming of the site remediation for SDG 17 is once again the lack of international outreach of any kind. This means that most of the targets for SDG 17, Partnerships for The Goals, are not met. Contrastly, all targets which relate to domestic partnerships for achieving the goal of remediating the M52 Superfund Site are met. Targets like Target 17.14 through Target 17.19 are all met due to site remediation being a sustainable development with multi-stakeholder partnerships. These partnerships were effective at sharing and mobilizing the knowledge through meetings with the community. Accomplishing so many goals makes SDG 17 highly applicable to the site remediation from this case study receiving a score of 5 out of 5. Cumulative list of applicability of various SDG for Case study 1 using the scale of 5 is shown in Table 2.

2.2 Case Study 2: Montreal, Canada

Case study 2 gives details on the benefits of the phytoremediation of brownfields and focuses on a brownfield remediation project in Montreal, Canada. Phytoremediation refers to the use of green plants and trees to treat contaminated sites. This remediation approach both reduces the mobility of contaminants while not generating any secondary waste that would need treatment. Brownfield sites refer to abandoned industrial sites that are potentially contaminated from prior use. Contamination in brownfield sites usually affects both the soil as well as the groundwater.

Phytoremediation is a natural solution for brownfields because it is proficient in treating both soil and groundwater for organic and inorganic compounds while contributing to sustainable development. In the case of the brownfield site in Montreal, Canada, in 2016, phytoremediation was implemented to 4 hectares of brownfield to treat contamination of heavy metals and organics such as As, Ba, Cd, Cu, Mn, Pb, Se, and Zn. Plants such as different types of willow and green shrubbery were used for the remediation as these are fast growing and have the best traits for absorption of pollutants. Over a two-year period, the site was shown to have reduced levels of pollutants such as cadmium and zinc.

The United Nations goals that this case directly contributes to are zero hunger, clean water, industry (innovation and infrastructure), sustainable cities and communities, responsible consumption, climate action, and life on land and water. Phytoremediation allows for contaminated sites to be treated in one of the most sustainable ways. It contributes to overall soil health on top of contaminant reduction as well

as the hydrological cycle by mitigating flood risk and reducing stormwater runoff. Phytoremediation also naturally reduces CO_2, is known to increase air quality, and reduces concentrations of airborne particles. It is also known to decrease urban air and soil temperature in the area, a U.K. study showed that greenspaces reduced summer soil temperatures by 5.7 °C [5]. These examples show the direct relationship to SDGs 6,13,14, and 15 (as seen in Table 2) which are clean water and sanitation, climate action, and life on land and water. When using phytoremediation, the cleaning of the site is obviously the main priority, but using this technology, it contributes to more than just the site. The plants used, along with contributing to soil and water health, contribute to the local climate and increase biodiversity in the area.

Projects such as the Montreal case study are not only known to benefit the environmental aspects but also promote social justice and cohesion of communities. Urban brownfields are most located in working class or low-income neighborhoods, and the implementation of a green project allows for community participation with the applicable prerequisites. Some ways that these projects can contribute to communities include community participation with the implementation of plants and trees to the site and use of the phytoremediation site for educational purposes such as school field trips. These communal aspects directly relate to the SDGs 11 and 4, which are sustainable cities, communities, and quality education. Phytoremediation also indirectly contributes to SDGs 3 and 17 which are good health and well-being and the overall partnership for the goals. The SDGs that were not very applicable to this case were 1, 5, and 10 (as seen in Table 2), which were no poverty, gender equality, and reduced inequalities. These goals were not applied to this case because there was no effect on poverty, inequalities, or gender equality, if the project's aim was to cover all the Sustainable Development Goals, it would be possible to somehow integrate these goals to be applicable. Overall, phytoremediation is shown to be one of the most green site remediation techniques and is a great contributor to the UN Sustainable Development Goals.

2.3 Case Study 3: Hartford, Illinois

Case Study 3 focuses on the Chemetco Superfund site located in Hartford, Illinois. This location was formerly a copper smelting facility and encompasses 41 acres of land. The area surrounding the plant is mainly agricultural, and the site contains wetlands and a seasonal tributary to Long Lake, a tributary of the Mississippi river referenced as SLL. However, a 10-inch diameter pipe was discovered to be ejecting contaminants into the surrounding area and water for years until the Illinois EPA discovered the contamination. The list of contaminants found on the site would include zinc oxide, oil, grease, volatile organic compounds (VOCs), and heavy metals such as lead and cadmium [6]. These metals were discovered at levels hazardous to human health and this site contaminated the nearby lake, SLL, wetlands, soils, groundwater, and surface water. Initially, Chemetco fulfilled a removal of the contamination within the area as per the 1997 IEPA, and the site officially shut down

in October of 2001. The Chemetco site was then placed on the NPL in 2010 and was therefore an established Superfund site. The area is still going through a preliminary stage of risk assessment and choosing which site remediation method is best for the community and stakeholders [7]. The remediation technologies considered would include landfilling and soil extraction of toxic equipment, phytoremediation, and biosimulation near the wetlands or areas of ecological importance, in situ or ex situ soil washing, and vitrification for the severe areas of contamination.

The SDGs that are directly applicable to the case study include 3,13,14,15, as seen in Table 2. These SDGs are directly related to this case study due to how the USEPA is impacting the environment, life on land, water and helping with climate change through their site remediation of the toxic contaminants in the area. This not only promotes environmental justice but also helps build the partnership and effort to remediate future Superfund sites. When determining the applicability of SDGs, the boundary of application was a range of 1–15 miles surrounding the Chemetco site in Hartford, Illinois. This is limited to the direct contact of the contaminants with the surrounding wetlands and tributary SLL, therefore the spread enabled by the water stream is not considered. The SDGs that are indirectly applicable to the case study would include 6, 8, 11, 16, and 17, because they are addressed in the aftermath of remedial completion. For example, the pursuit of the cleanup process expresses the government's advancement toward environmental justice and implementing mandatory cleanup to contaminated sites, reflecting SDG 16. In September of 2013, Paradigm Minerals and Environmental Services LLC (Paradigm) was approved to begin a Superfund removal action. Paradigm is the trustee and potential purchaser of the land. Therefore, this reflects SDG 17. SDG 6 is indirectly applicable because the remediation of this site would deter the contamination of groundwater in the area, thus providing clean water and sanitation. This case study is indirectly applicable to SDGs 8 and 11 because the process will provide jobs during and after the remediation. The aftermath of the process will contribute to a more sustainable community. The SDGs that do not apply to the site include 1, 2, 4, 5, 7, 12, as seen in Table 2. These SDGs are not applicable because they are not addressing poverty or hunger, gender equalities, the education system, energy, or production/consumption. Overall, this case study is an ongoing investigation to see which site remediation is the most applicable for the stakeholders and community residents.

2.4 Case Study 4: Chicago, Illinois

Case study 4 focuses on the recommendation of the Indian Ridge Marsh, which was formerly an industrialized wetland site located in the south side of Chicago, Illinois [8]. The contaminants identified include pesticides, volatile organic compounds (VOCs), polycyclic aromatic hydrocarbons (PAHs), heavy metals, and petroleum hydrocarbons. All the contaminants found threaten human health and where are all found in the soil, sediments, surface, and groundwater in the former wetland. The wetland was considered of ecological importance due to how the site was a former

prairie and wetlands ecosystem as well as how endangered species of birds still use the area as their home. These considerations were essential factors in choosing the site remediation technology. The recommended site remediation technology would include in situ phytoremediation with native species of plants and microorganisms' biosimulation [9]. It was determined that a passive remediation technology method was desired to minimize damage to the area. This would reduce the disturbance to the ecosystem while cleaning the area at the same time. However, it would increase the time for remediation compared to the traditional methods. The plants used would include trees such as willow, poplars, and cottonwood due to their long root systems to filter out the contaminants from the water table as well as their growth rates.

The SDGs directly applicable to the case study if the remediation was done would include 13, 14, 15. SDG 13 is climate action, SDG 14 is life below water, and SDG 15 is life on land. These SDGS received a 4 and 5 on the scale, as seen in Table 2, due to how they are directly related to this case study by impacting the environment, life on land, water, and helping with climate change. This type of remediation is actively cleaning the soil to help facilitate the growth of the native species of wetland fauna to remove the toxins from the land as well as helping filter out the water. Through these remediation efforts, the endangered species of birds can thrive in their new setting and help against climate change by promoting biodiversity and green technology. These plants used in phytoremediation will remove the toxic pollutants and reduce the carbon footprint by helping remove $C0_2$ or other greenhouse gases from the atmosphere.

The boundary of the applicability of the SDGs would be limited to the south side of Chicago. This includes the residents who live in a 5–10 mile radius of the Indian Ridge marsh. The SDGs that are indirectly applicable to the case study would include 2, 3, 4, 6, 12, 16, 17. SDG 3 can be defined as good health and well-being, SDG 4 is quality education, SDG 6 is clean water and sanitation, SDG 16 is peace, justice, and strong institutions, and SDG 17 is partnerships for the goals. The Indian marsh ridge helps with the zero hunger SDG 2 by allowing fishing in the lake, allowing the residents food in the summer months. The case study promotes good health and well-being by cleaning up the contaminants that are hazardous to human health and helping the health of the animals in the wetland. This allows people to visit the site and promotes a healthy environment through exercise with hiking trails. The education aspect also applies in the case study. Throughout the Indian Ridge Marsh, some informational billboards and signs inform the public about the history and the local ecosystem covering SDG 4. The plants used in phytoremediation also help with cleaning water; however, it is not complete sanitation of the water for human consumption benefits the surrounding aquatic species which covers SDG 6. SDG 12, which is responsible for human consumption and production, is covered by managing and reducing the waste of the chemicals present in the marsh to acceptable levels through remediation. Furthermore, the reduction of these chemicals as well as stopping the site from producing these chemicals helps add to the initiative of responsible human consumption.

The site also promotes environmental justice by fixing the land destroyed by former industries through remediation, which covers SDG 16. The case study also

adds to the effort of the Great Lakes initiative to help improve the land area and partnerships between governmental bodies to improve brownfield or contaminated sites which covers SDG 17. Overall, while these SDGs are not highly ranked, it can be stated that they are indirectly applicable to the case study, which is why they were given ratings between 2–3, as seen in Table 2.

These SDGs that do not apply to the case study include 1, 5, 7. These SGDs do not apply due to how it does not directly or indirectly impact the poverty in the south side of Chicago, which fails SGD 1. SDG 5 does not apply due to how the case study does not help gender equality in the workforce or in other areas. Furthermore, the case does not go over clean energy because it does not use clean power or have any green structures, SDGs 7, respectively. It should be noted that this article is a recommendation on the steps that should be taken, and the results are only predictions of why these steps are recommended to be done on the site. Overall, this case study is an example of how site remediation technology is selected and the applicable in site remediation methods to help fix an industrialized wetland. Below is the collective list of Sustainable Development Goals applicable to each of the case study using the scale 1–5.

3 Trends and Technologies

After the analysis of the four case studies, the results showed some common trends among Sustainable Development Goals that were commonly met across some or all case studies. Beginning with the SDGs that were most applicable to all case studies were SDG 12—responsible consumption and production, and SDG 15—life on land. These are from the nature of site remediation directly cleaning the land from contaminants. Regardless of the technology used in the remediation, there will be a reduction in contaminants which relates to sustainability by improving the environment. There were some Sustainable Development Goals that were not applicable to any of the case studies being evaluated. These include SDG 1—no poverty and SDG 5—gender equality. The case studies did not address any of these SDGs to any capacity as these goals tend to be more legislative. There are still ways that site remediation can incorporate these SDGs. To better apply SDG 1, sites can build a sort of civil infrastructure, such as a levee or solar/wind farm, that increases a community's resilience to climate, economic, social, or environmental disasters. For SDG 5, the site can be used to build commercial buildings that support companies to help bridge the gap in gender equality or schools/universities that create more opportunities for women in education. Another SDG that had very low applicability was SDG 7—affordable and clean energy. This SDG ranked low in these four case studies despite alternative energies becoming very common in all corners of engineering. With the rapid increase in alternative energies usage, site remediation should look to implementing alternative energies when using various remediation technologies. Further, inclusion of clean energy to site remediation can be turning remediated sites into solar or wind farms if the site allows.

Various technologies are better at addressing some of the SDGs than others and trends among case studies using these technologies allowed for a clear comparison of each. Phytoremediation is a remediation technology used in two of our case studies. It is considered to be one of the greenest and most sustainable remediation methods as it contributes greatly to the ecosystem in the area it is implemented. While reducing the contamination of the site, phytoremediation also contributes to air, soil, and water quality as well as increasing biodiversity and community inclusion. As seen in Table 2, case studies 2 and 4, the phytoremediation cases, were shown to cover more SDGs and were shown to be more applicable to SDGs such as 2 and 11. Due to its variety of benefits other than contamination reduction, phytoremediation is one of the site remediation methods that naturally applies to more SDGs than other standard remediation technologies due to how it 'is a passive, in situ, and minimally invasive method.

4 Challenges and Barriers

The challenges and barriers that site remediation faces toward the full application of the Sustainable Development Goals include variables relating to economic, political, and social challenges. Many laws play a role of inhibiting the application of some SDGs to certain areas where remediation may be occurring. The nature of site remediation practices will inherently cover some SDGs but not others, as seen in the case studies presented. However, there must be incentive and an initiative given to apply all the SDGs using site remediation. Some economic challenges include lack of economic incentives, high costs for construction, and costs of maintenance.

These economic challenges can influence the current policy makers political affiliation and views, as well as current regulations and laws that can prohibit the usage of the remediated land going that can further the application of SDGs. This includes certain zoning laws and EPA regulations which can dictate whether the land can be used for commercial, residential, or mixed purposes. Often these laws will restrict the construction of buildings such as schools, businesses, and nature reserves that would help achieve many of the SDGs. Political challenges might include local, state, and federal officials supporting or challenging the site remediation and the future of the land usage. This political barrier can come in the form of lobbying from specific companies, influential individuals, or community activists who can dictate the application of SDGs to their needs.

Furthermore, specific states as well as countries have various laws regulating site remediation, land development, and economic subsidies which all play a role into the application of the SDGs using site remediation. Social challenges can include systemic racism toward specific minorities and communities which often get less funding for specific projects such as brownfield sites or food deserts. Time is also another challenge due to how long-certain site remediation technologies take and how long the site will be developed depending on the requirements. Through these lists of challenges, it can be determined that although site remediation covers many

aspects that contribute to SDGs, there are many challenges that it faces when trying to apply the goals in their entirety. Covering all SDGs is important but may not be practical to focus on in site remediation due to increased cost and effort. Although site remediation faces challenges when dealing with SDGs relating to social and political aspects, it is possible for all the SDGs to be addressed. Overall, site remediation can be applied to all of the SDGs if needed but doing so may not be optimal. Standard site remediation practices are still great contributors to the SDGs and is a field that is focusing on implementing sustainable practices.

5 Conclusion

Sustainable Development Goals set by the United Nations are essential for more significant equitable development around the world. Through achieving these goals, more people will have access to better education, more food, and successful futures. Site remediation is essential today, as the past industries have left contaminated sites that need proper restoration. In recent years, site remediation has implemented many sustainability practices that naturally contribute to the Sustainable Development Goals. In doing this, site remediation is an industry-leading way in green and sustainable practices. By examining the case studies presented, it can be seen the critical role of sustainability in site remediation. The level of sustainability, a site remediation project can achieve can be noted by seeing how the Sustainable Development Goals apply to the project. While not all of the SDGs applied to the four case studies, the potential for all SDGs to be used will depend on the variables that affect site remediation, such as politics, economics, and societal needs. If these factors are addressed, and each SDG is planned to be fulfilled, site remediation can integrate the Sustainable Development Goals to help directly contribute to the United Nations sustainability plan.

References

1. Sustainability (2021) United nations-academic impact. https://www.un.org/en/academic-impact/sustainability. Last accessed 18 November 2021
2. Sustainable Development (2021) UNESCO. https://en.unesco.org/themes/education-sustainable-development/what-is-esd/sd. Last accessed 18 November 2021
3. Sharma HD, Reddy KR (2004) Geoenvironmental engineering: site remediation, waste containment, and emerging waste management technologies. John Wiley & Sons, New Jersey
4. Foley RW, Wiek A, Kay B, Rushforth R (2017) Ideal and reality of multi-stakeholder collaboration on sustainability problems: a case study on a large-scale industrial contamination in Phoenix, Arizona. Sustain Sci 12(1):123–136
5. Nissim WG, Labrecque M (2021) Reclamation of urban brownfields through phytoremediation: implications for building sustainable and resilient towns. Urban For Urban Greening 65:127364
6. EPA, Environmental Protection Agency (2021). https://www.epa.gov/enforcement/case-summary-settlement-reached-chemetco-superfund-site. Last accessed 22 November 2021

7. Fact sheet 1 (2021) Illinois Environmental Protection Agency. https://www2.illinois.gov/epa/topics/community-relations/sites/chemetco/Pages/fact-sheet-1.aspx. Last accessed 22 November 2021
8. Indian Ridge Marsh (2021) Chicago District, U.S. army corps of engineers, https://www.lrc.usace.army.mil/Missions/Civil-Works-Projects/Indian-Ridge-Marsh. Last accessed 22 November 2021
9. Yargicoglu EN, Reddy KR (2013) Green and sustainable remediation of contaminated Indian Ridge marsh site in Chicago, USA. In: Manassero et al (eds) Proceedings of Coupled Phenomena in Environmental Geotechnics (CPEG). Taylor & Francis Group, London

Sustainable In-Ground Permeable Reactive Filter for the Treatment of Urban Stormwater Runoff

Alesia Fiocca, Andrew Barbeau, Alesia Payasok, Fatimah Yousef, Jyoti K. Chetri, and Krishna R. Reddy

Abstract Lake Michigan and the various beaches throughout Chicago have a long history of surface water contamination issues due to the impermeable landscapes and nonpoint source pollution associated with dense urban environment. During rain events, urban stormwater runoff can collect and concentrate pollutants that are then mobilized to surface waters within the watershed. Pollutants of concern include suspended solids, nutrients, organic chemicals like non-aqueous phase liquids or oils, polycyclic aromatic hydrocarbons, heavy metals, and bacteria. Stormwater management tools such as detention ponds and green infrastructure (bioswales, permeable pavements) are not or may not be practical in urban environments due to limited space and functionality of these tools. The City of Chicago currently must run same day testing for urban beaches to give swimmers notice of potential health risks and beach closures due to elevated E. Coli levels. In-ground reactive stormwater filters might be a viable solution to treat the contamination associated with urban runoff and improve the water quality of Chicago's beaches. Utilizing three pre-tested filter designs from a previous study, the sustainability of each is evaluated and ranked using a triple bottom line (environmental, economic, and social) sustainability assessment within a conceptual site model in Chicago including contaminant removal efficiency.

Keywords Sustainability · In-ground reactive filter · Stormwater

1 Introduction and Project Background

Urban stormwater runoff sometimes poses serious problems to beaches when the stormwater mixed with contaminants finds its way into the beach waters [1]. Beach closures are issued every year repeatedly due to the presence of disease-causing microorganisms and other pollutants in beach water that can harm public health [1]. Impermeable surfaces combined with industrial and human activity create nonpoint sources that are difficult to provide water quality treatment. Urban stormwater

A. Fiocca · A. Barbeau · A. Payasok · F. Yousef · J. K. Chetri · K. R. Reddy (✉)
Department of Civil, Materials, and Environmental Engineering, University of Illinois at Chicago, 842 West Taylor Street, Chicago, IL 60607, USA
e-mail: kreddy@uic.edu

© The Author(s), under exclusive license to Springer Nature Singapore Pte Ltd. 2023

K. R. Reddy et al. (eds.), *Recent Advances in Sustainable Environment*, Lecture Notes in Civil Engineering 285, https://doi.org/10.1007/978-981-19-5077-3_22

Table 1 Synthetic stormwater concentrations

Contaminants	Average range in actual stormwater (mg/L)	Synthetic stormwater concentration (mg/L)
Total phosphorous	0.01–7.3	0.5
Total nitrogen	0.07–16.0	1
Cadmium	0.00005–13.73	30
Chromium	0.001–2.30	5
Copper	0.00006–1.41	5
Lead	0.00057–26.0	50
Nickel	0.001–49.0	100
Zinc	0.0007–22.0	50
Naphthalene	0.000036–0.0023	0.01
Phenanthrene	0.000045–0.01	0.01
Benzo(a)pyrene	0.0000025–0.01	0.01
E. Coli	12–4700	10,000
Total suspended solids	1–36,200	150

management is especially difficult because Chicago, like many other big cities, was not designed with these things in mind. We are now beginning to move in the direction of green infrastructure with recent developments of green roofs, rain gardens, the deep tunnel, permeable pavement, and now possibly in-ground filters. The objective of an in-ground permeable reactive filter strategically located directly at the beach is to remove harmful pollutants before they reach the water.

In Chicago, large-scale laboratory test and field pilot scale demonstrations were conducted recently to evaluate the performance of permeable mixed-media filter systems. Column studies were performed to determine the removal efficiencies of contaminants using different permeable filter medium [1]. Diverse types of contaminants with variable concentrations in actual stormwater were used to develop synthetic stormwater concentrations (mg/L) and are shown in Table 1. Studies included testing different filter materials with different absorption capacity to remove pollutants from synthetic runoff. A pilot scale in-ground filter was constructed at Rainbow Beach in Chicago, IL.

1.1 Technical Design Alternative

The three filter mix designs shown to be effective were: (1) calcite, sand, zeolite (C + S + Z), (2) calcite, sand, iron fillings (C + S + FeO), and (3) calcite, sand, zeolite, and iron filings (C + S + Z + FeO). Figure 1 shows each filter material's efficiency for

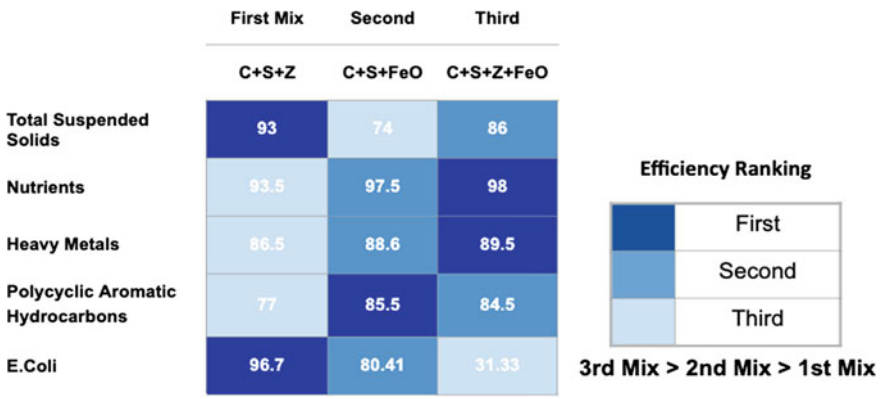

Fig. 1 Ranking of filter media's contaminant removal efficiencies

the removal of total suspended solids, nutrients, heavy metals, polycyclic aromatic hydrocarbons, and E-Coli. C + S + Z + FeO is the best choice for removing nutrients and heavy metals. This study utilized the results of these filter tests along with technical aspects of the Rainbow Beach pilot-test to evaluate the sustainability of a conceptual design at Oak Street Beach in Chicago. The environmental, economic, and social sustainability assessments will be considered using the triple bottom line approach and condensed into a single score index using MIVES (Sect. 3.4) to weight and rank the components. This model will help stakeholders make decisions in future using real data and a comprehensive method of analysis.

2 Methodology

2.1 Goal and Scope

The goals are to: (1) design an in-ground reactive filter unit with a mixed-media filter system that will prevent pollutants (mostly nonpoint source) from reaching the surface waters of Lake Michigan at Ohio Street Beach, Chicago, IL, USA; (2) identify the most sustainable mixed-media filter for urban stormwater runoff; and (3) evaluate the sustainability of the filters based on triple bottom line sustainability assessment (environmental, economic, and social aspects). In terms of water quality, the efficiency of the filter media during storm events and overall contaminant removal will be evaluated by looking at urban stormwater runoff versus lake water quality standards. The focus will be kept local by following Lake Michigan and Chicago's rules and regulations including pricing and sourcing materials and labor locally.

Fig. 2 Drainage area

2.2 Study Area

The watershed area at Ohio Street Beach in Chicago, IL includes two parks: The Jane Addams Memorial Park and the Olive Park Woodlands. Both parks partially drain into the beach. An online publicly available elevation tool [2] was used to determine trends in the topography to calculate the drainage area. Since the elevation of the parks peaks right down the center, the assumption is that anything outside of the drainage area shown in Fig. 2 would drain to the stormwater conveyance systems on Grand Avenue, Chicago.

2.3 Technical Design of the Filter

The in-ground tank made of concrete includes an access gate for maintenance, three different mixed-media filters, one primary inlet, and four small outflow pipes placed under the filter materials [3–5]. The design materials include filter materials (calcite, zeolite, sand, and iron filings), pre-cast concrete, construction equipment, fluid cement (mortar) for the foundation and setting the drainage inlet, 200 feet of polyethylene slotted inlet pipe to capture the watershed runoff, a cast iron grate for maintenance, CA-7 limestone for the drainage layer, CA-6 limestone for the subbase of the filter bed, and 28 feet of perforated polyethylene pipe for outflow drainage. A typical design for an in-ground reactive filter is included in shown in Fig. 3.

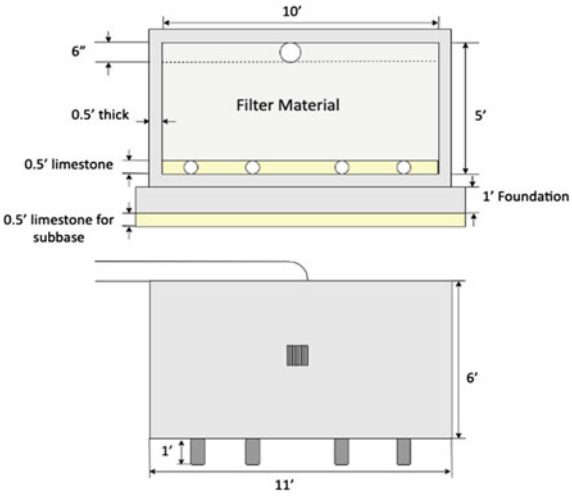

Fig. 3 Overall filter design

The technical design of an in-ground filter starts with the rational method for peak flow which includes rainfall intensity, values for permeable versus impermeable areas, and the total drainage or watershed area. The permeable surfaces refer to the grass and the sand at the top of the beach. Rainfall intensity in Chicago is 8.57 inches for a 24-h, 100-year storm. The area is about 3.78 acres for the watershed area. The peak flow is 0.4 cubic feet per second, and a factor of safety of 1.25 was included, making the peak flow equal to 0.5 cubic feet per second, which is used for filter capacity design in this study.

A 100-year 24-h storm event in Northeastern Illinois was assumed to get the rainfall intensity (Bulletin 70). The tank design was assumed to be based on the lowest hydraulic conductivity with calcite and sand being the limiting factors, each had a hydraulic conductivity (K) of 0.30 cm/s. The velocity through the filter was 0.00984 ft/s. The surface area for the filter material was found to be 50 square feet.

The design surface area was 5 × 10 ft, with a wall thickness of 0.5 ft. The hydraulic calculations for the filters include three different mixture ratios. Mixture #1 includes calcite, zeolite, and sand at a ratio of 1:1:1. Mixture #2 includes calcite, sand, and iron fillings at a ratio of 1:1:2. Mixture #3 includes calcite, zeolite, sand, and iron fillings at a ratio of 1:1:1:2. The bulk densities vary from 1.1 to 2.5 g/cm^3. The characteristics of each specific filter material are listed in Table 2.

A filter depth of 4 feet was chosen, so the volume needed was 200 cubic feet. This volume with an additional 1 foot of depth for the tank to store water before filtration gives the interior dimensions of 5 × 10 × 5 ft. The wall thickness is 0.5 ft gives an exterior dimension of 6 × 11 × 6 ft, as shown in Fig. 4. The concrete volume needed is 146 ft^3, with a corresponding weight of 10.6 tons. The collection pipe is a slotted inlet pipe that is 6-inches by 200 feet, however, we also added 20 feet for contingency. Our outflow corrugated perforated PE pipes are 4-inches in diameter and placed at the bottom of the filter at a length of 7 feet, coming out to a total of 28

Table 2 Physical and chemical properties of filter media

Filter material	Effective particle size, D_{10} (mm)	Average particle size, D50 (mm)	Dry density (g/cm^3)	Organic content (%)	pH	Oxidation–reduction potential (mV)	Electrical conductivity	Hydraulic conductivity (cm/s)
Calcite	0.5	0.7	1.6	0.0	9.0	−117.1	0.01	0.3
Zeolite	0.6	1.2	1.0	6.8	7.8	−58.0	0.10	0.4
Sand	0.5	0.6	1.8	0.3	8.4	−95.3	0.02	0.3
Iron filings	0.5	0.9	2.3	0.0	5.3	87.6	30.5	0.6

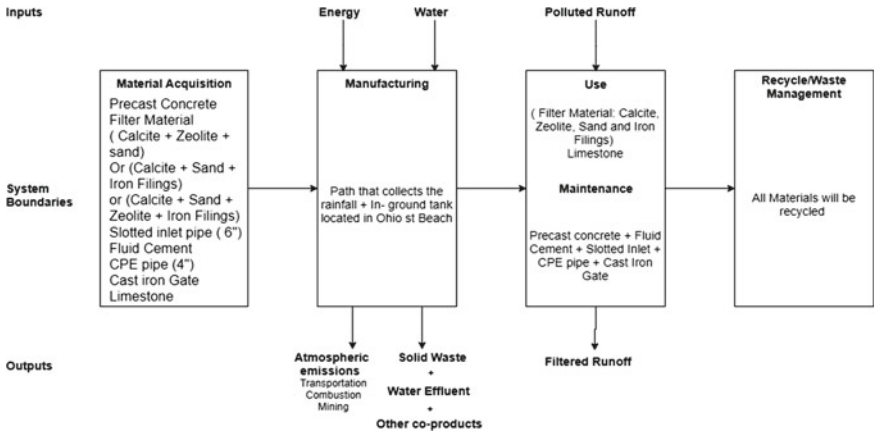

Fig. 4 System boundaries for LCA

ft. The perforated polyethylene pipes were designed to collect runoff further down the beach.

2.4 Life Cycle Assessment

Life cycle assessments (LCAs) are generally from cradle to grave and include major stages during the lifetime of the product [6]. Typical stages are raw material acquisition, manufacturing/production, operation/maintenance/use, and recycling/disposal. Transportation is often an overarching component affecting the other four stages and broadly incorporated in the assessment. When applying triple bottom line sustainability environmental, economic and social aspects are evaluated using the LCA approach. Environmental sustainability is addressed by using software such as SimaPro which evaluates the environmental impact of the product, in this case an in-ground reactive filter. Economical LCA aspects include direct cost, indirect cost, and maintenance cost. Social aspects include general social impacts as well as 4 specific social categories; socio-individual, socio-communal, socio-economic, and socio-environmental impacts. Considering the life and operation of the filters was a key component in having a complete picture in the assessment. Stormwater filtration systems constructed with mixed media showed a significant decrease of infiltration capacity after 5–7 years of operation due to the formation of a clogging layer at the surface of the filters, while the lifespan of the materials themselves were 20–35 years with proper maintenance. Hydraulic performance of the system could be recovered by scraping off the surface accumulated particle layer and replacement of the geotextile on periodic bases, approximately every 7 years. Thus, the mixed media must be inspected at least twice annually to determine if the permeability has decreased.

3 Sustainability Assessment

Environmental sustainability of the filter designs was determined using LCA SimaPro 8.0 [7]. The inputs, outputs, and system boundaries of four stages; raw material acquisition, transportation, construction, and maintenance are shown in Fig. 4. The functional unit of an in-ground reactive filter box design was considered to understand the operation and evaluate filter mix options, construction, and maintenance using a lifespan of 20 years. Economic sustainability was determined using standard materials, equipment, and labor from locally sourced vendors and reputable publicly available rates. Transportation was calculated based on mode of transit, fuel consumption, and weight of load. Other indirect and social costs were included using StepWise from SimaPro and the USEPA Social Cost of Carbon. Some costs were not included because they were either negligible or the same across every design. Social sustainability was done using the SSEM tool developed by Reddy et al. [8], and a survey was conducted to assess the social sustainability.

3.1 Environment Sustainability

The goal was to evaluate the environmental impacts of raw material acquisition, transportation, construction, and maintenance of an in-ground reactive filter box. Using the technical design specifications, side-by-side comparisons of the TRACI 2.1 V1.01/US 2008 methodology were run for environmental impact assessment of each filter mix design in order to have quantitative data associated with each design.

The quantitative outputs evaluated were ozone depletion, global warming, smog, acidification, eutrophication, carcinogens, as well as non-carcinogens, respiratory effects, ecotoxicity, and fossil fuel depletion.

3.2 Economic Sustainability

This involves evaluating the impacts of different processes and materials in the life cycle stages on monetary value. This project consisted of generating a cost estimate for the filter bed materials, the construction process costs, equipment and labor, maintenance costs, as well as the three different filter media mixtures, and transportation costs.

The maintenance costs were calculated by assuming that it will occur twice annually to check on the filter material and the tank. 10% contingencies were added to the original maintenance inspections. The maintenance inspection includes filter permeability, cracks, clogged pipes, and potential leakage.

The social cost of carbon was monetized using different monetization techniques: USEPA and StepWise. USEPA technique quantifies the emissions using SimaPro

and was converted into the corresponding costs using USEPA 3% discount rate—42$ per metric ton of CO_2 emissions in the year 2020, the present value of climate change damages. The StepWise technique allows for the full monetization of environmental impacts (expressed in USD 2002 that converted to USD 2020). StepWise is calculating the cost of carbon to be more than two and a half times the prediction of USEPA social cost of carbon.

3.3 Social Sustainability

The social impacts were evaluated using SSEM. Since the difference between design alternatives is only the filter material, the social evaluation mostly will be affected by the site construction and how it will affect the community. Hence, only the filter scenario (remediation) versus no filter (no remediation) was evaluated. This was conducted with the team's opinion as well as 17 peer opinions via a survey. The scoring was +2 for ideal social sustainability, +1 for improved, 0 for no impact or not applicable, −1 for diminished, then −2 for unacceptable. The focus was on the effects of the proposed scenario on quality-of-life issues post-construction, public health and wellness, effect on local businesses and life during construction, and the degree to which the project will improve water quality and/or reduce contaminants.

3.4 Integrated Sustainability Assessment

The overall sustainability of the three mixed-media filter options was assessed with the help of integrated value model for sustainability assessment (MIVES) method involving value functions [9]. For the environmental, the indicators were the impact categories obtained from the LCA. For the economic, the indicators were the various direct and indirect costs associated with the project. For the social, the indicators were the ones defined for the survey.

4 Results and Discussion

4.1 Environmental Sustainability

The final outputs from SimaPro are shown in Figs. 5 and 6. Environmental impact categories as listed in Sect. 3.1 can be seen shown below with respective contributions from each LCA stage. The most environmentally friendly design was filter mix 2. The dark green and dark blue represent the raw material acquisition and typically represent the most negative influence for each indicator. Only the maintenance of

the designs is comparable but is taking into account a 20-year lifespan of operating the system. Ozone depletion is also most heavily influenced by transportation and gas/diesel fuel consumption from combustion engines.

Using the TRACI 2.1 V1.01/US 2008 methodology, filter mix 2 had the best outcomes regarding environmental sustainability. In each and every category, mix design 2 was less impactful than mix designs 1 and 3 as can be seen in Fig. 6. This is mostly due to the use of zeolite. While zeolite is phenomenal at removing E. Coli from contaminated stormwater, the tradeoff is the environmental impacts of mining the resource. While filter mix 3 also uses zeolite, the combination of using all 4 materials somehow reduces the contamination removal efficiency. Since, filter mix 2 is able to adequately reduce concentrations across a broad array of pollutants, and it also uses more environmentally materials in its design.

Some exceptions to the SimaPro model include: components that were the same across all the 3 filter designs, a total account of end of life—recycling and waste management, as well as the net positive impacts of surface water quality improvements. In addition to the quantitative analysis, the impacts of global warming and respiratory health effects to the most negative components of construction the filters all together were also evaluated.

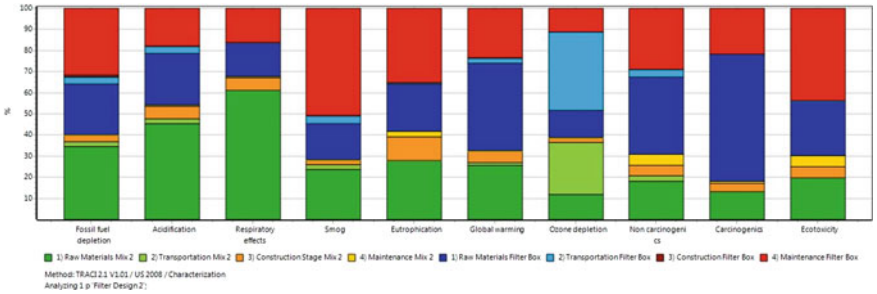

Fig. 5 Stage contributions to the different environmental impacts from TRACI model

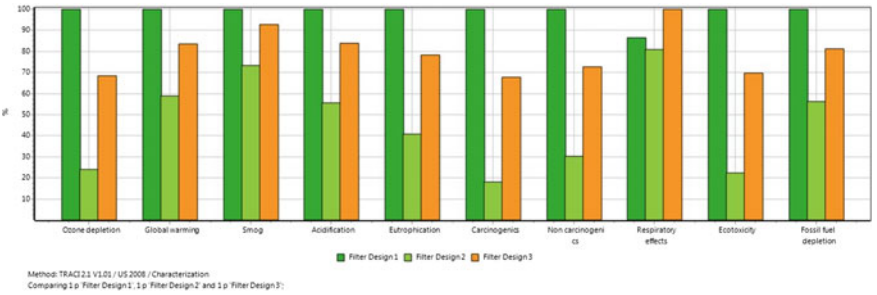

Fig. 6 Comparison of the environmental impacts of the three filter mix designs

4.2 Economic Sustainability

The costs for filter designs 1, 2, and 3 were approximately $44,460, $51,077, and $54,278, respectively. Filter design 1 is the cheapest, and filter design 3 is the most expensive, entirely due to transportation costs of zeolite. The filter material zeolite is sourced from Idaho, and even after checking the environmental impacts had it been sourced locally—there is still not much of a difference due to the invasive materials acquisition and mining process. It is still the most expensive due to the distance, it must be transported—which is not economically sustainable for a filter project. The labor costs included about 80 people at an average of $175 per hour, which came to a total of about $14,000 for each filter unit. The construction costs were also the same for each unit with 19 cubic yards of site work and about $21 per hour for excavation and equipment, making a total of $400. The materials included calcite, zeolite, sand, iron fillings, limestone, pre-cast concrete tank, fluid cement, soil disposal, slotted 6″ pipe, 4″ perforated polyethylene pipes, cast iron grate, excavator, and an aggregate mixer.

The indirect costs were derived as an output via the SimaPro program. An inflation rate of 43% for USD 2002 to 2020 was assumed. Filter design 1's indirect cost was given as $4,840 to $6,923.59. Filter design 2's indirect cost went from $2,720 to $3,890.95, and design 3 went from $4,260 to $6,093.91.

The social costs of carbon were derived from the USEPA [10] and StepWise results. StepWise is calculating the cost of carbon to be more than 2.5 times the prediction of USEPA social cost of carbon. The results are shown in Table 3.

In MIVES, the cost estimates and environmental impacts were weighted for direct cost, maintenance cost, indirect cost, and social cost at weighted values of 60%, 29%, 7%, and 3%, respectively. The direct cost has the highest weight and focuses on design materials, equipment, setup, and installation, as well as transportation and labor. The results for economic assessment showed filter design #1 as the best and most affordable, followed by filter design #2 and filter design #3. The filter mixes #1 has the most effective cost and direct cost. The filter mixes #2 has the most effective indirect cost, which means it has the lowest impact on the environment.

Table 3 Social cost of carbon related to the three filter mixes

Filter mix	Social cost of carbon (USEPA)		
	USEPA (USD 2020)	StepWise (USD 2002)	StepWise (USD 2020)
Filter design #1	1087.80	2070.00	2961.00
Filter design #2	638.40	1220.00	1745.20
Filter design #3	907.20	1730.00	2474.76

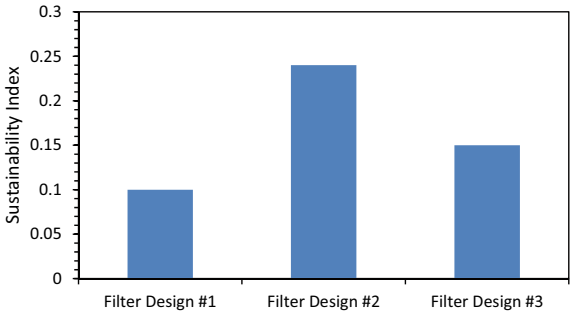

Fig. 7 Sustainability index for three filter designs

4.3 Social Sustainability

The team scored different dimensions of social sustainability as ideal, improved, diminished, or unacceptable. A survey was then sent out to various academic peers to compare the team predictions with a poll opinion. As an overall trend, the social dimension had improved social sustainability with the filter for both our assessment and the survey results. For the socio-institutional dimension, the team results were similar to the survey. For the socio-economic dimension, the 'no filter' option was at a negative score compared to the survey because of a loss of job creation for construction and maintenance. For the socio-environmental dimension, the team results were similar to the survey for the filter option, however, the survey results for no filter came back at a very low score. In the end, having a filter is better for the community than not having a filter to protect the beach from pollutants. The filter had an overall positive impact on social sustainability, whereas no filter had either no impact or a negative impact on social sustainability.

4.4 Integrated Assessment

The final MIVES score or integrated sustainability index for each filter mix is shown in Fig. 7. Equal weightages were given to the three pillars of sustainability: environmental, economic, and social. Filter design #2 appeared to be the most sustainable option among the three filter designs.

5 Conclusions

Using the MIVES, filter design #2 proved to be the most sustainable design. In the environmental assessment, filter design #2 came out to be the most sustainable, followed by filter design #3 and filter design #1, respectively. For the economic

assessment, filter design #1 has the most effective total cost and direct cost, whereas filter design #2 has the most effective indirect cost with the lowest environmental impacts. The social sustainability assessment ranking filter versus no filter conducted through the SSEM found the addition of filter at Ohio Street Beach to be favored over no filter; when coupled with the MIVES analysis, filter design #2 had the preferable social sustainability.

Environmental impacts were most influenced by the raw material acquisition, and finding sustainable sources of materials is a key component to a design with less environmental impacts. The indirect costs of any sort of major civil construction can have more influence than expected. Social and environmental costs can easily be thousands of dollars and are worth considering. Social sustainability is hard to quantify. When possible if the details of a design can be differentiated regarding social impacts to the point that people can accurately assess the design; then, the value of social quantification/statistics is immensely more beneficial in analysis.

References

1. Reddy KR, Kumar G (2017) Permeable reactive filter system for treatment of urban stormwater runoff with mixed pollutants. Geotechnical frontiers, Orlando, FL
2. Topographic Maps (2019) Chicago topographic map, relief map, elevations map. OVH SAS, 2 rue Kellermann, 59100 Roubaix, France. Web. https://en-gb.topographic-map.com/maps/lpjy/Chicago/
3. Reddy KR, Xie T, Dastgheibi S (2013) PAHs removal from urban storm water runoff by different filter materials. J Hazard Toxic Radioact Waste 18(2):04014008
4. Reddy KR, Xie T, Dastgheibi S (2014) Removal of heavy metals from urban stormwater runoff using different filter materials. J Environ Chem Eng 2(1):282–292
5. Reddy KR, Xie T, Dastgheibi S (2014) Mixed-media filter system for removal of multiple contaminants from urban storm water: Large-scale laboratory testing. J Hazard Toxic Radioact Waste 18(3):04014011
6. International Standardization Organization (ISO) (2006) Environmental management—life cycle assessment—principles and framework ISO 14040
7. Pré. SimaPro 8.5 LCA software. Amersfoort, The Netherlands (2018)
8. Reddy KR, Sadasivam BY, Adams JA (2014) Sustainability evaluation matrix (SSEM) to quantify social aspects of sustainable remediation. In: ICSI 2014: Creating infrastructure for a sustainable world, pp 831–841. ASCE
9. Reddy KR, Kumar G (2019) Application of triple bottom line sustainability framework to select remediation method at industrial contaminated site. In: Proceedings of geocongress, ASCE, Reston, VA
10. USEPA (2017) The social cost of carbon. https://19january2017snapshot.epa.gov/climatechange/social-cost-carbon_.html. Accessed 29 Jan 2018

Life Cycle Analysis of Low-volume Rural Hill Roads Using PCR

Akhilesh Nautiyal, Akhilesh Kumar, and Arunava Poddar

Abstract This article presents an approach to forecasting the behavior of pavements in rural hill roads in their overall life cycle and the prediction of its performance throughout their service life. In the present study, two major factors were considered to determine the overall performance of the pavement, i.e., pavement condition ratings and pavement age. Rutting, raveling, cracking, patching, and pothole were the five major defects that have been considered to evaluate the overall condition of the pavement. Linear regression analysis, polynomial regression analysis, and exponential regression analysis were adopted for evaluation purposes. Among chosen three approaches, the linear regression analysis approach gives better results while predicting a relationship between pavement age and pavement condition rating (PCR), which depicts a scientific relationship to predict the remaining service life of pavements in rural roads in hilly regions. The validation of the study was done based on a conducted case study of 18 low-volume rural hill roads constructed under a government scheme in the Hamirpur district of Himachal Pradesh, India.

Keywords Pavement maintenance · Linear regression · Hill road · Regression analysis · Himachal Pradesh

A. Nautiyal
Department of Civil Engineering, National Institute of Technology, Himachal Pradesh, Hamirpur 177005, India

A. Kumar (✉)
Department of Civil Engineering, Chitkara University Institute of Engineering & Technology, Chitkara University, Punjab 140401, India
e-mail: akhileshsharma54@gmail.com

A. Poddar
Department of Civil Engineering, Shoolini University, Himachal Pradesh, Solan 173229, India

© The Author(s), under exclusive license to Springer Nature Singapore Pte Ltd. 2023

K. R. Reddy et al. (eds.), *Recent Advances in Sustainable Environment*, Lecture Notes in Civil Engineering 285, https://doi.org/10.1007/978-981-19-5077-3_23

1 Introduction

The major objective of most transportation systems is to provide the rapid, safe, and convenient movement of goods and people from one spot to the next [1]. A good and effective transportation system enhances the economic activity and development of any country [2]. The presence of a huge network of roads throughout the globe makes roads a primary and most important mode of transportation. Roads are also said to be a basic infrastructural need in the development of any country [3]. Therefore, the life cycle assessment of pavements becomes necessary for effective movement of traffic on it throughout its service life. Subsequently, the role of a good pavement maintenance and management system (PMMS) becomes very important. A good PMMS covers all the necessary aspects after pavement construction, which includes pavement maintenance, pavement evaluation, and pavement research [4].

Life cycle assessment (LCA) of pavement is a process that covers all the features of pavement performance throughout its service life. LCA includes assessment of pavements at regular time intervals and the prediction of their performance. Remaining service life (RSL) prediction is a major factor for the LCA of any pavement. RSL is the time from the present to the time to which a pavement can perform adequately with the effective movement of traffic on it.

Zimmerman et al. [5] discuss the various issues integrating pavement maintenance and management. From the literature survey, the researchers conclude that various factors needed to be considered in selecting preventive-maintenance treatments: type and extent of distress, climate, cost of treatment, availability of qualified contractors, time of the year of placement, facility down-time, traffic loading, existing pavement type, expected life, availability of high-quality materials, pavement noise, and surface friction. Combination of distress types as part of its condition-survey procedures is sealed versus unsealed cracks, crack width (crack severity), raveling or weathering, friction, shoving, flushing (bleeding), and oxidation. Positive effects on pavement performance by preventive-maintenance treatments are delay the onset of cracking, improve pavement ride, improve surface friction, and reduce moisture infiltration. Chan et al. [6] in Tennessee investigate the effects of asphalt pavement conditions on traffic accidents on 4 urban interstates using negative binomial regression models, accident history database (AHD), RD models, IRI models, and PSI models. This study utilized the Tennessee pavement management system (PMS) and accident history database (AHD) to investigate the relationship between accident frequency and pavement distress variables. The various factors considered in this study are Rut depth (RD), international roughness index (IRI), present serviceability index (PSI).

1.1 Service Life Expansion

The service life expansion depicts the advantage from a pavement maintenance activity in the form of an extra number of years the pavement segment will perform

at or better than the threshold value. The threshold value could likewise be the states of the pavement segment at the hour of the pavement maintenance. In this case, pavement maintenance life is the benefit. The major distinction between the two is the threshold value and the amount of time over which the pavement condition is anticipated. Both strategies are examined in more detail below.

2 Remaining Service Life

Pavement service life can be characterized as the projected number of years between construction or rehabilitation of pavement to when the pavement segment arrives at a given condition or threshold limit [7]. Around then, the pavement segment is normally exposed to restoration or preservation activities [8]. The service life of a pavement is characterized as the period from the completion (or opening to traffic) of pavement to the state of the pavement being considered unsuitable, and recovery/replacement is required. Conventionally, the pavement service life prediction model was classified as either deterministic or probabilistic model. Maximum of the literature is based on this classification framework [9–11]. The performance of pavement is used as a random variable in probabilistic models.

The two most widely used strategies for the determination of pavement maintenance benefits are (1) the expansion in pavement service life because of a given maintenance technique or (2) the estimation of the area between the pavement performance curve and a given threshold value. The life extension method plays a significant role in stretching the pavement service life. Selecting a pavement maintenance technique and time with the most minimal expense to profit proportion could be considered "optimal". Nowadays, much statistical software performs very accurately, and all types of regression analysis and probabilistic models or curves can be established [12–16]. In any case, it would be beneficial particularly at the network level, for pavement construction and maintenance planners to figure out all essential data like traffic, maintenance, and rehabilitation type, performance information for a large number of pavement segments from the opening of pavements to traffic to present date. Furthermore, organizations cannot give a wide range of information that the prediction models required, for example, environmental conditions and non-destructive testing information, which are firmly identified with the expectation of pavement structural performance.

3 Study Area

Verification of the overall study was done by applying it to a case study of a total of 18 roads constructed under the PMGSY scheme of the government of India. All roads fall in the same district, i.e., Hamirpur of Himachal Pradesh state in India. As we know that worst climatic conditions increase the rate of decay of pavements w.r.t.

the good climatic condition of place but in our case, it can be neglected because all of these roads are within 20 km square area of road network, so there is not much change in climatic conditions for pavement deterioration rates. These roads are village link roads which connect villages to its nearest town, so there is a very little volume of traffic on these pavements. The temperature of the Hamirpur district varies between a maximum of 40 °C in hot humid summers and a minimum of up to 3 °C in cold winters. IRC 82 2015 [17] codal provisions of practice for maintenance of bituminous road surface are used to evaluate the distress criteria and evaluation. Manual visual surveys were conducted on all 18 roads and the measurements of each distress, and its severity was done by keeping in mind all the provisions as suggested by IRC 82 2015. A digitized map of the study area developed in ArcGIS is shown below as Fig. 1.

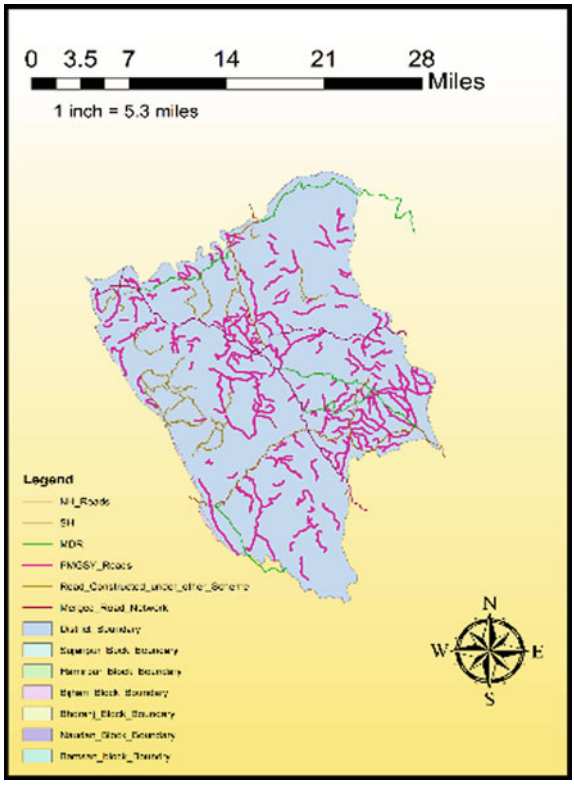

Fig. 1 Digitized road map of the study area

4 Methodology

4.1 Design Life (DL)

Design life is the total number of years for which the pavement can withstand a serviceable condition without reaching its threshold value.

4.2 Pavement Life (PL)

It is defined as an actual number of years a pavement is in serviceable condition, i.e., from the year of pavement construction to the year of pavement failure. Therefore, pavement life includes many cycles of pavement maintenance and rehabilitation activities.

4.3 Remaining Service Life (RSL)

The remaining service life is defined as the total number of years from today to the day when the pavement reaches to pre-specified distress threshold. For a long pavement weighted average, RSL of all pavement sections is considered as an RSL of pavement. When a pavement is newly constructed, its RSL is equal to its design life, and when a defect is treated with adequate maintenance techniques, its RSL is equal to the design life of the applied maintenance technique. If the condition of a pavement section reaches its threshold value, its RSL becomes zero. RSL value can never be negative. Road ID, name, length, construction year, overlay year, survey year, and pavement age assessment are shown in Table 1.

5 Pavement Condition Data

Pavement condition data include the collection of various types of distress that are acting as triggering factors for pavement decay. In this study, cracking, pothole, patching, rutting, and raveling are selected as five major distress commonly found on the low-volume rural roads. The percentage area and severity levels of this distress were collected for each pavement. Based on its severity levels, each distress was categorized into three major categories, i.e., low, medium, and high-severity levels. IRC82:2015 [16] guidelines were used to define the category of severity levels of each distress. Various studies have adopted different methodologies in the literature [17, 18]. The percentage of various distress for all pavements in the network has been shown in Fig. 2.

Table 1 Evaluation of pavement age

Road ID	Name	Length	Construction year	Overlay year	Survey year	Pavement age
HL022	Link road to village Anu Khurd	1.6	2004	2018	2017	13
HL036	Tuklehra Laleen road	2.1	2013	2013	2017	4
HL038	Link road to village Lingwin	2.2	2002	2016	2017	15
HL043	Daruhi to Barnwar road	1.7	2005	2017	2017	12
HL044	Matani to Sastar road	2.0	2015	2015	2017	2
HL045	Chamarari Khagal	7.0	2000	2018	2017	17
SL028	Lumbri Rangar road	6.5	2003	2018	2017	14
SL033	Link road to village Sapahal	1.7	2014	2014	2017	3
SL034	Link road to village Duhak	6.3	2006	2016	2017	11
SL040	Bhater Graoru Dadwalan road	6.5	2002	2014	2017	15
SL048	Jateru Bharmar road	5.3	2005	2012	2017	12
SL050	Link road to village Meharpura	1	2013	2013	2017	4
SL053	Matial Tikkar road	2	2017	2017	2017	0
NL027	Sassan to Putrial	2.5	2014	2014	2017	3
NL064	Janglu Salyan to Bhadrun Bassi	2.0	2014	2017	2017	3
NL092	Patta Jalari to Maan	2.0	2013	2013	2017	4
NL100	Chaurun to Batali Road	2.5	2003	2018	2017	14
NL101	Jalari Tillu road	2.5	2000	2018	2017	17

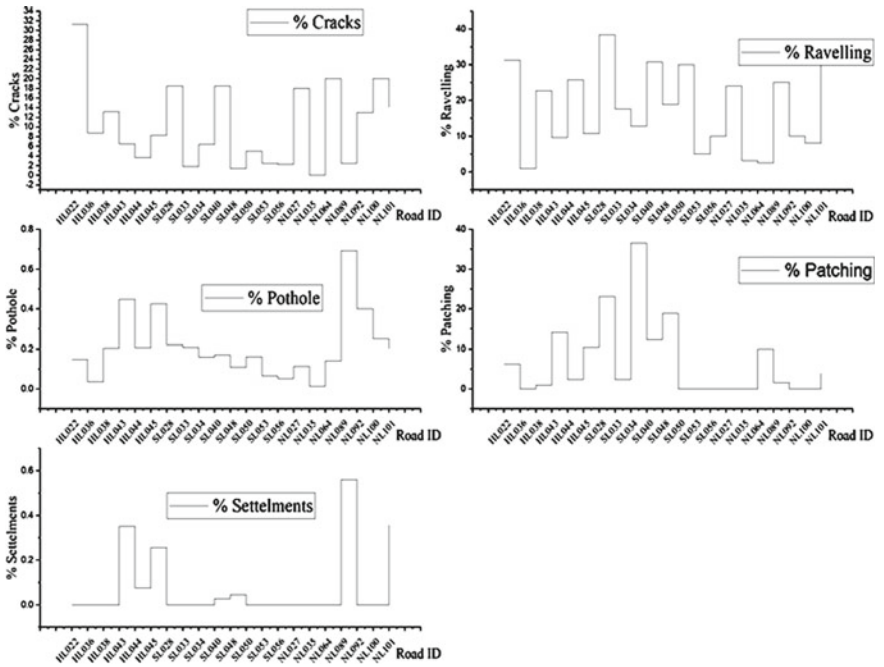

Fig. 2 Percentage of various distress for all pavements in the network

Since the value of present pavement life alone cannot replicate the serviceability of any pavement section, and the design life of a pavement ought to be founded on certain rules which depend on various criteria and threshold values defined by many states/countries. Therefore, it is not sensible to simply utilize the number of years a pavement was in service before rehabilitation as the value of pavement performance life. Pavement performance prediction needs to be considered very seriously for developing a good pavement life expectancy model. International roughness index (IRI), present serviceability index (PSI), pavement condition rating (PCR), and traffic volume are extensively used pavement performance prediction indices. Hence, comparison between performance indices and threshold values referred to pavement types, and conditions can help in the estimation of appropriate pavement life.

After collection of each distress, we need to convert all distress into a single performance index that will give a common equivalent index value for a pavement. In this study, the pavement condition rating (PCR) of all pavements is determined considering all collected distresses data by converting into a single PCR value. IRC 82 2015 [17] guidelines were used to determine the PCR value of all pavements in this study. The PCR values of all roads are shown in Fig. 3.

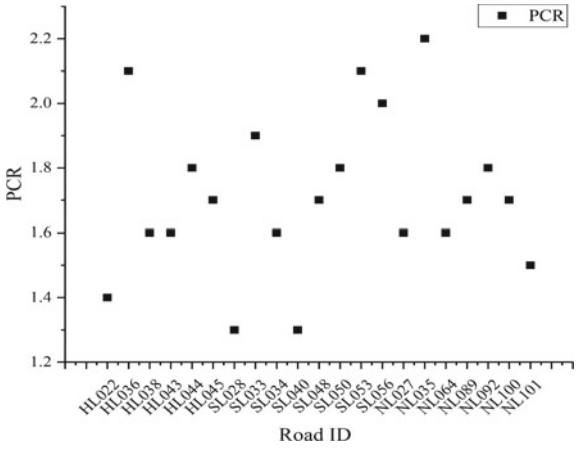

Fig. 3 Pavement condition rating for each pavement in the network

6 Estimation of RSL

Various distress indices are combined into a single equivalent unit of distress index for the evaluation of the RSL of the pavement network. The distress data variation over time is also very handy in RSL calculations and verifications. The computation of RSL is done employing the following steps.

Firstly, a manual pavement condition survey is conducted on each pavement. This survey includes the collection of various pavement distress data, for this percentage area of each distress on pavement section, is determined. After collection of pavement distress data, it is converted into a single equivalent unit, i.e., *PCR*. PCR value depicts its present condition. Now, determination of pavement age is done considering various factors. Now when we have evaluated both PCR value and pavement age of each pavement, then various regression plots are plotted between these two. These regression plots give the RSL value of pavement networks.

6.1 Life Cycle Analysis of Pavements

Forecasting of RSL is very helpful for LCA of pavements. In the present study, linear regression analysis was used to develop a relationship between pavement age and its PCR value. Pavement age is considered as the total duration (in years) that pavement has served till today without major maintenance and rehabilitation on it. If the overlay is laid over a pavement after the initial date of construction, then the date of overlay is said to be a new data of construction of pavements.

7 Result and Discussion

The study was conducted using three types of regression model analysis, i.e., linear regression analysis, polynomial regression analysis, and exponential regression analysis. These were applied to each pavement data for evaluation purposes. All the regression analyzes were performed using regression tool in Microsoft Excel software. The regression equations for each road are shown in Table 2.

Table 2 Regression equations for each road

Road ID	Exponential	Linear	Polynomial
HL022	$y = 3e^{-0.059x}$	$y = -0.1231x + 3$	$y = -0.1231x + 3$
HL036	$y = 3e^{-0.089x}$	$y = -0.225x + 3$	$y = -0.225x + 3$
HL038	$y = 3e^{-0.042x}$	$y = -0.0933x + 3$	$y = -0.0933x + 3$
HL043	$y = 3e^{-0.052x}$	$y = -0.1167x + 3$	$y = -0.1167x + 3$
HL044	$y = 3e^{-0.255x}$	$y = -0.6x + 3$	$y = -0.6x + 3$
HL045	$y = 3e^{-0.033x}$	$y = -0.0765x + 3$	$y = -0.0765x + 3$
SL028	$y = 3e^{-0.06x}$	$y = -0.1214x + 3$	$y = -0.1214x + 3$
SL033	$y = 3e^{-0.152x}$	$y = -0.3667x + 3$	$y = -0.3667x + 3$
SL034	$y = 3e^{-0.057x}$	$y = -0.1273x + 3$	$y = -0.1273x + 3$
SL040	$y = 3e^{-0.056x}$	$y = -0.1133x + 3$	$y = -0.1133x + 3$
SL048	$y = 3e^{-0.047x}$	$y = -0.1083x + 3$	$y = -0.1083x + 3$
SL050	$y = 3e^{-0.128x}$	$y = -0.3x + 3$	$y = -0.3x + 3$
SL056	$y = 3e^{-0.135x}$	$y = -0.3333x + 3$	$y = -0.3333x +$ 3implePara>
NL027	$y = 3e^{-0.21x}$	$y = -0.4667x + 3$	$y = -0.4667x + 3$
NL064	$y = 3e^{-0.21x}$	$y = -0.4667x + 3$	$y = -0.4667x + 3$
NL092	$y = 3e^{-0.128x}$	$y = -0.3x + 3$	$y = -0.3x + 3$
NL100	$y = 3e^{-0.041x}$	$y = -0.0929x + 3$	$y = -0.0929x + 3$
NL101	$y = 3e^{-0.041x}$	$y = -0.0882x + 3$	$y = -0.0882x + 3$

* In Table, "y" denotes PCR value, and "x" denotes pavement age

Table 3 Pavement age, PCR, and RSL of all roads

Road ID	Overall pavement life (years)	Served life/pavement age (years)	PCR	RSL (years)
HL022	16.24	13	1.4	3.24
HL036	8.88	4	2.1	4.88
HL038	21.43	15	1.6	6.43
HL043	17.13	12	1.6	5.13
HL044	3.33	2	1.8	1.33
HL045	26.14	17	1.7	9.14
SL028	16.47	14	1.3	2.47
SL033	5.45	3	1.9	2.45
SL034	15.71	11	1.6	4.71
SL040	17.65	15	1.3	2.65
SL048	18.46	12	1.7	6.46
SL050	6.67	4	1.8	2.67
SL053	6.006	0	2.1	6.006
NL027	4.28	3	1.6	1.28
NL064	4.28	3	1.6	1.28
NL092	6.67	4	1.8	2.67
NL100	21.52	14	1.7	7.52
NL101	22.67	17	1.5	5.67

PCR value 1 or below is assumed to be the threshold PCR value. When a pavement reaches PCR value 1, it is not in a serviceable condition and needs immediate reconstruction. So, the design life of pavement in terms of PCR value is the number of years from the initial construction of pavement when it is having PCR value 3 to its degradation of PCR value till 1. Pavement age, PCR, and RSL of all roads are shown in Table 3.

For checking of all the functions, pavement condition data surveys of these roads were done for the next 4 years, and pavement condition rating was evaluated each year. It was seen in actual trends that linear regression analysis gives the most accurate results w.r.t other two regression analyzes for pavement service life prediction.

8 Conclusions

In the study, three types of regression approaches were applied, i.e., linear regression analysis, polynomial regression analysis, and exponential regression analysis to each collected pavement data. RSL depicts the present condition of pavement and the rate of deterioration. The study proves that RSL may be utilized to (i) determine

the weighted average RSL or the life span of the pavement network. (ii) Figure out the percent of the pavements in each RSL category and decide the appropriation of the pavement's comparative with these categories. Uniform dispersion infers consistent workload starting with one year then onto the next. (iii) Determination of the overall condition of the pavement network, i.e., percentage of good, fair, and poor pavement sections. (iv) Determination of the advantages of the pavement protection and recovery programs by breaking down their effect on the weighted average RSL of the overall network. (v) Set up an ideal strategy to expand the pavement life span within the maximum available budget. (vi) Improve correspondence with officials concerning pavement construction and maintenance needs. (vii) Measure the effect of different budget levels on the soundness of the pavements. (viii) Permit the arranging of a yearly adjusted program. (ix) RSL is very handy in the setup of quality control checks on pavement defects.

Acknowledgements The authors would like to extend many thanks to the Department of Civil Engineering, National Institute of Technology (NIT), Hamirpur, Himachal Pradesh, India for their help in offering us the resources for carrying out the current study.

Grant Support Details The present research did not receive any financial support.

Conflict of Interest The authors declare that there is not any conflict of interest regarding the publication of this manuscript. In addition, the ethical issues including plagiarism, informed consent, misconduct, data fabrication and/or falsification, double publication and/or submission, and redundancy have been completely observed by the authors.

References

1. Nautiyal A, Sharma S (2021) J Clean Prod 127649. https://doi.org/10.1016/j.jclepro.2021.127649
2. Pereira P, Pais J (2017) J Traffic Transp Eng (Engl Ed) 4(4):316–346
3. Byzyka J, Rahman M, Chamberlain DA (2017) J Traffic Transp Eng (Engl Ed) 4(4):360–371
4. Nautiyal A, Sharma S (2021). J Qual Maint Eng. https://doi.org/10.1108/JQME-12-2019-0111
5. Zimmerman KA, Peshkin DG (2004) Transp Res Rec 1889(1):13–20
6. Chan CY, Huang B, Yan X, Richards S (2010) J Adv Transp 44(3):150–161
7. Nautiyal A, Sharma S (2019) Compusoft 8(7):3261–3268. https://ijact.joae.org/index.php/ijact/article/view/981
8. Raab C, Camargo I, Partl MN (2017) J Traffic Transp Eng (Engl Ed) 4(4):388–394
9. Fwa TF, Chan WT, Hoque KZ (2000) J Transp Eng 126(5):367–374
10. Kumari S, Poddar A, Kumar N (2021) Model. Earth Syst Environ. https://doi.org/10.1007/s40808-021-01181-w
11. Kumar A, Sharma RK, Bansal VK (2018) Environ Earth Sci 77:719. https://doi.org/10.1007/s12665-018-7896-2
12. Kumar A, Sharma RK, Bansal VK (2019) Innov Infrastruct Solut 4:28. https://doi.org/10.1007/s41062-019-0215-2
13. Kumar A, Sharma RK, Mehta BS (2020) J Earth Syst Sci 129:135. https://doi.org/10.1007/s12040-020-01396-y
14. Kumar A, Sharma RK, Bansal VK (2019) Lecture notes in civil engineering, vol 21. Springer, Cham. https://doi.org/10.1007/978-3-030-02707-0_9

15. Kumar A (2021) Lambert Academic Publishing
16. IRC:82-2015 (2015) Code of practice for maintenance of bituminous road surface. Indian Road Congress, New Delhi
17. Nautiyal A, Kumar A, Poddar A, Parajuli N (2021) J Achiev Mater Manuf Eng 109(1). https://doi.org/10.5604/01.3001.0015.5857
18. Nautiyal A, Sharma S (2019) Compusoft 8(7):3261–3268

Influence of Exchangeable Sodium and Calcium Contents on Consistency Limits of Expansive Soils: A Critical Review

Peddireddy Sreekanth Reddy, Bijayananda Mohanty, and Bendadi Hanumantha Rao

Abstract Owing to the difficulty in interpretation or non-availability of costly equipment, numerous researchers attempted to predict swelling properties with easily measured consistency limits. Swelling behaviour is primarily depended on associated mineralogy, exchangeable cations (sodium, Na, and calcium, Ca) specific surface area, and their quantity. Past studies, especially, conducted on bentonite attributed Na and Ca contents are one of the principal elements for expansive soils exhibiting significant volume change characteristics. In comparison with bentonite, contents of these cations are lesser quantity in natural soils. Moreover, studies report an inherent variation in these cations contents with the origin. Though, numerous studies highlight the effects of these cations on consistency properties, delineating their exact influence on these properties has not attracted greater attention. In this paper, an attempt is made to critically review the influence of Na and Ca contents on consistency limits. The objective of the paper is to establish relationships between exchangeable cations and consistency limits of expansive clays. For the study purpose, pertinent data are collected from the literature, and a series of correlations are developed between Na and Ca contents versus consistency limits. The study reveals that the variation in cation content of soil influences the thickness of diffuse double layer results in the variation of consistency limits. This is due to the forces of attraction and repulsion are affected by the valence and size of exchangeable cations adhered on the clay mineral surfaces. It is found from the interpretation of results that Na has superior influence over Ca. The results help the reader to have in-depth knowledge on exchangeable cations (Na^+ and Ca^{2+}) and their influence on the geotechnical performance of soils.

Keywords Expansive soils · Exchangeable cations · Consistency limits

P. S. Reddy · B. Mohanty
Department of Civil Engineering, NIT Mizoram, Aizawl 796012, India

B. H. Rao (✉)
School of Infrastructure, IIT Bhubaneswar, Argul 752050, India
e-mail: bhrao@iitbbs.ac.in

© The Author(s), under exclusive license to Springer Nature Singapore Pte Ltd. 2023

K. R. Reddy et al. (eds.), *Recent Advances in Sustainable Environment*, Lecture Notes in Civil Engineering 285, https://doi.org/10.1007/978-981-19-5077-3_24

1 Introduction

Expansive soils rolled out across the world and posing challenging issues in practical applications till date. It undergoes volume change in contact with the moisture content, which imparts distress in the structure, differential settlements, failure in pavements, etc. [1]. In this context, numerous studies predicted the behaviour of expansive soils from geotechnical properties and established relationships [2, 3]. Though the relationships were well established, it is little suspected to adopt as the behaviour is controlled by chemical contents. Amongst different parameters, cation exchange capacity (CEC) is the most promising factor to be considered in the case of expansive soils. CEC is the exchange of cations on the surface of clay particles with the contacted pore fluid [4]. Studies reported that the CEC can affect the consistency and swelling behaviour of expansive soils [5, 6]. But most of the studies available in the literature are confined to the quantification of exchangeable cations only, not in establishing the relationships. Cation exchange is a surface phenomenon and generally happens in soils comprise of clay minerals and organic content [7]. Several studies employed different methods and determined CEC depend on the soil condition. The methods include ammonium acetate [8], $BaCl_2$ compulsive exchange [7], methylene blue test [9], US EPA 9081 [10], Kappen's method [11], etc. Amongst all, $BaCl_2$ compulsive exchange is recommended to be accurate for field conditions [7, 12]. The saturation of samples with index cation is the common and primary task amongst the methods mentioned above. The results obtained from the analysis in turn depend on this cation nature, the pH of soils as well as extraction solution [13]. The accurate prediction of chemical contents can fetch an advantage in the indirect estimation of consistency limits and swelling behaviour of soils.

CEC on the higher side imparts maximum consistency and swelling properties. In order to mitigate that, numerous studies treated expansive soils with Ca-based additives. When treated with the additive, Na^+ will be replaced with Ca^{2+} results in a waning of diffuse double layer thickness. As stabilization is a complex chemical reaction between the soils and additive, knowledge on chemical contents is necessary. In this regard, the chemical contents play a key role in the selection of additive contents for controlling higher consistency and swelling behaviour. Studied reported the overdosage of additive with the current techniques, which poses a negative impact on the performance as well as environment.

2 Objective of the Study

Several studies reported that chemical contents influence consistency behaviour of expansive soils, but limited to the statements. As the chemical contents are the triggering parameter behind the changes in thickness of diffuse double layer in turn effects consistency limits. Numerous studies quantified the chemical contents in

exchangeable form by resorting to different methods, but fail to establish relationships, which offer a concrete understanding on different properties. Also, these fetch an advantage in the selection of additive based on exact influence. In order to address the same, the chemical contents in exchangeable form and their relevant consistency limits were collected from the literature. The objective of current paper is to establish relationships between exchangeable cations and consistency limits of expansive clays and to define the impact of exchangeable cations on consistency limits.

3 Results and Discussion

Chemical contents such as sodium, Na and calcium, Ca can influence the consistency behaviour of the expansive soils. To portray the same chemical contents in exchangeable form has been collected from the literature comprise of both bentonite soils (BS) and natural expansive soils (NES), and plots were drawn against consistency limits (i.e. liquid limit, w_L, and plasticity index, w_{PI}) as depicted in Figs. 1, 2 and 3. Figures 1 and 2 depict the influence of Na and Ca in exchangeable form on consistency limits. From the figures, it can be observed that the chemical contents can vary as a function of location. It can be observed from Figs. 1 and 2 that both w_L and w_{PI} increased linearly with Na_{CEC}. This is due to the fact that Na content possesses higher ionization energies and is attracted towards the clay surface than Ca and poses higher consistency limits. In addition, a linear fit was employed, and empirical equations are obtained with an R^2 value of (i) 0.85 for Na_{CEC} versus w_L (ii) 0.84 for Na_{CEC} versus w_{PI}, which indicates a good degree of relationship. Further, the empirical equations displayed in Figs. 1a and 2a can be used for the prediction of w_L and w_{PI} from Na in exchangeable form. On the other hand, there is no definite trends for both w_L and w_{PI} with the Ca content in exchangeable form.

Also, there is a huge scatter of data in the case of Figs. 1b and 2b conveying no relationship exists between these parameters and is not useful for determining the consistency limits of expansive soils. From the close observation of Figs. 1a and 2a, $w_L < 100\%$ and $w_{PI} < 60\%$ belongs to NES and beyond it corresponds to BS. Generally, NES is dominated with Ca rather than Na, which might be the reason behind constant trend beyond 40 meq/100 g of Ca_{CEC} in Figs. 1b and 2b. The dominance of Ca replaces the Na content descends the thickness of diffuse double layer is the reason behind constant trend.

Soil is composite of different chemical contents rather than a single element/ion. The presence of multiple elements/ions can influence one over the other, which makes it difficult to draw a conclusion that whose effect is superior. In order to reduce that effect, the ratio of Ca and Na contents is considered. Figure 3 depicts the influence of Ca/Na ratio in exchangeable form on w_L and w_{PI}. From the figure, it can be noticed that there is no significant relationship between these parameters. Compared to the ratio, individual form of Na_{CEC} is a useful parameter for predicting the w_L and w_{PI} of

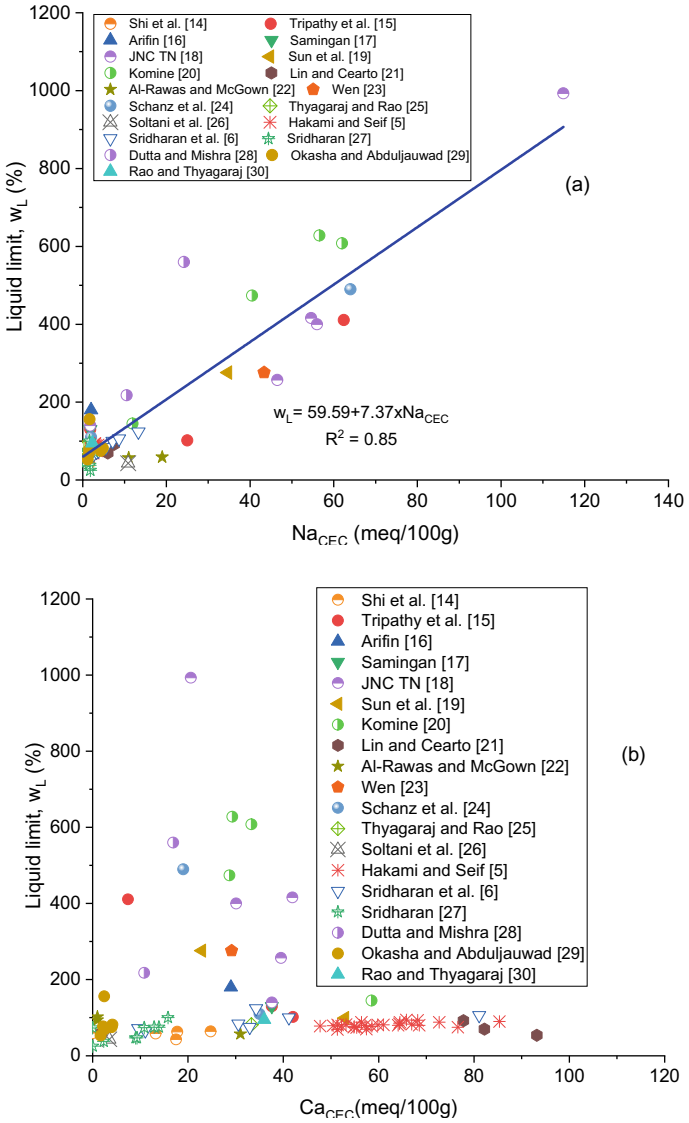

Fig. 1 Influence of **a** Na in exchangeable form, **b** Ca in exchangeable form on liquid limit of expansive soils

expansive soils. Also, Ca/Na ratio less than unity corresponds to Na dominated soils with high w_L and w_{PI}. Beyond the unity belongs to Ca dominated soils, generally of NES.

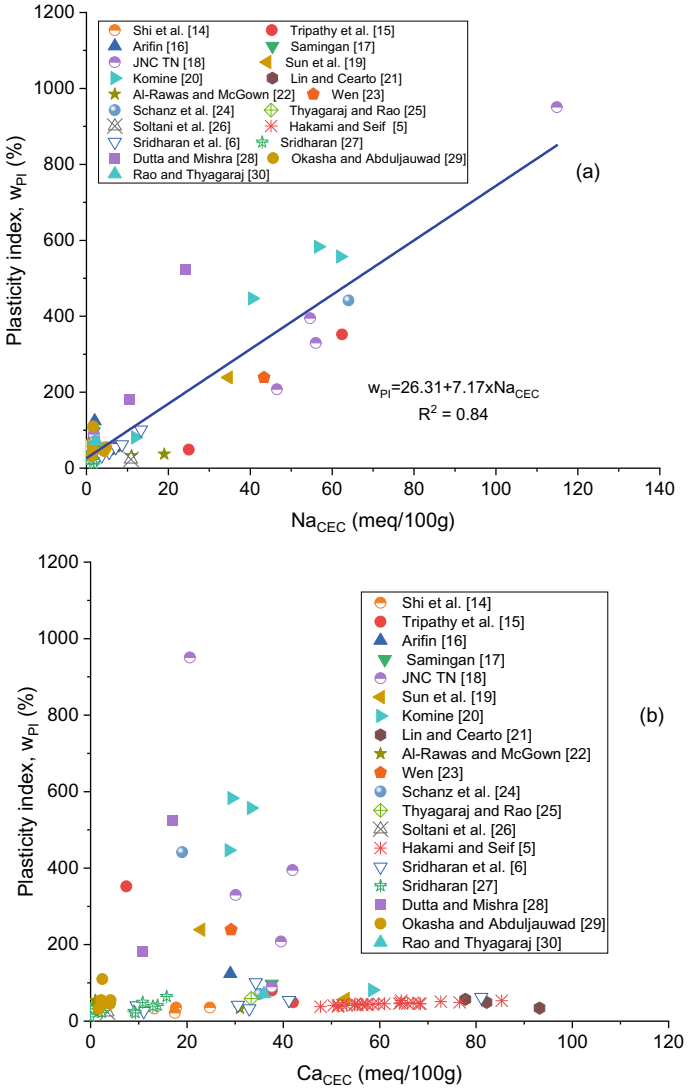

Fig. 2 Influence of **a** Na in exchangeable form, **b** Ca in exchangeable form on plasticity index of expansive soils

4 Conclusions

The current study investigates the influence of exchangeable cations on the consistency limits of expansive soils. For the same, the pertinent literature data have been collected, and relationships are established. From the observations, the below conclusion are drawn:

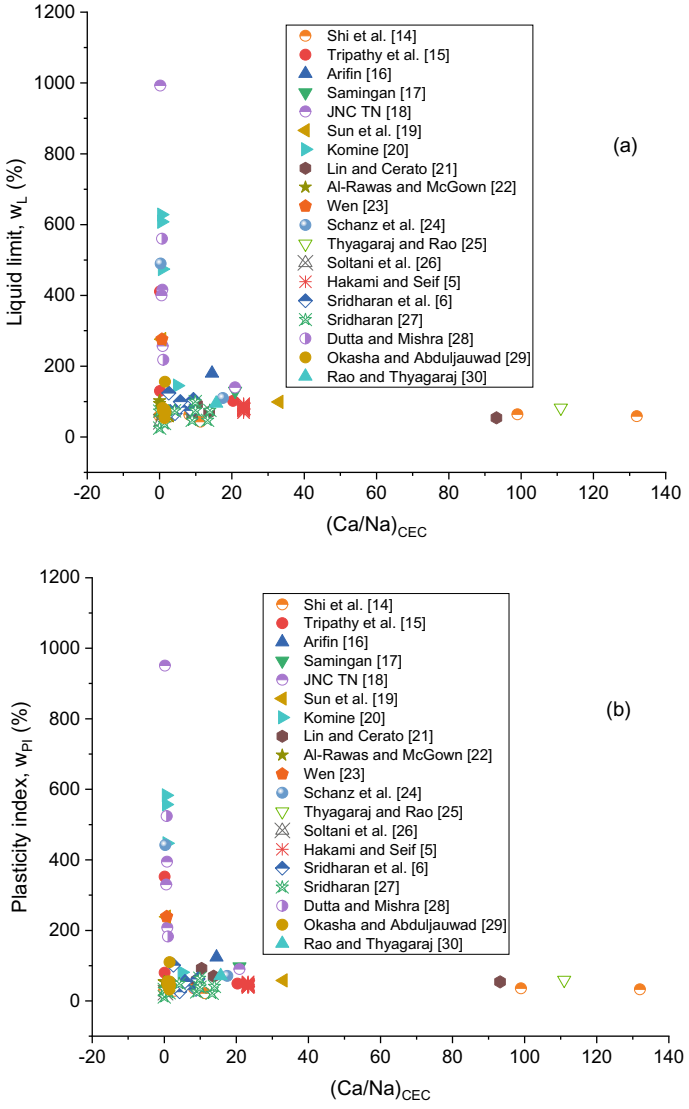

Fig. 3 Influence of Ca/Na ratio of exchangeable form on **a** liquid limit, **b** plasticity index

1. The chemical contents in exchangeable form vary as a function of soil sample location.
2. Both w_L and w_{PI} were found to be increased linearly with $Na_{CEC,}$ and exhibited a good relationship with an R^2 value of 0.85 and 0.84, respectively.
3. It is found that the $w_L < 100\%$ and $w_{PI} < 60\%$ belong to NES and beyond it corresponds to BS.

4. Compared to the ratio, the individual form of Na_{CEC} is a useful parameter for predicting the w_L and w_{PI} of expansive soils.

References

1. Chen FH (1988) Foundations on expansive soils, 2nd edn. Elsevier Science, New York
2. Rao BH, Venkataramana K, Singh DN (2011) Studies on the determination of swelling properties of soils from suction measurements. Can Geotech J 48(3):375–387
3. Erzin Y, Erol O (2007) Swell pressure prediction by suction methods. Eng Geol 92(3–4):133–145
4. Chen FH (1975) Foundations on expansive soils. Elsevier Science, Amsterdam, The Netherlands
5. Hakami BA, Seif ESSA (2019) Expansive potentiality of sabkha soils of Rabigh Lagoon, Saudi Arabia: a case study. Arab J Geosci 12(4):107
6. Sridharan A, Rao AS, Sivapullaiah PV (1986) Swelling pressure of clays. Geotech Test J 9(1):24–33
7. Chapman HD (1965) Cation-exchange capacity. In: Black CA (ed) Methods of soil analysis—chemical and microbiological properties. Agronomy 9:891–901
8. Gillman GP, Sumpter EA (1986) Modification to the compulsive exchange method for measuring exchange characteristics of soils. Aust J Soil Res 24:61–66
9. Cokca E, Birand A (1993) Determination of cation exchange capacity of clayey soils by the methylene blue test. Geotech Test J 16(4):518–524
10. US EPA Method 9081 (1986) Cation-exchange capacity of soils (sodium acetate)
11. Kappen H (1929) Bodenazidität: Nach agrikulturchemischen gesichtspunkten dargestellt. Springer, Berlin
12. Rhoades JD (1982) Cation exchange capacity. In: Page AL (ed) Methods of soil analysis. Part 2: Chemical and microbiological properties. Agronomy 9:149–157
13. Jaremko D, Kalembasa D (2014) A comparison of methods for the determination of cation exchange capacity of soils. Ecol Chem Eng 21(3):487–498
14. Shi B, Jiang H, Liu Z, Fang HY (2002) Engineering geological characteristics of expansive soils in China. Eng Geol 67(1–2):63–71
15. Tripathy S, Sridharan A, Schanz T (2004) Swelling pressures of compacted bentonites from diffuse double layer theory. Can Geotech J 41(3):437–450
16. Arifin YF (2008) Thermo-hydro-mechanical behavior of compacted bentonite-sand mixtures: an experimental study. Doktor – Ingenieur thesis, Bauhaus-University, Weimar
17. Samingan AS (2005) An experimental study on hydro-mechanical characteristics of compacted bentonite-sand mixtures. Doktor – Ingenieur thesis, Bauhaus-University, Weimar
18. JNC TN (2000) Project to establish the scientific and technical basis for HLW disposal in Japan. Japan Nuclear Cycle Development Institute, H12, JNC TN1410 2000-003
19. Sun D, Sun W, Fang L (2014) Swelling characteristics of Gaomiaozi bentonite and its prediction. J Rock Mech Geotech Eng 6(2):113–118
20. Komine H (2004) Simplified evaluation for swelling characteristics of bentonites. Eng Geol 71(3–4):265–279
21. Lin B, Cerato AB (2012) Prediction of expansive soil swelling based on four micro-scale properties. Bull Eng Geol Environ 71(1):71–78
22. Al-Rawas AA, McGown A (1999) Microstructure of Omani expansive soils. Can Geotech J 36(2):272–290
23. Wen Z (2006) Physical property of China's buffer material for high-level radioactive waste repositories. Yanshilixue Yu Gongcheng Xuebao/Chin J Rock Mech Eng 25(4):794–800
24. Schanz T, Nguyen-Tuan L, Datcheva M (2013) A column experiment to study the thermo-hydro-mechanical behaviour of expansive soils. Rock Mech Rock Eng 46(6):1287–1301

25. Thyagaraj T, Rao SM (2013) Osmotic swelling and osmotic consolidation behaviour of compacted expansive clay. Geotech Geol Eng 31(2):435–445
26. Soltani A, Taheri A, Khatibi M, Estabragh AR (2017) Swelling potential of a stabilized expansive soil: a comparative experimental study. Geotech Geol Eng 35(4):1717–1744
27. Sridharan A (1991) Engineering behaviour of clays—a fundamental approach. Indian Geotech J 21:1–136
28. Dutta J, Mishra AK (2016) Influence of the presence of heavy metals on the behaviour of bentonites. Environ Earth Sci 75(11):993
29. Okasha TM, Abduljauwad SN (1992) Expansive soil in Al-Madinah, Saudi Arabia. Appl Clay Sci 7(4):271–289
30. Rao SM, Thyagaraj T (2003) Lime slurry stabilisation of an expansive soil. Proc Inst Civ Eng Geotech Eng 156(3):139–146

CFD Analysis for Wind Flow Characteristics of Varying Cross-Section Tall Building Using ANSYS

Bhagya Jayant, Ark Rukhaiyar, Kunal Dahiya, and Ritu Raj

Abstract With growing population, urbanization, and industrialization, land availability is depreciating; demanding for vertical designing of structures to accommodate more population in limited available space. Therefore, designing of tall buildings has found its significance in recent times. Tall buildings are designed majorly for its serviceability and sensitivity. Tall buildings are slender structures which are prone to lateral buckling due to lateral loads like wind and earthquake. Therefore, to prevent structural failure that can be potentially hazardous to the mankind and environment, more emphasis on sensitivity analysis of tall buildings is made in recent times. In the present study, another such sensitivity analysis for determining the wind flow characteristics is performed using ANSYS: CFX mode (analysis of systems in computational fluid dynamics program) on an isolated G + 64 tall building (192 m in height) having varying cross sections ("square" and "plus"; exactly above the "square" for 96 m height each). Wind of magnitude 10 m/s is incident at wind angles 0° and 90°. Pressure contours obtained on analysis indicate that for incident wind angles 0° and 90°, all lateral faces of the proposed design model show similar pressure impact. Plotting of vertical and horizontal streamlines indicates the phenomenon of flow separation and flow reattachment. Horizontal streamlines indicate the occurrence of vortex formation in the wake region of the building for incident wind angles, 0° and 90°. This study aims to investigate and strengthen the acceptance of complex shapes like plus cross section in the designing of tall buildings by adopting a CFD approach.

Keywords Tall building · CFD · ANSYS · Pressure contours · Velocity streamlines

B. Jayant · A. Rukhaiyar · K. Dahiya · R. Raj (✉)
Department of Civil Engineering, Delhi Technological University, Delhi, India
e-mail: rituraj@dtu.ac.in

B. Jayant
e-mail: bhagyajayant_2k18ce032@dtu.ac.in

A. Rukhaiyar
e-mail: arkrukhaiyar_2k18ce025@dtu.ac.in

K. Dahiya
e-mail: kunaldahiya_2k18ce052@dtu.ac.in

© The Author(s), under exclusive license to Springer Nature Singapore Pte Ltd. 2023

K. R. Reddy et al. (eds.), *Recent Advances in Sustainable Environment*, Lecture Notes in Civil Engineering 285, https://doi.org/10.1007/978-981-19-5077-3_25

1 Introduction

As the population density sores, the optimization of space for better accommodation has led to advancements in engineering; proposing revisions in acceptable heights across the world. Heights provide space, therefore, tall buildings or high-rise buildings are key solution to this urban crawl. Although tall buildings do not have a single definition, it may be defined as to be considerably higher than the surrounding buildings or its proportion is slender enough to give the appearance of tall building (Council on tall Buildings and Urban Habitat, 2016) or a building having more than 11 stories (The City of Burlington, 2017). As tall buildings solve the problem of space unavailability, it has benefits of business growth as more lease is charged for more floors on the same piece of land, economically profitable as less land for construction, provides space for public transport, provides bountiful experience to the habitants, etc. However, it imposes drawbacks such as air pollution leading to poor visibility and possible structural damage due to effect of winds on it and due to nearby cluster of tall buildings. Other minor problems include maintenance and repairing issues, inaccessibility to fair share of municipal services like water, electricity and sewage, social congestion, delay in emergency services like fire exits, etc.

In tall buildings, according to Connors (2003) [16], lateral stiffness against wind loads predominates over the structural strength. Earlier, symmetrical shapes were necessary for building optimized, serviceable, and stable G + 11 designs as per Harman (2017) [13]. However, Moon (2018) [11] proved that tapered (twisted and irregular) forms in tall buildings produced superior structural performance in terms of resisting static and dynamic responses, saves limited natural resources to be used as building material for a more sustainable and architecturally effective structure satisfying different design requirements. Ding F. et al. (2020) [5] used aerodynamic shape tailoring or implementing a dynamic façade to counter the effects of changing wind environment. Their findings offer enormous potential in using AI agents and modern morphing technologies to mitigate wind-induced effects, thus controlling their impact on the performance and safety of civil infrastructures. Karimimoshaver, M. et al. [9] proposed a model using visual analysis approach to locate tall buildings based on technical and visual criteria from fuzzy visibility results. Fuka, V. et al. (2018) [12] compared the scalar dispersion in an array of uniform height buildings with flow and dispersion in an array with another building three times its height and found that the former showed more sensitivity to small changes in wind direction when the approaching flow faced the longest face of the building. This implied that great care needs to be taken in arranging the wind tunnel model so as to produce a symmetric flow field. It also implies that long time averaging is necessary in LES to converge to nearly symmetric mean fields. This paper aims to fill the research gap of less investigation on sensitivity analysis for determining wind flow characteristic of varying cross-section tall building (G + 64) using ANSYS by adopting a computational fluid dynamics (CFD) approach.

For analysis of wind flow characteristics of tall buildings, wind speed and wind direction are governing factors. Nicola et al. (2017) [14] in their study of the impact

of wind loads on slender buildings investigated the strength and design criteria and found the potential of damping enhancement to lessen the design loads and vibrations, thereby providing optimal balance among resilience, serviceability, and sustainability requirements. Other methods like gust factor methods and wind tunnel methods are also used to find out the shear and deflection of tall buildings and have conforming results. It was observed that the gust factor method or dynamic-wind method by IS 875—2015 provided more factor of safety, however, the wind tunnel gave more accurate results complying closer with actual site conditions as per Er, Deshmukh, Pranil et al. (2020) [10].

2 Methodology

In this study, integral scale is a more relevant factor than the turbulence intensity for wind–loading simulation of the proposed design model. Thus, computational fluid dynamics technique is utilized to analyze G + 64 tall building having two types of cross sections—square and plus, dimensions of which are as shown in Fig. 2. The results are interpreted in terms of the pressure coefficient values and streamlines obtained for proposed design model called model A. The model is validated with the help of a reference isolated model, called model X which is also a 192 m height model having only "square" as its cross section throughout as shown in Fig. 1. Since, IS 875 (Part III)—2015 gives a range of deflection for pressure coefficient for simple cross-section shapes, therefore, if model X is in agreement with the code, model A will also conform consequently.

Numerical flow simulation is carried out for analysis of model A and model X which were modeled using AutoCAD: 3D modeling (computer-aided design) and analyzed using ANSYS: CFX mode (analysis of system in computational fluid

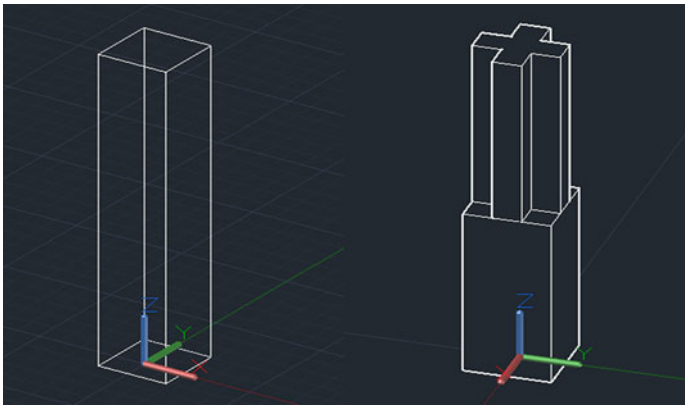

Fig. 1 Model X and model A, respectively

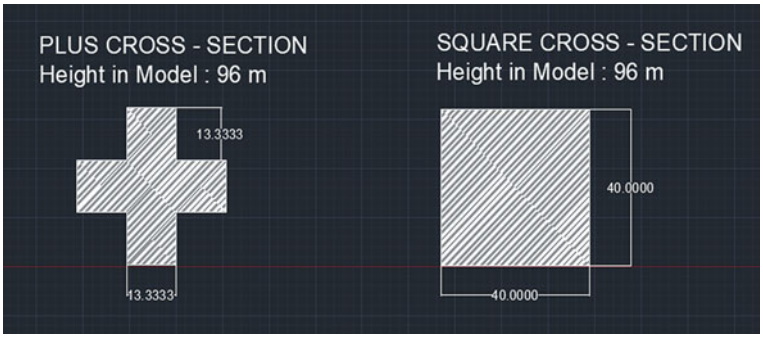

Fig. 2 Types of cross section in model A

dynamics program). It generally involves selection of building shape, selecting the dimension of domain, type, and size of meshing, defining the boundary conditions and flow characteristics, running the simulation, process the output in post CFX, and representation of various results into distinct forms. Therefore, flow behavior of tall building analyzed using ANSYS: CFX mode has 5 broad steps—geometry, meshing, setup, solution, and results. Beginning with the export of the proposed 3D model of tall building (model A) from AutoCAD to ANSYS. A reference isolated model with square section (model X) is also exported in this step for carrying out the validation study. In this *geometry step,* domain is generated as per IS standards. In the next step, *meshing* is performed for the entire domain along with inflation separately for the tall buildings or models. The meshing element is tetrahedral in shape having size of 0.2 m for domain and 0.07 m for models. In the *set-up* step, power law is used for finding out the pressure values for all faces. The program is then run for about an hour before the results are evaluated in the *solution* step. Finally, in the *result* step, pressure contours and streamlines are obtained which infer about variable coefficient of pressure (a flow parameter) values on every face of the model and conclude the study.

3 Numerical Model Development

3.1 Geometric Modeling

In the present study, model A is designed in AutoCAD: 3D modeling and is compared with a reference isolated model X, which is as depicted in Fig. 1. The types of cross section in model A are as shown in Fig. 2.

The procedure for analysis using ANSYS is divided into 5 steps—geometry, mesh, setup, solution, and result. The domain is set in accordance to Indian Standards such that the boundaries of the domain are at a distance of 5 h from the wind ward face

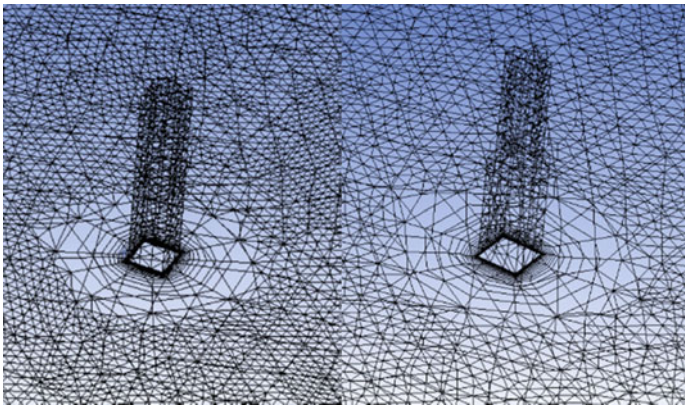

Fig. 3 Meshing in model X and model A, respectively

(A), lateral faces (C&D), and roof of the model and at a distance of 15 h from the leeward face (B) to avoid flow re-circulation (where let h be the height of the model). Meshing for the domain is done using the tetrahedral elements having element size of 0.2 m. Meshing inflation with 15 layers is provided at the boundaries of the model A and model X for allowing smooth flow and is represented in Fig. 3.

3.2 Basic Equations

The study aims to interpret the fluid–structure interaction in terms of various contours and streamlines obtained as a result of analysis in ANSYS and validate the observations to conform with IS: 875 (Part III)—2015. It utilizes the research in effect of wind on low-rise buildings and turbulence study using standard k−ε, standard k−ω, and SST k−ω models. The terms of the equations are brief about in appendix section.

Standard k−ε model. K−ε model is a two-equation model of computational fluid dynamics used to replicate flow characteristics for turbulent flow conditions. For turbulent kinetic energy,

$$\frac{\partial(\rho k)}{\partial t} + \frac{\partial(\rho k u_i)}{\partial x_i} = \frac{\partial}{\partial x_j}\left[\frac{\mu_t}{\sigma_k}\frac{\partial k}{\partial x_j}\right] + 2\mu_t E_{ij}E_{ij} - \rho\varepsilon \tag{1}$$

For dissipation,

$$\frac{\partial(\rho\varepsilon)}{\partial t}+\frac{\partial(\rho\varepsilon u_i)}{\partial x_i}=\frac{\partial}{\partial x_j}\left[\frac{\mu_t}{\sigma_\varepsilon}\frac{\partial\varepsilon}{\partial x_j}\right]+C_{1\varepsilon}\frac{\varepsilon}{k}2\mu_t E_{ij}E_{ij}-C_{2\varepsilon}\rho\frac{\varepsilon^2}{k} \tag{2}$$

Standard k−ω model. It is a two-equation model, generally used for flows having low Reynold's number used to interpret turbulent flow conditions. For turbulent kinetic energy,

$$\frac{\partial(\rho k)}{\partial t}+\frac{\partial(\rho\varepsilon u_i)}{\partial x_i}=\frac{\partial}{\partial x_j}\left[\Gamma_k\frac{\partial k}{\partial x_j}\right]+G_k-Y_k+S_k \tag{3}$$

Specific dissipation rate,

$$\frac{\partial(\rho\omega)}{\partial t}+\frac{\partial(\rho\omega u_i)}{\partial x_i}=\frac{\partial}{\partial x_j}\left[\Gamma_\omega\frac{\partial\omega}{\partial x_j}\right]+G_\omega-Y_\omega+S_\omega \tag{4}$$

SST k−ω model. SST, acronym for shear stress transport, is used to obtain better flow separation prediction for adverse pressure gradient conditions. For turbulent kinetic energy,

$$\frac{\partial(\rho k)}{\partial t}+\frac{\partial(\rho k u_i)}{\partial x_i}=\frac{\partial}{\partial x_j}\left[\Gamma_k\frac{\partial k}{\partial x_j}\right]+\tilde{G}_k-Y_k+S_k \tag{5}$$

Specific dissipation rate,

$$\frac{\partial(\rho\omega)}{\partial t}+\frac{\partial(\rho\omega u_i)}{\partial x_i}=\frac{\partial}{\partial x_j}\left[\Gamma_k\frac{\partial\omega}{\partial x_j}\right]+G_\omega-Y_\omega+D_\omega+S_k \tag{6}$$

3.3 CFD Pre-Simulations

Power law is used for interpreting the results in ANSYS in setup and solution steps. The inputs for the set-up step are $\alpha = 0.147$, $Z_{ref} = 1$ m, and $U_{ref} = 10$ m/s. Power law is used for calculation of pressure (Eq. 7).

$$P = U_{ref}\left(\frac{Z^\alpha}{Z^\alpha_{ref}}\right) \tag{7}$$

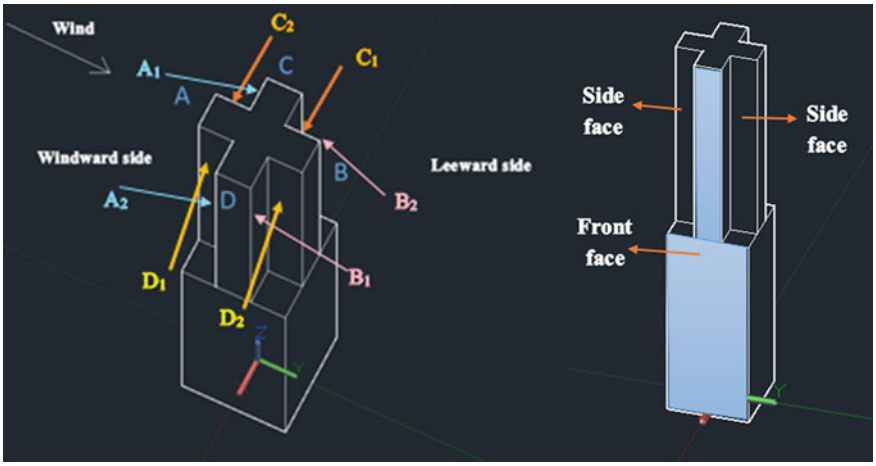

Fig. 4 Representation of front and side faces of model A

The program is run for about an hour before the results are evaluated. The variable coefficient of pressure is then found out (Eq. 8). V_{ref} is assumed to be 10 m/s.

$$C_P = \frac{(P - P_{ref})}{(\frac{1}{2}\rho_a V_{ref})} \tag{8}$$

Thus, value of pressure density comes out to be, $p_a = 1.225$ kg/m^3.

The wind load effect on model A is analyzed for 17 faces. Windward side is that side which is facing the on-coming wind. The side resisting this on-coming wind is called as the Leeward side. Classification of faces is done majorly based on four directions into faces A, B, C, and D as the "front faces". The remaining faces are classified into subscripts of 1 and 2 of front face as "side faces". As represented in the Fig. 4, each direction or front face will have 2 side faces. The side face to the left of front face is subscripted to 1 ($A_1/B_1/C_1/D_1$), while the one to the right is subscripted to 2 ($A_2/B_2/C_2/D_2$).

4 Validation

For validating the study, an isolated reference model named model X was designed and analyzed. Model X was designed such that the entire model was formed with a single square cross section having dimensions 40 m × 40 m throughout the height of 192 m (Fig. 1). Coefficient of pressure, $C_{p,}$ values for each face (A, B, C, D) classified similarly as discussed above was got after analysis using ANSYS: CFX mode and is as listed in Table 1 below. It is compared with the acceptable values as given in IS: 875 (Part III) – 2015.

Table 1 Comparing C_p values of model X with acceptable C_p values in accordance to IS: 875 (Part III) – 2015

Coefficient of pressure, C_p	Faces of model X			
	A	B	C	D
According to IS: 875 (Part III)−2015	+ 0.8	− 0.25	− 0.8	-0.8
Model X	+ 0.659769	− 0.277905	− 0.65153	-0.65153

From Table 1, it is said that C_p values for faces A, B, C, and D of model X varied by 17.528%, 11.162%, 18.558%, and 18.55875%, respectively.

5 Results and Discussion

5.1 Pressure Contours

Contours are used to indicate the change in constant pressure values over a surface. A contour plot with color bands which has discrete colored regions while the display of a variable on a locator (such as a boundary) shows a finer range of color detail by default. The following observations of pressure contours for all faces are classified into different cases as below. The cases are classified into 1 and 2 on the basis of incident wind angle—0° and 90°. The following pressure contours are evaluated using ANSYS for model A and model X. Note that for side faces, left contours are for "1" subscripted side face, while right contours are for "2".

Case 1. Incident wind angle is 0°

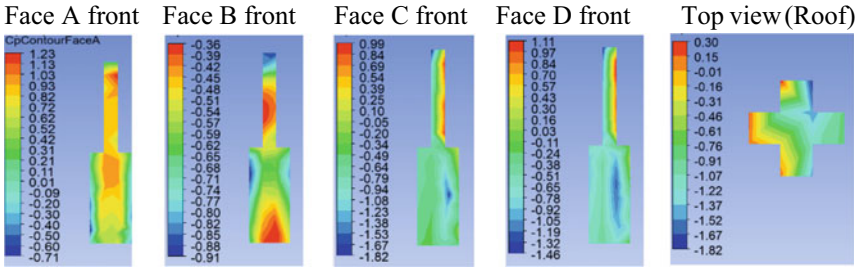

Face A sides Face B sides Face C sides Face D sides

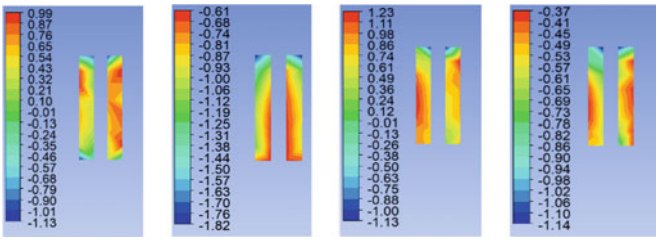

Face A front Face B front Face C front Face D front Top view (roof).
Face A sides Face B sidesFace C sides Face D sides.

Case 2. Incident wind angle is 90°

Face A front Face B front Face C front Face D front Top view (Roof)

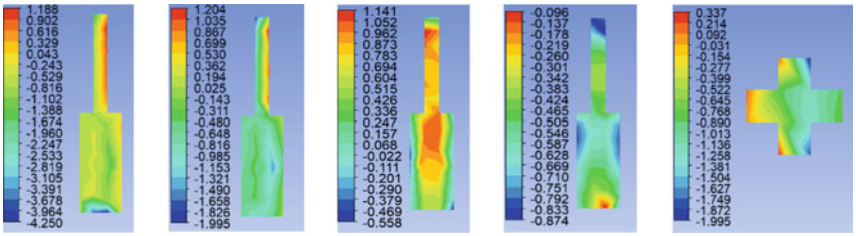

Face A sides Face B sides Face C sides Face D sides

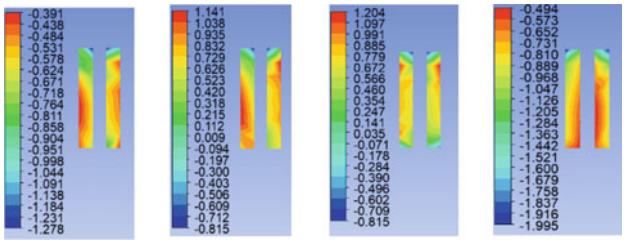

Face A front Face B front Face C front Face D front Top view (roof).
Face A sides Face B sides Face C sidesFace D sides.

Model X. For model X, pressure contours were obtained for wind incident angle 0°.

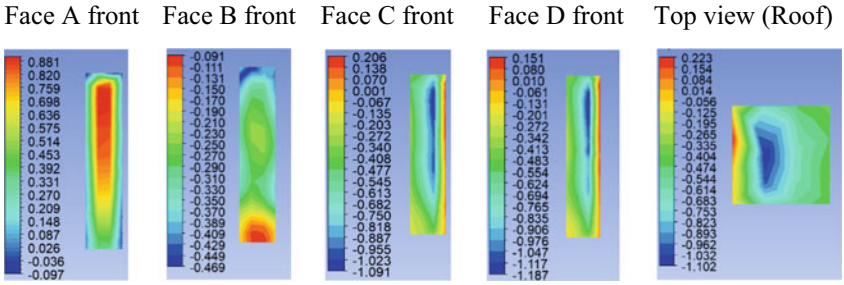

Face A front Face B front Face C front Face D front Top view (roof).
The following conclusions are drawn from the pressure contours obtained.

- For 0° incident wind angle on model A, value of C_p lies in the range ϵ [–0.86084, 0.666623]. Maximum negative and positive coefficients of pressure of –0.86084 acted on the face B_2 and 0.666623 acted on the face $D_{1,}$ respectively. Therefore, faces B_2 and D_1 are the critical faces in this case. Independent groups of side faces (A_1 and A_2, B_1 and B_2, C_1 and C_2, D_1 and D_2) have similar pressure impact. Faces A, B, C, D have almost equal value of coefficient of pressure, $C_p \approx 0.6$.
- For 90° incident wind angle on model A, value of C_p lies in the range ϵ [-0.85415, 0.642927]. Maximum negative and positive coefficients of pressure of -0.85415 acted on the face D_1 and 0.642927 acted on the face $B_{2,}$ respectively. Therefore, faces $D_{1\text{ and }}$ B_2 are the critical faces in this case. The range of C_p in this case is similar to 0° case. Independent side faces (A_1 and A_2, B_1 and B_2, C_1 and C_2, D_1 and D_2) have similar pressure impact. Faces A, B, C, D have almost equal value of coefficient of pressure, $C_p \approx 0.6$.
- For model X, value of C_p lies in the range ϵ [-0.734214, 0.623015]. Maximum negative and positive coefficients of pressure of -0.734214 acted on the face D and 0.623015 acted on the face A, respectively. The range of C_p for model X is similar to model A (0° case).

5.2 Streamlines

The wind in the present study is taken to be a fluid body. Streamline is a path of imaginary particles suspended in the fluid and carried along with it. The vertical and horizontal streamlines are evaluated and represented in the following sub-sections.

Vertical streamlines. For model A –

Case 1. Incident wind angle is 0°

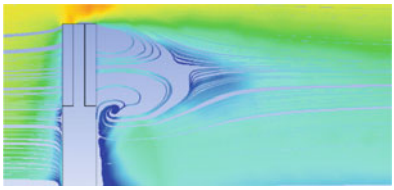

Case 2. Incident wind angle is 90°

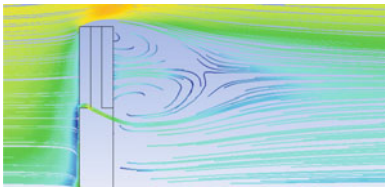

The following conclusions are drawn from the vertical streamlines obtained.

- For 0° incident wind angle on model A, it is observed that wind direction reverses in the wake region, creating a separation zone. Increased velocity is observed at the top—most point of the building or model A from where the streamlines change direction. It is observed that the streamlines are symmetrical and therefore will have minimum wind effect on structure.
- For 90° incident wind angle on model A, formation of re-circulation zone at the leeward side of the building is observed. Fewer flow lines are observed. Increased velocity is observed at the top—most point of building or model A from where the streamlines change direction.

Horizontal streamlines. For model A –
Case 1. Incident wind angle is 0°

Case 2. Incident wind angle is 90°

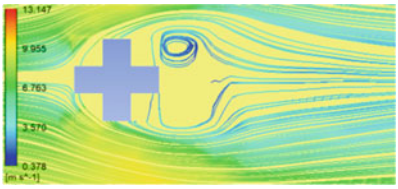

For model X, horizontal streamlines were obtained for four cases 1, 2, 3, and 4 representing wind flow at a height of 192 m, 144 m, 96 m, and 48 m, respectively, for incident wind angle 0°.

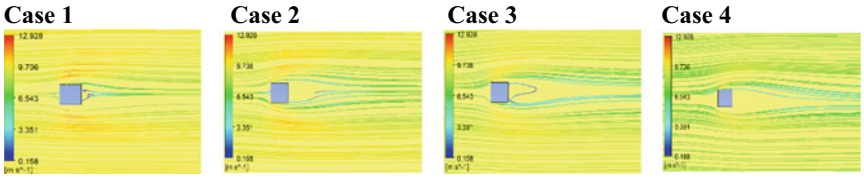

The following conclusions are drawn from the horizontal streamlines obtained.

- For 0° incident wind angle on model A, two vortices or re-circulation zones are formed symmetrical on both its sides near faces C_1 and B_2 and B_1 and D_2.
- For 90° incident wind angle on model A, vortex or re-circulation zone formation is observed near the faces C_1 and D_2. This region is not good for providing openings for windows, etc.
- For model X, symmetrical horizontal streamlines are observed with minimal turbulence and no re-circulation zone nearby indicating ideal cross-section shape for tall buildings. It is safely designed and shows minimal effect of wind on the structural damage component.

6 Conclusion

Complex nature of wind is due to its turbulent and gutsy nature that gives rise to many flow conditions upon interaction with tall buildings. Therefore, the study of wind flow characteristics on tall buildings is necessary for investigating the behavior of these slender flexible structures. The following conclusions are drawn from this paper.

- International standards are used for analyzing wind effects on tall buildings having simple shapes as cross section only. Therefore, in this study, complex shapes (plus) for varying cross-section tall building (model A) have been analyzed by adopting CFD analysis in ANSYS: CFX mode for interpreting the wind effect.
- As discussed in the validation section, the C_p values obtained for model X were in agreement with those given by IS:875 (Part III)—2015. Therefore, model A is also validated by consequence.

- Wind flow characteristics were determined for all faces of model A in terms of pressure contours, vertical, and horizontal streamlines for incident wind angles 0° and 90°. It is observed that for wind incident angle 0° and 90°, faces A, B, C, and D have approximately equal pressure impact ($C_p \approx 0.6$).
- Use of CFD for wind analysis in tall buildings is better than other popular methods like wind tunnel testing as it is less time-consuming and cost-effective.

Acknowledgements Authors would like to convey the exceptional thanks and appreciation to our Institute, Delhi Technological University for providing the resources to the authors to submit the paper within the allowable time.

References

1. Ritu Raj, Arun Kumar (2021) Study of pressure distribution on an irregular octagonal plan oval—shape building using CFD. Civ Eng J. https://doi.org/10.28991/cej-2021-03091760
2. Agarwal, Ashish, Irtaza, Hassan (2021) Turbulent wind flow through permeable claddings mounted on elevated scaffold using CFD simulation. Engineering Reports. 3. https://doi.org/10.1002/eng2.12350
3. Ahirwar, Ritu, Srinivasan, Anbukumar, Meena, Rahul (2021). Numerical Investigation of Wind Load on Side Ratio of High-Rise Buildings. https://doi.org/10.1007/978-981-16-6557-8_76
4. Nagar SK, Raj R, Dev N (2021) Proximity effects between two plus-plan shaped high-rise buildings on mean and RMS pressure coefficients. Scientia Iranica, 0(0), 0–0. https://doi.org/10.24200/sci.2021.55928.4484
5. Ding F, Kareem A (2020) Tall Buildings with Dynamic Facade Under Winds. Engineering 6(12):1443–1453. https://doi.org/10.1016/j.eng.2020.07.020
6. Pradeep Shekhar B, Madhira R, Nadu T, Professor A (2020) Aerodynamic Effect of Tall Building over a Small Building. Int Res J Eng Technol. Retrieved from www.irjet.net
7. rtall buildings of different shapes. Wind and Structures, An Int J, 31(5), 441–453. https://doi.org/10.12989/was.2020.31.5.431
8. Raj R, Jha S, Singh S, Choudhary S (2020) Response analysis of plus shaped tall building with different bracing systems under wind load. Int J Adv Res Eng Technol, 11(3), 371–380. https://doi.org/10.34218/IJARET.11.3.2020.032
9. Karimimoshaver M, Hajivaliei H, Shokri M, Khalesro S, Aram F, Shamshirband S (2020) A model for locating tall buildings through a visual analysis approach. Applied Sciences (Switzerland), 10(17). https://doi.org/10.3390/app10176072
10. Er. Deshmukh, Pranil, Shiyekar MR (2020) Wind analysis of Tall Building. Int J Eng Sci & Res Technol (IJESRT). 147−155. https://doi.org/10.29121/ijesrt.v9.i7.2020.14
11. Moon KS (2018) Comparative evaluation of structural systems for tapered tall buildings. Buildings, 8(8). https://doi.org/10.3390/buildings8080108
12. Fuka V, Xie ZT, Castro IP, Hayden P, Carpentieri M, Robins AG (2018) Scalar fluxes near a tall building in an aligned array of rectangular buildings. Bound-Layer Meteorol 167(1):53–76. https://doi.org/10.1007/s10546-017-0308-4
13. Harman, Dr. Hemant Sood (2017) Analyzing the Effect of Cross-Sectional Change of Column on Symmetrical R.C.C. Frame Structure. Int J Eng Res & Technol (IJERT) 06: 06 (June 2017), https://doi.org/10.17577/IJERTV6IS060211
14. Nicola Longarini, Luigi Cabras, Marco Zucca, Suvash Chapain, Aly Mousaad Aly. (2017). Structural Improvements for Tall Buildings under Wind Loads: Comparative Study. Shock and Vibration, vol. 2017, Article ID 2031248, 19 pages. https://doi.org/10.1155/2017/2031248

15. Ali MM, Al-Kodmany K (2012) Tall buildings and Urban habitat of the 21st century: A global perspective. Buildings 2(4):384–423. https://doi.org/10.3390/buildings2040384
16. Connor JJ (2003) Introduction to structural motion control. Upper Saddle River, N.J: Prentice Hall Pearson Education
17. Mehta KC (1984) Wmd induced damage observations and thek impucations for design practice. J Eng Struct, ASCE 6(1984):242–247

Grasshopper Optimization Technique for PV Array Reconfiguration to Achieve Higher GMPP Under PSCs

Rupendra Kumar Pachauri, Mohit Kumar, Ankur Kumar Gupta, Ahmad Faiz Minai, and Akhilesh Sharma

Abstract Partial shading has adverse impacts on photovoltaic (PV) systems performance, e.g. power losses (PL) and existence of multiple power maxima points on power-voltage (P–V) curves. To diminish the shading effect, game puzzles are most favourable methods to enhance PV system performance. In addition, the swarm optimization techniques are playing efficient role to find the optimized location of PV module to disperse the shading effect on entire PV array system. The grasshopper optimization (GHO) modified total-cross-tied (TCT) technique, i.e. GHO-TCT and the conventional series–parallel (SP), total-cross-tied (TCT) techniques are used to diminish the adverse impacts of partial shading conditions (PSCs). Using this optimization method to alter PV modules in an array system, greater global maximum power point (GMPP) is accomplished under non-uniform irradiance. MATLAB/Simulink study is carried out to achieve higher power output especially in GHO configuration of PV array system under PSCs. As a result, distinguished performance indices, e.g. power and voltage at GMPP, PL, and FF are observed. During extensive comparison, GHO arrangement produced efficient results to mitigate the impact of PSCs.

Keywords Solar energy · Power system · Optimization technique · Power loss

R. K. Pachauri (✉)
Electrical and Electronics Engineering Department, School of Engineering, University of Petroleum and Energy Studies, Dehradun 248007, India
e-mail: rpachauri@ddn.upes.ac.in

M. Kumar
Electrical Engineering Department, Sant Longowal Institute of Technology, Sangrur, Punjab, India

A. K. Gupta
Research & Development Department, IIMT University Meerut, Uttar Pradesh, Meerut, India

A. F. Minai
Electrical Engineering Department, Integral University, Uttar Pradesh, Lucknow, India

A. Sharma
Electrical Engineering Department, North Eastern Regional Institute of Science and Technology, Nirjuli, Arunachal Pradesh, India

© The Author(s), under exclusive license to Springer Nature Singapore Pte Ltd. 2023

K. R. Reddy et al. (eds.), *Recent Advances in Sustainable Environment*, Lecture Notes in Civil Engineering 285, https://doi.org/10.1007/978-981-19-5077-3_26

1 Introduction

Although, major power generation is based on fossil fuels such as diesel, petrol, coal, and gas. Due to scarcity and limited storage capacity of fossil fuel, researcher explored alternative energy sources such as renewable energy (RE) sources. In current technological era, RE sources are most promising and reliable for grid and stand-alone power distribution generation system. Amongst the RE sources, solar PV is gaining more popularity due to environmental friendly nature and less skill required for utilization to establish at stand-alone level. One of the main problems with the use of solar PV systems is the effect of PSCs, which reduce the power output and enhance PL. The major causes of PSCs are due to various factors, e.g. the falling of dry leaves on PV system, nearby telecom towers, passing clouds, nearby trees, and high-rise buildings. These PSCs are basic cause of non-uniform irradiations and accomplished multiple power maxima points, e.g. GMPP and LMPP on power-voltage (P–V) curves. Thus, to reduce the adverse impacts of partial shading on PV modules, game puzzle methods are utilized in various numbers of research articles. Due to high-wire length requirement, these game puzzle methods have limitation. In this context, swarm optimization methods are used for extensive research outputs under PSCs. In this paper, GHO-based configuration of PV system is compared with TCT configuration to show the effective higher response.

1.1 Literature Review

The authors reviewed recent research articles in order to extract valuable research activities for the remarkable study. Furthermore, an experimental test is carried out to validate the results obtained through the MATLAB/Simulink analysis. The authors of [6] investigated and validated the growth of enhanced performance of honey-comb (HC), bridge-link (BL), ladder (LDR), and TCT connections in the Su-Do-Ku arrangement-based PV array system. In BL configuration, the increment in power enhancement at time instants from t_1 to t_6 are 11.92%, 17.24%, 12.77%, 12.77%, 12.04% and 13.41%, respectively, compared to SP configuration. During the MATLAB/Simulink study, total five different PV array configurations are investigated under six distinguished shading patterns [7]. The mismatch losses for TCT under shading case-1 to 6 are observed as 45.38 W, 311.52 W, 82.22 W, 334.9 W, 348.04 W, and 281.05 W. To anticipate PV characteristic behaviour under PSCs, a MATLAB/Simulink study is carried out in [8]. The authors verified the findings to demonstrate efficient performance through experimental results. For the analysis of PSC's, TCT and RTCT configurations are used on a 6×6 size PV array. The gain in FF for reconfigured TCT (RTCT) PV system at distinguished shading scenarios are 8.94 %, 16.98%, 12.56%, 12.21%, 15.11%, and 9.32%, respectively. In RTCT, the losses are experienced due to shading scenarios at time instants from t_1 to t_6 are 4.79%, 15.69%, 11.34%, 10.87%, 13.42%, and 5.2%, respectively. Experimental

validation is carried out through the extensive investigation on series, parallel, and SP configurations [9]. Later on new PV array reconfiguration methodologies are introduced in [10, 11], Su-Do-Ku puzzle-based PV array enhanced shade dispersion property within non-uniform sun irradiation levels as 100–700 W/m^2 to 1000 W/m^2. The improved version of So-Do-Ku to reconfigure PV array is adopted and compared with existing SP, BL, HC, TCT, Su-Do-Ku, and optimal Su-Do-Ku configurations to verify the performance indices such as efficiency, FF, and mismatch losses by 11.79%, 65.8%, and 11.25%, respectively. In [12], the authors have proposed a reconfiguration method and compared to existing SP, BL, and TCT PV array configured systems under obscured sun irradiation levels from 400 W/m^2, 500 W/m^2, 700 W/m^2, and 1000 W/m^2. The RM configuration enhanced the system performance in terms of global power values as 3.71 kW, compared to the conventional SP, BL, and TCT configurations such as 3.6 kW, 3.42 kW, and 3.6 kW, respectively.

1.2 Novelty Work

The following are the key points in the current research article to support the novelty explained in the paper as,

- A meta-heuristic approach, such as GHO, is used to modify the TCT PV array configuration, demonstrating the current balancing method in shadowing cases.
- Existing PV array configurations, e.g. SP, TCT are compared with GHO-based configuration under considered shading scenarios. GHO has higher performance with respect to the PL and improved FF.

2 Photovoltaic Technology

2.1 PV Module: Modelling

PV cell voltage is shown in Eq. (1), and equivalent circuit is affixed in Fig. 1 as follows,

$$V_{PV} = \frac{AkT_C}{e} \ln\left(\frac{I_{Ph} + I_S - I_{cell}}{I_S}\right) - I_{cell}\left(\frac{R_{se}R_{sh}}{R_{se} + R_{sh}}\right) \tag{1}$$

where PV output voltage stands for V_{PV} and A stands for ideality factor, k represents for Boltzmann's constant, I_{Ph}, I_{cell}, and I_{DS} are shown for PV photo-current, module current, and diode saturation current. Moreover, R_S and R_{sh} stand for series shunt resistance.

The specifications at standard test conditions (STCs) of PV module are given for MATLAB/Simulation of PV arrays are shown in Table 1 as,

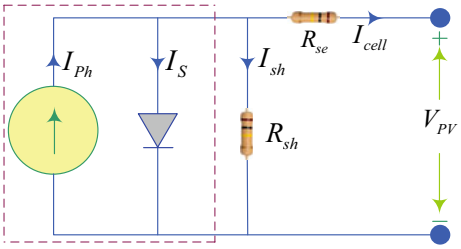

Fig. 1 Electrical circuit of a PV cell [13, 14]

Table 1 PV module specifications at STCs (SFTI18P5: Manf. Solar Univ. India)

Parameters	Specifications
S. C. current (I_{SC})	$0.55A$
O. C. voltage (V_{OC})	$11.25V$
Max. current (I_m)	$0.52A$
Max. voltage (V_m)	$9.62V$
Max power (P_m)	$5W$

2.2 PV Array Systems

(i) ***SP configuration***: To enhance voltage and current, 6 × 6 size PV array system is developed which is called SP configuration and shown in Fig. 2a.

(ii) ***TCT configuration***: These cross-tied connections between the strings improve the branches current during PSCs. The connection diagram of the TCT configuration is shown in Fig. 2b.

(iii) ***GHO-based configuration***: GHO technique is based on social interaction network. In present optimization concept, two main phases are existed (i) exploration, (ii) exploitation for sudden and travels of search agents correspondingly.

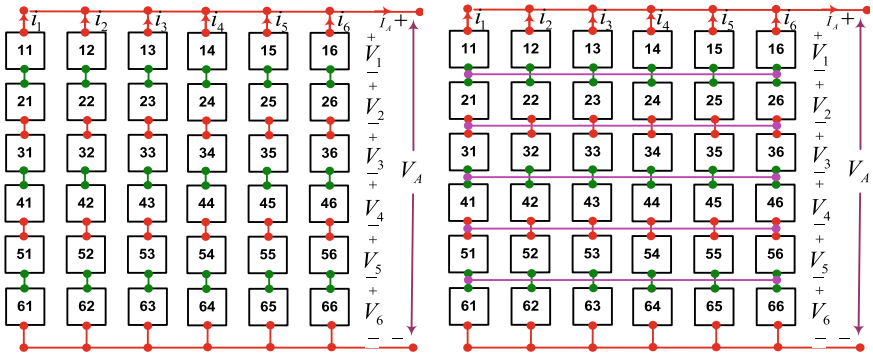

Fig. 2 **a** SP **b** TCT arrangement of 6 × 6 size PV array

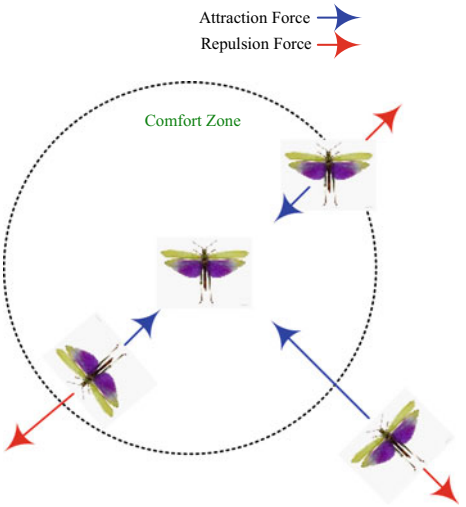

Fig. 3 Grasshopper's network interaction [15]

Figure 3 illustrates the social interaction of the grasshoppers to understand the behaviour as,

To analyze the behaviour of grasshoppers is expressed through mathematical approach in Eq. (2) as follows,

$$x_p(t+1) = c\left(\sum_{j=1}^{N} c\frac{Jb_d - Kb_d}{c} s(E)\frac{x_q(t) - x_p(t)}{d_{pq}}\right) + T_n \tag{2}$$

where $x_p(t+1)$ is the pth grasshopper's position at $t+1$ iteration, s is a function of social force strength. Moreover, f represents the attraction strength, r is a distance, Jb_d and Kb_d represent for upper and lower bounds. In addition, distance between pth and qth grasshoppers is shown as d_{pq}, C is reduction factor and T_n is the target of 'n' dimensional position [15, 16]. Error calculation is carried out as expressed in Eq. (3). In addition, the associated steps to execute GHO technique are shown in Fig. 4.

$$E = \left|\left(x_j(t) - x_i(t)\right)\right| \tag{3}$$

In Fig. 5, the methodology to show GHO technique for current equalization is shown as follows,

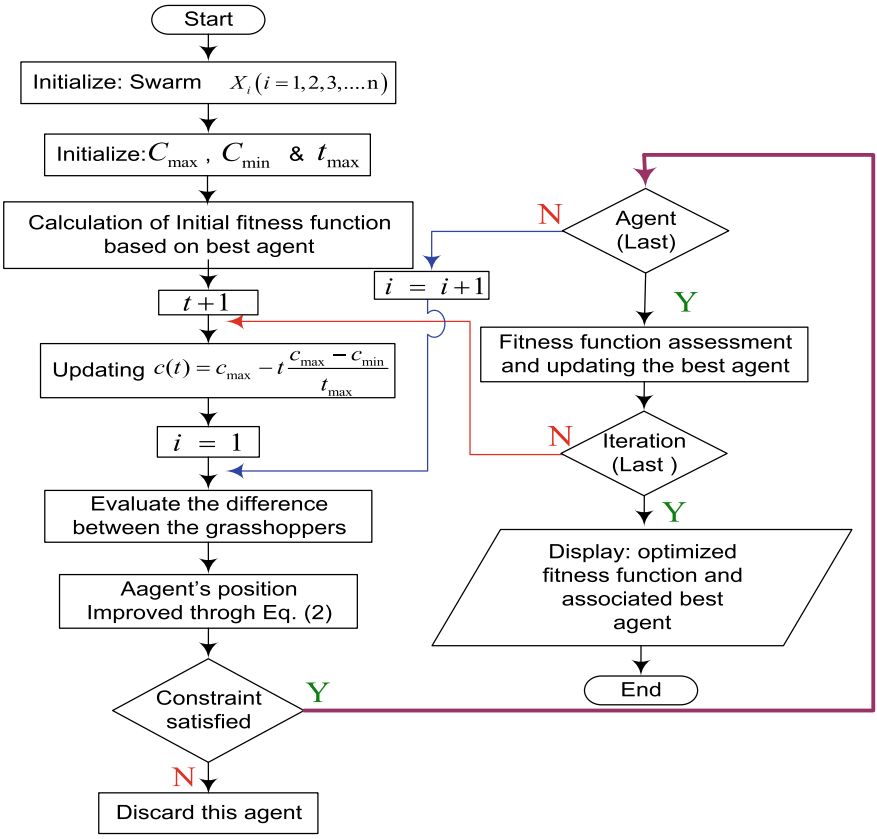

Fig. 4 GHO algorithm flow chart [15, 16]

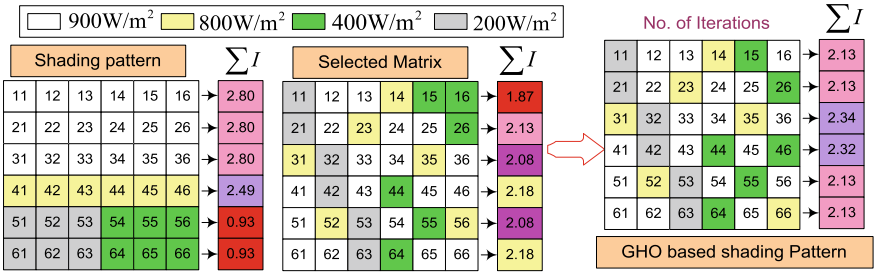

Fig. 5 Shade dispersion techniques using GHO method

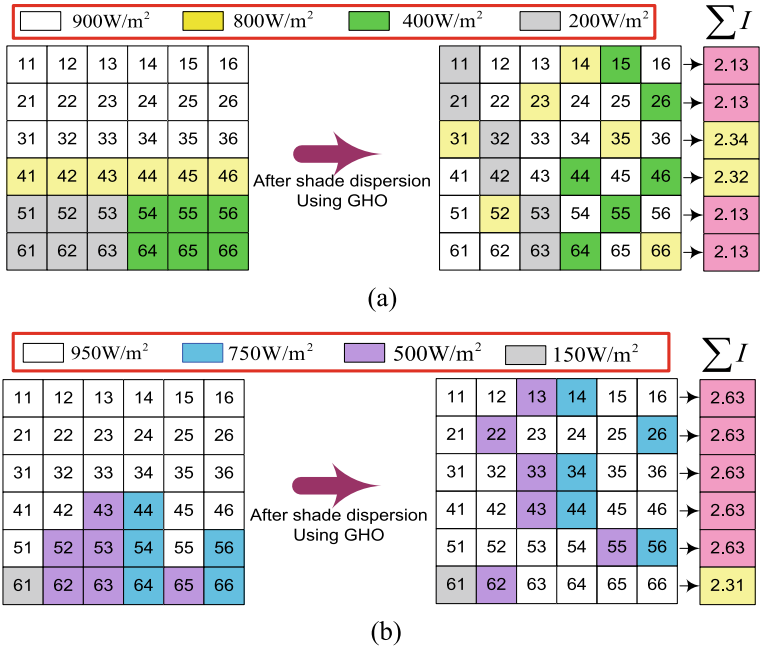

Fig. 6 Shading cases: I–II

2.3 Shading Scenarios

Two realistic conditions-based shading scenarios are considered in this paper for PV system performance evaluation. In the first shading pattern, distinguishing sun irradiance levels such as 900, 800, 400, and 200 W/m^2 and are reported for extensive study. Furthermore, the second shading pattern consists of nearly identical irradiation levels such as 950, 750, 500, and 150 W/m^2 for extensive study. Both shading patterns are depicted in Fig. 6a, b as follows,

3 Performance Assessment Indices

3.1 Power Maxima and Voltage at GMPP

Multiple power maxima are perceived on P–V performance curves because of uneven sun irradiance levels. Power maxima points such as LMPP and GMPP exist to show the effective maximum power and voltage for obtaining the PV system performance.

3.2 Fill Factor

At first glance, the FF parameter appears to be the most significant performance index for the PV system efficiency assessment and expressed in Eq. (4).

3.3 Power Loss

In first impressions, FF is the most important performance index parameter for defining efficiency and understanding PV performance. The PL assessment is carried out with the difference between MPP during uniform irradiance and GMPP at non-uniform irradiance and is expressed in Eq. (5).

$$FF = \frac{V_m \times \mathrm{I}_m}{V_{OC} \times I_{SC}} \tag{4}$$

$$PL = MPP_{at\ uniform\ irradiation} - GMPP_{at\ PSCs} \tag{5}$$

In addition, theoretical estimation of current values for SP, TCT, and GHO-TCT-based 6 × 6 PV array configurations is expressed through Eqs. (6)–(8) for case-I as,

$$I_{r1} = I_{r2} = I_{r3} = \left(\frac{900}{1000}\right)\mathrm{I}_m + \left(\frac{900}{1000}\right)\mathrm{I}_m + \left(\frac{900}{1000}\right)\mathrm{I}_m + \left(\frac{900}{1000}\right)\mathrm{I}_m + \left(\frac{900}{1000}\right)\mathrm{I}_m + \left(\frac{900}{1000}\right)\mathrm{I}_m = 5.4\mathrm{I}_m \tag{6}$$

$$I_{r4} = \left(\frac{800}{1000}\right)\mathrm{I}_m + \left(\frac{800}{1000}\right)\mathrm{I}_m + \left(\frac{800}{1000}\right)\mathrm{I}_m + \left(\frac{800}{1000}\right)\mathrm{I}_m + \left(\frac{800}{1000}\right)\mathrm{I}_m + \left(\frac{800}{1000}\right)\mathrm{I}_m = 4.8\mathrm{I}_m \tag{7}$$

$$I_{r5} = I_{r6} = \left(\frac{200}{1000}\right)\mathrm{I}_m + \left(\frac{200}{1000}\right)\mathrm{I}_m + \left(\frac{200}{1000}\right)\mathrm{I}_m + \left(\frac{400}{1000}\right)\mathrm{I}_m + \left(\frac{400}{1000}\right)\mathrm{I}_m + \left(\frac{400}{1000}\right)\mathrm{I}_m = 1.8\mathrm{I}_m \tag{8}$$

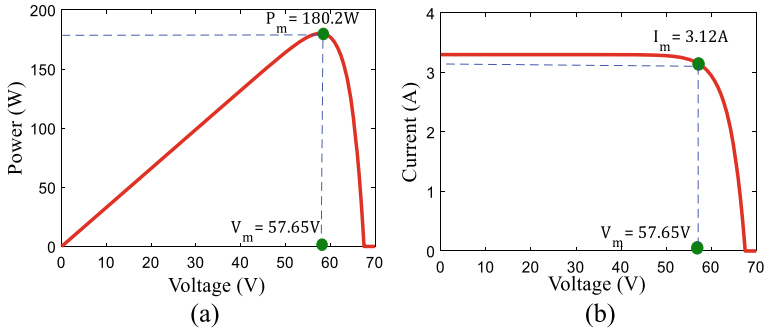

Fig. 7 P–V and I–V curves at ideal irradiations (1000 W/m^2)

4 Results and Discussion

4.1 P–V and I–V Curves Under Ideal Conditions

To assess the shading impact on PV system performance, performance characterization (P–V and I–V curves) is carried out for 6 × 6 size PV system under ideal irradiation conditions as shown in Fig. 7. Obtained power at MPP is found as 180.2 W in ideal conditions, found through P–V curve.

4.2 P–V and I–V Curves Under Shading Cases: I–II

A remarkable study is carried out and observed GMPP and LMPP as power maxima points under PSCs. During both the shading cases, the GMPPs for GHO-based configuration are reflected higher side as 113.9 W and 142.3 W compared to SP (96.96 W and 113.3 W) and TCT (99.89 W and 117.1 W) configurations. The performance behaviour of P–V and I–V curves is depicted in Figs. 8 and 9.

During the investigation, quantitative observations are made under both shading cases: I–II. Table 2 summarizes all of the performance indicators as.

4.3 Global Maximum Power and Voltage

To demonstrate the effective comparison of PV systems under shading scenarios, a bar chart representation is required. At GMPP, performance parameters such as power and voltage are measured and compared. Due to its good shade dispersion capability, a GHO-based configured PV system produces more power under both

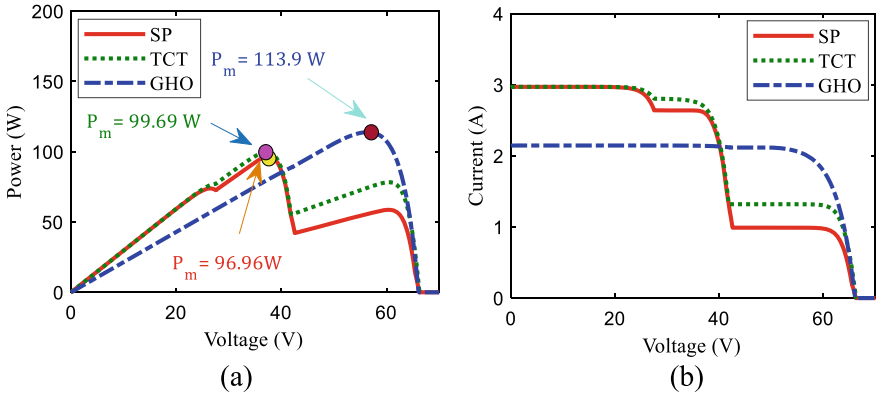

Fig. 8 P–V and I–V curves (during shading pattern-I)

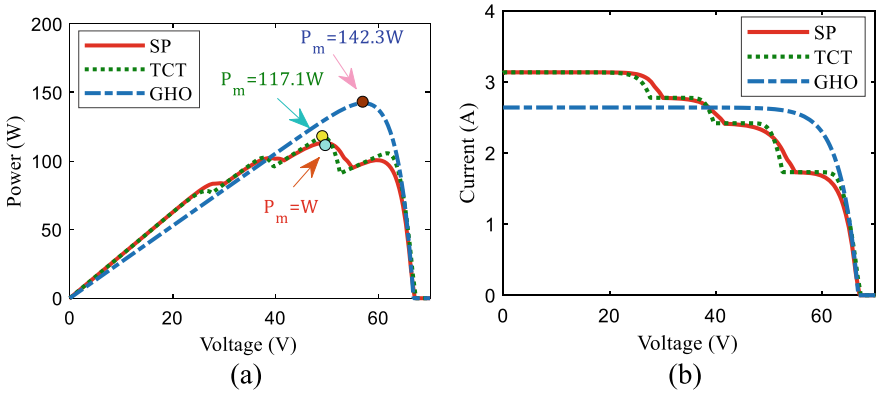

Fig. 9 P–V and I–V curves under shading pattern-II

Table 2 Quantitative analysis of PV array systems during shading scenarios: I–II

Parameters	Shading case–I			Shading case–II		
	SP	TCT	GHO	SP	TCT	GHO
$V_{OC}(V)$	65.74	65.74	65.74	66.48	66.48	66.48
$I_{SC}(A)$	2.95	2.97	2.145	3.12	3.16	2.64
$V_m(V)$	37.5	37.22	56.74	49.54	48.71	57.29
$I_m(A)$	2.58	2.68	2.00	2.28	2.40	2.48
$P_{GMPP}(W)$	96.96	99.89	113.9	113.3	117.1	142.3
FF	0.499	0.511	0.807	0.54	0.56	0.809
$PL(W)$	83.24	80.31	66.3	66.9	63.1	37.9
$PG(W)_{\%}$	–	3.02	17.47	–	3.35	25.59

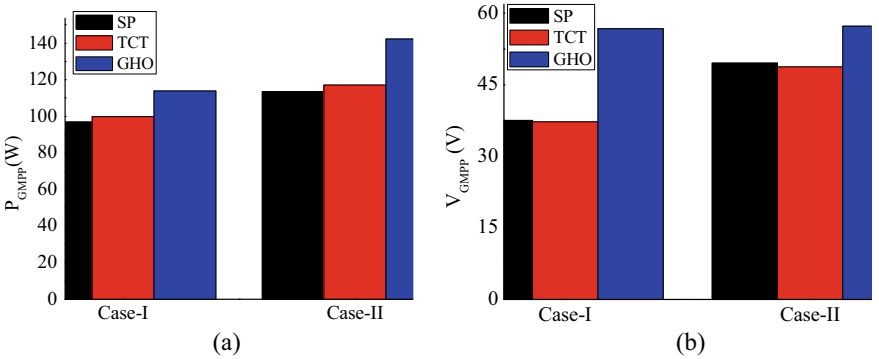

Fig. 10 **a** Power, **b** voltage at GMPP

shading patterns I and II. Power and voltage at GMPP are depicted in Fig. 10a, b, respectively.

4.4 FF and PL Analysis

During present study, PL is found minimized for GHO-based configured PV systems as 66.3 and 37.9 W compared to existing PV array systems. In a first perception, FF assessment is necessary to evaluate the PV system efficiency. During both the shading cases I–II, FF is investigated and observed higher for GHO-based PV array configuration as 0.807 and 0.809 compared to SP (0.49 and 0.54) and TCT (0.51 and 0.56) configurations, respectively. PL and FF analysis are shown Fig. 11a, b using bar chart representation as.

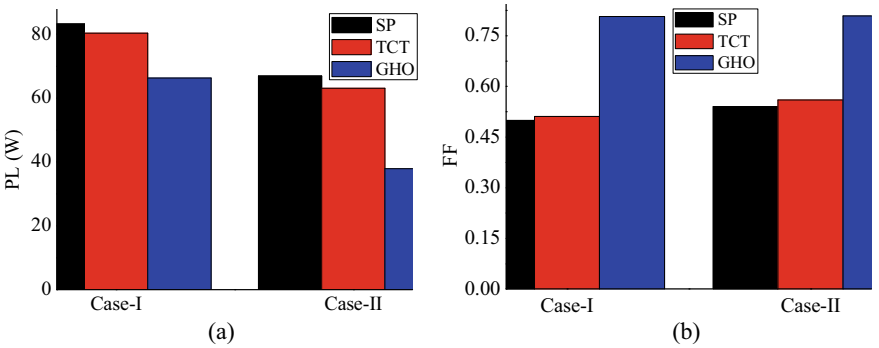

Fig. 11 **a** PL, **b** FF representation

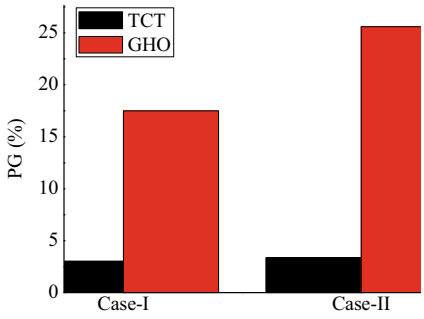

Fig. 12 PG analysis

4.5 Power Gain

For higher shade dispersion is helpful to enhance the PV performance. In this context, GHO technique is found best compared to conventional configurations. In this paper, GHO and TCT configured PV systems are having higher PG as 17.47%, 3.02%, and 25.59%, 3.35%, respectively, w. r. t. SP configured array, shown in Fig. 12 as.

5 Conclusion

The current study is examined for SP, TCT, and GHO technique-based configurations (9 × 9 size). Furthermore, during shading, cases I and II are considered, and the following are the key findings:

- Under shading cases: I–II, the highest GMPP is found as 113.9 W and 142.3 W for GHO configuration compared to conventional configurations.
- Furthermore, in GHO-based configurations, the PL is much lower, viz. 63.3 W and 37.9 W, when compared to SP (83.24 W and 66.9 W) and TCT (80.31 W and 63.1 W) configurations.
- Furthermore, the improved FF for GHO-based PV configurations is 0.807 and 0.809 when compared to conventional configurations.

Overall, the current study demonstrated that a higher shade dispersion factor helps to improve the performance of PV array configurations.

References

1. Gupta A, Chauhan YK, Pachauri RK (2016) A Comparative investigation of maximum power point tracking methods for solar PV system. Sol Energy 136:236–253

2. Bhadoria VS, Pachauri RK, Tiwari S, Jaiswal SP, Alhelou HH (2020) Investigation of different BPD placement topologies for shaded modules in a series-parallel configured PV array. IEEE Access 8:216911–216921
3. Bai J, Sun L, Pachauri RK, Wang G (2021) Investigate on photovoltaic array modeling and the MPPT control method under partial shading conditions. Int J Photo Energy 2021:1–16
4. Pachauri RK, Alhelou HH, Bai J, Golshan MEH (2021) Adaptive switch matrix for PV module connections to avoid permanent cross-tied link in PV array system under non-uniform irradiations. IEEE Access 9:45978–45992
5. Tao Y, Bai J, Pachauri RK, Sharma A (2020) Parameter extraction of photovoltaic modules using a heuristic iterative algorithm. Energy Convers Manag 224:1–18
6. Vijayalekshmy S, Bindu GR, Rama Iyer S (2015) Analysis of various photovoltaic array configurations under shade dispersion by Su-Do-Ku arrangement during passing cloud conditions. Indian J Sci Technol 8(35):1–20
7. Maharana SM, Mohapatra A, Saiprakash C, Kundu A (2020) Performance analysis of different PV array configurations under partial shading condition. Int Conf Comput Intell Smart Power Syst Sustain Energy CISPSSE 2020 5–9
8. Bindu SVGR, Iyer SR (2015) Performance improvement of partially shaded photovoltaic arrays under moving shadow conditions through shade dispersion. J Inst Eng Ser B
9. Junhong Z, Xueye W, Tianlong Z (2015) Research on the output characteristics of photovoltaic array under the non-uniform light 8(10):431–444 (2015)
10. Babu TS, Ram JP, Dragicevic T, Miyatake M, Blaabjerg F, Rajasekar N (2018) Particle swarm optimization based solar PV array reconfiguration of the maximum power extraction under partial shading conditions. IEEE Trans Sustain Energy 9(1):74–85
11. Sai Krishna G, Moger T (2019) Improved Su-Do-Ku reconfiguration technique for total-cross-tied PV array to enhance maximum power under partial shading conditions. Renew Sustain Energy Rev 109:333–348
12. Ul-Haq A, Alammari R, Iqbal A, Jalal M, Gul S (2020) Computation of power extraction from photovoltaic arrays under various fault conditions. IEEE Access 8:47619–47639
13. Gupta A, Kumar P, Pachauri RK, Chauhan YK (2014) Effect of environmental conditions on single and double diode PV system: a comparative study. Int J Renew Energy Res 4(4):849–858
14. Singh AS, Pachauri RK, Chauhan YK (2016) Comprehensive investigation of PV arays with puzzle shade dispersion for improved performance. Solar Energy 129:256–285
15. Fathy A (2018) Recent meta-heuristic grasshopper optimization algorithm for optimal reconfiguration of partially shaded PV array. Sol Energy 171:638–651
16. Pachauri RK (2022) Imperative role of optimization techniques to reconfigure solar photovoltaic array systems to diminish shading effects. Int J Circuit Theory Appl 50(1):317–353

Comparative Study of Wind Loads on Low-Rise Pitched and Circular Arch Roof Structures Based on CFD

Aditya Kumar Jha, Amartya Sinha, and Ritu Raj

Abstract This study compares the effect of wind load acting on a pitched roof and a circular arch roof of similar plan area of a storage building having one wall opening through computational fluid dynamics (CFD) simulations. CFD studies have been performed by many researchers to understand the flow behavior and find out coefficient of pressure on faces of regular building shapes having other types of roofs. However, no comparative study has been carried out for pitched and circular arch roofs building. Ansys (CFX) fluid flow software has been used to carry out the study using a standard k–ε turbulence model. The simulations have been carried out for −90° to 0° (clockwise) and +90° to 0° (anticlockwise) wind directions at an interval of 30°. Pressure, drag, and lift coefficients generated on the roofs were compared. It was found that, although variation in these coefficients w.r.t the wind incidence angles are similar for both the roofs types, coefficients of the sharp-edged pitched roof are higher in magnitudes than the smooth arch roof.

Keywords Wind load · Pitched roof · Arch roof · Ansys CFX · Pressure coefficients

1 Introduction

With the rapid economic growth in the country and transportation of goods from one place to another, storage facilities such as warehouses, cold storages, and bunkers. have become a need of the hour. Also, to compete with the global economy, increase in air transportation networks are being envisaged. Hangars are an important structure at airports for upkeep, maintenance, and storage of aircrafts. Such houses are built

A. K. Jha · A. Sinha (✉) · R. Raj
Delhi Technological University, Delhi, India
e-mail: amartyasinha_2k18ce018@dtu.ac.in

A. K. Jha
e-mail: adityakumarjha_2k18ce011@dtu.ac.in

R. Raj
e-mail: rituraj@dtu.ac.in

© The Author(s), under exclusive license to Springer Nature Singapore Pte Ltd. 2023

K. R. Reddy et al. (eds.), *Recent Advances in Sustainable Environment*, Lecture Notes in Civil Engineering 285, https://doi.org/10.1007/978-981-19-5077-3_27

with big dimensions with truss roof technologies. Wind flow has a significant effect on such roofs. Both, the roof geometry and the roof slope are essential factors in the structure's wind load resistance. Therefore, estimating wind loads on roofs is critical for designing a safe and cost-effective roof structures and its supporting truss. The wind load estimation can be done from numerical solutions for the wind pressures in which, a model of the structure is exposed to a wind flow profile in an artificially created wind tunnel domain with the help of computational fluid dynamics (CFD) simulations. The present study has been done as a preliminary step to analyze wind effect of the roof of such buildings through numerical simulation. In the present study, the time averaged wind flow Raynold's average Navier Stokes (RANS) equations of continuity and momentum has been considered using Ansys (CFX) solver with standard k–ε turbulent model. It is the simplest form of numerical simulation which requires the boundary conditions to be provided similar to the natural wind conditions. The differential equations of RANS are solved along the discretized elements of the domain and bluff body, and the process is iterated multiple times. The results of the flow parameters can be visualized, and post result data can be taken. The same process can be done in wind tunnel experiment also, but it is time consuming and cost of experiment also increases.

Wind pressures can also be measured directly on the existing prototype buildings by measuring the wind pressure acting on different critical points with the help of pressure sensors as done by Blackmore [1], Gerhardt and Kramer [2], Meecham [3], and Mehta et al. [4] who established that wind flow in the vicinity of buildings vary significantly with the edge and shape modifications in the buildings.

Wind loads display varied patterns on distinct localized locations on the faces and roofs of buildings, because the effects of wind loading on a structure are unique and wind flow behaves according to the structure's profile. Paul and Dalui [5], Mallick et al. [6], Chakraborty et al. [7], Mukherjee et al. [8], Sanyal and Dalui [9, 10], Kumar and Raj [11], and Gaur and Raj [12] have worked on high-rise buildings of various shapes like Z, C, +, Y, octagonal-oval, etc. by using experimental as well as numerical studies. From these works, it has been observed that different plan shapes of the buildings exhibit unique wind flow in the vicinity of the buildings, resulting into altogether different wind pressure patterns.

For low-rise structures, roof becomes the critical component of the building, and different roof geometries have shown unique behaviors when subjected to wind loads. Singh and Roy [13–16] have worked on CFD simulation on wind effects over pyramidal roofs and have studied the effect of wind direction and roof slope for single and double storied pyramidal roof buildings. Verma and Ahuja [17] and Zhou et al. [18] have studied wind effects on dome structures, which provided a completely unique shape of the roofs, using wind tunnel tests CFD analysis, respectively. Verma and Ahuja [19] have studied the effect of cylindrical roofs in single span as well as double span configurations.

In this study, an attempt to compare pitched roof and arch roof structures has been made for a low-rise rectangular plan building by employing CFD simulations which are performed by using the standard k-ε turbulence model corresponding to 10% (high) turbulence intensity in the Ansys CFX fluid flow package.

2 Computational Domain, Model, and Meshing Grid

For the analysis, a structure with 1 m × 0.6 m plan area and 0.5 m wall height is considered as shown in Fig. 1. The pitched roof is inclined at an angle of 20° with the horizontal which results in a maximum elevation of 0.6092 m at the center of the roof. For comparison with an arch roof, a circular arch is considered as a roof which has the same central elevation. The models are created with a wall thickness of 0.01 m, and one side of the models is kept open, in order to subject the structure with internal wind pressure also. A length scale of 1:10 has been adopted for the model in this study for the scope of future experimental verification. The Eqs. (1) and (2) represent the profile of the pitched roof and circular arch roof.

$$z = 0.6092 - 0.364|x| \tag{1}$$

$$z = 0.1425 + \sqrt{0.4667^2 - x^2} \tag{2}$$

For validating the flow setup, a validation model without opening from one side of same plan area and height was taken. At the inlet of the domain, a uniform homogeneous wind flow of 10 m/s was provided since the considered structure is low-rise, and the wind flow around the structure is the part of atmospheric surface layer, where the velocity profile can be treated as a uniform profile for simplicity in the analysis.

The domain volume meshing grid size was finalized as 0.2 m and the model faces and roofs meshing sizes as 0.05 m; much smaller as the focus in the present study is to map the pressure effect on the roofs of the model. The domain sides and top were defined as free slip walls ($T_{\text{wall}} = 0$ and $V_{\text{wall}} \neq 0$), where T_{wall} is the shear stress at the wall, and V_{wall} is the velocity along the wall surface. But, component of velocity normal to the wall surface is 0. The model faces and the ground were defined as no slip walls ($V_{\text{wall}} = 0$) which means component of fluid velocity along the boundary of wall is zero. Relative pressure at outlet was defined with 0 Pa.

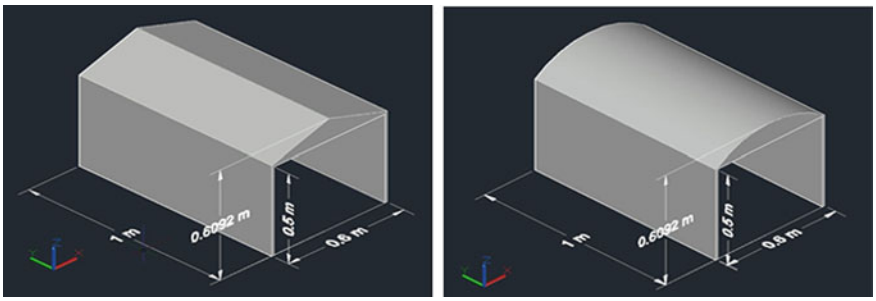

Fig. 1 Pitched roof and circular arch roof structure

Size of the computational domain for the simulation is created as per the recommendation of Franke et al. [20]. The domain size is taken in accordance with the recommendations so that reflection of fluid flow from the domain boundary does not alter the fluid interaction with the model. At the same time, blockage ratio remain below 3%. Accordingly, the inlet and outlet distances were kept as 5H and 15H, respectively, where H is the maximum height of the model. The sides of the domain walls and the top clearance from the model roof were kept as 5H each.

The C_{pe} on faces and roofs obtained on the validation model was compared with the values given in IS 875 (Part 3) [21], BS 6399-2 [22], AS-NZS 1170-2 [23], and ASCE 7-10 [24] standards as shown in Fig. 2. It can be observed that the coefficient of pressure values in different international codes/standards differs within themselves, and CFD values are within acceptable range of 15–20%. Models were then simulated under similar domain conditions and flow parameters for the study. The wind incidence angles were varied from −90° to 0° (clockwise) and +90° to 0° (anticlockwise) at an interval of 30°, 0° direction being the positive x axis which is normal to the axis of symmetry of the models as shown in Fig. 3.

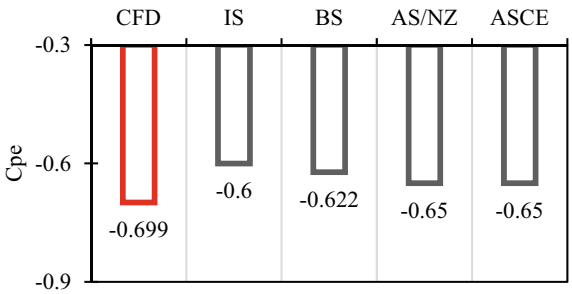

Fig. 2 Comparison of C_{pe} obtained with standard C_{pe} values given by different wind codes

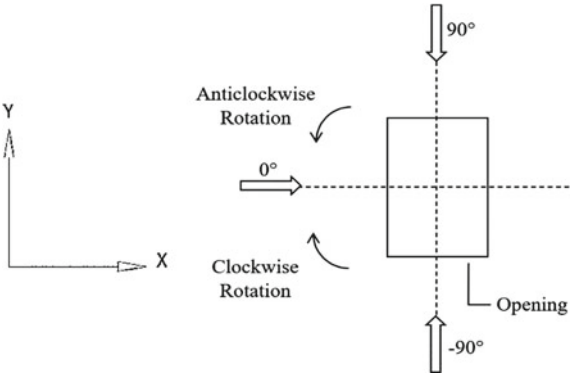

Fig. 3 Model orientation

3 Pressure Coefficient

Pressure coefficient (C_p) is a dimensionless quantity which provides a numerical representation for the relative pressure at any point w.r.t the design wind pressure. It is defined as shown in the Eq. (3).

$$C_p = \frac{\text{Pressure}}{\frac{1}{2} \cdot \rho \cdot V^2} \tag{3}$$

where ρ and V are the density of air and wind velocity, respectively. Based on the above relation, the contours of C_p for the arch and the pitched roof surfaces were plotted for 7 wind incidence angles with the interval of 30°. The present study focuses on the C_p contours for 0°, 90°, and −90° wind incidence angles.

Figure 4 represents the C_p contours for the external and internal faces of the arch and pitched roofs (roof face A and B combined) for 0° wind incidence. For the external roof face, the C_p is entirely negative for both the pitched and arch roofs with a slight increase in the suction pressure coefficient for the pitched roof. This can be attributed to the sharp edge present at the rooftop in the pitched roof due to which eddies form on the leeward side of the roof producing more suction. The effect of vortex shedding is quite evident in this case. The C_p contours for the internal roof faces for both the roofs are almost uniform. However, negative pressure coefficient of pitched roof is having lower magnitude than that of arch roof. It is due to the absence of smooth circular surface of arch roof which offers less resistance for air circulation in internal environment.

The C_p contours in Fig. 5 are obtained by the anticlockwise (+ve angles) and clockwise (−ve angles) rotation of building w.r.t the wind incidence for +90° and −90° as explained above. These cases represent closed and open side of the building facing the domain inlets, respectively. The contour variation for the external faces of both the roofs for both the wind incidence shows negative C_p values throughout the roof surface. The minimum C_p value for the external roof faces for both wind incidence angles is higher for the pitched roof due to its bluff body nature and the splitting of the wind streamline at the rooftop.

For the internal roof faces, the values of C_p are negative as expected for +90° wind incidence because of the suction created for the internal roof face by the closed wall, and positive for the −90° case because of the outward pressure exertion on the roof face due to the opening. The maximum values for both the roof cases are almost identical, however, the minimum value for the −90° case is nearly 2.12 times higher for the pitched roof case because of the sharp edge present in the pitched roof.

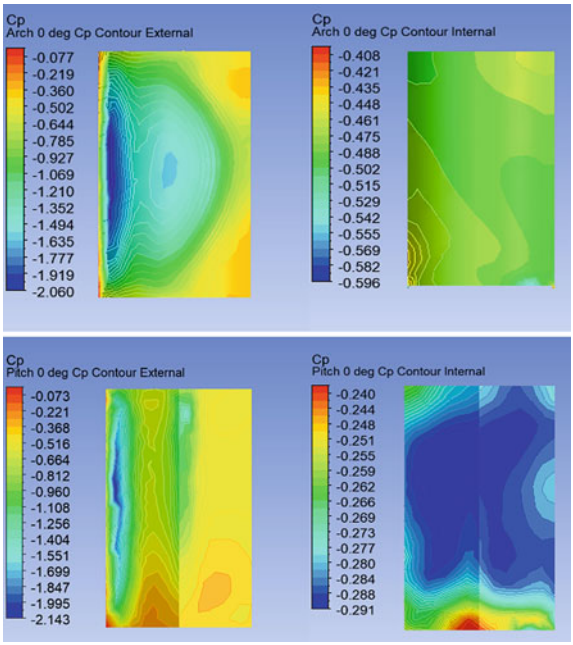

Fig. 4 C_p contours for 0° wind incidence

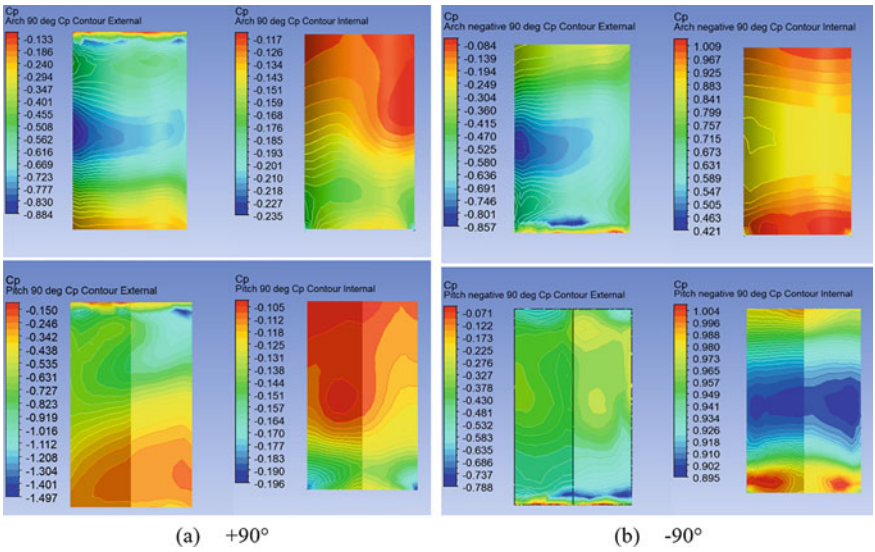

(a) +90° (b) -90°

Fig. 5 C_p contours for ±90° wind incidence

4 Drag and Lift Coefficients

Drag coefficient (C_d) and lift coefficient (C_l) are important parameters for the design of buildings and roofs against wind loadings. It can be applied on prototype building for calculating wind load on the building acting in the along and across wind directions, respectively. These coefficients also provide a platform to compare the behavior of the structures against wind flow. The C_d and C_l for both the arch and pitch roof buildings are calculated for the different angles of wind in the study of the two roofs are based on Eqs. (4) and (5).

$$C_d = \frac{F_{\text{along}}}{\frac{1}{2} \cdot \rho \cdot V^2 \cdot L_y \cdot H} \tag{4}$$

$$C_l = \frac{F_{\text{across}}}{\frac{1}{2} \cdot \rho \cdot V^2 \cdot L_x \cdot H} \tag{5}$$

where ρ and V are the density of air and wind velocity, respectively; F_{along} and F_{across} represent the forces on the building along the wind direction and perpendicular (across) wind direction, respectively; H is maximum height of the model (= 0.6092 m); L_x is the projected length along wind direction, and L_y is the projected length across wind direction which depend on the orientation of the model. The variation of C_d and C_l for both the arch and the pitched roof buildings is with the angles of wind incidence are represented in Figs. 6 and 7.

The nature of the variations of both C_d and C_l with the wind incidence angles is almost similar with very slight variations in magnitudes at the different wind incidence angles among both the roof types. However, a significant increase in the values of both C_d and C_l is seen at 0° for the pitched roof building (by nearly 1.15 and 4.60 times, respectively), and this happens because of its sharp roof edge which induces a larger force in the along wind direction and splits the wind streamline for a larger wind force in the across direction.

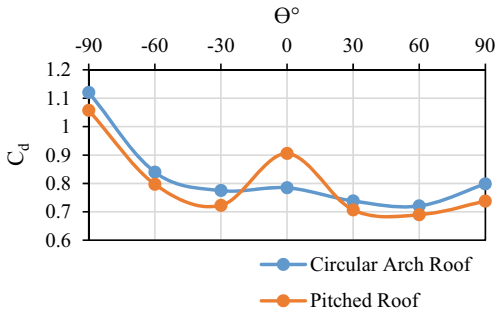

Fig. 6 Drag coefficient (C_d) versus wind incidence angle (Θ°)

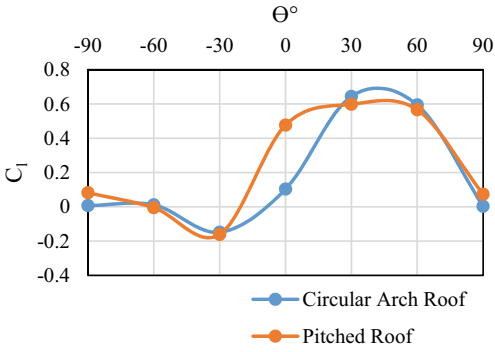

Fig. 7 Lift coefficient (C_l) versus wind incidence angle ($\Theta°$)

5 Conclusion and Future Work

In this study, a comparison has been done between a pitched roof and a circular arch roof low-rise structure. Both the type of roofs are prevalent in the industries and have similar frontal projections. When the dimensions of the building and the central rise of the roofs are kept the same, it all comes down to the shape and the curvature of these roofs, in terms of their behavior under wind loading. The opening provided on one side of the building leads to different behavior in the external and internal roof faces.

While for the 0°, the sharp edges of the pitched roof bring about positive C_p values on the external faces, it is observed that the clockwise rotation of the building w.r.t the wind results in the increase in the C_p values on the internal face of both the roofs, corresponding to larger openings w.r.t the wind and with higher magnitudes for the pitched roof owing to its sharp edge. The anticlockwise rotations, however, yield negative C_p values on both the external and internal roof faces with higher magnitudes for the arch roof.

The drag and lift coefficients calculated along and across the wind directions, respectively, also show similar variation for both the roofs, however, the magnitudes are slightly higher, particularly at 0° wind incidence angle for the pitched roof. The sharp-edged roof top for this roof is again responsible for this increment in coefficients due to the better splitting of the wind streamline.

The results and conclusions established in this study would have direct implications on similar studies on the other roof types. This comparative study provides key insight on the difference created by the shape and curvature of the roof on the pressure, force, moment and drag, lift coefficients which could be extended to other families of roofs. This would prove to be beneficial in the study of the structural soundness of the roof types under wind load conditions, accompanied with an economic design.

References

1. Blackmore PA (1988) Load reduction on flat roofs—the effect of edge profile. J Wind Eng Ind Aerodyn 29(1):89–98
2. Gerhardt HJ, Kramer C (1992) Effect of building geometry on roof wind loading. J Wind Eng Ind Aerodyn 43(1):1765–1773
3. Meecham D (1992) The improved performance of hip roofs in extreme winds—a case study. J Wind Eng Ind Aerodyn 43(1):1717–1726
4. Mehta KC, Levitan ML, Iverson RE, McDonald JR (1992) Roof corner pressures measured in the field on a low building. J Wind Eng Indus Aerodyn 181–192
5. Paul R, Dalui SK (2016) Wind effects on 'Z' plan-shaped tall building: a case study. Int J Adv Struct Eng 8(3):319–335
6. Mallick M, Kumar A, Patra KC (2019) Experimental investigation on the wind-induced pressures on C-shaped buildings. KSCE J Civ Eng 23(8):3535–3546
7. Chakraborty S, Dalui SK, Ahuja AK (2014) Experimental investigation of surface pressure on '+' plan shape tall building. Jordan J Civil Eng 8(3):251
8. Mukherjee S, Chakraborty S, Dalui SK, Ahuja AK (2014) Wind induced pressure on 'Y' plan shape tall building. Wind Struct Int J 19(5):523–540
9. Sanyal P, Dalui SK (2021) Effects of internal angle between limbs of 'Y' plan shaped tall building under wind load. J Build Eng 33
10. Sanyal P, Dalui SK (2021) Effects of side ratio for 'Y' plan shaped tall building under wind load. Build Simul 14(4):1221–1236
11. Kumar A, Raj R (2021) Study of pressure distribution on an irregular octagonal plan oval-shape building using CFD. Civil Eng J 7(10)
12. Gaur N, Raj R (2021) Aerodynamic mitigation by corner modification on square model under wind loads employing CFD and wind tunnel. Ain Shams Eng J (2021)
13. Singh J, Roy AK (2019) Effects of roof slope and wind direction on wind pressure distribution on the roof of a square plan pyramidal low-rise building using CFD simulation. Int J Adv Struct Eng 11(2):231–254
14. Singh J, Roy AK (2019) CFD simulation of the wind field around pyramidal roofed single-story buildings. SN Appl Sci 1(11)
15. Singh J, Roy AK (2019) Wind pressure coefficients on pyramidal roof of square plan low rise double storey building. Comput Eng Phys Model 2(1):1–16
16. Singh J, Roy AK (2021) Wind loads on roof of low-rise buildings. Disaster Adv 14(5):83–98
17. Verma A, Ahuja AK (2015) Wind pressure distribution on rectangular plan buildings with multiple domes. Int J Eng Tech Res (IJETR) 3(7):129–133
18. Zhou P, Tang B, Liu P, Zheng G (2019) Study on wind load distribution on the surface of dome structure based on CFD numerical simulation. J Phys Conf Ser 1176(5)
19. Verma A, Ahuja AK (2015) Wind pressure distribution on low-rise buildings with cylindrical roofs. In: Implementing innovative ideas in structural engineering and project management, pp 1211–1216
20. Franke J et al (2004) Recommendations on the use of CFD in wind engineering. In: Proceedings of the international conference on urban wind engineering and building aerodynamics
21. IS 875 (Part 3) (2015) Design loads (other than earthquake) for buildings and structures-code of practice part 3 wind loads (3rd revision)
22. BS 6399-2 (1997) Loading for buildings—part 2: code of practice for wind loads
23. AS/NZS-1170.2: Standards Australia/Standards New Zealand (2011) Structural design action—part 2: wind actions
24. SEI/ASCE 7-02: American Society of Civil Engineers (2002) Minimum design loads for buildings and other structures

Physical and Hydraulic Conductivity Behavior of Sand- and Slag-Bentonite Mixes Modified Using Nanoclay Particles

Arvind Kumar Jha and Md. Arshad

Abstract The effective uses of nanotechnology and nanomaterials for geotechnical applications such as dams, water retaining structures and landfill liner/barrier are still the matter of current research. Hence, it has been aimed in the present study to explore the potential use of nanoclay particles to modify the physical and hydraulic conductivity behavior of sand (i.e., a natural earth material) and slag (i.e., a by-product of iron industry). Detailed experimental investigations such as Atterberg's limits, compaction characteristics and hydraulic conductivity are conducted on bentonite-amended sand and slag with nanoclay particles (i.e., 1–3%). The results show that the nanoclay increases the plasticity index of both mixes. Further, addition of 2% nanoclay has shown promising results in terms of increase in MDD and hydraulic conductivity of both mixes. However, it is revealed that minimal nanoclay content can reduce the bulk amount of bentonite content to be utilized for various geotechnical constructions activities.

Keywords Bentonite · Hydraulic conductivity · Nanoclay · Slag

1 Introduction

Applications of various additives and stabilizers such as lime, cement, fly ash and asphalt are being examined since several decades despite certain limitations. However, the possible and effective uses of nanotechnology and nanomaterials in the field of geotechnical and geoenvironmental engineering to modify the desired properties of different geomaterials are the matter of current research. The nanomaterials that have been used commonly for soil modification are nanoclay, nanocarbon tubes, nanocarbon, nanosilica, nanosoil, nanoaluminum, nanocupper and other metal oxides. On comparison, nanoclay, which is predominated with montmorillonite minerals, has many advantageous characteristics such as higher specific surface area, high water adsorption capacity, high cation exchange capacity, ability to form

A. K. Jha (✉) · Md. Arshad
Department of Civil and Environmental Engineering (DCEE), Indian Institute of Technology Patna, Patna 801103, Bihar, India
e-mail: jhaarvind@iitp.ac.in

© The Author(s), under exclusive license to Springer Nature Singapore Pte Ltd. 2023

K. R. Reddy et al. (eds.), *Recent Advances in Sustainable Environment*, Lecture Notes in Civil Engineering 285, https://doi.org/10.1007/978-981-19-5077-3_28

thixotropic gel, good thermal conductivity, higher aspect ratio of particle as well as low expensive [1–6]. Hence, its utilization has been appeared to be more beneficial for geotechnical applications such as dams, water retaining structures and landfill liner/barrier. Some of the relevant researches carried out to understand the potential of nanomanterials are listed in Table 1. It can be noticed clearly with contradiction in results that despite numerous findings and research works, several issues still need to be studied for their effective utilizations and behavior with various materials and under different environmental conditions.

Table 1 Research findings by using various nanomaterials to modify the properties of soil

Authors	Materials used		Experiments	Findings	
	Soil	Nanomaterial		Increased	Decreased
Persoff et al. [7]	Sand	Nanosilica	UCS, permeability	Strength	Hydraulic conductivity
Noll et al. [8]	Sand	Nanosilica	Permeability test	–	Coefficient of permeability
Taha [9]	Clay	Nanosoil	UCS, Atterberg limits	Strength	Plasticity index (PI)
Taha and Ying [10]	Clay	Carbon nanotube	Atterberg limits; consolidation	PI Swelling index, compressibility	Hydraulic conductivity
Baziar et al. [11]	Clay	Nanoclay	Atterberg limits	PI	–
Sani et al. [12]	Sand	Nanoclay	Atterberg limits; direct shear test	Shear strength parameters (c & φ)	PI
Ghazi et al. [13]	Clay	Nanoclay	UCS	Compressive Strength	–
Majeed and Taha [14]	OL	Nanoclay	UCS; Atterberg limits; compaction	PI, MDD, strength properties	–
Janalizadeh et al. [15]	Clay	Nanoclay	Permeability	–	Hydraulic conductivity
Bahmani et al. [16]	Clay, cement	Nanosilica	Atterberg limits; permeability	PI	Hydraulic conductivity
Choobbasti et al. [17]	Sand	Nanosilica	Compaction characteristics	OWC	MDD
Baziar et al. [11]	Sand, clay	Nanoclay	Permeability, UCS, dynamic strength	UCS	Damping Ratio
Samala and Mir [18]	Clay	Nanosilica	UCS, compaction	UCS	MDD

Note OL Organic silts and organic silty clays of low plasticity; *UCS* Unconfined Compressive Strength

The present study has focused to investigate the effect of nanoclay particles on the physical properties and hydraulic conductivity of two different sources of materials, i.e., sand and slag amended with bentonites. The objectives are achieved by finding the various properties such as Atterberg's limits, compaction characteristics [maximum dry density (MDD) and optimum water content (OWC)] and hydraulic conductivity. Further, detailed characterizations of parent materials are conducted in order to understand the variation in experiment results of both sand-bentonite and slag-bentonite mixes with nanoclay content.

2 Materials Used and Methodologies Followed

2.1 Geotechnical Properties of Materials Used

The geotechnical properties of parent materials [sand (S), slag (Sg) and bentonite (B)] used in the present study and methodologies followed are presented in Table 2. The tests are conducted as per procedures of Indian Standard (IS).

The sand is collected from Holy River Ganga located in Patna, Bihar, India. The particle size analysis confirmed the presence of predominated amount of sand sized particles (4.75–0.075 mm), i.e., 88.30%. The minimum and maximum densities of sand are 1.23 and 1.52 g/cc, respectively. Slag, a by-product industrial waste material, is collected from iron industry located in Patna, India. Slag is predominated with sand sized particles (4.75–0.075 mm), i.e., 91.56%. The minimum and maximum densities of slag are observed to be 1.81 and 2.34 g/cc, respectively. On comparison, the specific gravity (i.e., 3.54) and maximum dry density (MDD) (i.e., 2.42 g/cc) of slag are more than that of the same with sand i.e., 2.71 and 1.86 g/cc, respectively, whereas optimum water content (OWC) of slag (i.e., 14.33%) is lower than that of the sand (i.e., 22.00%). According to Indian Standard Soil Classification System (ISSCS), sand and slag are classified as poorly graded sand (SP) and well graded sand (SW), respectively. However, both sand and slag are found as non-plastic (NP) in nature.

Bentonite used in the present study is obtained from Bikaner district of Rajasthan, India. The geotechnical properties (Table 1) of bentonite are same as per Jadda and Bag [19]. The bentonite is classified as a sodium (Na^+) bentonite (i.e., monovalent bentonite) having total specific area of 320 m^2/g measured by EGME. Nanoparticle used in the present study is nanoclay (NC). The commercially available nanoclay is purchased for experimental purpose. Based on data supplied by manufacturer, nanoclay is categorized as a montmorillonite clay which contains 15–35 wt.% octadecylamine and 0.5–5 wt.% aminopropyltriethoxysilane.

Table 2 Geotechnical properties of parent materials

Properties	Sand	Slag	Bentonite [19]
Specific gravity	2.71	3.54	2.76
Sand (4.75–0.075 mm)	88.30	91.56	2.00
Silt (0.075–0.002 mm)	11.70	8.44	23.00
Clay (<0.002 mm)	–	–	75.00
Coefficient of uniformity (Cu)	2.53	8.68	–
Coefficient of curvature (Cc)	0.92	1.53	–
Liquid limit (%)	10.32	5.35	230.00
Plastic limit (%)	NP	NP	187.00
Plastic index (%)	NP	NP	43.00
Max. dry density (g/cc)	1.86	2.42	1.57
Optimum water content (%)	22.00	14.33	27.00
Minimum density (g/cc)	1.23	1.81	1.57
Maximum density (g/cc)	1.52	2.34	27.00
Hydraulic conductivity (cm/s)	$4.22 * 10^{-4}$	$8.97 * 10^{-4}$	$7 * 10^{-11}$

2.2 Mineralogical Analysis and Microstructural Examination of Materials Used

X-ray diffraction (XRD) is used to perform the mineralogical analysis of samples (Fig. 1a–d). It is observed that quartz is predominant mineral in the sand (Fig. 1a), whereas slag is composed of quartz (Q), iron aluminum oxide (IAO), ferrite (F) and magnetite (Ma) (Fig. 1b). The XRD analysis of bentonite is confirmed the presence of halloysite (H) (i.e., aluminum silicate hydroxide hydrate), kaolinite-montmorillonite (K-M) (i.e., sodium aluminum silicate hydroxide hydrate), quartz (Q) and aluminum oxide (Al) (Fig. 1c). Nanoclay is predominated with montmorillonite (M) (i.e., sodium magnesium aluminum silicate hydroxide hydrate), octadecylamine hydrochloride (OH) and quartz (Q) (Fig. 1d).

The microstructural examinations of materials used are conducted by using scanning electron microscope (SEM) and are presented in Fig. 2a–d. SEM image of sand illustrates the irregular and varying size and physical appearance of particles (Fig. 1a). SEM image of slag has pronounced the varying range of particles shape and size with appearing distinct crystal and angularity patterns (Fig. 2). The SEM

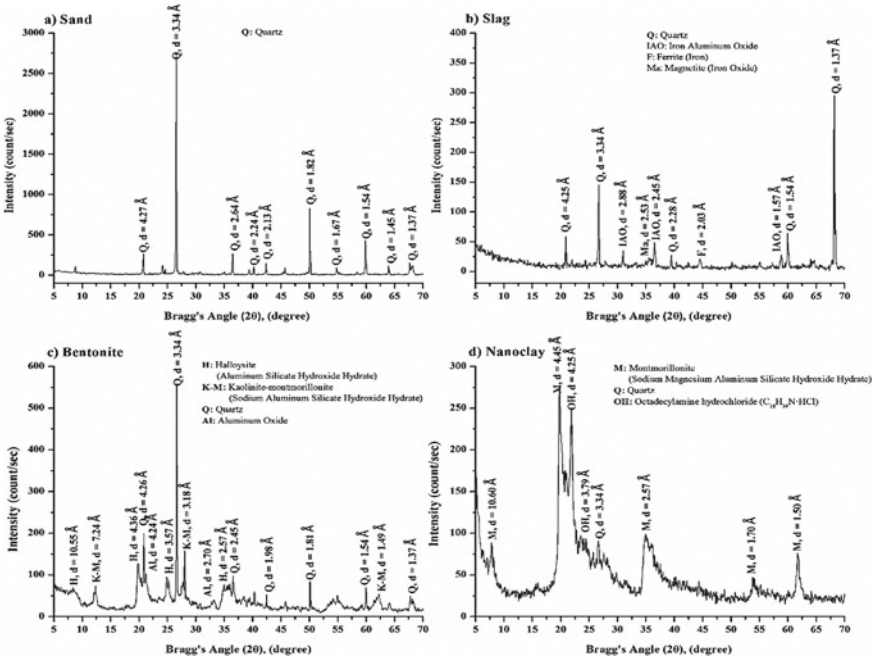

Fig. 1 XRD analyses of parent materials

image of bentonite has exhibited the accumulation of different size of needle-like structures within plate shape particles (Fig. 1c). Further, the platy shape sheet-like particles are observed in SEM image of nanoclay (Fig. 1d). The appearance of platy sheet-like particles in SEM images of bentonite and nanoclay confirmed the presence of montmorillonite in materials.

2.3 Sample Preparation and Mix Combinations

In the present study, sand and slag are selected as main constituents, whereas bentonite and nanoclay are used as additives. It is mentioned that sand and slag are non-plastic in nature and having poor in gradation. For that reason, bentonite (i.e., commonly used for barrier/liner material) contents of 5% and 10% are used to improve the plasticity behavior as well as to reduce the amount of nanoclay for economical aspect with sand and slag. The sand and slag are substituted with appropriate amount of bentonite by dry weight basis. Further, varying percentages of nanoclay (NC) (1–3%) are incorporated to evaluate their effects on the properties of each S-B and Sg-B mixes.

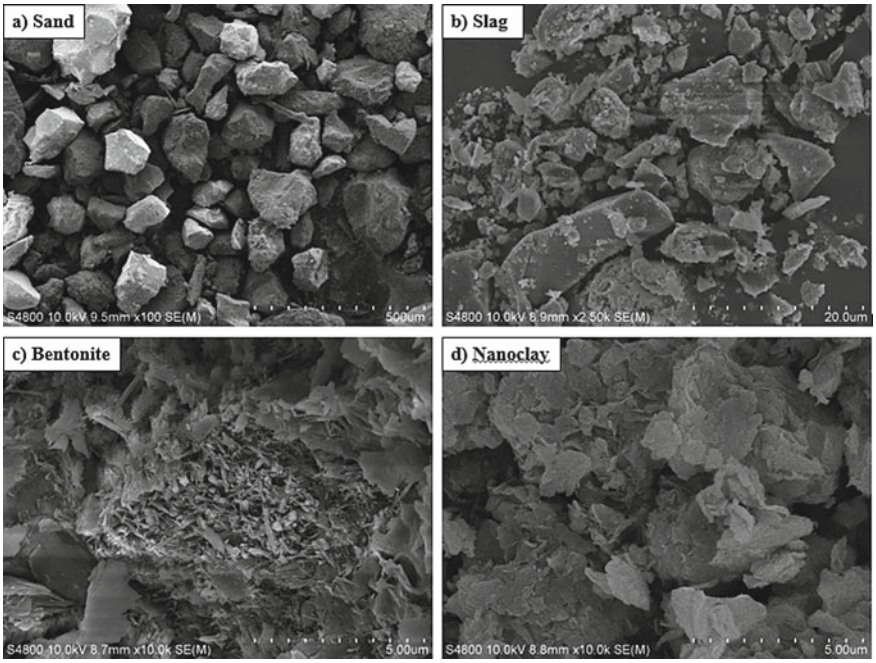

Fig. 2 Microstructural examination of parent materials

3 Results and Discussions

3.1 Atterberg's Limits of S-B and Sg-B Mixes with Nanoclay Particles

The effect of nanoclay on the liquid limit, plastic limit and plastic index of each combination of S-B and Sg-B mixes is present in Fig. 3.

It is observed that addition of bentonite results an increase in the plasticity of sand and slag. However, both plastic limit and liquid limit of both S-B and Sg-B mixes reduce with nanoclay content, whereas the derivative of liquid limit and plastic limit, i.e., plasticity index increases marginally with nanoclay. This is attributed to the requirement of additional water to flow with application of minimal shear force due to the increase in the shape aspect ratio of the mixture [11]. Further, higher surface area (SSA) of nanoclay enhances the water absorption capacity, resulting an increase in plasticity index [17, 20].

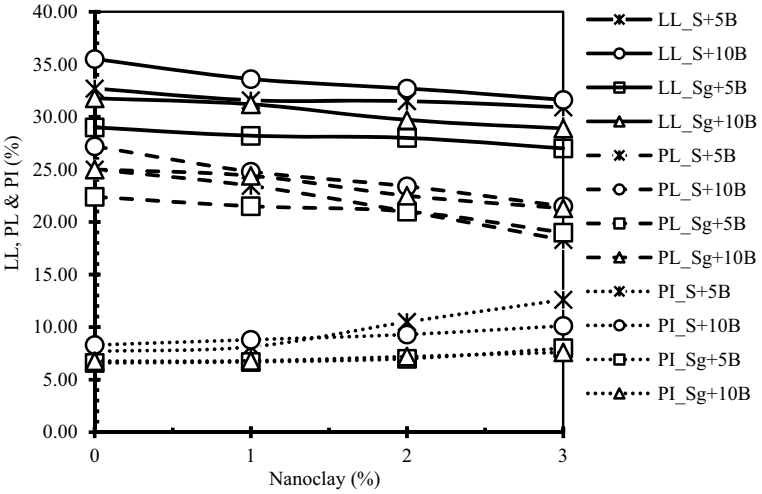

Fig. 3 Atterberg's limits of parent materials

3.2 Compaction Characteristics of S-B and Sg-B Mixes with Nanoclay Particles

The effect of nanoclay contents on the compaction characteristics of S-B and Sg-B mixes is shown in Figs. 4 and 5. It is interesting to note that effect of bentonite on the MDD value has pronounced more with slag as compared to sand. MDD of sand (i.e., 1.86 g/cc) with 5 and 10% bentonite has reduced to 1.60 g/cc and 1.65 g/cc, whereas the same with slag (i.e., 2.42 g/cc) is observed to be 2.36 g/cc and 2.33 g/cc, respectively. The reduction in the MDD of sand and slag is due to the lower MDD value and replacement of coarser size particles with clay size particles of bentonite. Further, OWC of sand and slag is observed to be increased with addition of bentonite to both sand and slag. This may be due to the higher water absorption capacity and OWC value of bentonite compared to sand and slag.

Inclusion of nanoclay up to 3% has increased the MDD of both S-B and Sg-B mixes. However, it is of interesting to observe that MDD of both mixes has appeared to be optimum at 2% NC and declined thereafter with 3% NC. The MDD values at 2% NC are 1.62 and 1.68 g/cc for sand, and 2.40 and 2.36 g/cc for slag with 5 and 10% bentonite contents, respectively. Initially, lower amount of nanoclay particles of very tiny in size acts as a filler material to form the compacted matrix, resulting an enhancement in MDD. On contrary, use of excess dosage beyond optimum limit causes its agglomeration and poor dispersion within the soil matrix, leading to the increase in void ratio/porosity, which in turn reduces the MDD [11, 21]. However, the OWC of both S-B and Sg-B mixes reduces with an inclusion of nanoclay. However, the reduction in OWC is only within 2%. The rate of reduction in OWC is found more in slag as compared to sand.

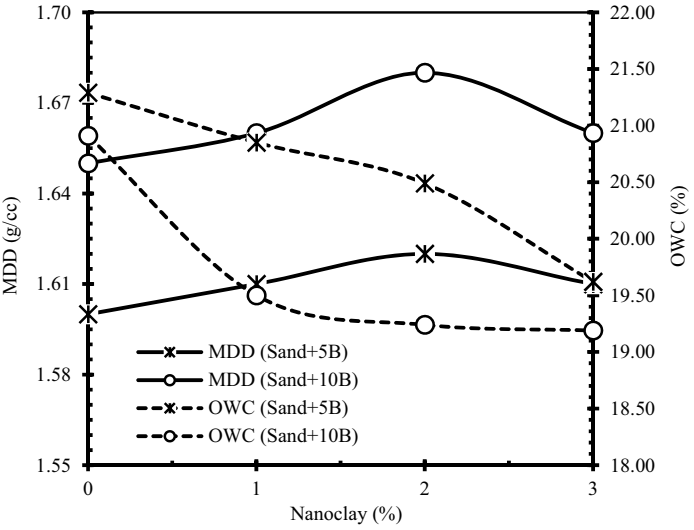

Fig. 4 Effect of nanoclay on compaction characteristics of S-B mixes

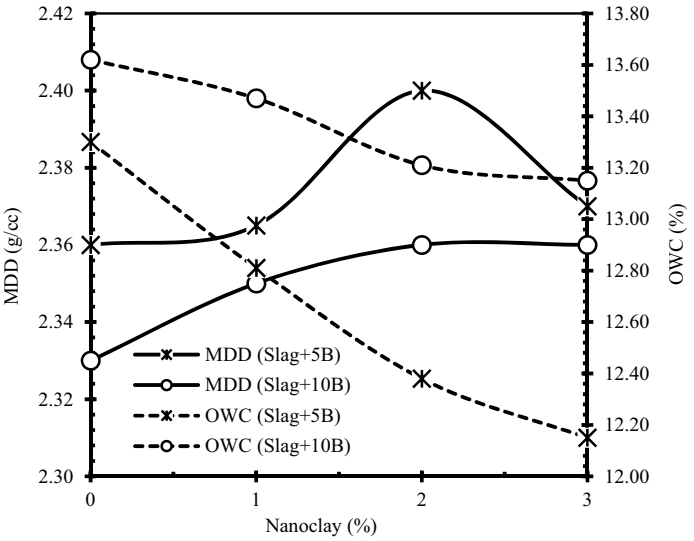

Fig. 5 Effect of nanoclay on compaction characteristics of Sg-B mixes

3.3 Hydraulic Conductivity of S-B and Sg-B Mixes with Nanoclay Particles

The effect of nanoclay content on the hydraulic conductivity of both S-B and Sg-B mixes is presented in Fig. 6. It is observed that addition of bentonite content causes a reduction in hydraulic conductivity of sand and slag, which is well-known fact and is due to its lower hydraulic conductivity. More interestingly, hydraulic conductivity reduces slightly with 5% bentonite content to slag and sand, which pronounces drastically with 10% bentonite content. Addition of 5 and 10% bentonite reduces the hydraulic conductivity to $3.870 * 10^{-6}$ and $1.744 * 10^{-9}$ m/s for sand (i.e., $4.22 * 10^{-6}$ m/s), and $3.870 * 10^{-6}$ m/s and $8.230 * 10^{-9}$ m/s for slag (i.e., $8.97 * 10^{-6}$ m/s), respectively. Further, it is interesting to note that addition of minimal amount of nanoclay up to 2% has shown drastic reduction in hydraulic conductivity of sand and slag amended with 5% bentonite and has increased thereafter. However, effect of nanoclay content has minimal influence in hydraulic conductivity of sand and slag with 10% bentonite mixes. This signifies positively that application of bulk amount of bentonite or clay can be minimized by using tiny amount of nanoclay in various geotechnical projects such as landfill liner/barrier and dams. The reduction in hydraulic conductivity of both mixes is due to the advantageous characteristics of nanoclay such as (1) ability to act as a filler material to fill the micro-void of

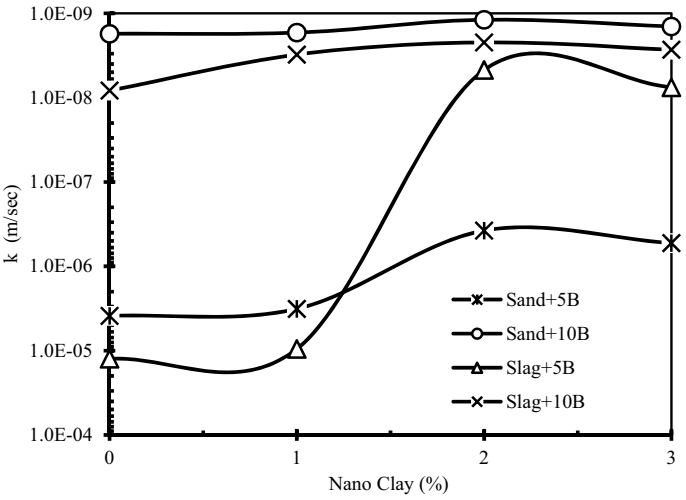

Fig. 6 Effect of nanoclay on hydraulic conductivity of S-B and Sg-B mixes

sample, (2) block the void/pore due to its swelling characteristics and (3) capacity to absorbed/hold more water and accelerate the rate of chemical reaction due to its higher specific surface area and surface charge [22, 23]. On contrary, utilization of excess nanoclay content causes its agglomeration within soil matrix, leading to increase the void/pore and consequently a decrease in the dry density and hydraulic conductivity.

4 Conclusion

Key conclusions of present findings are as follows:

1. Nanoclay enhances the plasticity index by lowering of liquid limit and plastic limit of S-B and Sg-B mixes.
2. Lower amount of nanoclay up to 2% increases the MDD of both S-B and Sg-B mixes. However, OWC of mixes reduces minimally.
3. Minimal amount of nanoclay up to 2% reduces the hydraulic conductivity of sand and slag amended with 5% bentonite significantly. However, hydraulic conductivity of sand and slag with 10% bentonite mixes increases minimally even with 3% nanoclay. This revealed that application of bulk amount of bentonite or clay can be minimized by using very small amount of nanoclay in various geotechnical projects such as landfill liner/barrier and dams.

References

1. Coo JL, So ZP, Ng CW (2016) Effect of nanoparticles on the shrinkage properties of clay. Eng Geol 213:84–88
2. LeBaron PC, Wang Z, Pinnavaia TJ (1999) Polymer-layered silicate nanocomposites: an overview. Appl Clay Sci 15(1–2):11–29
3. Liu G, Wu S, van de Ven M, Molenaar A, Besamusca J (2010) Characterization of organic surfactant on montmorillonite nanoclay to be used in bitumen. J Mater Civ Eng 22(8):794–799
4. Low IM, Hakamy A, Shaikh F (2017) High performance natural fiber-nanoclay reinforced cement nanocomposites. Springer International Publishing
5. de Melo JVS, Trichês G (2016) Effects of organophilic nanoclay on the rheological behavior and performance leading to permanent deformation of asphalt mixtures. J Mater Civ Eng 28(11):04016142
6. Uddin F (2008) Clays, nanoclays, and montmorillonite minerals. Metall Mater Trans A 39(12):2804–2814
7. Persoff P, Apps J, Moridis G, Whang JM (1999) Effect of dilution and contaminants on sand grouted with colloidal silica. J Geotech Geoenviron Eng 125(6):461–469
8. Noll MR, Bartlett C, Dochat TM (1992) In situ permeability reduction and chemical fixation using colloidal silica. In: Proceedings of the sixth national outdoor action conference, Las Vegas, NV, pp 443–457
9. Taha MR (2009) Geotechnical properties of soil-ball milled soil mixtures. In: Nanotechnology in construction, vol 3. Springer, Berlin, Heidelberg, pp 377–382

10. Taha MR, Ying T (2010) Effects of carbon nanotube on kaolinite: basic geotechnical behavior. ICCE-18, Anchorage, Alaska, USA
11. Baziar MH, Saeidaskari J, Alibolandi M (2018) Effects of nanoclay on the treatment of core material in earth dams. J Mater Civ Eng 30(10):04018250
12. Sani AM, Arabani M, Haghi AK, Chenari RJ (2010) Effect of nanoclay additive on the geotechnical properties of silty sands. In: Proceedings of 4th international conference on geotechnical engineering and soil
13. Ghazi H, Baziar MH, Mirkazemi SM (2011) The effects of nano-material additives on the basic properties of soil. In: Proceedings of 14th Asian regional conference on soil mechanics and geotechnical engineering, Hong-Kong, pp 23–27
14. Majeed ZH, Taha MR (2012) Effect of nanomaterial treatment on geotechnical properties of a Penang soft soil. J Asian Sci Res 2(11):587
15. Janalizadeh A, Nazarpoor H, Ebrahimi M (2014) Effect of nanoclay on permeability of silty sand. In: Proceedings of 8th national congress on civil engineering. Babol Noshirvani University of Technology, Mazandaranan, Iran
16. Bahmani SH, Huat BB, Asadi A, Farzadnia N (2014) Stabilization of residual soil using SiO_2 nanoparticles and cement. Constr Build Mater 64:350–359
17. Choobbasti AJ, Vafaei A, Soleimani Kutanaei S (2018) Static and cyclic triaxial behavior of cemented sand with nanosilica. J Mater Civ Eng 30(10):04018269
18. Samala HR, Mir BA (2020) Some studies on microstructural behaviour and unconfined compressive strength of soft soil treated with SiO_2 nanoparticles. Innov Infrastruct Solut 5(1):1–12
19. Jadda K, Bag R (2020) Variation of swelling pressure, consolidation characteristics and hydraulic conductivity of two Indian bentonites due to electrolyte concentration. Eng Geol 272:105637
20. Soleimani Kutanaei S, Janalizadeh Choobbasti A (2017) Effects of nanosilica particles and randomly distributed fibers on the ultrasonic pulse velocity and mechanical properties of cemented sand. J Mater Civ Eng 29(3):04016230
21. Assaedi H, Shaikh FUA, Low IM (2016) Effect of nano-clay on mechanical and thermal properties of geopolymer. J Asian Ceram Soc 4(1):19–28
22. Ng CWW, Coo JL (2015) Hydraulic conductivity of clay mixed with nanomaterials. Can Geotech J 52(6):808–811
23. Zhang G (2007) Soil nanoparticles and their influence on engineering properties of soils. In: Advances in measurement and modeling of soil behavior, pp 1–13

Performance Investigation of the Ejector Humidification Dehumidification (EHD) Cycle for Fresh Water and Cooling Generation

Deepak Singh, Srinivas Tangellapalli, and Rajeev Kukreja

Abstract Water purification, space conditioning, and energy saving are global necessities. Humidification–dehumidification (HDH) desalination is a water cycle-based process that includes air humidification and condensation. When compared to a single output device, two or three outputs from a single energy source result in overall high energy utilization factor (EUF). In this work, HDH desalination system has been expanded with the addition of a cooling system. Polygeneration of desalinated water and conditioned air utilizing solar energy fulfills the entire requirement simultaneously. This investigation is done by HDH desalination with ejector refrigeration system. The performance is investigated analytically, with the help of mass–energy balance equations. The maximum fresh yield water recorded at a particular ambient temperature (T_{Amb}) was approximately 36.08 LPH at 0.1 kg/s of airflow and 0.1 kg/s hot water flow rate in the humidifier and the cooling load, and energy utilization factor obtained from the system are 3.3 kW and 1.25, respectively. According to the findings, the suggested system has a maximum energy utilization factor is 1.26 when the evaporator temperature is −10 °C. The refrigerant used in ERC is R-134a.

Keywords Humidification–dehumidification · Ejector cycle · Cooling generation · Air pre-heater

Abbreviations

HDH	Humidification–dehumidification
ERC	Ejector refrigeration cycle
DS	Desalination system
GOR	Gain output ratio
P	Pressure (kPa)
COP	Coefficient of performance

D. Singh (✉) · S. Tangellapalli · R. Kukreja
Department of Mechanical Engineering, Dr. B. R. Ambedkar National Institute of Technology, Jalandhar, Punjab 144011, India
e-mail: deepaks.te.20@nitj.ac.in; deepaksingh22894@gmail.com

© The Author(s), under exclusive license to Springer Nature Singapore Pte Ltd. 2023

K. R. Reddy et al. (eds.), *Recent Advances in Sustainable Environment*, Lecture Notes in Civil Engineering 285, https://doi.org/10.1007/978-981-19-5077-3_29

T_{Amb}	Ambient temperature
$\dot{m}_a$	Mass flow rate of air
Q	Rate of heat transfer (kW)
w	Humidity ratio
W_p	Pump work (kW)
η	Efficiency
MR	Mass ratio
C	Specific heat
$\dot{m}$	Mass flow rate (kg/s)
P_w	Pure water
ε	Effectiveness
$\dot{m}_b$	Brine water
ω	Entrainment ratio
a,b,1,2….	State point in the system
a_s	Isotropic condition of state a

1 Introduction

The rise in global population, combined with an increase in agricultural and industrial activity, has resulted in an excess of demand for power, space cooling, and water. As a result, process integration provides numerous advantages and is the best method for decentralized power/energy production. Multiple outputs can be obtained from a single energy source. The current large-scale centralized desalination plants that produce and supply a large amount of desalinated water to urban areas use reverse osmosis. Decentralized plants, on the other hand, are more sustainable for development and have received significant attention in recent years. Mohamed et al. [1] investigated, theoretical and experimental, a closed-air cycle-based solar HDH water desalination technology is being investigated. The influence of water to air mass ratio (MR), air flow rate and cooling water flow rate on water productivity, and gain output ratio has been investigated. As the temperature of the water rises, the productivity and gain output ratio (GOR) increases. The average productivity is 1.46 kg/h, 2.59 kg/h, 4.40 kg/h, and 6.99 kg/h and gain output ratio is 0.71, 0.74, 0.78, and 0.81 at 40 °C, 50 °C, 60 °C, and 70 °C, respectively. The highest GOR of 0.86 is measured at a water to $\dot{m}_a$ ratio of 5. Askalany et al. [2] Presented a unique ejector and adsorption cycle integration to create cooling power and fresh water. Using a regeneration temperature of 75 °C the ACS and ACEJ produced SCPs of 107.5 and 115.5 W/kg, respectively. At a regeneration temperature of 95 °C, adding an ejector to ACS boosts the COP by 15%. The half-cycle time was 400 s. And 95 °C regeneration temperature, the SDWP is increased by a factor of 5.0 when compared to ADS when employing both an ejector condenser and an evaporator in an IHR system. Also when the IHR circuit is used, the COP is shown to be unaffected by the temperature of regeneration. ADEJ-HR has a COP of around 1.5. With an 85 °C desorption temperature. Boman

and Garimella [3] investigated an absorption heat drive that provides air conditioning and water purification while also providing secondary water purification via HDH. At baseline operating conditions, the HDH cycle outperforms similar cycles that use reverse and forward osmosis film purification by 12% and 19%, respectively. As a result of the high air flow rate required for air conditioning, the cycle's performance is insensitive to humidity and T_{Amb}. Though, after the heat transfer fluid input rates and heat exchanger dimensions have been determined; nevertheless, cycle performance is sensitive to water load. With a 12% reduction when the water output ratio is adjusted, there is a change in performance from 7% under to 7% overhead the baseline. Ali et al. [4] recommended using an adsorption desalination system (ADS) to bridge the gap between water availability and demand. To significantly increase freshwater output, this study suggests combining ADS with a liquid–vapor ejector. The present findings are compared to those of the ACS and the ADS, which are both standalone adsorption cooling systems. At a desorption temperature of 95 °C, ADEJ delivers a specific daily freshwater of 52.67 m^3/ton of silica gel with heat recovery. This value is 5.0 times greater than the one produced by the ADS. When the ejector is integrated with silica gel or water ADS, the COP is 1.47, which is higher than the usual technique of ADS by a factor of 2.7. Abdulateef et al. [5] investigated the basic background and development of solar-driven ERC which are used not only for air conditioning also but also for refrigeration applications and ice making to fulfill the demand for energy management and environmental protection. Numerous types of working fluids can be used in the cycle. Dry fluids, such as butane, isobutene, R114, R141b, and R114, which is require less excessive energy for superheating and thus perform superior than wet fluids and isentropic fluids at the same working temperatures. In steady state system, performance is determined by the operating condition, type of refrigerant, and ejector geometry. Sadeghi et al. [6] suggested a novel multigenerational hybrid system. ERC, as well as desalination system based on HDH processes, comprise the system. Two situations are used to perform the optimization. With the cooling capacity of 91.25 kW and a net power production of 57.03 kW, the first scenario achieves a maximum total energy efficiency of 17.12 percent. The Pareto frontier results in a gross generated power of 52.19 kW and the refrigeration capacity of 120.4 kW for the second example. On the basis of these facts, 16.46 percent total energy efficiency is computed.

2 Setup Description

ERC–HDH desalination system description and the procedure were changed by employing regular water in the dehumidifier for condensation of hot and humid air as well as the refrigerant to condense humid and hot air. By feeding hot water to the APH and humidifier, you can manage the heating and humidification of the air. When HDH desalination is paired with ERC, the outcome is combined desalination and cooling load. In the ERC, R134a is a working fluid. For various T_{Amb}, hot water temperature, evaporator temperature, and RH, the proposed system performance

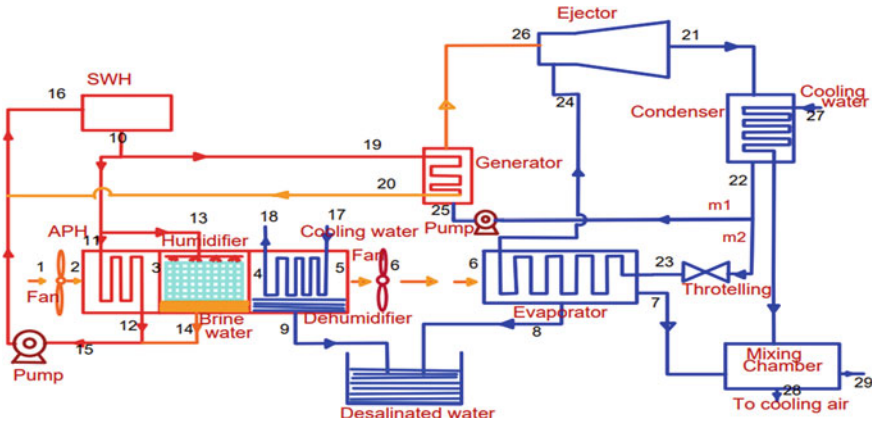

Fig. 1 Setup of an ejector HDH system

such as distilled water, cooling load, EUF, GOR, and COP is studied. The current study includes a thermodynamic analysis of the HDH desalination system with ERC, which includes APH, humidifiers, a normal water cooled dehumidifier, and an ERC unit. The ERC unit use R-134a as a refrigerant. At the system's input, a blower is employed to drive ambient air through the APH. Hot saline water circulates through the APH and heats the forced air then the hot water pump in the APH circulates hot saline water heated by the solar water heater (Fig. 1).

The high-temperature air from the APH is then sent to the system's humidifier, where hot saline water supplied by SWH is sprinkled over the high-temperature ambient air from the APH to humidify it. Following heating and humidification, heated humid air is routed to a conventional water cooled dehumidifier. The humid air has a higher WBT than the evaporator surrounded air. As a result, when humid air collides with evaporative air, it condenses. The saturated air is sent to the refrigerant-cooled evaporator after passing through the HDH. The primary goal of including a refrigerant evaporator in the cycle is to increase desalination production and provides cooling. Cooled air is sent to the mixing chamber after the refrigerant evaporator. Finally, the air from the mixing chamber is followed by the human comfort condition parameters, which are depicted in the flow diagram of the proposed humidification–dehumidification ERC.

2.1 System Model

In the RC, the refrigerant is a perfect gas with a constant C ratio. The system's thermodynamic model is numerically solved by using the given assumptions below.

- 1D and steady flow.
- The system's heat dissipation to the environment is negligible.

- The flow of air and water is assumed to be steady state
- Air flow rate is 100 m^3/h and temperature of inlet air is 28 °C
- Ø of supply air is 67%
- ε of air pre-heater is 0.6
- $T_{hot\ water}$ at inlet is 50 °C
- $T_{hot\ water}$ drop is 8 °C
- Water in condenser at 20 °C
- Evaporator maintain at 6 °C.

2.2 Numerical Investigation

Reference values have been taken from the Al-Mahammad. Air flow rate is 100 m^3/h, inlet air temperature in the air pre-heater is 24 °C, Ø of inlet air in the air pre-heated is 65%, and air pre-heater effectiveness (ε) is 0.6

$$\textbf{Mass of air(wet air)}\ \dot{m}_{air} = \frac{P_{air}\ V_{air}\ M_{air}}{R_{air}\ T_{air}} \tag{1}$$

$$\dot{m}_{da} = \frac{\dot{m}_{air}}{1+\omega} \tag{2}$$

To determine the flow rate of APH, the $T_{hot\ water}$ in and out has been fixed. The APH's energy balance equation [7] yields the hot water flow rate at the known $\dot{m}_a$, which is fixed according to the air exit temperature, is determined from its ε.

$$\varepsilon = \frac{(T3 - T2)}{(T12 - T11)} \tag{3}$$

To find out the mass of hot water, apply the energy balance [7] in the air pre-heater

$$\dot{m}_{hw}(T_{11} - T_{12}) = \dot{m}_{da}(T_3 - T_2) \tag{4}$$

At the humidifier inlet temperature and w, the humidifier inlet $T_{hot\ water}$ is greater than the air inlet temperature ($T_{13} > T_3$), so heating and humidification takes place in the humidifier.

$$\eta = \frac{\omega_4 - \omega_3}{\omega_{max} - \omega_3} = \frac{(T_4 - T_3)}{T_{max} - T_3} \tag{5}$$

Now finding out the hot water mass inter into the humidifier

$$\dot{m}_{13} = \frac{\dot{m}_{da}(h_4 - h_3)}{C_{pw}(T_{13} - T_{14})} \tag{6}$$

On the psychometric chart, heating and humidification process progresses toward the $T_{\text{hot water}}$, with the extreme humidification limit, i.e., 100% Ø, at this $T_{\text{hot water}}$ and Ø the exit, and mass of wet air from the humidifier is ($\dot{m}_4$)

$$\dot{m}_4 = \dot{m}_{da}\omega_3 + \dot{m}_{da}(\omega_4 - \omega_3) \tag{7}$$

Because of the air humidification, the $\dot{m}_b$ collected at the bottom of the humidifier is less than the $\dot{m}_{\text{hot water}}$ supply. The hot water spray in the humidifier has been determined based on the MR, a constant rate of air flow.

$$\dot{m}_b = \dot{m}_{13} - \dot{m}_{da}(\omega_4 - \omega_3) \tag{8}$$

Heat rate in the humidifier

$$Q_h = \dot{m}_{da}(h_4 - h_3) \tag{9}$$

Now use energy balance equation [7] and find out the exit temperature of the water.

$$\omega_5 = \omega_4 - \frac{(\omega_4 - \omega_{\min})(T_4 - T_{\min})}{T_4 - T_{17}} \tag{10}$$

Relative humidity of air is 100%, $h = h_{max}$, and mass of water in the air is.

$$\dot{m}_5 = \dot{m}_{da}(\omega_4 - \omega_3) \tag{11}$$

Circulating water required in the dehumidifier is

$$\dot{m}_w = \frac{\dot{m}_{da}(h_4 - h_5)}{C_{pw}(T_{18} - T_{17})} \tag{12}$$

Heat is out going from the dehumidifier, i.e., Q_{dh}

$$Q_{dh} = \dot{m}_{da}(h_4 - h_5) \tag{13}$$

Assume inlet condition of the ejector is saturated vapor, i.e., in the ejector, it is isentropic process so the properties are taken from property table

$$h_{26} = h(T_{26}, x = 1) \tag{14}$$

$$h_{24} = h(T_{24}, x = 1) \tag{15}$$

Energy balance applied into ejector before entering into the ejector and after exiting the ejector.

$$\dot{m}_1 h_{26} + \dot{m}_2 h_{24} = (\dot{m}_1 + \dot{m}_2) h_{21} \tag{16}$$

$$\omega = \frac{\dot{m}_1}{\dot{m}_2} \tag{17}$$

The is the ratio of mass flow through the evaporator to mass flow via the generator, where 1 and 2 are the primary and secondary flows, respectively. The employed fluid is totally condensed in the condenser, the specific enthalpy of state 22 equals the enthalpy of saturated liquid at state 21 and may be written as:

$$h_{22} = h(T_{21}g, x = 0) \tag{18}$$

$$h_{26} + \omega h_{24} = (1 + \omega) h_{21} \tag{19}$$

T_{21}g is the temperature of the condenser. Because the vapor in state 21 can be super-heated, T_{21} can be higher than the condenser.

$$h_{22} = h(T_{21}g, x = 0) \tag{20}$$

Between states 22 and 23, the working fluid goes via the expansion valve, hence the specific enthalpy remains constant, i.e.:

$$h_{22} = h_{23} \tag{21}$$

Furthermore, the pump's effort may be insignificant, implying that the specific enthalpy stayed almost constant, implying that pump work was ignored.

$$\frac{V_{a2}}{2} = (h_{26} - h_a) \tag{22}$$

The convergent–divergent nozzle exit is represented by state (a); whereas, the divergent nozzle exit is represented by state (b). The states inside the ejector have governing equations, which are described below.

$$\frac{V_{b2}}{2} = (h_{21} - h_b) \tag{23}$$

The mixing section's equivalent of the fluid momentum conservation equation [4] can be written as:

$$V_{a1} + w V_a^2 (1 + \omega) V_b \tag{24}$$

$$h_{\mathrm{b}} = h_{21} - (h_{26} - h_a)/(1 + \omega)^2 \tag{25}$$

To compute the specific enthalpy at state, use the following system of equations [4].

$$x_{\text{as}} = \frac{(S_{\text{as}} - S_{\text{fas}})}{(S_{\text{gas}} - S_{\text{fas}})} \tag{26}$$

$$S_{\text{as}} = S(T_{26}, x = 26) \tag{27}$$

$$\eta_{26\text{a}} = (h_{26} - h_a)h_{26} - h_{\text{as}} \tag{28}$$

The evaporator's saturated liquid and vapor enthalpies are h_{fas}, h_{gas}, and the evaporator's saturated liquid and vapor entropies, i.e., S_{fas} and S_{gas}, respectively.

$$\eta_{b21} = \frac{(h_b - h_{21\text{s}})}{(h_b - h_{21\text{new}})} \tag{29}$$

$$x_b = \frac{(h_b - h_{\text{fas}})}{(h_{\text{gas}} - h_{\text{fas}})} \tag{30}$$

$$h_{21\text{s}} = h(P_{21}, S = S_b) \tag{31}$$

Generator

$$Q_g = \dot{\text{m}}_1(h_{26} = h_{25}) \tag{32}$$

Condenser

$$Q_c = \dot{\text{m}}_t(h_{21} = h_{22}) \tag{33}$$

Evaporator

$$Q_e = m_2(h_b - h_{23}) \tag{34}$$

$$\text{COP} = \frac{Q_e}{Q_g + W_p} = \frac{w(h_2 - h_5)}{h_1 - h_4} \tag{35}$$

The proportion of each stream's actual enthalpy change to the maximum possible enthalpy change is used to calculate the humidifier and dehumidifier, as demonstrated below:

$$\varepsilon = \frac{\Delta H}{\Delta H_{\text{max}}} \tag{36}$$

As follows, the MR is defined as the ratio of water to air flow rate

$$\mathrm{MR} = \frac{\dot{m}_w}{\dot{m}_{\mathrm{da}}} \tag{37}$$

Performance of an HDH cycle is calculated through GOR. As demonstrated in Eq. [4], it is the ratio of the evaporation latent heat of water to that of energy input.

$$\mathrm{GOR} = \frac{(\dot{m}_{\mathrm{pw}}\ h_{\mathrm{fg}})}{Q_h} \tag{38}$$

The EUF is the proportion of the combined system's output energy to its intake energy may be used to indicate the hybrid system's performance. The overall fresh-water enthalpy of generation and ejector cycles load for refrigeration is represented by the output energy.

$$\mathrm{EUF} = \frac{Q_e + \dot{m}_{\mathrm{pw}} h_{\mathrm{fg}}}{Q_g + Q_h + W_p} \tag{39}$$

2.3 Preliminary Results

Sr. no	Parameter	Value
Ejector cooling cycle		
1	Condenser temperature (°C)	20
2	Evaporator temperature (°C)	6
3	Entrainment ratio	3.5
4	Generator temperature (°C)	50
5	Condenser heat rate kW	172.6
HDH desalination system		
6	Air pre-heater temperature (°C)	24
7	Humidifier maximum temperature (°C)	50
8	Humidifier minimum temperature (°C)	37
9	Heat rate in humidifier kW	1.713
10	Dehumidifier maximum temperature (°C)	27
11	Heat rate in dehumidifier kW	2.53
12	MR	1.296

(continued)

(continued)

Sr. no	Parameter	Value
13	COP	0.1715
14	Gain output ratio	1.98
15	Effective utilization factor	1.25

Figure 2 shows the fluctuation of COP as a function of evaporator temperature (T_e), demonstrating the tendency that as the temperature of the evaporator rises, the COP of the ERC first declines, and then rises.

Figure 3 shows variation of effective utilization factor with evaporator temperature in an opposing trend with increasing the air temperature in the hybrid humidification–dehumidification cooling cycle.

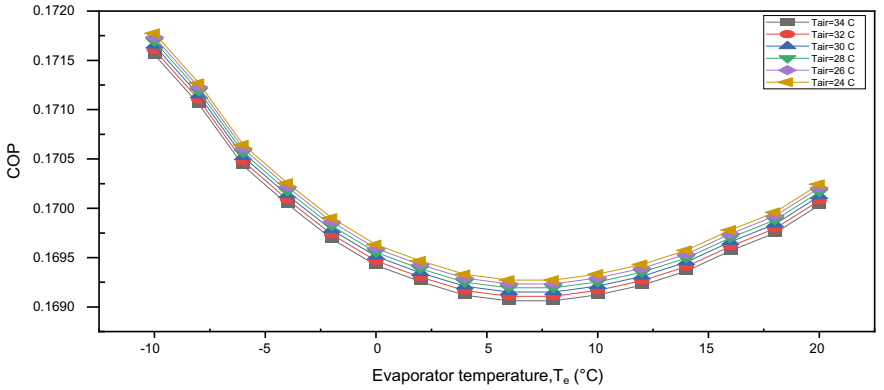

Fig. 2 The fluctuation of COP with the change of T_e

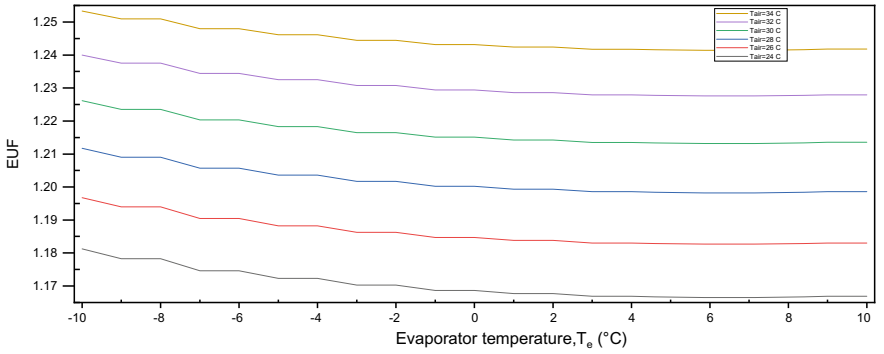

Fig. 3 Variation of effective utilization factor with the changing of evaporator temperature

3 Conclusion

The study was carried out to investigate the performance prediction of humidification–dehumidification ERC. The operational parameters listed above emphasize the most critical requirements for controlling desalination. In unit performance, such as hot water temperature and relative humidity of the atmosphere, there are two types of temperatures: T_{Amb} and evaporative temperature. Because of the vast range of input elements that might impact the overall performance of the desalination unit, a computer application and the MATLAB software have been written to analyze and simulate the desalination system. The peak value of $T_{\text{hot water}}$, η_{h}, and dehumidifier ε generates a substantial quantity of desalination as well as cool air. We were able to obtain 36.08 LPH of freshwater and 11.616 TR cooling load at 0.1 kg/s mass flow rate air seawater.

References

1. Ali ES, Mohammed RH, Qasem NA, Zubair SM, Askalany A (2021) Solar-powered ejector-based adsorption desalination system integrated with a humidification-dehumidification system. Energy Convers Manage 238:114113
2. Alkhulaifi YM, Baata E, Al-Sulaiman FA, Ibrahim NI, Ben-Mansour R (2021) Performance and exergoeconomic assessment of a novel combined ejector cooling with humidification-dehumidification (HDH) desalination system. Desalination 500:114843
3. Ali ES, Mohammed RH, Askalany A (2021) A daily freshwater production of 50 m^3/ton of silica gel using an adsorption-ejector combination powered by low-grade heat. J Clean Prod 282:124494
4. Al-Mahmoud HA, Ibrahim NI, Al-Sulaiman FA, Zubair SM (2020) Thermodynamic performance evaluation of a hybrid ejector cooling and humidification-dehumidification desalination system. Energy Convers Manage 225:113450
5. Boman DB, Garimella S (2021) Performance improvement of a water-purifying absorption cooler through humidification-dehumidification. Appl Therm Eng 185:11632
6. Chafidz A, Al-Zahrani S, Al-Otaibi MN, Hoong CF, Lai TF, Prabu M (2014) Portable and integrated solar-driven desalination system using membrane distillation for arid remote areas in Saudi Arabia. Desalination 345:36–49
7. Tangellapalli S (2021) Humidification-dehumidification and heat pump integration for water purifier and air conditioning. Energy Convers Manage 244:114472

Assessment of Subsurface Migratory Behavior of Lead (Pb) Laden Leachate Generated from a Waste Dumpsite in Srinagar, Kashmir, India

Abdul Waris Kenue, Eedy Sana, Avishek Adhikary, Majid Hussain, and Supriya Pal

Abstract Contamination of groundwater due to leachate percolation is an alarming issue globally. Developing countries in the sub-continent are no exception, and the present work focuses on assessing a similar issue in one of the landfills of the Himalayan region, Kashmir. The work entails the identification of prominent heavy metals in surface water, subsurface water, and leachate present in and around the landfill site. Geotechnical properties and sorption studies were carried out to determine the input parameters required to model contaminant flow using the HYDRUS 1D and 3D package, and the models were validated with the laboratory-scale dynamic assays. The modeling was carried out in a bid to provide a better work plan for policy-makers and government agencies to remediate the two primary problems at hand: problems of flooded leachate pools in the vast open spaces of the landfill and direct draining out of untreated leachate through drainage lines/pipes into the nearby stream. This work concludes that the remediation work on untreated leachate drainage into the river stream must take precedence over the flooded leachate pool in the landfill as the subsurface migration of the prominent contaminant Pb does not pose a significant threat in the near future. The flooded leachate pool can therefore be pumped out, at convenience, through remediated drainage lines which would save labor and time.

Keywords Landfill · Contaminant transport and migration · Groundwater · Lead

A. W. Kenue (✉) · A. Adhikary · S. Pal
National Institute of Technology Durgapur, Durgapur, West Bengal 713209, India
e-mail: abdulwariskenue@gmail.com

S. Pal
e-mail: supriya.pal@ce.nitdgp.ac.in

E. Sana
National Institute of Technology Silchar, Fakiratilla, Silchar, Assam 788010, India

M. Hussain
National Institute of Technology Srinagar, Hazratbal, Srinagar, Jammu and Kashmir 190006, India
e-mail: majid.h@nitsri.ac.in

© The Author(s), under exclusive license to Springer Nature Singapore Pte Ltd. 2023

K. R. Reddy et al. (eds.), *Recent Advances in Sustainable Environment*, Lecture Notes in Civil Engineering 285, https://doi.org/10.1007/978-981-19-5077-3_30

1 Introduction

The migration of the population from rural to urban areas has increased the pressure on landfills which receive the ever-increasing dump load leading to direct consequences on the environment and creating waste management issues for municipalities, companies, and governments [1]. Above 90% of the waste is openly dumped by municipalities of developing countries, such as India [2]. In India, municipal solid waste (MSW) management falls short of the desired standards, as the system employed is outdated [3]. Even though the Central Pollution Control Board (CPCB) and Ministry of Environment (2000) clearly state the specification of landfill base, which should have leachate collection/treatment systems, a 1.5 mm thick high-density polyethylene (HDPE) for containing the leachate [4]. But in India, such practices are seldom implemented, and if implemented, proper maintenance is rarely taken care of due to unscientific and ad hoc based approaches on the field [5]. These landfills harbor numerous hazardous compounds such as aromatic hydrocarbons, halogenated compounds, phenols, antibiotics, and heavy metals [6].

In India, most MSW disposal is done by unengineered open field dumping, posing a risk to the environment in soil and groundwater contamination since the leachate emanates from the waste and percolates into the subsurface, contaminating the groundwater. The solid waste consists of plastic items, batteries, tyres, food, e-waste, and scrap, produced in the city [7]. Poor infrastructure, inefficient management of landfills, low investment by the government, poor maintenance and check, and non-abidance to the environmental laws have made landfills a source of permanent pollution: air, soil, and water pollution [1]. The landfill in Kashmir, though equipped with leachate treatment plants (LTPs), engineered cell structures cannot be called an efficient engineering landfill because it still has issues of inferior maintenance, ineffective/dysfunctional LTPs, and unscientific open dumping practice into the only available cell.

Lead may be present in the form of combined minerals or organic compounds [8]. It is very harmful if it accumulates in body organs, causing plumbism (lead poisoning) or even death. The brain, central nervous system, gastrointestinal tract, and kidneys are affected by the presence of lead. No amount of lead has been found free of harmful effects [9]. The high concentration of Pb in leachate could pose the risk of groundwater contamination in the future [7].

In this article, the authors have attempted to model the subsurface transport and migration of lead using the HYDRUS package to ascertain the vulnerability of geoenvironmental pollution by percolation of lead from the spilled-out leachate flooded in the large open spaces at the Achan landfill site. This work would help prioritize whether immediate remediation is required for the subsurface percolation or for treating the leachate which directly drains into the river stream or for both simultaneously.

Fig. 1 Map of Achan landfill site depicting the situation at hand

1.1 Area of Interest

Srinagar is the summer capital and the largest city of the state of Jammu and Kashmir, India [10]. Srinagar is housed in Kashmir Valley, which is surrounded by picturesque mountain ranges in the lap of the Himalayas [2] This city produces the highest per capita per day of MSW in the Kashmir region. The only landfill site for the disposal of wastes from all the different areas of Srinagar is Achan [10]. The Achan landfill area (see Fig. 1) was first started as an open dumping site back in 1985 CE with a land area of 26 hectares approximately. As per the 2015–2016 data, the per day collection of waste in Srinagar city alone was 400 metric tons [3]. This landfill is near the once magnificent Anchar freshwater lake, deteriorating rapidly due to premature aging. One of the reasons could be contamination from the unscientific landfill drains, which directly drain into a nearby stream and leachate percolation through the subsurface soil [10, 11].

2 Material and Methodology

2.1 Geotechnical Investigations of the Soil

Soil samples were collected at a depth of 0.50 m from the ground level. Undisturbed soil samples were collected in core cutters, and disturbed soil samples were collected in polypropylene bags and transported to the geotechnical engineering laboratory at the National Institute of Technology, Srinagar.

Index and engineering properties including Atterberg's limits, in situ water content, optimum moisture content and maximum dry density, coefficient of permeability (falling head permeability test), bulk density, grain size analysis, and the organic content of the soil were determined. All tests were performed following the

IS standard codes except for organic content determination, where ASTM D2974 was used [12].

2.2 Sampling, Storage, and Analysis of Leachate

The leachate, surface, and subsurface water samples were collected from different places in and around the landfill site. These samples were immediately transported to Residue and Quality Analysis (RCRQA) laboratory at Sher-e-Kashmir University of Agricultural Sciences and Technology (SKUAST) for determining the heavy metals using flame atomic absorption spectrophotometer (FAAS). The samples were acidified (pH < 2) and kept at a temperature of 4 °C in a refrigerator, later filtered through Whatman Grade1 filter paper. These leachate samples were analyzed for heavy metals (Zn, Pb, Cu, Mn, Ni, Cr, and Fe) using the FAAS [13]. The instrument used was the Agilent (Make) model 240 FS.

2.3 Batch Adsorption Tests

The adsorption test was conducted on the local soil by following the ASTM code, Organization for Economic Co-operation and Development (OECD) recommendations, and available literature [14–20]. Geomedia sample was air-dried, crushed, and passed through a 2 mm sieve. Moisture content was determined to calculate the mass equivalent oven-dried sample from the air-dried sample using Eq. (1).

$$M_A = M_s * [1 + (M/100)] \tag{1}$$

where M_A denoted the original air-dried mass, M_s denoted the mass of equivalent (desired) oven-dried sample, and M was the moisture content in %age. Here,

$$M_A = 5 * (1 + 0.023) = 5.115 \text{ g}$$

Then, 5.00 g equivalent oven-dried samples were placed in the flasks, and 100 ml of contaminant solution was added to form the sorbate-to-sorbent (solid/liquid) ratio of 1:20 (in terms of mass). The appropriate amount of solution was prepared to determine the initial concentration. Conical flasks along with geomedia and solution were put in the incubator shaker while maintaining an rpm count of 150, at the temperature of 20 ± 5 °C. Appropriate intervals for determining the concentration of the solution were chosen, and the intervals were taken as 0, 15, 30, 60, 120, 240, 480, and 1440 min initially, but then in the later tests 4 h duration sufficed the test, as equilibrium was achieved early on. The geomedia phase was separated from the solution via decantation, and the supernatant was poured into the 15 ml tube, centrifuged,

and then acidified (5% addition of acid HNO_3) to determine the concentration of solution using FAAS. As per ASTM recommendations, three method blanks were also prepared without geomedia [14].

Once this was done, isotherm studies and kinetic studies were carried out. Different isotherm models such as linear, Freundlich, Langmuir, and Temkin were compared with the obtained experimental isotherm data. Similarly, various models were analyzed for chemical kinetic studies, such as the pseudo-first-order, pseudo-second-order, intraparticle diffusion, and Elovich kinetic model for the obtained experimental data. Linear (straight) lines were plotted for isotherm and kinetic studies, and the parameters were obtained from their slope and intercept values. The goodness-of-fit was determined by the R-squared value available in the MS excel program.

2.4 Fixed-Bed Column Test (Dynamic Assays)

Laboratory-scale column tests were conducted, and exit concentrations were determined at different time intervals. These were performed to obtain the breakthrough curves and validate the models generated using the HYDRUS 3D package. The bed depth of geomedia was varied (20 and 30 mm) for a constant Pb concentration of 10 ppm, the maximum concentration limit at the landfill site.

2.5 Modeling of Fate and Transport of Prominent Contaminant Using Hydrus

The experimental laboratory-scale fixed-bed columns and the subsurface migration of prominent contaminants through the soil at the landfill were modeled via the HYDRUS standard solute transport module. The input data was obtained from the local soil's geotechnical properties and sorption studies (batch adsorption assays). The chosen Pb^{2+} concentration for modeling purposes was 10 ppm, and the maximum concentration determined at the site. In the case of fill media over the local soil, appropriate sorption data was chosen from the literature, which matched its grain size analysis [21]. The sorption parameters for the two soil layers are mentioned in Table 3. The modeling for the subsurface was performed for 2400 mm total soil depth with 1900 and 500 mm of fill media and local soil, respectively.

Table 1 Geotechnical properties of the soil sample at Srinagar's only landfill site

Geotechnical properties		(Units)
In situ water content	33.95	%
In situ bulk density	19.39	kN/m^3
Sand fraction	14.82	%
Silt fraction	81.38	%
Clay fraction	3.8	%
Liquid limit	27.53	%
Plastic limit	20.20	%
Shrinkage limit	20.10	%
Organic content	6.97	%
Soil type	ML	-
Sedimentation analysis remarks	*Fine-grained soil depicts high silt content*	-
Optimum moisture content	16.38	%
Maximum dry density, γ_{dmax}	18.07	kN/m^3
Coefficient of permeability at 27 °C	2.795 * 10^{-6}	cm/s

3 Results and Discussion

3.1 Geotechnical Investigation of the Soil at the Site

The basic geotechnical properties of the soil from the landfill site as determined by IS codes are mentioned in Table 1. The soil is classified as low-plasticity silt.

3.2 Heavy Metals in Leachate and Water Samples in and Around the Site

Leachate and groundwater samples were analyzed for heavy metals (Table 2), and it was found that lead is a prominent contaminant in all the leachate (L) and water (W) samples. This poses a risk of surface and groundwater contamination [8].

Lead could have been produced by dumping materials like lead batteries, cable covers, ammunitions, solders, electronic waste, pipes, and paints [8, 22]. Emissions from poorly maintained dumping vehicles which remain in a queue to dump the waste in the overloaded cell-2 could also have contributed to the higher concentration of Lead than permissible [23].

Table 2 Heavy metal in three leachate samples and three water samples

Heavy metals	*L2*	*L3*	*L5*	*W1*	*W2*	*W3*	IS10500:2012	IS 2490 PART 1—1981
Zn	0.88	0.84	0.87	0.11	0.06	0.04	5	5
Pb	**1.67**	**1.58**	**8.41**	**0.18**	**0.17**	**0.17**	**0.05**	**0.1**
Cu	0.32	0.51	0.80	0.02	0.03	0.01	0.05	3
Mn	0.14	0.17	0.40	0.08	0.05	0.03	0.1	–
Ni	0.82	1.06	1.48	0.05	0.03	0.03	0.02	3
Cr	0.33	0.92	0.74	BDL	BDL	BDL	0.05	2
Fe	1.29	7.40	7.56	0.13	0.09	0.05	0.3	–

All concentrations are in mg/l; *BDL* Below detection line

Table 3 Langmuir and Freundlich parameters

Langmuir parameters	Local soil	Freundlich parameters	Fill soil
Q_{max} (mg/g)	0.3652	K_f (mg/g)	0.681
k_L (L/mg)	0.2271	n	0.481
R^2	0.9408	R^2	0.8542

3.3 Sorption Results

Batch adsorption

Removal Efficiency and Equilibrium adsorption capacity. The results revealed that the removal efficiency for the concentration range of 0.5–10.0 ppm was anywhere in the range between 70 and 90% in the experimental batch adsorption tests (Fig. 3). The removal percentage was maximum for 10 ppm. Initially, with a 10 ppm concentration of Lead, 24 h tests were executed with equilibrium attained within 2 h, with much of the removal happening rapidly in the first 15 min. This could be attributed to Lead's spontaneous adsorption or chemisorption onto the geomedia. Therefore, all other tests were terminated at 4 h with the assumption that equilibrium would have reached by then [16, 24, 25].

Isotherm Studies. Isotherm studies provide essential information about the adsorbate–adsorbent interaction mechanism and its surface characteristics and describe adsorbent capacity [26]. Data from the equilibrium adsorption capacity test was utilized for the isotherm study (Fig. 4). Based on the goodness-of-fit value (R^2), the defining model for the local soil followed Langmuir's model with the highest R^2 value of 94.08. The Langmuir adsorption isotherm is based on ion adsorption in a monolayer on the adsorbent's surface, the system energy is also considered constant, and the binding sites are uniformly distributed across the adsorbent surface [27]. This model implies that the adsorbent is homogenous. In our case, 81% of the soil fraction is silt (Table 1).

Kinetic Studies. Figure 2 shows the experimental data's kinetic model, which closely approximates the pseudo-second-order reaction with an R^2 value of 0.999. Thus, the adsorption reaction is primarily chemisorption, which is also indicated by the swift adsorption reaction time in attaining equilibrium.

HYDRUS modeling

Laboratory-Scale Fixed-bed column test. Figure 5 depicts the graphical representation of normalized exit concentration and time for experimental and predicted results, which show an excellent corelation. The numerical models generated in HYDRUS 3D establishes the flow of lead solution with a concentration of 10 ppm at the upstream end of the soil column with a constant head of 100 mm. The lead saturation level reached 90% for local soil under 100 mm head in 4 and 5 days for a soil depth of 20 and 30 mm, respectively. This could be attributed to the low hydraulic permeability of soil due to the high fraction of fine particles (Table 1). This provides confidence for the results to be modeled for the contamination transport through the local soil at the site (Fig. 6).

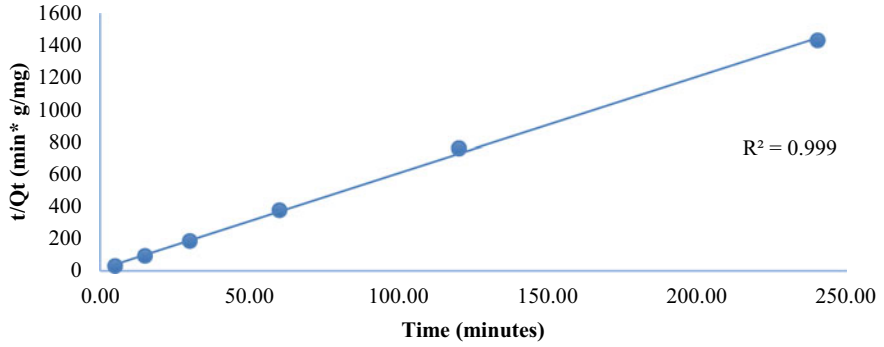

Fig. 2 Pseudo-second-order kinetic study graph

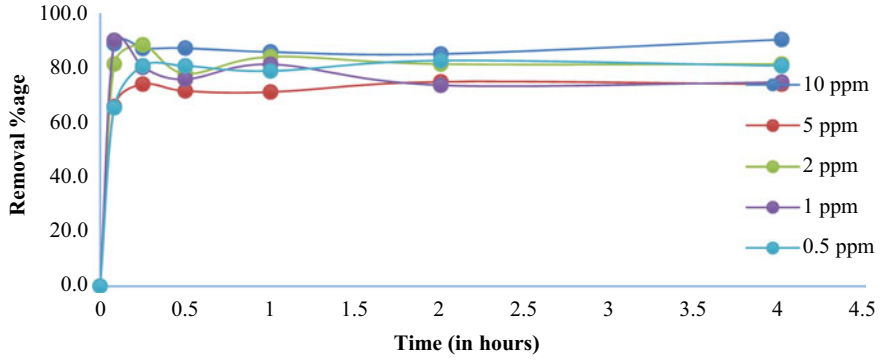

Fig. 3 Removal efficiency of Pb in the local soil

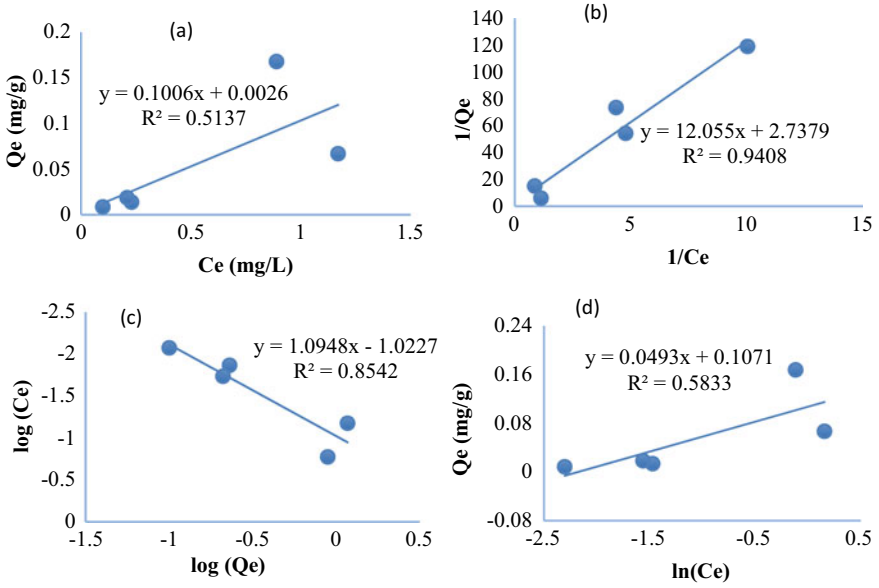

Fig. 4 Isotherm models of local soil from static assays. **a** Linear **b** Langmuir **c** Freundlich **d** Temkin

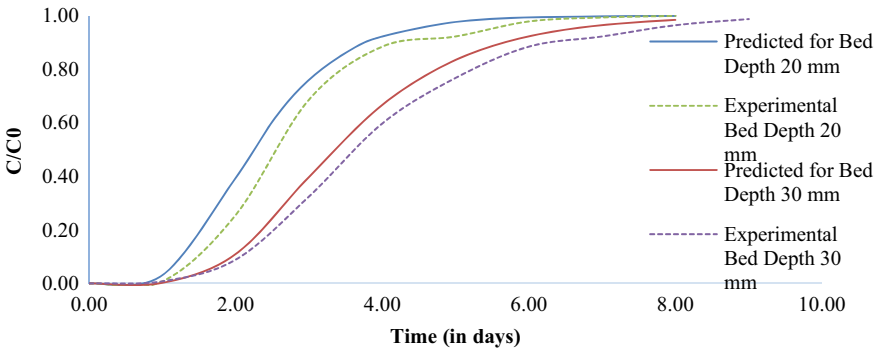

Fig. 5 Experimental and predicted breakthrough curves for local soil

Vulnerability of Groundwater contamination. Owing to the excellent corelation between the laboratory-scale fixed-bed column tests and the modeled results in Fig. 5, the BTC curve was modeled at two observation points (Fig. 6), with one observation point at the fill and local soil interface, and the other at the interface of local soil and groundwater. The Pb^{2+} migration was predicted using HYDRUS 1D, and Fig. 6 depicts that the water table contamination vulnerability was low as the time taken by the contaminant to migrate through the subsurface to reach the WT is about 500 days. This result highlights the need to prioritize the remediation of untreated

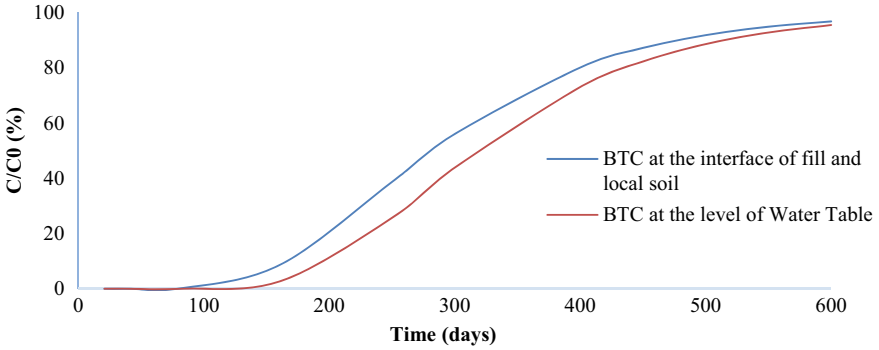

Fig. 6 HYDRUS generated BTC for the soil profile at the landfill

draining wastewater leachate into the stream by exploring nature-based bio-inspired constructed wetland along the drainage lines.

4 Conclusion

The following conclusions can be drawn based on the experimental and numerical modeling results presented in the paper:

- This study presents a preliminary investigation of the contamination problem of lead laden leachate and explores the vulnerability of groundwater contamination at Srinagar's lone landfill.
- The soil collected from the nearby area of the landfill was found to have good uptake and attenuation capacity for lead and thus can expect to effectively participate in the retention and removal of lead.
- The isotherm studies conducted on the soil showed that Langmuir isotherm is the best fitting isotherm with an R^2 value of 0.9408. Similarly, from the kinetic study, pseudo-second-order kinetics is the best fitting kinetics bearing an R^2 value of 0.999.
- The numerical modeling results showed the need to prioritize the remediation of untreated leachate draining into the stream over the flooded leachate problem in the open spaces.
- The authors suggest that the remediation technique that could be explored is the usefulness of constructed wetlands. The flooded leachate in open spaces can then be pumped out into the available drains, which could be equipped with CWs. After this study, the problem can be planned by policy-makers and government agencies in a sustainable, time-saving, and cost-effective manner.

References

1. Veselaj T, Morina R, Gashi V, Sallaku F (2019) Assessment of leachate and soil contamination with heavy metals around deposit sites in Podujeva and Prizren
2. Mushtaq J, Dar AQ, Ahsan N (2020) Physio-chemical characterization of municipal solid waste and its management in high-altitude urban areas of North-Western Himalayas. Waste Dispos Sustain Energy 2(2):151–160. https://doi.org/10.1007/s42768-020-00040-1
3. Jammu and Kashmir Housing and Urban Development Department (2016) SWM state action plan J&K. [Online]. http://jkhudd.gov.in/pdfs/SWM%20State%20Action%20Plan%20J&K.pdf. Accessed 10 Dec 2021
4. CPCB and FCC Ministry of Environment (2000) Municipal solid wastes (management and handling) rules, 2000. [Online]. https://www.mpcb.gov.in/sites/default/files/solid-waste/MSWrules200002032020.pdf. Accessed 18 Dec 2021
5. Naveen BP, Mahapatra DM, Sitharam TG, Sivapullaiah Pv, Ramachandra Tv (2017) Physico-chemical and biological characterization of urban municipal landfill leachate. Environ Pollut 220:1–12, Elsevier Ltd. https://doi.org/10.1016/j.envpol.2016.09.002
6. Devare M, Bahadir M (1994) Biological monitoring of landfill leachate using plants and luminescent bacteria. Chemosphere 28(2):261–271. https://doi.org/10.1016/0045-6535(94)90123-6
7. Adhikari K, Pal S (2016) Assessment of pollution potential of soil and groundwater in a non-engineered MSW landfill site. Int J Environ Sci Dev 7(3):207–210. https://doi.org/10.7763/IJESD.2016.V7.769
8. Wuana RA, Okieimen FE (2011) Heavy metals in contaminated soils: a review of sources, chemistry, risks and best available strategies for remediation. ISRN Ecol 2011:1–20. https://doi.org/10.5402/2011/402647
9. Lead poisoning (2021) [Online]. https://www.who.int/en/news-room/fact-sheets/detail/lead-poisoning-and-health. Accessed 11 Oct 2021
10. Bhat RA, Dervash MA, Mehmood MA, Hakeem KR (2017) Municipal solid waste generation and its management, a growing threat to fragile ecosystem in Kashmir Himalaya. Am J Environ Sci 13(6):388–397. https://doi.org/10.3844/ajessp.2017.388.397
11. Lone AM, Shah RA, Achyuthan H, Fousiya AA (2018) Geochemistry, spatial distribution and environmental risk assessment of the surface sediments: Anchar Lake, Kashmir Valley, India. Environ Earth Sci 77(3). https://doi.org/10.1007/s12665-018-7242-8
12. Reddy KR (n.d.) Organic matter determination. Retrieved from CME315 Soil Mechanics laboratory. https://cemmlab.webhost.uic.edu/Experiment%202-Organic%20Content.pdf
13. (1983) Methods for chemical analysis of water and wastes. US EPA
14. ASTM D4646-16 (2016) Standard test method for 24-h batch-type measurement of contaminant sorption by soils and sediments. https://doi.org/10.1520/D4646-16
15. Barna R, Fernandez A, Hlavackova P (2007) Assessment methodologies for copper and zinc mobility in a neutral synthetic soil: the influence of pH. Colloids Surf A Physicochem Eng Aspects 306(1–3 SPEC. ISS):56–67. https://doi.org/10.1016/j.colsurfa.2007.06.027
16. Mouni L, Merabet D, Robert D, Bouzaza A (2009) Batch studies for the investigation of the sorption of the heavy metals Pb2+ and Zn2+ onto Amizour soil (Algeria). Geoderma 154(1–2):30–35. https://doi.org/10.1016/j.geoderma.2009.09.007
17. OECD and OCDE (2000) OECD guidelines for the testing of chemicals: OECD guidelines for the testing of chemicals
18. Pal S, Mukherjee S, Ghosh S (2014) Estimation of the phenolic waste attenuation capacity of some fine-grained soils with the help of ANN modeling. Environ Sci Pollut Res 21(5):3524–3533. https://doi.org/10.1007/s11356-013-2315-4
19. Rakesh R, Singh DN, Pandit G, Pathak P (2014) Determination of distribution coefficient: a critical review
20. Pathak P, Singh DN, Pandit GG, Rakesh RR (2016) Guidelines for quantification of geomaterial-contaminant interaction. J Hazard Toxic Radioact Waste 20(1):04015012. https://doi.org/10.1061/(ASCE)hz.2153-5515.0000292

21. Keçeci M, Usta S, Uygur V (2020) Lead adsorption in soils and the effect of soil properties: case study from Turkey. Environ Earth Sci 79(18). https://doi.org/10.1007/s12665-020-09156-3
22. Boateng TK, Opoku F, Akoto O (2019) Heavy metal contamination assessment of groundwater quality: a case study of Oti landfill site, Kumasi. Appl Water Sci 9(2). https://doi.org/10.1007/s13201-019-0915-y
23. Lu Y, Gong Z, Zhang G, Burghardt W (2003) Concentrations and chemical speciations of Cu, Zn, Pb and Cr of urban soils in Nanjing, China. Geoderma 115(1–2):101–111. https://doi.org/10.1016/S0016-7061(03)00079-X
24. Huang G et al. (2011) Recent progress in research on the adsorption of lead in soil. In: Proceedings—3rd international conference on measuring technology and mechatronics automation, ICMTMA 2011, vol 2, pp 966–969. https://doi.org/10.1109/ICMTMA.2011.523
25. Ahmed IM, Helal AA, el Aziz NA, Gamal R, Shaker NO, Helal AA (2019) Influence of some organic ligands on the adsorption of lead by agricultural soil. Arab J Chem 12(8):2540–2547. https://doi.org/10.1016/j.arabjc.2015.03.012
26. Patel H (2020) Batch and continuous fixed-bed adsorption of heavy metals removal using activated charcoal from neem (*Azadirachta indica*) leaf powder. Sci Rep 10(1). https://doi.org/10.1038/s41598-020-72583-6
27. Awual MR, Hasan MM (2019) A ligand based innovative composite material for selective lead(II) capturing from wastewater. J Mol Liq 294:111679. https://doi.org/10.1016/j.molliq.2019.111679

Assessment of Efficacy of Silty-Sandy Soil to Treat Carbendazim-Laden Wastewater

Debasmita Datta, Abdul Waris, Avishek Adhikary, Supriya Pal, and Kalyan Adhikari

Abstract Pesticides are used in the agricultural field in order to destroy harmful pests and weeds. Nowadays, the excessive use of pesticides also produces a detrimental effect on the ecosystem. Though many European countries have banned its use, some countries like India still allow it. In this study, laboratory-scale batch experiments were conducted with the help of response surface methodology to determine the sorption behavior of a commonly used fungicide Carbendazim on a locally available silty sandy soil of the Durgapur region, West Bengal, having a saturated hydraulic conductivity of 1.66×10^{-5} cm/s. The soil proved to be moderately efficient in removing Carbendazim at the rate of 63.93% for a selective dose of Carbendazim as 12 mg/L within a contact time of 2 h. The Langmuir isotherm model and pseudo-second-order kinetic model proved to be the best fit with R^2 values of 0.99 and 0.98, respectively.

Keywords Pesticide · Fungicide · Response surface methodology · Isotherm · Kinetics

1 Introduction

A pesticide is a substance introduced into the environment to prevent insects, weeds, fungi, and other harmful pests. It has been seen that 40% of agricultural products are lost due to plant diseases and problems. So, pesticides protect those damages significantly increase crop production and reduce economic losses [1]. The use of

D. Datta (✉) · K. Adhikari
Department of Earth and Environmental Studies, National Institute of Technology Durgapur, Durgapur 713209, West Bengal, India
e-mail: d.datta23@gmail.com

K. Adhikari
e-mail: kalyan.adhikari@ees.nitdgp.ac.in

A. Waris · A. Adhikary · S. Pal
Department of Civil Engineering, National Institute of Technology Durgapur, Durgapur 713209, West Bengal, India

© The Author(s), under exclusive license to Springer Nature Singapore Pte Ltd. 2023

K. R. Reddy et al. (eds.), *Recent Advances in Sustainable Environment*, Lecture Notes in Civil Engineering 285, https://doi.org/10.1007/978-981-19-5077-3_31

pesticides started from the ancient Romans, and during world war two, a significant outbreak of synthetically prepared pesticides occurred.

Carbendazim(methyl 1H-benzimidazol-2-yl carbamate) is a systematic fungicide used to treat ascomycetes, fungi imperfecti, and other fungal diseases. It is widely used on vegetables and fruits like bananas, mango, strawberry, and orange. It is also used in the paint, textile, paper, and leather industries. Carbendazim is classified as a possible human carcinogen [2]. Its long-time accumulation can contaminate the ecosystem and bring detrimental effects on human and animal beings. Due to its toxicity and persisting nature, it has been banned in Australia, most European Union, and the USA [3]. However, developing countries like India, China, and Brazil are still allowing their production and uses. So, there is a high chance that Carbendazim can contaminate our environment via leaching and runoff from the agricultural ground.

Earlier researchers have conducted a study about the sorption of Carbendazim with different types of soil. Its sorption behavior has been tested on four soils, ranging from hilly to desert areas of Pakistan [4]. The low value of distribution coefficient K_d (3.59–11.60 ml/μg) indicates low adsorption. It has been seen that the soil firmly retained adsorbed fungicide and is almost irreversible. Another study showed Carbendazim's sorption and other five pesticides in Hungarian agricultural soil [5]. Carbendazim is most strongly adsorbed with a higher Freundlich coefficient K_f value.

These studies encouraged us to study the sorption behavior of Carbendazim on locally available silty-sandy soil in the Durgapur region, West Bengal. Soil's physicochemical properties were determined as per IS:2720 [6]. Batch adsorption has been performed like the previous researcher [7] and kinetic isotherm study, and results are compared with response surface methodology (RSM) to check optimum removal efficacy.

2 Materials and Methods

2.1 Silty-Sandy Soil

Locally available silty-sandy soil used in this study was collected from local agricultural land near the Durgapur Barrage area. The physical property of soil is determined as per IS:2720 [6] and given below in Table 1.

2.2 Batch Adsorption Study and Response Surface Methodology

The batch tests were carried out to determine the removal efficiency of the synthetically generated stock solution as adsorbate and soil as an adsorbent. This was

Table 1 Physicochemical properties of silty sandy soil

Sl. no	Parameters	Output
1	Saturated hydraulic conductivity	$1.6556 * 10^{-5}$ cm/s
2	Specific gravity	2.635
3	Soil **P**H	7.4
4	Maximum dry density	1.725 gm/cc
5	Optimum moisture content	9.65%
6	Particle size distribution	Sand 61% silt 39% clay 10%

done using Stat-Ease Inc.'s Design-Expert software. In this investigation, the Box–Behnken model in Design-Expert was utilized to optimize the process parameters for maximal contaminant removal from the aqueous solution. The initial concentration of Carbendazim (mg/L), soil dose (g/L), and contact time (min) were the input variables in the Box–Behnken model. The Box–Behnken Design (BBD) of response surface methodology provided 15 different combinations, with soil dosage ranging from 10 to 40 g/L, contact time ranging from 2 to 8 hr, and initial solute concentration ranging from 4 to 12 mg/l [7]. The percentage removal of Carbendazim is obtained using Eq. (1).

$$\%\text{removal} = \frac{C0 - Ce}{C0} * 100 \tag{1}$$

where C_0 and Ce are initial and final concentrations, respectively.

2.3 Adsorption Isotherm

This study was done by varying the initial concentrations from 2 to 12 mg/L and keeping soil dose and contact time constant 10 g/L and 2 hr. After the equilibrium is reached, the adsorption capacity value, qe (mg/gm), is calculated using Eq. (2).

$$\text{qe} = \frac{(C0 - Ce) * V}{M * 1000} \tag{2}$$

where V(ml) is the synthetic solution volume taken for each batch setup, and M (gm) is the adsorbent mass used.

2.4 Adsorption Kinetics

This study was done by varying the contact time from 40 to 120 min, maintaining the fixed value of soil dose and initial concentration as 10 g/L and 12 mg/L.

The sorption capacity at time t for qt (mg/g) of soil was computed using Eq. (2).

3 Results and Discussions

3.1 Batch Results

Among 15 runs, different removal efficiencies are obtained. Later, the optimum condition is obtained by the ramp plots. Response values are mentioned in Table 2.

The quadratic model is best fitted for our case depending on regression coefficient R^2 values among different models. The predicted R^2 of 0.7376 is reasonable with the adjusted R^2 of 0.9356, as the difference is less than 0.2. Results are depicted below in Table 3. ANOVA for the quadratic model is shown in Table 4.

Model Equation: The actual equation to determine the removal efficiency as obtained by RSM is mentioned in Eq. 3.

Table 2 Response values for various experimental conditions

Sl. No	Soil dose (g/L)	Contact time (h)	Initial conc (mg/L)	Predicted removal efficiency %	Actual removal efficiency %
1	25	5	8	25.26	26.5 ± 0.5
2	40	5	4	42.44	40.1 ± 0.7
3	10	2	8	38.26	37.1 ± 0.4
4	25	2	4	45.28	41.6 ± 0.9
5	40	5	12	36.14	34.4 ± 0.3
6	25	5	8	26.58	29.2 ± 1.1
7	25	8	4	50.55	49.8 ± 0.5
8	25	8	12	53.39	48.5 ± 0.8
9	25	5	8	26.44	30.9 ± 1.2
10	10	8	8	36.85	34.9 ± 1.5
11	25	2	12	55.22	53.7 ± 0.9
12	10	5	4	29.48	26.4 ± 0.8
13	40	2	8	19.49	25.6 ± 0.4
14	10	5	12	53.21	51.9 ± 0.6
15	40	8	8	37.45	34.7 ± 0.7

Table 3 Comparison between different models

Source	Sequential p-value	Lack of fit p-value	Adjusted R^2	Predicted R^2	
Linear	0.6764	0.0389	−0.1143	−0.6870	
2FI	0.4210	0.0363	−0.0986	−1.5527	
Quadratic	**0.0005**	**0.4570**	**0.9356**	**0.7376**	**Suggested**
Cubic	0.4570		0.9461		Aliased

Table 4 ANOVA for quadratic model

Source	Sum of squares	df	Mean square	F-value	P-value	
Model	1257.78	9	139.75	23.59	0.0014	Significant
A-soil dose	30.91	1	30.91	5.22	0.0712	
B-contact time	11.87	1	11.87	2.00	0.2161	
C-initial concentration	117.44	1	117.44	19.82	0.0067	
AB	31.34	1	31.34	5.29	0.0698	
AC	242.73	1	242.73	40.96	0.0014	
BC	44.93	1	44.93	7.58	0.0401	
A2	33.19	1	33.19	5.60	0.0642	
B2	193.40	1	193.40	32.64	0.0023	
C2	559.50	1	559.50	94.42	0.0002	
Residual	29.63	5	5.93			
Lack of fit	19.72	3	6.57	1.33	0.4570	Not significant
Pure error	9.91	2	4.95			
Cor total	1287.41	14				

$$\text{Removal Efficiency}(\%) = 54.09 + 1.26 * \text{soil dose} - 6.96 * \text{contact time} - 6.71 * \text{initial conc} + 0.062198 * \text{soil dose} * \text{contact time} - 0.13 * \text{soil dose} * \text{initial conc} - 0.28 * \text{contact time} * \text{initial conc} - 0.28 * \text{contact time} * \text{initial conc} - 0.013 * \text{soil dose}^2 + 0.804 * \text{contact time}^2 + 0.77 * \text{initial conc}^2 \quad (3)$$

Ramp Plots: The plots in Fig. 1 signify optimal conditions for Carbendazim removal, further validated in the laboratory with triplicates resulting in 61% removal, which was close to the model results.

Adsorption Isotherm Tests Results: Among all four models, Langmuir isotherm provided the best fit here with the highest regression coefficient value 0.994, as presented in Fig. 2. The adsorption coefficient K_L was found to be 0.6213 L/mg.

Kinetic Results: Adsorption kinetics helps determine the rate of solute uptake and duration of the adsorption process. All the adsorption-kinetics models are plotted, among which pseudo-second-order provided the best fit for our case, with the highest R^2 value shown in Fig. 3.

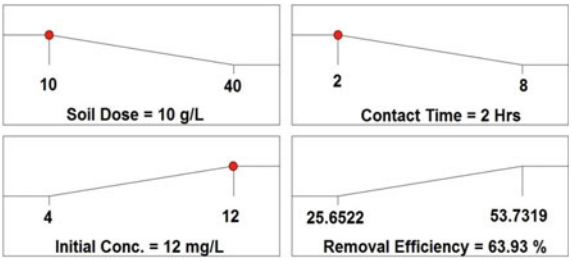

Fig. 1 Ramp plot for three variables and removal efficiency as a response

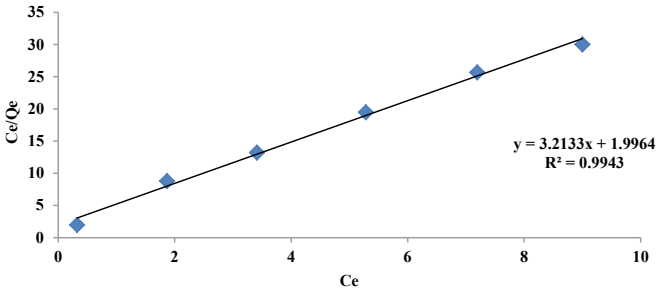

Fig. 2 Langmuir isotherm plot

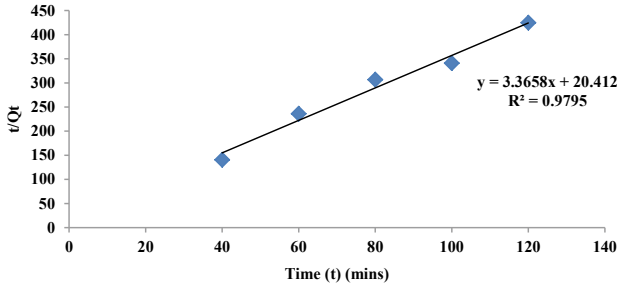

Fig. 3 Pseudo-second-order reaction plot

4 Conclusions

The following conclusions can be drawn based on the experimental and numerical modeling results presented in the paper:

- The groundwater in the vicinity of agricultural lands releasing pesticides such as Carbendazim is highly contaminated due to the leaching of discharged wastewater.

- The studied silty-sandy soil collected from the nearby area of the Durgapur Barrage was found to have good uptake and attenuation capacity for Carbendazim and thus can expect effectively participate in the retention and removal of Carbendazim.
- The isotherm studies conducted on the soil showed that Langmuir isotherm is the best fitting isotherm with an R^2 value of 0.994. Similarly, from the kinetic study, pseudo-second order kinetics is the best fitting kinetics bearing an R^2 value of 0.979.
- •The quadratic model obtained from response surface methodology technique showed removal efficiency around 64% in optimized condition, which closely followed the experimental results after validation.
- This study presents a preliminary investigation of the contamination problem due to indiscriminate disposal of Carbendazim. The outcome of this research is expected to present a guideline toward mitigation of this type of problem. Even though fairly good removal efficiency is obtained from the batch adsorption test results, the exit concentration of Carbendazim is still considered on the higher side. So, further amendments of the soil along with various remediation techniques must be incorporated to enhance the removal efficiency of Carbendazim from wastewater.

References

1. Webster JPG, Bowles RG, Williams NT (1999) Estimating the economic benefits of alternative pesticide usage scenarios: wheat production in the United Kingdom. Crop Prot 18:83–89
2. Goodson WH et al (2015) Assessing the carcinogenic potential of low-dose exposures to chemical mixtures in the environment: the challenge ahead. Carcinogenesis 36:S254–S296. https://doi.org/10.1093/carcin/bgv039
3. Huan Z, Luo J, Xu Z, Xie D (2016) Acute toxicity and genotoxicity of Carbendazim, main impurities and metabolite to earthworms (*Eisenia foetida*). Bull Environ Contam Toxicol 96:62–69. https://doi.org/10.1007/s00128-015-1653-y
4. Ahmad KS, Rashid N, Nazar MF, Tazaiyen S (2013) Adsorption and desorption characteristic of benzimidazole based fungicide carbendazim in Pakistani soils. J Chem Soc Pak 34(3):1017–1024
5. Nemeth-Konda L, Füleky Gy, Morovjan Gy, Csokan P (2002) Sorption behaviour of acetochlor, atrazine, Carbendazim, diazinon, imidacloprid and isoproturon on Hungarian agricultural soil. Chemosphere 48(5):545–552
6. Adhikary A, Konar P, Chakraborty T, Pal S, Ghosh S (2021) Efficacy assessment of silty-sandy soil as bed material in constructed wetland to treat naphthalene-laden wastewater: physical and numerical modeling. J Hazard Toxic Radioact Waste 26(2):04021064. https://doi.org/10.1061/(ASCE)HZ.2153-5515.0000670
7. Li X, Zhou Q, Wei S, Ren W, Sun X (2011) Adsorption and desorption of Carbendazim and cadmium in typical soils in northeastern China as affected by temperature. Geoderma 160(3–4):347–354. https://doi.org/10.1016/j.geoderma.2010.10.003

Prediction of Interface Friction Angle Between Landfill Liner and Soil Using Machine Learning

Faizanjunaid Mohammed, Sasanka Mouli Sravanam, and K. V. N. S. Raviteja

Abstract This study employs machine learning (ML) techniques and artificial neural networks (ANN) to predict the interface friction angle between the landfill liner and the soil. The interface behavior is majorly affected by the thickness of landfill liner (t), mass of landfill liner (m), tensile strength of landfill liner (T), cohesion of soil (cu), angle of shearing resistance of soil (Φ), shear strength (τ), and normal stress (σ). As the stability of landfill liner varies significantly from that of the soil due to the non-homogeneity and anisotropic character of the soil, it is critical to comprehend the interface behavior between the landfill liner and the soil. However, no prior research employing machine learning techniques to analyze the interface behavior between landfill liners and soil has been reported; a study using machine learning algorithms and artificial neural networks is carried out on 66 datasets to probe the interface behavior with the help of an ANACONDA navigator. Further, to understand the impact of input variables on the output variable, Pearson's correlation coefficients were determined. Mean absolute error (MEA) is considered as a loss function, and the best model was chosen based on the r^2-value. Random forest regressor (RFR) model is determined to be the best model among the available models with an r^2-score of 0.99 and a minimum mean absolute error of 0.46.

Keywords Interface friction angle · Regression analysis · Person's correlation coefficients · Support vector machine · Random forest regressor · Decision tree regressor · Artificial neural networks · Mean absolute error · r^2-score

F. Mohammed · S. M. Sravanam (✉)
Department of Civil Engineering, VNRVJIET, Hyderabad, Telangana, India
e-mail: sasankamouli_s@vnrvjiet.in

K. V. N. S. Raviteja
Department of Civil Engineering, SRM University, Amaravati, Andhra Pradesh, India

© The Author(s), under exclusive license to Springer Nature Singapore Pte Ltd. 2023

K. R. Reddy et al. (eds.), *Recent Advances in Sustainable Environment*, Lecture Notes in Civil Engineering 285, https://doi.org/10.1007/978-981-19-5077-3_32

1 Introduction

The study of geotechnical engineering deals with rock and soil mass. The nature of soil mass depends on its transportation and formation from its parent rock. As soil is formed from the disintegration of rock either by a physical or chemical process, the eventually obtained soil mass will be non-homogenous and anisotropic. Therefore, researchers have to reckon on many assumptions while perusing complex and simple hypotheses. However, these assumptions are limited to some extent only. Therefore, several researchers have embarked on different solutions [1–3] to overcome these problems based on the outputs obtained from field and laboratory tests. Machine learning is one of the most coherent solutions to overcome these problems [4]. However, as it requires several test data to analyze and predict the outcome, it becomes challenging for the researchers to carry out machine learning algorithms. Apart from this, machine learning gives accurate output by developing suitable equations. It takes various input and output data from dependent and independent variables and generates an appropriate equation.

In these times, fast and sensible work is additional most well-liked instead of time-taking work. Although, as we know, the tests to determine the interface friction angle between soil mass and landfill liner are a time-taking process, it ought to get replaced with comparatively quick and reliable solutions during this epoch. It takes numerous test data from the results obtained from past tests and gives the required data in the output [5]. Thus, it is potential with machine learning and deep learning algorithms.

2 Methodology

Machine learning is mostly data-driven and task-driven. As a result, the accuracy of machine learning is highly dependent on the data. It is necessary to comprehend data before beginning the analysis using machine learning algorithms.

2.1 Data Collection

The world in which we live is a data-rich environment. This data is acquired from various areas, including journals and articles, as well as by conducting relevant tests on a prototype [5–25]. It may be of various formats, including text, number, picture, and voice. Analysis can be carried out with two types of data, i.e., numerical and categorical data. The parameters that are included in this study are shown in Table 1. Numerical data is reported, and analysis is carried out using ML and ANN algorithms.

Table 1 Parameters used in this study

Input parameters	Thickness of landfill liner (t), mass of landfill liner (m), tensile strength of landfill liner (T), cohesion of soil (cu), angle of shearing resistance of soil (Φ), shear strength (τ), and normal stress (σ)
Output parameter	Interface friction angle (δ)

2.2 Data Cleaning

Data cleaning is the process of detecting missing data (NAN values) and attempting to fill the dataset using appropriate data preprocessing techniques, i.e., standardizing the data in the range of 0 to +1. In other words, anytime data is acquired from many sources, it is collected in its raw form, which makes analysis unfeasible. Therefore, data cleaning is required in order to make it appropriate for analysis. It may be done by using statistical methods like mean, median, mode or by studying the trend of the available data whichever is best suitable. In this study, the trend of the available data is studied and NAN values are filled after standardizing the data in the range of 0 to +1.

2.3 Hyper-Parameter Tuning

The model's performance depends on the type of parameters used to determine the loss function and also upon the division of the dataset. The parameters may include the magnitude of exponent, number of estimators and epochs, type of kernels, activation functions, and optimizers. Grid search was used for hyper-parameter tuning to determine the optimum architect of the model. Table 2 lists the parameters acquired using grid search.

3 Results and Discussions

The dataset consists of 67 load test results shown in Table 3. From this dataset, seven variables were considered to predict interface friction angle. The thickness (t) of landfill liner varies between 0.0006 and 0.00385 m, while the mass per unit area (m) varies between 0.1 and 1.9 kg/m^2, and the tensile strength (T) varies between 7 and 138.8 kN. The angle of shearing resistance (ϕ) ranges from 6.2′ to 46′, whereas soil cohesion (cu) ranges from 0 to 25.3 kPa. Normal stress (σ) varies from 4.5 to 478 kPa, while soil shear strength (τ) extends from 51 to 470.73 kPa: The relationship between the input and output parameters was calculated using Pearson's correlation coefficient [6] matrix, which is portrayed in Table 4.

Table 2 Architect of the ML and ANN models

Sl. No.	Models	Test size	Hyper-parameters	
1	Multivariate linear regression	0.1	Default	
2	Multivariate polynomial regression	0.1	Exponent (a)	2
3	Support vector machine	0.1	Kernel	Radial bias function (rbf)
4	Random forest regression	0.1	Number of estimators	10
5	Decision tree regression	0.1	Default	
6	Artificial neural networks	0.45	Epochs Input layers Output layer Activation function Hidden layer (1) Activation function Hidden layer (2) Activation function Optimizer Loss function	5000 7 1 Linear 14 ReLu 7 ReLu Adam Mean absolute error

3.1 Results of Linear Models

The linear model is composed of two types of machine learning algorithms. The multivariate linear regression (MLR) model is the first, while the multivariate polynomial regression (MPR) model is the second. Linear and polynomial regression studies were performed on the dataset shown in Table 3, filled with appropriate input and output variables. As the test size is an essential key factor that affects the model's design, therefore the analysis was carried out by varying the dataset's test size. After running ML algorithms on this dataset, the test results were acquired. The selection of the optimum model was carried out based on the loss function of the dataset acquired from the analysis. It was seen that mean absolute error changes (MAE) when test size varies, and it can be concluded that MAE doesn't remain constant upon changing test size. In MLR analysis, at a test size of 0.1, a minimum MAE of 0.74 and 0.81 kPa occurs in the training and testing stages, respectively, as shown in Figs. 1 and 2.

As a result, 0.1 was chosen as an appropriate MLR model test size. Following the study, by carrying out the analysis using MPR algorithm, it was discovered that MAE in the training and testing phases was quite low (Fig. 3). Therefore, MPR over-fits the dataset and is ineffective in predicting the interface friction angle between the landfill liner and soil. Based on the results obtained from MLR analysis, an Eq. (1)

Table 3 Load-test dataset

Liner configuration	Soil type	t (m)	m (kg/m^2)	T (kN)	cu (kPa)	ϕ (′)	τ (kPa)	σ (kPa)	δ (′)
HDPE	SM4.5	0.00112	0.97419	18	22	26.558	209.05	12.1	24
HDPE	S4	0.0015	1.28994	20.36	0	26.414	132.35	230.3	18
HDPE	SC3.5	0.00174	0.96675	35	15	32	88.77	372.18	14
HDPE	S4	0.0025	1.262	28.4	0	35	156.47	20.7	20
PVC	S4	0.0025	0.404	59.6	0	31	298.02	20.7	30
SHDPE	C3.1	0.0015	0.55678	138.8	0	14.5	51	240	12
SHDPE	C3.1	0.0015	0.45115	158.7	0	14.5	98.14	478	11.6
SHDPE	C3.1	0.0015	0.66584	118.0	0	21.4	52.68	240	12.45
SHDPE	C3.1	0.0015	0.88185	75.75	0	21.4	114.91	478	13.5
SHDPE	C3.2	0.0015	1.11559	26.99	0	16.8	64.39	240	15.1
SHDPE	C3.2	0.0015	0.56941	136.4	0	16.8	102.22	478	12.05
SHDPE	C3.2	0.0015	0.95066	61.86	0	20.35	59.37	240	13.9
SHDPE	C3.2	0.0015	0.93413	65.22	0	20.35	117.78	478	13.8
SHDPE	S4	0.0025	0.96675	58.57	0	29	88.77	100	14
RHDPE	S4	0.0025	0.48299	50.79	0	29	282.39	100	29
PVC	S4	0.0006	0.48299	50.79	0	29	282.39	100	29
SHDPE	S4	0.0025	0.34001	66.27	0	33	313.96	350	31
PVC	S4	0.0006	0.2947	70.24	0	33	330.2	350	32
GT	SC3.5	0.0011	0.48299	65	19.23	22.993	282.39	61.52	29
SHDPE	S4	0.0015	1.14694	17.6	0	38	182.05	142.51	22
SHDPE	S4	0.0015	1.23602	17.6	0	38	115.26	275.72	16.5

(continued)

Table 3 (continued)

Liner configuration	Soil type	t (m)	m (kg/m^2)	T (kN)	cu (kPa)	ϕ ($'$)	τ (kPa)	σ (kPa)	δ ($'$)
SHDPE	S4	0.0015	0.34001	17.6	0	46	313.96	48.4	31
SHDPE	S4	0.0015	0.34001	17.6	0	46	202.17	119.03	23.5
RHDE	S4	0.0015	0.2947	17	0	38	330.21	42.9	32
RHDE	S4	0.0015	0.97419	17	0	38	209.05	112.1	24
RHDE	S4	0.0015	0.47706	17	0	46	415.88	23.55	37
RHDE	S4	0.0015	0.62155	17	0	46	259.54	73.65	27.5
GTN	S4	0.00201	0.47706	75	0	41	415.88	23.55	37
GTN	S4.2	0.00115	0.404	75	5	35	298.02	54.56	30
GTN1	S4.1	0.002	0.1	7	0	31	282.39	4.5	29
GTN2	S4.1	0.002	0.2	12	0	31	313.96	4.5	31
GTN3	S4.1	0.0026	0.3	20	0	31	313.96	4.5	31
GTN4	S4.1	0.0045	0.6	37	0	31	313.96	4.5	31
GTW1	S4.1	0.0004	0.138	22	0	31	267.07	4.5	28
GTW2	S4.1	0.0006	0.222	35	0	31	298.02	4.5	30
GTW3	S4.1	0.0004	0.141	24	0	31	267.07	4.5	28
GM1	S4.1	0.001	1.38	14	0	31	209.05	4.5	24
GM2	S4.1	0.002	1.9	33	0	31	209.05	4.5	24
GM3	S4.3	0.0026	0.3	20	0	32	330.2	4.5	32
GTW1	S4.3	0.0004	0.141	24	0	32	282.39	4.5	29
GM1	S4.3	0.001	1.38	14	0	32	209.05	4.5	24
GM2	S4.3	0.002	1.9	33	0	32	223.06	4.5	25

(continued)

Table 3 (continued)

Liner configuration	Soil type	t (m)	m (kg/m^2)	T (kN)	cu (kPa)	ϕ (′)	τ (kPa)	σ (kPa)	δ (′)
GM3	S4.3	0.001	0.98	33	0	32	330.21	4.5	32
GTN3	C3	0.0026	0.3	20	22	36	330.21	4.5	32
GM2	C3	0.002	1.9	33	22	36	267.07	4.5	28
GM3	C3	0.001	0.98	33	22	36	470.73	4.5	40
GT	S4	0.00108	0.87538	5.875	0	35	223.06	99.42	25
GM	S4	0.00115	0.404	59.6	0	35	298.02	54.56	30
HDPE	SM4.5	0.0015	0.93413	65.23	0	31.8	86.77	381.23	13.8
HDPE	S4	0.0015	0.97306	22	0	18	175	370.4	14.04
GT	S4	0.00122	0.34001	70	0	35	313.96	48.39	31
SHDPE	S4	0.0025	1.12775	24.28	0	29	101.27	425	15.21
PVC	S4	0.0005	0.45794	53.62	0	29	287.05	300	29.3
SHPDE	S4	0.0025	0.64029	32.68	0	33	256.69	425	27.3
PVC	S4	0.00075	0.28731	76.55	0	33	335.63	300	32.3
SHDPE	SC3.5	0.0015	1.4	4.3	16.2	36.8	119.73	212.5	16.9
SHDPE	SC3.5	0.0015	1.4	4.3	25.3	36.4	125.41	200	17.4
THDPE	SC3.5	0.0015	1.4	4.3	16.2	36.8	127.71	300	17.6
GT	SC3.5	0.001	1.07	8	16.2	36.8	85.77	200	13.7
GM	C3	0.0014	1.24025	23.1	13.4	19.5	162.73	170.6	20.5
SHDPE	S4	0.001	947	35.5	0	23.2	278.53	32	28.75
THDPE	S4	0.001	0.946	33	0	16.1	373.85	7.2	34.6
PVC	S4	0.001	1.35	14	0	20.1	323.67	12	31.6

(continued)

Table 3 (continued)

Liner configuration	Soil type	t (m)	m (kg/m^2)	T (kN)	cu (kPa)	ϕ ($'$)	τ (kPa)	σ (kPa)	δ ($'$)
GT	SC3.5	0.00309	0.65834	3.81	16.9	14.2	66.75	108	11.7
GT	G1	0.0038	0.65834	3.81	0	29.5	44.77	108	9.1
GM	S4	0.0019	0.21964	3.54	0	26.9	117.49	108	16.7
GM	C3	0.0015	0.21964	3.54	14.3	6.2	151.53	108	19.6

Table 4 Pearson's correlation coefficients

Parameters	t (m)	m (kg/m^2)	T (kN)	cu (kPa)	ϕ (′)	τ (kPa)	σ (kPa)	δ (′)
t (m)	1	–	–	–	–	–	–	–
m (kg/m^2)	−0.097	1	–	–	–	–	–	–
T (kN)	−0.0995	−0.0107	1	–	–	–	–	–
cu (kPa)	0.00583	−0.0593	0.248239	1	–	–	–	–
ϕ (′)	0.00345	−0.1019	0.345243	0.007046	1	–	–	–
τ (kPa)	−0.1629	0.0658	−0.11643	0.077253	0.416918	1	–	–
σ (kPa)	−0.0198	−0.09	0.451376	0.068499	0.304724	0.548186	1	–
δ (′)	−0.1747	0.07313	0.162325	−0.07206	0.447466	0.985478	0.605788	1

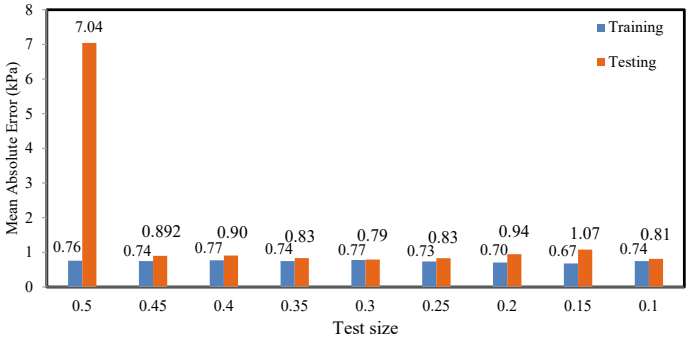

Fig. 1 Mean absolute error for MLR with varying test size

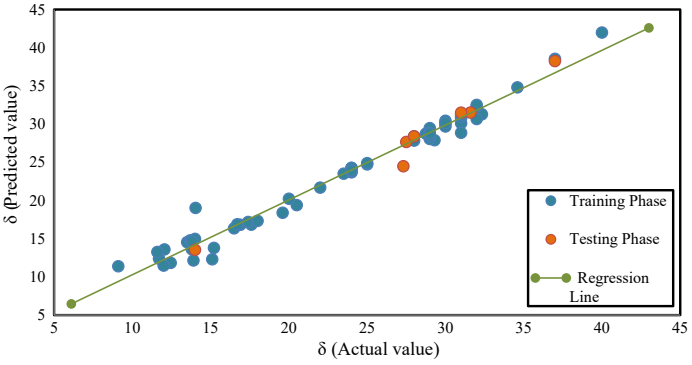

Fig. 2 Result of multivariate linear regression analysis

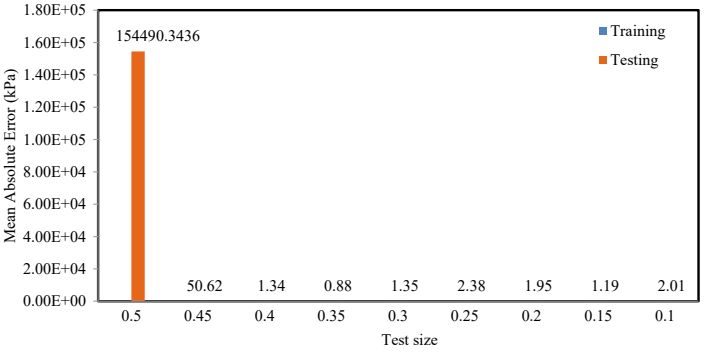

Fig. 3 Mean absolute error for MPR with varying test size

was proposed to calculate interface friction angle (δ), as shown below

$$\delta = -3.62\text{e}+02 * \text{t} + 2.64\text{e}-04 * \text{m} + 1.65\text{e}-03 * \text{T} - 8.94\text{e}-03 * \text{cu} + 3.99\text{e}-02 * \phi + 6.76\text{e}-02 * \tau - 6.05\text{e}-03 * \sigma + 9.22. \quad (1)$$

3.2 Results of Nonlinear Models

Using nonlinear methods such as support vector machine, random forest, decision tree, and nonlinear regression analysis was carried out to assess the model's performance. The performance of the model to be utilized is solely determined by the model's test size.

As the machine gave varied outcomes as the testing size was changed, the minimum MAE was 0.51 kPa, while the maximum MAE was 0.71 kPa (Fig. 4). The performance of the decision tree regressor (DTR) is varied in training phases that can be seen in Fig. 5. The machine gave varied outcomes as the testing size as changed. In the training and testing phases, the minimum MAE was 0.27 and 0.88 kPa, respectively, resulting to an optimum test size of 0.1 and an overall r^2-score of 0.998. The results obtained with DTR analysis show that MAE varies depending on the test size. MAE was much higher in the testing phase than in training. As a result, the DTR model over-fits the available data in the training phase, resulting in a high inaccuracy in the testing phase. Finally, DTR is ineffective in anticipating the interface friction angle between the landfill liner and the soil because it leads to huge mistakes that are difficult to relay. Since the random forest (RFR) is an enhanced model of DTR, it was discovered that the DTR model over-fits the data by generating a single decision tree. The RFR model was utilized in this work to tackle the problem of over-fitting. RFR created random trees instead of a single tree and provided an appropriate output that was optimal for the trees that were generated in the training and testing phases,

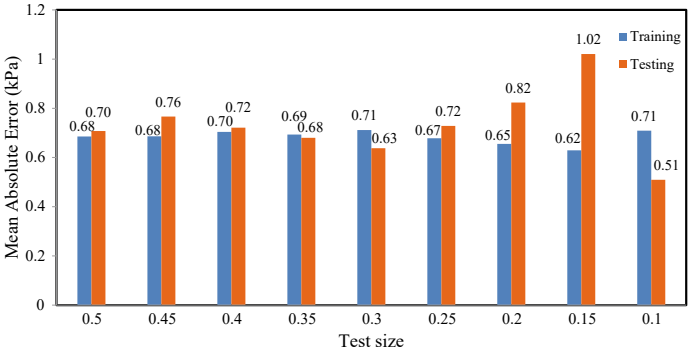

Fig. 4 Mean absolute error for SVM with varying test size

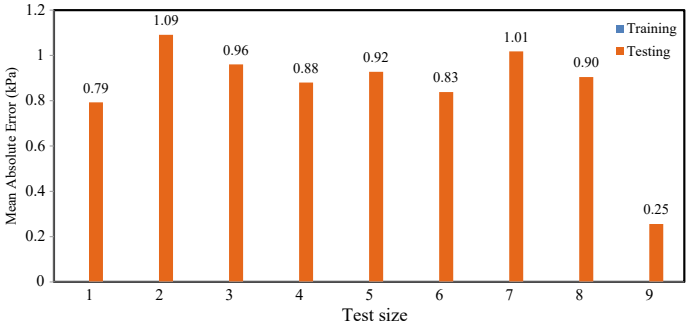

Fig. 5 Mean absolute error for DTR with varying test size

with the minimum MAE as 0.35 and 0.57 kPa, respectively (Figs. 6 and 7), resulting to a test size of 0.1 and an overall r^2-score of 0.99. It may be concluded that DTR is not adequate for forecasting the interface friction angle based on the findings of nonlinear analysis utilizing various nonlinear machine learning methods. SVM and RFR both had r^2-scores of 0.98 and 0.99, respectively.

As a result, RFR models were shown to have the best fit for predicting the interface friction angle between the landfill liner and the soil. When comparing linear and nonlinear models shown in Table 5, an RFR nonlinear model with an r^2-score of 0.99 complies best for predicting the interface friction angle.

4 Artificial Neural Networks (ANN)

An artificial neural network is a subset of ML. Over-fitting is a significant problem that can be seen in ANN. To minimize this problem, hyper-parameter tuning was carried out to determine the optimum number of hidden layers and epochs. This

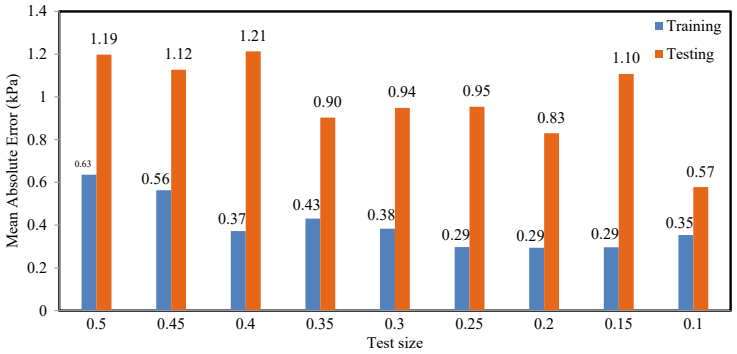

Fig. 6 Mean absolute error for RFR with varying test size

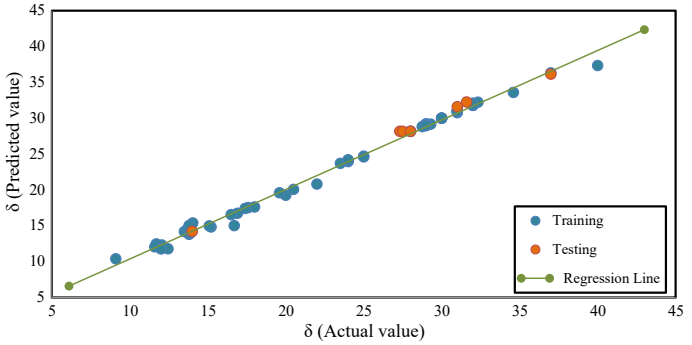

Fig. 7 Result of Random Forest Regression analysis

Table 5 Statistical parameters of ML algorithms

Models	Regressors	Statistical parameter	Phase		Overall performance
			Training	Testing	
Linear model	MLR	MAE (kPa)	0.74	0.81	0.78
		r^2-score	0.97	0.96	0.97
	MPR	MAE (kPa)	0.27	0.88	0.56
		r^2-score	0.99	0.94	0.97
Non-linear model	SVM	MAE (kPa)	0.70	0.50	0.60
		r^2-score	0.97	0.98	0.98
	DTR	MAE (kPa)	0	0.25	0.12
		r^2-score	1	0.98	0.98
	RFR	MAE (kPa)	0.35	0.57	0.46
		r^2-score	0.99	0.99	0.99

hyper tuning was carried out by feeding the machine with the data that is available in Table 1. The results of hyper-parameter tuning are shown in Table 2. Since the range of output data was greater than +1, the ReLu function was finalized as an activation function to the hidden layers. The results of ANN are shown in Fig. 8, which portrays upon changing the number of epochs, variation of MEA can be seen. Therefore, the analysis was carried out by varying the test size along with the number of epochs. Figure 9 shows the plot of actual and predicted value of δ with a regression line. The results of ANN are shown in Table 6 with a 5000 number of epochs that consists of MAE as 0.76 kPa and 0.84 kPa along with the coefficient of determination as 0.98 and 0.96 in training and testing phases, respectively. Therefore, ANN can also be used in the prediction of interface friction angle between landfill liner and soil.

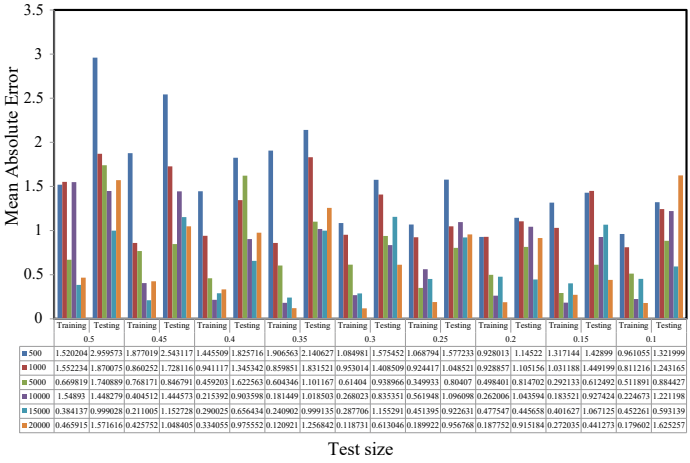

	Training	Testing	Training	Testing	Training	Testing	Training	Testing	Training	Testing	Training	Testing	Training	Testing	Training	Testing	Training	Testing
	0.5		0.45		0.4		0.35		0.3		0.25		0.2		0.15		0.1	
500	1.520204	2.959573	1.877019	2.543117	1.445509	1.825716	1.906563	2.140627	1.084981	1.575452	1.068794	1.577233	0.928013	1.14522	1.317144	1.42899	0.961055	1.321999
1000	1.552234	1.870075	0.860252	1.728116	0.941117	1.345342	0.859851	1.831521	0.953014	1.408509	0.924417	1.048521	0.928857	1.105156	1.031188	1.449199	0.811216	1.243165
5000	0.669819	1.740889	0.768171	0.846791	0.459203	1.622563	0.604346	1.101167	0.61404	0.938966	0.349933	0.80407	0.498401	0.814702	0.292133	0.612492	0.511891	0.884427
10000	1.54893	1.448279	0.404512	1.444573	0.215392	0.903598	0.181449	1.018503	0.268023	0.835351	0.561948	1.096098	0.262006	1.043594	0.183521	0.927424	0.224673	1.221198
15000	0.384137	0.999028	0.211005	1.152728	0.290025	0.656434	0.240902	0.999135	0.287706	1.155291	0.451395	0.922631	0.477547	0.445658	0.401627	1.067125	0.452261	0.593139
20000	0.465915	1.571616	0.425752	1.048405	0.334055	0.975552	0.120921	1.256842	0.118731	0.613046	0.189922	0.956768	0.187752	0.915184	0.272035	0.441273	0.179602	1.625257

Fig. 8 Result of artificial neural network analysis

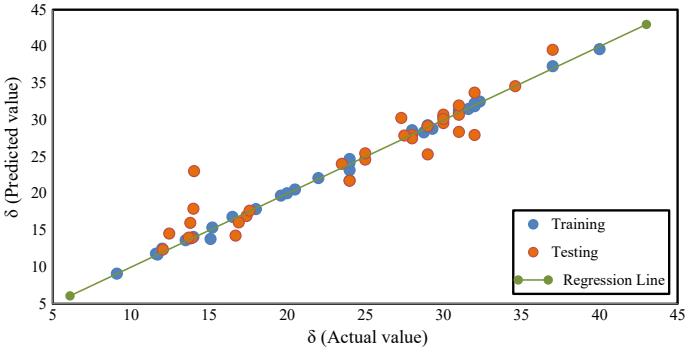

Fig. 9 Result of artificial neural network analysis for 5000 epochs

Table 6 Statistical parameters of ANN algorithms

Models	Number of epochs	Statistical parameter	Phase		Overall performance
			Training	Testing	
Artificial Neural networks	5000	MAE (kPa)	0.76	0.84	0.07
		r^2-score	0.985	0.975	0.98

5 Conclusions

The interface friction angle was calculated using a various machine learning algorithms, including linear and nonlinear regression models, on the basis of which the following conclusions are drawn.

1. The MAE and r^2-scores were determined to be 0.779, and 0.972 kPa, respectively, using the multivariate linear regression (MLR) model. As a result, the suggested MLR equation may be used to compute the interface friction angle, improving accuracy and reducing variability.
2. After finding the correlation coefficients, it was concluded that the mass and tensile strength of a landfill liner, angle of shearing resistance of soil, shear strength, and normal stress were positively correlated with the interface friction angle.
3. As demonstrated in the training phase, multivariate polynomial regressor (MPR) and decision tree regressor (DTR) over-fits the data.
4. With a minimal mean absolute error of 0.46 kPa and highest precision (r^2-score $= 0.99$), the random forest regression (RFR) model was shown to be the best model for predicting interface friction angle between landfill liner and soil.
5. ANN displayed better results with a minimum mean absolute error of 0.07 and with the closest precision of 0.98 when compared to RFR. Therefore, ANN can also be used to predict the interface friction angle between landfill liner and soil. Therefore, ANN can be adopted in the case of small dataset at it gave good results with a test size of 0.45.

References

1. Fishman KL, Pal S (1994) Further study of geomembrane/cohesive soil interface shear behavior. Geotext Geomembr 13(9):571–590
2. Palmeira EM (2009) Soil–geosynthetic interaction: modelling and analysis. Geotext Geomembr 27(5):368–390
3. Stark TD, Poeppel AR (1994) Landfill liner interface strengths from torsional-ring-shear tests. J Geotech Eng 120(3):597–615
4. Monteiro CB, Araújo GLS, Palmeira EM, Neto MPC (2013) Soil-geosynthetic interface strength on smooth and texturized geomembranes under different test conditions. In: Proceedings of the 18th international conference on soil mechanics and geotechnical engineering. Paris, pp 3053–3056

5. Raviteja KVNS, Munwar B, Basha S (2015) Variability associated with interface friction between geomembrane and soil. In: 50th Indian geotechnical conference, Pune, India
6. Dadhich S, Sharma JK, Madhira M (2021) Prediction of ultimate bearing capacity of aggregate pier reinforced clay using machine learning. Int J Geosynth Ground Eng 7(2):1–16
7. Ali F, Salman FA, Subramaniam S (2012) Influence of surface texture on the interface shear capacity of landfill liner. Electron J Geotech Eng 17:101–114
8. Stark TD, Choi H, Lee C, Queen B (2012) Compacted soil liner interface strength importance. J Geotech Geoenviron Eng 138(4):544–550
9. Vaid YP, Rinne N (1995) Geomembrane coefficients of interface friction. Geosynth Int 2(1):309–325
10. Palmeira EM, Lima NR Jr, Mello LGR (2002) Interaction between soils and geosynthetic layers in large-scale ramp tests. Geosynth Int 9(2):149–187
11. Rinne NF (1989) Evaluation of interface friction between cohesionless soil and common construction materials. Doctoral dissertation, University of British Columbia
12. O'rourke TD, Druschel SJ, Netravali AN (1990) Shear strength characteristics of sand-polymer interfaces. J Geotech Eng 116(3):451–469
13. Esterhuizen JJ, Filz GM, Duncan JM (2001) Constitutive behavior of geosynthetic interfaces. J Geotech Geoenviron Eng 127(10):834–840
14. Mitchell JK, Seed RB, Seed HB (1990) Kettleman Hills waste landfill slope failure. I: liner-system properties. J Geotech Eng 116(4):647–668
15. Koerner RM, Hwu BL (1991) Stability and tension considerations regarding cover soils on geomembrane lined slopes. Geotext Geomembr 10(4):335–355
16. Seed RB, Boulanger RW (1991) Smooth HDPE-clay liner interface shear strengths: compaction effects. J Geotech Eng 117(4):686–693
17. Hullings DE, Sansone LJ (1997) Design concerns and performance of geomembrane anchor trenches. Geotext Geomembr 15(4–6):403–417
18. Villard P, Gourc JP, Feki N (1999) Analysis of geosynthetic lining systems (GLS) undergoing large deformations. Geotext Geomembr 17(1):17–32
19. Izgin M, Wasti Y (1998) Geomembrane–sand interface frictional properties as determined by inclined board and shear box tests. Geotext Geomembr 16(4):207–219
20. Chareyre B, Briançon L, Villard P (2002) Theoretical versus experimental modeling of the anchorage capacity of geotextiles in trenches. Geosynth Int 9(2):97–123
21. De A, Vellone DA (2005) Experimental and numerical modeling of geosynthetic anchor trench. In: Geosynthetics research and development in progress, pp 1–7
22. Fleming IR, Sharma JS, Jogi MB (2006) Shear strength of geomembrane–soil interface under unsaturated conditions. Geotext Geomembr 24(5):274–284
23. Ezzein FM, Bathurst RJ (2014) A new approach to evaluate soil-geosynthetic interaction using a novel pullout test apparatus and transparent granular soil. Geotext Geomembr 42(3):246–255
24. Pirnia P, Duhaime F, Manashti J (2018) Machine learning algorithms for applications in geotechnical engineering. In: Proc. GeoEdmonton, pp 1–37
25. Gao JL, Zhang MX, Zhang WJ (2010) Interface frictional property between sand and geomembrane. In: Advances in environmental geotechnics. Springer, Berlin, Heidelberg, pp 822–827

Effect of Lead on the Geotechnical Behaviour of Fine-Grained Soil

Bhoomi A. Kamdar and Chandresh H. Solanki

Abstract Heavy metal contamination of soils and its control has become a challenging issue globally. Accumulation of heavy metals in environment causes serious health issues on living organisms due to its harmful effects on the soil biota, crop yield and pollution of ground water table. It is also found that heavy metals mineralization into more stable form does not occur easily. The present study investigated the impact of lead heavy metal on geotechnical characteristics of fine-grained soil. A silt soil with low plasticity (ML) is artificially contaminated with high concentration of lead, i.e. 5000 and 10,000 mg/kg. Then the contaminated soil is subjected to different laboratory experiments to observe the changes in Atterberg limits, specific gravity, compaction characteristics and shear strength of soil. The results indicated that liquid limit, plastic limit and MDD increased for both concentrations of lead polluted soil, whereas specific gravity and OMC value were reduced. The strength test results concluded that with the increase in lead content from 0 to 10,000 mg/kg, the UCS value increases compared to the uncontaminated soil. The main cause for this can be the reduction in thickness of diffuse double layer of soil particles during the interaction with lead. Overall, it can be said that heavy metal greatly influences the geotechnical behaviour of fine-grained soil.

Keywords Heavy metal contamination · Unconfined compressive strength · Diffuse double layer

B. A. Kamdar (✉) · C. H. Solanki
Department of Civil Engineering, Sardar Vallabhbhai National Institute of Technology, Surat 395007, India
e-mail: bkamdar91@gmail.com

C. H. Solanki
e-mail: chs@amd.svnit.ac.in

© The Author(s), under exclusive license to Springer Nature Singapore Pte Ltd. 2023

K. R. Reddy et al. (eds.), *Recent Advances in Sustainable Environment*, Lecture Notes in Civil Engineering 285, https://doi.org/10.1007/978-981-19-5077-3_33

1 Introduction

The rapid expansion of industry and human activities in urban areas has resulted in a rise in heavy metal concentrations in soil layers [1]. When these metals accumulate in the natural environment as a result of anthropogenic activities and are detected in large quantities, they contribute to the disruption of human metabolism. Emissions from the industry and the use of gasoline, paints, fertilizers and pesticides can seriously affect the environmental quality and human health [2]. Lead (Pb) is a bluish-grey metal that is found in low contents in the earth's crust but certain man-made activities contribute to its release in high amounts. Lead enters the human body in a variety of ways, remains in the body for an extended period of time and accumulates in tissues. Plumbism is one of the disorders that might be caused by lead ingestion. Considering the long-term effects of lead in the environment, it is necessary to investigate its influence on soil properties as well.

Several studies have been carried out on soils which are contaminated by heavy metals to investigate the geotechnical condition of these soils which is necessary for engineering projects. (Negahdar et al.) investigated the impact of lead and zinc nitrate contamination on sandy clay. Results of the direct shear test concluded that as heavy metal contamination increased, soil cohesiveness reduced for both types of contaminant. However, the presence of heavy metal impurities had no effect on the internal friction angle of the samples [3]. Based on laboratory studies, (Negahdar and Nikghalbpour) evaluated the effects of different quantities of lead nitrate and zinc nitrate hexahydrate heavy metals in pore fluid on the geotechnical properties of kaolinite–sand mixtures. The results indicate that the presence of Pb(II) and Zn(II) would decrease the initial void ratio and sedimentation of samples which is attributed to the noticeable changes in soil microstructure [4]. Impact of heavy metals such as lead (Pb^{2+}), copper (Cu^{2+}) and zinc (Zn^{2+}) on different bentonite's characterization was investigated by (ray et al.) [5]. It was found that liquid limit and swelling properties of bentonite decreased with increase in heavy metal concentration in soil. Also, a high value of UCS of more than 200 kPa was obtained for different metal concentrations in soil. Moghal et al. examined the effect of six different heavy metal contamination on geotechnical properties of semiarid soils [6]. The swell, compressibility and the unconfined compressive strength (UCS) behaviour of metal spiked soils are studied for both control and lime-treated cases. Results indicated that UCS strength of soil increased with metal spiking and compression behaviour had some contrasting results for different metal contents in soil. Impacts of lead nitrate contamination on the geotechnical properties of clayey soil was studied by (Karkush et al.), and it was inferred that Atterberg limits, permeability and OMC value decreases with addition of lead nitrate whereas causes increment in MDD and compression index of soil [7].

Studies from the past have found to have contrasting results for various geotechnical properties for lead contaminated soils. Apart from this it is important to understand the soil behaviour at high concentrations of heavy metals which is lacking in the previous studies. Hence, the following research aims to get a clearer idea on how

Table 1 Physicochemical properties of lead contaminated soil

	Pb0	Pb0.5%	Pb1%
Specific gravity (G)	2.55	2.20	2.08
Liquid limit (%)	49	60.2	62
Plastic limit (%)	34.5	40.8	41.6
Plasticity index	14.5	19.4	20.4
pH	7.98	7.50	7.27
Free swell index	40	60	50

the presence of heavy metal can affect the geotechnical behaviour of fine grained soils. For this purpose, a silty soil with low plasticity (ML) has been contaminated artificially with two different concentrations of lead (5000 and 10,000 mg/kg) to study its effect on Atterberg limit, specific gravity, compaction characteristics and shear strength of soil.

2 Materials and Methodology

2.1 Properties of Virgin Soil

The virgin soil used as control was collected from Surat, India and homogenized by passing through 2 mm sieve. Table 1 represents the physicochemical properties of soil which have been determined according to the ASTM standards. Soil was classified as ML type based on the USCS method. Atterberg limits, specific gravity, optimum moisture content (OMC) and maximum dry density (MDD) were determined as per ASTM-D4318 (ASTM 2010), ASTM-D854-92 (ASTM 1994) and ASTM-D698 (ASTM 2012), respectively. Also, pH of soil was measured according to ASTM standard D4972. For observing the effect of lead on soil, heavy metal solution of $Pb(NO_3)_2$ was used in experiments.

2.2 Preparation of Lead Specimen

For preparing contaminated soil specimen, the necessary volume of stock solution made with analytical grade lead nitrate hexahydrate $Pb(NO_3)_2.6H_2O$ was added to the air-dried soil until the stock solution content reached soil's optimum moisture content (OMC) [8]. The concentration of lead contaminated soil was kept at 5000 mg/kg (0.5%Pb) and 10,000 mg/kg (1%Pb) for observing their effect on the geotechnical properties of soil.

2.3 Estimation of Geotechnical Characteristics

To study the effect of lead contaminant on geotechnical parameters of fine grained ML soil, the experiments of Atterberg limit determination, compaction test and unconfined compression tests were done on the samples according to ASTM-D4318 (ASTM 2010), ASTM-D698 (ASTM 2012) and ASTM D2166, respectively. For performance of UCS test, soil specimens of 50 mm diameter and 100 mm height were prepared and compacted to achieve the desired MDD. Specific gravity of contaminated and uncontaminated soils was determined based on ASTM-D854-92 (ASTM 1994).

3 Result and Discussion

3.1 Atterberg Limits

The Atterberg limits are found to be a useful measure for predicting soil behaviour. Engineering properties like permeability and shear strength are closely related to consistency limits of soil. Figure 1 depicts the variations in liquid limit and plastic limit with increase in lead contamination from 0 to 5000 and 10,000 mg/kg in soil. Table 1 shows the values of Atterberg limits and plasticity index for uncontaminated and lead contaminated soil. It is observed that as the lead content increase in the soil, both liquid limit and plastic limit increases. Plasticity index of uncontaminated soil was 14.42% which shows an increment to 19.38% for lead contamination of 5000 mg/kg in soil. A slight increment in Atterberg limits is observed when lead content increases from 5000 to 10,000 mg/kg in soil.

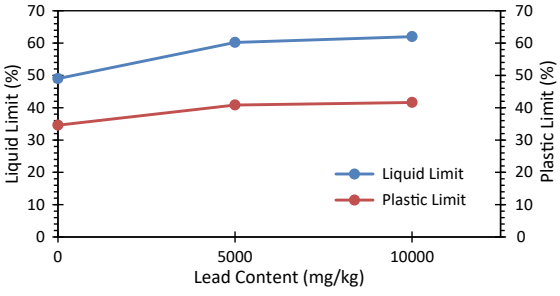

Fig. 1 Atterberg limits of lead contaminated soil

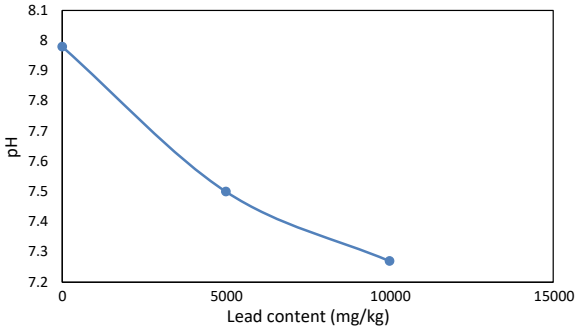

Fig. 2 Variation in soil pH

3.2 Specific Gravity

Specific gravity values of uncontaminated soil along with contaminated soils are shown in Table 1. The specific gravity of virgin soil was 2.55, but lead contamination of 5000 and 10,000 mg/kg reduced the values to 2.20 and 2.08, respectively.

3.3 PH

Figure 2 presents the soil pH results with the rise of lead content in the soil. The natural pH of soil was found to be alkaline. With increase in the lead content, pH value decreases significantly. The main reason for decrease in the soil pH is ascribed to the hydrolysis reaction of lead with soil system [4]. Reduction in soil pH due to addition of lead further causes reduction in double layer thickness developing a flocculated structure in the soil.

3.4 Compaction Properties

Figure 3 illustrates the variation of OMC and MDD with increasing lead content in soil. The MDD and OMC values for uncontaminated soil are 1.57 g/cm^3 and 26%. It can be observed that as the lead concentration increases from 0 to 5000 mg/kg in soil, MDD value is greatly increased and OMC reduces. For further increment in lead concentration to 10,000 mg/kg, the MDD value decreases and OMC value increases compared to Pb0.5% soil. But, the MDD value remains high for both contaminated soils in comparison to the control. Similarly, OMC value reduces with increase in contamination in soil. The principle reason for this compaction behaviour can be attributed to the reduction in thickness of double diffused layer surrounding the soil particles. This brings the particles closer to each other under the same compaction energy, thus increasing the MDD and reduction in OMC values [1, 9].

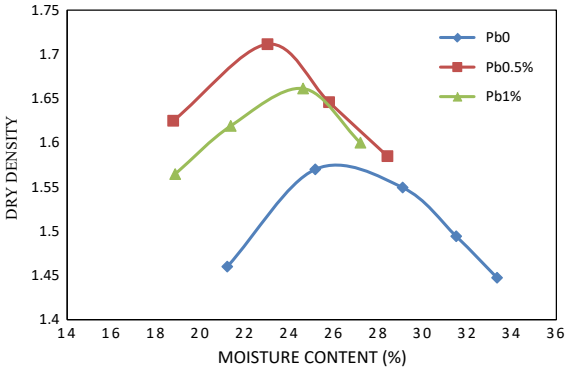

Fig. 3 Compaction characteristics of lead contaminated soil

3.5 Mechanical Strength

Results of unconfined compressive strength test for control soil and lead spiked with two different concentrations in soil are represented in Fig. 4. It was encountered that addition of lead to soil contributed to increase in the UCS value. The strength increment was 1.78 and 0.56 times more than the value obtained for the virgin soil. The development of solid complexes with the hydroxyl groups present in the fine-grained soil was linked to the higher UCS value for the lead spiked condition [6]. Also, reduction in the thickness of the DDL of the soil after addition of lead at higher concentrations forms strong soil particles agglomerates leading to increment in shear strength [5, 6]. Further, it was also observed that with increase in the lead concentration from 5000 to 10,000 mg/kg, the UCS value decreases. This could be due to the change in compaction behaviour as the MDD value decreases and OMC increases at 10,000 mg/kg lead concentration in soil [5].

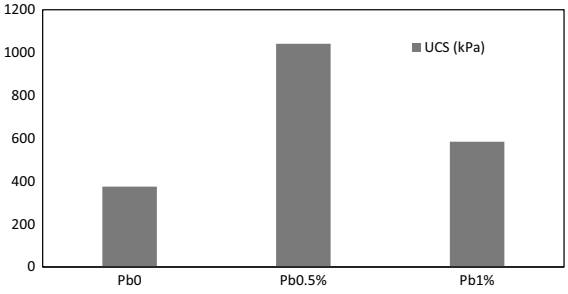

Fig. 4 Unconfined compressive strength of lead contaminated soil

4 Conclusion

Present study investigated the effect of lead metal on geotechnical properties of a fine-grained soil. For this purpose, ML type soil was artificially contaminated in a laboratory condition with two high concentrations of lead and tested for understanding the changes in consistency limits, compaction characteristics and shear strength of soil. The following critical observations were made:

- The Atterberg limits have increased in the presence of lead and a further increment is observed as its concentration increased.
- The value of specific gravity reduced as the lead content in the soil increases. Also, pH value decreased continuously for lead contaminated soil compared to the control.
- Compaction test results showed an increment in MDD value and reduction in OMC as the lead content increased from 0 to 10,000 mg/kg in soil. This could be attributed to the lessening in the DDL thickness at high concentrations of lead in soil.
- The UCS value of lead spiked soils increased compared to the strength of uncontaminated soil. Highest UCS value was obtained for lead content of 5000 mg/kg after which it decreased for 10,000 mg/kg amount of lead addition in soil. The main reason for strength increment could be the formation of strong soil particles agglomerates due to the reduction in thickness of diffused double layer after addition of lead in the soil. The findings of this study can be utilised for forecasting the behaviour of fine-grained soils that have been exposed to such high concentration of heavy metals.

Additional studies can be conducted to modify contaminated soils by adopting stabilization method using various materials like lime, agricultural waste and construction demolition waste [10, 11]. Such modified soils can be further applied as a construction material.

References

1. Nazari Heris M, Aghajani S, Hajialilue-Bonab M, Vafaei Molamahmood H (2020) Effects of lead and gasoline contamination on geotechnical properties of clayey soils. Soil and Sediment Contam 29(3):340–354. https://doi.org/10.1080/15320383.2020.1719973
2. Turer D (2007) Effect of heavy metal and alkali contamination on the swelling properties of kaolinite. Environ Geol 52(3):421–425. https://doi.org/10.1007/s00254-006-0557-x
3. Negahdar A, Shabanian MR, Nikghalbpour M (2018) Amirkabir journal of civil engineering the effect of heavy metal contaminants on the strength parameters of sandy clay. Civil Eng 50(5):263–266. https://doi.org/10.22060/ceej.2017.12869.5287
4. Negahdar A, Nikghalbpour M (2020) Geotechnical properties of sandy clayey soil contaminated with lead and zinc. SN Appl Sci 2(8). https://doi.org/10.1007/s42452-020-3115-3
5. Ray S, Mishra AK, Kalamdhad AS (2022) Effect of lead, copper, and zinc on mechanical properties of compacted bentonites. J Hazard, Toxic, Radioact Waste 26(2). https://doi.org/10.1061/(ASCE)HZ.2153-5515.0000690

6. Moghal AAB, Ashfaq M, Al-Shamrani MA, Al-Mahbashi A (2020) Effect of heavy metal contamination on the compressibility and strength characteristics of chemically modified semi-arid soils. J Hazard, Toxic, Radioact Waste 24(4):04020029. https://doi.org/10.1061/(asce)hz.2153-5515.0000527
7. Karkush MO, Ali SD, Karkush MR, Ali SD (2020) Impacts of lead nitrate contamination on the geotechnical properties of clayey soil
8. Du YJ, Jiang NJ, Liu SY, Jin F, Singh DN, Puppala AJ (2014) Engineering properties and microstructural characteristics of cement-stabilized zinc-contaminated kaolin. Can Geotech J 51(4):289–302. https://doi.org/10.1139/cgj-2013-0177
9. J. shan Li, Q. Xue, P. Wang, and Z. ze Li, "Effect of lead (II) on the mechanical behavior and microstructure development of a Chinese clay. Appl Clay Sci 105–106:192–199. https://doi.org/10.1016/j.clay.2014.12.030
10. Sharma A, Sharma RK (2019) Effect of addition of construction–demolition waste on strength characteristics of high plastic clays. Innov Infrastruct Solutions 4(1). https://doi.org/10.1007/s41062-019-0216-1
11. Sharma A, Sharma RK Sub-grade characteristics of soil stabilized with agricultural waste, constructional waste, and lime. 2047. https://doi.org/10.1007/s10064-020-02047-8/Published

Energy Assessment of a Hybrid Multiple Stage Evaporator Using Metaheuristic Algorithms

Smitarani Pati and Om Prakash Verma

Abstract This paper encases the energy optimization of an energy integrated heptad-based Multiple Stage Evaporator (MSE) used to escalate the solid concentration of the aqueous black liquor obtained from the pulp and paper mill. A standalone MSE is designated as the most energy-intensive unit, hence, various Energy Reduction Schemes (ERSs) are integrated to enhance the energy efficiency of this unit. Steam Consumption (SC) and Steam Economy (SE) are the two major energy efficiency parameters to judge the energy performance of the MSE. Hence, a single objective optimization problem is developed by considering the interrelation of SE and SC as the objective function for the hybrid MSE. The dependency of the problem variables is stated by the constraint functions developed by employing thermo-dynamical laws that create a couple of nonlinear equations for each stage of MSE. The solution to this optimization problem is obtained using two metaheuristic approaches named Differential Evolution Algorithm and Archimedes Optimization Algorithm. Employment of these algorithms provides excellent performance in searching for optimized unknown process parameters with enhanced energy efficiency for this complex optimization problem.

Keywords Multiple Stage Evaporator · Energy Reduction Schemes · Energy efficiency · Metaheuristic approaches

Nomenclature and Acronyms

A	Area of heat transfer (m^2)
h	Enthalpy of liquor (kJ/h)
Cp	Specific heat
f	Fitness function
H	Enthalpy of vapor (kJ/h)

S. Pati · O. P. Verma (✉)
Department of Instrumentation and Control Engineering, Dr. B. R. Ambedkar National Institute of Technology, Jalandhar, Punjab 144011, India
e-mail: vermaop@nitj.ac.in

© The Author(s), under exclusive license to Springer Nature Singapore Pte Ltd. 2023

K. R. Reddy et al. (eds.), *Recent Advances in Sustainable Environment*, Lecture Notes in Civil Engineering 285, https://doi.org/10.1007/978-981-19-5077-3_34

k	Split fraction of feed liquor
L	Flow rate of input liquor (kg/h)
m	Vapor split fraction sent to the 7th stage
PH	Preheater
T	Temperature (°C)
U	Heat transfer coefficient (kW/m^2 °C)
V	Vapor flow rate (kg/h)
x	Black liquor concentration
y	Split fraction of steam
z	Decision variables

Greek Letters

Δ	Difference
λ	Latent heat of vaporization (kJ/kg)

Subscript

f	Feed
i	Stage number
L	Liquor
v	Vapor

Abbreviations

ERSs	Energy Reduction Schemes
MSE	Multiple Stage Evaporator
SC	Steam Consumption (kg/h)
SE	Steam Economy
TVC	Thermo-vapor compressor
WBL	Weak Black Liquor

1 Introduction

Multiple Stage Evaporator (MSE) is the cascade combination of evaporator units used to escalate the solid concentration of the feed solution. It consumes a high portion of the total industrial energy and is a very high energy-intensive unit. A countable amount of energy-saving may be recovered by incorporating different Energy Reduction Schemes (ERSs) such as thermo-vapor compressor (TVC), steam-, and feed- splitting, and feed preheater [1–9]. To integrate different ERSs, it is imperative to understand the effect of operational parameters on system performance. Hence, mathematical correlations are established between the system operating parameters to assess the performance of the MSE in detail. A considerable amount of foregoing researches are present on mathematical modeling, simulation, and optimization related to the MSE house [6, 10–13].

The main focus of this paper is to optimize the energy efficiency of the MSE in terms of Steam Consumption (SC) and Steam Economic (SE). These two parameters show interdependency with an inverse relationship and depend on some unknown process parameters, making the model a constrained optimization problem. This study mainly investigates the maximization of SE to urge the best optimal solution of the unknown process parameters in terms of temperatures of vapor (T_i, $i = 1, 2, 3 \ldots 6$), flow rates of liquor (L_i, $i = 1, 2 \ldots 7$), and amount of steam supplied (V_0) for the hybrid ERSs incorporated MSE.

Optimization is the process of searching the optimal value of the decision variables of a given system by considering all possible choices to maximize or minimize the objective function. Usually, stochastic optimization algorithms treat an optimization problem as a black box due to its high flexibility. In this paper, the proposed problem is a gray-box optimization problem as the input parameters are known. Several well-known optimization approaches have been applied to solve such industrial problem, such as PSO, DE, GA [13] along with some other metaheuristic approaches ABC, TLBO, GWO, WCA, AEFA, SCA, etc., [14–17] to check the efficiency of these algorithms toward such complex industrial problem. However, the proposed optimization problem in these works is unconstraint optimization problems, and these can also be expressed as constrained optimization problem. Hence, this work suggests a constrained optimization problem by considering the SE as the objective function and formulated energy models as the equality constraints.

Further, as in recent years, a number of newly developed metaheuristic approaches have been introduced in optimization; their efficiency also needs to be checked for this kind of industrial optimization problems. Hence, in this study, a newly developed metaheuristic approach called Archimedes Optimization Algorithm (AOA) has been considered to obtain the optimized process parameters along with the maximized energy efficiency. The algorithms are employed to observe the performance of systems. Again, the obtained results are compared with a well-known optimization algorithm named Differential Evolution (DE) algorithm. Further, a comparative analysis has also been performed with the plant-operated model to validate the proposed MSE model.

2 Problem Statement

A heptad-based backward feed falling film MSE is considered to study the effect of various ERSs on SC, operated at a north Indian pulp and paper industry as represented in Fig. 1. The vapor produced at the 7th stage of the evaporator generally treated as waste, but with the utilization of the TVC this amount of vapor is recompressed with the high pressure input steam to produce a medium pressure vapor that fed as heating input to the MSE unit. The intermediate steam obtained from TVC is split into two parts and send to the first two stages. The output vapor obtained from these two stages is combined together and send as input to the 3rd stage. The vapor out from the 3rd stage is sent to the 4th stage and similar process is carried out to 6th stage. However, the vapor from the 6th stage is split with a fraction of *m* and send to the 7th stage, The left vapor is send to operate the preheater that preheats feed liquor. Further, the feed is split with a split fraction of *k* and send to the 7th stage and remaining is send to the 6th stage along with the output liquor obtained from the 7th stage. The concentrated product is obtained from the 1st stage of the MSE unit.

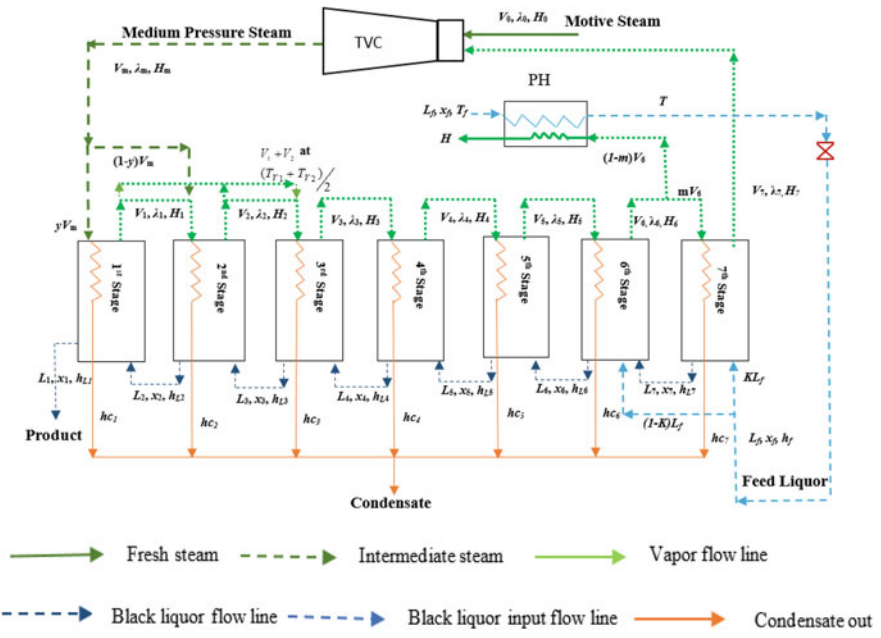

Fig. 1 Structural representation of hybrid ERSs incorporated MSE

3 Model Formulation

The energy equations developed for the proposed hybrid MSE are nonlinear. To formulate these equations, certain assumptions are considered as listed below:

I. The model is considered under steady-state operating conditions.
II. The system is operated in the ideal condition that no plant complexities are considered.
III. The concentration of the solution is constant throughout the process.

The mathematical models for the proposed heptad-based MSE are developed as represented in [15]. To develop these energy models, the 1st law of thermodynamics has been employed around each stage of the MSE by considering the thermo-physical properties of the vapor and liquor fed to concentrate through it. Due to the integration of TVC, the fresh steam enter into the TVC first combined with the steam out from the 7th stage of the MSE. The intermediate steam is split with split fraction of y and $(1-y)$ and send as heating medium for the 1st and 2nd stage, respectively, as illustrated in Fig. 1. Applying enthalpy balance around the 1st and 2nd stage, the obtained equations are expressed as in Eq. (1)–(4).

$$yV_m(\lambda_m - hc_m) + L_1(H_1 - h_1) + L_2(h_2 - H_1) = 0 \tag{1}$$

$$U_1A_1(T_m - T_1) - yV_m(\lambda_m - hc_m) = 0 \tag{2}$$

$$(1-y)V_m(\lambda_m - hc_m) + L_2(H_2 - h_2) + L_3(h_3 - H_2) = 0 \tag{3}$$

$$U_2A_2(T_1 - T_2) - (1-y)V_m(\lambda_m - hc_m) = 0 \tag{4}$$

The output vapor from the 1st and 2nd stage are combined and fed as the heating medium for the 3rd stage of the MSE with an average temperature of T_{avg} and the energy equations for this stage are represented as in Eq. (5)–(6).

$$(L_3 - L_1)(\lambda_{avg} - hc_{avg}) + L_3(H_3 - h_3) + L_4(h_4 - H_3) = 0 \tag{5}$$

$$U_3A_3(T_2 - T_3) - (L_3 - L_1)(\lambda_{avg} - hc_{avg}) = 0 \tag{6}$$

Similarly, for the 4th and 5th stages of the MSE, the energy equations are deduced as in Eqs. (7)–(8).

$$(L_i - L_{i-1})(\lambda_i - hc_i) + L_i(H_i - h_i) + L_{i+1}(h_{i+1} - H_i) = 0 \tag{7}$$

$$U_iA_i(T_{i-1} - T_i) - (L_i - L_{i-1})(\lambda_i - hc_i) = 0 \tag{8}$$

where i denotes the stage number of the 4th and 5th stages. Further, employment of feed split operation to the 6th and 7th stages with a split fraction of (1-k) and k, respectively. The energy balance equation get modified and rendered as in Eqs. (9)–(12).

$$\begin{aligned}&(L_6 - L_5)(\lambda_5 - hc_5) + L_6(H_6 - h_6) + L_7(h_7 - H_6)\\&+ (1-k)L_f(h_f - H_6) - (1-k)L_f Cp\Delta T = 0\end{aligned} \tag{9}$$

$$U_6A_6(T_5 - T_6) - (L_6 - L_5)(\lambda_5 - hc_5) + (1-k)L_f Cp\Delta T = 0 \tag{10}$$

$$\begin{aligned}&m(L_7 + (1-k)L_f - L_6)(\lambda_6 - hc_6) + L_7(H_7 - h_7)\\&+ kL_f(h_f - H_7) - kL_f Cp\Delta T = 0\end{aligned} \tag{11}$$

$$U_7A_7(T_6 - T_7) - m(L_7 + (1-k)L_f - L_6)(\lambda_6 - hc_6) + kL_f Cp\Delta T = 0 \tag{12}$$

These fourteen nonlinear equations of the MSE treated as equality constraints with fourteen number unknown decision variables such as fresh steam supplied (V_0), output temperature of each stage (T_i (i = 1, 2,…,6)), and output liquor flow rates (L_i (i = 1, 2,…,7)). Equations (13)–(14) illustrate the side constraints of T_i and L_i for the mentioned stages of the proposed MSE to maintain a continuous process with feasible bound of [0:3] (kg/s) of fresh steam (V_0), required to accelerate the continuous process. The boundary values of T_i and L_i that are subjected to compute the optimal results are mentioned in Table 1.

$$\begin{aligned}&T_i > T_{i+1},\ (i = 2, 3 \ldots 7) T_7 > 52\,(T_8)\\&L_{i+1} > L_i,\ (i = 1, 2 \ldots 7)\end{aligned} \tag{13}$$

$$T_i > 0,\ (i = 2, 3 \ldots 7) \text{ and } L_i > 0,\ (i = 1, 2 \ldots 7) \tag{14}$$

Various approaches are reported in the literature to smoothly deal with the constraints functions, from which penalty functions are the simplest ones. The proposed objective function is penalized concerning the violation of the constraints. In this work, the fitness function is represented as in Eq. (15).

$$F = -f(z) + p_m\omega \tag{15}$$

Table 1 Boundary values of T_i and L_i for ith stages of proposed ERSs integrated MSE

T_i(°C) ∈ [90 : 125; 70 : 120; 66 : 90; 60 : 75; 55 : 65; 52 : 63], (i = 1, 2 . . . 6)
L_i(kg/s) ∈ [1.5 : 5; 3 : 6; 4 : 8; 6.5 : 10.5; 9 : 12; 6 : 13; 6 : 14, (i = 1, 2 . . . 7)

where F is the fitness function value, the negative sign indicates it is a maximization problem, $f(z)$ is the objective function, p_m is the penalty factor, and ω is the total penalty for constraints' violation.

a. **Objective function**

There are two objectives in the current investigation: to minimize the SC and maximize the SE of the proposed ERSs integrated MSE as SE is defined as the ratio of the difference between the amount of feed liquor and product liquor concerning the amount of SC by the MSE. Hence, this problem is turned into a single objective optimization problem with several constraints. The problem for the MSE is formulated as in Eq. (16).

$$\begin{aligned} \text{Maximize: } & f(z) = SE = \frac{L_f - L_1}{V_0} \\ \text{Subjected to: } & g_i(z_1, z_2, \ldots, z_n) \geq 0 \\ & h_i(z_1, z_2, \ldots, z_n) = 0 \end{aligned} \tag{16}$$

where i is the number of inequality/equality constraints and n number of unknown decision variables. But in this work, no inequality constraint is present only equality constraints are considered.

b. **Solution Algorithm**

In this section, two different metaheuristic approaches have been proposed named Differential Evolution Algorithm (DEA) [18] and Archimedes Optimization Algorithm (AOA) [19], inspired from two different natural phenomena of evolutionary computation and laws of physics to solve the constrained optimization problem. DEA is developed three decade before that provides a promising result for unknown decision variables, whereas AOA is developed in 2020, and its performance toward this industrial constraint optimization problem is steel a matter of search. Hence, to perform the comparative analysis among the obtained optimized energy efficiency parameters and decision variables, these two algorithms are considered from two different periods. The pseudocode of the proposed algorithms for the proposed models are given in Table 2.

4 Result Analysis

Based on the above discussions, population-based algorithms can solve real-life problems with the unknown, challenging, and constrained search space due to high exploration and local optima avoidance that heighten the utilization of different metaheuristic approaches. The algorithms mentioned above (DE and AOA) are employed with 100 search agents and 1000 iterations with 30 runs to solve this problem. A comparative analysis of these two algorithms is mentioned the Table 3, and the

Table 2 Pseudocode of DEA and AOA

DEA	**AOA**

Define objective function *f(z)*
Set input values (L_f, T_1, A_i, x_i,$\forall i$ =1 to7) // Table 2
Algorithm Parameters
LB & UB // Table 1
Number of Population (N=100)
Search space Dimension (D=14)
Crossover probability (P_c=0.8)
Max iteration (*maxite*=1000)
Initialization
Random population generation (P)
Calculate the fitness with the random population
for t=1*: maxite*
for i=1*:N*
Mutation: Generate the donor vector (V_i)
$V_i = x_{r1} + Fx_{r2} - x_{r3}$ // F=constant [0, 2]
Crossover: Generate offspring (U_j)
$U_i = \begin{cases} V_i & if\ r \le P_c\ or\ i = \delta \\ X_i & if\ r > P_c\ and\ i \ne \delta \end{cases}$ // $\delta \in (1, 2 \ldots D)$
end for
for i=1:*N*
Bound U_i
Calculation of the fitness function f_{Ui}
Performing greedy selection using f_{Ui} and f_i
Update P
end for
end for
Display the optimum results
	Define objective function *f(z)*
	Set input values (L_f, T_1, A_i, x_i,$\forall i$ =1 to7) // Table 2
	Algorithm Parameters
	LB & UB // Table 1
	Number of Population (N=100)
	Search space Dimension (D=14)
	Max iteration (*maxite*=1000)
	Define C_1 (2), C_2 (6), C_3 (2), C_4 (0.5), u (0.9), and l (0.1)
	Initialization
	Object population with random positions, densities, and volume
	Calculate the fitness of the first set and find the best one
	Set iteration counter, t = 1
	while t<=maxite
	for i=1:*N*
	Update density and volume of each object
	Update transfer and density decreasing factors (*TF* and *d*)
	$TF = \exp\left(\frac{t - \max ite}{\max ite}\right)\ d^{t+1} = \exp\left(\frac{\max ite - t}{\max ite}\right) - \left(\frac{t}{\max ite}\right)$
	if TF<=0.5 // exploration phase
	Update and normalize acceleration
	Update direction flag F and position
	end if
	end for
	Perform greedy selection to update population if there is better solution
	end while
	Display the optimum results

convergence curve for 30 runs of AOA and for best runs of DE and AOA are shown in Fig. 2 and Fig. 3, respectively. AOA converges faster and better among these two algorithms but needs more execution to achieve better fitness value in less time.

According to the unknown process variables and objective function value, the performance of these two population-based algorithms belongs to two different classes of inspiration (Evolutionary technique and mathematics-based technique). Specifically for this constraint gray-box optimization problem with fourteen decision variables, these two algorithms are approaching very likely, as represented in Table 4. The energy efficiency parameters SC and SE obtained by two approaches show a deviation of 8.96% and 3.75%, respectively. The AOA algorithm performs

Table 3 Comparison of proposed algorithm parameters

Algorithms parameters	DE	AOA
Population size (N)	100	100
Number of iterations (T)	1000	1000
Number of execution	30	30
Best execution	16	13
Average computational time (s)	35.698	24.84

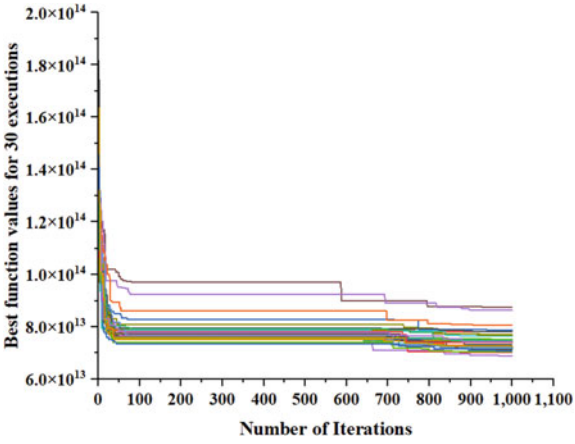

Fig. 2 Convergence curve for thirty runs for AOA

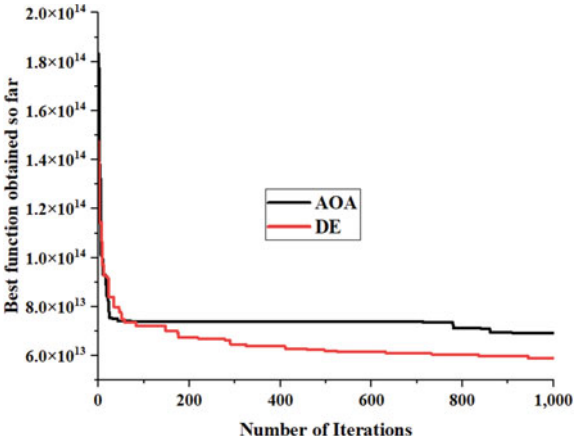

Fig. 3 Convergence curve for best runs of DE and AOA

very competitively and produces better results than the DEA. Comparing it with real-time plant data, the SE is increased by 83.5% due to the incorporation of different ERSs, and similarly, the SC is decreased by 39.9%, as illustrated in Fig. 4. The variation in liquor flow rate (L_i) with respect to the temperature (Ti) is demonstrated in Fig. 5.

5 Conclusion

A constrained gray-box optimization employed to a real-life problem with higher dimensions often demands conventional iterative methods' heavy computational

Table 4 Optimal parameters obtained by DE and AOA for the proposed MSE model

Process parameters	Algorithms	1st	2nd	3rd	4th	5th	6th	7th	Output
T (°C)	DE	110.08	100.08	78.186	70.017	63.046	57.6	54.52	52
	AOA	111.499	101.499	86.058	69.157	62.528	58.098	54.205	52
L (kg/sec)	DE	4.259	5.998	7.023	9.29	11.183	12.791	12.667	NA
	AOA	3.2088	5.29	5.47	7.44	9.69	11.87	12.23	NA
V (kg/sec)	DE	2.994	1.739	1.025	2.267	1.893	1.608	1.561	1.383
	AOA	3.285	2.081	0.18	1.97	2.25	2.18	1.921	1.819
SC (kg/sec)	DE	1.611							
	AOA	1.4666							
SE	DE	8.2072							
	AOA	8.5147							

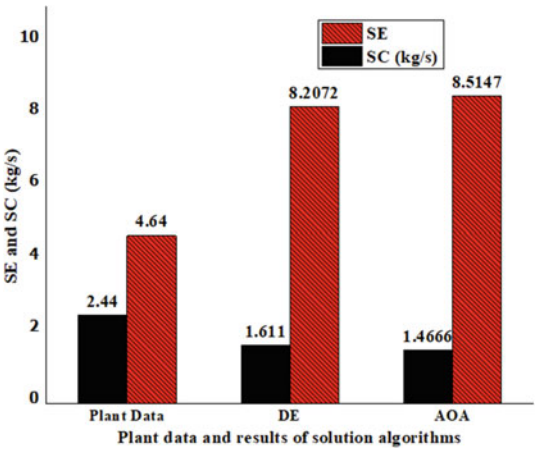

Fig. 4 Variation of SE and SC for DE and AOA

effort. In this situation, approximated solutions arise, obtained by different metaheuristic algorithms. The case study is a complex process industry problem of fourteen dimensionalities with a single objective function and fourteen constraints. The aim is to maximize the SE that reduces the SC of MSE used for the Kraft recovery process and ensures higher energy efficiency. Energy integration escorts the system toward self-sustainability and cost-saving. The principle of process integration and numerical optimization with the utilization of metaheuristic approaches (DE and AOA) stands as the most imperative way to decrease energy utilization and enhance the provision of waste heat reutilization of the mentioned energy-intensive unit. This work has evolved a steady-state nonlinear energy modeling of the proposed ERSs-integrated MSE. The model is validated by comparing it with the plant-operated MSE model with available data. This investigation shows efficient energy reduction

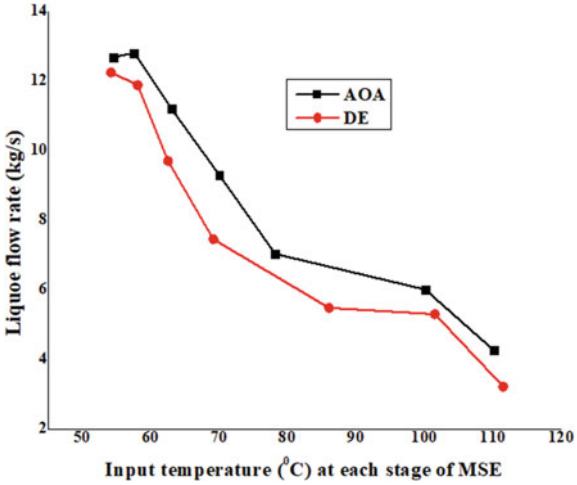

Fig. 5 Variation in liquor flow rate with respect to the temperature for DE and AOA

through SC (33.97%) and enhancement in SE (88.77%), leading to economic and environmental savings.

References

1. Sharan P, Bandyopadhyay S (2016) Integration of thermo-vapor compressor with multiple-effect evaporator. Appl Energy 184:560–573. https://doi.org/10.1016/j.apenergy.2016.10.037
2. Chen T, Ruan Q (2016) Modeling and energy reduction of multiple effect evaporator system with thermal vapor compression. Comput Chem Eng 92:204–215. https://doi.org/10.1016/j.compchemeng.2016.05.011
3. Hassan AS, Darwish MA (2014) Performance of thermal vapor compression. Desalination 335:41–46. https://doi.org/10.1016/j.desal.2013.12.004
4. El-Dessouky HT, Ettouney HM (1999) Multiple-effect evaporation desalination systems: thermal analysis. Desalination 125: 259–276. https://doi.org/10.1016/S0011-9164(99)00147-2
5. Shen S, Zhou S, Yang Y, Yang L, Liu X (2011) Study of steam parameters on the performance of a TVC-MED desalination plant. Desalin Water Treat 33:300–308. https://doi.org/10.5004/dwt.2011.2653
6. Verma OP, Mohammed TH, Mangal S, Manik G (2016) Optimization of steam economy and consumption of heptad's effect evaporator system in Kraft recovery process. Int J Syst Assur Eng Manag 1–20. https://doi.org/10.1007/s13198-016-0488-1
7. Bhargava R, Khanam S, Mohanty B, Ray AK (2008) Selection of optimal feed flow sequence for a multiple effect evaporator system. Comput Chem Eng 32:2203–2216. https://doi.org/10.1016/j.compchemeng.2007.10.012
8. Kaya D, Ibrahim SH (2007) Mathematical modeling of multiple-effect evaporators and energy economy. Energy 32:1536–1542. https://doi.org/10.1016/j.energy.2006.09.002
9. Al-Mutaz IS, Wazeer I (2014) Development of a steady-state mathematical model for MEE-TVC desalination plants. Desalination 351: 9–18. https://doi.org/10.1016/j.desal.2014.07.018
10. Verma OP, Suryakant, Manik G (2017) Solution of SNLAE model of backward feed multiple effect evaporator system using genetic algorithm approach. Int J Syst Assur Eng Manag 8:63–78. https://doi.org/10.1007/s13198-016-0533-0

11. Bhargava R, Khanam S, Mohanty B, Ray AK (2008) Simulation of flat falling film evaporator system for concentration of black liquor. Comput Chem Eng 32:3213–3223. https://doi.org/10.1016/j.compchemeng.2008.05.012
12. Miranda V, Simpson R (2005) Modelling and simulation of an industrial multiple effect evaporator: Tomato concentrate. J Food Eng 66:203–210. https://doi.org/10.1016/j.jfoodeng.2004.03.007
13. Pati S, Yadav D, Verma OP (2020) Synergetic fusion of energy optimization and waste heat reutilization using nature-inspired algorithms: a case study of Kraft recovery process. Neural Comput Appl. https://doi.org/10.1007/s00521-020-04828-4
14. Pati S, Verma OP (2021) Performance optimization of multiple stage evaporator using interior-point method and metaheuristic approaches in environment of real-time plant complexities. Int J Green Energy 1–18. https://doi.org/10.1080/15435075.2021.1884868
15. Pati S, Verma OP (2022) Energy integration of solar assisted Multiple Stage Evaporator and optimum parameter selection. Energy 239:122162. https://doi.org/10.1016/J.ENERGY.2021.122162
16. Yadav D, Verma OP (2020) Energy optimization of Multiple Stage Evaporator system using Water Cycle Algorithm. Heliyon 6:e04349. https://doi.org/10.1016/j.heliyon.2020.e04349
17. Pati S, Verma OP (2022) Integration of solar field with multiple stage evaporator to sustain eco-energy in pulp and paper plant. J Clean Prod 333: 130148. https://doi.org/10.1016/J.JCLEPRO.2021.130148
18. Storn R, Price K (1997) Differential evolution: a simple and efficient heuristic for global optimization over continuous spaces. J Glob Optim 11:341–359. https://doi.org/10.1023/A:1008202821328
19. Houssein EH, Hashim FA, Hussain K, Mabrouk MS, Al-Atabany W (n.d.) Archimedes optimization algorithm: a new metaheuristic algorithm for solving optimization problems. https://doi.org/10.1007/s10489-020-01893-z

Numerical Verification of FEM Model for Jute FRP Wrapped RC Beams Under Shear Failure Criteria

Tara Sen

Abstract Many past earthquakes and environmental degradation have resulted in severe damage in several concrete structures, retrofitting and rehabilitation aids in extending the service life of such damaged structures. ACI-440 codal provisions aids in analytical verification of various parameters of FRP wrapped concrete structures. Also, finite element analysis aids in evaluation of the same. This paper deals with the comparative study of the analytical verification carried out using the ACI-440 codal provisions with that of finite element analysis of the RC beams wrapped jute FRP (jute in woven textile form). The results obtained from the analytical study and that using the finite element analysis came in close agreement with enhanced shear strength being displayed by FEM model under ultimate shear failure criteria. This supports the fact that finite element analysis carried out with efficient meshing results in evaluation of various structural parameters which satisfies all the equations of ACI-440 codal provisions.

Keywords Finite element analysis · Nonlinear analysis · Shear failure · FRP · Jute · RC beams

1 Introduction

Various RC structures are in need of urgent strengthening, because of various factors such as existing flexure and shear cracks in them, carbonation effect, sulphate attacks, freeze–thaw cycles resulting in concrete distress, re-cycled steel being used, constructional errors in site, faulty design in load carrying capacities, and faulty reinforcement designs and detailings, etc. The utilization of textile FRPs, i.e. fibre reinforced polymer composites (FRP) in textile form has rendered these structures with sufficient enhancement in load carrying capacities and also enhanced their resistance to various environmental degradation effects, when attached to cracked (post-cracked or pre-cracked) structures with conjunction with epoxy resin. Carbon FRP (CFRP),

T. Sen (✉)
Department of Civil Engineering, National Institute of Technology Agartala, Barjala, Jirania, Agartala 799046, India
e-mail: tarasen20@gmail.com

© The Author(s), under exclusive license to Springer Nature Singapore Pte Ltd. 2023

K. R. Reddy et al. (eds.), *Recent Advances in Sustainable Environment*, Lecture Notes in Civil Engineering 285, https://doi.org/10.1007/978-981-19-5077-3_35

basalt FRP (BFRP), glass FRP (GFRP), and various natural fibres in the form of natural FRP (NFRP) and also aramid FRP (AFRP) attached with specified epoxiy resin have pointed out at manifestation in enhancement in structural load as well as environmental resistance. The experimental investigations of the suitability of using FRPs in various forms are enormous in nature. Various researchers have worked in this field which has effectively established the utilization of various FRPs for enhanced structural flexure or shear load carrying capacities [1–10]. All these experimental investigations are incumbent to heavy cost and expenditure, as a result of which nonlinear finite element analysis of various FRP wrapped RC beams has evolved, which can pave the way for effective virtual analysis and hence result in cost saving. Also, since huge experimental data is already available, even a comparative study to judge the effectiveness of nonlinear analysis can be performed, which many researchers have done so as to establish the FEM method of analysis as a reliable one [11–19]. The ACI 440.2R-02 [20] codal provisions basically deal with the 'Guide for the Design and Construction of Externally Bonded FRP Systems for Strengthening Concrete Structures'. The shear failure studies are very important in FRP strengthened RC structures, since shear failure is completely a brittle type of failure, and can be highly catastrophic in nature without any prior signs or warnings [1–3, 5, 9]. This paper deals with the comparative study of the analytical method of analysis obtained through the theory of ACI 440.2R-02 and that of the nonlinear finite element method of analysis of RC beams which are deficient in shear and have been wrapped with jute FRP, for enhancing their shear carrying characteristics.

2 RC Beam Models and Description

The reinforcement design of the reinforced concrete (RC) beam was carried out according to IS- 456: 2000 [21]. Beams were made deficient in shear, so that shear cracks in the beams appeared before flexural effect could begin. Table 1 describes the representative models.

Table 1 RC model beams

Beam designations	Description of the model	Type of failure
Model JF	Controlled RC beam where no FRP was bonded	Shear
Model JSF	RC beam model where jute FRP was bonded in full wrapping configuration (100% wrap ping)	Shear

2.1 Design of RC Beam for Shear Failure

The RC beam was designed such that it underwent shear failure before any flexural effect resulting in flexural stress could begin. So that the shear carrying capacity of the beam could be accessed, the RC beam was designed as a beam which have to first fail in shear-brittle failure. The beam was designed such that inclined shear cracks would appear in the shear regions of the beam. The beam was tested in the FEM platform using Ansys 12.0 using the two point loading configuration for the development of pure shear in the shear regions of the beam under this loading scheme. The beam design length was considered as 1.4 m. In accordance to the RC beam design, as per the stated the total area of steel for flexural requirement was obtained at 106.29 mm^2. So, using 8 mm dia bar in the tension zone, we provided three numbers of tor steel bars. But, since it was required here that the beam undergoes failure in shear only and not in flexure, hence extra flexural strengthening was carried out. Hence, the tensile reinforcement was increased by 50%, which turned out to be 159.435 mm^2. In order to provide shear resistance at the supports (so as to ensure shear failure in the beams), two legged 8 mm stirrup @ 130 mm C/C was provided throughout the beam. The entire reinforcement detailing of the RC beams for shear failure, which was followed for all the three groups of beams is shown in Fig. 1.

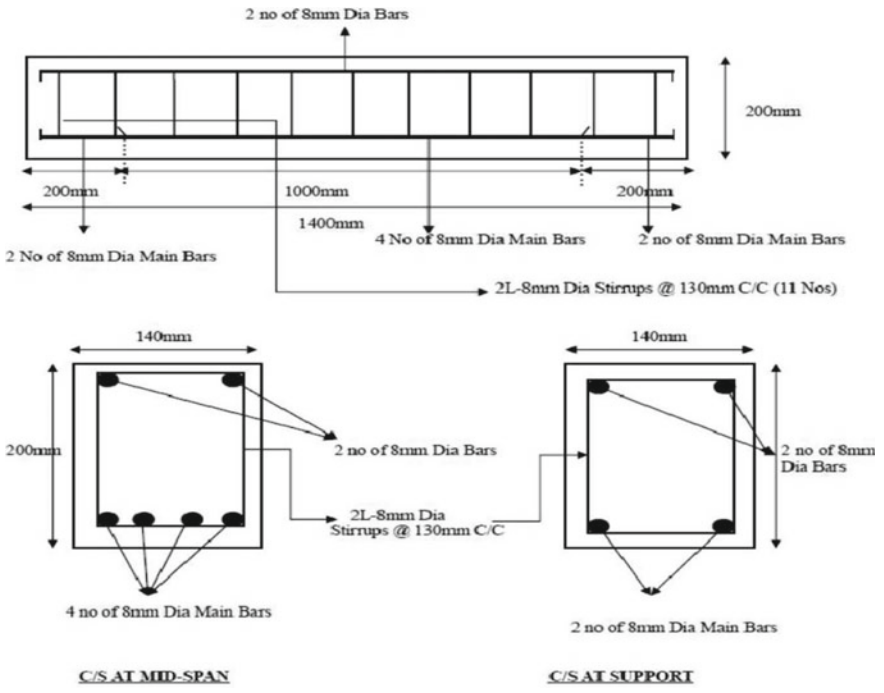

Fig. 1 FRP bonded on three sides of the RC beam FEM model, in U wrapping scheme

3 Finite Element Model Development in Ansys 12.0

3.1 Finite Element Modelling and Build-Up

Suitable finite elements were used for building up the entire model in FEM platform. SOLID65 was used for discretization of concrete, LINK8 was used for discretization of reinforcement steel, SOLID45 was used for discretization of steel plates for loadings and supports, and finally, the jute FRP composite sheet was discretized using SOLID layered46 element. The discretization and the meshing of the various components (volumes) in the finite element analysis were based on previous studies conducted by many researchers in this field [22–26]. Mapped meshing was selected for meshing the entire structure, since the accuracy of results using mapped meshing is very high; hence, this feature was used. The mapped meshing uses uniform and straight edged subelements for elemental discretization. Hence, it was used for obtaining better inter-nodal connectivity which can only be obtained if straight edged elements are used instead of irregular ones. Discrete modelling was carried out with individual characteristic inputs for concrete, reinforcements, FRP composite sheets and steel plates separately. After the discretization, and mapping, the overlapping or gluing of all the volumes was done, so that the entire unit act as monolithic. When the "edge option" was utilized in the Ansys platform, then it fetched just the outline boundary of the entire model, which basically indicated that the entire model along with the RC beam (concrete element) with the steel reinforcements inside, the steel plates (for loading and support), and the jute FRP composite sheet (wrapped around the beam in U-wrapping configuration), all act as one single unit, and there are no individual distortions when subjected to load.

Figure 2a is the FEM reinforcements detailing so as to aid in shear failure, and Fig. 2b is the outline or boundary of the entire FEM model with the "edge-only" option, which basically depicts that the entire FEM model acts as a monolithic volume. Figure 3 presents the symmetrical boundary conditions used on the axis of symmetry of the FEM model, this was done, since only one-half of the beam was modelled in the FEM platform so as to save computational time since the model was symmetric. Figure 4 shows the point load along the entire top surface nodal elements in the steel plate, used for load transferring to the RC-FRP wrapped FEM beam model. Figure 5 presents the displacement constraints carried out so as to model a simple support, on which the RC beam rests.

3.2 Finite Element Method of Modelling the FEM Beam Models

The RC beams were modelled using the ANSYS 12.0 finite element method (FEM) software, as per the plan and the beam designations as described in Table 1. The analysis done was for static conditions and also for small-deflection problems. During

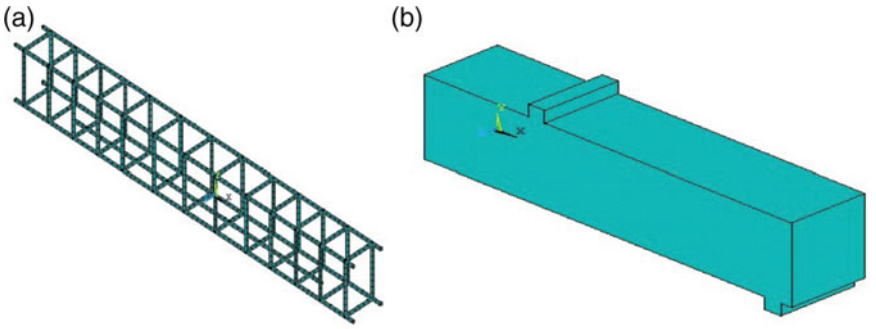

Fig. 2 FEM model for reinforcements **a** for flexural failure **b** boundary of the entire FEM model with "edge-only" option

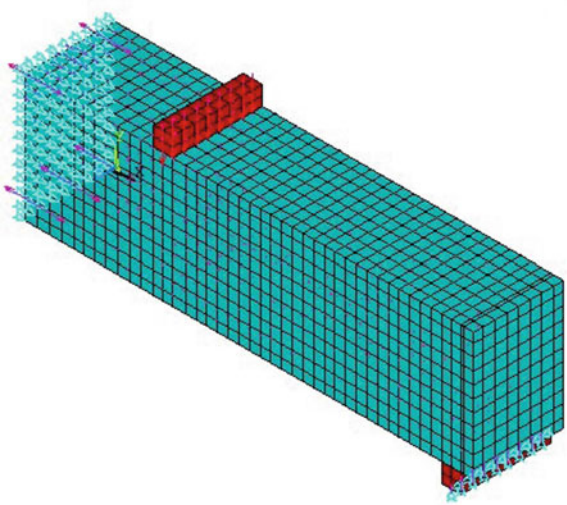

Fig. 3 FEM model displaying symmetrical boundary conditions on the axis of symmetry

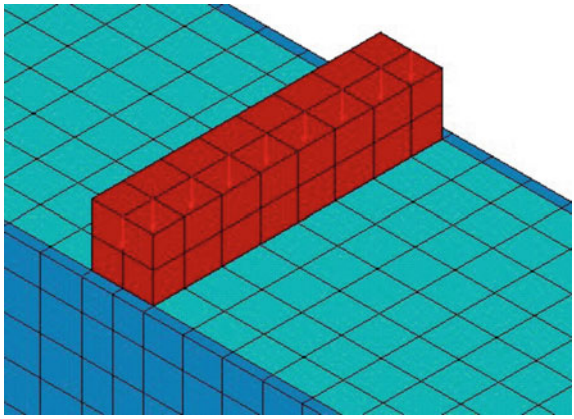

Fig. 4 Load application through the steel loading plates in the FEM model

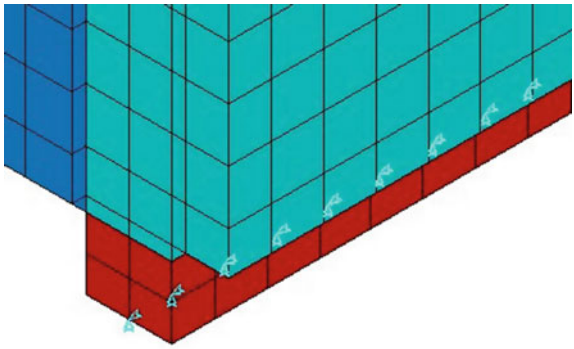

Fig. 5 Displacement constraints in the steel support

modelling of the JF beam, no FRPs were modelled on the three faces of the beam, while during the modelling of the JSF beam, on the three faces, i.e. the three sides of the beam (in the U wrapping configurations), jute FRP was modelled separately in 3D and was glued to the three faces of the beam alongside establishment of inter-nodal connectivity, this is as shown in Fig. 6. The inter-nodal connectivity of all the FRP, loading plate and RC beam model is shown in Fig. 7. The representative figure as depicted in Fig. 7 shows the established inter-nodal connectivity between the jute FRP composite sheet (dark-blue colour), the RC beam (light blue colour) and one of the loading plates on the RC beam (red colour). Failure of the reinforced concrete element is based on the Von Misses failure criterion and the Willam and Warnke model [27, 28], which defines the failure surface of the concrete. Containment of different displacement boundary conditions was carried out so as to constraint the model for getting unique solution. The symmetric boundary conditions (symmetrical BC) and the support boundary conditions for modelling of simple support was done. The force applied at each node was divided by the total number of nodes selected in the steel plate used for loading, and it was applied UY direction. The finite element model was capable of predicting failure for concrete materials, i.e. both cracking and crushing failure modes were accounted for. Finally, after the nonlinear finite element analysis, all the crack patterns were obtained in ANSYS 12.0, at the corresponding ultimate stages of loadings. The study of the ultimate shear failure load obtained using the nonlinear finite element analysis by ANSYS 12.0, revealed good agreement with the analytical obtained results using the ACI 440 codal provisions.

3.3 Shear Cracking Failure as Obtained from FEM Analysis

Many researchers have carried out a lot of research on the cracking-crushing characteristics of concrete failure in finite element analysis [2, 6, 12–14]. The red lines in the output FEM models represent cracks with smaller crack width. The blue-green lines in the FEM models represent concrete cracks with larger crack widths. The

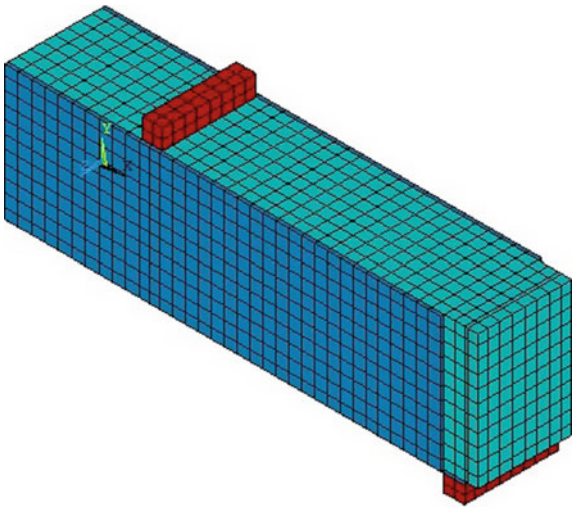

Fig. 6 Jute FRP bonded on three sides of the RC beam model in FEM platform

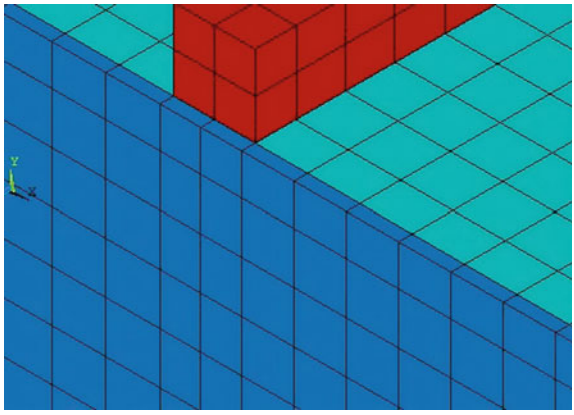

Fig. 7 Inter-nodal connectivity establishment between FRP, loading plates and RC beam in the FEM platform

cracking pattern as displayed by cracking in the JF beam FEM model, the shear cracks, i.e. diagonal tensile cracks at the shear zone of this model is clearly shown in Fig. 8b. Accompanied by some flexural cracks as well as flexure-shear cracks, the blue-green colour indicating excessive concrete cracking was observed at almost 45° inclined manners in the pure shear zone, also there was generation of alternate flexure-shear cracks near the end of the flexure zone. The excessive concrete cracking can be observed to be extending from the support towards the load and was predominant in the shear zone of the model. The cracking pattern as displayed by the JSF model, shows massive shear cracks, i.e. diagonal tensile cracks at the shear zone of the model. The blue-green excessive concrete cracking was observed to be mainly localized in the pure shear zone, also the generation of alternate flexure-shear cracks near the end of the flexure zone was very evident. The failure of the model

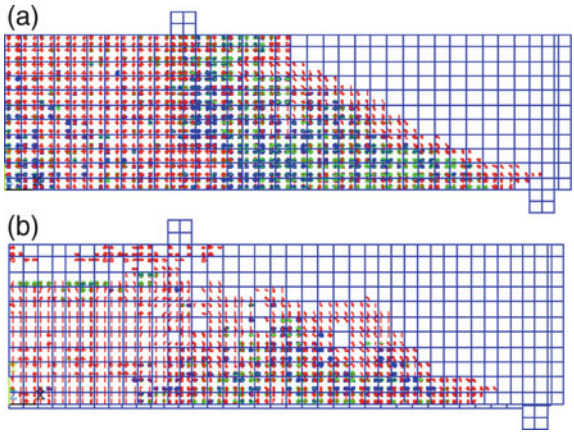

Fig. 8 Shear cracking and crushing of concrete in the FEM models **a** shear cracking in controlled JF FEM beam model, **b** shear cracking in JSF FEM beam model wrapped with jute FRP in 100% configuration

was marked by massive diagonal shear cracks almost inclined at an angular direction of 45° in the pure shear zone, with the direction of excessive concrete cracking extending from near the support towards the load. Figure 8 presents the diagonal tensile flexural cracking in the FEM models in (a) controlled beam (b) JF RC beams wrapped with jute FRP in the U-wrapping configuration in 100% wrapping.

4 Analytical Study Based on ACI-440.2R-02

The FRP contribution to the shear strength of strengthened RC beams pre-strengthened using three sided continuous U wrap, in full wrapping technique, was calculated in accordance to Fig. 8, which is based on the ACI 440.2R-02 [65] guidelines for shear strengthening using FRP systems (Fig. 9).

The following steps were carried out for the verification and checking of the U-wrapping scheme of shear revitalization for group II beams. The design ultimate tensile strength of FRP f_{fu} was calculated using the following equation.

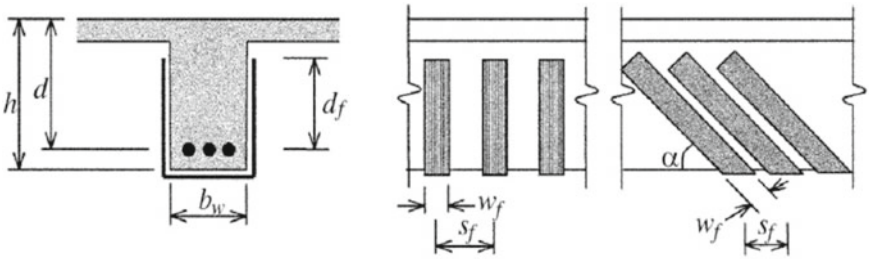

Fig. 9 Illustration of the dimensional variables used in shear-strengthening calculations for repair, retrofit or strengthening using FRP laminates as per ACI 440.2R-02

$$f_{fu} = C_E f_{fu}* \tag{1}$$

where C_E is the environmental-reduction factor and $f_{fu}*$ is the ultimate tensile strength of FRP as reported by the manufacturer. The effective strain in FRP wraps was determined using the bond-reduction coefficient *Kv* given by the following equation.

$$K_v = (K_1 * K_2 * l_e)/(11900 * \varepsilon_{fu}) \leq 0.75 \tag{2}$$

where active bond length, $l_e = 23{,}300/((n\ t_f\ E_f)\ \text{^}0.58)$, modification factor 1, i.e. $K_1 = (f'c/27)\text{^}(2/3)$, modification factor 2, i.e. for U wraps, $K_2 = (d_f - l_e)/d_f$. The effective strain level in the FRP ε_{fe} was then computed using the following equation.

$$\varepsilon_{fe} = (K_v * \varepsilon_{fu}) \leq 0.004 \tag{3}$$

The area of FRP shear reinforcement was obtained using the following equation.

$$A_{fv} = 2 * \mathrm{n} * t_f * w_f \tag{4}$$

where *wf* is the total width of the FRP, *n* is the number of plies, i.e. the number of layers of FRP reinforcement and *tf* is the nominal thickness of one ply of the FRP reinforcement. The effective stress *ffe* in the FRP was obtained using the following Eq. 5.

$$f_{fe} = E_f \varepsilon_{fe} \tag{5}$$

where *Ef* is the modulus of elasticity of different FRPs, and ε*fe* is the effective strain in the FRPs. The shear contribution by the FRP was obtained using the following equation.

$$V_f = [A_{fv} * f_{fe}(\mathrm{Sin}\alpha + \mathrm{Cos}\alpha) * d_f]/s_f \tag{6}$$

where $A_{fv} = 2n\ t_f\ w_f$ mm^2 and A_{fv} are the area of FRP shear reinforcement, and s_f is the spacing of FRP shear reinforcement in strips, since, here continuous U wraps were utilized; hence, width of the strip along entire length was considered, i.e. w_f is equal to the spacing of the strips s_f. Also, α is the angle of inclination of the FRP, here $\alpha = 90^{\circ}$, and *df* is depth of the FRP shear reinforcement. For jute FRP $V_f = 66.964$ KN. Finally, the design shear strength was calculated using the following equation.

$$\phi V_n = \phi[V_c + V_s + (\Psi_f * V_f) \tag{7}$$

Table 2 Comparative study of results

Beam designations in FEM analysis	Ultimate shear load carrying capacity obtained through FEM analysis (KN)	Ultimate shear load carrying capacity obtained through ACI440 codal provisions (KN)	PAnalytical/PFEM	Percentage difference (%)
Model JF	98	62.7	0.64	43
Model JSF	162	119.6	0.74	30

where V_c is the contribution to shear by concrete, and V_s is the contribution to shear by stirrup, reinforcing steel, in IS-456:200, we have combined effect of contribution by concrete as well as stirrup, which is $V_{u\ provided}$ and its calculated value was, $V_{u\ provided} = (V_c + V_s) = 62.678$ KN $= 62{,}678$ N, and we also have, $\Psi_f = 0.85$, *for U Wraps,* where Ψ_f is the additional strength reduction factor. For jute FRP wrapped RC beam, $\phi V_n = 119.597$ KN. The anticipated shear force on the RC beams is V_u, which is 30 KN.

Therefore, we see that ϕV_n for jute FRP wrapped beam is much greater than V_u, and hence, the design of jute FRP wrapped beam was safe under shear failure criteria.

Table 2 gives a comparison of the ultimate shear load carrying capacity as obtained from nonlinear finite element analysis, and that obtained the analytical method using the ACI-440.2R-02 codal provisions, for the JF beam and also the JSF beam. The ultimate shear load carrying capacity was found to be in good agreement with that obtained from nonlinear finite element analysis. The values of ultimate shear load carrying capacities as obtained from ACI codal provisions were found to be very reserve in nature.

References

1. Al-Amery R, Al-Mahaidi R (2006) Coupled flexural–shear retrofitting of RC beams using CFRP straps. Compos Struct 75:457–464
2. Barros JAO, Dias SJE, Lima JLT (2007) Efficacy of CFRP-based techniques for the flexural and shear strengthening of concrete beams. Cement Concr Compos 29:203–217
3. Dong J, Wang Q, Guan Z (2013) Structural behaviour of RC beams with external flexural and flexural–shear strengthening by FRP sheets. Compos Part B 44:604–612
4. Esfahani MR, Kianoush MR, Tajari AR (2007) Flexural behaviour of reinforced concrete beams strengthened by CFRP sheets. Eng Struct 29:2428–2444
5. El-Ghandour AA (2011) Experimental and analytical investigation of CFRP flexural and shear strengthening efficiencies of RC beams. Constr Build Mater 25:1419–1429
6. Hashemi S, Al-Mahaidi R (2012) Flexural performance of CFRP textile-retrofitted RC beams using cement-based adhesives at high temperature. Constr Build Mater 28:791–797
7. Almusallam TH (2006) Load–deflection behavior of RC beams strengthened with GFRP sheets subjected to different environmental conditions. Cement Concr Compos 28:879–889
8. Correia JR, Branco FA, Ferreira JG (2007) Flexural behaviour of GFRP–concrete hybrid beams with interconnection slip. Compos Struct 77:66–78

9. Sundarraja MC, Rajamohan S (2009) Strengthening of RC beams in shear using GFRP inclined strips—an experimental study. Constr Build Mater 23:856–864
10. Correia JR, Valarinho L, Branco FA (2011) Post-cracking strength and ductility of glass–GFRP composite beams. Compos Struct 93:2299–2309
11. Al-Rousan R, Haddad R (2013) NLFEA sulfate-damage reinforced concrete beams strengthened with FRP composites. Compos Struct 96:433–445
12. Demakos CB, Repapis CC, Drivas D (2013) Investigation of structural response of reinforced concrete beams strengthened with anchored FRPs. Open Constr Build Technol J 7:146–157
13. Hawileh RA (2012) Nonlinear finite element modelling of RC beams strengthened with NSM FRP rods. Constr Build Mater 27:461–471
14. Hawileh RA, El-Maaddawy TA, Naser MZ (2012) Nonlinear finite element modelling of concrete deep beams with openings strengthened with externally-bonded composites. Mater Des 42:378–387
15. Hawileh RA, Naser MZ, Abdalla JA (2013) Finite element simulation of reinforced concrete beams externally strengthened with short-length CFRP plates. Compos Part B 45:1722–1730
16. Jindal A (2012) Finite element modelling of reinforced concrete exterior beam-column joint retrofitted with externally bonded fiber reinforced polymer (FRP). Master's thesis, Department of civil engineering, Thapar University, Patiala, Punjab
17. Kachlakev D, Miller T (2001) Finite element modelling of reinforced concrete structures strengthened with FRP laminates final report SPR 316, Oregon department of transportation. For Oregon Department of Transportation Research Group200 Hawthorne SE, Suite B-240Salem, OR 97301–5192 and Federal Highway Administration, 400 Seventh Street SW, Washington, DC 20590
18. Luo Y, Li A, Kang Z (2012) Parametric study of bonded steel–concrete composite beams by using finite element analysis. Eng Struct 34:40–51
19. Özcan DM, Bayraktar A, Sahin A, Haktanir T, Türker T (2009) Experimental and finite element analysis on the steel fiber-reinforced concrete (SFRC) beams ultimate behavior. Constr Build Mater 23:1064–1077
20. ACI 440.2R-02. Guide for the design and construction of externally bonded FRP systems for strengthening concrete structures. Reported by ACI Committee 440
21. IS- 456: 2000. Indian Standard, plain and reinforced concrete-code of practice (4th Revision)
22. Omran HY, El-Hacha R (2012) Nonlinear 3D finite element modelling of RC beams strengthened with prestressed NSM-CFRP strips. Constr Build Mater 3:74–85
23. Padmarajaiah SK, Ramaswamy A (2002) A finite element assessment of flexural strength of prestressed concrete beams with fiber reinforcement. Cement Concr Compos 24:229–241
24. Potisuk T, Higgins CC, Miller TH, Yim SC (2011) Finite element analysis of reinforced concrete beams with corrosion subjected to shear. Advances in civil engineering, vol 2011. Hindawi Publishing Corporation, 14 pp. Article ID 706803
25. Santhakumar R, Chandrasekaran E (2004) Analysis of retrofitted reinforced concrete shear beams using carbon fiber composites. Electron J Struct Eng 4:66–74
26. Saifullah I, Hossain MA, Uddin SMK, Khan MRA, Amin MA (2011) Nonlinear analysis of RC beam for different shear reinforcement patterns by finite element analysis. Int J Civil Environ Eng 11(01):63–74
27. Willam KJ, Warnke EP (1974) Constitutive model for triaxial behaviour of concrete. In: Seminar on concrete structures subjected to triaxial stresses. In: International association of bridge and structural engineering conference, Bergamo, Italy, p 174
28. Wolanski AJ (2004) Flexural behavior of reinforced and prestressed concrete beams using finite element analysis. Master of Science thesis, Faculty of the Graduate School, Marquette University, Milwaukee, Wisconsin

Aspergillus Fumigatus NTCC1222 for Mitigation of Phenol-Related Environment Pollution

Abhishek Pandey, Shalini Singh, and Divya Prakash

Abstract Biodegradation, one of the most sought after methods to mitigate environmental pollution, is also found to very effective, safe, and well accepted for reduction of environmental pollution owing to presence of phenol and phenolic compounds in industrial effluents. The given study evaluates an indigenously isolated filamentous fungal strain of *Aspergillus fumigatus* for degradation of phenol so as to explore possible use of the given fungus in reducing phenol-related environmental pollution. Around 26% phenol degradation was seen for 7 day incubation period, at pH 7 and 32 °C at a phenol concentration of 1.5 g/L, when used as sole carbon source in the fermentation medium. The study provides valuable insight to the use of *Aspergillus fumigatus* for degradation of phenol, and possibly other phenolic compounds too, which might prove helpful in reducing environmental load of these industrial pollutants.

Keywords Biodegradation · Phenol · *Aspergillus fumigatus*

1 Introduction

Phenol and many phenolic compounds are considered serious pollutants present in waste waters generated from industries like, pesticides, pulp and paper, textile, timber, plastic, dyes, pharmaceuticals, tanneries, paints, gas and coke, synthetic rubber, fertilizers, steel, oil refineries, etc. Such chemicals, when disposed into the environment, have toxic effects on aquatic flora and fauna and affect the ecological balance [1–4].

A. Pandey · S. Singh (✉)
School of Bioengineering and Biosciences, Lovely Professional University, Phagwara 144411, Punjab, India
e-mail: shalinisingh.iit@gmail.com

S. Singh
Amity Institute of Microbial Technology, Amity University, Jaipur 307007, India

D. Prakash
School of Agriculture and Environmental Sciences, Shobhit University Gangoh, Saharanpur 247341, India

© The Author(s), under exclusive license to Springer Nature Singapore Pte Ltd. 2023

K. R. Reddy et al. (eds.), *Recent Advances in Sustainable Environment*, Lecture Notes in Civil Engineering 285, https://doi.org/10.1007/978-981-19-5077-3_36

One of the major phenolic derivatives, o-phenyl phenol, 2-phenylphenol, and its water soluble salt, sodium ortho-phenylphenate, are used as antimicrobial agents in bacteriostatic agents, fungicides, and sanitizers. O-phenyl phenol is moderately toxic in animal studies. In higher animal studies, both these agents have been associated with carcinomas [5]. Chlorophenols constitute a major category of pollutants often associated with paper industry effluents, wood industries, pesticide industries, etc. [6].

Inappropriate treatment of such materials has widely contaminated soil and groundwater, and associated toxicity is capable of causing serious health hazards in living organisms [7].

Biological methods to mitigate pollution related to phenolics in industrial waste waters have been used and are popular as they offer safe and environment friendly solutions for the removal of phenolics from waste water [7].

A number of microorganisms [8] have been found to be capable of degrading phenol and its derivatives. Reports suggest that bacteria [9–16] and yeast [17–19] have been majorly evaluated for phenol degradation. Fungal forms (filamentous), on the other hand, have been evaluated lesser for phenol degradation than bacteria or yeast [20–23].

The filamentous fungi, with wide range of enzymatic activities and ability to survive in extreme environmental conditions, are considered to have great ability to degrade wide varieties of pollutants and thus, have huge potential in bioremediation [24]. The genus *Aspergillus* and *Penicillium*, are known for their ability to metabolize and breakdown phenol and its derivatives [7, 25], but very few studies report ability of *Aspergillus fumigatus* to degrade phenol derivatives [21].

As a continuous search for newer, potent microbial strains for biodegradation of aromatic compounds continues, even though much information has been gathered during the years, and as *Aspergillus* sp. are important candidates in mitigation of industrial pollutants, the current study evaluates *Aspergillus fumigatus* for biodegradation of phenol. *Aspergillus fumigatus* NTCC1222 has previously been characterized for crude amylases [26–33], and the current study evaluates the strain for degradation of phenol.

2 Materials and Methods

2.1 Microbial Culture and Its Maintenance

Aspergillus fumigatus NTCC1222 procured from laboratory of Microbiology, Lovely Professional University, Punjab, India, was used in the present study. The culture was maintained on Potato dextrose agar medium (PDA), incubated at 37 °C for 3 days, and then stored in refrigerator at 4 °C. For long time preservation, the fungal mycelium and spores were suspended (15% v/v) sterile glycerol and stored at −20 °C [30].

2.2 Fermentation Conditions

About 250 ml Erlenmeyer flasks were taken, to which 100 ml of the fermentation medium (sodium nitrate 2.0 g/L, potassium phosphate (dibasic) 1.0 g/L, potassium chloride 0.5 g/L, magnesium sulfate heptahydrate 0.5 g/L, and ferrous sulfate heptahydrate 0.01 g/L and phenol as sole carbon source, 2.0 g/L) [7] was added. The initial pH of the medium was adjusted to 5.5 followed by steam sterilization (autoclaving: 121 °C temperature and 15 psi pressure) of the medium. Subsequently, the medium was cooled, inoculated with 2 discs (each of 5 mm diameter) of *Aspergillus fumigatus* NTCC 1222 and incubated at 27 °C, under shaking (150 rpm) [25, 30) conditions. After appropriate incubation period (flasks were harvested, every 24 h till the enzyme activity decreased). The contents of each flask were filtered through a pre-weighed Whatman filter paper 1. The pellet was then used to determine the microbial biomass [34], while the supernatant was used for determination of catechol 1, 2-dioxygenase activity, and spectrophotometric determination of phenol degradation rate [7].

Similarly, the effect of incubation pH and temperature on phenol degradation using test fungal isolate was also determined under desired fermentation conditions, while varying the pH (6.0, 6.5, 7.0, and 7.5) and incubation temperature (27, 32, and 37 °C) of the fermentation medium and keeping other conditions constant. For each experimental set up, the flasks were harvested, and the contents of the flasks were used to determine biomass [34] and phenol degradation [7].

Analytical methods

Determination of Catechol 1, 2-dioxygenase activity

5 μL of cell free extract in Eppendorf tube to which 20 μL of 10 mM catechol (substrate) was added. The final volume was adjusted to 1 mL with 50 mM sodium phosphate buffer (pH 7.0). The samples were then spectrophotometrically analyzed (260 nm) at 25 °C [7].

Determination of Biomass

Whatman filter paper 1 was dried at 100 °C until constant weight was achieved. The content of the flasks were filtered through Whatman filter paper 1 and the pellets so collected over the surface of the filter paper, were dried again at 100 °C until constant weight was achieved [34].

Biomass determination was calculated as:

Biomass determination (g/ml) = {[pellet (g) + filter paper (g)] – [filter paper (g)] / [Sample volume (mL)] X 1000}.

Determination of phenol degradation

About 0.3 mL freshly prepared sodium carbonate (200 g/L) and 0.1 mL folin-ciocalteau phenol reagent (folin-ciocalteu phenol reagent 0.1 mL and sodium carbonate 0.3 mL) were added to 2 mL of cell free extract. The mixture was then

vortexed and subsequently incubated at room temperature for 1 h. After incubation, 1 mL of distilled water was added into the mixture and again vortexed. The mixture was then subjected to spectrophotometer analysis at 750 nm [7, 36].

Phenol degradation rate was calculated as:

Percentage of phenol degradation = {[Initial phenol concentration (g) – Final phenol concentration (g)]/[Initial phenol concentration] X100}.

2.3 Statistical Analysis

3 Result and Discussion

Phenol (Table 1) degradation increases with increasing time, up to, 7th day of incubation (Table 1) with a maximum of 19.2% when tested for variable incubation time. The catechol 1, 2 dioxygenase activity [35] showed a similar pattern with highest activity being observed (66.72 U/mL) on 7th day of incubation, followed by a decrease in the enzyme activity on the 8th day of incubation. A corresponding increase in fungal biomass (4 gm/L) seen for 7th day of incubation was also seen.

With variable pH (Table 2), phenol degradation changed from 11.5% (pH 5) to 14.6% (pH 7.5), with the highest degradation being (19.9%) observed for neutral pH (pH 7.0). At a lower pH (pH 6.5) than the optimum, the phenol degradation rate decreased by almost 16%, while a decrease of 26.6% in phenol degradation was seen at pH 7.5. At very low or high pH, acids or bases can penetrate in to cells more easily, because they tend to exist in un-dissociated form under these conditions [39] and thus, might influence the degradation rate with varying amount of relevant enzymes produced.

Table 1 Effect of incubation period on degradation of phenol by *Aspergillus fumigatus* NTCC1222

Days	Biodegradation (%)	Biomass (g/ml)	Catechol 1, 2 dioxygenase activity (U/ml)
1	10.67	0.2	43.59
2	12.39	0.9	44.78
3	14.32	1.7	48.04
4	16.56	2.2	54.42
5	17.45	3.1	56.94
6	18.32	3.5	63.02
7	19.22	4.0	66.72
8	14.63	3.4	47.45

Cultural conditions
Temperature, °C: 27
pH: 5.5
Phenol concentration: 2 g/L

Table 2 Effect of incubation pH, temperature and initial phenol concentration on degradation of phenol by *Aspergillus fumigatus* NTCC1222

Optimization parameter	Range of values	Biodegradation (%)	Biomass (g/mL)
Incubation pH	**5.0**	11.5 ± 0.10	2.1 ± 0.03
	5.5	12.1 ± 0.03	4.4 ± 0.04
	6.0	13.3 ± 0.03	4.7 ± 0.01
	6.5	16.8 ± 0.08	4.8 ± 0.03
	7.0	19.9 ± 0.05	5.7 ± 0.06
	7.5	14.6 ± 0.10	3.5 ± 0.09
Incubation conditions: Incubation temperature, °C: 27 Incubation time, days: 7 Phenol concentration: 2 g/L			
Incubation temperature, °C	**27**	18.2 ± 0.10	4.2 ± 0.08
	32	22.0 ± 0.21	5.2 ± 0.22
	37	15.6 ± 0.17	2.9 ± 0.11
	42	11.9 ± 0.10	1.0 ± 0.15
	47	11.0 ± 0.11	0.17 ± 0.07
Incubation conditions: Incubation pH: 7.0 Incubation time, days: 7 Phenol concentration: 2 g/L			
Initial Phenol concentration, g/L	**1.0**	19.5 ± 1.01	4.1 ± 0.08
	1.5	25.5 ± 0.20	6.6 ± 0.13
	2.0	20.1 ± 0.82	5.9 ± 0.10
	2.5	12.2 ± 0.04	3.8 ± 0.31
Incubation conditions: Incubation pH: 7.0 Incubation time, days: 7 Incubation temperature, °C: 32			

Along with the nutrient availability, incubation temperature (Table 2), also play significant role in degradation of organic pollutants [39]. The biodegradation of phenol was highest (22%) at 32 °C followed by a decrease of 15.6% at 37 °C. As enzymatic activities are temperature dependent, it is expected that phenol degradation along with the enzyme responsible for the same, might decrease beyond the optimum temperature and also be less active below the optimum. The biomass increase also followed a similar pattern where the highest biomass was obtained at 32 °C and further increase resulted in lesser biomass accumulation.

Studies indicate that as phenol metabolism in mycelial fungi still needs to be extensively investigated and as in many of such studies, phenol has been shown to be metabolized by the beta-ketoadipate pathway, through ortho-fission of catechol, a basic evaluation of catechol 1, 2 dioxygenase activity in our experimental set up was

also done so as to possibly co-relate the given enzyme activity (if found produced by the test fungi) with phenol degradation. Litova et al. [38] has also shown, through genome sequencing that *Aspergillus fumigatus* (*Aspergillus fumigatus* Af293) carry the gene for catechol 1, 2-dioxygenase [37, 38]. The aim was thus to preliminary check whether the given enzyme was being produced or not as reported in Table 1. The enzyme activity showed similar pattern as phenol degradation, with best enzyme activity seen on 7th day of incubation. Further no optimization for catechol 1, 2 dioxygenase was done as the prime aim was to evaluate the fungal strain was its phenol degradation ability only.

Phenol degradation by the test fungi was also found to be dependent on substrate (phenol) concentration, as shown by decrease in phenol degradation beyond 1.5 g/L (25.5% biodegradation) of phenol in fermentation medium (Table 2). At 2 g/L phenol concentration, a decrease of 21.7% in degradation was seen. Similar observations about phenol degradation being concentration dependent, have been made by others too [39]. *Pseudomonas putida* has shown to degrade phenol in water in the concentration range 100–1000 ppm, with inhibition effects predominant above 500 ppm concentration by Bandhyopadhyay et al. [4].

4 Conclusion

The findings of the current study suggest that *Aspergillus fumigatus* NTCC 1222 might be explored for its phenol degradation ability. As observed, catechol 1, 2 dioxygenase was found to increase with increase in phenol degradation, indicating some phenol degradation linked production of the given enzyme. The maximum phenol degradation rate was obtained at pH 7, temperature 32 °C and incubation time of 7 days with the test fungal strain under aerobic conditions. Further, work will aim to understand the metabolic pathway via which phenol degradation is being carried out by the test fungi, and also will evaluate the possible use in mitigating phenol and phenolic compound related waste water treatment so as to understand the real time value of the microbial strain for the given application.

References

1. Saputera WH, Putrie AS, Esmailpour AS, Sasongko D, Suendo V, Mukti RR (2021) Technology advances in phenol removals: current progress and future perspectives. Catalysts 11:998-1-45
2. Nair CI, Jayachandran K, Shashidhar S (2008) Biodegradation of phenol. Afr J Biotechnol 7(25):4951–4958
3. Hobson MJ, Millis NF (1990) Hemostat studies of a mixed culture growing on phenolics. Res J Water Pollut Control Fed 62:684–691
4. Bandhopadhyay K, Das D, Maiti BR (1999) Kinetics of phenol degradation using *Pseudomonas putida* MTCC 1194. Bioprocess Eng 18:373–377
5. Anonymous (2022) https://www.cdc.gov/biomonitoring/Orthophenylphenol_BiomonitoringSummary.html. Last accessed on 27 January 2022

6. Rape C (1980) Chloroaromatic compounds containing oxygen. In: Hutzinger O (ed) The handbook of environmental chemistry. Springer KG, Berlin, pp 157–179
7. Stoilova I, Krastanov A, Stanchev V, Daniel D, Maria G, Zlatka A (2006) (2006) Biodegradation of high amounts of phenol, catechol, 2,4-dichlorophenol and 2,6-dimethoxyphenol by *Aspergillus awamori* cells. Enzyme Microbial Technol 39:1036–1041
8. Mathur N, Nigam V, Kumar A, Ghosh P (2008) Biodegradation of phenol by oxygenase producing thermophilic microorganisms. Asian J Exp Sci 22:55–65
9. Hinteregger CR, Leinter M, Loidl A, Streichshier F (1992) Degradation of phenol and phenolic compounds by *Pseudomonas* EKII. Appl Microbiol Biotechnol 37:252–295
10. Kwon KH, Yeom SH (2009) Optimal microbial adaptation routes for the rapid degradation of high concentration of phenol. Bioprocess Biosyst Eng 32:435–442
11. Seker S, Beyenal H, Salih B, Tomas A (1997) Multi-substrate growth kinetics of *Pseudomonas putida* for phenol removal. Appl Microbiol Biotechnol 47:610–614
12. Margesin R, Fonteyne PA, Redl B (2005) Low-temperature biodegradation of high amounts of phenol by *Rhodococcus* spp. and basidiomycetous yeasts. Res Microbiol 156:68–75
13. Buswell JA (1975) Metabolism of phenol and cresols by *Bacillus stearothermophilus.* J Bacteriol 124:1077–1083
14. Topalova Y, Dimkov R, Merdzhanov D (1995) Two steps for speeding up of phenol detoxication. Biotechnol Biotechnol Equip 9:55–59
15. Muller D, Schlomann M, Reineke W (1996) Maleylacetate reductases in chloroaromatic-degrading bacteria using the modified ortho pathway: Comparison of catalytic properties. J Bacteriol 178:298–300
16. Banerjee A, Ghoshal AK (2010) Phenol degradation by Bacillus cereus: Pathway and kinetic modeling. Bioresour Technol 101(14):5501–5507
17. Krastanov A, Alexieva Z, Yemendzhiev H (2013) Microbial degradation of phenol and phenolic derivatives. Eng Life Sci 2013(13):76–87
18. Shivaraman N, Kumaran P, Parhad NM (1978) Phenol degradation by *Candida Tropicalis* and influence of other toxicants. Ind J Environ Health 20(2):101–111
19. Aleksieva Z, Ivanova D, Godjevargova T, Atanasov B (2002) Degradation of some phenol derivatives by *Trichosporon cutaneum* R57. Process Biochem 37:1215–1219
20. Anselmo AM, Novais JM (1992) Degradation of phenol by immobilized mycelium of *Fusarium floccieferum* in continuous culture. Water Sci Technol 25:161–168
21. Jones KH, Trudgill PW, Hopper DJ (1995) Evidence of two pathways for the metabolism of phenol by *Aspergillus fumigatus.* Arch Microbiol 163:176–181
22. Santos VL, Heilbuth NM, Braga T, Monteiro AS, Linardi VR (2003) Phenol degradation by a *Graphium* sp. FIB4 isolated from industrial effluents. J Basic Microbiol 43:238–248
23. Kennes C, Lema JM (1994) Simultaneous biodegradation of p-cresol and phenol by the basidiomycete *Phanerochaete chrysosporium.* J Ind Microbiol 13:311–314
24. Deshmukh R, Khardenavis AA, Purohit HJ (2016) Diverse metabolic capacities of fungi for bioremediation. Ind J Microbiol 56(3):247–264
25. Ghanem KM, Al-Garni SM, Al-Shehri AN (2009) Statistical optimization of cultural conditions by response surface methodology for phenol degradation by a novel Aspergillus flavus isolate. Afr J Biotechnol 8(15):3576–3583
26. Singh S, Cheema SK, Kaur B, Mann NK (2013) Influence of ethanol on growth alpha-amylase production for *Aspergillus fumigatus* NTCC1222 under solid state fermentation. Int J Eng Res Technol 6(8):67–69
27. Singh S, Cheema SK, Kaur B, Mann NK (2013) Sorbitol: an enhancer of growth and alpha-amylase production for *Aspergillus fumigatus* NTCC1222 using wheat bran as substrate. Int J Biotechnol Bioeng Res 4(6):555–560
28. Singh S, Kaur B, Mann NK, Cheema SK (2013) Influence of Calcium Chloride on growth and alpha-amylase production for wild and UV-mutated Strains of *Aspergillus fumigatus.* Int J Biotechnol Bioeng Res 4(7):697–702
29. Singh S, Mann NK, Kaur B, Cheema SK (2013) Effect of toluene on fungal growth and amylase production—a step towards exploration of enzymes for industrial applications. Int Rev Appl Eng Res 4(2):117–122

30. Singh S, Singh S, Sharma L, Bali V, Mangla J (2014) Production of fungal amylases using cheap, readily available agri-residues, for potential application in textile industry. BioMed Res Int 9. Article ID 215748
31. Singh S, Cheema SK, Kaur B, Mann NK (2015) Effect of Ferrous sulphate on growth and alpha-amylase production for *Aspergillus fumigatus* NTCC1222. Orient J Chem 31(2):1181–1184
32. Singh S, Singh S, Mangla J (2016) Physical and chemical mutation for enhanced alpha-amylase production by *Aspergillus fumigatus* NTCC1222 under solid state fermentation conditions using agri-residue waste. J Pharm Nutr Sci 6(1):22–26
33. Singh S, Mangla J, Singh S (2021) Evaluation of *Aspergillus fumigatus* NTCC1222 as a source of enzymes for detergent industry. Res Environ Sustain 5:100030
34. Aneja KR (2003) Experiments in microbiology and plant pathology. New Age Int Pvt. Ltd., New Delhi
35. Varga JM, Neujahr HY (1970) Purification and properties of catechol 1,2-oxygenase from *Trichosporoon cutaneum*. Eur J Biochem 12:427–434
36. Box JD (1983) Investigation of the Folin-Ciocalteau phenol reagent for the determination of polyphenolic substances in natural waters. Water Res 17:511–525
37. Tuckwell D, Denning DW, Bowyer P (2011) A public resource for metabolic pathway mapping of *Aspergillus fumigatus* Af293. Med Mycol 49(Supl.1):114–119
38. Litova K, Manasiev J, Gerginova M, Peneva N, Alexieva Z (2015) Sequence analyses of genes coding key enzymes responsible for degradation of phenolic compounds by Aspergillus fumigatus strain AL3. J Biosci Biotechnol 195–203
39. Balamurugan P, Preetha B, Virithagiri T (2012) Study on effect of operating parameters on biodegradation of phenol by *Aspergillus fumigatus*. Int J Eng Res Appl (IJERA) 2(2):981–986

Soil Fertility Evaluation and Management by SFM Model in IIA-IDD Zone of Rajasthan

Jyoti Sihag and Divya Prakash

Abstract Soil is dynamic and natural that present in the uppermost layer of earth's crust. Soil fertility of IIA-IDD zone was assessed. The fertilization status were assessed using sand, silt, clay, texture, calcium carbonate, bulk density, electrical conductivity (EC), soil pH, organic carbon (OC), organic matter (OM), nitrogen (N), potassium (K), phosphorus (P), zinc (Zn), copper (Cu), manganese (Mn), iron (Fe), enzyme activity of acid phosphates, alkaline phosphates, dehydrogenase, and urease in soil of IIA-IDD zone. According to data, the most deficiency of nitrogen, phosphorus, potassium, organic carbon, zinc, iron, and copper were analyzed in farmland and wasteland soil of IIA-IDD zone. SFM model recommended bio-fertilizers like *Bacillus megaterium*, *Azotobacter*, *Bacillius*, *Pesudomonas*, *Rhizobium*, and *Aspergillus*, etc., and organic-fertilizers to enhance the deficiency of related nutrients and organic carbon in soil of analyzed zone. The suggestions of SFM model are applicable to nutrient management, environmental management, fertility management, and sustainable eco-friendly agricultural field management.

Keywords Dynamic · Dehydrogenase · Agricultural field

1 Introduction

In agriculture, the influences of soil are tremendous on crop health because the soil is a natural critical pool that is capable to provide water and nutrition, etc., to crops [1, 2]. The health of the soil is closely associated with plant and environmental health, food quality and food safety [3–6]. So, soil management is one of the important tasks to improve agriculture and its production. Several definitions of soil health have been provided over the years. The term 'Soil fertility' is generally used in soil science and it includes soil organic carbon and soil nutrients, etc., explained by Desbiez et al. [7]. The fertility of the soil is comprehensive [8], therefore, it

J. Sihag · D. Prakash (✉)
Shobhit University Gangoh, Saharanpur, India
e-mail: divya.prakash@shobhituniversity.ac.in

© The Author(s), under exclusive license to Springer Nature Singapore Pte Ltd. 2023

K. R. Reddy et al. (eds.), *Recent Advances in Sustainable Environment*, Lecture Notes in Civil Engineering 285, https://doi.org/10.1007/978-981-19-5077-3_37

can't be assessed only by certain parameters. To evaluate soil fertility, it is necessary to estimate physical, chemical, and biological attributes [9–24] that are linked to soil functions, called indicators or parameters of soil fertility. Soil texture, soil content (sand, silt, and clay), percentile, and bulk density are included in physical parameters. Whereas chemical parameters include soil pH, electrical conductivity, organic carbon, sulfur concentration, nitrogen concentration, phosphorus concentration, potassium concentration, zinc concentration, iron concentration, copper concentration, manganese concentration, heavy metal concentration, and biological parameters include microbial quantity, biochemical test, microbial biomass, and enzyme activity [25–28]. These parameters are capable to characterize the soil fertility.

In the present scenario, high agrarian production is essential to accomplish the demands of rapidly and regularly growing population. As well as, the reclamation and conservation of the product quality is necessary to maintain the health of present and future generation. Now, moving to the aspect of soil fertilization management of IIA-IDD zone of Rajasthan. Soil fertilization management is a major concern in IIA-IDD zone. The total geographical area of IIA-IDD zone is 31380 km^2 (37.11%). In which 3829.49 km^2 area is covered by wasteland according to the sources of the Rajasthan government. The remaining 27,550.51 km^2 area is utilized for agricultural purposes. For the economic development and sustainable agriculture, it is very essential to analyze chemically, physically, and biologically the wasteland and arable soil that help to understand the present challenges of soil and the problem of soil fertility degradation of studied zone. In this respect, the main aim of the present work is assessment of the fertilization status for agricultural and wasteland soil by different soil parameters of IIA-IDD zone of Rajasthan.

The modeling technique is helpful and important in the land management agenda because it is an excellent way of transferring and providing the consequent information to other people [29]. We already discussed about model, classification, development, and its importance in previous paper [30, 31]. Developed computational model has been used to achieve the long-term fertility improving and sustainability development on studied zone. The aim of this work is to analyze the actual problem of soil and also maintain its fertility by help of computational model in IIA-IDD zone of Rajasthan.

2 Materials and Methods

2.1 Study Area

Present investigations have been carried out in the IIA-Internal Drainage Dry (IDD) zone of Rajasthan of India (Fig. 1). The districts Sikar, Nagaur, and Jhunjhunu are situated in IIA-IDD zone. In the IIA-IDD zone, the FLS samples were collected from Sikar district, while the WLS samples were collected from Nagaur district. The north side of the IIA-IDD zone is surrounded by Bikaner and Churu districts. The

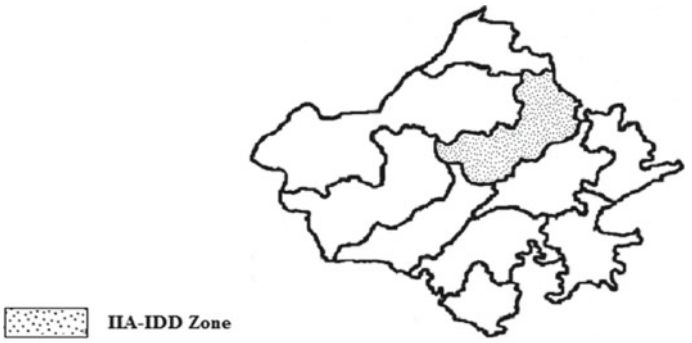

Fig. 1 Location of the IIA-IDD zone in Rajasthan

west side is covered by Jodhpur district, on the south side there are Ajmer, Pali, and Jaipur. The north-east region is covered by Haryana state, while the south-east region is covered by Jaipur.

The climate of the studied zone is semi-arid. For the IIA-IDD zone, the total annual rainfall is 300–350 mm. The rainfall is erratic and unevenly distributed. Also, maximum rainfall is received in the monsoon season which mainly starts from July and continues to September month. In this zone, variation in temperature is found because storms are very common in summer and during winters fog is seen. The average maximum temperature is 39.7 °C, and the minimum temperature is 5.3 °C (Source: Government of Rajasthan Department of Agriculture). The *Aridisols*, *Inceptisols*, and *Vertisols* soil orders are mainly dominant in the IIA-IDD zone of Rajasthan.

Neem (*Azadirachta indica*), bhurut (*Cenchrus biflorus*), khejri (*Prosopis cineraria*), aak (*Calotropis procera*), babul (*Prosopis cineraria*), bordi (*Zizyphus jujube*), shisham (*Dalbergia sisssoo*), rohira (*Tecomella undulata*), imali (*Tamaaindus Indica*), kairi (*Acacia senegal*), dhaab (*Desmostachya bipinnata*), ganthia (*Dactyloctenium scindicum*), and lampla (*ristida purpurea*) are found in natural vegetation of IIA-IDD zone. Mustard (*Brassica juncea*), moong (*Vigna radiata*), cotton (*Gossypium hirsutum*), bajra (*Pennisetum glaucum*), guar (*Cyamopsis tetragonoloba*), barley (*Hordeum vulgara*), wheat (*Triticum aestivum*), gram (*Cicerarietinum*), and cowpea (*Vigna sinensis*) are majorly grown in this zone. In vegetables, tomato (*Lycopersicon esculentum*), cabbage (*Brassica oleracea var. capitata*), onion (*Allium cepa*), tinda (*Citrullus vulgaris var. fistulosus*), phog (*Calligonum polygonoides*), brinjal (*Solanum melongena*), moth bean (*Vigna aconitifolia*), carrot (*Daucus carota*), fenugreek (*Trigonella foenum graecum*), bottle gourd (*Lagenaria riceraria*), cauliflower (*Brassica oleracea var. botrytis*), water melon (*Citrullus lanatus*), pea (*Pisum sativum*), indian spinach (*Beta vulgaris*), pearl millet (*Pennisetum glaucum*), sesame (*Sesamum indicum*), and musk melon (*Cucumis melo*) are grown in IIA-IDD zone.

2.2 Soil Sampling

All soil samples were separately collected from IIA-IDD zone of Rajasthan. Soil samples were collected from different field sites such as farmland and wasteland sites of IIA-IDD zone of Rajasthan. Before the soil sampling, the soil from the upper layer was scraped off to remove foreign elements and litter. For soil sampling, we made 'V' shaped cut with the help of a spade. Then we obtained a uniformly thick slice of soil from the surface to 30 cm plough depth for both types of soil collection. Soil samples from farmland and wasteland soil were separately packed in white clean polythene bags as well as correctly marked with the help of a marker. A part of the soil samples was dried in shade at room temperature conditions for chemical and physical parameters evaluation. After the drying, soil samples were grinded by a grinder and sieved using a sieve. Sampled soils were passed through a 2 mm sieve for chemical analysis. Soils of agricultural sites were collected after the harvesting of crops and before the irrigation of the field and sowing because at that time fertilizers are least effective or active. Roots were excluded from the farmland soil samples. Remaining soil samples sieved (<5 mm) and stored in a refrigerator at 4 °C for biological parameter and enzyme activity analysis [32]. Finally, we have determined the soil parameters of collected samples in the laboratory.

2.3 Physical, Chemical and Biological Measurement

The texture of the soil samples was observed according to the procedures outlined by Hydrometer method [33]. Soil bulk density was examined as per Mathur (2001) [34]. Soil pH was estimated by a glass electrode pH meter [33]. Electrical conductance of soil was measured by the conductivity method [35]. Soil organic carbon was analyzed by the wet-digestion method [36]. Soil organic matter was calculated by multiplying organic carbon content by the Van Bemmelen factor 1.724, based on the assumption that soil organic matter is composed of fifty-eight percent carbons [37]. Soil nitrogen was observed by the alkaline potassium permanganate method described by Subbiah and Asija (1956) [38]. The sodium bicarbonate extractable method of Olsen et al. (1954) was followed for the evaluation of phosphorus concentration in soil samples [39]. Potassium nutrient was determined by flame photometer method [40]. The soil sulfur determination was done as per Williams and Steinberg's (1959) [41]. Soil micronutrient concentration like zinc, manganese, iron and copper was analyzed by DTPA extracted method [42]. Heavy metals like lead, cadmium and chromium of soil were examined by tri-acid mixture digestion method [43]. For determination of calcium carbonate in soil, rapid titration method was used [44].

The dehydrogenase enzyme activity of soil was determined by 2-3-5-Triphenyl tetrazolium chloride (TTC) reduction technique [45]. The acid phosphatase enzyme activity was tested using the method described by Tabatabai and Bremner (1969) [46]. Alkaline phosphatase enzyme activity was also observed by the method described

by Tabatabai and Bremner (1969) [46]. Urease enzyme activity was determined by the method of McGarity and Myers (1967) [47]. Fluorescein diacetate activity of soil was analysed by following the procedure of Schnürer & Rosswall (1982) [48]. The bacterial isolation was done as per Kannan et al. (2018) [49] and Jasuja et al. (2013) [50]. Citrate utilization test, indole test, methyl red test, voges-proskauer and catalase test were done as per Bhattacharya et al. (2014) [51]. For fungal, soil dilution method was done as per Waksman (1927) [52] and Raja et al. (2017) [53]. The fungus identification was done by Lactophenol blue method. Biomass carbon of soil was done by chloroform fumigation extraction method [54].

2.4 Development of SFM Model

The model for the soil fertility management (SFM) has been developed in C# using windows form in visual studio 2019 IDE. The developed model is categorized in two modules. In the first module, the data inputs of soil parameters are entered. The data input is provided in 25 parameters. The input parameters include pH, EC, OC, P, N, K, Zn, Cu, Fe, Mn, S, Pd, Cd, Cr, sand, silt, clay, bulk density, carbon biomass, acid phosphates activity, alkaline phosphatase activity, dehydrogenase activity, urease activity, and FDA activity. Based on these values, the next module has been developed to compare the analyzed value of soil parameters with their reference criteria. At the end, the model shows the cumulative information of the deficient and toxic elements etc. of soil fertility status in dialog boxes. Fertilization status of soil is also shown in three classes, i.e., fertile, low fertile and nonfertile. Along with it, the model also recommends effective bio-fertilizer and organic fertilizer on the basis of analysis of the various input parameters of soil, in order to improve the fertility of wasteland soil and manage the fertility of agricultural land soil of IIA-IDD zone.

2.5 Working of Model

Firstly, we provide the input data values of soil parameters such as pH value, electrical conductivity, organic carbon, nitrogen, phosphorus, potassium, zinc, iron, copper, manganese, sulfur, lead, chromium, cadmium, calcium carbonate, sand, silt, clay, bulk density, carbon biomass, acid phosphatase activity, alkaline phosphatase activity, dehydrogenase, FDA, and urease activity in the respective input boxes. Thereafter, we click on 'calculate soil fertility' option. The input values are thereafter analyzed after acceptance and passed through various test conditions. Finally, the results are provided, which categorize the soil as either non-fertile, low fertile, or fertile. Wherein the soil fertilization status after analysis is derived as non-fertile or low fertile, then the model provides details of the parameters which are low or have toxic level. Further, it also suggests bio-fertilizer and organic fertilizers, which can be used for managing fertility of the soil. All the outputs means results and recommendations

are displayed in a "Message Dialog Box", to display the information. This model is extremely beneficial to resolve soil fertility problems of studied zone by suggesting effective and suitable bio-fertilizer and organic fertilizer, in a time efficient manner.

3 Result and Discussion

3.1 Physico-Chemical Parameter and Biological Parameter Evaluation of Farmland Soil (FLS)

Loamy sand was assessed as more dominant texture for FLS of IIA-IDD zone. Similar soil texture was observed for Sri Madhopur panchayat samiti of Sikar [55]. The majority of soils were found sandy in nature for Sri Madhopur tehsil of Sikar [56]. The textural class of IIA zone varied from loamy sand to sandy loam according to Kameriya [57].

The content of sand, silt, and clay ranged from 72.34 to 91.96, 7.21 to 26.2, and 1.26 to 6.36%, respectively. Mean value of sand, silt, and clay content was assessed as 79.84, 16.77, and 3.71%, respectively. However, mean value of silt and clay content were examined as 6.5 and 7.6%, respectively, for Palsana of Sikar [58]. According to Kumar and Babel (2011), sand, silt, and clay content varied between 76.70 to 90.40, 1.30 to 7.50 and 5.2 to 12.9%, respectively, for soil of Jhunjhunu [59]. The silt plus clay content in soils of Nagaur district of Rajasthan varies from 7.9 to 21.8 with a mean value of 12.9% [60]. Soil bulk density varied from 1.43 to 1.46 g/cc with mean value of 1.44 g/cc.

Soil pH values varied between 7.32 and 9.76 in soil of farmland. Mean value was assessed as 7.89 for pH exercise. In FLS, 63.33% of samples showed pH in normal (6.6 to 7.5) range. Remaining 26.66 and 10% of FLS showed pH in mild alkaline and strongly alkaline range, respectively. Highly alkaline soil was observed for Sri Madhopur panchayat Samiti of Sikar [55]. Sanwal et al. (2014) reported slightly alkaline nature of soil for Sri Madhopur Tehsil, Sikar [56]. Mean pH value was assessed as 7.91 for Sikar [61].

Range of electrical conductivity was assessed in 0.11 to 2.86 dS m^{-1}. Mean electrical conductivity was calculated as 1.09 dS m^{-1}. The electrical conductivity of soil was assessed in normal (<0.8 dS m^{-1}) range for 40% FLS samples. While 20 and 23.33% FLS were assessed in the range of 0.8 to 1.6 dS m^{-1} and 1.6 to 2.5 dS m^{-1}, respectively. But, in EC values, 16.66% FLS samples showed above 2.5 dS m^{-1} suggesting injurious to all crops. Most of Jhunjhunu's soils were reported in non-saline and moderately alkaline nature [59]. But, mean electrical conductivity was assessed as 0.14 dS/m for Sikar soil [61]. Normal range of pH and electrical conductivity was observed for Jhunjhunu [62].

Soil organic carbon content varied from 0.01 to 2.20% with 0.24% mean value. Soil organic carbon was present in the medium range for 3.33% of FLS. Remaining 93.33 and 3.33% of soil of IIA-IDD zone were found in low and high range of organic

carbon, respectively. Deficient availability of soil organic carbon was observed for Sri Madhopur tehsil of Sikar [56].

The soil organic matter varied from 0.01 to 3.79% in FLS. Mean value of organic matter was calculated as 0.40% for FLS of IIA zone. Organic carbon was reported as low to medium status for IIA zone [57]. Gupta (1986) obtained almost similar trends of organic matter for Palsana (Sikar) [58]. Kumar and Babel (2011) obtained low status of organic carbon for Jhunjhunu [59]. According to data of Verma et al. (2016b), organic carbon content was examined from 0.35 to 0.39% with an average value of 0.37% for Sikar [63]. Soil organic matter is important for crop production as it provides nutrients and modified physical properties of soil [64].

The mean value of nitrogen concentration was measured as 141.53 kg ha^{-1} within the range of 94 to 558 kg ha^{-1}. Nitrogen concentration was observed in low level for 96.66 and medium level for 3.33% of FLS samples, respectively. Low nitrogen status was observed for soil of Jhunjhunu [62]. Low nitrogen concentration directly affects plant growth, because it is a primordial part of chlorophyll and control development of plant. It plays a significant role in formation protein and amino acid [65].

We found potassium concentration range from 95 to 972 kg ha^{-1} in farmland soil. The mean concentration of potassium was measured as 239.3 kg ha^{-1}. For 13.33 and 56.66% FLS samples were determined in low and medium potassium range, respectively. In remaining 30.01% soil samples, potassium was found higher than the 335 kg ha^{-1} critical status given by Muhr et al. (1965) [66]. Potassium deficiency was more pronounced in agricultural field [67]. Nutrient potassium is essential and plays a vital role in energy metabolism, plant development, and starch synthesis, as well as increase plant resistance to pests and disease [68].

Soil phosphorus varied from 5.5 to 56 kg ha^{-1}. The mean value of phosphorus concentration was observed as 23.75 kg ha^{-1} in the farmland soil of IIA-IDD zone. The P concentration was found in low range for 26.66% soil samples. Concentration of phosphorus was assessed in medium and high range for 53.33 and 20% FLS, respectively. While medium to high availability of potassium and phosphorus found for IIA zone [57]. Medium concentration of phosphorus and potassium were observed for 42.9 and 55.4%, respectively, soil of Jhunjhunu [62]. Phosphorus is important for normal plant growth and maturity, energy storage, energy transfer, protein synthesis, water regulation, photosynthesis, and carbohydrate synthesis [65]. Deficiency of phosphorus was spread all over Jhunjhunu [67].

Ranges of zinc and iron concentration varied between 0.45 to 2.26 ppm and 2.23 to 6.52 ppm for farmland soil of IIA-IDD zone. In FLS, the mean values of zinc and iron concentration was calculated as 1.07 and 4.81 ppm, respectively. Sufficient availability of zinc and iron was assessed in 60 and 63.33%, respectively, soil sample of farmland. While 40 and 36.66% soil of farmland were found in deficient range for Zn and Fe, respectively. Seventy percent soil of Jhunjhunu was assessed in zinc deficiency [59]. Deficiency of zinc was widespread in both rainfed and irrigated agriculture fields of Jhunjhunu [67]. The concentration of copper micro-nutrient was found from 0.17 to 0.49 ppm in FLS. Average concentration of copper appeared as 0.31 ppm in farmland soil. In farmland, 86.66% soil samples were in a sufficient range of copper. However, deficiency of copper was observed in 13.33% soil samples

of farmland. The concentration of manganese and sulfur was assessed from 2.18 to 5.26 ppm and 10.10 to 32.17 ppm, respectively. Sanwal et al. (2014) observed range of zinc and manganese concentrations from 0.28 to 3.24 mg/kg and 2 to 5.62 mg/kg, respectively [56]. The ranges of copper, zinc, iron, and manganese nutrient varied between 0.17 to 3.32, 0.12 to 1.30, 1.22 to 5.87 and 2.03 to 5.67 mg/kg for Jhunjhunu [59]. Mean concentration of manganese and sulfur was observed as 3.8 and 21.93 ppm, respectively, in farmland soil samples. Manganese was observed in sufficient range for whole FLS. Manganese is constituent of plant enzymes and activates plant enzymes in many processes like photosynthesis, protein synthesis, metabolism, and respiration [65]. Soils of Jhunjhunu were adequate in copper, iron, and manganese micronutrient [67]. Sulfur concentration in 56.66% of soil was observed in medium (10–20 ppm) range, while 43.33% of farmland soil samples were assessed in high (>20 ppm) range.

The calcium carbonate was observed from 1.7 to 2.94% with an average value of 2.30%. In FLS, all soils were estimated in non-calcareous in terms of the limits classified by FAO (1973) [69]. Slightly calcareous soil nature was reported for Sri Madhopur tehsil of Sikar [56]. According to Kumar and Babel (2011), calcium carbonate varied from 3.90 to 12% with an average value of 8.24% for soil of Jhunjhunu [59].

Lead and chromium concentration varied between 9.12 to 33.26 mg/g and 5.27 to 14.9 mg/g, respectively. Mean concentration value of lead and chromium was observed as 18.32 and 9.08 mg/g, respectively in farmland soil of IIA-IDD zone. Concentration of cadmium varied from 0.08 to 0.18 mg/g. For farmland soil samples, mean concentration of cadmium was observed as 0.12 mg/g. The non-toxic availability of heavy metals, viz., lead, cadmium, and chromium were observed in farmland soil samples.

Soil enzymes play a vital role in nutrient cycling in particular since they are constantly being synthesized, accumulated, activated and decomposed in soil [70]. Soil acid phosphatase enzyme activity varied from 3.22 to 4.98 pkat g^{-1} with a mean value 4.15 pkat g^{-1}. However, range of alkaline phosphatase activity was observed from 73.2 to 78.6 pkat g^{-1} in farmland soil samples of IIA-IDD zone. The mean value of alkaline phosphatase activity was observed as 76.2 pkat g^{-1} in FLS samples. Enzyme activity of dehydrogenase varied from 4.03 to 4.19 pkat g^{-1}. Mean activity of dehydrogenase enzyme was calculated as 4.12 pkat g^{-1} in farmland soil samples. For all the farmland samples, the mean value of urease enzyme activity was calculated as 0.016 NH_4^+-N g^{-1} dry soil 3 h^{-1}. The urease enzyme activities ranged from 0.012 to 0.018 NH_4^+-N g^{-1} dry soil 3 h^{-1}. FDA activity in farmland soil ranged between 1621 and 1878 pkat g^{-1}. The mean value of FDA enzyme activity was found as 1753 pkat g^{-1} in soil samples.

Biomass carbon was assessed from 33 to 258 ppm for farmland soil samples of IIA-IDD zone. Mean value of microbial carbon biomass was calculated as 146 ppm. The bacterial population in farmland soil of IIA-IDD zone was observed as 2.5×10^8 CFU/ml for farmland soil of IIA-IDD zone. The gram-positive and cocci-shaped bacteria was observed in bacterial identification. Positive results were assessed for

methyl red and simmons citrate test. Bacteria *E. coli.*, *Shigella* spp., *Salmonella* spp., and *Klebsiella Pneumoniae* may be present in farmland soil of IIA-IDD zone.

3.2 Physico-Chemical Parameter and Biological Parameter Evaluation of Wasteland Soil (WLS)

The content sand, silt, and clay were observed from 20.24 to 43.15, 29.01 to 37.17, and 24.5 to 47.79%, respectively. Mean values of sand, silt, and clay content were observed as 32.48, 32.74, and 34.78%, respectively, for FLS (Table 1). According to Sharma et al. (2003), silt plus clay varied between 7.9 and 21.8% with an average value of 12.9% for Nagaur [60].

The soils were categorized as clay loamy for wasteland of IIA-IDD. But, loamy sand soil texture was observed for Didwana of Nagaur [71]. Soil bulk density of wasteland of IIA-IDD zone was found from 1.43 to 1.50 g/cc. Mean bulk density was calculated as 1.46 g/cc for wasteland soil samples.

Soil pH value was varied from 6.67 to 9.53 in wasteland soil of IIA-IDD zone. The mean pH was measured as 7.62 values for WLS. The pH value of 56.66% of

Table 1 Mean result of FLA and WLS for physico-chemical parameters

Parameters	Units	Mean of FLS	Mean of WLS
Sand	%	79.84	32.48
Silt	%	16.77	32.74
Clay	%	3.71	34.78
Texture	–	Loamy sand	Clay loam
Bulk density	g/cc	1.44	1.46
pH	–	7.89	7.62
EC	dS m^{-1}	1.09	0.84
OC	%	0.24	0.11
N	kg ha^{-1}	141.53	198
P	kg ha^{-1}	23.75	21.28
K	kg ha^{-1}	239.3	300
S	ppm	21.93	26.25
Zn	ppm	1.07	0.57
Fe	ppm	4.81	4.19
Cu	ppm	0.31	0.24
Mn	ppm	3.8	2.14
$CaCO_3$	%	2.30	1.16
Pb	mg g^{-1}	18.32	5.87
Cr	mg g^{-1}	9.08	13.88
Cd	mg g^{-1}	0.12	0.33

WLS was found in the normal range (6.6–7.5). Remaining 30 and 13.33% WLS were found in mild and strongly alkaline nature, respectively. A similar pH trend was assessed for Nagaur [61]. Normal and alkaline soil nature was assessed as 88 and 12%, respectively, soil of Nagaur [62]. Mean pH value was observed as 8.16 for Didwana of Nagaur [71]. Moderately alkaline nature of soil was assessed for Degana tehsil of Nagaur, which varied from 8.04 to 9.45 [72].

Data on electrical conductivity was found from 0.10 to 2.06 dS m^{-1} with an average value of 0.84 dS m^{-1}. The electrical conductivity of 43.33% WLS was observed in the normal range. Remaining 26.66 and 30% of soil were found in 0.8 to 1.6 dS m^{-1} and 1.6 to 2.5 dS m^{-1} range, i.e., critical range for salt sensitive and tolerant crops, respectively. Mean EC value was observed as 0.19 dS/m for Nagaur [61]. Normal and saline soil nature was assessed for 89.3 and 10.7% soils of Nagaur, respectively [62]. But, for Didwana of Nagaur, mean electrical conductivity was reported as 0.29 dS/m [71].

Organic carbon and organic matter varied from 0.03 to 0.20 and 0.05 to 0.34%, respectively, in WLS. For this zone, average value of organic carbon content and organic matter was assessed as 0.11 and 0.18%, respectively, in wasteland soil samples. For WLS of IIA-IDD zone, organic carbon content was assessed in deficient. Low organic carbon was more pronounced in Nagaur [63, 71, 73]. Similarly, organic matter was also assessed in deficiency.

The range of nitrogen nutrient was found from 54 to 380 kg ha^{-1} with mean value of 198 kg ha^{-1}. Medium availability of nitrogen nutrient was found in 3.33% WLS. And, 96.66% soil samples were assessed in nitrogen deficiency. Low nitrogen concentration was assessed for 70% of soil of Nagaur [62].

The phosphorus concentration ranged between 5 to 47.4 kg ha^{-1} with a mean value of 21.28 kg ha^{-1}. The P concentration was observed in low status for 36.66, medium for 46.66, and high levels for 16.66% WLS samples, respectively. Phosphorus is an important factor in several plant processes like cell division, growth process, respiration, photosynthesis, and plant development process [65].

Nutrient potassium concentration was found in the range of 104–629 kg ha^{-1}. Further, medium and high potassium concentration was found in 56.66 and 20% of samples, respectively. Low K concentration was observed for 23.33% soil samples. The mean concentration of potassium appeared as 300 kg ha^{-1}. Soil P and K were assessed in low concentration for 50.5 and 28.8% soil of Nagaur [62]. In Degana (Nagaur), phosphorus as well as potassium nutrient were present in soil in medium range however the availability of organic carbon was low [72].

Concentration of zinc micronutrients varied between 0.18 to 1.74 ppm with a mean value of 0.57 ppm. Similarly, concentration of iron was found between 2.49 and 5.61 ppm, with a mean value of 4.19 ppm. Zinc and iron deficiency were found in 46.66 and 30% of WLS samples, respectively. Zinc deficiency affects many processes like oxidation, synthesis of auxin indole acetic acid, transformation of carbohydrates, and further also affects the function of enzymes activitiy [65]. Iron and zinc were available within sufficient range in 70 and 53.33% of WLS samples, respectively. The concentration of Cu nutrient was found between 0.09 and 0.37 ppm, with a mean value of 0.24 ppm; and, the concentration of Mn nutrient was between 1.08

and 3.79 ppm, with a mean value of 2.14 ppm. Copper was available within sufficient range in 90% of WLS samples. The availability of Mn was sufficient for all the WLS.

Sulfur was measured from 17.64 to 44.67 ppm in WLS with mean value of 26.25 ppm. Availability of sulfur was analyzed in medium for 40% of soil of wasteland and in high range for 60% soil of wasteland.

Calcium carbonate varied from 0.1 to 2% and the mean value was 1.16%. All wasteland soil samples were found in non-calcareous nature as the classification proposed by FAO (1973) [69].

Heavy metal lead concentration in wasteland soil samples was between 3.19 and 24.01 mg/g. The mean lead concentration was calculated as 5.87 mg/g for WLS. Cadmium and chromium metal were observed between 0.13 to 0.78 and 4.21 to 29.56 mg/g, respectively. In WLS, mean concentration of cadmium and chromium was observed as 0.33 and 13.88 mg/g, respectively. For whole WLS, non-toxic concentrations of lead, cadmium, and chromium were observed.

Enzyme activity of acid phosphatase varied from 3.49 to 4.52 pkat g^{-1}, with a mean value of 4.01 pkat g^{-1}, whereas enzyme activity of alkaline phosphatase was between 15.3 and 22.4 pkat g^{-1}, and the mean concentration of alkaline phosphatase enzyme activity was 19 pkat g^{-1}. Dehydrogenase enzyme activity was found from 4.23 to 6.27 pkat g^{-1}. For WLS, mean dehydrogenase enzyme activity was calculated as 5.25 pkat g^{-1}. Range of urease enzyme activity varied from 0.01 to 0.019 NH_4^+-N g^{-1} dry soil 3 h^{-1} in wasteland soil samples of IIA-IDD zone. For WLS, mean value of urease was calculated as 0.013 NH_4^+-N g^{-1} dry soil 3 h^{-1}. The mean activity of FDA was measured as 1381 pkat g^{-1}. The FDA ranged between 1226 and 1466 pkat g^{-1} in WLS.

Biomass of carbon ranged between 14 and 80 ppm for wasteland soil samples of IIA zone. For soil samples of wasteland, average value of microbial carbon biomass was observed as 54 ppm (Table 2). For wasteland soil samples of IIA-IDD zone, 1.5 $\times$ 10^8 bacterial populations were assessed. According to morphological characterization, gram-positive and cocci shaped bacteria were observed. Positive results for methyl red were observed for wasteland soil. Bacteria *E. coli*., *Salmonella* spp. and *Shigella* spp. may be present in wasteland soil of IIA-IDD zone.

Table 2 Mean result of FLS and WLS for biological parameters

Parameters	Units	Mean of FLS	Mean of WLS
AP	pkat g^{-1}	4.15	4.01
ALP	pkat g^{-1}	76.2	19
DH	pkat g^{-1}	4.12	5.25
Urease	NH_4^+-Ng^{-1} dry soil 3 h^{-1}	0.016	0.013
FDA	pkat g^{-1}	1753	1381
Biomass C	Ppm	146	54

3.3 *Data Analysis by Computational Model*

After the analysis of soil samples, we obtained data of farmland as well as wasteland soil. The functioning and details of the said computational model have already been explained. To illustrate the functioning of the model, we have randomly selected data of one sample of wasteland and entered those values in the developed model. The selected sample is shown below (Fig. 2):

(a) **Data of WLS sample 8 of IIA-IDD zone in SFM model** (Fig. 2)

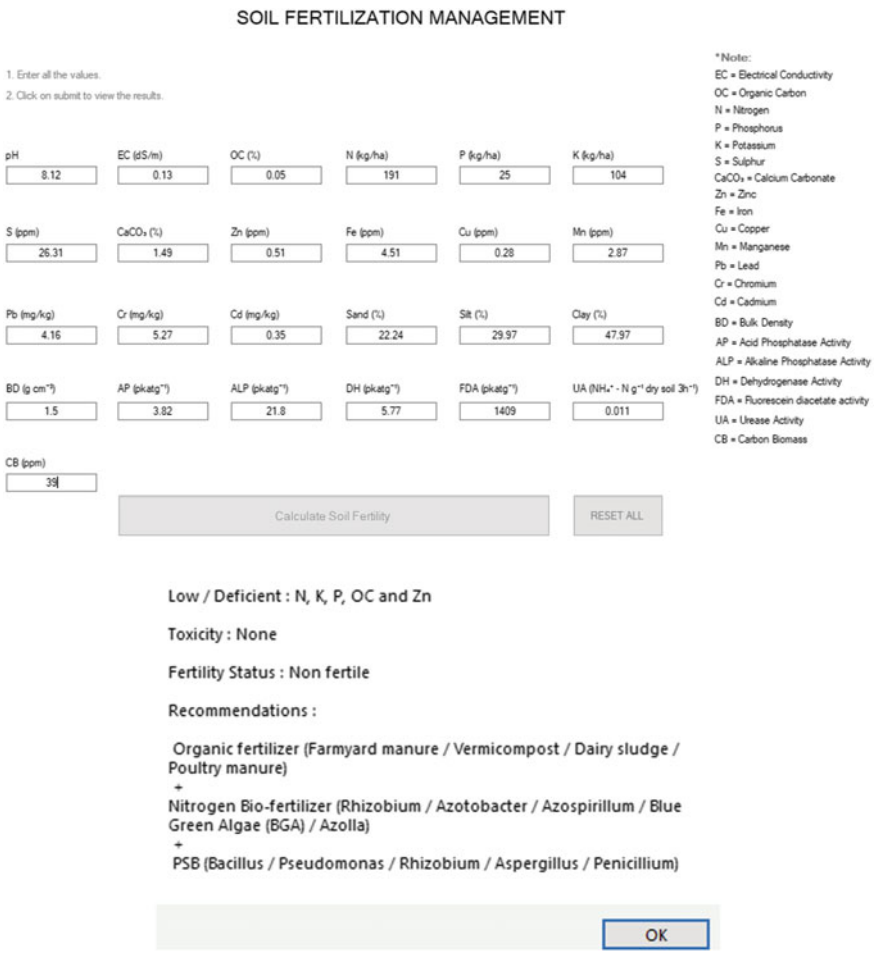

Fig. 2 Soil status of WLS sample 8 of IIA-IDD zone by SFM model

4 Conclusions

Overall in IIA-IDD zone, it was found that loamy sand and clay loam was present in FLS and WLS, respectively. The pH value has been observed in the normal (natural) range for 60% soils of IIA-IDD zone. While in the remaining soils 28.33% and 11.66% soils have shown pH in slightly alkaline and strong alkaline range, respectively. In farmland soil of IIA-IDD zone, the normal soil pH was maximum. The data revealed that 41.66% of soil samples were found in normal electrical conductivity range. Further, low range of organic carbon, nitrogen, potassium, and phosphorus was observed in 96.66%, 96.66%, 18.33%, and 31.66% of soils, respectively. However, a medium range of nitrogen, potassium, phosphorus, sulfur, and organic carbon in soil was observed in 3.33%, 56.66%, 50%, and 48.33% of the samples, respectively. Deficiency of organic carbon was more pronounced in all wasteland soil samples of IIA-IDD zone.

It was observed that in farmland and wasteland of IIA-IDD zone the deficiency of nitrogen is maximum. Sufficient availability of zinc, iron, copper and manganese has been observed in 56.66%, 66.66%, 88.33%, and 100% soil samples, respectively. The remaining 43.33%, 33.33%, and 11.66% of soil samples were found deficient in zinc, iron, and copper, respectively. It has been observed that in wasteland soils of IIA-IDD zone, the deficiency of zinc was maximum; and, farmland soil of IIA-IDD zone was most sufficient in terms of zinc. In farmland and wasteland soil of IIA-IDD zone of Rajasthan the sufficiency of manganese was maximum. The highest deficiency of iron has been observed in farmland soil of IIA-IDD.

The non-calcareous soil nature was found in all soil samples of IIA-IDD zone of Rajasthan. No toxicity of lead and chromium has been found in any of the soil samples of IIA-IDD zone. Similarly, normal cadmium concentration (no toxicity) was observed in IIA-IDD (FLS and WLS). In farmland soil of IIA-IDD zone, the acid phosphatase enzyme activity was maximum. However, highest alkaline phosphatase enzyme activity was observed in farmland soil of IIA-IDD zone of Rajasthan. High dehydrogenase enzyme activity has been observed in wasteland soil of IIA-IDD zone. Further, in farmland soil of IIA-IDD zone, maximum FDA hydrolysis and biomass carbon was observed.

After experiment, the data of parameters were analyzed in farmland and wasteland soil of IIA-IDD zone. According to data, SFM model suggested bio-fertilizers and organic-fertilizers because it is beneficial to enhance the deficiency of nutrients and organic carbon in soil of analyzed zone. The suggestions of this study are applicable to nutrient management, environmental management, fertility management, and sustainable eco-friendly agricultural field management.

References

1. Sihag J, Prakash D (2019) An assessment of the soil fertilization status of IB-INW zone of Rajasthan. Int J Mech Prod Eng Res Develop. 9(2):137–150

2. Sihag J, Prakash D, Yadav P (2019) Comparative study of soil fertility based on SFM computational model for IB-INW and IC-HAPI zone. Int J Mech Prod Eng Res Develop 9(4):499–508
3. Parr JF, Papendick RI, Hornick SB, Meyer RE (1992) Soil quality: attributes and relationship to alternative and sustainable agriculture. Am J Altern Agric 5–11 (1992)
4. Halvorson JJ, Smith JL, Papendick RI (1997) Issues of scale for evaluating soil quality. J Soil Water Conserv 52(1):26–30
5. Nielsen MN, Winding A, Binnerup S (2002) Microorganisms as indicators of soil health
6. Yilmaz E, Sönmez M (2017) The role of organic/bio–fertilizer amendment on aggregate stability and organic carbon content in different aggregate scales. Soil Tillage Res 168:118–124
7. Desbiez A, Matthews R, Tripathi B, Ellis-Jones J (2004) Perceptions and assessment of soil fertility by farmers in the mid-hills of Nepal. Agr Ecosyst Environ 103(1):191–206
8. Bautista-Cruz A, Carrillo-González R, Arnaud-Viñas MR, Robles C, de León-González F (2007) Soil fertility properties on Agave angustifolia Haw. Plantations Soil Tillage Res 96(1–2):342–349
9. Sinclair TR, de Wit CT (1975) Photosynthate and nitrogen requirements for seed production by various crops. Science 189(4202):565–567
10. Sihag J, Prakash D, Yadav P, Gupta P (2019) Physico-chemical characteristics with enzyme activity of topsoil for farmlands management of Ajmer, Rajasthan. Res Rev Int J Multi 4(3):1547–1552
11. Spiertz JHJ, De Vos NM (1983) Agronomical and physiological aspects of the role of nitrogen in yield formation of cereals. Plant Soil 75(3):379–391
12. Tiessen H, Cuevas E, Chacon P (1994) The role of soil organic matter in sustaining soil fertility. Nature 371(6500):783–785
13. Romig DE, Garlynd MJ, Harris RF, McSweeney K (1995) How farmers assess soil health and quality. J Soil Water Conserv 50(3):229–236
14. Doran JW, Parkin TB (1997) Quantitative indicators of soil quality: a minimum data set. Methods Assessing Soil Qual 49:25–37
15. Abbott LK, Murphy DV (eds) (2003) Soil biological fertility: a key to sustainable land use in agriculture. Springer Science & Business Media
16. He ZL, Yang XE, Baligar VC (2003) Microbiological and biochemical indexing systems for assessing acid soil quality. Adv Agron 78:89–138
17. Bot A, Benites J (2005) The importance of soil organic matter: key to drought-resistant soil and sustained food production (No. 80). Food & Agriculture Organization of the United Nations Rome, pp 1–59
18. Van Dang M (2007) Quantitative and qualitative soil quality assessments of tea enterprises in Northern Vietnam. Afr J Agric Res 2(9):455–462
19. Herridge DF, Peoples MB, Boddey RM (2008) Global inputs of biological nitrogen fixation in agricultural systems. Plant Soil 311(1–2):1–18
20. Johnston AE, Poulton PR, Coleman K (2009) Soil organic matter: its importance in sustainable agriculture and carbon dioxide fluxes. Adv Agron 101:1–57
21. Spiertz JHJ (2009) Nitrogen, sustainable agriculture and food security: a review. In: Sustainable agriculture. Springer, Dordrecht, pp 635–651
22. Sharma SK, Ramesh A, Sharma MP, Joshi OP, Govaerts B, Steenwerth KL, Karlen DL (2010) Microbial community structure and diversity as indicators for evaluating soil quality. In: Biodiversity, biofuels, agroforestry and conservation agriculture. Springer, Dordrecht, pp 317–358
23. Baruah BK, Das B, Medhi C, Misra AK (2013) Fertility status of soil in the tea garden belts of golaghat district, Assam, India. J Chem 2013:1–6
24. Kekane SS, Chavan RP, Shinde DN, Patil CL, Sagar SS (2015) A review on physico-chemical properties of soil. Int J Chem Stud 3(4):29–32
25. Karlen DL, Mausbach MJ, Doran JW, Cline RG, Harris RF, Schuman GE (1997) Soil quality: a concept, definition, and framework for evaluation (a guest editorial). Soil Sci Soc Am J 61(1):4–10

26. Marinari S, Mancinelli R, Campiglia E, Grego S (2006) Chemical and biological indicators of soil quality in organic and conventional farming systems in Central Italy. Ecol Ind 6(4):701–711
27. Vasconcellos RDF, Bonfim JA, Andreote FD, Mendes LW, Baretta D, Cardoso EJBN (2013) Microbiological indicators of soil quality in a riparian forest recovery gradient. Ecol Eng 53:313–320
28. Vasconcellos RL, Bonfim JA, Baretta D, Cardoso EJ (2016) Arbuscular mycorrhizal fungi and glomalin-related soil protein as potential indicators of soil quality in a recuperation gradient of the Atlantic forest in Brazil. Land Degrad Dev 27(2):325–334
29. Dourado-Neto D, Teruel DA, Reichardt K, Nielsen DR, Frizzone JA, Bacchi OOS (1998) Principles of crop modelling and simulation: II. The implications of the objective in model development. Scientia Agricola 55(spe):51–57
30. Sihag J, Prakash D (2019) A review: importance of various modeling techniques in agriculture/crop production. Soft Comput Theor Appl 699–707
31. Sihag J, Prakash D, Yadav P (2020) Evaluation of soil physical, chemical parameter and enzyme activities as indicator of soil fertility with SFM model in IA–AW zone of Rajasthan. In: Soft computing: theories and applications, vol 1154. Springer, Singapore, pp 1107–1121 (2020)
32. Sihag J, Prakash D, Gupta H (2020) Soil fertilization status assessment for IC-HAPI Zone of Rajasthan with SFM computational model. In: Pant M, Sharma T, Verma O, Singla R, Sikander A (eds) Soft computing: theories and applications. Advances in intelligent systems and computing, vol 1053. Springer, Singapore, pp 1425–1439
33. Bishnoi RR, Brar SPS (1988) A handbook of soil testing. Punjab Agricultural University, Ludhiana, India
34. Mathur GM (2001) Status availability and transformation of zinc in irrigated north west plain soils of Rajasthan (SKNAU). PhD, Doctoral dissertation, SKNAU)
35. Piper CS (1950) Soil and plant analysis. Adelaide University (1950)
36. Walkley A, Black IA (1934) An examination of the Degtjariff method for determining soil organic matter and a proposed modification of the chromic acid titration method. Soil Sci 37:29–38
37. Kahle P, Beuch S, Boelcke B, Leinweber P, Schulten HR (2001) Cropping of miscanthus in central Europe: biomass production and influence on nutrients and soil organic matter. Eur J Agron 15(3):171–184
38. Subbiah BV, Asija GL (1956) A rapid procedure for the determination of available nitrogen in soils. Curr Sci 25:259–260
39. Olsen SR (1954) Estimation of available phosphorus in soils by extraction with sodium bicarbonate (no 939). US Department of Agriculture
40. Black CA (1965) Methods of soil analysis, part 2. American Society of Agronomy, Madison, WI, USA
41. Williams CH, Steinbergs A (1959) Soil sulfur fractions as chemical indices of available sulfur in some Australian soils. Aust J Agric Res 10(3):340–352
42. Lindsay WL, Norvell WA (1978) Development of a DTPA soil test for zinc, iron, manganese, and copper. Soil Sci Soc Am J 42(3):421–428
43. Behera PK (2006) Soil and solid waste analysis: a laboratory manual. Dominant Publishers and Distributors
44. Puri AN (1930) A new method of estimating total carbonates in soils. Government of India Central Publication Branch
45. Tabatabai MA (1982) Soil enzymes. In: Page AL (ed) Methods of soil analysis. Part 2: chemical and microbiological properties, 2nd ed. American Society of Agronomy, Madison, Wisconsin, USA, pp 903–947
46. Tabatabai MA, Bremner JM (1969) Use of p-nitrophenyl phosphate for assay of soil phosphatase activity. Soil Biol Biochem 1(4):301–307
47. McGarity JW, Myers MG (1967) A survey of urease activity in soils of northern New South Wales. Plant Soil 217–238
48. Schnürer J, Rosswall T (1982) Fluorescein diacetate hydrolysis as a measure of total microbial activity in soil and litter. Appl Environ Microbiol 43(6):1256–1261

49. Kannan MN, Sethi S, Badoni A, Chamoli V, Bahuguna NC (2018) Isolation and characterization of bacterial isolates from agriculture field soil of Roorkee region. J Pharmacognosy Phytochem SP5:108–110
50. Jasuja ND, Saxena R, Joshi SC (2013) Isolation and identification of microorganism from polyhouse agriculture soil of Rajasthan. Afr J Microbiol Res 7(41):4886–4891
51. Chitra B, Harshab P, Sadhana G, Soni R (2014) Isolation characteriazation of bacterial isolates from agricultural soil at durg district. Indian J Sci Res 4(1):221–226
52. Waksman SA (1927) Principle of soil microbial. Williams & Wilkins Co. Baltimore, Md, pp 1–65
53. Raja M, Praveena G, William SJ (2017) Isolation and identification of fungi from soil in Loyola college campus, Chennai, India. Int J Curr Microbiol App Sci 6(2):1789–1795
54. Brookes PC, Kragt JF, Powlson DS, Jenkinson DS (1985) Chloroform fumigation and the release of soil nitrogen: the effects of fumigation time and temperature. Soil Biol Biochem 17(6):831–835
55. Rahul C, Kumawat BL, Ajeet S, Sharma DK (2014) Evaluation of underground irrigation water quality and its associated effects on irrigated soils of Sri Madhopur Panchayat Samiti of district Sikar (Rajasthan). Ann Agri Bio Res 19(2):268–275
56. Sanwal RC, Yogesh S, Reager ML, Tak SR (2014) Available zinc and manganese status and their relationship with soil physico-chemical properties and its content in wheat crop of internal drainage dry zone of Rajasthan. Int J Agric Sci 10(2):685–690
57. Kameriya PR (1995) Characterization of soils of agro-climatic zone of transitional plains of inland drainage (Zone IIA) of Rajasthan. J Indian Soc Soil Sci 42:100–101
58. Gupta JP (1986) Moisture and thermal regimes of the desert soils of Rajasthan, India, and their management for higher plant production. Hydrol Sci J 31(3):347–359
59. Kumar M, Babel AL (2011) Available micronutrient status and their relationship with soil properties of Jhunjhunu tehsil, District Jhunjhunu, Rajasthan, India. J Agric Sci (Toronto) 3(2):97–106
60. Sharma RP, Singh M, Sharma JP (2003) Correlation studies on micronutrients vis-à-vis soil properties in some soils of Nagaur district in semi-arid region of Rajasthan. J Indian Soc Soil Sci 51(4):522–527
61. Verma N, Tarafdar JC, Srivastava KK, Sharma B (2016) Correlation of soil physico-chemical factors with AM fungal diversity in *Ailanthus excelsa* Roxb. under different agroecological zones of Western Rajasthan. Int J Life Sci Sci Res 2(4)
62. Seth SP, Mehta KN (1963) Fertility survey and soil test summaries of some districts of arid region of Rajasthan. Ann Arid Zone 11(1):61–68
63. Verma N, Tarafdar JC, Srivastava KK, Sharma B (2016) Arbuscular mycorrhizal (AM) diversity in *Acacia nilotica* subsp. indica (Benth.) Brenan under arid agroecosystems of western Rajasthan. Int J Adv Res Biol Sci 3(3):134–143
64. Kononova MM (1961) Soil organic matter, its nature, its role in soil formation and in soil fertility. Soil organic matter, its nature, its role in soil formation and in soil fertility
65. Hodges SC, Crozier C (1996) Soil fertility basics. North Carolina State University, Soil science extension
66. Muhr GR, Datta NP, Shankar Subramany N, Dever F, Lecy VK, Donahue RR (1965) Soil testing in India. USDA Publication, p 120
67. Kumar M, Raina P, Sharma BK (2011) Soil fertility appraisal under dominant land use systems in north-eastern part of arid Rajasthan. Ann Arid Zone 50(1):11–15
68. Etesami H, Emami S, Alikhani HA (2017) Potassium solubilizing bacteria (KSB): Mechanisms, promotion of plant growth, and future prospects a review. J Soil Sci Plant Nutr 17(4):897–911
69. Food and Agriculture Organization of the United Nations (FAO) (1973) FAO Soils Bulletin 21. Calcareous Soils. FAO, Rome
70. Balota EL, Chaves JCD (2010) Enzymatic activity and mineralization of carbon and nitrogen in soil cultivated with coffee and green manures. Rev Bras Ciênc Solo 34(5):1573–1583
71. Mathur N, Singh J, Bohra S, Vyas A (2007) Arbuscular mycorrhizal status of medicinal halophytes. Int J Soil Sci 2(2):119–127

72. Singh B (2005) Appraisal of fertility, salinity and alkalinity indices of soils in relation to under ground water of Degana tehsil of Nagaur district (Rajasthan). M.Sc. (Ag.) Thesis, Rajasthan Agricultural University, Bikaner
73. Joshi DC (1984) Micronutrient status of soils for developing agro-forestry in arid regions. In: Shankarnarayan KA (ed) Agroforestry in aid and semi arid zones. Central Arid Zone Research Institute, Jodhpur, pp 35–38 (1984)